

# Identifying Isoprene and Toluene Gas-Phase Oxidation Products to Better Constrain Ozone and Secondary Organic Aerosol Formation in the Atmosphere

Thesis by  
Rebecca Helen Schwantes

In Partial Fulfillment of the Requirements for the  
degree of  
Doctor of Philosophy



CALIFORNIA INSTITUTE OF TECHNOLOGY  
Pasadena, California

2017  
Defended October 11, 2016

© 2017

Rebecca Helen Schwantes  
ORCID: 0000-0002-7095-3718

All rights reserved



## ACKNOWLEDGEMENTS

First I would like to thank my PhD advisers John Seinfeld and Paul Wennberg. I appreciate all the opportunities and invaluable guidance both of you have given me during my time at Caltech. I was very fortunate to be able to work so closely with both of you. John, thank you for patiently providing me advice and support throughout my entire PhD. Your style of mentoring has helped me become an independent scientist such that I feel ready to pursue my own research interests. Paul thank you for helping me understand atmospheric chemistry. Your willingness to help me discover the chemical details of all my projects has helped improve my work and made me a better scientist. I would also like to thank Rick Flagan for providing very detailed assistance and guidance with the Differential Mobility Analyzer. Also I would like to thank Mitchio Okumura for being the chair of my committee.

So many fellow students, post doctoral scientists, and staff scientists have helped me throughout my time at Caltech. I truly appreciate all the support I have been given. Specifically, I thank Lindsay Yee for being my first mentor at Caltech and for teaching me how to use the Chemical Ionization Mass Spectrometer (CIMS). I also thank John Crounse and Jason St. Clair for always being available to give me guidance with CIMS data analysis and maintenance. The Chamber CIMS would not be working as well without you both.

I also appreciate Christine Loza for sharing with me all of her immense knowledge about running the atmospheric chamber facility. I thank Tran Nguyen for consistently giving me advice on science and my future. I wholeheartedly appreciate all the fun and interesting collaborations I had with all the core Seinfeld group members (Kelvin Bates, Jill Craven, Matt Coggon, Christine Loza, Rennee McVay, Tran Nguyen, Kate Schilling, Lindsay Yee, and Xuan Zhang). I will miss working with all of you, and I hope we will continue to keep in touch and perhaps work together again. Additionally, I thank all the students in the Wennberg lab with whom I have collaborated. I will miss our lunch and social hour discussions. I wish the best of luck to the new group of students taking over the chamber lab. I have enjoyed working with you over the last year.

Lastly, I thank my boyfriend, friends, and family for their support throughout my entire PhD. I know there were times when I was consistently late to everything

because of experiments and temperamental instruments. I really appreciate all of your understanding and patience with me. I want to also thank everyone who took the time to venture into the mountains with me to go on hikes, camping trips, and trail runs. All these trips were immensely important for maintaining my happiness, optimism, and sanity at Caltech.

## ABSTRACT

Anthropogenic pollutants such as  $\text{NO}_x$  interact with volatile organic compounds (VOCs) such as isoprene and toluene to produce ozone ( $\text{O}_3$ ) and oxidized low volatility compounds that are responsible for forming secondary organic aerosol (SOA). Understanding the processes that form  $\text{O}_3$  and SOA from VOCs is important for understanding climate interactions and air quality. Both  $\text{O}_3$  and SOA are harmful air pollutants.  $\text{O}_3$  directly contributes to warming while the influence of aerosols is far more complicated, but ultimately leads to regional cooling. Understanding the chemistry that produces  $\text{O}_3$  and SOA will help better predict how future regulations will influence climate and air quality. A series of experiments using the Caltech chamber facility were designed and performed to better understand the influence of isoprene and toluene gas-phase oxidation products on  $\text{O}_3$  and SOA formation.

First, in order to conduct experiments, the new Caltech chamber facility was characterized. Second, to understand the oxidation products from isoprene in the presence of anthropogenic pollutants such as  $\text{NO}_x$ , a chemical ionization mass spectrometer (CIMS) was used to identify the gas-phase products from the oxidation of isoprene by the nitrate radical ( $\text{NO}_3$ ). First-generation nitrates were identified to be predominantly  $\delta$ -nitrates while first-generation nitrates formed from OH oxidation of isoprene in the presence of NO are predominantly  $\beta$ -nitrates. This has important consequences for  $\text{NO}_x$  recycling and  $\text{O}_3$  generation because these  $\beta$ - and  $\delta$ -nitrates react with  $\text{O}_3$  and OH at different rates and form different products. Photooxidation products from nitrooxy hydroperoxide, a product from isoprene +  $\text{NO}_3$  oxidation (in the presence of hydroperoxy radical- $\text{HO}_2$ ), were identified to be predominantly propanone nitrate and nitrooxy hydroxy epoxide. Nitrooxy hydroxy epoxide undergoes reactive uptake to seed aerosol similar to isoprene dihydroxy epoxide, suggesting it may be important for SOA formation.

Lastly, first- and later-generation photooxidation products from cresol and benzaldehyde oxidation were identified. Cresol and benzaldehyde are products from toluene OH oxidation. Low volatility ring-retaining products produced from cresol oxidation were detected in the gas phase by the CIMS and in the particle phase using offline direct analysis in real time mass spectrometry (DART-MS). Products detected included polyols such as dihydroxy, trihydroxy, tetrahydroxy, and pentahydroxy toluenes and benzoquinones such as hydroxy, dihydroxy, and trihydroxy methyl benzoquinones. These results suggest that even though the cresol pathway

only contributes  $\sim 20\%$  to gas-phase toluene oxidation, products from the cresol channel potentially generate a significant fraction ( $\sim 20\text{--}40\%$ ) of toluene SOA.

## PUBLISHED CONTENT AND CONTRIBUTIONS

Nguyen, T. B. et al. (2014). “Overview of the Focused Isoprene eXperiment at the California Institute of Technology (FIXCIT): Mechanistic Chamber Studies on the Oxidation of Biogenic Compounds”. In: *Atmos. Chem. Phys.* 14, pp. 13531–13549. DOI: 10.5194/acp-14-13531-2014.

RHS participated in the design of experiments, preparation of the Caltech chamber facility, and implementation of experiments for the FIX-IT field campaign.

Schwantes, R. H., R. C. McVay, et al. (2016). “Science of the Environmental Chamber (In Review)”. In: *Advances in Atmospheric Chemistry*. Singapore: World Scientific Publishing. Chap. 1, pp. 1–92.

RHS designed and performed experiments associated with characterizing the atmospheric chamber, analyzed data, and participated with writing the paper.

Schwantes, R. H., K. A. Schilling, et al. (2016). “Formation of Highly Oxygenated Low-Volatility Products from Cresol Oxidation”. In: *Atmos. Chem. Phys. Disc.* DOI: 10.5194/acp-2016-887.

RHS designed and performed experiments, analyzed data, and wrote the paper.

Schwantes, R. H., A. P. Teng, et al. (2015). “Isoprene NO<sub>3</sub> Oxidation Products from the RO<sub>2</sub> + HO<sub>2</sub> Pathway”. In: *J. Phys. Chem. A*. 119,40, pp. 10158–10171. DOI: 10.1021/acs.jpca.5b06355.

RHS designed and performed experiments, analyzed data, and wrote the paper.

Zhang, X., R. H. Schwantes, M. M. Coggon, et al. (2014). “Role of Ozone in SOA Formation from Alkane Photooxidation”. In: *Atmos. Chem. Phys.* 14, pp. 1733–1753. DOI: 10.5194/acp-14-1733-2014.

RHS operated the chemical ionization mass spectrometer used in these experiments and participated in data analysis.

Zhang, X., R. H. Schwantes, R. C. McVay, et al. (2015). “Vapor Wall Deposition in Teflon Chambers”. In: *Atmos. Chem. Phys.* 15, pp. 4197–4214. DOI: 10.5194/acp-15-4197-2015.

RHS operated the chemical ionization mass spectrometer used in these experiments and participated in data analysis.

## TABLE OF CONTENTS

|   |      |
|---|------|
| Acknowledgements . . . . .  | iii  |
| Abstract . . . . .  | v    |
| Published Content and Contributions . . . . .   | vii  |
| Table of Contents . . . . .   | viii |
| List of Illustrations . . . . .   | x    |
| List of Tables . . . . .  | xv   |
| Chapter I: Introduction . . . . .   | 1    |
| Chapter II: Science of the Environmental Chamber . . . . .  | 9    |
| 2.1 Introduction . . . . .  | 9    |
| 2.2 Reactor Type . . . . .  | 9    |
| 2.3 Characterization of the Environmental Chamber . . . . .   | 11   |
| 2.4 Chemical Environment in the Chamber . . . . .   | 22   |
| 2.5 Secondary Organic Aerosol (SOA) Formation . . . . .   | 37   |
| 2.6 Particle Deposition onto Chamber Walls . . . . .  | 40   |
| 2.7 Vapor Deposition on Chamber Walls . . . . .   | 49   |
| 2.8 The Continuously Mixed Flow Reactor (CMFR) . . . . .  | 55   |
| 2.9 The Flow Tube Reactor . . . . .   | 66   |
| 2.10 Time Scales and Regimes of Behavior for Chamber Processes . . . . .  | 77   |
| Chapter III: Isoprene NO <sub>3</sub> Oxidation Products from the RO <sub>2</sub> + HO <sub>2</sub> Pathway . . . . .   | 84   |
| 3.1 Abstract . . . . .  | 84   |
| 3.2 Introduction . . . . .  | 84   |
| 3.3 Experimental Methods . . . . .  | 86   |
| 3.4 Results . . . . .   | 91   |
| 3.5 Discussion . . . . .  | 98   |
| 3.6 Atmospheric Relevance . . . . .   | 110  |
| 3.7 Conclusions . . . . .   | 111  |
| 3.8 Acknowledgments . . . . .   | 112  |
| 3.9 Supporting Information . . . . .  | 112  |
| Chapter IV: Formation of Highly Oxygenated Low-Volatility Products from<br>Cresol Oxidation . . . . .   | 154  |
| 4.1 Abstract . . . . .  | 154  |
| 4.2 Introduction . . . . .  | 154  |
| 4.3 Methods . . . . .   | 157  |
| 4.4 Results . . . . .   | 170  |
| 4.5 Discussion . . . . .  | 183  |
| 4.6 Supporting Information . . . . .  | 193  |
| Chapter V: Conclusions and Future Work . . . . .  | 229  |
| Appendix A: CIMS Sensitivities and Reactions Included in the Kinetic Mechanism<br>Developed to Better Understand Isoprene NO <sub>3</sub> Oxidation . . . . . | 232  |

|  |     |
|--|-----|
| Appendix B: Overview of the Focused Isoprene eXperiment at the California<br>Institute of Technology (FIXCIT): mechanistic chamber studies on the<br>oxidation of biogenic compounds . . . . . | 264 |
| Appendix C: Vapor wall deposition in Teflon chambers . . . . .   | 284 |
| Appendix D: Role of ozone in SOA formation from alkane photooxidation . .  | 309 |

## LIST OF ILLUSTRATIONS

| <i>Number</i>   | <i>Page</i> |
|---|-------------|
| 2.1 Spectral actinic flux versus wavelength for blacklights in the Caltech chamber facility. . . . .  | 15          |
| 2.2 Chamber mixing time for Caltech chamber . . . . .   | 17          |
| 2.3 Ozone and ammonium sulfate concentrations during flushing of the two Caltech chambers (near and far). . . . .   | 18          |
| 2.4 Ozone, NO, and NO <sub>2</sub> concentrations, particle number concentration, and particle volume formation during a blank photooxidation experiment with clean injection air. . . . .  | 20          |
| 2.5 Formation of ozone, NO, and NO <sub>2</sub> during blank experiment with added hydrogen peroxide. . . . .   | 20          |
| 2.6 Aerosol Mass Spectrometer measurements during a blank photooxidation experiment with clean air. . . . .   | 22          |
| 2.7 Reactions of the peroxy radicals generated by OH oxidation of <i>n</i> -hexane. . . . .   | 25          |
| 2.8 Fate of the RO <sub>2</sub> radical as a function of the initial mixing ratio of NO <sub>x</sub> at different times in <i>n</i> -hexane photooxidation for a system of 50 ppb initial <i>n</i> -hexane and 1000 ppb initial hydrogen peroxide. . . . .  | 26          |
| 2.9 Fate of the RO <sub>2</sub> radical as a function of the initial mixing ratio of NO <sub>x</sub> at different times in <i>n</i> -hexane photooxidation with 50 ppb initial <i>n</i> -hexane and 10 ppb initial hydrogen peroxide. . . . .   | 27          |
| 2.10 Fate of the RO <sub>2</sub> radical as a function of [VOC] <sub>o</sub> /[NO <sub>x</sub> ] <sub>o</sub> (after 4 h of reaction) in experiments starting with variable <i>n</i> -hexane and [NO <sub>x</sub> ] <sub>o</sub> concentrations each with 10 ppb of H <sub>2</sub> O <sub>2</sub> . . . . .   | 28          |
| 2.11 Fate of the RO <sub>2</sub> radical as a function of [VOC] <sub>o</sub> /[NO <sub>x</sub> ] <sub>o</sub> (after 4 h of reaction) in experiments starting with variable <i>n</i> -hexane and [NO <sub>x</sub> ] <sub>o</sub> concentrations each with 1000 ppb of H <sub>2</sub> O <sub>2</sub> . . . . . | 29          |
| 2.12 Fate of the RO <sub>2</sub> radical as a function of [ <i>n</i> -hexane] <sub>o</sub> /[NO <sub>x</sub> ] <sub>o</sub> at [H <sub>2</sub> O <sub>2</sub> ] <sub>o</sub> /[ <i>n</i> -hexane] <sub>o</sub> = 20 after 4 h of reaction. . . . .  | 30          |
| 2.13 Fate of the RO <sub>2</sub> radical as a function of [VOC] <sub>o</sub> /[NO <sub>x</sub> ] <sub>o</sub> at [H <sub>2</sub> O <sub>2</sub> ] <sub>o</sub> /[VOC] <sub>o</sub> = 0.2 after 4 h of reaction. . . . .   | 31          |
| 2.14 Temporal profile of the fate of the RO <sub>2</sub> radical for a system with 500 ppb <i>n</i> -hexane and 10 ppb CH <sub>3</sub> ONO. . . . .   | 32          |



|      |  |     |
|------|--|-----|
| 2.15 | Temporal profiles of particle number distribution as a result of particle wall deposition. . . . .   | 40  |
| 2.16 | Determination of the particle-wall deposition rate constant. . . . .   | 41  |
| 2.17 | SOA yield (expressed as the total organic aerosol mass formed, $\Delta M_o$ , vs. the total hydrocarbon mass reacted, $\Delta HC$ ) from the photooxidation of toluene under low-NO conditions . . . . .   | 47  |
| 2.18 | Computed temporal profiles of semivolatile organic compound $i$ in the gas phase ( $C_{g,i}$ ) and on the chamber wall ( $C_{w,i}$ ) during 10-h vapor-wall interaction. . . . .   | 52  |
| 2.19 | Evolution of the parent VOC (species A) and two progressive oxidation products (species B and C) in the gas phase (top panel), aerosol phase (middle panel), and wall phase (bottom panel). . . . .  | 62  |
| 2.20 | Comparison of the performance between a batch chamber and a CMFR in SOA formation. . . . .   | 63  |
| 2.21 | Flow tube reactor designs. . . . .   | 68  |
| 2.22 | Cooling jacket arrangements typically used to control the temperature within a flow tube reactor. . . . .  | 71  |
| 2.23 | Inlet designs used by (A) the Potential Aerosol Mass reactor (PAM) (B) the UC Irvine flow tube and (C) the Caltech flow tube. . . . .  | 74  |
| 2.24 | UV-visible transmission spectra of glass flow tube materials (Quartz and Pyrex, dotted lines), and cooling liquid (50/50 mix of ethylene glycol/water, solid line) . . . . .   | 76  |
| 3.1  | Isoprene reactant partner distribution and nitrooxy alkylperoxy ( $INO_2$ ) radical reactant partner distribution. . . . .   | 90  |
| 3.2  | Diagram of the main products formed from $NO_3$ oxidation of isoprene. . . . .   | 92  |
| 3.3  | Photooxidation products (e.g., $C_5$ nitrooxy hydroxyepoxide (INHE)) of the dominant $\beta$ - and $\delta$ - $C_5$ nitrooxy hydroperoxide (INP). . . . .  | 93  |
| 3.4  | Major nitrates detected by the CIMS and predicted by the kinetic mechanism . . . . .   | 94  |
| 3.5  | GC-ToF-CIMS data (markers) and kinetic mechanism results (lines) for $\delta$ - and $\beta$ -isomers of INP and INHE. . . . .  | 106 |
| 3.6  | Experimental results (markers, 1 min averages) and kinetic mechanism results (lines) for propanone nitrate (red), ethanal nitrate (cyan), $C_4$ carbonyl hydroxynitrate (blue), and $C_4$ carbonyl hydroperoxynitrate (magenta) from experiment 8. . . . . | 107 |

|      |   |     |
|------|---|-----|
| 3.7  | The dominant decomposition products from the reaction of INP, IHN, and ICN with OH. . . . .   | 108 |
| 3.8  | C <sub>5</sub> nitrooxy hydroperoxide + C <sub>5</sub> nitrooxy hydroxyepoxide + C <sub>5</sub> dihydroxy nitrate; C <sub>5</sub> carbonyl nitrate (ICN); C <sub>5</sub> hydroxy nitrate (IHN); and primary decomposition products for several weeks during the SOAS 2013 field campaign. . . . . | 111 |
| 3.9  | OH oxidation of Isoprene nitrates . . . . .   | 118 |
| 3.10 | Possible H-shifts from OH oxidation of ICN. . . . .   | 120 |
| 3.11 | GC-ToF-CIMS chromatographs for experiment 8 as a function of time following the initiation of the photochemistry . . . . .  | 123 |
| 3.12 | Main products proposed for the 1,5-H-shift of (a) <i>trans</i> -1,4-INO, and (b) <i>cis</i> -1,4-INO . . . . .  | 135 |
| 3.13 | GC-ToF-CIMS chromatographs for C <sub>5</sub> hydroxy carbonyl nitrate, C <sub>5</sub> dihydroxy nitrate/ $\delta$ -INHE, and C <sub>5</sub> hydroxy hydroperoxy nitrate . . .  | 135 |
| 3.14 | Main products formed from the 1,6-H-shift of <i>trans</i> -1,4-INO <sub>2</sub> . . . . .   | 136 |
| 3.15 | (a) INHE gas phase loss detected by CIMS and (b) total organic mass growth detected by the AMS. . . . .   | 138 |
| 3.16 | (a) AMS spectrum (percent of total organic) for hydrated MgSO <sub>4</sub> ·H <sub>2</sub> SO <sub>4</sub> (1:1) seed at peak growth. (b) AMS fragments (percent of total organic) proposed to be tracers for IEPOX . . . . .   | 139 |
| 3.17 | AMS difference spectrum (percent of total organic) between hydrated MgSO <sub>4</sub> ·H <sub>2</sub> SO <sub>4</sub> (1:1) and hydrated (NH <sub>4</sub> ) <sub>2</sub> SO <sub>4</sub> seed. . . . .  | 140 |
| 3.18 | Proposed products of $\beta$ -[4,1]-INHE that form in the particle phase under hydrated acidic conditions. . . . .  | 140 |
| 3.19 | Change in N:C and O:C ratios for hydrated (NH <sub>4</sub> ) <sub>2</sub> SO <sub>4</sub> seeds (circles), hydrated MgSO <sub>4</sub> + H <sub>2</sub> SO <sub>4</sub> seeds (squares), and dry (NH <sub>4</sub> ) <sub>2</sub> SO <sub>4</sub> seeds (triangles). . . . .                        | 143 |
| 4.1  | Toluene photooxidation pathways as exemplified by the Master Chemical Mechanism (MCM) v3.3.1 including cresol isomer distribution. .  | 156 |
| 4.2  | Kinetic model predictions (Version 1 solid lines) compared to CIMS measurements (markers) under low-NO (a, experiment 4) and high-NO (b, experiment 3) oxidation of toluene for cresol (red) and dihydroxy toluene (blue). . . . .  | 171 |
| 4.3  | Gas-phase chemical mechanism for <i>o</i> -cresol photooxidation under low-NO conditions. . . . .   | 172 |

|      |  |     |
|------|--|-----|
| 4.4  | Gas-phase chemical mechanism for <i>o</i> -cresol photooxidation under high-NO conditions. . . . .   | 173 |
| 4.5  | Proposed decomposition pathways for bicyclic intermediate compounds formed from OH oxidation of <i>o</i> -cresol and 3-methyl catechol. . . . .  | 176 |
| 4.6  | Proposed decomposition pathways for bicyclic intermediate compounds formed from OH oxidation of trihydroxytoluene and tetrahydroxytoluene. . . . .   | 177 |
| 4.7  | Gas-phase chemical mechanism for benzaldehyde photooxidation under low- and high-NO conditions. . . . .  | 178 |
| 4.8  | Particle-phase products detected by DART-MS during oxidation of toluene under low-NO conditions (a, experiment 13) and high-NO conditions (b, experiment 14) . . . . .   | 181 |
| 4.9  | CIMS signals for trihydroxy toluene (panel a) and the following compounds (panel b): 3-methyl catechol (blue), hydroxy methyl benzoquinone (red), dihydroxy methyl benzoquinone (black), and tetrahydroxy toluene (cyan) during experiment 9. . . . .  | 185 |
| 4.10 | Kinetic model predictions (Version 1 solid lines, Version 2 dashed lines, Version 3 dotted lines) versus CIMS measurements (markers) for <i>o</i> -cresol oxidation under low-NO (a) and high-NO (b) conditions and 3-methyl catechol oxidation under low-NO (c) and high-NO (d) conditions. . . . . | 190 |
| 4.11 | CIMS MS signals of 3-methyl catechol oxidation products (panel a) and MS/MS signals of tetrahydroxy toluene (panel b) for experiment 10. . . . .   | 193 |
| 4.12 | CIMS measurements (markers) compared to predictions from version 1 of kinetic model (lines) for benzaldehyde low-NO oxidation . . . . .  | 201 |
| 4.13 | CIMS measurements (markers) compared to predictions from the kinetic model (solid lines version 1 and dotted lines version 3) for benzaldehyde oxidation under high-NO conditions . . . . .  | 202 |
| 4.14 | CIMS measurements (markers) compared to predictions from version 3 of the kinetic model (lines) for 3-methyl catechol oxidation under low-NO conditions . . . . .  | 203 |
| 4.15 | Linear fit to natural log of wall deposition rate constant versus natural log of $C^*$ used to estimate wall deposition of compounds that cannot be directly measured. . . . .   | 205 |

- 4.16 Epoxide pathway oxidation mechanism under both low- and high-NO conditions as recommended by MCM v3.3.1 . . . . . 223
- 4.17 Products detected by DART-MS in the particle phase during oxidation of *o*-cresol under high NO conditions (experiment 15) with boxes identifying the following types of compounds: polyols (black), methyl benzoquinone type compounds (magenta), decomposition products from the bicyclic intermediate pathway (cyan), products with more than 7 carbons (gold), and nitro compounds (green). . . . 224

## LIST OF TABLES

| <i>Number</i>  | <i>Page</i> |
|--|-------------|
| 2.1 Environmental Chamber Characterization Tests. . . . .  | 11          |
| 2.2 Photolysis rate constants in Caltech Environmental Chamber . . . . .   | 14          |
| 2.3 Lifetimes of <i>n</i> -hexane peroxy radicals against reaction with NO, HO <sub>2</sub> ,<br>and RO <sub>2</sub> for various conditions of <i>n</i> -hexane oxidation by OH, as<br>calculated by MCM. Lifetimes are calculated at 4 h of photooxidation. | 33          |
| 2.4 Variables and Parameters Important in the Environmental Chamber . . . . .  | 48          |
| 2.5 Dynamic Continuously Mixed Flow Reactor (CMFR) Model . . . . .   | 58          |
| 2.6 CMFR Simulation Parameters. . . . .  | 60          |
| 3.1 List of isoprene NO <sub>3</sub> oxidation chamber experiments. . . . .  | 87          |
| 3.2 Molar yield per isoprene reacted for main products detected by the<br>CIMS during experiment 8 (at 2.5 h) compared to yields reported<br>previously. . . . .   | 95          |
| 3.3 Proposed isomer distribution for INP, ICN, and IHN including un-<br>certainties due to peak integration and CIMS sensitivity. . . . .  | 97          |
| 3.4 Isomer specific IHO <sub>2</sub> + IHO <sub>2</sub> rate constants compared to estimated<br>INO <sub>2</sub> + INO <sub>2</sub> rate constants. . . . .  | 101         |
| 3.5 Isomer dependent product distribution of INO <sub>2</sub> + HO <sub>2</sub> . . . . .  | 104         |
| 3.6 List of isomers assigned to each peak labeled in Figure 3.11. . . . .  | 124         |
| 3.7 Yields for products formed during experiments 3-5 and experiment 8.  | 128         |
| 4.1 Description of Experiments . . . . .   | 158         |
| 4.2 Fraction of CIMS signal detected from the transfer reaction, complex<br>formation, or fragmentation . . . . .  | 162         |
| 4.3 Estimated vapor pressures and saturation mass concentrations for<br>main products detected by CIMS from toluene oxidation . . . . .  | 164         |
| 4.4 Estimated CIMS sensitivity factors . . . . .   | 194         |
| 4.5 Water curve correction and sensitivity factors applied to each com-<br>pound of interest . . . . .   | 200         |
| 4.6 Reactions and reaction rate constants added to chemistry in MCM<br>v3.3.1 to test proposed chemistry. . . . .  | 206         |
| 4.7 Abbreviations used in Table 4.6 . . . . .  | 209         |
| 4.8 Chamber conditions based on kinetic model (Version 1) . . . . .  | 210         |
| 4.9 DART-MS data from low NO toluene oxidation (experiment 13). . . . .  | 213         |
| 4.10 DART-MS data from high NO <i>o</i> -cresol oxidation (experiment 15). . . . .   | 215         |

|      |   |     |
|------|---|-----|
| 4.11 | DART-MS data from high NO toluene oxidation (experiment 14). . .                                | 218 |
| A.1  | Sensitivities used in this study for the triple-CIMS (experiments 3-5)<br>and ToF-CIMS. . . . . | 233 |
| A.2  | List of the general reactions in the kinetic mechanism. . . . .                                 | 234 |
| A.3  | List of isoprene related reactions in the kinetic mechanism. . . . .                            | 239 |
| A.4  | List of photolysis reactions in the kinetic mechanism. . . . .                                  | 253 |
| A.5  | Full name of abbreviations used in the kinetic mechanism. . . . .                               | 257 |

*Chapter 1*

## INTRODUCTION

Volatile organic compounds (VOCs) are emitted into the atmosphere from both biogenic and anthropogenic processes. Once in the atmosphere, these VOCs are oxidized by the hydroxyl radical (OH), nitrate radical (NO<sub>3</sub>), or ozone (O<sub>3</sub>). In some cases oxidation leads to decomposition and in other cases oxidation leads to highly functionalized compounds. The exact chemical mechanism that occurs is important as it will influence both aerosol and ozone formation.

Aerosols are particles suspended in the gas-phase. There are two classifications of aerosols based on their formation: primary and secondary. Primary aerosol is directly emitted into the atmosphere and secondary aerosol is formed in the atmosphere by nucleation of gas-phase compounds or partitioning of gas-phase compounds to preexisting particles (Seinfeld et al., 2006). Particles are also classified by their chemical composition (e.g., organic, sulfate, and nitrate).

Aerosols have been shown to negatively impact human health by numerous studies (e.g.,(Dockery et al., 1993)), and aerosols influence climate directly by absorbing and scattering radiation and indirectly by impacting cloud formation. Globally, estimates suggest that aerosols have offset nearly 50% of warming caused by emissions of greenhouse gases (Raes et al., 2009). More specifically, secondary organic aerosol (SOA) formed from biogenic VOCs in the presence of anthropogenic pollutants cool the southeastern United States (Goldstein et al., 2009).

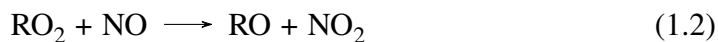
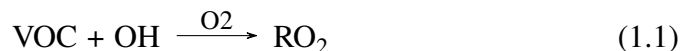
There are still large uncertainties in how aerosols impact the global radiative force and cloud formation (Stocker et al., 2013). In order to reduce these uncertainties better understanding of aerosol composition is needed. Organics comprise a large fraction (as much as 80-90%) of aerosol (Zhang et al., 2007; Murphy et al., 2006). Secondary organic aerosol formation is a complicated dynamic process where low-volatility gas-phase organics partition to the particle phase. Once in the particle phase, these low-volatility compounds potentially react with other compounds to form new products. These new products will be either lower in volatility (e.g., oligomers), enhancing the likelihood the carbon will remain in the particle phase or decomposition products, enhancing the likelihood the carbon will ultimately partition back to the gas phase. This study examines the process of SOA formation

from two systems (isoprene and toluene) with an emphasis on identifying gas-phase oxidation products monitored by a chemical ionization mass spectrometer that have the potential to form SOA. Once the process of SOA formation is better understood, the process can be accurately included and parameterized in large global chemistry models.

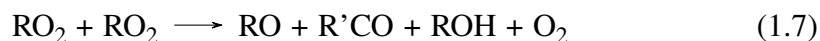
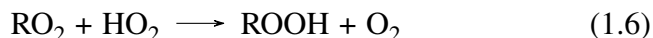
Toluene and isoprene oxidation are interesting systems to study for very different reasons. Isoprene is the dominant biogenic non-methane VOC emitted into the atmosphere. With such high emissions ( $\sim 470$  Tg C annually) (Guenther et al., 2012), even minor oxidation pathways of isoprene are relevant in the atmosphere. For example, isoprene has a relatively low SOA mass yield, but isoprene derived SOA is still projected by global chemical transport models to make up a large portion ( $\sim 30$ -80%) of total global SOA (Carlton et al., 2009, and references therein). In order to better predict how much isoprene derived SOA contributes to the total, better understanding of the chemical processes that occur during SOA formation are needed. Toluene is emitted in much lower quantities than isoprene into the atmosphere ( $\sim 7$  Tg C annually) (Henze et al., 2008). Because toluene is one of the dominant aromatic compounds emitted into the atmosphere, it is a good example system to better understand how aromatic oxidation occurs. Despite low emissions of aromatic compounds compared to isoprene emissions, around 10% of all SOA is derived from aromatics due to the high aromatic SOA mass yields (Henze et al., 2008).

Ozone ( $O_3$ ) is harmful to human health and crops. Ozone is a regulated pollutant and ozone standards have recently been strengthened by the U.S. EPA to protect human health (USEPA, 2015). Ozone is difficult to regulate because for the most part it is not directly emitted into the atmosphere. Instead, ozone is produced in the atmosphere when anthropogenic or biogenic VOCs interact with nitrogen oxides ( $NO_x$ ).  $NO_x$  is emitted from anthropogenic processes and natural processes such as lightning and soil. A peroxy radical forms when the hydroxyl radical (OH) adds to a double bond or abstracts a hydrogen from a volatile organic compound (VOC) with subsequent  $O_2$  addition (R1.1). This peroxy radical can react with nitric oxide (NO) to form an alkoxy radical and nitrogen dioxide ( $NO_2$ ) (R1.2) or an organic nitrate (R1.3) (Orlando et al., 2012). The yield of organic nitrates and the amount of  $NO_x$  recycling that occurs in sequential steps are both important for predicting  $O_3$  formation accurately.





Organic nitrates act as temporary reservoirs of  $\text{NO}_x$ . The fate of the organic nitrate will determine if it is a terminal sink (e.g., dry deposition), is a continued reservoir for  $\text{NO}_x$  (e.g., reaction with  $\text{OH}/\text{O}_3$  to form secondary organic nitrates), or releases  $\text{NO}_x$  back into the atmosphere (e.g., photolysis or reaction with  $\text{OH}$  to release  $\text{NO}_2$ ). Organic nitrates are also generated when the nitrate radical ( $\text{NO}_3$ ) reacts with a VOC.  $\text{NO}_3$  adds to a double bond on a VOC with subsequent  $\text{O}_2$  addition to form a peroxy radical (R1.5). In general, this peroxy radical will then react with  $\text{HO}_2$  (R1.6),  $\text{RO}_2$  (R1.7), or  $\text{NO}_3$  (R1.8) (Orlando et al., 2012):



where  $\text{ROOH}$  is a hydroperoxide,  $\text{RO}$  is an alkoxy radical,  $\text{R}'\text{CO}$  is an aldehyde or ketone, and  $\text{ROH}$  is an alcohol. The organic nitrate yield from  $\text{NO}_3$  oxidation is often much higher than that produced via the photooxidation pathway and will depend on the degree of fragmentation that occurs to release  $\text{NO}_2$ . In the atmosphere, due to the fast photolysis of  $\text{NO}_3$  during the day, typically  $\text{NO}_3$  oxidation produces organic nitrates at night and  $\text{OH}$  oxidation produces organic nitrates during the day.

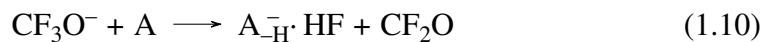
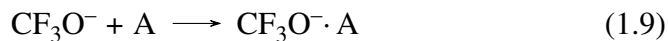
The yield of organic nitrates from either pathway  $\text{OH}/\text{NO}$  or  $\text{NO}_3$  oxidation varies depending on the parent hydrocarbon. Understanding the yield and fate of organic nitrates from the significant VOCs present in the atmosphere is important in order for global chemical transport models to simulate ozone accurately. If global chemical transport models simulate ozone correctly for the right reasons, these models can be used to better understand which regulations will best mitigate ozone formation in a specific region (e.g., reducing  $\text{NO}_x$  or reducing VOCs). Ozone production

from  $\text{NO}_x$  and VOCs is a complicated non-linear process. A study by Farmer et al. (2011) explains an example where decreasing certain VOC emissions without corresponding reductions in  $\text{NO}_x$  can actually increase ozone formation.

This work will be particularly useful in better simulating ozone in regions with low emissions of NO and high emissions of biogenic VOCs such as isoprene. In this regime, the ozone production efficiency is quite sensitive to the  $\text{NO}_x$  level and the  $\text{NO}_x$  level is sensitive to the formation and fate of the organic nitrates present in the atmosphere. As  $\text{NO}_x$  increases the ozone production efficiency also increases (Seinfeld et al., 2006). For example, F. Paulot et al. (2012) explored how isoprene oxidation chemistry impacts simulated tropical ozone formation in GEOS-Chem, a global chemical transport model. F. Paulot et al. (2012) determined that the fate of first- and later-generation organic nitrates derived from isoprene oxidation greatly impact tropical ozone formation. The formation and fate of later-generation isoprene derived organic nitrates are less understood than their first-generation counterparts, but are important for accurately understanding  $\text{NO}_x$  levels in the atmosphere. The present work begins to clarify some of this less understood later-generation isoprene chemistry.

There is a complicated mixture of VOCs and oxidants all interacting and reacting simultaneously in the atmosphere. Atmospheric chambers provide a clean, systematic, and controlled environment (e.g., consistent temperature, light flux, pressure, humidity) to investigate chemical processes occurring in the atmosphere. Atmospheric chambers are typically used in order to examine the chemistry of one VOC (e.g., isoprene) reacting with one oxidant (e.g.,  $\text{NO}_3$ ) proceeding down one pathway (e.e., optimizing  $\text{RO}_2 + \text{HO}_2$  reactions, R1.6). This simplification is important for explicitly determining reaction rate constants and products. Chapter 2 explains how such atmospheric chambers are characterized and used in order to explore the chemical processes occurring in the atmosphere. Chapters 3 and 4 describe examples of how laboratory chamber experiments are used to better understand how ozone and SOA are produced from  $\text{NO}_3$  oxidation of isoprene (Chapter 3) and how SOA is produced from OH oxidation of toluene (Chapter 4).

Integral to both Chapters 3 and 4, is correctly identifying functionalized gas-phase organic compounds. To do this, a chemical ionization mass spectrometer using the reagent gas  $\text{CF}_3\text{O}^-$  is utilized.  $\text{CF}_3\text{O}^-$  forms a complex with an analyte (A) (R1.9) or a transfer reaction (R1.10):



Acidic compounds are more likely to undergo a transfer reaction. The  $\text{CF}_3\text{O}^-$  CIMS used in this work is a custom-modified triple quadrupole mass analyzer (Varian, 1200) (St. Clair et al., 2010). This mass spectrometer is operated in two modes: MS mode, which scans through a selected range of masses or MS/MS mode, which selects one molecular “parent” ion in quadrupole 1, fragments the molecular ion to various “daughters” in quadrupole 2, and selects one of these daughters in quadrupole 3. The daughters that form from a parent molecular ion can be used to understand which functional groups (e.g., carboxylic acid, hydroperoxide) are present. MS/MS mode can also be used to separate out isobaric compounds (i.e., compounds with the same molecular mass) (St. Clair et al., 2010; Fabien Paulot et al., 2009a; Crounse et al., 2006).

Chapter 3 describes the identification of products suspected to be important for SOA formation from isoprene  $\text{NO}_3$  oxidation. More specifically, first generation organic nitrates produced from  $\text{NO}_3$  oxidation of isoprene are generated in the chamber.  $\text{NO}_3$  oxidation largely occurs at night. Traditionally, chamber experiments have focused on examining isoprene oxidation via  $\text{NO}_3$  or OH. However, in the atmosphere, the first generation organic nitrates produced at night become further oxidized at sunrise when OH radicals form. To simulate this in the atmospheric chamber, after  $\text{NO}_3$  oxidation products were generated, UV lights were turned to generate OH. A new potential precursor (nitrooxy hydroxy epoxide) for isoprene SOA that would form in the early hours of the morning was identified from these experiments.

Organic nitrate production from isoprene oxidation by  $\text{NO}_3$  is also discussed in Chapter 3. As stated above, the fate of the organic nitrates is important for understanding  $\text{NO}_x$  recycling and thereby  $\text{O}_3$  formation. In Chapter 3, the isomer distribution of organic nitrates formed from isoprene oxidation by  $\text{NO}_3$  was measured. This is important because the isoprene organic nitrate isomers have different fates in the atmosphere. For example, isoprene oxidation by OH forms mostly  $\beta$ -organic nitrates (Nguyen et al., 2014) and isoprene oxidation by  $\text{NO}_3$  forms mostly  $\delta$ -organic nitrates (~70-100% depending on the organic nitrate, Schwantes et al. (2015)).  $\beta$  and  $\delta$ -organic nitrates will react with oxidants such as OH and  $\text{O}_3$  at different reaction rate constants and to form different products. Photooxidation of the

organic nitrates produced from  $\text{NO}_3$  oxidation will produce more propanone nitrate than ethanal nitrate. Propanone nitrate has a longer lifetime in the atmosphere than ethanal nitrate (Muller et al., 2014). Because propanone nitrate is longer lived, a greater proportion will deposit removing  $\text{NO}_x$  from the atmosphere. Additionally, longer lived organic nitrates can transport  $\text{NO}_x$  to more rural and less polluted areas where the  $\text{O}_3$  formation potential is higher.

In Chapter 4, products important for SOA formation from toluene oxidation by OH under low and high- $\text{NO}$  conditions were identified. Toluene oxidation by OH produces the following first generation products: benzaldehyde, cresol, bicyclic intermediate products, and epoxide products. In Chapter 4, a simple and direct pathway for toluene SOA formation was determined from the cresol channel. Although the cresol channel is relatively minor in the gas phase ( $\sim 20\%$ ), based on the low-volatility products that form from the cresol pathway, it is estimated to contribute significantly ( $\sim 20\text{--}40\%$ ) to toluene SOA. Although this study only looks at toluene oxidation, the phenolic pathway of other aromatic compounds is also likely to be important for SOA formation.

Developing a comprehensive chemical mechanistic understanding for SOA formation is important. The entire gas-phase and particle-phase chemical mechanism for every VOC emitted into the atmosphere cannot be included into global models due to computational constraints. However, understanding the key chemical processes that lead to SOA formation is integral to developing accurate SOA parameterizations that can then be used in global chemical transport models. This work identifies key pathways important for SOA formation from isoprene and toluene. These SOA formation pathways can be extended to other compounds to better predict SOA formation in general.

## References

- Carlton, A. G., C. Wiedinmyer, and J. H. Kroll (2009). "A Review of Secondary Organic Aerosol (SOA) Formation from Isoprene". In: *Atmos. Chem. Phys.* 9, pp. 4987–5005.
- Crounse, John D. et al. (2006). "Measurement of Gas-Phase Hydroperoxides by Chemical Ionization Mass Spectrometry". In: *Anal. Chem.* 78, pp. 6726–6732.
- Dockery, D. W. et al. (1993). "An Association between Air Pollution and Mortality in Six U.S. Cities". In: *N Engl J Med* 329, pp. 1753–1759.
- Farmer, D. K. et al. (2011). "Impact of Organic Nitrates on Urban Ozone Production". In: *Atmos. Chem. Phys.* 11, pp. 4085–4094.

- Goldstein, A. H. et al. (2009). “Biogenic Carbon and Anthropogenic Pollutants Combine to Form a Cooling Haze over the Southeastern United States”. In: *P. Natl. Acad. Sci. USA* 106.22, pp. 8835–8840.
- Guenther, A. B. et al. (2012). “The Model of Emissions of Gases and Aerosols from Nature version 2.1 (MEGAN2.1): an extended and updated framework for modeling biogenic emissions”. In: *Geosci. Model. Dev.* 5, pp. 1471–1492. DOI: 10.5194/gmd-5-1471-2012.
- Henze, D. K. et al. (2008). “Global modeling of secondary organic aerosol formation from aromatic hydrocarbons: high- vs. low-yield pathways”. In: *Atmos. Chem. Phys.* 8, pp. 2405–2421.
- Muller, J. F., J. Peeters, and T. Stavrakou (2014). “Fast Photolysis of Carbonyl Nitrates from Isoprene”. In: *Atmos. Chem. Phys.* 14, pp. 2497–2508.
- Murphy, D. M. et al. (2006). “Single-particle mass spectrometry of tropospheric aerosol particles”. In: *J. Geophys. Res.* 111. DOI: 10.1029/2006JD007340.
- Nguyen, T. B. et al. (2014). “Overview of the Focused Isoprene eXperiment at the California Institute of Technology (FIXCIT): Mechanistic Chamber Studies on the Oxidation of Biogenic Compounds”. In: *Atmos. Chem. Phys.* 14, pp. 13531–13549. DOI: 10.5194/acp-14-13531-2014.
- Orlando, John J. and Geoffrey S. Tyndall (2012). “Laboratory Studies of Organic Peroxy Radical Chemistry: An Overview with Emphasis on Recent Issues of Atmospheric Significance”. In: *Chem. Soc. Rev.* 41.19, pp. 6294–317. DOI: 10.1039/c2cs35166h.
- Paulot, F., D. K. Henze, and P. O. Wennberg (2012). “Impact of the isoprene photochemical cascade on tropical ozone”. In: *Atmos. Chem. Phys.* 12, pp. 1307–1325. DOI: 10.5194/acp-12-1307-2012.
- Paulot, Fabien et al. (2009a). “Unexpected Epoxide Formation in the Gas-Phase Photooxidation of Isoprene”. In: *Science* 325, pp. 730–733. DOI: 10.1126/science.1172910.
- Raes, F. and J. H. Seinfeld (2009). “New Directions: Climate Change and Air Pollution Abatement: A bumpy Road”. In: *Atmos. Environ.* 43, pp. 5132–5133.
- Schwantes, R. H. et al. (2015). “Isoprene NO<sub>3</sub> Oxidation Products from the RO<sub>2</sub> + HO<sub>2</sub> Pathway”. In: *J. Phys. Chem. A* 119.40, pp. 10158–10171. DOI: 10.1021/acs.jpca.5b06355.
- Seinfeld, J. H. and S. N. Pandis (2006). *Atmospheric Chemistry and Physics*. Hoboken, New Jersey: John Wiley & Sons, Inc.
- St. Clair, Jason M. et al. (2010). “Chemical Ionization Tandem Mass Spectrometer for the in Situ Measurement of Methyl Hydrogen Peroxide”. In: *Rev. Sci. Instrum.* 81, pp. 094102–094102. DOI: 10.1063/1.3480552.

- Stocker, T.F. et al. (2013). *Technical Summary. In: Climate Change 2013: The Physical Science Basis. Contribution of Working Group I to the Fifth Assessment Report of the Intergovernmental Panel on Climate Change* [Stocker, T.F., D. Qin, G.-K. Plattner, M. Tignor, S.K. Allen, J. Boschung, A. Nauels, Y. Xia, V. Bex and P.M. Midgley (eds.)] Cambridge, United Kingdom and New York, NY, USA: Cambridge University Press.
- USEPA (2015). *National Ambient Air Quality Standards for Ozone: Final Rule*. Vol. 206, pp. 65292–65468.
- Zhang, Q. et al. (2007). “Ubiquity and dominance of oxygenated species in organic aerosols in anthropogenically-influenced Northern Hemisphere midlatitudes”. In: *Geophys. Res. Lett.* 34. DOI: 10.1029/2007GL029979.

## Chapter 2

### SCIENCE OF THE ENVIRONMENTAL CHAMBER

Schwantes, R. H. et al. (2016). “Science of the Environmental Chamber (In Review)”. In: *Advances in Atmospheric Chemistry*. Singapore: World Scientific Publishing. Chap. 1, pp. 1–92.

#### 2.1 Introduction

The environmental chamber is used to isolate atmospheric chemistry under well-controlled conditions. Both gas-phase chemistry and secondary organic aerosol (SOA) formation and growth are studied in such chambers. SOA is formed when volatile organic compounds (VOCs) undergo oxidation to form low volatility products that subsequently partition into the particle phase. Numerous environmental chambers have been constructed and are in use worldwide. The science underlying the environmental chamber can be divided into four parts: (1) design of the chamber; (2) characterization of the chamber; (3) execution of experiments; and (4) interpretation of the data. The purpose of this chapter is to discuss each of these aspects so as to elucidate the considerations in the use of an environmental chamber to perform studies of atmospheric chemistry and aerosol formation. A critical aspect of environmental chamber experiments is the suite of instrumentation used to characterize the gas and particle phases in the chamber. We will address the measurement of particle size distributions in chambers; a number of reviews of gas- and particle-phase chemical composition measurements exist, so we do not address these here.

#### 2.2 Reactor Type

Two broad types of environmental reactors are in common use. The first is simply a batch reactor, the contents of which are well mixed. This type of reactor is referred to as an *environmental chamber*. The second type is a tubular flow reactor into which reactants are introduced at one end and products are withdrawn at the other end, with reactions proceeding as the material flows down the tube. This type of reactor is referred to as a *flow tube reactor*.

There are two modes of operation of the environmental chamber: *batch* and *con-*

*tinuous*. In batch mode, the chamber is initially filled with specified gases (and perhaps particles). After time is allowed for reactants to become sufficiently mixed, reactions are initiated through the introduction of reactants or by radiation. The chamber walls can be flexible or fixed. Over the duration of an experiment, samples of chamber air containing both gases (and particles) are withdrawn for analysis. The duration of a batch mode experiment is ultimately limited by the volume of chamber air withdrawn for analysis over the course of an experiment and by the magnitude of the accumulated deposition of particles and gases to the walls of the chamber. In a flexible walled chamber, the chamber volume decreases as material is withdrawn for measurement. In a fixed wall chamber, air must be continually replenished to maintain atmospheric pressure in the chamber. Chambers may or may not incorporate active mixing within the chamber. Mixing occurs as a result of the flows used to introduce reactants and withdraw chamber samples, and perhaps as a result of natural movements of the flexible walls of the chamber.

An alternative to the batch-mode (time-dependent) chamber operation is the steady-state continuous flow mode, in which case the reactor is referred to as a *continuously mixed flow reactor* (CMFR). The CMFR is analogous to the batch chamber in physical configuration, but differs in that throughout the course of an experiment there is a continuous flow of reactants into the chamber and a continuous flow (unreacted reactants and reaction products) out of the chamber. After an initial transient start-up period in a CMFR, the gases (and particles) in the reactor eventually achieve steady state. The contents of the CMFR are usually well mixed, whether actively or not, so that the concentrations in the outflow are essentially identical to those in the bulk of the chamber. Continuous sampling of the effluent permits accumulation of arbitrarily large quantities of gases and particles for analysis. The characteristic time scale of a CMFR is the mean residence time in the reactor, which is the ratio of the volume of the reactor to the volumetric flow rate of air through the chamber.

In the Flow Tube Reactor, reactants are introduced at one end of a tubular reactor and reaction products are withdrawn from the other end. The flow rate through the tube is adjusted to achieve a desired residence time in the reactor. The flow rate of air through the tube and the diameter of the tube itself determine the state of the flow: laminar or turbulent. Like the CMFR, the Flow Tube Reactor affords continuous sampling of the effluent.

A common material used for flexible-walled batch environmental chambers is flu-



orinated ethylene propylene (FEP) Teflon film, usually of thickness 0.05 mm (2 mil). Irradiation of the chamber with actual or artificial sunlight is usually required, and Teflon film has the attribute that it is essentially transparent to ultraviolet and visible radiation. While Teflon is a relatively inert material, there is evidence that particles and certain organic molecules can deposit and adhere to the Teflon walls of a chamber. These “wall effects” play an important role in the interpretation of data, and they will be addressed later in this chapter in some detail. Permanent materials for fixed-wall chamber construction are stainless steel and glass. These materials offer the advantage that they can be cleaned between experiments and that, if desired, experiments can be carried out at pressures lower than atmospheric. The flow tube reactor is commonly constructed of glass or steel, with appropriate attention to transmission of radiation.

### 2.3 Characterization of the Environmental Chamber

Characterization of the environmental chamber is essential prior to its use in studying atmospheric chemistry. In this section we outline a number of characterization tests and illustrate the results of such tests carried out on the Caltech chambers. Table 1 summarizes these tests. Earlier reports of chamber characterizations are those of Cocker et al. (2001) and Carter, Cocker, et al. (2005) and Carter, Heo, et al. (2012) and Wang et al. (2011).

**Table 2.1:** Environmental Chamber Characterization Tests.

| Characterization Test | Procedure  |
|-----------------------|--|
| Leak rate             | Evaluate the extent to which ambient air outside of the chamber leaks into the chamber.  |
| Aerosol background    | Use DMA (Differential Mobility Analyzer) coupled to CPC (Condensation Particle Counter) to determine the background particle concentration in the chamber when the chamber is filled with purified air and irradiated. |
| Mixing time           | Evaluate the characteristic mixing time in the chamber: Add an inert gas (e.g., CO), take measurements at different ports and determine the amount of time it takes for the gas to become well mixed.                  |
| Irradiation spectrum  | Use a portable spectroradiometer to measure the irradiance spectrum of the light source and compare this irradiance spectrum to the solar spectrum.  |

**Table 2.1:** Environmental Chamber Characterization Tests.

| Characterization Test  | Procedure  |
|--|--|
| Light homogeneity  | Evaluate the extent to which the radiant flux in the chamber enclosure is uniform: Place photodiodes at varying locations in the chamber enclosure. Record the signal hitting the top (direct) and bottom (reflected) of the photodiode.   |
| Photolysis frequencies of NO <sub>2</sub> and O <sub>3</sub> | Calculate photolysis rates by converting the irradiance spectrum determined by the spectroradiometer into actinic flux, and then using the absorption spectrum for the molecule.   |
| Cleaning protocol  | Flush chamber with ~10 chamber volumes of clean air over 24 h. During this, periodically bake under full blacklights at 50 °C.   |
| NO <sub>x</sub> -air photolysis                              | Photolyze varying amounts of initial NO <sub>2</sub> and monitor the concentrations of NO <sub>2</sub> , NO, O <sub>3</sub> , and HONO over time.  |
| Vapor wall deposition  | Calculate the first-order wall deposition rate from the decrease in the concentration of a spectrum of compounds under dark conditions. Test vapor wall deposition under different relative humidity levels (e.g., for glyoxal in Caltech chamber: $k_w$ (dry) = $9.6 \cdot 10^{-7} \text{ s}^{-1}$ , but $k_w$ (RH = 61%) = $4.7 \cdot 10^{-5} \text{ s}^{-1}$ )  |
| Propene-NO <sub>x</sub> photooxidation                       | Add initial amounts of propene and NO <sub>x</sub> to the chamber and monitor the concentration of NO <sub>2</sub> , NO, O <sub>3</sub> , propene, and secondary organic compounds (e.g., HCHO, CH <sub>3</sub> CHO, HCOOH, and PAN) during photooxidation. Compare measured concentrations to those predicted by the Master Chemical Mechanism (MCM) for propene. Evaluate HO <sub>x</sub> sources and sinks. |
| Species off-gassing from walls                               | During the experiments above (e.g., photolysis of NO <sub>x</sub> alone and photolysis of propene in the presence of NO <sub>x</sub> ), use CIMS to evaluate the extent to which species might be off-gassing from the walls.  |

**Table 2.1:** Environmental Chamber Characterization Tests.

| Characterization Test  | Procedure  |
|--|--|
| Photolysis of NO <sub>x</sub> in the presence of ammonium sulfate seed aerosol | Add ammonium sulfate seed aerosol and NO <sub>x</sub> to the chamber and irradiate this mixture over ~5 h to determine the background SOA production from any residual organic gases in the chamber.   |
| Aerosol generation   | Test the aerosol generation equipment by atomizing various solutions of (NH <sub>4</sub> ) <sub>2</sub> SO <sub>4</sub> and H <sub>2</sub> SO <sub>4</sub> into the chamber and monitoring the aerosol size distribution and aerosol mass concentration resulting.   |
| Secondary organic aerosol formation  | Carry out dark ozonolysis of $\alpha$ -pinene under dry conditions, in the absence of an OH scavenger. $\alpha$ -pinene ozonolysis leads to SOA that is only weakly dependent on the presence or absence of seed particles and chemical properties of the seed. Repeat for dry seed, dry conditions; dry seed, elevated relative humidity; wet seed, elevated relative humidity.   |
| Particle wall deposition   | Model particle dynamics as a result of wall deposition by $dN(D_p, t)/dt = -\beta(D_p)N(D_p, t)$ where $\beta(D_p)$ = particle wall deposition coefficient. Determine experimentally by atomizing monodisperse (NH <sub>4</sub> ) <sub>2</sub> SO <sub>4</sub> aerosol of different sizes into the chamber and measuring decay of each size class over time. For longer experiments, owing to extraction of air for sampling, the volume of the chamber decreases with time, increasing the surface-to-volume ratio. To simulate this effect, run the same tests with (NH <sub>4</sub> ) <sub>2</sub> SO <sub>4</sub> seed particles, but at the beginning of the experiment remove ~ one-third of the air from the chamber. |

### Photolytic Environment

Since the ultimate driving force for atmospheric chemistry is solar radiation, an environmental chamber requires a source of radiation that is either the Sun itself or a source that approximates the solar spectrum. The earliest environmental chambers

were constructed outdoors, to take advantage of sunlight as the source of radiation. For indoor chambers, two types of artificial lights are used: (1) radiation sources like argon or xenon arc lamps with specially designed UV filters which give a UV and visible spectrum similar to that of sunlight; and (2) blacklights. For example, xenon lamps, which mimic the solar spectrum, are used in the CESAM (Experimental Multiphasic Atmospheric Simulation Chamber) chamber in Laboratoire Inter-universitaire des Systemes Atmospheriques (LISA) at Universite Paris VII (Wang et al., 2011).

As shown in Figure 2.1, the blacklight spectral actinic flux differs from that of the Sun. The blacklight spectrum is intended primarily to drive the photolysis of ozone and  $\text{NO}_2$ . For example,  $j_{\text{NO}_2}$ , the first-order photolysis rate constant of  $\text{NO}_2$ , was calculated from the spectral actinic flux determined for the Caltech chamber at full irradiation to be  $6.63 \times 10^{-3} \text{ s}^{-1}$ . The actual  $j_{\text{NO}_2}$  value on Earth depends on many factors, such as latitude, time of day, extent of cloudiness, etc. For comparison, the  $j_{\text{NO}_2}$  value was calculated using the global solar spectral actinic flux shown in Figure 2.1 to be  $9.6 \times 10^{-3} \text{ s}^{-1}$  and  $5.8 \times 10^{-3} \text{ s}^{-1}$  for zenith angles  $0^\circ$  and  $60^\circ$ , respectively. The  $j_{\text{NO}_2}$  value was confirmed by sending  $\text{NO}_2$  gas through a quartz flow cell and measuring the resulting concentrations of  $\text{NO}$ ,  $\text{O}_3$ , and  $\text{NO}_2$  under blacklight irradiation.  $j_{\text{NO}_2}$  values calculated from spectroradiometer measurements fall within the range of the  $j_{\text{NO}_2}$  values calculated by this method. Table 2.2 summarizes photolysis rate constants in the Caltech environmental chamber.

**Table 2.2:** Photolysis rate constants in Caltech Environmental Chamber

| Photolysis Reactions   | Value of $j \text{ (s}^{-1}\text{)}$ <sup>a</sup> |
|--|---|
| $\text{NO}_2 + h\nu \longrightarrow \text{NO} + \text{O}$                      | $6.63 \times 10^{-3}$                             |
| $\text{NO}_3 + h\nu \longrightarrow \text{NO}_2 + \text{O}$                    | $3.34 \times 10^{-3}$                             |
| $\longrightarrow \text{NO} + \text{O}_2$                                       |   |
| $\text{O}_3 + h\nu \longrightarrow \text{O}(^1\text{D}) + \text{O}_2$          | $7.48 \times 10^{-6}$                             |
| $\text{CH}_3\text{ONO} + h\nu \longrightarrow \text{CH}_3\text{O} + \text{NO}$ | $1.67 \times 10^{-3}$                             |
| $\text{HONO} + h\nu \longrightarrow \text{OH} + \text{NO}$                     | $1.62 \times 10^{-3}$                             |
| $\text{H}_2\text{O}_2 + h\nu \longrightarrow 2 \text{OH}$                      | $4.85 \times 10^{-6}$                             |

<sup>a</sup> Photolysis rate constants calculated using the irradiance spectrum measured for 100% UV lights in the chamber and absorption cross sections and quantum yields from Sander et al. (2011).

To assess the degree of homogeneity of radiative flux in the chamber enclosure,

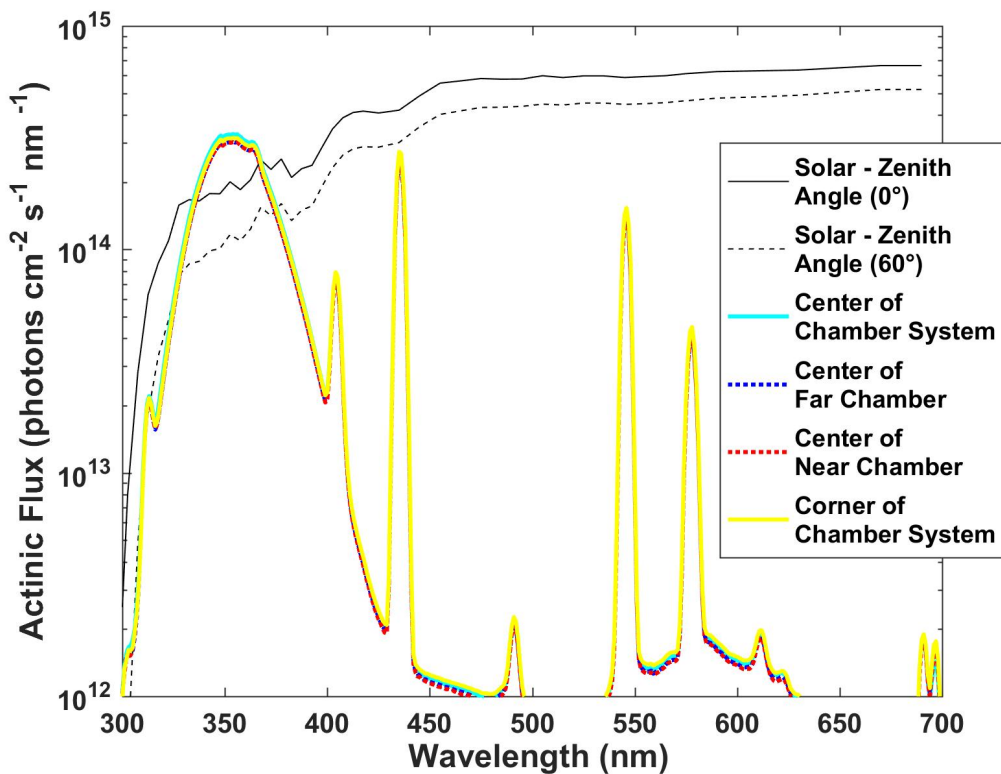


**Figure 2.1:** Spectral actinic flux versus wavelength for blacklights in the Caltech chamber facility. “Near” and ‘Far’ is the designation for the two otherwise identical chambers. Global solar spectral actinic flux is shown for comparison at zenith angles 0° and 60°.

a spectroradiometer can be used to measure the irradiance (for example from 300 to 850 nm). The irradiance is then converted into spectral actinic flux, as shown in Figure 2.1. The spectroradiometer can be placed in various locations of the chamber enclosure, to assess the extent of homogeneity of the radiative flux. The irradiances detected in each direction can be averaged since natural air movements in the chamber will mix the fluid elements. Figure 2.1 shows that for the Caltech chamber the spectra do not change appreciably depending on location in the chamber. If the radiation field is found to be inhomogeneous, then adjustments in the chamber configuration may need to be made.

### Chamber Mixing State

An inert tracer compound that is conveniently measured, such as CO or hydrogen peroxide ( $\text{H}_2\text{O}_2$ ), can be injected into the chamber in order to estimate mixing time in the chamber (i.e., the amount of time it takes for the concentration of an injected

compound to become essentially well-mixed in the chamber). In the case in which  $\text{H}_2\text{O}_2$  is used as the tracer, chemical ionization mass spectrometry (CIMS) can be used to monitor the relative concentration of  $\text{H}_2\text{O}_2$  over time. ( $\text{H}_2\text{O}_2$  can be heated in a closed glass bulb for  $\sim 10$  min and then the amount of  $\text{H}_2\text{O}_2$  vaporized during this period can be injected into the chamber for  $\sim 2$  min.) The chamber mixing time is then established by the time it takes for the measurement signal to stabilize following injection. Mixing time in the presence and absence of additional inflow air (mixing air) can also be tested. Two ports, 1 and 2, are used in the Caltech chamber for injection of gases. As an example, the mixing time for injection at port 1, with and without mixing air is shown in Figure 2.2. The mixing time is shorter if extra mixing air is flowing into the chamber. Injection of tracer at different ports led to similar mixing times in both cases. For example, the average mixing time for injection at port 1 in the chamber with and without air flowing into the chamber was 2 and 8 min, respectively, while the average mixing time for injection at port 2 in the chamber with and without air flowing into the chamber was 2 and 11 min, respectively.

### Wall Penetration

For Teflon chambers, transport of molecules may occur through the Teflon polymer matrix or in minute leaks at seams. The purpose of penetration testing is to determine the extent to which transport of material into or out of the chamber is occurring. Isoprene as a molecular tracer, for example, can be injected into the chamber and monitored simultaneously with gas chromatography (GC) and CIMS. Isoprene is an effective tracer for the presence of leaks because it exhibits virtually no wall deposition.

Water vapor may also leak into the chamber through minute gaps in the seams. In a test on the Caltech chamber, over a 14-h period, the chamber relative humidity increased by  $\sim 1\%$  over 14 h. Based on the temperature and relative humidity readings, the change in the mixing ratio of water increased from 1.9 to 2.1 parts per thousand for one chamber and 2.1 to 2.3 parts per thousand for the other chamber. The CIMS signals  $(-103 \text{ (CF}_3\text{O}^- \cdot \text{H}_2\text{O)})$  and  $(-121 \text{ (CF}_3\text{O}^- \cdot (\text{H}_2\text{O})_2))$  are highly water-dependent as they represent the reagent ion-water complex. Infusion of this small amount of water vapor was deemed acceptable in terms of its potential effect on chemistry occurring in the chamber. The change in water vapor should be monitored for all experiments, so that appreciable leaks in the chamber can be detected and repaired.

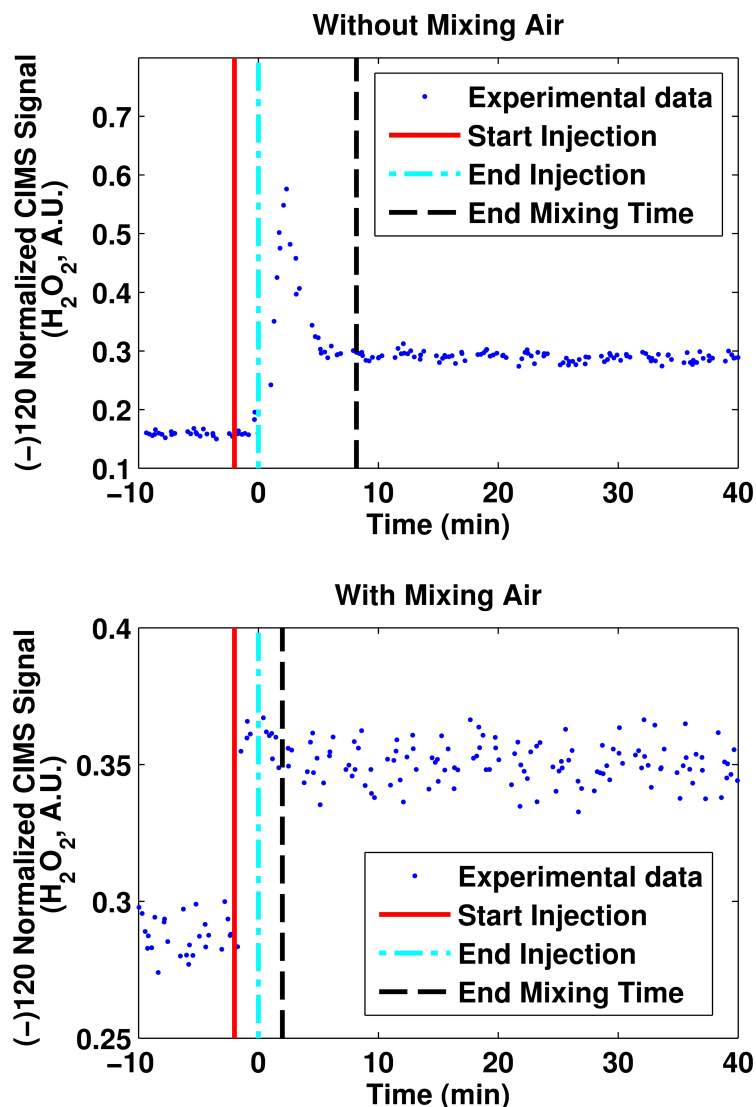


**Figure 2.2:** Chamber mixing time for Caltech chamber with and without mixing air (flowing additional air into the chamber other than that carrying the injected hydrogen peroxide).

### Flushing/Cleaning Procedure

After completion of an experiment, the chamber is routinely flushed with clean air. Results of flushing experiments on the Caltech chamber are shown in Figure 2.3. Ozone and ammonium sulfate seed particles were injected into both chambers (termed the near and far chambers). Ozone and particle number concentrations were monitored over time as purified air was injected into the chamber at the same rate as air was flushed out. As expected, the concentration of species decays exponentially during flushing (concentration  $\sim \exp(-t/\tau)$ , where  $\tau$  is the mean residence time of air in the chamber at the particular flow rate of air). Using ozone as a tracer and

assuming constant volume and a well-mixed system, it was estimated that the flow during these dry flushing experiments was  $370 \text{ L min}^{-1}$ . The mean residence time  $\tau$  for both chambers for this flow was estimated as 1.1 h. Ozone and particles were flushed sufficiently within five residence times,  $\sim 5 \text{ h}$ . A typical protocol is to flush the chamber for 24 h between experiments.

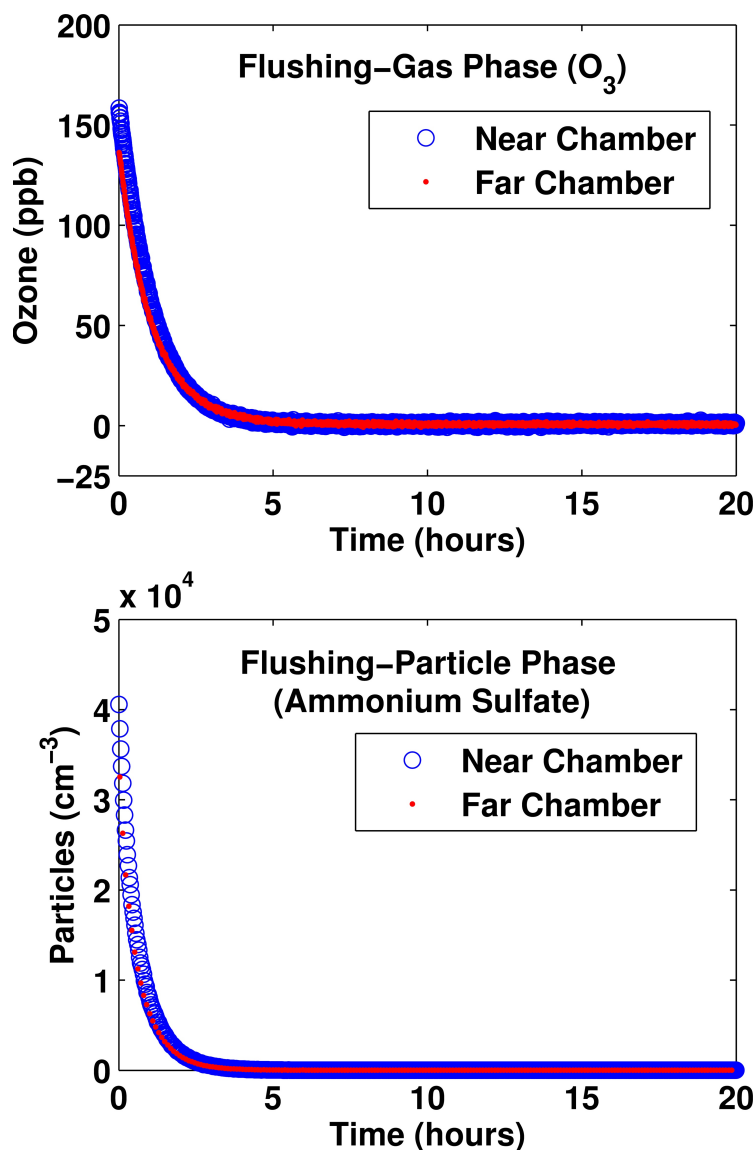


**Figure 2.3:** Ozone and ammonium sulfate concentrations during flushing of the two Caltech chambers (near and far).

### Chemical Blank Experiments

The purpose of so-called *blank experiments* is to assess the chemical reactivity of the chamber under conditions when it is filled only with purified air or an



oxidant-generating species. Such experiments can reveal chemistry involving residual species present either in the purified air system or from material degassing from the walls of the chamber.

### **Blank Experiments with Injection Air Only**

The first test is to feed only purified injection air into the chamber. A typical protocol for such a test is as follows. After filling with injection air ( $\sim 1$  h), the lights are turned on. After 5 h with lights on at  $20^\circ\text{C}$ , the temperature is increased at a constant rate over 2 h to  $40^\circ\text{C}$ . After another  $\sim 13$  h, lights are turned off, and the experiment terminates. Results of such a test for one (far) of the Caltech chambers are shown in Figure 2.4. One indication of chemistry occurring during this test is generation of aerosol from gas-phase reactions involving residual species. The volume concentration of aerosol formed in the blank experiment was found to be greater in the near chamber ( $\sim 1.1 \mu\text{m}^3 \text{ cm}^{-3}$ ) than in the far chamber ( $\sim 0.2 \mu\text{m}^3 \text{ cm}^{-3}$ ). Prior to this test, the far chamber had been flushing for considerably longer, and this difference is reflected in the amount of aerosol volume generated. As shown in Figure 2.4,  $\text{O}_3$  also formed during the blank experiment. Even though the  $\text{NO}_2$  signal remained below its detection limit, it is likely that  $\text{O}_3$  formed from photolysis of trace amounts of  $\text{NO}_2$ .

### **Blank Experiments with OH Generation**

A second blank experiment is one in which OH radicals are intentionally generated in the chamber in the presence of injection air only. In a test of this nature, 210 ppb  $\text{H}_2\text{O}_2$  was injected into the Caltech chamber, and the same experiment as the blank with injection air only was carried out. Results for this test in the far chamber are shown in Figure 2.5. A similar amount of ozone and particle volume was generated as in the blank experiment in the absence of  $\text{H}_2\text{O}_2$ . This observation supports the argument that  $\text{NO}_x$  is the likely agent leading to ozone formation. Adding more oxidant does not increase the ozone concentration significantly, so it is likely that the formation of  $\text{NO}_x$  is the limiting factor. The aerosol mass and volume concentrations generated for the two chambers were  $< 0.4 \mu\text{g m}^{-3}$  and  $0.5 \mu\text{m}^3 \text{ cm}^{-3}$ . For aerosol-generation experiments in which a low aerosol concentration is anticipated, a background aerosol level of this magnitude may be unacceptable. These results emphasize the importance of running blank experiments prior to each new set of experiments to confirm that backgrounds, which will change as the life

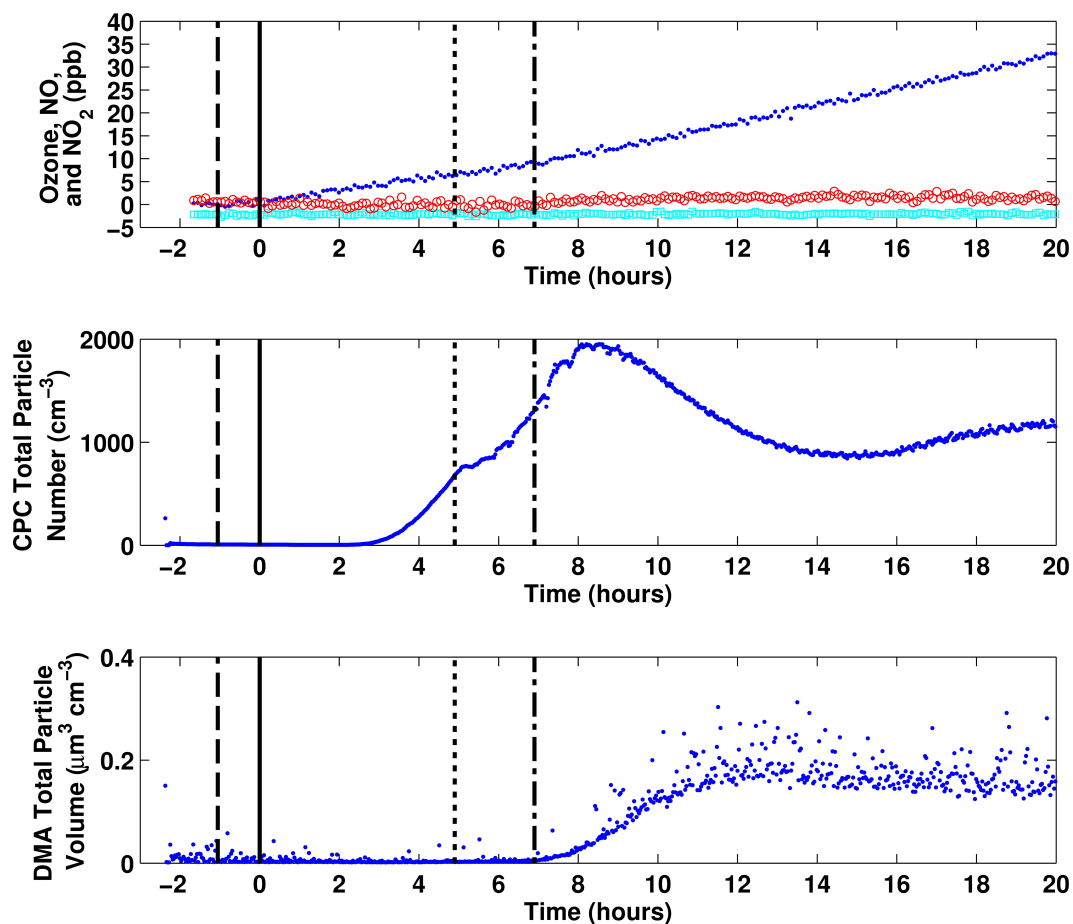


**Figure 2.4:** Ozone, NO, and NO<sub>2</sub> concentrations, particle number concentration, and particle volume formation during a blank photooxidation experiment with clean injection air.

of the chamber increases, will not impact the results.

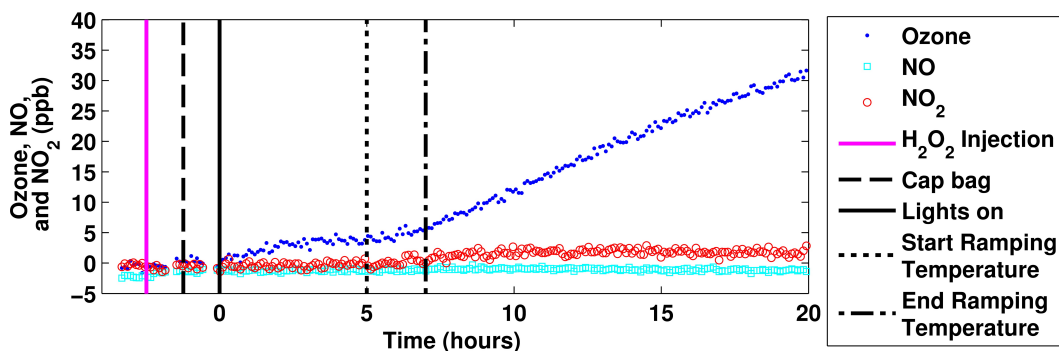


**Figure 2.5:** Formation of ozone, NO, and NO<sub>2</sub> during blank experiment with added hydrogen peroxide.

Aerosol Mass Spectrometer (AMS) measurements of particle composition for the

near chamber initial blank experiment with  $\text{H}_2\text{O}_2$  are shown in Figure 2.6. From the normalized carbon spectrum, the  $m/z$  44 signal is indicative of the presence of oxidized organic species in the particles. The aerosol also contains reduced carbon species, as indicated by the signals for  $m/z$  55, 57, 69, and 71. Overall, the AMS data show that the aerosol is carbonaceous in nature, suggesting that the particles result from the oxidation of trace organic species. Additional tests are warranted to determine whether the source of the primary organic material is the injection air or desorption from the chamber walls.

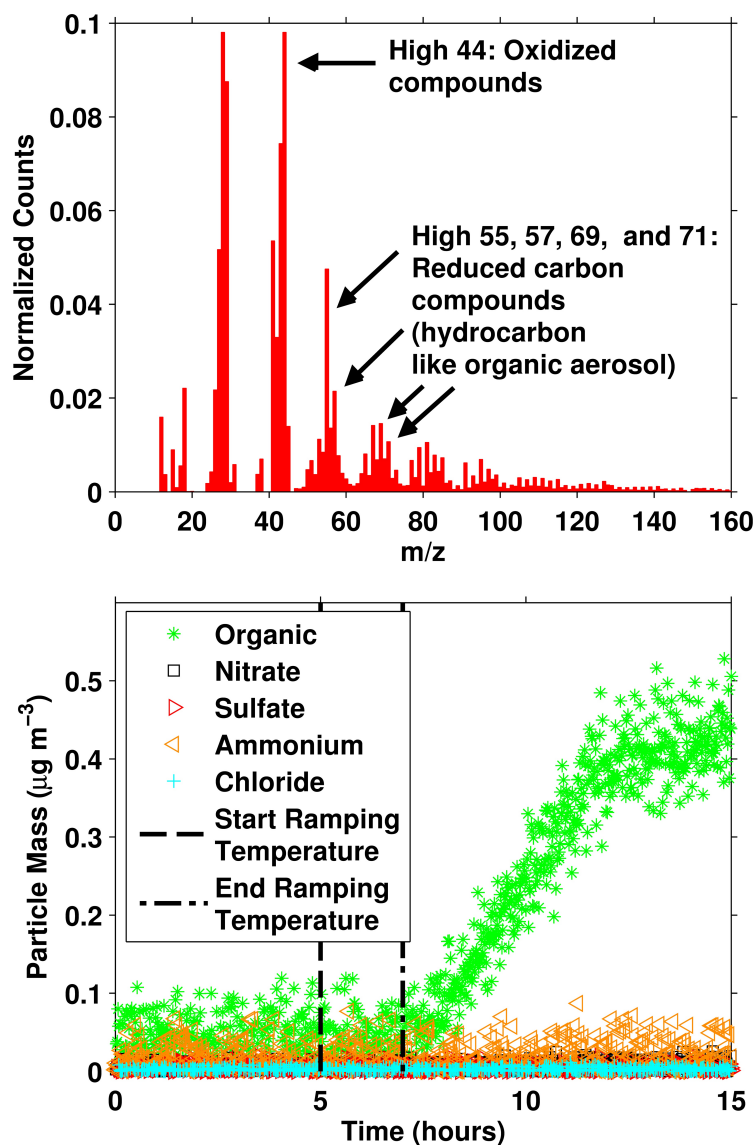


**Figure 2.6:** Aerosol Mass Spectrometer measurements during a blank photooxidation experiment with clean air. The top panel shows the normalized average organic spectrum at time of peak growth. The bottom panel shows the chemical composition of the aerosol formed.

## 2.4 Chemical Environment in the Chamber

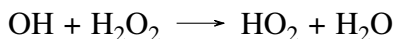
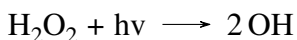
### Hydroxyl Radical Generation

In the atmosphere, OH radicals are generated via the reaction of  $\text{H}_2\text{O}$  with singlet ( $\text{O}(^1\text{D})$ ) oxygen atoms produced from  $\text{O}_3$  photolysis at wavelengths  $< 319$  nm. In chamber facilities, the spectrum and wavelength-dependent intensities of radiation sources govern the choice of the OH precursor. For example, blacklights with a spectrum that peaks at 350 nm do not provide sufficient photon intensity to sustain

the O<sub>3</sub> photolysis chemistry. OH sources that have been widely used in chambers include H<sub>2</sub>O<sub>2</sub>, HONO, and CH<sub>3</sub>ONO.

### **H<sub>2</sub>O<sub>2</sub> Radical Source**

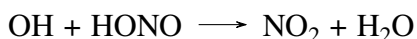
Photolysis of H<sub>2</sub>O<sub>2</sub> yields two OH radicals, which subsequently react with H<sub>2</sub>O<sub>2</sub>, producing HO<sub>2</sub> radicals:



The relatively slow H<sub>2</sub>O<sub>2</sub> photolysis rate, together with the suppression of OH propagation by reaction with H<sub>2</sub>O<sub>2</sub> itself, makes it possible to sustain a steady OH concentration over a long timescale.

### **HONO Radical Source**

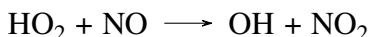
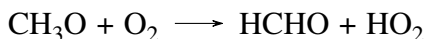
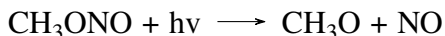
HONO photolyzes to produce one OH radical and one NO radical. Because NO is produced even if no additional NO<sub>x</sub> is added to the system, the RO<sub>2</sub>+NO reaction will always dominate under typical chamber conditions. Thus, for experiments in which HONO is used as a radical source, the peroxy radical will always react preferentially with NO, regardless of the [VOC]<sub>o</sub>/[NO<sub>x</sub>]<sub>o</sub> ratio or initial HONO concentration:



Due to the substantial photolysis rate of HONO, OH radicals generated usually peak at the beginning of the experiment and then rapidly decay to zero. Thus, multiple HONO injections are required for extended duration experiments.

### **CH<sub>3</sub>ONO Radical Source**

CH<sub>3</sub>ONO photolysis produces the methoxy radical, CH<sub>3</sub>O, and NO. The methoxy radical rapidly reacts with oxygen to yield formaldehyde and HO<sub>2</sub>. HO<sub>2</sub> and NO then react to yield OH and NO<sub>2</sub>. Thus, in contrast to HONO, which yields OH and NO, the ultimate yield of CH<sub>3</sub>ONO photolysis is OH and NO<sub>2</sub>:



$\text{NO}_2$  can then photolyze to generate  $\text{NO}$  and  $\text{O}_3$ . One needs also to consider the effect on the system from subsequent reactions of  $\text{HCHO}$ .

### High- versus Low-NO Conditions

In atmospheric chemistry the terms “high-NO” and “low-NO” are used to classify photooxidation conditions of volatile organic compounds (VOCs). (The common terminology relating to these conditions has been low- $\text{NO}_x$  and high- $\text{NO}_x$ , but it is the  $\text{NO}$  concentration that governs the fate of the peroxy radical in the system, so low- and high-NO are more appropriate descriptions.) In VOC oxidation, these terms are intended to delineate the gas-phase fate of the peroxy radicals ( $\text{RO}_2$ ) generated by VOC reaction with  $\text{OH}$ . The peroxy radicals can react via one of three main pathways, as illustrated for n-hexane ( $\text{C}_6\text{H}_{14}$ ) in Figure 2.7: reaction with  $\text{NO}$ , reaction with  $\text{HO}_2$ , and reaction with other  $\text{RO}_2$  radicals. Reaction with  $\text{NO}$  generates either an alkoxy radical or an alkyl nitrate. Reaction with  $\text{HO}_2$  generates a hydroperoxide. Reaction with another  $\text{RO}_2$  radical generally yields two alkoxy radicals or the combination of an alcohol and a carbonyl (Atkinson, 1994). For some VOCs, such as isoprene, a fraction of peroxy radicals may undergo isomerization (autoxidation) under conditions when the lifetime of the peroxy radical against reaction is sufficiently long (Crounse et al., 2011). In a so-called high-NO regime, reaction with  $\text{NO}$  dominates the fate of the  $\text{RO}_2$  radicals. In a low-NO regime, the  $\text{RO}_2$  radical may react with  $\text{HO}_2$ , with  $\text{RO}_2$  or undergo intra-molecular isomerization. Kroll et al. (2006) demonstrated that  $\text{H}_2\text{O}_2$  may be used as a radical source to isolate the  $\text{RO}_2 + \text{HO}_2$  reaction because the slow photolysis rate of  $\text{H}_2\text{O}_2$  produces a continuous supply of  $\text{OH}$  and  $\text{HO}_2$  (from  $\text{OH} + \text{H}_2\text{O}_2$ ). However, the terms high- and low-NO alone are inadequate to characterize the conditions of a VOC photooxidation. A more precise description of the regime of a system is based on the specific fate of the peroxy radicals.

Using hexane as the illustrative VOC, we quantify the conditions needed to isolate different peroxy radical pathways. For specified initial concentrations of hexane and  $\text{H}_2\text{O}_2$  (50 ppb and 1000 ppb, respectively), we present simulations of the subsequent chemistry at different initial  $\text{NO}$  levels (assuming a 1:1 initial ratio of  $\text{NO}:\text{NO}_2$ ) ranging from 0 to 20 ppb. The fate of the  $\text{RO}_2$  radicals at any instant of time is determined from the fractional contribution of each pathway,  $\text{RO}_2+\text{NO}$ ,  $\text{RO}_2+\text{HO}_2$ , and  $\text{RO}_2 + \text{RO}_2$ . The mechanism for  $\text{OH}$  oxidation of hexane is derived from the Master Chemical Mechanism (MCM) v3.2 (<http://mem.leeds.ac.uk/MCM>) (Saunders et al., 2003). Photolysis rates for all species are calculated using the UV

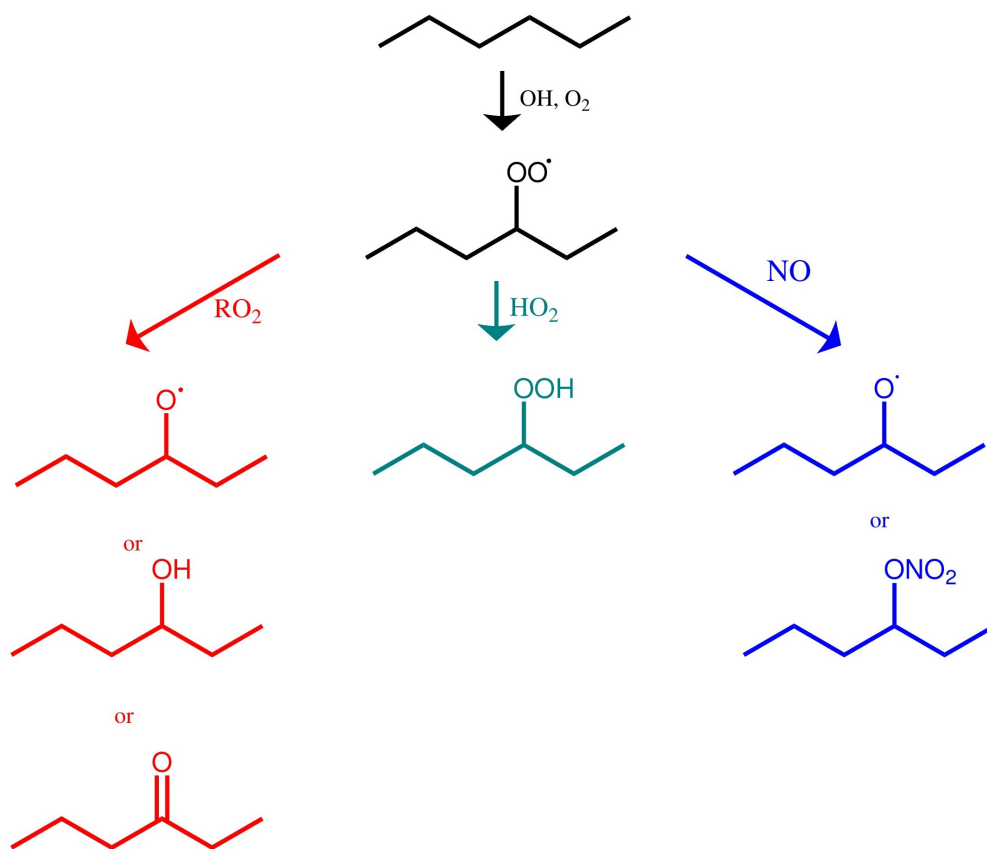


**Figure 2.7:** Reactions of the peroxy radicals generated by OH oxidation of *n*-hexane.

spectrum of the Caltech laboratory chamber ( $j_{\text{NO}_2} = 6.63 \times 10^{-3} \text{ s}^{-1}$ ). We examine  $\text{H}_2\text{O}_2$ ,  $\text{HONO}$ , and  $\text{CH}_3\text{ONO}$  as OH sources.

The relative amounts of  $\text{RO}_2$ ,  $\text{NO}$ , and  $\text{HO}_2$  can vary substantially over the course of a photooxidation. For example,  $\text{NO}$  tends to be at its maximum concentration at the onset of oxidation prior to consumption by reaction with  $\text{RO}_2$  and other species. Consequently, the  $\text{RO}_2 + \text{NO}$  reaction can be disproportionately dominant at the beginning of a photooxidation. This trend is illustrated in Figure 2.8, where the fate of the  $\text{RO}_2$  radical is shown at the start of a hypothetical experiment (solid lines), after 4 h (dashed lines), and after 8 h (dotted lines). As evident in Figure 2.8, the  $\text{RO}_2 + \text{NO}$  reaction dominates at the start of the experiment, even for what may be considered “low” values of  $[\text{NO}_x]_0$ , i.e., 5 ppb. After 4 h, the peroxy radical reacts predominantly with  $\text{HO}_2$  for practically all values of  $[\text{NO}]_0$  because the substantial initial concentration of  $\text{H}_2\text{O}_2$ , 1000 ppb, eventually generates an excess of  $\text{HO}_2$ . The behavior of the system at 4 and 8 h is essentially identical. The evolution of the

peroxy radical fate over the course of the oxidation is noteworthy, as products from the  $\text{RO}_2 + \text{NO}$  reaction are generated even in the presence of relatively low values of  $[\text{NO}_x]_0$  until sufficient levels of  $\text{HO}_2$  are attained. Figure 2.9 shows the same case as Figure 2.8 but with an initial  $\text{H}_2\text{O}_2$  mixing ratio of 10 ppb. In this case, the level of OH generation is considerably smaller and peroxy radical reaction with NO dominates.

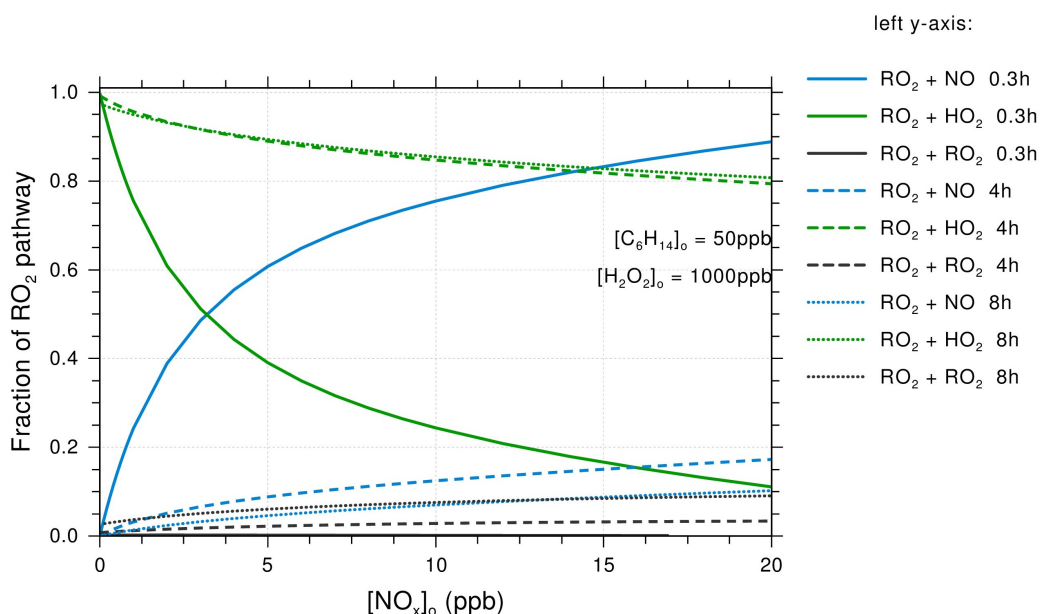


**Figure 2.8:** Fate of the  $\text{RO}_2$  radical as a function of the initial mixing ratio of  $\text{NO}_x$  at different times in *n*-hexane photooxidation for a system of 50 ppb initial *n*-hexane and 1000 ppb initial hydrogen peroxide. The sum of all  $\text{RO}_2 + \text{NO}$  reactions is shown in blue, all  $\text{RO}_2 + \text{HO}_2$  reactions in green, and all  $\text{RO}_2 + \text{RO}_2$  reactions in black. The fractions at the start of the experiment are shown by solid lines, the fractions after 4 h are shown by dashed lines, and the fractions after 8 h are shown by dotted lines.

The ratio of initial VOC to  $\text{NO}_x$  concentrations alone does not adequately define the behavior of the peroxy radical when applied to a wide range of initial VOC concentrations and initial  $\text{H}_2\text{O}_2$  concentrations, as demonstrated in Figures 2.10 and 2.11. Figure 2.10 shows the fate of the  $\text{RO}_2$  radical as a function of  $[\text{VOC}]_0/[\text{NO}_x]_0$  for three different initial hexane mixing ratios and a range of  $[\text{NO}_x]_0$ , each initially with 10 ppb of  $\text{H}_2\text{O}_2$ . The transition from a  $\text{RO}_2 + \text{NO}$  regime to an  $\text{RO}_2 + \text{RO}_2$  regime for these systems is not well predicted by the ratio  $[\text{VOC}]_0/[\text{NO}_x]_0$ . Depending on the initial VOC mixing ratio, the  $[\text{VOC}]_0/[\text{NO}_x]_0$  ratio at which the transition occurs ranges from 75 for a low initial hexane concentration to 1500 for



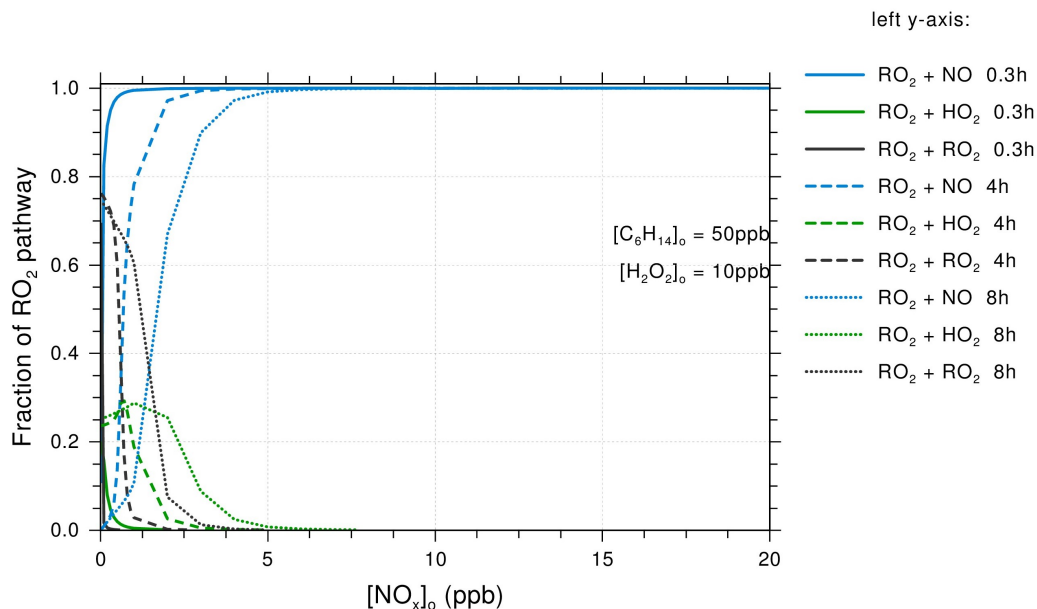


**Figure 2.9:** Fate of the  $\text{RO}_2$  radical as a function of the initial mixing ratio of  $\text{NO}_x$  at different times in *n*-hexane photooxidation with 50 ppb initial *n*-hexane and 10 ppb initial hydrogen peroxide. The sum of all  $\text{RO}_2 + \text{NO}$  reactions is shown in blue, all  $\text{RO}_2 + \text{HO}_2$  reactions in green, and all  $\text{RO}_2 + \text{RO}_2$  reactions in black. The fractions at the start of the experiment are shown by solid lines, the fractions after 4 h are shown by dashed lines, and the fractions after 8 h are shown by dotted lines.

a high initial hexane concentration. Thus,  $[\text{VOC}]_o/[\text{NO}_x]_o$  alone is not a reliable predictor of the fate of the  $\text{RO}_2$  radical for these systems. For an initial  $\text{H}_2\text{O}_2$  mixing ratio of 1000 ppb (Figure 2.11), the  $\text{RO}_2 + \text{NO}$  pathway is negligible for almost all values of  $[\text{VOC}]_o/[\text{NO}_x]_o$ . The amount of initial VOC (represented by different line styles), not the  $[\text{VOC}]_o/[\text{NO}_x]_o$  ratio, dictates those systems for which the peroxy radical reacts with  $\text{RO}_2$  or with  $\text{HO}_2$ . For a low initial hexane mixing ratio of 50 ppb, the  $\text{RO}_2$  radical reacts predominately with  $\text{HO}_2$  at all  $[\text{VOC}]_o/[\text{NO}_x]_o$  ratios. For higher initial hexane values, 500 ppb and 1000 ppb, roughly equal amounts of  $\text{RO}_2$  react with  $\text{HO}_2$  and  $\text{RO}_2$ .

For the systems in both Figures 2.10 and 2.11, the different behavior at a particular  $[\text{VOC}]_o/[\text{NO}_x]_o$  ratio does not occur simply as a result of the different initial VOC concentrations. Rather, the behavior at a particular  $[\text{VOC}]_o/[\text{NO}_x]_o$  ratio changes both with initial VOC concentration and with initial  $\text{H}_2\text{O}_2$  concentration. A more precise classification of the fate of the peroxy radical in an experiment in which  $\text{H}_2\text{O}_2$  is the radical source is based on the ratio  $[\text{VOC}]_o/[\text{NO}_x]_o$  at a specific  $[\text{H}_2\text{O}_2]_o/[\text{VOC}]_o$ . That is, for a specified  $[\text{H}_2\text{O}_2]_o/[\text{VOC}]_o$  ratio, the fate of the

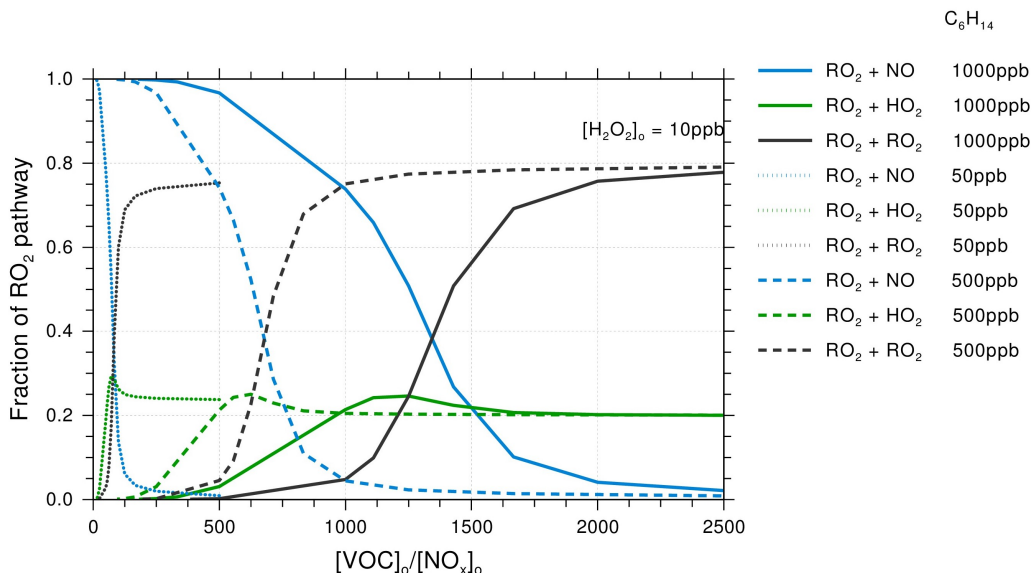


**Figure 2.10:** Fate of the  $\text{RO}_2$  radical as a function of  $[\text{VOC}]_o/[\text{NO}_x]_o$  (after 4 h of reaction) in experiments starting with variable *n*-hexane and  $[\text{NO}_x]_o$  concentrations each with 10 ppb of  $\text{H}_2\text{O}_2$ . The  $\text{RO}_2 + \text{HO}_2$  pathway is shown in green, the  $\text{RO}_2 + \text{RO}_2$  pathway in black, and the  $\text{RO}_2 + \text{NO}$  pathway in blue. Different line styles are used for different initial *n*-hexane concentrations: solid lines for 1000 ppb, dots for 50 ppb, and dashes for 500 ppb.

$\text{RO}_2$  radical can then be distinguished on the basis of the ratio  $[\text{VOC}]_o/[\text{NO}_x]_o$ . Figure 2.12 shows the results of simulated photooxidation at two initial hexane levels, each at  $[\text{NO}_x]_o$  levels ranging from 0.1 ppb to 20 ppb. For each of the simulations,  $[\text{H}_2\text{O}_2]_o/[\text{VOC}]_o = 20$ . The same trend is observed for each simulation with this ratio. Thus, specifying  $[\text{H}_2\text{O}_2]_o/[\text{VOC}]_o$  is necessary in order to classify the behavior of a system based on the ratio,  $[\text{VOC}]_o/[\text{NO}_x]_o$ . For  $[\text{H}_2\text{O}_2]_o/[\text{VOC}]_o = 20$ ,  $\text{RO}_2 + \text{NO}$  is the dominant reaction below a  $[\text{VOC}]_o/[\text{NO}_x]_o$  ratio of  $\sim 0.5$ . Above a  $[\text{VOC}]_o/[\text{NO}_x]_o$  ratio of  $\sim 20$ , the  $\text{RO}_2 + \text{HO}_2$  reaction dominates. Between  $[\text{VOC}]_o/[\text{NO}_x]_o$  ratios of 0.5 and 20, a transition region exists in which both peroxy radical pathways are significant. Figure 2.13 shows the results of simulations of two initial hexane concentrations for a range of  $[\text{NO}_x]_o$  values, both with an  $[\text{H}_2\text{O}_2]_o/[\text{VOC}]_o$  ratio of 0.2. For this  $[\text{H}_2\text{O}_2]_o/[\text{VOC}]_o$  ratio,  $\text{RO}_2 + \text{NO}$  dominates below a  $[\text{VOC}]_o/[\text{NO}_x]_o$  ratio of  $\sim 25$ . Above  $[\text{VOC}]_o/[\text{NO}_x]_o \sim 150$ , the  $\text{RO}_2 + \text{RO}_2$  reaction dominates, although the  $\text{RO}_2 + \text{HO}_2$  reaction contributes about 20%.

For both of these  $[\text{H}_2\text{O}_2]_o/[\text{VOC}]_o$  ratios, a  $[\text{VOC}]_o/[\text{NO}_x]_o$  ratio is sufficient to describe the fate of the peroxy radical for a system. These conditions can be

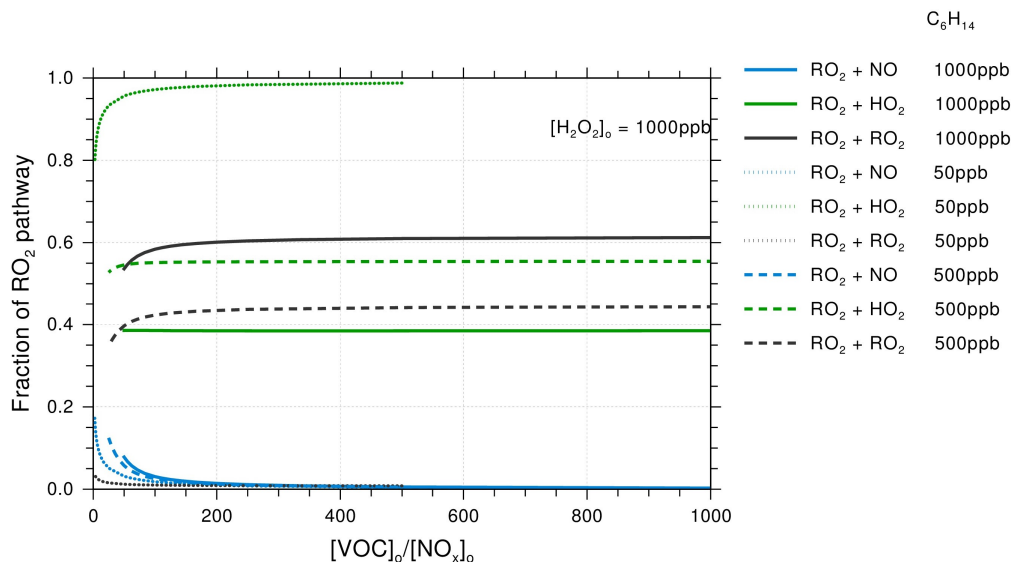


**Figure 2.11:** Fate of the  $RO_2$  radical as a function of  $[VOC]_o/[NO_x]_o$  (after 4 h of reaction) in experiments starting with variable  $n$ -hexane and  $[NO_x]_o$  concentrations each with 1000 ppb of  $H_2O_2$ . The  $RO_2 + HO_2$  pathway is shown in green, the  $RO_2 + RO_2$  pathway in black, and the  $RO_2 + NO$  pathway in blue. Different line styles are used for different initial  $n$ -hexane concentrations: solid lines for 1000 ppb, dots for 50 ppb, and dashes for 500 ppb.

generalized into the following two rules of thumb: (1) the  $RO_2 + HO_2$  reaction can be isolated by using an initial  $H_2O_2$  concentration at least an order of magnitude higher than the initial VOC concentration at a moderately high  $[VOC]_o/[NO_x]_o$  ratio; (2) the  $RO_2 + RO_2$  reaction can be isolated by using an initial  $H_2O_2$  concentration at least an order of magnitude lower than the initial VOC concentration at a high  $[VOC]_o/[NO_x]_o$  ratio. However, the latter result should be viewed with caution due to the uncertainty and variability in the rate constants for  $RO_2 + RO_2$  reactions. Owing to the large number of permutation reactions of  $RO_2 + RO_2$ , MCM assumes that each peroxy radical reacts with a pool of all other peroxy radicals with a generic rate constant calculated from the structure of the organic group and general trends of peroxy reactivity (Jenkin et al., 1997). Thus it is difficult to state with certainty when the  $RO_2 + RO_2$  reaction will be dominant. The  $RO_2 + NO$  reaction can be isolated for any combination of initial  $H_2O_2$  and VOC concentrations but only at very low  $[VOC]_o/[NO_x]_o$  ratios. With these cautionary considerations, these conditions enable the design of experiments to isolate the three main pathways of the peroxy radical.

For chamber conditions similar to those used in the simulations for  $H_2O_2$  and HONO,

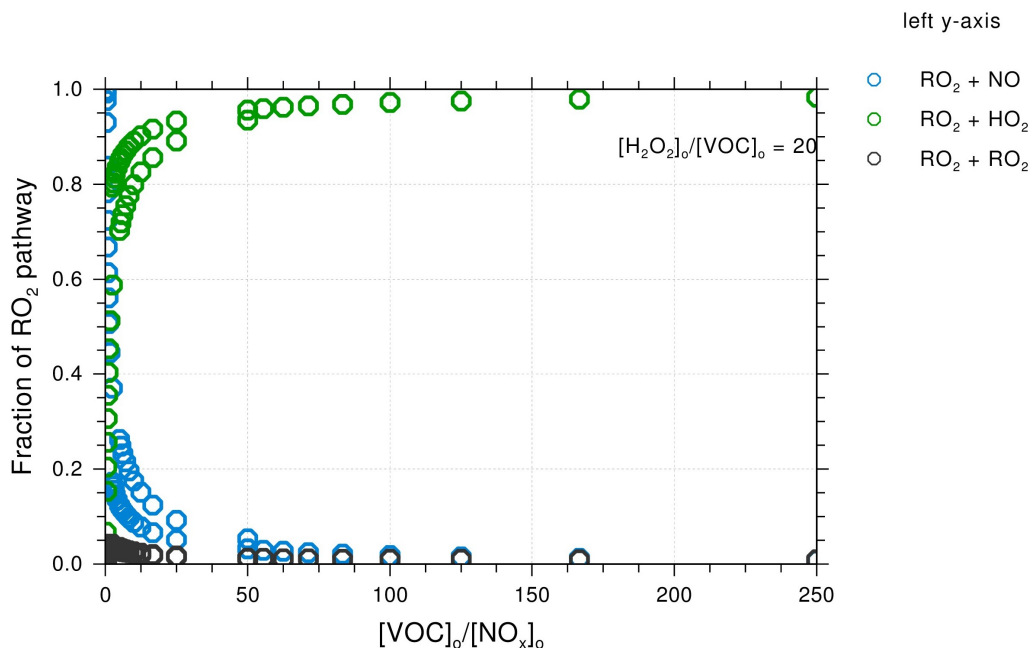


**Figure 2.12:** Fate of the  $\text{RO}_2$  radical as a function of  $[\text{n-hexane}]_o/[\text{NO}_x]_o$  at  $[\text{H}_2\text{O}_2]_o/[\text{n-hexane}]_o = 20$  after 4 h of reaction. Two different combinations were simulated to produce this ratio, both under a large range of  $[\text{NO}_x]_o$  conditions: 1000 ppb  $\text{H}_2\text{O}_2$ /50 ppb  $\text{n-hexane}$  and 100 ppb  $\text{H}_2\text{O}_2$ /5 ppb  $\text{n-hexane}$ .

when  $\text{CH}_3\text{ONO}$  is the OH source, sufficient NO is generated via photolysis that the  $\text{RO}_2 + \text{NO}$  reaction is dominant throughout the experiment even with no additional  $\text{NO}_x$ . For most of the duration of the experiment,  $\text{RO}_2 + \text{NO}$  is essentially the sole peroxy fate. After 8 to 10 h, as  $\text{CH}_3\text{ONO}$  is depleted and NO diminishes, the  $\text{RO}_2 + \text{HO}_2$  reaction increases to  $\sim 5\%$  of the peroxy reactions (Figure 2.14,  $j_{\text{NO}_2} = 6.63 \times 10^{-3} \text{ s}^{-1}$ ). If the photolysis rate of  $\text{NO}_2$  is reduced, the formation of NO can be suppressed, allowing other reactions to contribute significantly. For several simulations using  $\text{CH}_3\text{ONO}$  as the radical source, the photolysis rates for all species were calculated by scaling the chamber irradiance data by 1% ( $j_{\text{NO}_2} = 6.63 \times 10^{-5} \text{ s}^{-1}$ ). The lower UV intensity produces  $\text{HO}_2$  and NO mixing ratios of  $\sim 10$  ppt and  $\sim 50$  ppt, respectively, similar conditions to those generated in Crounse et al. (2011) by using only a single UV bulb ( $j_{\text{NO}_2} = 2.8 \times 10^{-5} \text{ s}^{-1}$ ). The effect of this lower UV intensity is shown in Figure 2.14 by comparing a simulation with identical initial conditions to that discussed in Section 4.2 but where  $j_{\text{NO}_2} = 6.63 \times 10^{-5} \text{ s}^{-1}$ . For this lower intensity, the  $\text{RO}_2 + \text{HO}_2$  reaction constitutes close to half of the total peroxy reactions for the first few hours of experiment and decreases to 20% towards the end of the experiment. Similar behavior for both UV intensities is predicted for

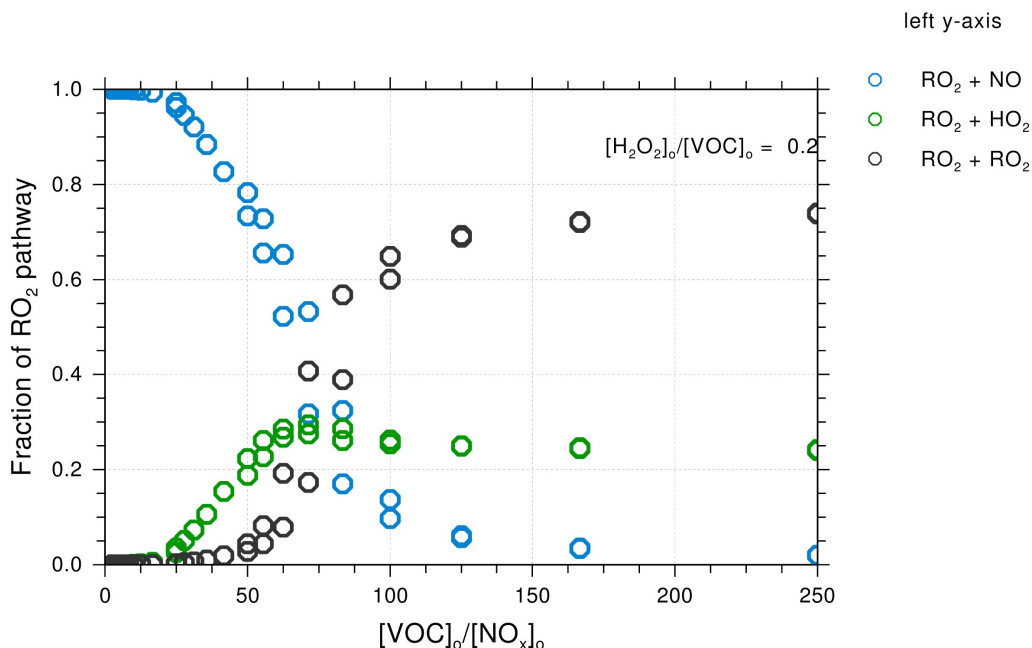


**Figure 2.13:** Fate of the  $\text{RO}_2$  radical as a function of  $[\text{VOC}]_o/[\text{NO}_x]_o$  at  $[\text{H}_2\text{O}_2]_o/[\text{VOC}]_o = 0.2$  after 4 h of reaction. Two different combinations were simulated to produce this ratio, both under a range of  $[\text{NO}_x]_o$  conditions: 10 ppb  $\text{H}_2\text{O}_2$ /50 ppb *n*-hexane and 100 ppb  $\text{H}_2\text{O}_2$ /500 ppb *n*-hexane.

different initial hexane and  $\text{CH}_3\text{ONO}$  concentrations. The  $\text{RO}_2 + \text{NO}$  and  $\text{RO}_2 + \text{HO}_2$  reactions are expected to co-exist in pristine and tropical atmospheres, and the photolysis of  $\text{CH}_3\text{ONO}$  at a lower UV intensity provides a convenient method to study these conditions.

It is useful to compare the chemical lifetime of the peroxy radical in each reaction, where the lifetime against reaction with NO is  $(k_{\text{RO}_2+\text{NO}}[\text{NO}])^{-1}$ , etc. The overall lifetime for a peroxy radical is then

$$\tau_{\text{Overall}} = (k_{\text{RO}_2+\text{NO}}[\text{NO}] + k_{\text{RO}_2+\text{HO}_2}[\text{HO}_2] + k_{\text{RO}_2+\text{RO}_2}[\text{RO}_2])^{-1}$$

Lifetimes for representative initial conditions for each of the categories considered, calculated using concentrations at 4 h, are given in Table 2.3. The dominant reaction for each set of conditions is that with the shortest lifetime, and these data reinforce the conclusions drawn from the simulations.

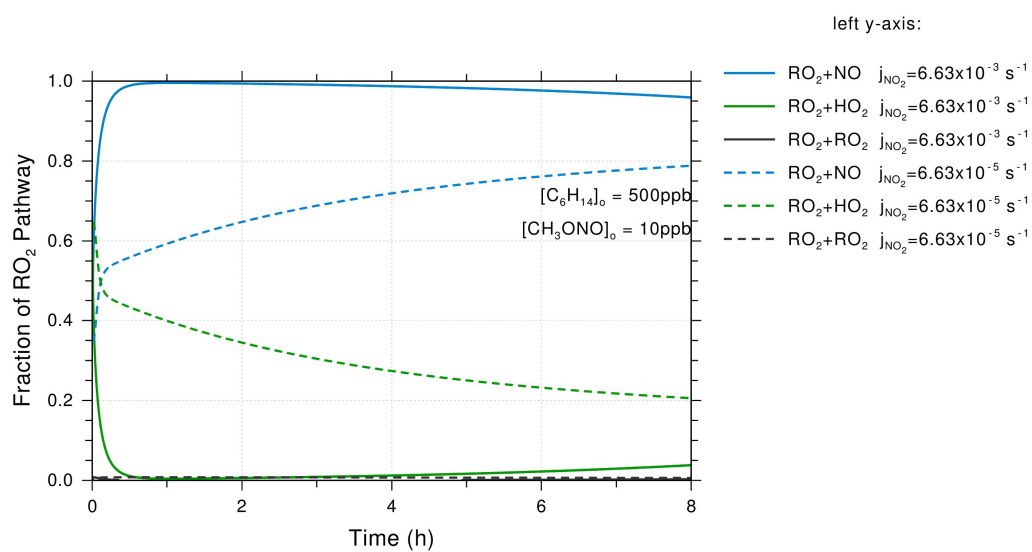


**Figure 2.14:** Temporal profile of the fate of the  $\text{RO}_2$  radical for a system with 500 ppb *n*-hexane and 10 ppb  $\text{CH}_3\text{ONO}$ .

**Table 2.3:** Lifetimes of *n*-hexane peroxy radicals against reaction with NO, HO<sub>2</sub>, and RO<sub>2</sub> for various conditions of *n*-hexane oxidation by OH, as calculated by MCM. Lifetimes are calculated at 4 h of photooxidation.

| OH Source/I.C.s                                 | C <sub>6</sub> H <sub>14</sub> (ppb) | NO <sub>x</sub> (ppb) | $\tau_{RO_2+NO}$ (s) | $\tau_{RO_2+HO_2}$ (s) | $\tau_{RO_2+RO_2}$ (s) | $\tau_{Overall}$ (s) |
|---|--------------------------------------|-----------------------|----------------------|------------------------|------------------------|----------------------|
| H <sub>2</sub> O <sub>2</sub> /VOC=20           |                                      |                       |                      |                        |                        |                      |
| High NO <sub>x</sub> : VOC/NO <sub>x</sub> =0.5 | 5                                    | 10                    | 17.8                 | 66                     | 3930                   | 14                   |
| Low NO <sub>x</sub> : VOC/NO <sub>x</sub> =10   | 50                                   | 5                     | 162                  | 10                     | 1270                   | 9.6                  |
| H <sub>2</sub> O <sub>2</sub> /VOC=0.2          |                                      |                       |                      |                        |                        |                      |
| High NO <sub>x</sub> : VOC/NO <sub>x</sub> =25  | 50                                   | 2                     | 13.8                 | 497                    | 4690                   | 13.4                 |
| Low NO <sub>x</sub> : VOC/NO <sub>x</sub> =100  | 500                                  | 5                     | 2365                 | 733                    | 103                    | 87.2                 |
| HONO  |                                      |                       |                      |                        |                        |                      |
| HONO=10 ppb                                     | 500                                  | 0                     | 3.3                  | 2360                   | 22980                  | 3.3                  |
| HONO=100 ppb                                    | 500                                  | 0                     | 0.3                  | 15010                  | 230240                 | 0.3                  |
| CH <sub>3</sub> ONO                             |                                      |                       |                      |                        |                        |                      |
| CH <sub>3</sub> ONO=10 ppb                      |                                      |                       |                      |                        |                        |                      |
| $j_{NO_2} = 6.63 \times 10^{-5} \text{ s}^{-1}$ | 50                                   | 0                     | 83                   | 168                    | 3370                   | 54.7                 |
| $j_{NO_2} = 6.63 \times 10^{-3} \text{ s}^{-1}$ | 50                                   | 0                     | 5.1                  | 650                    | 9200                   | 5.1                  |
| CH <sub>3</sub> ONO=100 ppb                     |                                      |                       |                      |                        |                        |                      |
| $j_{NO_2} = 6.63 \times 10^{-5} \text{ s}^{-1}$ | 50                                   | 0                     | 28                   | 44                     | 2210                   | 17                   |
| $j_{NO_2} = 6.63 \times 10^{-3} \text{ s}^{-1}$ | 50                                   | 0                     | 1.9                  | 563.6                  | 14290                  | 1.9                  |

It is also apparent that  $\text{RO}_2$  lifetimes can vary dramatically within systems characterized by same peroxy pathway. For conditions in which  $\text{RO}_2 + \text{NO}$  is the dominant reaction, the lifetime for reaction with NO can vary from 0.3 s at a high concentration of HONO to 18 s at low initial concentrations of both  $\text{H}_2\text{O}_2$  and  $\text{NO}_x$ . Using  $\text{CH}_3\text{ONO}$  at a lower UV intensity generates lifetimes similar to those of remote chemistry ( $\sim 30\text{--}60$  s) and allows study of these reactions.

Therefore, in addition to simply choosing initial conditions to isolate a particular peroxy pathway, it may also be necessary to design experiments to yield a particular  $\text{RO}_2$  lifetime.

### **Ozone-Alkene Oxidation and OH Scavenging**

Ozone-alkene reactions are important in gas-phase atmospheric chemistry and are a pathway to formation of secondary organic aerosol. The gas-phase reaction of ozone with alkenes proceeds by the addition of ozone across the  $\text{C}=\text{C}$  double bond to form an energy-rich primary ozonide, followed by decomposition of the primary ozonide to produce an energized carbonyl oxide species, known as the Criegee intermediate, and an aldehyde or ketone product (Calvert et al., 2000; Johnson et al., 2008). Further unimolecular decay of the Criegee intermediate leads to formation of OH radicals. The OH yield from ozonolysis depends on the alkene structure, increasing from  $\sim 10\%$  for ethene via the simplest Criegee intermediate  $\text{CH}_2\text{OO}$  to  $>60\%$  for trans-2-butene, which proceeds through the Criegee intermediate  $\text{CH}_3\text{CHOO}$ .

Because the OH radical itself is highly reactive toward alkenes, for an experiment intended to isolate ozone-alkene chemistry, it is necessary to remove the OH from the system, via a molecular OH scavenger. The necessary characteristics of an OH scavenger are twofold: (1) a molecule that is itself chemically inert toward alkenes, and (2) a molecule that upon reaction with OH does not generate products that are themselves reactive toward alkenes or that mimic products of the ozone-alkene chemistry. Hydroxyl radical scavengers that have been commonly used include cyclohexane, CO, alcohols, and aldehydes. Understanding the chemical role played by the OH scavenger is important in separating the effects of the scavenger itself from that of the intrinsic ozone-alkene reactions. Differences in observed products when different scavengers are used provide important clues to the gas-phase chemistry occurring in the system.

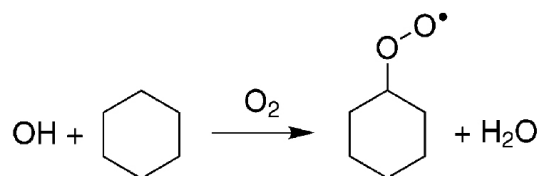
To illustrate the technicalities associated with choice of an OH scavenger in an ozone-alkene reaction, we consider the ozone-cyclohexene system (Keywood et



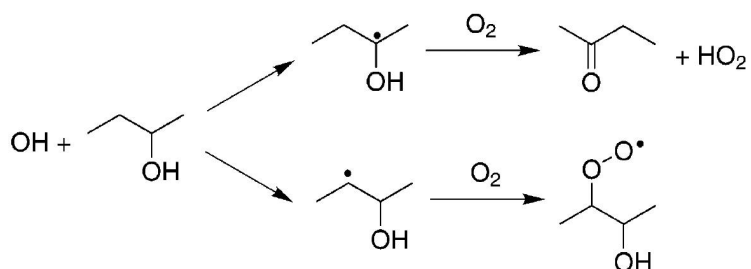
al., 2004). The reaction of ozone with cyclohexene forms OH radicals at a yield of  $\sim 0.6$ . Ozonolysis of cyclohexene in the presence of the OH scavengers, cyclohexane, 2-butanol, and CO, and in the absence of an OH scavenger was carried out in the Caltech chamber (the precursor to the current chambers). These experiments, carried out in the presence of ammonium sulfate seed aerosol, were directed at measuring the formation of secondary organic aerosol in this system. Each OH scavenger was injected at sufficient concentration that the reaction rate of OH radicals with the scavenger exceeded that of OH with the cyclohexene by a factor of  $\sim 100$ . The ratio of the mass concentration of secondary organic aerosol to the mass concentration of reacted cyclohexene, the so-called secondary organic aerosol (SOA) yield (see Section 5), was used as the metric for the behavior of the system. The use of cyclohexane as the OH scavenger resulted in the smallest SOA yield. 2-Butanol scavenger led to a higher SOA yield than that of cyclohexane. When no OH scavenger was used, the SOA yield was similar to that when 2-butanol was used, and when CO was used as the scavenger, the largest SOA yield occurred, even larger than that in the absence of any scavenger.

Understanding the reasons for the observed effects of the different OH scavengers on the observed aerosol yields provides a clue to the chemistry occurring in the system. One possible explanation lies in reactions of the stabilized Criegee intermediate (SCI) with the scavenger, which could potentially form low volatility products. In the case of cyclohexene ozonolysis, however, such reactions are unlikely to occur to an appreciable extent, as little SCI forms. Criegee intermediates from endocyclic alkenes are formed with more energy than those from exocyclic alkenes and so are less likely to be stabilized; SCI yields from cyclohexene ozonolysis are measured at only  $\sim 3\%$ . Also, it is unlikely that the reaction of the Criegee intermediate with CO would form products of lower volatility than those of the Criegee-2-butanol reaction. One concludes that reactions of the OH scavengers themselves with the Criegee intermediate probably do not affect the SOA yield appreciably.

A more likely explanation for the observed effects of the different scavengers on SOA yield lies in the radical products formed in the OH-scavenger reactions, especially the effect on production of  $\text{HO}_2$  and  $\text{RO}_2$ . In the case of CO, the  $\text{CO} + \text{OH}$  reaction produces only  $\text{HO}_2$ . By contrast, when cyclohexane is used as the OH scavenger, an alkylperoxy radical is formed:



When 2-butanol is used as the OH scavenger, either  $\text{HO}_2$  or  $\text{RO}_2$  is formed, which in the case of OH abstraction of a H atom from two of the different carbon atoms in 2-butanol leads to:



For these reactions, formation of  $\text{HO}_2$  is the major channel, with a branching ratio of  $\sim 70\%$ .

The  $\text{HO}_2/\text{RO}_2$  ratio from each of the scavengers ( $\text{CO} > \text{2-butanol} > \text{cyclohexane}$ ) matches that of the SOA yields, suggesting that increased formation of  $\text{HO}_2$  and/or decreased formation of  $\text{RO}_2$  favors SOA formation. In short, the  $\text{RO}_2$  radical from the ozonolysis reaction and the  $\text{HO}_2$  and/or  $\text{RO}_2$  from the OH-scavenger reaction promote the ensuing radical chemistry. In the absence of  $\text{NO}_x$ , the chemistry consists largely of self- and cross-reactions of peroxy species, i.e.,  $\text{HO}_2 + \text{HO}_2$ ,  $\text{RO}_2 + \text{RO}_2$ , and  $\text{HO}_2 + \text{RO}_2$ .

The cyclohexene- $\text{O}_3$  results show that selection of an OH scavenger in an ozone-alkene system must be made with careful attention to the subsequent chemistry that occurs following the scavenger-OH reaction.

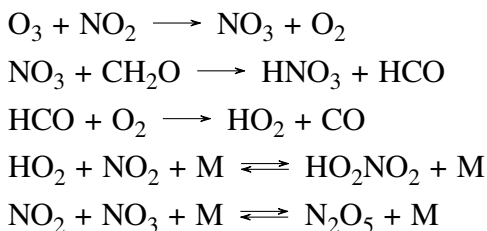
### **$\text{NO}_3$ Oxidation**

An important class of chamber oxidation studies involves the nitrate radical  $\text{NO}_3$  as the oxidant. Such studies are especially germane to nighttime chemistry. Because of its strong oxidizing capacity and its relatively high nighttime concentration, the  $\text{NO}_3$  radical can play an important role in the nighttime removal of alkenes. Although the reaction of  $\text{NO}_3$  with alkenes is 10 to 1000 times slower than that with OH,  $\text{NO}_3$  can be present in sufficiently high concentrations at night so that the overall consumption

of alkenes can be comparable for OH and NO<sub>3</sub>. Alkenes react predominantly with NO<sub>3</sub> through addition to the double bond, yielding an alkyl radical that rapidly adds O<sub>2</sub> to produce a nitratoalkyl peroxy radical. The high alkyl nitrate yields lead to significant loss of atmospheric NO<sub>x</sub>.

Two routes used to generate NO<sub>3</sub> *in situ* in chambers are: (1) decomposition of N<sub>2</sub>O<sub>5</sub>; and (2) reaction of O<sub>3</sub> and NO<sub>2</sub>. After initial NO<sub>3</sub> reaction with the organic of interest, the fate of the nitratoalkyl peroxy radical depends on the composition of the mixture in the chamber. Either of these two routes of generation of NO<sub>3</sub> optimizes conditions for RO<sub>2</sub> + NO<sub>3</sub> or RO<sub>2</sub> + RO<sub>2</sub>. Some HO<sub>2</sub> is expected to form from later-generation chemistry in these chamber experiments, but this is not sufficient to establish a dominant regime of RO<sub>2</sub> + HO<sub>2</sub> chemistry. This regime is expected to be important in nighttime chemistry, since HO<sub>2</sub> is not removed at night as effectively as OH. For example, in the BEARPEX field campaign, (Mao et al., 2012) estimated HO<sub>2</sub> mixing ratios at night to be ~4 ppt, while NO<sub>3</sub> mixing ratios were estimated as ~1 ppt (Bouvier-Brown et al., 2009). These observations suggest that RO<sub>2</sub> + HO<sub>2</sub> chemistry is important in the nighttime.

In order to optimize for the RO<sub>2</sub> + HO<sub>2</sub> pathway, formaldehyde (CH<sub>2</sub>O) can be injected into the chamber along with O<sub>3</sub> and NO<sub>2</sub>. Formaldehyde will react with NO<sub>3</sub> to form HCO, and HCO will react immediately with O<sub>2</sub> to form HO<sub>2</sub>:



Production of NO<sub>3</sub> and HO<sub>2</sub> are coupled through the formaldehyde reaction in such a manner that the ratio of NO<sub>3</sub> to HO<sub>2</sub> can be controlled throughout the experiment. It is still necessary to employ kinetic simulation to estimate the relative pathways of reaction of the RO<sub>2</sub> radicals produced by the initial NO<sub>3</sub> reaction. The high aldehyde concentrations can also impact aqueous/aerosol phase chemistry.

## 2.5 Secondary Organic Aerosol (SOA) Formation

Secondary organic aerosol (SOA) forms when volatile organic compounds (VOCs) are oxidized to yield products of sufficiently low volatility to condense into the particulate phase. This transformation rarely occurs in a single reaction step; rather, oxidation products undergo progressive oxidation steps, leading to products of de-

creasing volatility. The atmospheric evolution that leads to SOA can be described in terms of the number of oxidation steps undergone, or the “generation number” of products formed. In an alternative route to SOA formation, low molecular weight, water-soluble VOCs can dissolve in droplets or particles wherein they undergo oxidation to products that remain in the aqueous phase as dissolved SOA. When a droplet containing dissolved SOA eventually evaporates, a residual aerosol particle rich in oxidized organics remains. While experiments addressed at understanding aqueous-phase pathways to SOA formation have tended to employ “beaker scale” systems, studies with moist aerosols and in chambers are starting to emerge.

In the absence of a seed aerosol, low volatility VOC oxidation products may accumulate in the chamber until a point is reached at which homogeneous nucleation of these products occurs. (The point at which nucleation occurs in a VOC system depends crucially on the VOC itself and the nature of its oxidation products.) Experiments carried out in the absence of a seed aerosol are useful for determining the density of the pure secondary organic aerosol, since the particles will consist exclusively of organic oxidation products. In the absence of a seed aerosol, the nucleated particles tend to concentrate in a range of relatively small particle sizes that may present measurement challenges. In addition, smaller sized particles are more prone to loss by deposition on the wall of the chamber than larger particles (see Section 2.6).

From the point of view of measurement of the aerosol size distribution, it is often useful to employ a seed aerosol (for example, ammonium sulfate, ammonium bisulfate, sulfuric acid, sodium chloride, etc.) to maintain particle sizes in the region above 100 nm diameter, which is where conventional aerosol particle-size instrumentation is most accurate. Seeded experiments also facilitate condensation of oxidized organics more readily than when vapors must accumulate until homogeneous nucleation occurs. The earlier particle growth stimulated by the presence of seed aerosol also promotes condensation of vapors onto growing particles as opposed to the walls of the chamber. (SOA formation in the atmosphere also occurs in the presence of pre-existing aerosol.) The use of aerosol mass spectrometry allows direct measurement of the organic-to-inorganic mass ratio, which allows one to quantify the extent of particle deposition onto the walls of the chamber through a mass balance on the suspended inorganic concentration. By control of relative humidity with an inorganic seed aerosol, if an aqueous phase is desired in the particles, experiments can be conducted at an RH above the deliquescence RH of the

inorganic seed.

Ordinarily, an SOA formation chamber experiment is continued for several hours after the parent VOC is consumed, since the oxidation products themselves generally continue to react with the oxidant (usually OH) forming additional low volatility products and SOA. At the termination of the experiment, the *SOA yield* is customarily determined as the ratio of the mass concentration of SOA formed to the mass concentration of the parent VOC reacted. This single quantity is the manifestation of all the phenomena involved: gas-phase chemistry, particle-phase chemistry, compound volatility, etc. SOA yields exhibit a complex dependence on VOC-to-NO<sub>x</sub> ratio, VOC concentration and volatility, and oxidant exposure. While the definition of the SOA yield is straightforward, its determination is complicated by two phenomena that are a consequence of the presence of chamber walls. First, during the course of an experiment, the particles, which contain both the inorganic seed and condensed VOC oxidation products, deposit irreversibly onto the walls of the chamber. Thus, the aerosol suspended in the chamber at the termination of an experiment does not reflect fully the extent of SOA formation, since a portion of the SOA that formed is on the walls of the chamber. In computing the actual SOA yield, it is necessary to account for the SOA that has deposited on the chamber walls. Section 2.6 addresses particle deposition onto chamber walls and the computation of the SOA mass concentration accounting for that deposition. Secondly, the low volatility gas-phase oxidation products that condense on the particles to constitute SOA are themselves subject to deposition on the walls of the chamber (Section 2.7). In the absence of walls, these compounds would contribute to the SOA mass formed, so it is necessary to estimate the effect of vapor wall deposition to determine the actual SOA yield.

In chamber experiments it is desirable to mimic the degree of atmospheric oxidant exposure, the integral of the oxidant (e.g. OH) concentration and the reactor residence time. Environmental chambers operate at OH concentrations in the range of  $10^6$  to  $10^7$  molecules  $\text{cm}^{-3}$ , which are roughly equal to ambient daytime concentrations. Chamber experiments are ultimately limited in duration by wall deposition of particles and vapors to the order of 24–36 h or so. As a result, SOA chamber formation experiments tend to simulate an oxidant exposure of about a day or two.

## 2.6 Particle Deposition onto Chamber Walls

### Experimental Determination of Particle Wall Deposition Rates

Suspended particles in the chamber are transported to the walls by diffusion, gravitational settling and electrostatic forces (Crump et al., 1981; McMurry and Rader, 1985b). The particle wall deposition rate can be measured directly in wall deposition experiments, which is a routine procedure in most environmental chambers. Calibration particles over a range of sizes are often generated by atomizing aqueous ammonium sulfate solution ( $(\text{NH}_4)_2\text{SO}_4$ ) into the chamber. Figure 2.15 shows the hourly-averaged temporal profiles of the particle number distribution as a result of particle deposition to the chamber walls in the Caltech chamber. For a population of particles with diameters ranging from 10 nm to 1000 nm, those at an intermediate size exhibit the minimum deposition rate, which is a consequence of the combined effects of turbulent mixing in the chamber, particle diffusivity, and particle settling velocity.

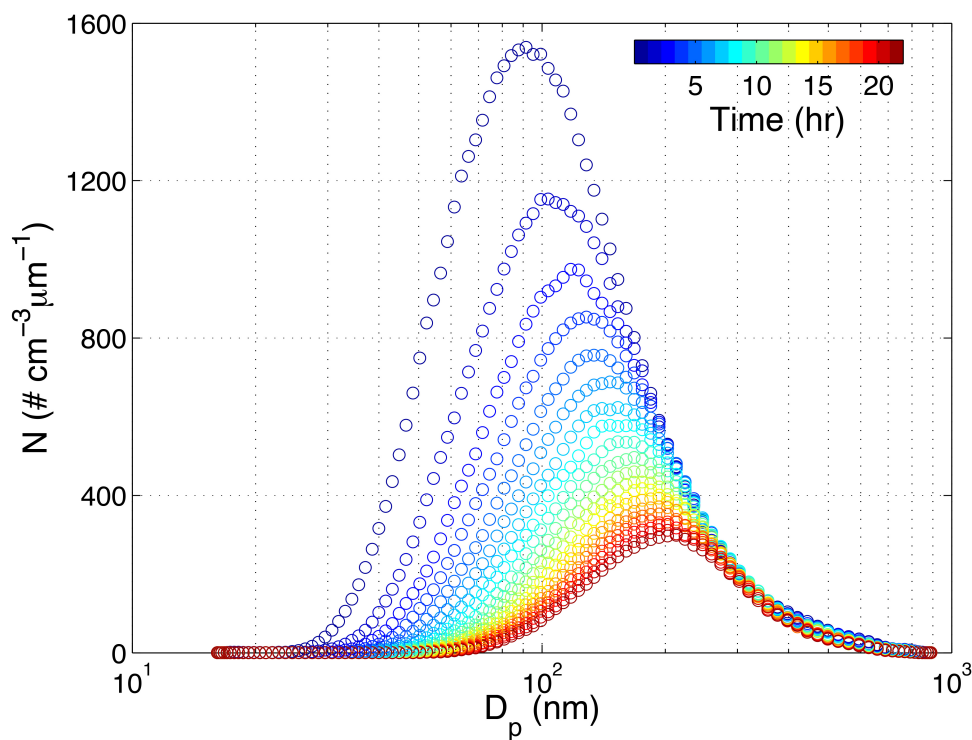


**Figure 2.15:** Temporal profiles of particle number distribution as a result of particle wall deposition.

The decay of particle number concentration in each size range is subsequently fitted to a first-order loss model in terms of a size-dependent wall loss rate coefficient,  $\beta_i$ ,

$$n_{s,i} = n_{0,i} \times \exp(-\beta_i t) \quad (2.1)$$

where  $n_{s,i}$  is the suspended particle number distribution in size bin  $i$  at time  $t$ , and  $n_{0,i}$  is the initial particle number distribution in size bin  $i$ . Figure 2.16 (panel a) shows the measured as well as fitted deposition rate of particles at  $D_p = 80$  nm as an illustration. Extending this analysis to particles over the complete range of relevant sizes will give the size-dependent particle wall deposition rate coefficients, as shown in Figure 2.16 (panel b). In the Caltech chamber, particle wall deposition rate coefficients are of the order of  $10^{-4}$  to  $10^{-2} \text{ min}^{-1}$ , that is, the half-life with respect to particle wall deposition ranges from  $\sim 70$  min to  $\sim 5$  d, depending on particle size. It is advantageous when carrying out experiments to generate SOA to employ seed aerosol that causes the size distribution of the SOA-containing particles to focus in the vicinity of the minimum of  $\beta_i(D_p)$ .

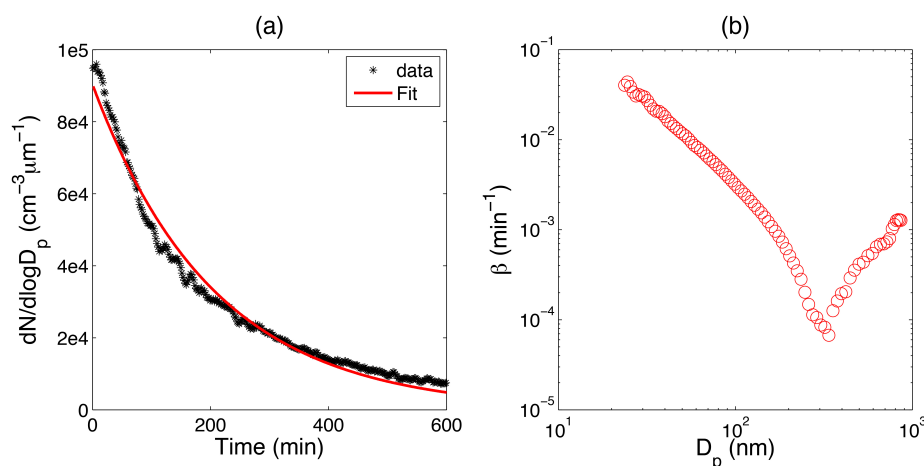


**Figure 2.16:** Determination of the particle-wall deposition rate constant. Panel A: Observed and fitted particle number concentration decay at  $D_p = 80$  nm. Panel B: Best-fit  $\beta$  as a function of particle diameter.

Throughout an experiment, the volume of the chamber decreases due to sampling, but the surface area of the walls remains the same. The increasing surface area-to-volume ratio might lead to an increase in the particle wall loss rates. The duration of a typical wall loss experiment is 18–24 h, shorter than that of the longest SOA aging experiments. To confirm that wall loss rates do not vary significantly as chamber volume decreases, an additional wall loss calibration experiment can be performed. These calibration experiments were conducted following the same protocol as a typical wall loss calibration; however, before ammonium sulfate seed aerosol is

injected, approximately 8 m<sup>3</sup> of air was removed from the chambers to simulate conditions at the end of an 18 h experiment. The wall loss rates determined from these lower-volume experiments were within the range of those observed in the fully inflated chambers.

### **SOA Yields Accounting for Particle Wall Deposition**

As noted earlier, to determine the total SOA mass concentration at the termination of a chamber experiment, particle wall losses must be taken into account. An inherent uncertainty exists in making this accounting: while the particle deposition is irreversible, the extent to which the deposited particles continue to interact with the gas-phase in the chamber remains uncertain. This uncertainty has given rise to two limiting assumptions concerning the estimate of the extent to which particle wall deposition affects the SOA yield (see, for example, Weitkamp et al. (2007), Hildebrandt, Donahue, et al. (2009) and Hildebrandt, Henry, et al. (2011), Loza, Chhabra, et al. (2012) and Loza, Craven, et al. (2014)).

In one limit, particles deposited on the wall are assumed to cease interaction with suspended vapors after deposition. In this case, the amount of organic material in the deposited particles does not change after deposition, and these particles remain at the same size at which they deposited for the remainder of the experiment. In the other limit, particles on the wall are assumed to continue to interact with vapors in the chamber after deposition as if they had remained suspended. Thus, in this case, the amount of organic material in the particles after deposition changes at the same rate as the amount of organic material in the suspended particles, and the deposited particles are assumed to continue to grow throughout the remainder of the experiment. This limit is analogous in theory to that of a chamber without walls. In either limit, the material on the walls is added to that which remains suspended at the end of the experiment to obtain the total amount of SOA formed. The extent to which salts that have deposited to chamber walls may continue to interact with chamber contents is unknown.

During particle growth, if an inorganic seed is present, the organic mass fraction of the suspended particles increases. In the first limit, the organic mass fraction of deposited particles ceases changing after particle deposition; therefore, this case produces a lower limit for SOA mass. In the second limit, deposited particles are assumed to continue growing; therefore, this case represents an upper limit for SOA mass. These two limits of wall loss corrected SOA mass are referred to as the *lower*



*bound* and *upper bound*, respectively.

The first limiting assumption has been widely used in analyzing data in chamber experiments. The size-dependent wall deposition rate coefficient ( $\beta_i$ ) estimated earlier can be applied to chamber experiments for particle wall loss correction. (A key assumption here is that particles of the same size, regardless of the chemical nature, exhibit the same deposition rate. It should be noted that particles of different phase states might have different affinities for the wall. For examples, solid particles might bounce off the wall instead of sticking onto the walls with unity accommodation coefficient.) For each size bin  $i$ , the number distribution of particles deposited to the wall ( $n_{w,i,j}$ ) over the time increment  $\Delta t$  from time step  $j$  to time step  $j + 1$ , is

$$n_{w,i,j} = n_{s,i,j}[1 - \exp(-\beta_i \Delta t)] \quad (2.2)$$

where  $n_{s,i,j}$  is the suspended particle number distribution in size bin  $i$  at time step  $j$ . The number distribution of deposited particles ( $n_{w,i,j}$ ) is added to the suspended particle number distribution ( $n_{s,i,j}$ ) to give the total particle number distribution ( $n_{tot,i,j}$ ),

$$n_{tot,i,j} = n_{w,i,j} + n_{s,i,j} \quad (2.3)$$

The total number concentration in size bin  $i$  at time step  $j$  ( $N_{tot,i,j}$ ) can be calculated by converting the number distribution based on  $d(\ln D_p)$  to  $d(D_p)$ ,

$$N_{tot,i,j} = \frac{n_{tot,i,j}}{D_{p,i} \ln 10} (D_{p,i+} - D_{p,i-}) \quad (2.4)$$

where  $D_{p,i}$  is the median particle diameter for size bin  $i$ ,  $D_{p,i+}$  is the upper limit of particle diameter for size bin  $i$ , and  $D_{p,i-}$  is the lower limit of particle diameter for size bin  $i$ . Assuming spherical particles, the total volume concentration at time step  $j$  ( $V_{tot,j}$ ) is:

$$V_{tot,j} = \sum_i \frac{\pi}{6} D_{p,i}^3 \times N_{tot,i,j} \quad (2.5)$$

The total organic mass ( $\Delta M_{o,j}$ ) at time step  $j$  can be obtained by,

$$\Delta M_{o,j} = \rho_p (V_{tot,j} - V_{seed}) \quad (2.6)$$

where  $\rho_p$  is the average particle density, and  $V_{seed}$  is the volume concentration of seed particles injected at the beginning of the experiment.

The upper bound limit on SOA mass is calculated by combining data from on-line aerosol mass spectrometry (the Aerodyne Aerosol Mass Spectrometer, AMS) and particle size distribution measurement (e.g., the Differential Mobility Analyzer, DMA, see Section 11). In experiments that utilize seed particles containing sulfate, the only process that decreases sulfate concentration in the suspended phase is wall deposition. The initial sulfate concentration is determined from the initial seed volume concentration. (Collection efficiency in the AMS increases as organic content of the particles increases, and because the seed particles usually do not contain organic material, they are more susceptible to bounce in the instrument and exhibit a collection efficiency that is less than unity (Matthew et al., 2008)). To calculate the mass of sulfate in the seed,  $m_{SO4}$ , the following equation is used,

$$m_{SO4} = V_{seed} \rho_{seed} \frac{MW_{SO4}}{MW_{seed}} \quad (2.7)$$

where  $\rho_{seed}$  is the density of the seed particles,  $MW_{SO4}$  is the molecular weight of sulfate, and  $MW_{seed}$  is the molecular weight of the seed particles. For dry AS seed,  $\rho_{seed} = 1.77 \text{ g cm}^{-3}$ . In the upper bound limit, both suspended and deposited particles are assumed to gain or lose organic material at the same rate; therefore, the organic-to-sulfate ratio of all particles of the same size is the same, and this ratio can be determined from unit mass resolution AMS data. (Differences in the organic-to-sulfate ratio,  $r_{OS}$ , between unit mass resolution and high-resolution data are less than 5%, except possibly during the early period of growth when organic loading is low.) To obtain the SOA mass,  $r_{OS}$  is multiplied by the initial mass of sulfate in the seed particles,

$$\Delta M_o = m_{SO4} r_{OS} \quad (2.8)$$

This equation is valid if the organic-to-sulfate ratio does not vary with particle size or if particle wall loss rates are constant over the particle size range of interest. When particle wall deposition rates depend on particle size, as they usually do, the latter assumption is not valid. Depending on the condensation behavior of the SOA,  $r_{OS}$  may depend on particle size (Hildebrandt, Donahue, et al., 2009; Riipinen et al., 2011).

The Aerosol Parameter Estimation (APE) model (Pierce et al., 2008) has been employed to compute the wall deposition corrected SOA yield under the upper limit assumption (Loza, Craven, et al., 2014). The suspended particle population evolves as a result of three processes: coagulation, condensation, and wall deposition (J. H. . Seinfeld et al., 2006),

$$\frac{\partial n_s(D_p, t)}{\partial t} = \left(\frac{\partial n_s(D_p, t)}{\partial t}\right)_{coagulation} + \left(\frac{\partial n_s(D_p, t)}{\partial t}\right)_{condensation} + \left(\frac{\partial n_s(D_p, t)}{\partial t}\right)_{wallloss} \quad (2.9)$$

where  $n_s(D_p, t)$  is the suspended particle number distribution. The change of suspended particle number distribution due to coagulation is,

$$\begin{aligned} \left(\frac{\partial n_s(D_p, t)}{\partial t}\right)_{coagulation} = & \frac{1}{2} \int_0^{D_p} K((D_p^3 - q^3)^{\frac{1}{3}}, q) \times n_s(D_p^3 - q^3)^{\frac{1}{3}}, t) n_s(q, t) dq \\ & - n_s(D_p, t) \int_0^{\infty} K(q, D_p) n_s(q, t) dq \quad (2.10) \end{aligned}$$

where  $K(D_{p1}, D_{p2})$  is the coagulation coefficient for collision of particles of diameters  $D_{p1}$  and  $D_{p2}$ . The first term of equation (2.10) represents the formation of particles with diameter  $D_p$  from the coagulation of smaller particles, and the second term represents the loss of particles with diameter  $D_p$  due to collisions with all available particles. The change of the suspended particle number distribution owing to wall deposition is represented by the first-order loss model as described earlier. The continuous form of this model can be written as,

$$\left(\frac{\partial n_s(D_p, t)}{\partial t}\right)_{wallloss} = -\beta(D_p) n_s(D_p, t) \quad (2.11)$$

The change of suspended particle number distribution due to condensation is given by,

$$\left(\frac{\partial n_s(D_p, t)}{\partial t}\right)_{condensation} = \frac{\partial}{\partial D_p} [I(D_p, t) n_s(D_p, t)] \quad (2.12)$$

where  $I(D_p, t)$  is the change in particle diameter due to condensation,

$$I(D_p, t) = \frac{dD_p}{dt} = \sum_i \frac{4\mathcal{D}_i MW_i}{RT D_p \rho_p} f(Kn, \alpha) (p_{\infty, i} - p_{s, i}) \quad (2.13)$$

where  $\mathcal{D}_i$  is the diffusion coefficient of species  $i$  in air,  $MW_i$  is the molecular weight of species  $i$ ,  $R$  is the gas constant,  $T$  is the temperature,  $f(Kn, \alpha)$  is a correction factor for non-continuum transport and imperfect surface accommodation,  $p_{\infty,i}$  is the partial pressure of species  $i$  in the bulk gas,  $p_{s,i}$  is the vapor pressure of species  $i$  over the particle surface,  $Kn$  is the Knudsen number ( $2\lambda/D_p$ ),  $\alpha$  is the accommodation coefficient for the species on the particle surface, and  $\lambda$  is the mean free path of the diffusing species. (See Table 2.4 for a listing of parameters and variables.) The mean free path of air molecules is  $\sim 70$  nm at 298 K, and diameters of particles of interest in chamber studies range from 10 nm to 1  $\mu$ m. Substituting equation (2.13) into equation (2.12) gives,

$$\left(\frac{\partial n_s(D_p, t)}{\partial t}\right)_{condensation} = -F_c \left[ \frac{1}{D_p^2} n_s(D_p, t) + \frac{1}{D_p} \frac{\partial n_s(D_p, t)}{\partial D_p} \right] \quad (2.14)$$

where the parameter  $F_c$  can be considered as a characterization of the condensation rate, and the expression of  $F_c$  includes all the unknown parameters in equation (2.14),

$$F_c = \sum_i \frac{4\mathcal{D}_i MW_i}{RT \rho_p} f(Kn, \alpha) (p_{\infty,i} - p_{s,i}) \quad (2.15)$$

The value of  $F_c$  can be obtained by optimal fitting of the APE model predictions to the measured particle size distribution at each time step over the course of the experiment. Once the  $F_c$  values are estimated, they can be applied to parameterize the growth of particles on the walls due to condensation of gaseous vapor and deposition of suspended particles (note that coagulation of particles deposited on the walls is not considered). A factor  $\Phi$  can be introduced to describe the extent of interaction between deposited particles and suspended vapors and is applied when summing aerosol masses in the chamber core and on the walls. As noted above, the upper limit estimate accounts for the maximum vapor transport to particles deposited on chamber walls by assuming the interaction of deposited particles with vapors is the same as that for suspended particles. The magnitude of vapor wall condensation on deposited particles is potentially overestimated under this assumption because the effect of a finite time-scale for vapor transport through the boundary layer adjacent to the wall is not accounted for (see Section 2.7).

Figure 2.17 gives an example of the SOA yield (expressed as the total organic aerosol mass formed,  $\Delta M_o$ , vs. the total hydrocarbon mass reacted,  $\Delta \text{VOC}$ ) from

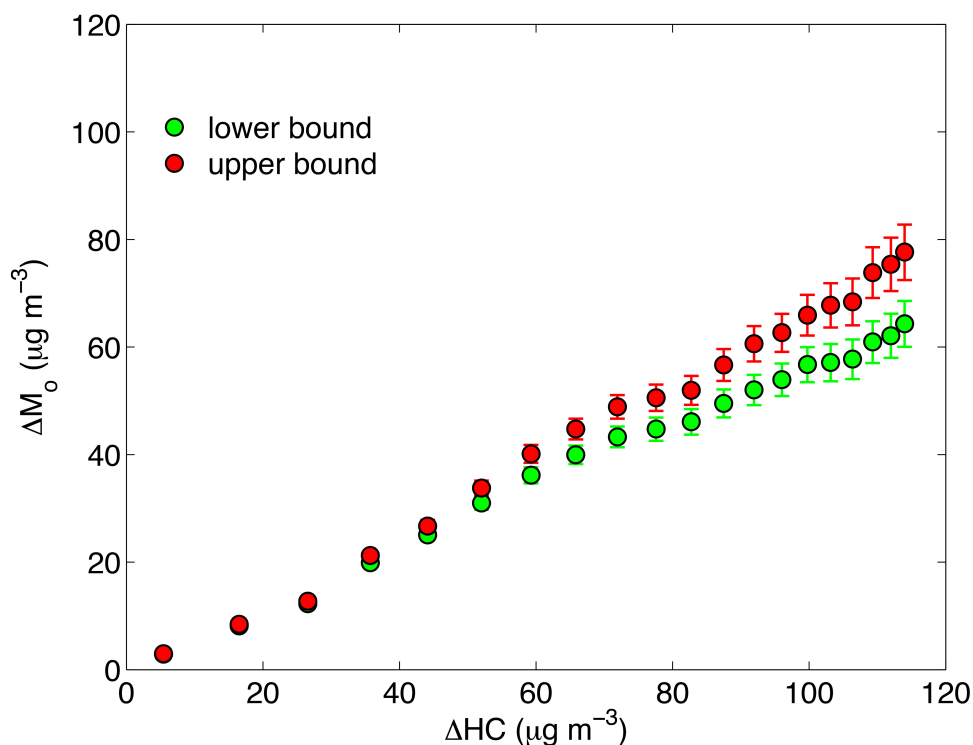


**Figure 2.17:** SOA yield (expressed as the total organic aerosol mass formed,  $\Delta M_o$ , vs. the total hydrocarbon mass reacted,  $\Delta\text{HC}$ ) from the photooxidation of toluene under low-NO conditions with both upper- and lower-bound particle wall deposition corrections. The error bars represent the 95% confidence interval from the particle wall deposition rate constant  $\beta$  fitting to experimental deposition data.

the photooxidation of toluene under low-NO conditions with both upper- and lower-bound particle wall deposition corrections estimated by the APE model. Specifically, the DMA measured particle number distribution at each timestep is used to optimize the single adjustable parameter  $F_c$  in the APE model. Thus  $F_c$  is regarded as a characterization of 1) the diffusion of gas-phase organic vapors to the particle surface and 2) subsequent uptake by particles at different sizes. When applying the best-fit  $F_c$  value to represent interactions of organic vapors with particles deposited on the chamber wall, the scaling factor  $\Phi$  is employed. When  $\Phi = 0$ , particles deposited on the walls cease to interact with gas-phase molecules and the particle size distribution remain the same as at the moment they deposited on the chamber wall. Summing up particle masses in the chamber air and on the chamber wall gives SOA yields with lower bound correction. When  $\Phi = 1$ , the growth rate of deposited particles due to interaction with organic vapors is assumed to be identical with that for

suspended particles. The overall SOA masses on the chamber wall result from two processes: deposition of suspended particles and condensation of organic vapors. As a result, SOA yield with upper bound correction can be derived as if no chamber wall exists. For the system shown in Figure 2.17, the SOA yields with upper bound corrections are, on average, 1.13 times higher than those corrected under the lower limiting assumption.

**Table 2.4:** Variables and Parameters Important in the Environmental Chamber

| Variable         | Description  |
|------------------|--|
| $\beta(D_p)$     | Particle wall deposition rate coefficient, as a function of particle diameter $D_p$                    |
| $\beta_i$        | Particle wall deposition rate coefficient, for diameter range $D_{pi}$                                 |
| $n_{w,i,j}$      | Number distribution of particles in size bin i deposited to the wall over time step $t_j$ to $t_j + 1$ |
| $n_{s,i,j}$      | Number distribution of suspended particles in size bin i at time step $t_j$ , or $n_s(D_p, t)$         |
| $n_{tot,i,j}$    | Total number distribution of particles in size bin i at time step $t_j$                                |
| $N_{tot,i,j}$    | Total number concentration of particles in size bin i at time step $t_j$                               |
| $D_{p,i}$        | Median particle diameter for size bin i  |
| $\Delta M_{o,j}$ | Total organic mass concentration at time $t_j$   |
| $V_{tot,j}$      | Total particle volume concentration at time $t_j$  |
| $V_{seed}$       | Volume concentration of seed aerosol   |
| $\rho_p$         | Average particle density   |
| $m_{SO4}$        | Mass concentration of sulfate in seed aerosol  |
| $\rho_{seed}$    | Density of seed aerosol  |
| $MW_{SO4}$       | Molecular weight of $SO_4$   |
| $MW_{seed}$      | Molecular weight of seed aerosol   |
| $r_{os}$         | Organic to sulfate ratio   |
| $\Delta M_o$     | Secondary Organic Aerosol (SOA) mass concentration   |
| $K(D_p, D'_p)$   | Brownian coagulation coefficient   |
| $I(D_p, t)$      | Rate of growth of particle of diameter $D_p$ by condensation of vapor                                  |
| $MW_i$           | Molecular weight of species i  |
| R                | Gas constant   |
| T                | Temperature  |
| $\lambda$        | Mean free path (for a formula see Table 5)   |
| $K_n$            | Knudsen number ( $2\lambda/D_p$ )  |

**Table 2.4:** Variables and Parameters Important in the Environmental Chamber

| Variable           | Description   |
|--------------------|---|
| $f(K_n, \alpha_p)$ | Correction factor for non-continuum transport (for formula see Table 5) |
| $\alpha_{p,i}$     | Accommodation coefficient for vapor species i on a particle             |
| $\alpha_{w,i}$     | Vapor-wall accommodation coefficient                                    |
| $p_{\infty,i}$     | Partial pressure of species i in the bulk gas                           |
| $p_{s,i}$          | Vapor pressure of species i over the particle surface                   |
| $C_w$              | Equivalent absorbing organic mass on the chamber wall                   |
| $\bar{C}_{v,i}$    | Concentration of vapor species i in the well-mixed core of the chamber  |
| $\bar{C}_{w,i}$    | Concentration of vapor species i in the thin layer adjacent to the wall |
| $A / V$            | Surface area-to-volume ratio of chamber                                 |
| $D_i$              | Molecular diffusivity of species i in air                               |
| $K_e$              | Coefficient of eddy diffusion in chamber                                |
| $\bar{C}_{tot,i}$  | Total concentration of vapor species i generated                        |
| $K_{w,i}$          | Gas-aerosol partitioning coefficient of species i                       |
| $\bar{c}_i$        | Molecular mean speed (for formula see Table 5)                          |

## 2.7 Vapor Deposition on Chamber Walls

Vapor molecules generated in the course of VOC oxidation can be removed upon contact with chamber walls. Whereas the rate of particle wall deposition depends essentially exclusively on particle size, deposition of vapor molecules on the wall varies in a complex, and generally unknown, manner depending on the chemical nature of the molecule and the nature of the wall itself. One hypothesis is that organic oxidation products can deposit to form a coating on the wall that acts as a medium for further absorption. In the case of a Teflon-walled chamber, it has also been hypothesized that the Teflon film itself can act as an absorbing medium, in a process akin to the sorption of small molecules by organic polymers. In order to formulate a model of vapor wall deposition, the microscopic nature of vapor-wall interactions need not be understood in detail, as the physico-chemical parameters that arise in the theory of vapor wall deposition must ultimately be determined from experimental data.

### Theoretical Description of Vapor Wall Deposition

Vapor molecules are transported from the well-mixed core of a chamber through a thin layer adjacent to the walls by a combination of molecular and turbulent diffusion. The transport rate across this layer depends on both the molecular properties of individual compounds, as well as the extent of mixing in the chamber. As a vapor molecule (species  $i$ ) encounters the chamber wall, the fraction of those encounters that lead to uptake is represented by the vapor wall accommodation coefficient ( $\alpha_{w,i}$ ), which depends, in principle, on the nature of the wall surface as well as the chemical nature of the vapor molecule. Species deposited on the walls may, in principle, re-evaporate, eventually leading to equilibrium between the gas-phase and the wall.

The rate at which gas-wall equilibrium is approached can be evaluated with a simple kinetic model that assumes a concentration of the deposited vapor in the wall layer can be defined. We define for a species A:

$A_g$ : concentration of species A in the gas-phase

$A_w$ : concentration of species A in the wall

$A_{Tot}$ : total concentration of species A, in both the gas-phase and the wall

$(\frac{A_g}{A_{Tot}})_{eq}$ : ratio of species present in the gas-phase to the total at equilibrium

$k_F$ : forward rate constant for vapor wall deposition

$k_R$ : reverse rate constant for evaporation from wall

The equations describing the dynamics of  $A_g$  and  $A_w$  are:

$$\frac{dA_g}{dt} = -k_F A_g + k_R A_w$$

$$A_w = A_{Tot} - A_g$$

$$\frac{dA_g}{dt} = -(k_F + k_R) A_g + k_R A_{Tot}$$

The general solution is

$$\frac{A_g}{A_{Tot}} = (\frac{A_g}{A_{Tot}})_{eq} + (1 - \frac{A_g}{A_{Tot}})_{eq} e^{-(k_F + k_R)t}$$

The time scale governing the approach to gas-wall equilibrium is

$$\tau_{gw} = \frac{1}{k_f + k_R}$$

The chamber walls have been characterized by a parameter defined as the equivalent absorbing organic mass on the wall ( $C_w$ ) (Matsunaga et al., 2010), which is analogous to the concentration of absorbing aerosol mass, in gas-particle equilibrium



partitioning theory (J. Seinfeld et al., 2003). Then, the time scale for approach to gas-wall equilibrium is

$$\tau_{gw} = \frac{1}{k_f(1 + \frac{C^*}{C_w})}$$

where  $C^*$  is the effective equilibrium mass concentration of the species at the temperature of interest. The time at which the wall concentration of deposited vapor reaches 90% of its equilibrium value is given by  $-\log(0.1)/(k_F + k_R)$ .

The above development assumes that a concentration of the vapor species in the wall layer can be defined. If  $C_w$  is sufficiently large, the wall presents essentially an infinite absorbing medium, and the concentration of the vapor species in the wall is effectively zero. In this case, vapor wall deposition is ultimately an irreversible process, and the reversible analysis above does not apply. It is important to note that the concept of an ‘equivalent absorbing organic mass’ does not necessarily imply that an actual layer of organic material exists on the chamber wall. In the case of a Teflon-walled chamber, the quantity  $C_w$  can be regarded simply as a proxy for the equilibrium solubility of individual organic molecules in FEP Teflon polymer.

The simple kinetic model above can be replaced by one that defines the quantities involved in the wall deposition process more explicitly. A dynamic balance on the concentration of vapor species  $i$  in the chamber,  $\bar{C}_{v,i}$ , that is undergoing solely wall deposition is (McMurry and Grosjean, 1985a; Zhang, Schwantes, et al., 2015),

$$\frac{d\bar{C}_{v,i}}{dt} = \left(\frac{A}{V}\right) \left( \frac{\alpha_{w,i}\bar{c}_i/4}{\pi\alpha_{w,i}\bar{c}_i/8(\mathcal{D}_i K_e)^{1/2} + 1} \right) \left( \frac{\bar{C}_{tot,i} - \bar{C}_{v,i}}{K_{w,i}C_w} - \bar{C}_{v,i} \right) \quad (2.16)$$

where this equation expresses the rate of change of the concentration in the core of the chamber as a result of transport through the wall layer at a rate determined by the difference between the concentration of the species immediately above the wall and that in the core of the chamber. The fraction of encounters at the wall that lead to uptake is represented by the vapor wall accommodation coefficient ( $\alpha_{w,i}$ ).  $K_e$  is the coefficient of eddy diffusion in the well-mixed chamber, and  $\mathcal{D}_i$  is the molecular diffusivity of species  $i$  in air.  $K_{w,i}$  is the gas-aerosol partitioning coefficient of species  $i$ .  $\bar{c}_i$  is the molecular mean speed of species  $i$ .

Figure 2.18 shows two case studies on the simulated wall-induced decay profiles of a semivolatile organic compound  $i$  ( $C^* = 10 \mu\text{g m}^{-3}$ ) under conditions in which the vapor wall interaction is controlled either by  $\alpha_{w,i}$  or  $C_w$ . For case 1, the wall accommodation of compound  $i$  is the limiting step that ultimately governs the overall

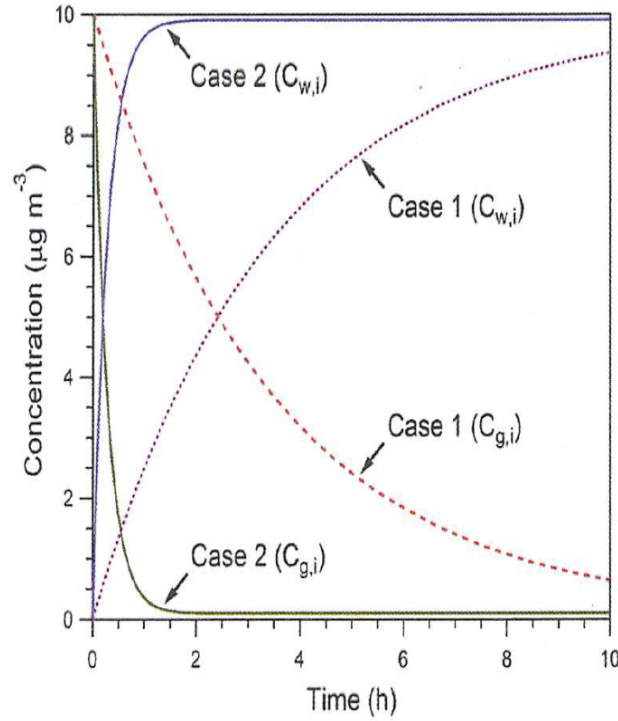


**Figure 2.18:** Computed temporal profiles of semivolatile organic compound  $i$  in the gas phase ( $C_{g,i}$ ) and on the chamber wall ( $C_{w,i}$ ) during 10-h vapor-wall interaction. Conditions for case 1:  $\alpha_{w,i} = 10^{-6}$  and  $C_w = 1 \text{ mg m}^{-3}$ ; and case 2:  $\alpha_{w,i} = 10^{-2}$  and  $C_w = 1 \text{ mg m}^{-3}$

deposition rate. The timescale for approaching gas-wall equilibrium is 18 h. This case has been confirmed by experimental data in the Caltech chambers. For case 2, the chamber wall accommodation of organic vapors is rapid and the vapor flux to the wall can be approximated as a constant that is related to the turbulent mixing state of the chamber. (Yeh et al., 2015), in experiments carried out in their chamber, observe that vapor-wall equilibrium is established rapidly and therefore that  $C_w$  is the sole governing parameter. In the case in which  $\alpha_{w,i}$  is the sole governing parameter, equation (2.16) becomes,

$$\frac{d\bar{C}_{v,i}}{dt} = -\left(\frac{A}{V}\right)\left(\frac{\alpha_{w,i}\bar{C}_i/4}{\pi\alpha_{w,i}\bar{C}_i/8(\mathcal{D}_i K_e)^{1/2} + 1}\right)\bar{C}_{v,i} \quad (2.17)$$

where the first-order vapor wall deposition rate constant for species  $i$  is,

$$k_{w,i} = \left(\frac{A}{V}\right)\left(\frac{\alpha_{w,i}\bar{C}_i/4}{\pi\alpha_{w,i}\bar{C}_i/8(\mathcal{D}_i K_e)^{1/2} + 1}\right) \quad (2.18)$$

Eq (2.18) reveals that two competing physical processes govern the vapor wall deposition rate: (1) gas-phase transport by molecular diffusion and turbulent mixing and (2) transfer across the gas-wall interface. For small  $\alpha_{w,i}$  which leads to the inequality  $\pi\alpha_{w,i}\bar{c}_i/8(\mathcal{D}_iK_e)^{1/2} \ll 1$ , the denominator of Eq (2.18) approaches unity, and Eq (2.18) simplifies to Eq (2.19a) below. In this case, one expects that the flux of vapor molecules to the chamber wall is limited by the accommodation of organic vapors by the wall surface. For large  $\alpha_{w,i}$  which leads to the inequality  $\pi\alpha_{w,i}\bar{c}_i/8(\mathcal{D}_iK_e)^{1/2} \gg 1$ , Eq (2.18) becomes Eq (2.19b) below. In this case, vapor molecules that encounter the wall are efficiently accommodated by the wall surface, and the supply of vapor molecules from the well-mixed core of the chamber becomes the limiting step,

$$k_{w,i} = \begin{cases} (\frac{A}{V})(\frac{\alpha_{w,i}\bar{c}_i}{4}) & \text{(equation a)} \\ \frac{\pi}{2}(\frac{A}{V})(\mathcal{D}_iK_e)^{1/2} & \text{(equation b)} \end{cases} \quad (2.19)$$

The maximum vapor wall deposition rate is eventually approached for highly oxygenated, extremely low-volatility compounds (which are precisely those compounds that are most prone to form SOA). For values of  $\alpha_{w,i} > 10^{-5}$ , the rate of transfer to the wall is limited by the rate of diffusion to the wall rather than surface accommodation (Zhang, C. D. Cappa, et al., 2014; Zhang, Schwantes, et al., 2015).

### Experimental Characterization of Vapor Wall Deposition

Chamber wall-induced decay of individual organic vapors can be measured experimentally. Organic vapors are directly injected by evaporating a known amount of chemical standards into the chamber or produced from photochemistry of the corresponding parent VOC (Matsunaga et al., 2010; Zhang, Schwantes, et al., 2015). Determining the initial vapor concentration is crucial in generating the entire temporal profile of organic vapors due to wall deposition. For the external vapor injection method, the mixing timescale of the chamber is required to be much shorter than that for establishing gas-wall partitioning equilibrium. If organic vapors are generated via photochemistry, a short reaction duration will minimize the interactions of vapors with the chamber wall prior to the onset of vapor-wall deposition. Given the measured vapor wall deposition profile, values for the two unknown parameters in Eq. (2.16),  $\alpha_{w,i}$  and  $C_w$ , can be obtained by optimal fitting of Eq. (2.16) to the observations.

### Correction of SOA Formation Data for Vapor Wall Deposition

In order to accurately predict SOA formation in chemical transport models, experimental data must be corrected for the effects of vapor wall deposition. Because the effects of vapor wall deposition change with species volatility, it is not possible to simply apply a first-order deposition coefficient as in the case of particle wall loss. Rather, an SOA formation experiment must be simulated with a full dynamic model that accounts for time-dependent gas-phase chemistry, vapor-particle condensation, and vapor wall loss. Examples of such models include the Statistical Oxidation Model (SOM) (C. Cappa and K.R., 2012; C. Cappa, Zhang, et al., 2013) and the Generator for Explicit Chemistry and Kinetics of Organics in the Atmosphere (GECKO-A) (Aumont, Szopa, et al., 2015; Aumont, Camredon, et al., 2015). In this section, the basic procedure of correcting SOA formation data will be explained, and then a brief example will be given using the SOM.

The model chosen to correct the data must include time-dependent chemistry. This chemistry can be in the form of a condensed chemical mechanism that has been fit to the experimental data (as in the SOM) or an explicit chemical mechanism (as in the GECKO-A). The model must track the evolving concentrations of individual species, as well as their volatility. The model must additionally include dynamic condensation to particles. Dynamic condensation rather than equilibrium partitioning must be employed because the relative timescales of gas-particle condensation and gas-wall deposition significantly impact the overall effects of this wall deposition (See Section 10). The rate of condensation to particles is controlled by the gas-phase diffusivity and the vapor-particle accommodation coefficient. This accommodation coefficient must be estimated or constrained by modeling, as described below. Condensation to particles is limited by gas-particle equilibrium, which depends on individual species volatilities and the concentration of absorbing aerosol mass. Finally, the model should include reversible vapor wall deposition, characterized by the first-order wall loss rate,  $k_w$ , and the rate of evaporation from the wall, which depends on the species volatility and the absorbing organic mass of the wall,  $C_w$ . Both  $k_w$  and  $C_w$  must be determined experimentally, but can be constrained by modeling the data, as described below.

The model should be used to generate curves of organic aerosol concentration  $C_{OA}$  as a function of time. These curves can then be compared with the experimental results. Sensitivity tests should be conducted for the three unknown parameters: the vapor-particle accommodation coefficient,  $\alpha_p$ , the first-order wall loss rate,  $k_w$ ,

and the absorbing organic mass of the wall,  $C_w$  to determine the optimal values that give the best fit for  $C_{OA}$ . When the predicted  $C_{OA}$  curve matches well with the experimental  $C_{OA}$  curve, the model can then be used to correct for the effects of vapor wall deposition. By setting vapor wall deposition within the model to zero but leaving all other parameters the same, the model can predict  $C_{OA}$  in the absence of vapor wall deposition. Yields determined from this curve are then considered to be the true yields that would be observed in the absence of chamber walls and are thus the appropriate yields to incorporate into chemical transport models.

The approach described above was used in Zhang, C. D. Cappa, et al. (2014) to correct SOA yields using the SOM. The SOM represents the multi-generational oxidation of a volatile organic compound and includes dynamic gas-particle condensation and vapor wall loss. Species are represented using a grid of number of carbon atoms and number of oxygen atoms, with an assigned volatility per grid box. The SOM has six tunable parameters to simulate the gas-phase chemistry: the probability that a reaction leads to fragmentation, the probabilities that a functionalization reaction leads to 1, 2, 3, or 4 oxygen atoms added, and the decrease in vapor pressure per each oxygen added (C. Cappa and K.R., 2012; C. Cappa, Zhang, et al., 2013). Two additional tunable parameters are the vapor-particle accommodation coefficient and the first-order wall loss rate  $k_w$ . In Zhang, C. D. Cappa, et al. (2014), these parameters were varied to provide the optimal fit to experimental  $C_{OA}$  data. When the optimal values were determined, the model was re-run with vapor wall loss set to zero to generate  $C_{OA}$  curves in the absence of vapor wall deposition (See Zhang, C. D. Cappa, et al. (2014), Figures S8, S9, or S10).

## 2.8 The Continuously Mixed Flow Reactor (CMFR)

### The Nature of the CMFR

The CMFR is a well-mixed environmental chamber with continuous feed of reactants and continuous withdrawal of reactor contents. After an initial start-up phase, the reactor is presumed to reach steady state conditions in which the reactor contents are no longer changing with time. For example, in the use of a CMFR to study secondary organic aerosol formation, a VOC/seed aerosol mixture is fed continuously to the reactor, and a comparable flow rate of unreacted VOC and reaction products, including seed aerosol coated with condensed oxidation products, is withdrawn from the reactor. An advantage of the CMFR is that the chamber contents can be sampled for as long a period of time as desired. The mean residence time of air in the chamber is the ratio of the volume of the chamber to the volumetric flow rate of

air.

As in batch mode, particles and vapors in a CMFR are subject to deposition on the walls of the reactor. Wall deposition of particles is irreversible, so this process needs to be accounted for as in the batch chamber. If vapor wall deposition is reversible, wall concentrations of deposited compounds increase until equilibrium between the gas phase and the wall is reached. The time scale associated with the approach of vapor wall deposition to equilibrium is not necessarily the same as the residence time of fluid in the chamber. In order to assess the time scale for approach of the reactor contents to steady state in the presence of vapor wall loss, it is necessary to account for the dynamic processes involving vapors occurring in the chamber. A key parameter in this assessment is  $C_w$ , which controls the wall concentrations of deposited species at equilibrium. Depending on the magnitude of  $C_w$ , vapor-wall equilibrium may or may not be achieved at steady state in the CMFR. For low values of  $C_w$  and semivolatile oxidation products, vapor-wall equilibrium is established within a reasonable timeframe. As the walls approach equilibrium, the net rate of transfer of species to the walls slows and the gas-phase concentrations increase. Therefore, vapor-wall equilibrium is a prerequisite for the CMFR to achieve steady state. If, instead,  $C_w$  is sufficiently large and the products have low volatilities, vapor wall deposition is essentially irreversible. If the walls never saturate, vapor wall loss depresses the SOA yield even at steady state since condensable species are continually being removed by the wall.

The variables, parameters, and governing equations of a CMFR model (in which coagulation is neglected) are given in Table 2.5. We will illustrate the application of this model using idealized gas-phase chemistry in which a VOC (denoted A) reacts to form products B and C of lower vapor pressures according to  $A \longrightarrow B \longrightarrow C$ . To demonstrate that steady state can be achieved even in the absence of vapor-wall equilibrium, we present the results of idealized simulations of the start-up period of a CMFR using the model in Table 2.5 and parameter values in Table 2.6. Wall uptake of vapors is modulated by the value of the equivalent absorbing organic mass on the wall,  $C_w$ . In batch chambers,  $C_w$  has been inferred to lie in the range of 2 and 24  $\text{mg m}^{-3}$  based on individual measured vapor decay rates. Particle wall deposition is represented by a size-dependent first-order loss coefficient, as detailed in Section 2.7. For sufficiently low particle number concentrations, the characteristic time scale for coagulation (see Section 10.2) is much longer than typical reactor residence times, so coagulation can be neglected. Though the vapor-particle accommodation coefficient

$\alpha_{p,i}$  is, in general, species-dependent, for convenience a single value  $\alpha_p$  is used in the simulations. The increase in particle size from the seed particle diameter to that in the chamber is calculated numerically using a moving-bin size distribution based on the total amount of organic aerosol condensed in each size bin (see equation in Table 2.5).

**Table 2.5:** Dynamic Continuously Mixed Flow Reactor (CMFR) Model

| Variables         | Definition  | Units                               |
|-------------------|---|-------------------------------------|
| $A_i^j$           | Organic aerosol concentration of species $i$ in size bin $j$<br>$\frac{dA_i^j}{dt} = -\frac{A_i^j}{\tau} + J_i^j n^j$   | $\mu\text{g m}^{-3}$                |
| $\bar{c}_i$       | Mean molecular speed<br>$\bar{c}_i = \left(\frac{8RT}{\pi M_i}\right)^{1/2}$  | $\text{m s}^{-1}$                   |
| $D_p^j$           | Diameter of particles in size bin $j$<br>$D_p^j = \left(\frac{6}{\pi \rho_p} \left(\frac{\pi}{6} \rho_p (D_{p0}^j)^3 + \frac{\sum_i A_i^j}{n^j}\right)\right)^{1/3}$                      | nm                                  |
| $f(Kn, \alpha_p)$ | Correction factor for non-continuum transport<br>$\frac{0.75\alpha_p(1+Kn)}{Kn^2+Kn+0.283Kn\alpha_p+0.75\alpha_p}$  |                                     |
| $G_i$             | Gas-phase concentration of species $i$<br>$\frac{dG_i}{dt} = \frac{G_{i,0}}{\tau} - \frac{G_i}{\tau} - k[OH]G_i + k[OH]G_{i-1} - k_{wall,on,i}G_i + k_{wall,off,i}W_i - \sum_j J_i^j n^j$ | $\mu\text{g m}^{-3}$                |
| $G_{i,eq}^j$      | Equilibrium gas-phase concentration of species $i$ in size bin $j$<br>$G_{i,eq}^j = \frac{A_i^j C_{i*}}{\sum_k A_k^j + M_{init}^{tot} \frac{n_0^j}{n_0^{tot}}}$                           | $\mu\text{g m}^{-3}$                |
| $J_i^j$           | Rate of condensation of species $i$ onto a particle of diameter $D_p^j$<br>$J_i^j = 2\pi D_i D_p^j (G_i - G_{i,eq}^j) f$  | $\mu\text{g m}^{-3} \text{ s}^{-1}$ |
| $Kn_i^j$          | $Kn_i^j = \frac{2\lambda_i}{D_p^j}$   |                                     |



**Table 2.5:** Dynamic Continuously Mixed Flow Reactor (CMFR) Model

| Variables        | Definition  | Units                         |
|------------------|---|-------------------------------|
| $K_w$            | Gas-wall partitioning coefficient<br>$K_w = \frac{RT}{M_w \gamma_w P_i^0}$  | $\text{m}^3 \mu\text{g}^{-1}$ |
| $k_{wall,on,i}$  | First-order wall deposition coefficient for species $i$<br>$k_{wall,on,i} = \left(\frac{A}{V}\right) \frac{\frac{\alpha_{wall,i} \bar{c}_i}{4}}{1 + \frac{\pi}{2} \left[ \frac{\alpha_{wall,i} \bar{c}_i}{4(K_e D_i)^{0.5}} \right]}$ | $\text{s}^{-1}$               |
| $k_{wall,off,i}$ | First-order wall desorption coefficient for species $i$<br>$k_{wall,off,i} = \frac{k_{wall,on,i}}{K_w C_w} = k_{wall,on,i} \left( \frac{C_i^* M_w \gamma_w}{C_w M_p \gamma_p} \right)$  | $\text{s}^{-1}$               |
| $\lambda_i$      | Mean free path<br>$\lambda_i = \frac{3D_i}{\bar{c}_i}$  | $\text{m}$                    |
| $n^j$            | Number concentration of particles in size bin $j$<br>$\frac{dn^j}{dt} = \frac{n_0^j}{\tau} - \frac{n^j}{\tau} - \beta^j n^j$  | $\text{cm}^{-3}$              |
| $P_i^0$          | Vapor pressure of species $i$<br>$P_i^0 = \frac{C_i^* RT}{M_p \gamma_p}$  | $\text{Pa}$                   |
| $W_i$            | Wall concentration of species $i$<br>$\frac{dW_i}{dt} = k_{wall,on,i} G_i - k_{wall,off,i} W_i$   | $\mu\text{g m}^{-3}$          |

**Table 2.6:** CMFR Simulation Parameters.

| Parameter        | Definition  | Base Value  |
|------------------|---|---|
| $\alpha_p$       | Accommodation coefficient of vapor species on particles   | 0.001   |
| $\alpha_{wall}$  | Accommodation coefficient of vapor species on the wall    | $10^{-5}$ <sup>a</sup>                            |
| $C_w$            | Effective wall organic aerosol concentration              | $10 \text{ mg m}^{-3}$                            |
| $K_e$            | Coefficient of eddy diffusion in chamber                  | $0.015 \text{ s}^{-1}$ <sup>b</sup>               |
| $k_{wall,on,i}$  | First-order vapor wall loss coefficient                   | $3.66 \times 10^{-4} \text{ s}^{-1}$ (not varied) |
| $\tau$           | Average residence time in chamber                         | 1, 3, 5 h   |
| $A/V$            | Surface-area-to-volume ratio of the chamber               | $3.0 \text{ m}^{-1}$                              |
| $C_i^*$          | Saturation concentration for species                      | $[10^0 \text{ } 10^{-1}] \mu\text{g m}^{-3}$      |
| $D_i$            | Gas-phase diffusivity of species $i$                      | $3 \times 10^{-6} \text{ m}^2 \text{ s}^{-1}$     |
| $G_{AO}$         | Feed parent VOC concentration (mixing ratio)              | $654 \mu\text{g m}^{-3}$ (80 ppb)                 |
| $\gamma_p$       | Activity coefficient in the particle                      | Cancels with $\gamma_w$                           |
| $\gamma_w$       | Activity coefficient in the wall layer                    | Cancels with $\gamma_p$                           |
| $M_i$            | Species molecular weight                                  | $200 \text{ g mol}^{-1}$                          |
| $M_{init}^{tot}$ | Absorbing organic material in seed aerosol                | $0.01 \mu\text{g m}^{-3}$                         |
| $M_p$            | Average molecular weight of the organic aerosol           | Cancels with $M_w$                                |
| $M_w$            | Effective molecular weight of the absorbing wall material | Cancels with $M_p$                                |
| $k_{wall,on,i}$  | First-order vapor wall loss coefficient                   | $3.66 \times 10^{-4} \text{ s}^{-1}$              |
| R                | Ideal gas constant  | $8.314 \text{ J mol}^{-1} \text{ K}^{-1}$         |
| $\rho_p$         | Particle density  | $1700 \text{ kg m}^{-3}$                          |
| T                | Temperature   | 298 K   |

<sup>a</sup> Estimated experimentally from semi-volatile alkanes, alkenes, alcohols, and ketones (Matsunaga et al., 2010). <sup>b</sup> For actively mixed chambers  $K_e$  has been estimated as  $0.02\text{--}0.12 \text{ s}^{-1}$ ; for chambers that are not intentionally mixed,  $K_e$  has been estimated as  $0.015\text{--}0.075 \text{ s}^{-1}$  (McMurry and Grosjean, 1985a) (Zhang, Schwantes, et al., 2015).

The transient start-up period of the CMFR begins when parent VOC and seed particles are introduced in the flow into the chamber at  $t = 0$ . The seed aerosol distribution is assumed to be lognormal with a mean diameter of 50 nm and a geometric standard deviation of 1.5, with number concentration =  $8000 \text{ cm}^{-3}$ . The

base values of the variable parameters,  $k_e$ ,  $\alpha_w$ , and  $\alpha_p$  are taken as those obtained by fitting SOA data in (Zhang, C. D. Cappa, et al., 2014).  $C_w$  is set to  $10 \text{ mg m}^{-3}$ . The inverse of the e-folding time for each step of progressive oxidation of the parent VOC and its oxidation products is taken as  $10^{-3} \text{ s}^{-1}$  (time scale  $\sim 20 \text{ min}$ ). A reactor residence time of 3 h is considered. Figure 2.19 shows the evolution of the parent VOC (species A) and two progressive oxidation products (species B and C) in the gas phase, aerosol phase, and wall phase. The gas-phase and aerosol-phase concentrations, which would be sampled in the outflow of the CMFR, each reach steady state after about 20 h. Even though the outflow of the CMFR is at steady state, the wall concentrations are still far from equilibrium and are continuing to increase. For these low volatility products and a large  $C_w$ , vapor wall loss appears to be irreversible and still affects the SOA yield even at steady state. Therefore, steady state in a CMFR does not necessarily imply that vapor wall loss is at equilibrium and no longer affects the SOA yield. These results suggest that experiments are useful to constrain the nature of wall deposition of vapors in a CMFR. These experiments can clarify the extent to which vapor-wall equilibrium is established during a typical experiment, or if vapor wall deposition is essentially irreversible and must be taken into account when interpreting SOA yields.

### **Comparison of the Secondary Organic Aerosol Yield Obtained in Batch vs. CMFR Chambers**

For a given SOA system, it is informative to ask: How do the SOA yields compare between batch and CMFR systems? For instance, CMFR studies have tended in a number of cases to achieve higher SOA yields than those observed in batch systems. This has been attributed to the walls of the CMFR reaching equilibrium (Chen et al., 2013). However, as we have shown, this may or may not be the case. If the walls do not reach equilibrium, why then would a CMFR achieve a higher SOA yield than a batch reactor? To address this question, we present the results of simulations using the batch and CMFR versions of the model in Table 2.5. Parameter values from Table 2.6 are used with some exceptions. The procedure will be to vary parameters one-by-one to explore the effect of the parameters on the SOA yield. The base values of the parameters for this comparison are:  $\alpha_p = 0.01$ ;  $C_w = 10 \text{ mg m}^{-3}$ ;  $\alpha_w = 10^{-5}$ ;  $\beta = 1.94 \times 10^{-5} \text{ s}^{-1}$  (assumed independent of particle size);  $\tau = 5.2 \text{ h}$ . To simplify the comparison, the gas-phase oxidation chemistry is represented as  $A \rightarrow B$ , with a 50% yield, where B is a low volatility product, with mass saturation concentration  $C^* = 0.01 \text{ } \mu\text{g m}^{-3}$ . The SOA yield in the batch reactor is taken as the maximum

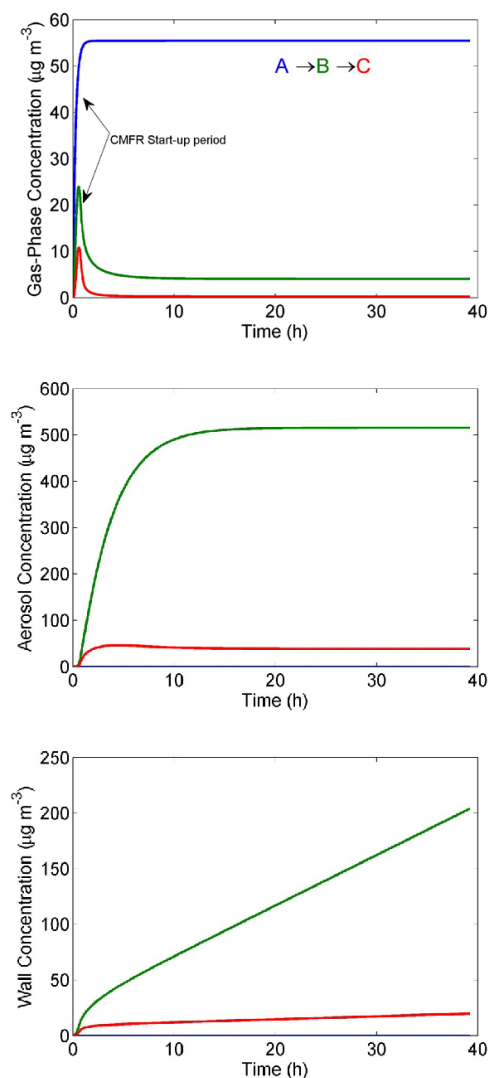


**Figure 2.19:** Evolution of the parent VOC (species A) and two progressive oxidation products (species B and C) in the gas phase (top panel), aerosol phase (middle panel), and wall phase (bottom panel). Saturation mass concentrations for species B and C are  $1 \mu\text{g m}^{-3}$  and  $0.1 \mu\text{g m}^{-3}$ , respectively.

value achieved over the course of the experiment, whereas the CMFR SOA yield is taken as that when the CMFR is at steady state conditions. The results of the

comparison are shown in eight panels in Figure 2.20, in which the SOA yield is compared between the two reactor configurations. In each panel one parameter is varied, while the remaining parameters are held at their nominal base values. We discuss the results panel by panel.

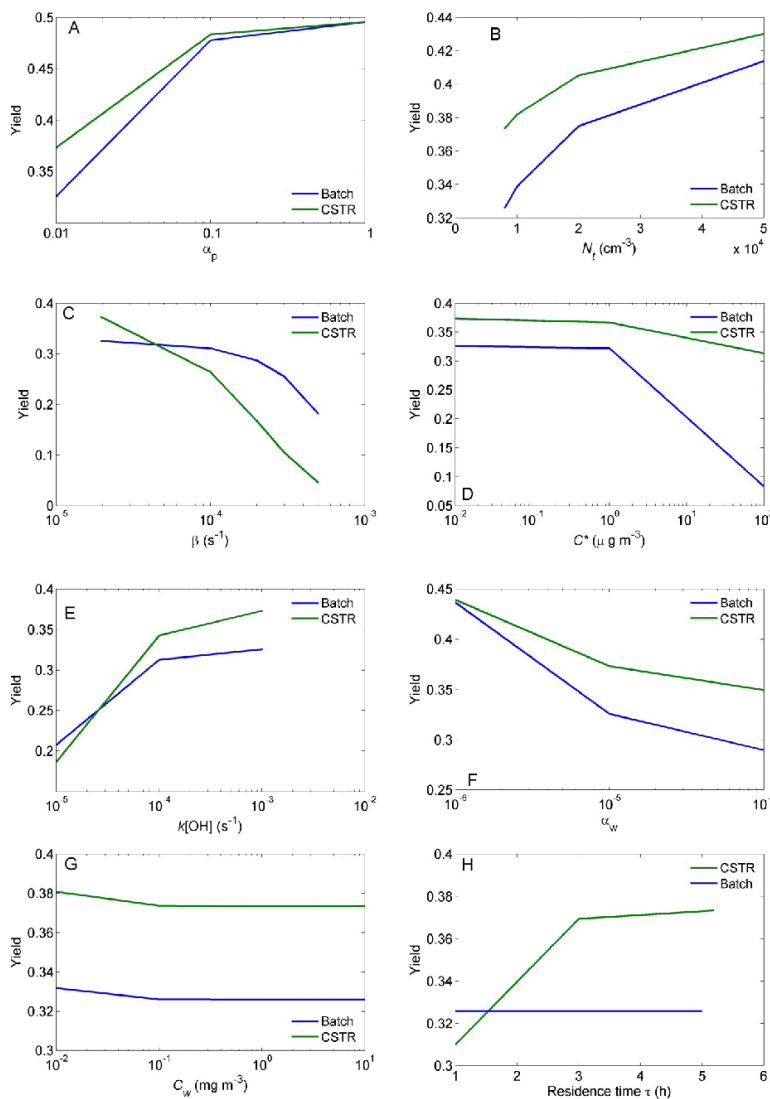


**Figure 2.20:** Comparison of the performance between a batch chamber and a CMFR in SOA formation. See text for explanation of panels A-H.

### **Figure 20A: Effect of $\alpha_p$ (0.01 to 1.0)**

SOA yield is larger in the CMFR for all values of  $\alpha_p$ , with the two yields approaching each other as  $\alpha_p$  approaches 1. As  $\alpha_p$  approaches 1, the resistance to vapor-particle mass transfer is lowered, the impact of vapor wall loss is lessened, and SOA yields approach 0.5, the highest possible yield since species B is assumed to be produced with a 50% yield in the gas phase.

### **Figure 20B: Effect of seed particle number concentration**

SOA yield is larger in the CMFR for all values of the aerosol number concentration. At the beginning of a batch chamber experiment, the seed aerosol is free of condensed organics, so there is a delay in growth, during which time vapor-wall deposition is occurring. Once steady state is reached in a CMFR, there is no “start-up” effect, and the seed aerosol has the steady state level of organics.

### **Figure 20C: Effect of particle wall deposition rate**

For a relatively fast wall deposition rate of particles, the SOA yield in the batch reactor exceeds that in the CMFR. In the batch reactor, vapor condensation occurs as soon as oxidation takes place when wall deposition of particles has not yet had an appreciable effect on particle concentrations, whereas in the steady state CMFR particles are effectively removed over the relatively long residence time in the reactor. Only when the particle wall deposition rate is very slow does the yield in the CMFR exceed that in the batch chamber.

### **Figure 20D: Effect of the volatility of the SOA oxidation product**

Yields in both reactors decrease as  $C^*$  increases, as expected, but that in the batch system decreases much faster as  $C^*$  increases. For  $C^* = 100 \mu\text{g m}^{-3}$  and only one condensable product, the equilibrium gas-phase concentration is  $100 \mu\text{g m}^{-3}$ . Because species B is continually being formed in a CMFR, the gas-phase concentration remains slightly above  $100 \mu\text{g m}^{-3}$  and the yield slowly increases over an exceedingly long time until steady state is achieved. In contrast, species B is rapidly depleted in a batch reactor since no new A is supplied to the chamber. Thus, the concentration of B decreases below  $100 \mu\text{g m}^{-3}$  and condensation to the particle phase no longer occurs. It is important to note that the time for the CMFR to achieve steady state for  $100 \mu\text{g m}^{-3}$  is so long that this result would not be observed experimentally.

**Figure 20E: Effect of the rate of oxidation ( $k[\text{OH}]$ )**

For a relatively slower rate of oxidation, the yield in the batch chamber exceeds that in the CMFR due to the shorter residence time in the CMFR. For a slower reaction rate and a fixed residence time, the extent of reaction is lowered in the CMFR. Less species B is produced, lowering the driving force for condensation on the particles and reducing the yield. As the reaction rate increases, the CMFR eventually supplants the batch reactor.

**Figure 20F: Effect of the vapor-wall accommodation coefficient  $\alpha_w$**

For a low vapor-wall accommodation coefficient, e.g.  $\alpha_w \sim 10^{-6}$ , there is very little vapor wall loss and the SOA yields in both reactors are essentially equal. As  $\alpha_w$  increases, proportionately more vapor product is lost early in the batch reactor. The larger impact of vapor wall deposition on the batch chamber is due to this “startup” effect. When the reaction begins in the batch chamber, there is no organic aerosol present. As species B forms and condenses on seed particles, it is also being lost to the walls, leading to a steadily decreasing driving force for condensation. In contrast, in a CMFR, owing to immediate dilution of B, wall loss occurs but has less impact as the CMFR evolves toward steady state. At steady state the concentration of B is a constant, and the driving force for condensation is sustained.

**Figure 20G: Effect of  $C_w$**

The large  $C_w$  values considered here signify that at vapor-wall equilibrium, the concentration of species B in the wall will greatly exceed that in the gas phase, and the reverse flux of species B from the wall to the gas phase is essentially negligible. This remains true even when reducing  $C_w$  by two orders of magnitude. Therefore the SOA yield is unaffected, and the CMFR achieves higher yields than the batch chamber regardless of the value of  $C_w$ .

**Figure 20H: Effect of CMFR residence time**

At relatively short CMFR residence times, the reaction does not have time to proceed sufficiently versus that in the batch chamber. As the CMFR residence time increases, the CMFR yield eventually exceeds that in the batch reactor.

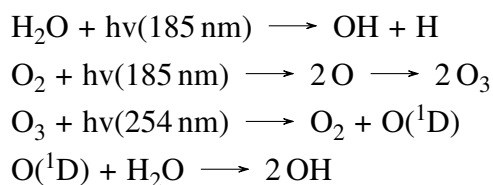
Although comparison of the batch chamber with the CMFR depends on a number of design features, a few general conclusions can be drawn. The CMFR generally

exhibits a higher SOA yield except when particle wall losses are high, VOC oxidation is slow, and the residence time in the CMFR is relatively short. The lower SOA yield exhibited in the batch chamber is the result of the wall deposition of condensable vapors at the beginning of the experiment that limits the ultimate amount of vapor available for SOA growth. Once steady state is reached in a CMFR, there is no corresponding “start up” effect. In the absence of vapor wall deposition, SOA yield is generally higher in a batch chamber; as the residence time in a CMFR is increased, the SOA yield in the CMFR will approach that in the batch chamber.

## 2.9 The Flow Tube Reactor

The flow tube reactor is an alternative to the large environmental chamber. This reactor offers the ability for a wide range of oxidant exposures over relatively short residence times and with reduced wall effects. One principal motivation for the development of flow tube reactors for studying SOA formation is the limitation on OH levels that can be generated in chambers. In flow tube reactors, it is possible to generate OH concentrations of the order of  $10^9$  molecules  $\text{cm}^{-3}$  and thereby to study SOA formation and evolution under conditions equivalent to multiple days of atmospheric OH exposure. The advent of flow reactors for the study of SOA formation can be considered to have begun with the introduction of the Potential Aerosol Mass (PAM) reactor (Kang, Root, et al., 2007; Kang, Toohey, et al., 2011). Other laboratory flow reactor systems have been used for a variety of SOA formation studies (A. Lambe, Ahern, et al., 2011; A. Lambe, Chhabra, et al., 2012; A. T. Lambe et al., 2015; Keller et al., 2012; Slowik et al., 2012; Chen et al., 2013). Modeling studies have investigated the radical chemistry in the oxidation flow reactor (Li et al., 2015).

As noted, a key aspect of the flow tube reactor is the ability to generate OH radical concentrations substantially exceeding those in environmental chambers. In a number of flow tube reactors designed for large OH exposure, low-pressure Hg lamps producing wavelengths of 185 and 254 nm are used to generate OH radicals under continuous flow conditions (Li et al., 2015). OH radicals are produced by photolysis of  $\text{H}_2\text{O}$  and by photolysis of  $\text{O}_3$  formed from  $\text{O}_2$  photolysis:





Under typical operating conditions, about 10% of  $O(^1D)$  reacts with  $H_2O$  to form 2 OH, the majority undergoing quenching to  $O(^3P)$ , reforming  $O_3$ . In  $H_2O$  photolysis, virtually all the H atoms formed react with  $O_2$  to form  $HO_2$ . The  $H_2O$  vapor concentration determines the relative importance of the formation pathways. Overall  $HO_x$  loss tends to be dominated by  $OH + HO_2$ , with a minor contribution by  $HO_2 + HO_2$ .

The OH concentration can be quantified by measuring the decay of  $SO_2$  by  $SO_2 + OH$ , for which the reaction rate constant is accurately known. OH concentrations, for example, can be generated in the range of  $2 \times 10^8$  to  $2 \times 10^{10}$  molecules  $cm^{-3}$ . At a reactor residence time of 100 s, the corresponding OH exposures are  $2 \times 10^{10}$  to  $2 \times 10^{12}$  molecules  $cm^{-3}$  s, equivalent to about 0.2 to 17 days of atmospheric OH exposure. Li et al. (2015) present an OH estimation equation as a function of experimental parameters. A. T. Lambe et al. (2015) have shown that the composition of SOA produced in a flow reactor by OH oxidation of gas-phase VOCs and in chambers is the same within experimental accuracy. One must be cautious, however, that the intense oxidation conditions may produce sufficiently high  $RO_2$  abundances that  $RO_2 + RO_2$  chemistry may dominate in a way that is uncharacteristic of the atmosphere.

### **Design Considerations: Introduction**

A flow tube reactor comprises three sections: an inlet/mixing section, a reaction section, and an exit section (Figure 2.21). We illustrate these components with three designs currently employed to study atmospheric chemistry. For example, the Potential Aerosol Mass (PAM) reactor employed by Kang, Root, et al. (2007) and A. Lambe, Ahern, et al. (2011) utilizes a 46 cm length x 22 cm diameter cylindrical design into which aerosol is introduced via standard 6.35 mm tubing and removed from the reactor via a large exhaust (Figure 2.21A). A characteristic of this system is the generation of high OH exposures in order to simulate multi-day atmospheric processing. The PAM achieves this high-intensity oxidation using four mercury lamps with peak emission wavelength at  $\lambda = 254$  nm. The system is operated at a flow rate of  $8.5 \text{ L min}^{-1}$ , yielding a plug-flow residence time of 106 s and an average velocity of  $0.37 \text{ cm s}^{-1}$ . The Reynolds number for this system is 55 (A. Lambe, Ahern, et al., 2011).

The PAM oxidation flow reactor of Li et al. (2015) is a 13 L cylindrical aluminum vessel with two or more low-pressure Hg lamps producing 185 nm and 254 nm light

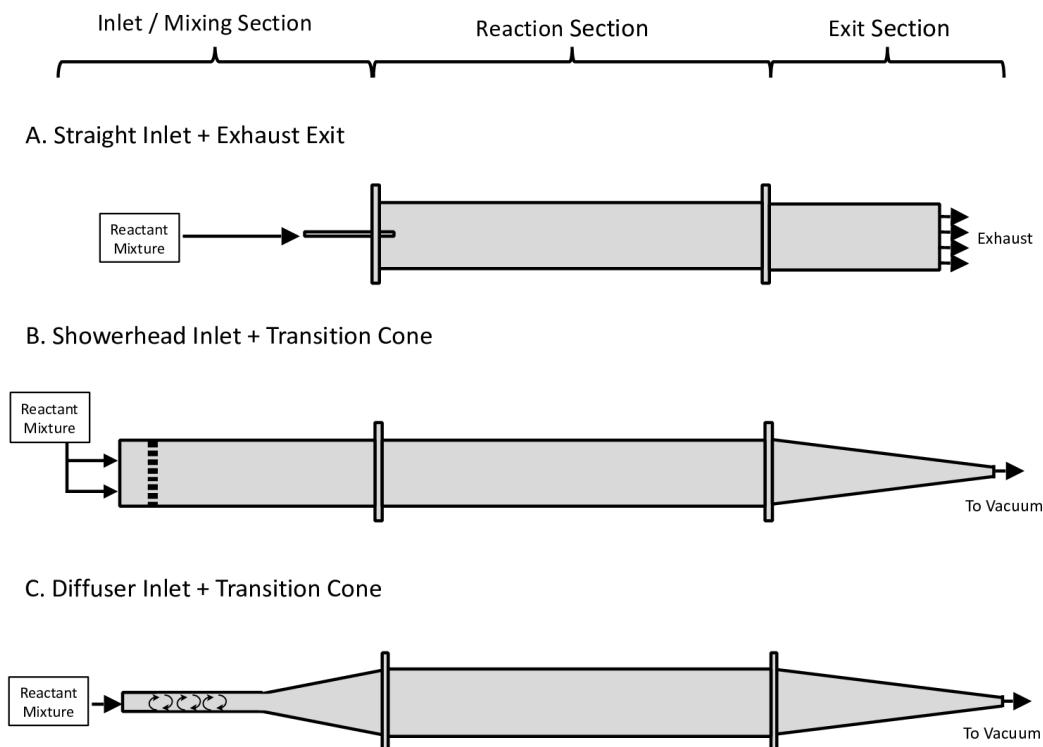


**Figure 2.21:** Flow tube reactor designs. The reactors presented here comprise inlet, reaction, and exit sections. Reactor (A) is a design similar to the Potential Aerosol Mass (PAM) tube (Kang, Root, et al., 2007; A. Lambe, Ahern, et al., 2011), reactor (B) is a design similar to the UC Irvine flow tube (Ezell et al., 2010), and reactor (C) is a design similar to the Caltech flow tube.

inside the reactor. Total OH exposure levels in the reactor can be varied from  $10^{10}$  to  $10^{12}$  molecules  $\text{cm}^{-3}$  s by changing the UV light intensity, absolute humidity, and residence time. The Hg lamps are enclosed in sleeves through which  $\text{N}_2$  flows to remove the heat generated by the lamps. Two types of sleeves are used. Teflon sleeves transmit both 185 and 254 nm light, as the shorter wavelength fosters the direct photolysis of  $\text{O}_2$  and  $\text{H}_2\text{O}$ . Quartz sleeves allow only 254 nm light to be transmitted. An important parameter governing the behavior of the reactor is the ratio of the photon intensities at 185 and 254 nm light. The effective photon flux at 185 nm is determined from the observed  $\text{O}_3$  mixing ratio in the reactor, and the effective photon flux at 254 nm is estimated from the ratio of the fluxes at 185 nm and 254 nm. Reactor flow is ordinarily 3.1 standard liters per minute, giving a residence time in the reactor of 4.2 min.

The UC Irvine flow reactor described by Ezell et al. (2010) utilizes a design em-

ploying a showerhead inlet and a transition cone exit section (Figure 2.21B). This system introduces gas and particles evenly along the cross section of the reaction tube and is designed to minimize turbulence and particle interactions with the walls. This 8.5 m length x 46 cm diameter flow tube reactor is operated at a flow rate of 20 L min<sup>-1</sup>, yielding a plug-flow residence time of 60 min and an average velocity of 0.2 cm s<sup>-1</sup>. The Reynolds number for this system is 61 (Ezell et al., 2010).

Figure 2.21C is a schematic of the Caltech flow reactor. This tube is designed to gently introduce reactants with a diffuser cone while providing prolonged exposure to UV light. The flow tube is 244 cm length x 15 cm diameter and is typically operated at a flow rate of 1 L min<sup>-1</sup>, yielding a plug-flow residence time of 44 min and an average velocity of 0.09 cm s<sup>-1</sup>. This system is operated with a typical Reynolds number of ~9.

### **Design Considerations: The Nature of the Flow in the Reaction Section**

Flow tube reactors can be operated in laminar or turbulent flow regimes. The radiation source can be external to the tube or inside the tube itself. If the radiation source is inside the reactor itself, one must consider the effect of that heat source on the velocity profile in the reactor. Here, we focus on the design of the reaction section since this is the component of the flow tube apparatus that is most susceptible to thermal mixing induced by heat emitted from the UV lights (Khalizov et al., 2006; Ezell et al., 2010).

The essential dimensionless group that differentiates laminar vs. turbulent flow is the Reynolds number,

$$Re = \frac{\rho U D}{\mu}$$

where  $\rho$  is the fluid density,  $U$  is the average velocity,  $\mu$  is the fluid viscosity, and  $D$  is the tube diameter. For cylindrical tubes,  $Re < 2100$  is the condition for laminar flow.

An advantage of laminar flow is that deposition of gases and particles on the tube wall is minimized; a disadvantage is that the residence time of fluid elements following independent streamlines is different. Nonetheless, the average residence time in laminar flow is precisely known. In contrast, the velocity profile in turbulent flow is uniform across the tube (so-called plug flow); however, the transport of material to the wall is greatly enhanced. For photochemical flow tube reactors in which the radiation source is inside the tube itself, mixing induced by natural convection is another concern. For example, Khalizov et al. (2006) modeled the effects of

temperature differentials for a variety of flow conditions and system geometries. The authors found that even for flow tubes with small diameters, a radial temperature differential of only 1K can induce convective mixing within the tube.

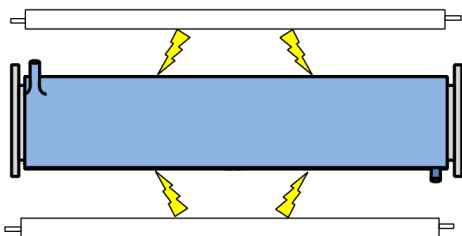
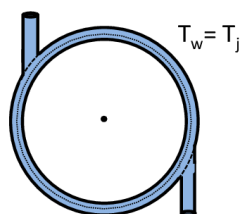
The Richardson number,  $Ri$ , is a measure of the relative contributions of natural and forced convection (Khalizov et al., 2006; Ezell et al., 2010),

$$Ri = \frac{g\beta_a\Delta TD}{U^2}$$

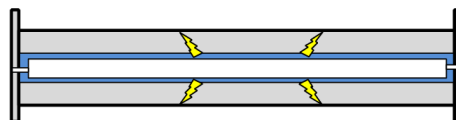
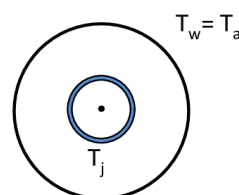
where  $\beta_a$  is the thermal expansion coefficient of air,  $g$  is the acceleration due to gravity,  $U$  is the velocity of the fluid, and  $\Delta T$  is the radial temperature differential within tube. For  $Ri > 1$ , natural convection will influence the velocity profile in the tube. For the PAM and UC Irvine flow tubes operated under the conditions described above, a value of  $Ri < 1$  exists only if radial temperature differences are  $< 1.5 \times 10^{-3}$  K and  $3 \times 10^{-4}$  K, respectively. In essence, when the source of radiation is in the tube itself, free convective mixing is unavoidable. To minimize convective mixing, Khalizov et al. (2006) recommend arranging flow tube reactors in a vertical position. This is feasible for reactor tubes that are short or have relatively small diameters, however this is impractical for larger systems.

Heat transfer control can be achieved using air or water-chilled jackets. Figure 2.22 demonstrates two radiation arrangements with jacketed components. Arrangement (A) is a representation of the Caltech flow tube jacket. With lights positioned on the outside of the tube, the exterior water jacket provides a heat transfer medium, while allowing UV radiation to drive photochemistry in the reactor. Since the wall temperature is constant,  $\Delta T$  is solely dependent on the temperature of the reactant mixture. If the fluid recirculation in the jacket is sufficiently rapid, the axial temperature gradient in the cooling jacket is small. In arrangement (B), the lights are contained within the flow tube reactor. The PAM and UC Irvine flow tubes utilize this arrangement. In this case, the reactor walls can be constructed from inexpensive, UV blocking materials. The jacket around the light source, however, must still allow UV penetration. Since the temperature at the reactor walls is affected by that of the surroundings, any jacket temperature maintained below or above ambient will lead to  $\Delta T > 0$ ; thus, the temperature gradient in this arrangement is dependent on the temperature of the reactant mixture, reactor walls, and cooling jacket. It may be difficult to avoid some degree of free-convective mixing with this radiation arrangement.

A. Exterior Lights and Cooling Jacket

Axial ViewRadial View

B. Interior Lights and Cooling Jacket

Axial ViewRadial View

**Figure 2.22:** Cooling jacket arrangements typically used to control the temperature within a flow tube reactor. Arrangement (A) employs an exterior cooling jacket with lights positioned on the outside of the tube. Arrangement (B) employs an interior cooling jacket with lights positioned on the inside of the tube.  $T_w$ ,  $T_j$ , and  $T_a$  are the temperatures of the reactor wall, cooling jacket, and ambient, respectively.

### Design Considerations: Particle Losses on Reactor Surfaces

For flow tubes constructed to study aerosol chemistry, a major consideration in the design of the reaction section is the extent of interaction between particles and the tube walls. As in atmospheric chambers, particle loss is a function of multiple processes including gravitational settling, particle diffusion, coagulation, and electrostatic interactions. Since particles travel along streamlines in a flow tube, particle losses may also occur by impaction upon surfaces within the tube. For example, the UC Irvine and Caltech flow tubes have sampling ports along the length of the reactor.

To evaluate the extent to which particle loss due to impaction on surfaces protruding into the flow may occur, one may evaluate the Stokes number, which is a measure of the tendency of a particle to follow streamlines of the flow or impact upon surfaces (J. H. . Seinfeld et al., 2006),

$$St = \frac{D_p^2 \rho_p C_c U}{18\mu L} \text{ where } C_c = 1 + \frac{2\lambda}{D_p} [1.257 + 0.4 \exp(-\frac{1.1 D_p}{2\lambda})]$$

where  $D_p$  is the particle diameter,  $\rho_p$  is the particle density,  $C_c$  is the Cunningham slip correction, and  $L$  is a characteristic length scale of the flow (e.g., sampling port diameter). The Cunningham slip correction factor accounts for non-continuum effects as the diameter of a particle approaches the mean free path of air ( $\lambda$ ). When  $St \ll 1$ , particles adapt to changes in fluid velocity quickly and impaction is unimportant. For a 500 nm ammonium sulfate particle (density =  $1770 \text{ kg m}^{-3}$ ) travelling around a standard 6.35 mm sampling tube under typical operating conditions, for example,  $St \ll 1$ .

Another potential factor contributing to particle loss is wall deposition. A. Lambe, Ahern, et al. (2011) observed nearly identical particle transmission efficiencies in the PAM system (ratio of surface area to volume,  $SA/V = 0.2 \text{ cm}^{-1}$ ) relative to the University of Toronto Photo-Oxidation Tube ( $SA/V = 0.97 \text{ cm}^{-1}$ ) when operated at the same residence time. Both tubes exhibit significant losses for particles  $< 100 \text{ nm}$  (50% transmission) with improved transmission for particles  $> 200 \text{ nm}$  (80–90% transmission). The authors attribute this behavior to: (1) flow disturbances that enhance deposition to the walls; or (2) electrostatic deposition due to the non-conductive flow tube walls. If the reactor is constructed with stainless steel walls, electrostatic deposition is minimized. For example, in the UC Irvine flow tube reactor, Ezell et al. (2010) report  $> 98\%$  transmission for particles  $< 300 \text{ nm}$ , 91% transmission for 800 nm particles, and 86% transmission for 1000 nm particles.

### **Design Considerations: Entrance and End Effects**

When calculating key fluid mechanical parameters such as  $Re$  and  $Ri$  under laminar flow conditions, one assumes that the flow inside the tube is fully developed as a parabolic profile. This assumption implicitly neglects entrance effects. The flow tubes depicted in Figure 2.21 introduce or remove reactants at the inlet and exit sections in a manner that minimizes turbulence or undesired mixing. This section addresses considerations in the design of the entrance region into a flow tube reactor.

For reactors that gently introduce reactants into the tube, there is an axial distance required for the flow to develop to the characteristic parabolic profile of laminar flow. This entrance length,  $L_e$ , is estimated to be  $0.035 D Re$  (Bird et al., 2002). For the Caltech, PAM, and UC Irvine reactors, the entrance lengths at nominal operating conditions are approximately 0.11 m, 0.42 m, and 1 m, respectively.

A number of possible arrangements exist to introduce reactants into a flow tube

reactor (Figure 2.23). Figure 2.23A depicts the injection method utilized by the PAM. Here, gas and particles are introduced into the reaction section through a short injection tube. The benefit of this design is its simplicity; however, it is challenging to distribute reactant mixtures evenly about the reactor cross section. This inlet method was tested on the Caltech flow tube, and the flow pattern was visualized by the injection of smoke (Figure 2.23A). In this system, the flow is controlled by a vacuum line attached to the exit section (see Figure 2.21); consequently, the gas-particle mixture is pulled into the reaction tube at a rate that is dictated by mass conservation. Smoke studies illustrate that the mixture concentrates in a plug focused at the center of the reactor. This “fire hose” effect can be attributed to the enhanced velocity at the exit of the injection tube ( $V_{\text{avg, injection}}$ ). When operating the flow tube with an overall flow rate of  $1 \text{ L min}^{-1}$ , the average velocity exiting a standard 6.35 mm tube (ID = 3 mm) is  $2.35 \text{ m s}^{-1}$ . This is nearly 2500 times the average velocity of the flow within the reactor ( $V_{\text{avg, bulk}} = 0.09 \text{ cm s}^{-1}$ ). As discussed by A. Lambe, Ahern, et al. (2011), this injection method has the potential to induce dead volume near the entrance of the reaction section and reactor-scale recirculation. Such behavior is typical for that occurring with a sudden expansion (Bird et al., 2002). A consequence is that the reactor behaves essentially like a CMFR.

The UC Irvine flow tube reactor utilizes a spoked-hub/showerhead disk inlet that distributes the reactants evenly about the reactor cross-section, provides sufficient mixing, and avoids the “fire hose” effect (Figure 2.23B). Ezell et al. (2010) designed the inlet with sufficient length to develop the laminar profile before gas and aerosol reach the reaction section. Here, we consider only the showerhead disk; we refer readers to Ezell et al. (2010) for the complete inlet design. With a showerhead disk, the reactants can be mixed and introduced into the tube in a controlled, gentle manner. The disk itself is perforated with a number of holes such that the fluid velocity at each hole exit ( $V_{\text{avg, i}}$ ) approaches that of  $V_{\text{avg, bulk}}$ . To determine the number of holes in a showerhead design that would sufficiently slow the flow to  $V_{\text{avg, bulk}}$ , one can calculate  $V_{\text{avg, i}}$ ,

$$V_{\text{avg, i}} = \frac{F_{\text{vol}}}{n_s \times A_c}$$

where  $F_{\text{vol}}$  is the total volumetric flow rate through the showerhead,  $n_s$  is the number of holes, and  $A_c$  is the cross-sectional area of each hole. To achieve a  $V_{\text{avg, i}}/V_{\text{avg, bulk}} = 25$  in the Caltech flow tube (a 100-fold reduction in velocity relative to a standard 3 mm pipe), a showerhead with 575 holes would be required. For perspective, the

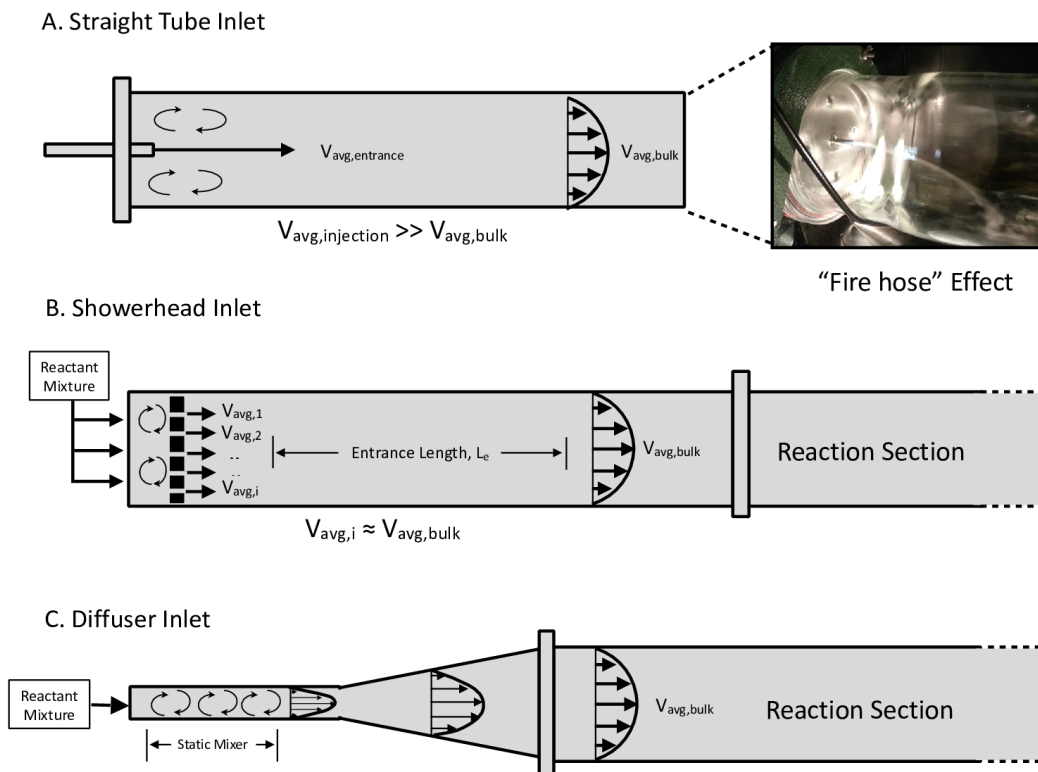


**Figure 2.23:** Inlet designs used by (A) the Potential Aerosol Mass reactor (PAM, Kang, Root, et al. (2007) and A. Lambe, Ahern, et al. (2011)) (B) the UC Irvine flow tube (Ezell et al., 2010) and (C) the Caltech flow tube.  $V_{avg,injection}$ ,  $V_{avg,bulk}$ , and  $V_{avg,i}$  are the average velocities at the PAM inlet, in the bulk reaction section, and at the exit of a showerhead hole. Inlet (A) also illustrates the “fire hose” effect, as demonstrated by the injection of smoke in the Caltech flow tube.

UC Irvine flow tube utilizes a showerhead with 940 equally spaced 3.2 mm diameter holes.

In the Caltech flow tube, reactants are injected via a diffuser cone design, after which a laminar flow profile develops. Like the showerhead disk, the advantage in the diffuser cone design is the reduction of the “fire hose” effect through the gradual decrease in the velocity profile. One consideration when designing a diffuser is flow separation from the wall of the cone, leading to concentration of reactants towards the center of the tube and recirculation within the reaction section. Fried et al. (1989) recommended that diffusers be designed with an angle of divergence  $< 7^\circ$  to avoid flow separation; alternatively, White (2008) recommends an angle  $< 15^\circ$ . Sparrow et al. (2009) modeled the flow of fluid through diffuser cones at various Re. For further discussion about flow separation within diffusers, the authors recommend



discussions by Tavoularis (2005). At the design stage, it is recommended that one simulate the diffuser cone numerically using a computational fluid dynamics code to determine if a particular cone design suits the needs of the reactor.

The exit section of a flow tube is primarily designed to minimize upstream disturbance. The UC Irvine and Caltech reactors utilize a transition cone in which the reactants are concentrated to a common sampling line that can be split among multiple instruments; thus, a representative measure of the entire tube cross-section is obtained. The PAM uses an exhaust exit, and sampling lines are directed in-line with the flow. Both a transition cone and exhaust configuration eliminate dead volume at the reactor exit; thus, flow recirculation due to exit effects is not expected.

### **Design Considerations: Construction Materials**

Flow tube construction materials are strongly dependent on the purpose of the reactor. The most commonly used glass materials are Pyrex (borosilicate) and Fused Quartz, and the selection should be based on the desired wavelengths of photolysis used to promote reactions as well as the placement of the UV lights. Quartz is considerably more expensive and fragile than Pyrex, but provides properties essential for photochemical studies, assuming the lights are placed outside the reaction vessel (see Figure 2.21A). Pyrex glass UV-wavelength cut-off is at 275 nm, whereas Quartz is transparent down to 170 nm (Figure 2.24). If the lights are placed inside the tube (Figure 2.21B), Pyrex and other more robust materials can be used to construct the flow reactor, but challenges related to mixing issues and structural considerations related to removing the heat produced by the light source need to be considered.

As mentioned in above, temperature-controlled studies require cooling of the flow reactor during irradiation; consequently, the cooling fluid should absorb as little UV radiation as possible while providing sufficient heat removal. Likewise, glass materials have a lower pressure threshold than other materials; thus, recirculation in the cooling jacket must be performed using a low-pressure pump. In the Caltech flow reactor (Figure 2.21A), coolant recirculation in the jacket is performed with a magnetic-drive pump rated to operate under 10 psi, which is ~20 psi below the fracture point of 6 mm thick Quartz glass tubes. The coolant liquid is either a 50/50 mix of ethylene glycol/water, which does not significantly absorb in the UV range dictated by the 350 nm lights (transmission cut-off at around 225 nm) and provides sufficient cooling to maintain reactor temperatures between -10 to 35 °C, or pure water which is transparent in the UV-visible range above 200 nm. Transmission

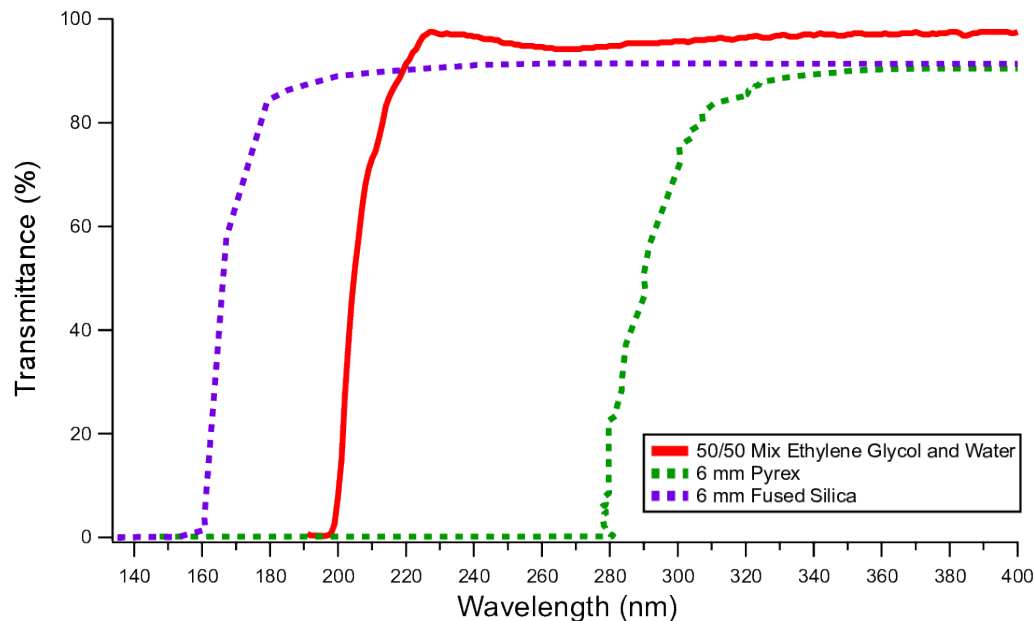


**Figure 2.24:** UV-visible transmission spectra of glass flow tube materials (Quartz and Pyrex, dotted lines), and cooling liquid (50/50 mix of ethylene glycol/water, solid line). Pure water is transparent in the UV-visible range above 200 nm. Quartz and Pyrex transmission data are from the Martin Fleischmann Memorial Project ([www.quantumheat.org](http://www.quantumheat.org)).

spectra of the 50/50 mix of water/ethylene glycol are included in Figure 2.24. Alcohol coolants such as methanol can be used to reach very low temperatures, but the possible UV-absorption of the cooling liquid needs to be considered.

In the internal cooling arrangement in the UC Irvine flow reactor, the photolysis lamps are inside the Pyrex tube at the center of the reactor. Heat generation from the lights is removed with  $460 \text{ L min}^{-1}$  airflow, which enters the lamp housing in the middle of the reaction/photolysis section. With this cooling arrangement, the temperature inside the reactor is 4-6 °C above the surrounding temperature. This system cools sufficiently to operate reactions at ambient temperatures.

In flow reactors designed for atmospherically relevant studies, commonly used light sources are broadband and narrowband blacklights and different arc lamps (xenon, argon, mercury), similar to those used in atmospheric chambers (see Section 3.1). The flow reactor construction should ideally allow changing of the lights to suit different photolysis needs, such as OH generation, photolysis at different wavelengths, etc. The PAM uses four  $\lambda = 275 \text{ nm}$  lights with variable intensity to produce a range of OH exposures within the reactor. The Caltech flow tube uses lights that have

peak emission between 300-350 nm, although they are interchangeable with other types of lights.

## 2.10 Time Scales and Regimes of Behavior for Chamber Processes

### Oxidation Time Scale

In most chamber experiments involving oxidation of a volatile organic compound, the oxidation time scale is simply  $(k [\text{Oxidant}])^{-1}$ , where  $k$  is the reaction rate constant ( $\text{cm}^3 \text{ molecule}^{-1} \text{ s}^{-1}$ ) and  $[\text{Oxidant}]$  is the oxidant (e.g., OH) concentration ( $\text{molecules cm}^{-3}$ ). If the oxidant concentration changes over the course of an experiment, one can use an average concentration to estimate the reaction time scale. The reaction time scale can be tuned experimentally by adjusting the oxidant concentration in the reactor.

### Particle Coagulation Time Scale

The coagulation time scale of a population of monodisperse particles of initial number concentration  $N_0$  ( $\text{cm}^{-3}$ ) undergoing Brownian coagulation can be estimated as  $2(K N_0)^{-1}$ , where  $K$  is the Brownian coagulation coefficient ( $\text{cm}^3 \text{ s}^{-1}$ ) for particles of the given size (J. H. Seinfeld et al., 2006). Using this relation, the coagulation time scale for typical laboratory chamber conditions can be estimated. The coagulation coefficient for monodisperse seed particles of diameter 100 nm is  $\sim 10^{-9} \text{ cm}^3 \text{ s}^{-1}$ . At an initial number concentration of  $10^4 \text{ cm}^{-3}$ , the coagulation time scale is  $\sim 55 \text{ h}$ . This time scale exceeds the duration of typical chamber experiments, so the effect of particle coagulation can generally be neglected.

### Particle Wall Deposition Time Scale

Wall deposition of particles is represented as a first-order process, with deposition rate coefficient of  $\beta(D_p)$  (Section 2.6). The time scale is just the inverse of this first-order rate coefficient. A typical functionality of  $\beta(D_p)$ , as determined in the Caltech chambers, was shown in Figure 2.16 (panel b). The longest particle wall deposition time scale is that for particles of the size corresponding to the minimum of  $\beta(D_p)$ . From Figure 2.16, the minimum in  $\beta(D_p)$  occurs at  $\sim 400 \text{ nm}$  diameter for which the time scale is  $\sim 333 \text{ h}$ .

### Vapor-Particle Equilibration Time Scale

In cloud-free air, secondary organic aerosol forms via three possible mechanisms: (1) effectively irreversible condensation of very low volatility organic vapors pro-

duced by gas-phase VOC oxidation; (2) reversible absorption of semi-volatile organic vapors into existing particles; and (3) absorption of semi-volatile and volatile organic vapors into existing aerosol followed by particle-phase reactions to form effectively nonvolatile products. A variety of studies have shown that secondary organic aerosol particles can exhibit the properties of semi-solids, in which case intra-particle diffusion of a species can be significantly retarded and does not occur instantaneously, as has been presumed for a liquid particle. This affects the time required for the dissolved species to equilibrate with the gas phase. Typical diffusivities  $D_b$  ( $\text{cm}^2 \text{s}^{-1}$ ) of organics are  $10^{-10}$  to  $10^{-5}$  for liquid,  $10^{-20}$  to  $10^{-10}$  for semi-solid, and  $< 10^{-20}$  for solid.

As semi-volatile vapors condense into particles, equilibrium is eventually reached at which the partial pressure of the vapor is equal to the vapor pressure of the species over the particle. Estimation of the vapor-particle equilibration time scale must, in principle, account for three transport time scales (in the absence of particle-phase chemical reactions): (1) the characteristic time for the profile of the gas-phase concentration around the particle to relax to its new steady state following a perturbation of the bulk gas-phase concentration; (2) the characteristic time for interfacial equilibrium to be re-established following a perturbation; and (3) the characteristic time for particle-phase diffusion to establish a uniform concentration in the particle (in the absence of particle-phase chemical reaction). Depending on the specifics of a given situation, any of these three transport processes can govern the overall vapor-particle equilibration time scale. The rate of condensation is controlled by the rate of diffusion of vapor molecules to the surface of the particle and by the accommodation coefficient,  $\alpha_p$ , of the vapor molecules at the particle surface. The accommodation coefficient  $\alpha_p$  embodies empirically the net rate of uptake of molecules at the particle surface and has to be determined experimentally from vapor uptake (or particle growth) measurements.

With the recognition of the role of wall deposition of vapor molecules involved in secondary organic aerosol formation in chambers, the competition between suspended particles and the chamber walls for VOC oxidation products plays a crucial role in determining the measured SOA yield, and the relative time scales for equilibration of the vapors between the suspended particles and the walls of the chamber become important in determining the extent to which the SOA yield is affected by vapor wall deposition. If the vapor-particle equilibration time scale is long compared to that for vapor-wall equilibration, then the effect of vapor wall loss on SOA

yield is exacerbated.

Shiraiwa et al. (2012) performed a theoretical analysis of the equilibration timescale  $\tau_{eq}$  of SOA partitioning in liquid, semi-solid, and solid particles using the numerical model KM-GAP, which resolves the mass transfer in both gas and particle phases. The model allows a systematic evaluation of the equilibration timescale  $\tau_{eq}$  as a function of SOA volatility, particle-phase diffusivity, surface accommodation coefficient, and particle size. Species volatility can be represented by the effective saturation mass concentration,  $C^*$ , expressed in units of  $\mu\text{g m}^{-3}$ . Values of  $C^*$  define volatility in the following ranges:  $10^3 - 10^5$  (Intermediate Volatility Organic Compounds, IVOC);  $10^{-1} - 10^3$  (Semi-Volatile Organic Compounds, SVOC);  $10^{-4} - 10^{-1}$  (Low Volatility Organic Compounds, LVOC);  $< 10^{-3}$  (Extremely Low Volatility Organic Compounds, ELVOC). The behavior of  $\tau_{eq}$  can be summarized as follows:

- 1) For liquid particles with diffusivities in the range of  $10^{-8} \text{ cm}^2 \text{ s}^{-1}$ ,  $\tau_{eq}$  increases as  $C^*$  decreases. In this case, the partial pressure gradient between the gas phase and the particle surface is larger for smaller  $C^*$ , that is a less volatile species, and the equilibration time is correspondingly longer.
- 2) For liquid particles as in 1) above, as the accommodation coefficient  $\alpha_p$  decreases,  $\tau_{eq}$  increases. At  $\alpha_p = 1$ , SOA growth is limited by gas-phase diffusion, but as  $\alpha_p$  decreases, SOA growth eventually becomes limited by surface accommodation.
- 3) For semi-solid particles, with particle-phase diffusivities in the range of  $10^{-10}$  down to  $10^{-20} \text{ cm}^2 \text{ s}^{-1}$ , the timescales for exchange between the surface and the particle bulk and diffusion in the bulk particle become longer than those for gas-phase diffusion and surface accommodation. In this case,  $\tau_{eq}$  is insensitive to the value of  $\alpha_p$  but sensitive to the value of the bulk diffusivity  $D_b$ . In this regime, decrease of  $D_b$  by an order of magnitude leads to roughly an order of magnitude increase in  $\tau_{eq}$ . For a typical situation,  $\tau_{eq}$  is the order of minutes for semi-solid particles with  $D_b \sim 10^{-15} \text{ cm}^2 \text{ s}^{-1}$ , increasing to days for  $D_b < 10^{-20} \text{ cm}^2 \text{ s}^{-1}$ .

For LVOC, the instantaneous gas-particle equilibrium model can overestimate the particle-phase concentration by an order of magnitude before equilibrium is established. The formation of oligomers and other multifunctional compounds in the particle phase with high molecular mass and low vapor pressure is one mechanism that can lead to high viscosity and low diffusivity. The occurrence of a semi-solid state and the associated effects may require a more detailed kinetic representation of SOA formation than has been the case for instantaneous equilibrium partitioning.

## References

- Atkinson, R. (1994). "Gas-phase tropospheric chemistry of organic compounds, Monograph No. 2". In: *Journal of Physical and Chemical Reference Data*.
- Aumont, B., M. Camredon, et al. (2015). "Modeling the influence of alkane molecular structure on secondary organic aerosol formation". In: *Faraday Discussions*.
- Aumont, B., S. Szopa, and S. Madronich (2015). "Modeling the evolution of organic carbon during its gas-phase tropospheric oxidation: Development of an explicit model based on a self generating approach". In: *Atmos. Chem. Phys.* 5, pp. 2497–2517.
- Bird, R.B., W.E. Stewart, and E.N. Lightfoot (2002). *Transport Phenomena, 2nd Ed.* New York: John Wiley.
- Bouvier-Brown, N. C. et al. (2009). "In-situ Ambient Quantification of Monoterpenes, Sesquiterpenes, and Related Oxygenated Compounds during BEARPEX 2007: Implications for Gas- and Particle-Phase Chemistry". In: *Atmos. Chem. Phys.* 9, pp. 5505–5518.
- Calvert, J.G. et al. (2000). *The Mechanisms of the Atmospheric Oxidation of the Alkenes*. Oxford, UK: Oxford University Press, Inc.
- Cappa, C.D. and Wilson K.R. (2012). "Multi-generation gas-phase oxidation, equilibrium partitioning and the formation and evolution of secondary organic aerosol." In: *Atmos. Chem. Phys.* 12, pp. 9505–9528.
- Cappa, C.D., X. Zhang, et al. (2013). "Application of the Statistical Oxidation Model (SOM) to secondary organic aerosol formation from photooxidation of C<sub>12</sub> Alkanes." In: *Atmos. Chem. Phys.* 13, pp. 1591–1606.
- Carter, W.P.L., D.R. Cocker, et al. (2005). "A new environmental chamber for evaluation of gas-phase chemical mechanisms and secondary aerosol formation". In: *Atmos. Environ.* 39, pp. 7768–7788.
- Carter, W.P.L., G. Heo, et al. (2012). *SOA formation: Chamber study and model development, Final Report to the California Air Resources Board*. Tech. rep.
- Chen, S. et al. (2013). "Modeling organic aerosol from the oxidation of -pinene in a Potential Aerosol Mass (PAM) chamber". In: *Atmos. Chem. Phys.* 13, pp. 5017–5031.
- Cocker, D.R., R.C. Flagan, and J.H. Seinfeld (2001). "State-of-the-art chamber facility for studying atmospheric aerosol chemistry". In: *Environ. Sci. Technol.* 35, pp. 2594–2601.
- Crounse, J. D. et al. (2011). "Peroxy Radical Isomerization in the Oxidation of Isoprene". In: *Phys. Chem. Chem. Phys.* 13, pp. 13607–13613. doi: 10.1039/c1cp21330j.

- Crump, J.G. and J.H. Seinfeld (1981). "Turbulent deposition and gravitational sedimentation of an aerosol in a vessel of arbitrary shape". In: *J. Aerosol Sci.* 12, pp. 405–415.
- Ezell, M.J. et al. (2010). "A new aerosol flow system for photochemical and thermal studies of tropospheric aerosols." In: *Aerosol Sci. Technol.* 44, pp. 329–338.
- Fried, E. and L.E. Idelchik (1989). *Flow Resistance: A Design Guide for Engineers*. New York: Hemisphere Publishing Corporation.
- Hildebrandt, L., N.M. Donahue, and S.N. Pandis (2009). "High formation of secondary organic aerosol from the photo-oxidation of toluene". In: *Atmos. Chem. Phys.* 9, pp. 2973–2986.
- Hildebrandt, L., K.M. Henry, et al. (2011). "Evaluating the mixing of organic aerosol components using high-resolution aerosol mass spectrometry". In: *Environ. Sci. Technol.* 45, pp. 6329–6335.
- Jenkin, M. E., S. M. Saunders, and M. J. Pilling (1997). "The Tropospheric Degradation of Volatile Organic Compounds: A Protocol for Mechanism Development". In: *Atmos. Environ.* 31.1, pp. 81–104.
- Johnson, D. and G. Marston (2008). "The gas-phase ozonolysis of unsaturated volatile organic compounds in the troposphere". In: *Chem. Soc. Rev.* 37, pp. 699–716.
- Kang, E., M.J. Root, et al. (2007). "Introducing the concept of Potential Aerosol Mass (PAM)". In: *Atmos. Chem. Phys.* 7, pp. 5727–5744.
- Kang, E., D.W. Toohey, and W.H. Brune (2011). "Dependence of SOA oxidation on organic aerosol mass concentration and OH exposure". In: *Atmos. Chem. Phys.* 11, pp. 1837–1852.
- Keller, A. and H. Bartscher (2012). "A continuous photo-oxidation flow reactor for a defined measurement of the SOA formation potential of wood burning emissions". In: *J. Aerosol Sci.* 49, pp. 9–20.
- Keywood, M.D. et al. (2004). "Secondary organic aerosol formation from cyclohexene ozonolysis: Effect of OH scavenger and the role of radical chemistry". In: *Environ. Sci. Technol.* 38, pp. 3343–3350.
- Khalizov, A.F. et al. (2006). "Modeling of flow dynamics in laminar aerosol flow tubes". In: *J. Atmos. Sci.* 37, pp. 1174–1187.
- Kroll, J. H. et al. (2006). "Secondary Organic Aerosol Formation from Isoprene Photooxidation". In: *Environ. Sci. Technol.* 40, pp. 1869–1877.
- Lambe, A. T. et al. (2015). "Effect of Oxidant Concentration, Exposure Time, and Seed Particles on Secondary Organic Aerosol Chemical Composition and Yield". In: *Atmos. Chem. Phys.* 15, pp. 3063–3075.

- Lambe, A.T., A.T. Ahern, et al. (2011). "Characterization of aerosol photooxidation flow reactors: Heterogeneous oxidation, secondary organic aerosol formation and cloud condensation nucleus (CCN) activity measurements". In: *Atmos. Meas. Tech.* 4, pp. 445–461.
- Lambe, A.T., P.S. Chhabra, et al. (2012). "Transitions from functionalization to fragmentation reactions of laboratory Secondary Organic Aerosol (SOA) generated from the OH oxidation of alkane precursors". In: *Environ. Sci. Technol.* 46, pp. 5430–5437.
- Li, R. et al. (2015). "Modeling the radical chemistry in an oxidation flow reactor: Radical formation and recycling, sensitivities, and OH exposure estimation equation". In: *J. Phys. Chem. A.* 119, pp. 4418–4432.
- Loza, C.L., P.S. Chhabra, et al. (2012). "Chemical aging of m-xylene secondary organic aerosol: Laboratory chamber study". In: *Atmos. Chem. Phys.* 12, pp. 151–167.
- Loza, C.L., J.S. Craven, et al. (2014). "Secondary organic aerosol yields of 12-carbon alkanes". In: *Atmos. Chem. Phys.* 14, pp. 1423–1439.
- Mao, J. et al. (2012). "Insights into Hydroxyl Measurements and Atmospheric Oxidation in a California Forest". In: *Atmos. Chem. Phys.* 12, pp. 8009–8020.
- Matsunaga, A. and P.J. Ziemann (2010). "Gas-wall partitioning of organic compounds in a Teflon film chamber and potential effects on reaction product and aerosol yield measurements". In: *Aerosol Sci. Technol.* 44, pp. 881–892.
- Matthew, B.M., A.M. Middlebrook, and T.B. Onasch (2008). "Collection efficiencies in an Aerodyne aerosol mass spectrometer as a function of particle phase for laboratory generated aerosols". In: *Aerosol Sci. Technol.* 42, pp. 884–898.
- McMurry, P.H. and D. Grosjean (1985a). "Gas and aerosol wall losses in Teflon film smog chambers". In: *Environ. Sci. Technol.* 19, pp. 1176–1182.
- McMurry, P.H. and D.J. Rader (1985b). "Aerosol wall losses in electrically charged chambers". In: *Aerosol Sci. Technol.* 4, pp. 249–268.
- Pierce, J.R. et al. (2008). "Constraining particle evolution from wall losses, coagulation, and condensation-evaporation in smog-chamber experiments: Optimal estimation based on size distribution measurements". In: *Aerosol Sci. Technol.* 42, pp. 1001–1015.
- Riipinen, I. et al. (2011). "Organic condensation: A vital link connecting aerosol formation to cloud condensation nuclei (CCN) concentrations". In: *Atmos. Chem. Phys.* 11, pp. 3865–3878.
- Sander, S. P. et al. (2011). *Chemical Kinetics and Photochemical Data for Use in Atmospheric Studies, Evaluation No. 17*. Jet Propulsion Laboratory, Pasadena: JPL Publication 10-6.



- Saunders, S. M. et al. (2003). "Protocol for the Development of the Master Chemical Mechanism, MCMv3 (Part A): Tropospheric Degradation of Non-Aromatic Volatile Organic Compounds". In: *Atmos. Chem. Phys.* 3, pp. 161–180.
- Seinfeld, J. H. and S. N. Pandis (2006). *Atmospheric Chemistry and Physics*. Hoboken, New Jersey: John Wiley & Sons, Inc.
- Seinfeld, J.H. and J.F. Pankow (2003). "Organic atmospheric particulate material". In: *Annual Review of Physical Chemistry* 54, pp. 121–140.
- Shiraiwa, M. and J.H. Seinfeld (2012). "Equilibration timescale of atmospheric secondary organic aerosol partitioning". In: *Geophys. Res. Lett.* 39, p. L24801.
- Slowik, J.G., J.P.S. Wong, and J.P.D. Abbatt (2012). "Real-time controlled OH-initiated oxidation of biogenic secondary organic aerosol". In: *Atmos. Chem. Phys.* 12, pp. 9775–9790.
- Sparrow, E.M., J.P. Abraham, and W.J. Minkowycz (2009). "Flow separation in a diverging conical duct: Effect of Reynolds number and divergence angle". In: *International Journal of Heat and Mass Transfer* 52, pp. 3079–3083.
- Tavoularis, S. (2005). *Measurement in Fluid Mechanics*. New York: Cambridge University Press.
- Wang, J. et al. (2011). "Design of a new multi-phase experimental simulation chamber for atmospheric photosmog, aerosol and cloud chemistry research". In: *Atmos. Meas. Tech.* 4, pp. 2465–2494.
- Weitkamp, E.A. et al. (2007). "Organic aerosol formation from photochemical oxidation of diesel exhaust in a smog chamber". In: *Environ. Sci. Technol.* 41, pp. 6969–6975.
- White, F.M. (2008). *Fluid Mechanics, 6th Ed.* Berlin: McGraw Hill.
- Yeh, G.K. and P.J. Ziemann (2015). "Gas-wall partitioning of oxygenated organic compounds: Measurements, structure-activity relationships, and correlation with gas chromatographic retention factor". In: *Aerosol Sci. Technol.* 49 (9), pp. 727–738.
- Zhang, X., C. D. Cappa, et al. (2014). "Influence of Vapor Wall Loss in Laboratory Chambers on Yields of Secondary Organic Aerosol". In: *P. Natl. Acad. Sci. USA* 111.16, pp. 5802–5807.
- Zhang, X., R. H. Schwantes, et al. (2015). "Vapor Wall Deposition in Teflon Chambers". In: *Atmos. Chem. Phys.* 15, pp. 4197–4214. doi: 10.5194/acp-15-4197-2015.

## Chapter 3

# ISOPRENE NO<sub>3</sub> OXIDATION PRODUCTS FROM THE RO<sub>2</sub> + HO<sub>2</sub> PATHWAY

Schwantes, R. H. et al. (2015). “Isoprene NO<sub>3</sub> Oxidation Products from the RO<sub>2</sub> + HO<sub>2</sub> Pathway”. In: *J. Phys. Chem. A*. 119.40, pp. 10158–10171. DOI: 10.1021/acs.jpca.5b06355.

### 3.1 Abstract

We describe the products of the reaction of the hydroperoxy radical (HO<sub>2</sub>) with the alkylperoxy radical formed following addition of the nitrate radical (NO<sub>3</sub>) and O<sub>2</sub> to isoprene. NO<sub>3</sub> adds preferentially to the C<sub>1</sub> position of isoprene (>6 times more favorably than addition to C<sub>4</sub>), followed by the addition of O<sub>2</sub> to produce a suite of nitrooxy alkylperoxy radicals (RO<sub>2</sub>). At an RO<sub>2</sub> lifetime of ~30 s,  $\delta$ -nitrooxy and  $\beta$ -nitrooxy alkylperoxy radicals are present in similar amounts. Gas-phase product yields from the RO<sub>2</sub> + HO<sub>2</sub> pathway are identified as 0.75-0.78 isoprene nitrooxy hydroperoxide (INP), 0.22 methyl vinyl ketone (MVK) + formaldehyde (CH<sub>2</sub>O) + hydroxyl radical (OH) + nitrogen dioxide (NO<sub>2</sub>), and 0-0.03 methacrolein (MACR) + CH<sub>2</sub>O + OH + NO<sub>2</sub>. We further examined the photochemistry of INP and identified propanone nitrate (PROPNN) and isoprene nitrooxy hydroxyepoxide (INHE) as the main products. INHE undergoes similar heterogeneous chemistry as isoprene dihydroxy epoxide (IEPOX), likely contributing to atmospheric secondary organic aerosol formation.

### 3.2 Introduction

NO<sub>3</sub> oxidation of alkenes typically occurs during the night because NO<sub>3</sub> readily photolyzes under solar radiation. Daytime NO<sub>3</sub> chemistry can, however, be important under conditions in which NO<sub>3</sub> photolysis is suppressed (e.g., below dense clouds or in thick forest canopies). The oxidation of isoprene, the most abundantly emitted alkene in the atmosphere, is of particular interest to global climate and tropospheric chemistry. While the rate of isoprene emission is low at night (Monson et al., 1989; Loreto et al., 1990), isoprene can accumulate in the boundary layer in the late afternoon when OH concentrations have diminished (Starn et al., 1998; Stroud et al., 2002; Steinbacher et al., 2005; Warneke et al., 2004; S. S. Brown, DeGouw, et al.,

2009a; Beaver et al., 2012). Although nighttime isoprene concentrations are highly variable, its mixing ratio has been measured to be as high as several ppb just before sunset, and upon nightfall typically declines, widely attributed to reaction with  $\text{NO}_3$  (Starn et al., 1998; Stroud et al., 2002).

The rate of  $\text{NO}_3$  formation is controlled by the concentrations of nitrogen dioxide ( $\text{NO}_2$ ),  $\text{O}_3$ , and temperature. In heavily populated urban areas, e.g., the Northeast US, the  $\text{NO}_3$  mixing ratio can approach 300 ppt during the night in the summer (S. S. Brown, Ryerson, et al., 2006). At night, OH concentrations approach zero, so isoprene will react either with  $\text{NO}_3$  or  $\text{O}_3$ . Even when  $\text{NO}_3$  mixing ratios are 104 times lower than those of  $\text{O}_3$ , reaction of isoprene with  $\text{NO}_3$  is still competitive due to the large disparity in the reaction rate constants of isoprene with  $\text{O}_3$  ( $1.3 \times 10^{-17} \text{ cm}^3 \text{ molec}^{-1} \text{ s}^{-1}$ , (Sander et al., 2011)) and  $\text{NO}_3$  ( $7.0 \times 10^{-13} \text{ cm}^3 \text{ molec}^{-1} \text{ s}^{-1}$ , (Atkinson et al., 2006)) at 298K.

Organic nitrates are the major product of the reaction of isoprene with  $\text{NO}_3$  (65-80%) (Barnes et al., 1990; Rollins, Kiendler-Scharr, et al., 2009; Perring et al., 2009; Kwan et al., 2012; Sprengnether et al., 2002; Chen et al., 1998; F. Paulot et al., 2009b). Based on this high nitrate yield, Horowitz et al. (2007) predicted that in the Southeast US, 50% of the isoprene nitrates are derived from  $\text{NO}_3$  chemistry, even though this process represents only 6% of isoprene loss. Using an updated mechanism of the Community Multiscale Air Quality (CMAQ) model, Xie et al. (2013) also predicted that a large portion of isoprene nitrates are attributable to  $\text{NO}_3$  oxidation (~40%). Thus, isoprene  $\text{NO}_3$  chemistry is important for understanding how formation of organic nitrogen impacts regional  $\text{NO}_x$  and  $\text{O}_3$  concentrations. Indeed in forested regions that are influenced by urban emissions, the formation of these nitrates in the oxidation of isoprene by  $\text{NO}_3$  can be a significant sink for  $\text{NO}_x$ .

Organic nitrates are likely involved in secondary organic aerosol (SOA) formation. Using SOA yield measurements from chamber studies, S. S. Brown, DeGouw, et al. (2009a) estimate that isoprene  $\text{NO}_3$  chemistry contributes more to SOA formation than isoprene OH chemistry in urban areas of the Northeast US. Rollins, Browne, et al. (2012) observed that the particulate nitrate fraction and total organic aerosol mass concentration are enhanced at night, implicating nitrates from  $\text{NO}_3$  oxidation as the cause.

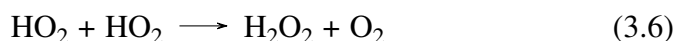
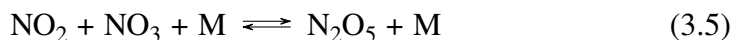
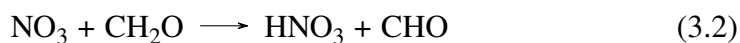
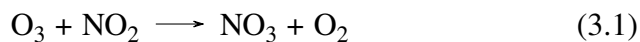
Isoprene oxidation by  $\text{NO}_3$  leads to the formation of peroxy radicals ( $\text{RO}_2$ ), and the subsequent chemistry will depend on which radical these  $\text{RO}_2$  react with (e.g.,  $\text{RO}_2$ ,  $\text{HO}_2$ ,  $\text{NO}_3$ ). Atmospherically-relevant studies of  $\text{NO}_3$  oxidation of biogenic

compounds require radical conditions similar to those encountered in forested environments. Measured HO<sub>2</sub> concentrations at night are often several ppt (Stone et al., 2012). For example, during the BEARPEX 2009 field campaign (located 75 km northeast of Sacramento, CA), the HO<sub>2</sub> mixing ratio at night was ~4 ppt (Mao, Ren, et al., 2012), while NO<sub>3</sub> was only ~1 ppt (Bouvier-Brown et al., 2009). Model calculations conducted by Xie et al. (2013) using CMAQ suggest that nearly half of the RO<sub>2</sub> reacts with HO<sub>2</sub> in the nighttime boundary layer. Consistent with these simulations, isoprene nitrooxy hydroperoxide (INP), a product from the RO<sub>2</sub> + HO<sub>2</sub> pathway, was detected during the BEARPEX 2009 (Beaver et al., 2012) and the Southern Oxidant and Aerosol Study (SOAS) 2013 field campaigns with a diurnal pattern consistent with a nighttime source (see Section 3.6). These findings support the importance of the RO<sub>2</sub> + HO<sub>2</sub> pathway in the atmospheric oxidation of isoprene by NO<sub>3</sub>.

To date, NO<sub>3</sub> radicals in laboratory chamber studies have been produced either via decomposition of N<sub>2</sub>O<sub>5</sub> or via reaction of O<sub>3</sub> and NO<sub>2</sub>. In these studies, a significant fraction of the isoprene derived alkylperoxy radicals (RO<sub>2</sub>) react with either NO<sub>3</sub> or with other RO<sub>2</sub>, which is dissimilar to the chemistry in most forested environments. In this study, we investigate the oxidation of isoprene by NO<sub>3</sub> in the presence of considerably higher concentrations of HO<sub>2</sub> radicals. We further investigate the photooxidation of the nitrates produced in this chemistry to understand the potential reactive uptake of these compounds to the particle phase.

### 3.3 Experimental Methods

We examined the products formed from NO<sub>3</sub> oxidation of isoprene in an environmental chamber. To study the RO<sub>2</sub> + HO<sub>2</sub> pathway, formaldehyde (CH<sub>2</sub>O) was injected into the chamber along with NO<sub>2</sub> and O<sub>3</sub> to enhance HO<sub>2</sub> production. The basic reactions summarizing the chemistry for this approach are shown below (Reactions 2.1-2.6). Table SA2 includes a more comprehensive list of general reactions.



This chemistry represents a new approach for studying  $\text{NO}_3$  oxidation with an independent  $\text{HO}_2$  source. It mimics atmospheric conditions in forested environments more closely than previous studies. With this approach, formation of  $\text{NO}_3$  and  $\text{HO}_2$  are coupled such that a nearly constant ratio of  $\text{NO}_3$  to  $\text{HO}_2$  is maintained throughout the experiment.

### Experimental Procedures

All experiments were carried out in either a 24  $\text{m}^3$  or a 1  $\text{m}^3$  Teflon chamber (see Table 1 for a list of experiments). Prior to each experiment, the 24- $\text{m}^3$  chamber was flushed with purified, dry air for 24 h such that all volatile organic compounds were below the detection limit, particle number concentration was  $< 10 \text{ cm}^{-3}$ , and particle volume concentration was  $< 0.01 \mu\text{m}^3 \text{ cm}^{-3}$ . Prior to each of the 1  $\text{m}^3$  experiments, the chamber was filled and flushed repetitively until all gas-phase products were below the detection limit.

**Table 3.1:** List of isoprene  $\text{NO}_3$  oxidation chamber experiments.

| Expt # | Chamber Size ( $\text{m}^3$ ) | $\text{CH}_2\text{O}$ (ppm) | $\text{NO}_2$ (ppb) | $\text{O}_3^A$ (ppb) | Isoprene (ppb) | Seed Type <sup>B</sup>                       | RH     |
|--------|-------------------------------|-----------------------------|---------------------|----------------------|----------------|--|--------|
| 1      | 24                            | 2.1                         | 300                 | 152, ~50             | 80             | None   | 31-41% |
| 2      | 24                            | 2.2                         | 300                 | 155, ~50             | 80             | $(\text{NH}_4)_2\text{SO}_4$                 | 34-42% |
| 3      | 24                            | 2.2                         | 300                 | 157, ~50             | 80             | $\text{MgSO}_4$ ,<br>$\text{H}_2\text{SO}_4$ | <3-6%  |
| 4      | 24                            | 2.2                         | 300                 | 160, ~50             | 80             | $(\text{NH}_4)_2\text{SO}_4$                 | <3-7%  |
| 5      | 24                            | 2.2                         | 300                 | 152, ~50             | 80             | None   | <3-3%  |
| 6      | 24                            | 4.7                         | 300                 | 153, ~50,<br>~50     | 60             | $\text{MgSO}_4$ ,<br>$\text{H}_2\text{SO}_4$ | <3-5%  |
| 7      | 1                             | 2.0                         | 330                 | ~150, ~50            | 85             | None   | -      |
| 8      | 1                             | 4.0                         | 100                 | 49                   | 24             | None   | -      |
| 9      | 24                            | 4.1                         | 100                 | 49                   | 18             | None   | <3-9%  |
| 10     | 1                             | 0                           | 100                 | 0                    | 97             | None   | -      |

<sup>A</sup> Multiple injections of  $\text{O}_3$  occurred in some experiments.  $\text{O}_3$  mixing ratios are listed according to injection order. <sup>B</sup> The atomizing solutions for the seed types used in this experiment were: 0.06 M  $(\text{NH}_4)_2\text{SO}_4$  and 0.03 M  $\text{MgSO}_4$  + 0.03 M  $\text{H}_2\text{SO}_4$ .

For experiments 1 and 2, the chamber was humidified prior to all injections. Dry, purified air was passed through a Nafion membrane humidifier (FC200, Permapure LLC) that is kept wet by recirculation of 27°C ultra-pure water (18M $\Omega$ , Millipore

Milli-Q). O<sub>3</sub> was introduced by flowing dry, purified air through an ozone generator (EMMET).

Gas phase CH<sub>2</sub>O was produced by flowing N<sub>2</sub> over paraformaldehyde solid (97% purity) in a heated glass bulb and subsequently through a 0°C trap to remove impurities. The CH<sub>2</sub>O was finally condensed and stored in a trap submerged in liquid nitrogen. CH<sub>2</sub>O was injected into the chamber after introduction of O<sub>3</sub> by filling a glass bulb with several Torr of pure CH<sub>2</sub>O and backfilling with dry N<sub>2</sub> gas. The final concentration in the glass bulb was ~1-2% CH<sub>2</sub>O. The CH<sub>2</sub>O mixing ratio in the bulb was measured using Fourier transform infrared spectroscopy (calculated from the HITRAN line list) and found to agree within ~14% of the concentration calculated from manometry. The mixing ratio in the bulb, however, decreased slowly over time indicating that some loss due to CH<sub>2</sub>O polymerization or deposition to the walls of the bulb occurs at these concentrations. Thus, CH<sub>2</sub>O was injected immediately into the chamber after the bulb was prepared to prevent further loss. For the ~24 m<sup>3</sup> chamber, the CH<sub>2</sub>O values reported in Table 3.1 were calculated assuming that the chamber volume was consistent for each experiment. With the exception of experiment 9, CH<sub>2</sub>O was not measured in the chamber.

NO<sub>2</sub> (488 ppm in N<sub>2</sub>, Scott Specialty Gases) was directly injected into the chamber through a mass flow controller. After 1 h, sufficient amounts of NO<sub>3</sub> and HO<sub>2</sub> were generated, and isoprene (99% purity) was introduced by injecting a known volume into a glass bulb fitted with a septum and flowing purified, clean air through the bulb into the chamber. The mixing ratios of NO<sub>3</sub> and HO<sub>2</sub> prior to isoprene injection varied by experiment, but as an example, the kinetic mechanism for experiment 8 predicts ~10 ppt NO<sub>3</sub> and ~70 ppt HO<sub>2</sub>.

For standard NO<sub>3</sub> oxidation experiments (1-5), additional O<sub>3</sub> was injected in the dark after 2.5-3 h of reaction to oxidize the remaining isoprene. After an additional 2.5-3 h, the UV lights were turned on ( $j_{NO_2} = 5 \times 10^{-3} \text{ s}^{-1}$ ) for 3 h to generate OH and photochemically oxidize the first-generation nitrates. Seed aerosols were subsequently introduced into the chamber (after 1 h dark equilibrium) to test SOA formation. To inject seed particles, dilute (0.03-0.06 M) aqueous solutions of various salts (Table 1) were atomized through a <sup>210</sup>Po neutralizer into the chamber. For humid experiments, the seeds were hydrated prior to injection into the chamber with a wet-wall denuder heated to ~90°C.

For experiment 6, O<sub>3</sub> was added 6.5 h after isoprene injection and then again 3 h later, in order to monitor second-generation products from NO<sub>3</sub> oxidation. At the end of

experiment 6, highly acidic seed was injected to investigate those products formed prior to photooxidation that undergo reactive uptake to seed aerosol. Experiments 7 and 8 were run in a 1-m<sup>3</sup> Teflon chamber ( $j_{NO_2} = 2.5 \times 10^{-3} \text{ s}^{-1}$ ). For experiment 7, all procedures were the same as the standard NO<sub>3</sub> experiments (1-5) described above. In experiment 8, more CH<sub>2</sub>O, and less isoprene, O<sub>3</sub>, and NO<sub>2</sub> were added to the chamber in order to slow down the chemistry and increase the fraction of isoprene reacting via the RO<sub>2</sub> + HO<sub>2</sub> pathway. Experiment 9 was run in the same way as experiment 8, but carried out during the Focused Isoprene eXperiment at the California Institute of Technology (FIXCIT) campaign (T. B. Nguyen, J. D. Crounse, Schwantes, et al., 2014). For experiment 10, second-generation chemistry was further minimized by injecting isoprene along with methyl nitrite (160 ppb), NO<sub>2</sub>, and H<sub>2</sub>O<sub>2</sub> (3.2 ppm) to create conditions in the chamber containing several oxidants (NO<sub>3</sub>, HO<sub>2</sub>, OH, and NO). After an initial photooxidation period (52 min,  $j_{NO_2} = 9.4 \times 10^{-5} \text{ s}^{-1}$ ) to generate HO<sub>2</sub>, lights were turned off and isoprene NO<sub>3</sub> oxidation began.

Figure 3.1 details the predicted isoprene oxidation fate and the nitrooxy alkylperoxy radical fate for a subset of the experiments (Table 3.1). To minimize the RO<sub>2</sub> + RO<sub>2</sub> chemistry, we find that the CH<sub>2</sub>O/isoprene ratio should be high (>70 in experiments 6 and 8). Experiment 8 had the most optimal conditions because the RO<sub>2</sub> + HO<sub>2</sub> pathway was clearly favored over the RO<sub>2</sub> + RO<sub>2</sub> pathway, and background OH was sufficiently small to limit second-generation chemistry that would not typically occur at night in the ambient atmosphere. This study focuses mainly on results from experiment 8. See the Supporting Information for analysis of the other experiments.

### Instrumentation

A gas chromatograph with a flame ionization detector (GC-FID, HP 6890N) using a HP-Plot-Q column was used to monitor isoprene, methyl vinyl ketone (MVK) and methacrolein (MACR). A -40°C cold trap upstream of the GC-FID was used to discriminate between authentic carbonyls and interfering hydroperoxides/epoxides (Liu et al., 2013; Rivera-Rios et al., 2014). The cold trap was warmed, cleaned, and dried every 2-3 h to avoid occluding sample flow with ice build-up. The cold trap was not used for experiments with high RH. Without the cold-trap, interferences increased MVK and MACR signals by ~10 and ~2 fold, respectively, suggesting that other hydroperoxides, such as INP, also interfere with the GC-FID detection of MVK and MACR in a manner similar to that observed for the first generation hydroxy hydroperoxides formed via oxidation of isoprene by OH (ISOPOOH) (Liu

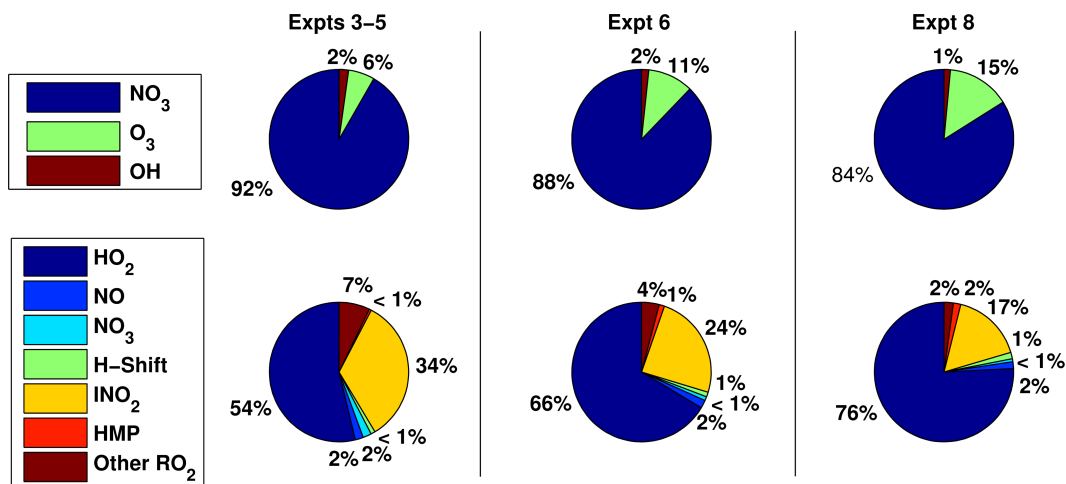


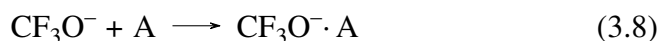
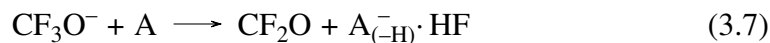
**Figure 3.1:** Isoprene reactant partner distribution (top graphs), and the nitrooxy alkylperoxy (INO<sub>2</sub>) radical reactant partner distribution (bottom graphs) predicted by the kinetic mechanism. Abbreviations not yet defined are hydroxy methyl peroxy radical (HMP).

et al., 2013; Rivera-Rios et al., 2014).

Relative humidity (RH) and temperature were monitored via a Vaisala HMM211 probe. O<sub>3</sub> was monitored using a Horiba O<sub>3</sub> analyzer (APOA-360). NO<sub>2</sub> and NO were monitored using a Teledyne NO<sub>x</sub> analyzer (Teledyne T200). Particle volume was monitored via a differential mobility analyzer (TSI, 3081) coupled with a condensation particle counter (TSI, 3010), and particle composition was monitored by a time-of-flight aerosol mass spectrometer (AMS) (Aerodyne Research, Inc.) (Drewnick et al., 2005). AMS data were processed using software (Squirrel 1.51H) (DeCarlo et al., 2006) with updated O:C ratios recommended by Canagaratna et al. (2015). The collection efficiency (0.75) in this work was assumed to be the same as that calculated for IEPOX derived organic aerosol (T. B. Nguyen, Coggon, et al., 2014).

A chemical ionization mass spectrometer (CIMS) using a custom-modified triple quadrupole mass analyzer (Varian, 1200) (Jason M. St. Clair et al., 2010) was used to monitor gaseous oxidized organic species. The CIMS uses CF<sub>3</sub>O<sup>-</sup> as the reagent ion. CF<sub>3</sub>O<sup>-</sup> interacts with an analyte (A) in either a transfer reaction (generally acidic species, R2.7) or a cluster complex (R2.8) (Jason M. St. Clair et al., 2010; Fabien Paulot et al., 2009a; John D. Crounse, McKinney, et al., 2006):



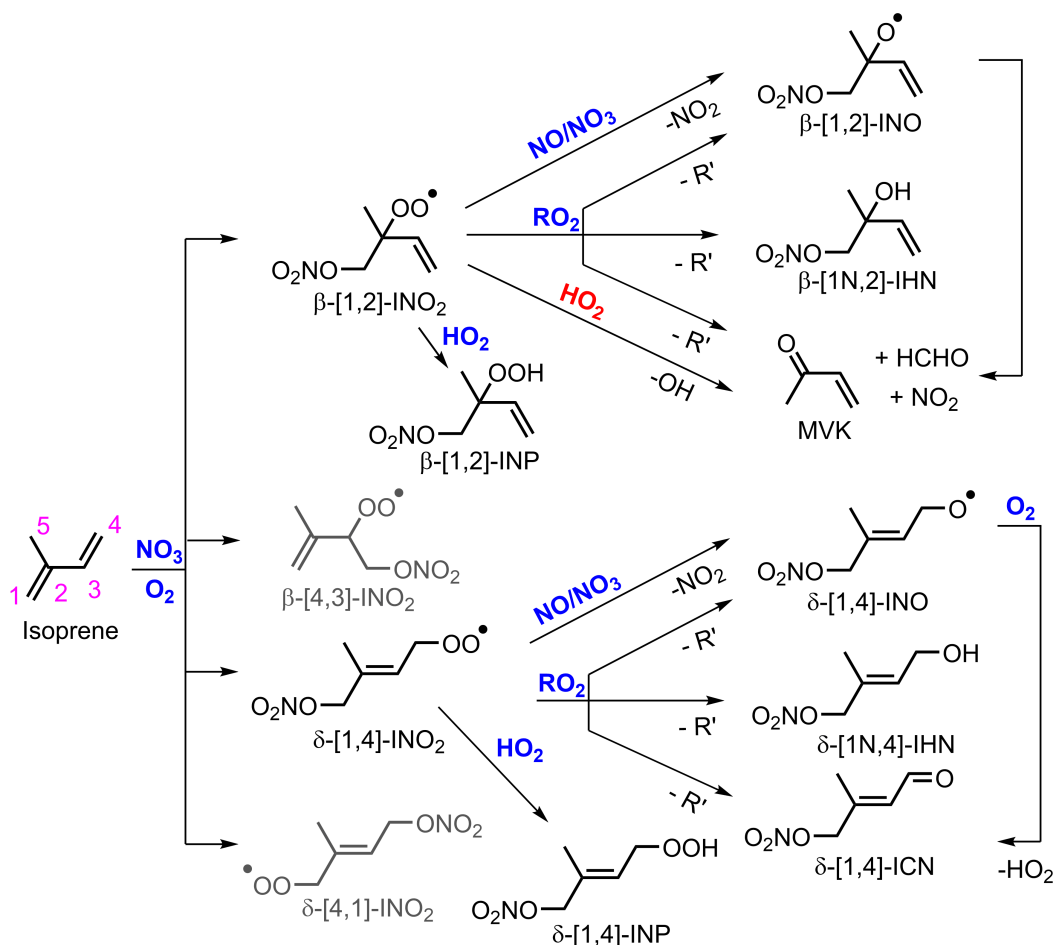


MS/MS mode was used on the triple quadrupole CIMS to separate isobaric compounds such as ISOPOOH and dihydroxy epoxide (IEPOX) (Fabien Paulot et al., 2009a).<sup>33</sup> In addition to a triple quadrupole CIMS (triple-CIMS), a Time-of-Flight CIMS (ToF-CIMS) coupled to a GC (Bates et al., 2014; Teng et al., 2015; Praske et al., 2015) was used during experiments 7-10. GC separation was achieved by cryofocusing products at the head of a 1m or 4 m GC column (RTX-1701 megabore) with a  $\sim -25^\circ\text{C}$  isopropanol cold bath. The oven temperature was set to ramp from 30-60°C at 3°C/min and 60-120°C at 10°C/min. Elution of products from the GC was monitored with the ToF- or triple-CIMS.

As synthetic standards are not available, the CIMS sensitivities for most of the isoprene nitrates formed in this work are not known. The large isoprene nitrates ( $\text{CF}_3\text{O}^-$  cluster ions with  $m/z \geq (-) 230$  except  $(-) 234$ , for which the sensitivity has been measured) were assumed to have the same sensitivity as IHN that was previously quantified using synthetic standards (T. B. Nguyen, J. D. Crounse, Schwantes, et al., 2014; Lance Lee et al., 2014). The uncertainty in the ToF-CIMS sensitivities is  $\pm 20\%$  for IHN. Based on theoretical calculations of the dipole moment and polarizability of the main nitrates (Kwan et al. (2012) (INP and ICN) and F. Paulot et al. (2009b) (IHN)), the sensitivities are expected to be similar, so we do not expect the uncertainty for the large nitrates formed in this work to exceed  $\pm 20\%$ . For non-nitrate species and the smaller nitrate species, synthesized standards or those of structurally similar compounds were used to calibrate the ToF-CIMS (measurement uncertainties  $\pm 20\%$ ).

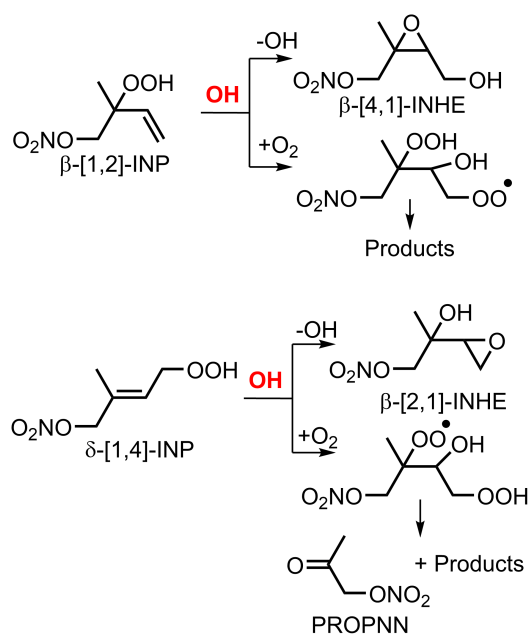
### 3.4 Results

The general isoprene- $\text{NO}_3$  reaction mechanism is shown in Figure 3.2. Four of the six nitrooxy alkylperoxy radical isomers are shown. The two *cis*- $\delta$  products also form, but for brevity are not shown. Structural isomers are named according to the oxidant addition site (first number) and  $\text{O}_2$  addition site (second number) on the isoprene skeleton (see Figure 3.2 for examples). For clarity, isoprene hydroxy nitrates (IHN) are labeled with an N next to the carbon number at which the nitrate group is attached since they arise from both OH and  $\text{NO}_3$  oxidation. Photooxidation products of the dominant  $\beta$ - and  $\delta$ -INP are shown in Figure 3.3.



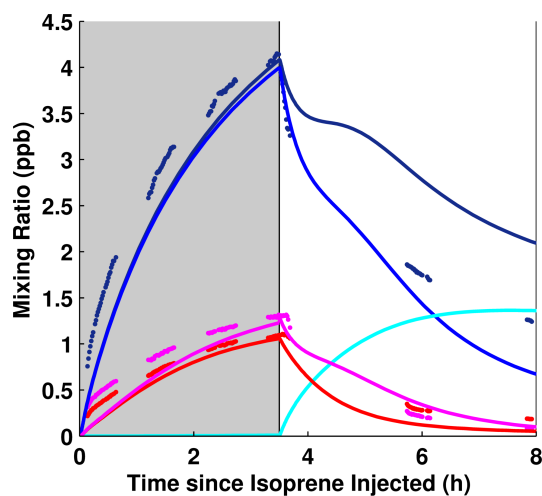
**Figure 3.2:** Diagram of the main products formed from  $\text{NO}_3$  oxidation of isoprene. For simplicity, products from only the dominant  $\beta$  and  $\delta$  isomer are presented. Well-established reactions are in blue. New or previously proposed reactions are in red (Rollins, Kiendler-Scharr, et al., 2009; Kwan et al., 2012). Carbon atom numbers for isoprene are shown in magenta. Acronyms used are nitrooxy alkylperoxy radical ( $\text{INO}_2$ ), nitrooxy alkoxy radical ( $\text{INO}$ ),  $\text{C}_5$  nitrooxy hydroperoxide (INP),  $\text{C}_5$  hydroxy nitrate (IHN), methyl vinyl ketone (MVK), and  $\text{C}_5$  carbonyl nitrate (ICN).

The main first-generation products formed from  $\text{NO}_3$  oxidation of isoprene are  $\text{C}_5$  nitrooxy hydroperoxide (INP),  $\text{C}_5$  carbonyl nitrate (ICN), and  $\text{C}_5$  hydroxy nitrate (IHN) (Figure 3.4 and Table 2). The molar yield of INP is higher than found in previous studies (Table 3.2), likely due to the significantly higher ratio of  $\text{HO}_2$  to  $\text{NO}_3$  in these experiments. The total molar yield of organic nitrates is estimated to be  $76 \pm 15\%$  (Table 3.2) of isoprene reacted; this includes isoprene loss due to  $\text{O}_3$  ( $\sim 15\%$ , see Figure 3.1), which presumably does not form nitrates. The nitrate yield determined in this study is similar to previous studies, which reported organic nitrate yields ranging from 65-80% (Barnes et al., 1990; Rollins, Kiendler-Scharr, et al.,



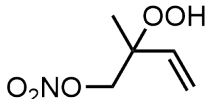
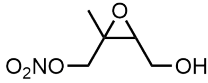
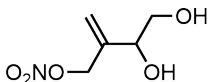
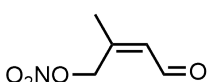
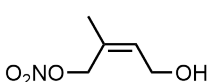
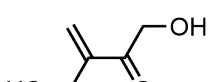
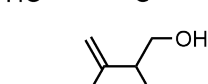
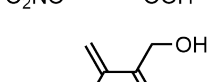
**Figure 3.3:** Photooxidation products (e.g., C<sub>5</sub> nitrooxy hydroxyepoxide (INHE)) of the dominant  $\beta$ - and  $\delta$ - C<sub>5</sub> nitrooxy hydroperoxide (INP).

2009; Perring et al., 2009). The product yields from other studies are also included as reference in Table 3.2, but comparing these yields directly is not possible because the contributions of  $\text{RO}_2 + \text{HO}_2$ ,  $\text{RO}_2 + \text{RO}_2$ , and  $\text{RO}_2 + \text{NO}_3$  are not equal between the studies. Refer to Figure 3.1 for the contribution of each pathway predicted by the kinetic mechanism for a subset of experiments in this study.

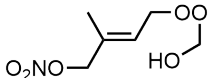
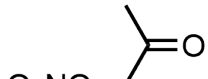


**Figure 3.4:** Major nitrates detected by the CIMS (markers, 1 min averages) and predicted by the kinetic mechanism (solid lines) for experiment 8 including C<sub>5</sub> nitrooxy hydroperoxide (INP) + C<sub>5</sub> nitrooxy hydroxyepoxide (INHE) + C<sub>5</sub> dihydroxy nitrate (IDHN) [dark blue], C<sub>5</sub> hydroxy nitrate (IHN) [red], and C<sub>5</sub> carbonyl nitrate (ICN) [magenta]. The kinetic mechanism results for INP [blue] and INHE [cyan] are also presented separately for reference. The white background indicates when photooxidation occurred.

**Table 3.2:** Molar yield per isoprene reacted for main products detected by the CIMS during experiment 8 (at 2.5 h) compared to yields reported previously.

| Name                                       | Abbrev. | Possible Structure   | m/z (-) | Est. VP (atm) <sup>A</sup> | Yield Here | Literature Yield                       |
|--|---------|--|---------|----------------------------|------------|--|
| C <sub>5</sub> nitrooxy hydroperoxide      | INP     |    | 248     | 1.0 x 10 <sup>-5</sup>     | 0.41       | 0.123 <sup>b</sup> , 0.18 <sup>c</sup> |
| C <sub>5</sub> nitrooxy hydroxyepoxide     | INHE    |    |         | 7.6 x 10 <sup>-6</sup>     |            |  |
| C <sub>5</sub> dihydroxy nitrate           | IDHN    |    |         | 3.2 x 10 <sup>-7</sup>     |            |  |
| C <sub>5</sub> carbonyl nitrate            | ICN     |    | 230     | 1.2 x 10 <sup>-4</sup>     | 0.12       | 0.356 <sup>b</sup> , 0.51 <sup>c</sup> |
| C <sub>5</sub> hydroxy nitrate             | IHN     |    | 232     | 2.4 x 10 <sup>-5</sup>     | 0.12       | 0.214 <sup>b</sup> , 0.27 <sup>c</sup> |
| C <sub>5</sub> dihydroxy carbonyl*         | IDHC    |  | 201     | 1.5 x 10 <sup>-6</sup>     | 0.03       | 0.012 <sup>b</sup>                     |
| C <sub>5</sub> hydroxy hydroperoxy nitrate | IHPN    |  | 264     | 3.0 x 10 <sup>-8</sup>     | 0.03       | 0.016 <sup>b</sup>                     |
| C <sub>5</sub> hydroxy carbonyl nitrate    | IHCN    |  | 246     | 3.6 x 10 <sup>-6</sup>     | 0.02       | 0.043 <sup>b</sup>                     |

**Table 3.2:** Molar yield per isoprene reacted for main products detected by the CIMS during experiment 8 (at 2.5 h) compared to yields reported previously.

| Name  | Abbrev. | Possible Structure   | m/z (-) | Est. VP (atm) <sup>A</sup> | Yield Here | Literature Yield   |
|---|---------|--|---------|----------------------------|------------|--|
| ROOR from INO <sub>2</sub> and HMP <sup>d</sup> * | INO2HM  |  | 278     | 8.5 x 10 <sup>-7</sup>     | 0.02       |  |
| Propanone nitrate                                 | PROPNN  |  | 204     | 4.5 x 10 <sup>-3</sup>     | 0.01       |  |
| Total Nitrates Detected                           |         |  |         |                            | 0.76       | ~0.80 <sup>e</sup> , 0.70 ± 0.08 <sup>f</sup> ,<br>0.65 ± 0.12 <sup>g</sup> , ~0.80 <sup>b</sup> |

Only a single isomer is shown. <sup>A</sup>Vapor pressure (atm, at 298K) is estimated using the method EVAPORATION.

(Compernelle et al., 2011). We note epoxides are not a functional group specifically within the scope of EVAPORATION.

\*Assignment of these compounds is tentative; observed signal could be impacted by other compounds. <sup>b</sup> (Kwan et al., 2012). <sup>c</sup> (Ng et al., 2008).

<sup>d</sup> ROOR from INO<sub>2</sub> and hydroxy methyl peroxy (HMP) or CIMS complex btw INP and CH<sub>2</sub>O. <sup>e</sup> (Barnes et al., 1990).

<sup>f</sup> (Rollins, Kiendler-Scharr, et al., 2009). <sup>g</sup> (Perring et al., 2009).

We quantify isomer specific yields of the main nitrates formed using the GC-ToF-CIMS (Table 3.3). INP fragments during ionization ( $\sim 12\%$ ) in the  $\text{CF}_3\text{O}^-$  CIMS. Data in Table 3.2 and Table 3.3 are corrected for this fragmentation (see Section 3.9 for more details). We use experiment 8 to determine the isomer-dependent yields for ICN and IHN because this experiment had the lowest oxidant concentrations, which minimized second-generation chemistry. The first GC-ToF-CIMS chromatograph (49 min after the start of isoprene  $\text{NO}_3$  oxidation) was used to calculate the fractions in Table 3.3 to limit the influence of wall loss and later generation chemistry.

**Table 3.3:** Proposed isomer distribution for INP, ICN, and IHN including uncertainties due to peak integration and CIMS sensitivity.

| Nitrate   | Distribution of $\beta/\delta$ -Isomers |                   | $\beta$ - and $\delta$ -Isomer Distribution |                    |
|---|---|-------------------|---|--------------------|
|   | Isomer                                  | Percent           | Isomer                                      | Percent            |
| C <sub>5</sub> Nitrooxy<br>Hydroperoxide<br>(INP) | $\beta$                                 | $30^{+9}_{-8} \%$ | $\beta$ -[1,2]                              | $88^{+4}_{-5} \%$  |
|   |   |                   | $\beta$ -[4,3]                              | $12^{+5}_{-4} \%$  |
|   | $\delta$                                | $70^{+8}_{-9} \%$ | $\delta$ -[1,4]                             | $84^{+7}_{-11} \%$ |
|   |   |                   | $\delta$ -[4,1]                             | $16^{+11}_{-7} \%$ |
| C <sub>5</sub> Carbonyl<br>Nitrate (ICN)          | $\beta$                                 | 0 %               | $\beta$ -[1,2]                              | NA                 |
|   |   |                   | $\beta$ -[4,3]                              | NA                 |
|   | $\delta$                                | 100%              | $\delta$ -[1,4]                             | $74^{+8}_{-9} \%$  |
|   |   |                   | $\delta$ -[4,1]                             | $26^{+9}_{-8} \%$  |
| C <sub>5</sub> Hydroxy<br>Nitrate (IHN)           | $\beta$                                 | $20^{+7}_{-6} \%$ | $\beta$ -[1,2]                              | 0 %                |
|   |   |                   | $\beta$ -[4,3]                              | 100 %              |
|   | $\delta$                                | $80^{+6}_{-7} \%$ | $\delta$ -[1,4]                             | $86^{+6}_{-8} \%$  |
|   |   |                   | $\delta$ -[4,1]                             | $14^{+8}_{-6} \%$  |

For INP,  $\text{RO}_2 + \text{RO}_2$  chemistry clearly impacts the isomer distribution even in experiment 8 when  $\text{RO}_2 + \text{RO}_2$  chemistry is limited (Figure 3.1). The first GC-ToF-CIMS results (39 min after photooxidation ended) for experiment 10 were used to determine the isomer distribution of INP. In this experiment  $\text{RO}_2 + \text{RO}_2$  chemistry was much less prominent than experiment 8. For example, in experiments 7, 8, and 10 the ratio of  $\beta$ -INP compared to  $\beta$ -[4,3]-IHN, the IHN isomer produced from the  $\text{RO}_2$  with the fastest expected  $\text{RO}_2 + \text{RO}_2$  rate constant, was 2.5, 4.4, and 14.6. Experiment 10 contained a mixture of products from OH and  $\text{NO}_3$  oxidation of isoprene, which made further use of this experiment difficult, but since INP forms only from isoprene and  $\text{NO}_3$  oxidation, this experiment was optimal for determining these isomer ratios.

Synthetic standards are not available for most of the nitrates formed in this work, so the relative GC-ToF-CIMS elution times of synthetic standards from ISOPOOH/IEPOX (Bates et al., 2014) and hydroxy nitrates from isoprene OH oxidation (T. B. Nguyen, J. D. Crounse, Schwantes, et al., 2014) are used to assign the peaks to INP/INHE, ICN, and IHN. Uncertainties in Table 3.3 are derived from the uncertainty in integration (1 sigma) and uncertainty in the relative sensitivity between the isomers (20%). Peak assignments are shown in Figure 3.11 and Table 3.6, and explanation for peak selection is discussed in Section 3.9. Transmission through the GC-ToF-CIMS for all isomers reported in Table 3.3 was  $\sim 100\%$ .

### 3.5 Discussion

To analyze these experiments, we develop a kinetic mechanism for the isoprene- $\text{NO}_3$  reaction based on available recommended literature rates and branching ratios. The first-generation products including the isomer distributions of the significant nitrates reported in Table 3.3 are incorporated into the kinetic mechanism. For the most part, we use the literature rates and branching ratios without attempting to optimize the chemistry due to the complexity of the chamber mixture. Three primary oxidants are present ( $\text{NO}_3$ ,  $\text{O}_3$ , and OH) within our experiments. The rates and products for reactions between these three oxidants and the isoprene nitrates produced via  $\text{NO}_3$  oxidation are not well known. As a result of the few constraints and large number of unknowns, a variety of solutions to the chemical mechanism can explain the observations equally well. Nevertheless, the kinetic mechanism developed here does inform our analysis and provide guidance for future studies.

We use the kinetic mechanism and the products detected to give insight on each step of isoprene oxidation by  $\text{NO}_3$ :

- $\text{NO}_3$  addition to isoprene and subsequent  $\text{O}_2$  addition to form a nitrooxy peroxy radical ( $\text{INO}_2$ )
- $\text{INO}_2$  reaction with either itself or another  $\text{RO}_2$ ,  $\text{HO}_2$ , or  $\text{NO}/\text{NO}_3$  to form nitrates, each with unique isomer distributions.
- The subsequent fate of these organic nitrates upon reaction with OH to form INHE, PROPNN, and other products, some of which (e.g., INHE) undergo reactive uptake to the aerosol phase.



### Isoprene Nitrooxy Peroxy Radical (INO<sub>2</sub>) Distribution.

NO<sub>3</sub> adds to isoprene followed by O<sub>2</sub> addition to form isoprene nitrooxy peroxy radical (INO<sub>2</sub>). There are few previous constraints (Skov et al., 1992; Berndt et al., 1997; Suh et al., 2001) on the INO<sub>2</sub> distribution, but this distribution is important to understand as it determines the lifetime and subsequent photoproducts of the first-generation compounds. To determine the INO<sub>2</sub> distribution, we use the products of the INO<sub>2</sub> + HO<sub>2</sub> reaction (Table 3.5-Column 2) and assume that each INO<sub>2</sub> reacts with HO<sub>2</sub> at the same rate, consistent with Michael E. Jenkin and Hayman (1995). Based on this INO<sub>2</sub> distribution, NO<sub>3</sub> adds to the C<sub>1</sub> position of isoprene 7±1 times faster than to the C<sub>4</sub> position. This range is on the high end of other experimental studies (3.5 (Skov et al., 1992) and 5.1-7.4 (Berndt et al., 1997)) and a theoretical study (5.6) (Suh et al., 2001).

We find that  $\delta$ -peroxy radicals are present in slightly higher quantities than  $\beta$ -peroxy radicals (~1.2:1), also consistent with previous studies. Skov et al. (1992) proposed that the dominant product is [1,4]-ICN, but no quantitative data were provided. In a theoretical study, Zhao et al. (2008) calculated that O<sub>2</sub> adds 1.15 times faster at the  $\delta$  position. However, the ratio of the O<sub>2</sub> addition rates does not necessarily determine the  $\delta/\beta$  distribution as (J. Peeters, T. L. Nguyen, et al., 2009; Jozef Peeters et al., 2014) have shown that the bond strength of the alkylperoxy radicals is sufficiently weak that, with a time constant of several seconds, the RO<sub>2</sub> will dissociate leading to a dynamic exchange between  $\beta$ - and  $\delta$ -isomers. Zhao et al. (2008) calculated that the energy differences (kcal mol<sup>-1</sup>) between INO<sub>2</sub> and isoprene-NO<sub>3</sub> + O<sub>2</sub> are between 15.63-17.20 for  $\beta$ -INO<sub>2</sub> and 11.97-14.06 for  $\delta$ -INO<sub>2</sub>, suggesting that the reverse reaction will likely be important for INO<sub>2</sub>.

Recently, a number of studies have highlighted the importance of RO<sub>2</sub> lifetime for isoprene oxidation by OH (J. Peeters, T. L. Nguyen, et al., 2009; Jozef Peeters et al., 2014). The lifetime influences the isomer distribution, which, in turn, influences later generation products and likely SOA formation. We suspect that the RO<sub>2</sub> lifetime is also important for isoprene oxidation by NO<sub>3</sub>. According to the kinetic mechanism developed here, the INO<sub>2</sub> lifetime at the beginning of experiments 5, 6, 8, and 10 was ~7 s, ~10 s, ~30 s, and ~20 s, respectively. However, across all experiments the estimated INO<sub>2</sub> lifetime increased with time. For example, the INO<sub>2</sub> overall lifetime prior to photooxidation in experiment 8 was estimated to be ~80 s. Reaction of INO<sub>2</sub> + NO<sub>2</sub> was not included in the INO<sub>2</sub> lifetime calculation because the peroxyxynitrate that forms is believed to quickly decompose back to INO<sub>2</sub>.

and NO<sub>2</sub> without altering the initial isomer distribution. The INO<sub>2</sub> distribution determined in this work is for an RO<sub>2</sub> lifetime of ~30 s as most of the distribution is based on the INP isomer fractions measured during experiment 10, and the average lifetime between the start of NO<sub>3</sub> oxidation and the first GC collection time is ~30 s. An RO<sub>2</sub> lifetime of ~30 s may be representative of that at night in the urban atmosphere (~50 s), but the lifetime for rural conditions may be much longer (~200 s), assuming HO<sub>2</sub> is 5 ppt and RO<sub>2</sub> is 20 ppt 48 for both conditions, and NO<sub>3</sub> is 1 ppt in rural (Bouvier-Brown et al., 2009) and 300 ppt in urban (Steven S. Brown et al., 2012) conditions with the rate constants assumed in the kinetic mechanism.

Our data suggest that for an INO<sub>2</sub> lifetime of ~30 s, the  $\delta$ -INO<sub>2</sub> concentration is 1.1-1.2 times more abundant than the  $\beta$ -INO<sub>2</sub> isomer. Based on theoretical calculations, Jozef Peeters et al. (2014) calculated that for OH-initiated oxidation of isoprene at 295 K the  $\beta$ -isomer would, in contrast, be nearly ~30 times higher than the  $\delta$ -isomer for RO<sub>2</sub> at a similar lifetime. This suggests that the alkylperoxy radical kinetics and thermodynamics are quite different for NO<sub>3</sub> derived peroxy radicals.

### **RO<sub>2</sub> + RO<sub>2</sub> Reaction Rates.**

As shown in Figure 3.2, INO<sub>2</sub> can react with itself or another RO<sub>2</sub> radical to form IHN and ICN or two alkoxy radicals (INO). In order to constrain the MVK and MACR yields from the RO<sub>2</sub> + HO<sub>2</sub> pathway, the yields of MVK and MACR from the RO<sub>2</sub> + RO<sub>2</sub> pathway need to be approximated. In experiment 8, IHN, ICN, and INO predominantly come from RO<sub>2</sub> + RO<sub>2</sub> reactions because NO and NO<sub>3</sub> levels are so low (Figure 1). The IHN and ICN isomer distributions can give insight into the RO<sub>2</sub> + RO<sub>2</sub> self-reaction rates of INO<sub>2</sub>. The alkoxy radical can either react with O<sub>2</sub> to form HO<sub>2</sub> and ICN or undergo a [1,5]-H-shift (Figure 3.12). We detect the same products Kwan et al. (2012) proposed formed from the [1,5]-H-shift of the trans-[1,4]-INO. Additionally, recent studies for similar alkoxy radicals (Jozef Peeters et al., 2014) suggest that the trans- and cis-[1,4]-INO may interconvert rapidly (see Section 3.9 for more details). Because of this, the ICN distribution favors the [4,1]-isomer more than the INP and IHN distribution (Table 3.3). The distribution of IHN, ICN, and the [1,5]-H-shift products are shown in Table 3.4, Column 2. To calculate this distribution we assumed that for every [1,2]-IHN or [4,3]-IHN detected there is a corresponding MVK or MACR formed. This product distribution is included in the kinetic mechanism.

MCM v3.2 recommends a single rate coefficient of  $1.3 \times 10^{-12} \text{ cm}^3 \text{ molec}^{-1} \text{ s}^{-1}$  for

**Table 3.4:** Isomer specific IHO<sub>2</sub> + IHO<sub>2</sub> rate constants compared to estimated INO<sub>2</sub> + INO<sub>2</sub> rate constants.

| Isomer          | RO <sub>2</sub> + RO <sub>2</sub><br>Product<br>Distribution | Normalized<br>RO <sub>2</sub> + RO <sub>2</sub><br>Product Distribution <sup>A</sup> | k <sub>IHO<sub>2</sub>+IHO<sub>2</sub></sub><br>(cm <sup>3</sup> molec <sup>-1</sup><br>s <sup>-1</sup> ) <sup>B</sup> | Estimated<br>k <sub>INO<sub>2</sub>+INO<sub>2</sub></sub><br>(cm <sup>3</sup> molec <sup>-1</sup> s <sup>-1</sup> ) |
|-----------------|--|--|--|---|
| $\beta$ -[1,2]  | 1.5 x 10 <sup>-3</sup>                                       | (3.5-3.6) x 10 <sup>-3</sup>   | 6.92 x 10 <sup>-14</sup>   | 1.8 x 10 <sup>-14</sup>   |
| $\beta$ -[4,3]  | 0.12   | 2.2-4.6  | 5.74 x 10 <sup>-12</sup>   | (1.1-2.3) x 10 <sup>-11</sup>   |
| $\delta$ -[1,4] | 0.73   | 1.6  | 3.90 x 10 <sup>-12</sup>   | (7.9-8.2) x 10 <sup>-12</sup>   |
| $\delta$ -[4,1] | 0.15   | 1.7  | 2.77 x 10 <sup>-12</sup>   | (8.3-8.6) x 10 <sup>-12</sup>   |

<sup>A</sup> The normalized RO<sub>2</sub> + RO<sub>2</sub> product distribution is the RO<sub>2</sub> + RO<sub>2</sub> product distribution (Column 2) divided by the INO<sub>2</sub> distribution estimated by the INO<sub>2</sub> + HO<sub>2</sub> products (Table 3.5-Column 2). <sup>B</sup>(Michael E. Jenkin, Boyd, et al., 1998)

all isomers of INO<sub>2</sub> + INO<sub>2</sub>. However, for isoprene RO<sub>2</sub> species from OH oxidation (IHO<sub>2</sub>), MCM v 3.2 recommends isomer specific rates based on a study done by Michael E. Jenkin, Boyd, et al. (1998) (Table 3.4, Column 4). To our knowledge, there are no direct studies on how nitrate groups influence RO<sub>2</sub> + RO<sub>2</sub> rates.  $\beta$ -chloro,  $\beta$ -bromo, and  $\beta$ -hydroxy functional groups seem, however, to similarly increase the RO<sub>2</sub> + RO<sub>2</sub> rates (Michael E. Jenkin and Hayman, 1995; Murrells et al., 1991; John N. Crowley et al., 1992). Similar to nitrooxy, all of these substituents are electron-withdrawing, so a priori we would expect that the RO<sub>2</sub> kinetics would follow a similar pattern.

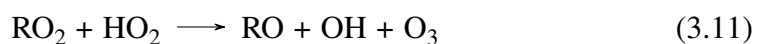
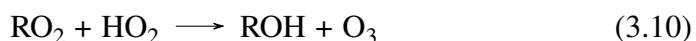
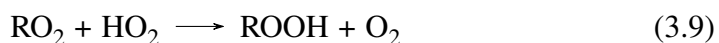
As shown in Figure 3.4, the kinetic mechanism best captures the formation rate of IHN when one uses a general rate constant for INO<sub>2</sub> + INO<sub>2</sub> of  $\sim 5 \times 10^{-12}$  cm<sup>3</sup> molec<sup>-1</sup> s<sup>-1</sup>. A general rate constant of  $\sim 3 \times 10^{-12}$  cm<sup>3</sup> molec<sup>-1</sup> s<sup>-1</sup> produces enough IHN in the kinetic mechanism to be within the uncertainty of the ToF-CIMS results. This general INO<sub>2</sub> + INO<sub>2</sub> rate constant is much larger than that included in MCM v3.2, CMAQ (Xie et al., 2013), or GEOS-CHEM (Mao, F. Paulot, et al., 2013). The present study, however, does not provide ideal conditions to measure the RO<sub>2</sub> + RO<sub>2</sub> reaction rates as CH<sub>2</sub>O and HO<sub>2</sub> will react reversibly to form the hydroxy methylperoxy radical (HMP) and the equilibrium constant for this reaction is not well-constrained (IUPAC (Atkinson, Baulch, Cox, J. N. Crowley, Hampson, Hynes, M. E. Jenkin, Rossi, Troe, and Subcommittee, 2006)). Additionally, it is possible that the HMP + HMP reaction rate constant is faster than that recommended by IUPAC. Thus, although the high general RO<sub>2</sub> + RO<sub>2</sub> rate constant used in this work

is necessary to constrain the products from the  $\text{RO}_2 + \text{RO}_2$  pathway, it is possible that this rate constant leads to a better fit of the data (Figure 3.4) merely because of uncertainties in HMP formation and subsequent reaction. It is recommended that a separate study be carried out to independently measure the general  $\text{INO}_2 + \text{INO}_2$  rate constant.

To estimate the isomer-specific self-reaction rates, we normalize by the  $\text{INO}_2$  distribution fractions based on the  $\text{INO}_2 + \text{HO}_2$  products (Table 3.5-Column 2). Although studies have confirmed that  $\text{RO}_2 + \text{HO}_2$  rate constants are influenced by carbon number (Saunders et al., 2003), it appears that the type of peroxy radical (i.e., primary, secondary, or tertiary) does not substantially impact the  $\text{RO}_2 + \text{HO}_2$  reaction rate constants (Michael E. Jenkin and Hayman, 1995). Provided that the  $\text{INO}_2 + \text{HO}_2$  rate constants are not isomer dependent, the ratio of the  $\text{RO}_2 + \text{RO}_2$  products to the  $\text{INO}_2 + \text{HO}_2$  products represents the relative  $\text{RO}_2 + \text{RO}_2$  reaction rate distribution between the isomers (normalized  $\text{RO}_2 + \text{RO}_2$  product distribution, Table 3.4-Column 3). The isomer specific  $\text{RO}_2 + \text{RO}_2$  reaction rate constants were estimated by combining the generalized reaction rate constant ( $\sim 5 \times 10^{-12} \text{ cm}^3 \text{ molec}^{-1} \text{ s}^{-1}$ ) based on IHN formation with the normalized  $\text{RO}_2 + \text{RO}_2$  product distributions based largely on the GC-ToF-CIMS results. The  $\beta$ -[4,3]-IHO<sub>2</sub> self-reaction rate constant is the largest (Table 3.4) consistent with the measured isomer dependent IHO<sub>2</sub> + IHO<sub>2</sub> rate constants (Michael E. Jenkin, Boyd, et al., 1998).

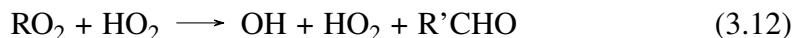
### **$\text{INO}_2 + \text{HO}_2$ Reaction Products.**

Hydroperoxides have typically been assumed to be the dominant product of the  $\text{RO}_2 + \text{HO}_2$  reaction pathway. Recent studies of acetylperoxy radical (Sulbaek Andersen et al., 2003; A. S. Hasson et al., 2004; Hurley et al., 2006; M. E. Jenkin et al., 2007; Dillon et al., 2008) and  $\alpha$ -carbonyl peroxy radical (Praske et al., 2015; A. S. Hasson et al., 2004; Alam S. Hasson et al., 2012; M. E. Jenkin et al., 2010) reactions with  $\text{HO}_2$  have found, however, that a variety of other products can form (R2.9-R2.11):



Rollins, Kiendler-Scharr, et al. (2009) and Kwan et al. (2012) proposed that the  $\text{INO}_2 + \text{HO}_2$  reaction produces OH as well as INP. Using the formation of isoprene

OH oxidation products (e.g., hydroxy hydroperoxide (ISOPOOH)) as tracers for OH chemistry, Kwan et al. (2012) suggested that 38-58% of the total  $\text{INO}_2 + \text{HO}_2$  reactions produce OH via channel R2.11. Hou, Deng, et al. (2005) and Hou and Wang (2005) have proposed a different reaction pathway (R2.12), in which OH,  $\text{HO}_2$ , and  $\text{R}'\text{CHO}$  form:



R2.12 has also been suggested to be important in the reactions of  $\text{RO}_2$  produced from  $\text{MVK} + \text{OH} + \text{O}_2$  with  $\text{HO}_2$  radicals (Praske et al., 2015).

The  $\beta$ -isomers, [1,2]- $\text{INO}_2$  and [4,3]- $\text{INO}_2$ , may react with  $\text{HO}_2$  to produce OH and MVK or MACR. The MVK and MACR yield from the  $\text{INO}_2 + \text{HO}_2$  pathway is inferred by subtracting all known sources of MVK and MACR (as predicted by the kinetic simulation) from the observations and assuming the remainder arises from the  $\text{INO}_2 + \text{HO}_2$  pathway. The overall MVK (12.3%) and MACR (4.8%) yields (relative to isoprene consumed) from experiment 6 were used, as experiments 1-5 have an unknown GC-FID interference following the subsequent injections of  $\text{O}_3$ . In experiment 6, we were able to quantify MVK and MACR after all  $\text{O}_3$  had reacted away. Additionally, a cold trap ( $-40^\circ\text{C}$ ) was used upstream of the GC-FID to remove interferences from hydroperoxides/epoxides (Liu et al., 2013; Rivera-Rios et al., 2014).

The yield of MVK from  $\text{RO}_2 + \text{HO}_2$  compared to  $\text{RO}_2 + \text{RO}_2$  reactions is expected to be quite high given that the  $\beta$ -[1,2]- $\text{INO}_2 + \text{RO}_2$  reaction rate constant is expected to be small. Conversely, MACR yields from the  $\text{RO}_2 + \text{HO}_2$  pathway will be difficult to constrain given that the  $\beta$ -[4,3]- $\text{INO}_2 + \text{RO}_2$  reaction rate constant is quite high. A general  $\text{RO}_2 + \text{HO}_2$  branching ratio of 0.22 for MVK best matches with the present experimental data, but the kinetic mechanism over-predicts MACR even without an additional yield from the  $\text{RO}_2 + \text{HO}_2$  pathway. This is likely a result of the assumption that for every [4,3]-IHN detected there is a corresponding MACR formed. The exact distribution of products from  $\text{RO}_2 + \text{RO}_2$  self- and cross-reactions is uncertain. We calculate the isomer dependent product distribution of  $\text{INO}_2 + \text{HO}_2$  based on the isomer distribution of INP (Table 3.3) and the kinetic mechanism determined MVK yields. For the MACR yield from  $\beta$ -[4,3]- $\text{INO}_2 + \text{HO}_2$  we report a range from 0 to the yield of MVK from  $\beta$ -[1,2]- $\text{INO}_2 + \text{HO}_2$  as

we expect less substituted nitrooxy peroxy radicals to produce less OH than their tertiary counterparts (Alam S. Hasson et al., 2012).

**Table 3.5:** Isomer dependent product distribution of  $\text{INO}_2 + \text{HO}_2$ .

| $\text{INO}_2$   | Fraction  | Products  | Yield  |
|------------------|-----------|---|--------|
| $\beta$ -[1,2]-  | 0.42      | OH + MVK + $\text{CH}_2\text{O}$ + $\text{NO}_2$  | 0.53   |
|                  |           | $\beta$ -[1,2]-INP                                | 0.47   |
| $\beta$ -[4,3]-  | 0.03-0.06 | OH + MACR + $\text{CH}_2\text{O}$ + $\text{NO}_2$ | 0-0.53 |
|                  |           | $\beta$ -[4,3]-INP                                | 0.47-1 |
| $\delta$ -[1,4]- | 0.44-0.46 | $\delta$ -[1,4]-INP                               | 1      |
| $\delta$ -[4,1]- | 0.08-0.09 | $\delta$ -[4,1]-INP                               | 1      |

The OH yield has only been measured for a small subset of alkylperoxy radicals. The  $\text{HO}_x$  recycling implied from the product distributions of  $\beta$ -[1,2]- $\text{INO}_2$  agrees with available data. For example, Alam S. Hasson et al. (2012) found that the secondary  $\text{RO}_2$   $\text{CH}_3\text{C}(\text{O})\text{CH}(\text{O}_2)\text{CH}_3$  produces 0.58 OH and Praske et al. (2015) found that the secondary  $\text{RO}_2$   $\text{CH}_3\text{C}(\text{O})\text{CH}(\text{O}_2)\text{CH}_2\text{OH}$  produces 0.66 OH from reaction with  $\text{HO}_2$ .

When an OH yield of 0.22-0.25 (i.e., co-product of MVK and MACR) is incorporated into the kinetic mechanism for the  $\text{RO}_2 + \text{HO}_2$  reaction, ISOPOOH formation is underpredicted prior to photooxidation for experiments 3-5 by  $\sim 29$ -34% (not shown), which may indicate “missing” OH in the experiment. However, the agreement is within the uncertainty of the Triple-CIMS measurements ( $\pm 35\%$ , see Section 3.9), and the yield of ISOPOOH will be dependent on the  $\text{RO}_2 + \text{RO}_2$  reaction rates used in the kinetic mechanism, which are not well constrained. MS/MS CIMS and the GC-ToF-CIMS verify that the initial chemistry produces only ISOPOOH, so formation of IEPOX, an isobaric compound, is not causing this discrepancy.

Furthermore, we confirm this potentially “missing” OH is not likely from the reaction of  $\delta$ - $\text{INO}_2 + \text{HO}_2 + \text{O}_2 \rightarrow \text{OH} + \text{HO}_2 + \text{ICN}$ . The ratios of INP:IHN and ICN:IHN are 2.4 and 1.5, respectively, for experiment 7 while for experiment 8 these ratios are 3.2 and 1.2, respectively. Given that  $\text{RO}_2 + \text{HO}_2$  reactions are more dominant in experiment 8 (Figure 1), if ICN is formed from  $\delta$ - $\text{INO}_2 + \text{HO}_2$  reactions, both the INP:IHN and ICN:IHN ratios should increase, but only the INP:IHN ratio increased from experiment 7 to 8. This strongly suggests that ICN is not a major product of the  $\text{RO}_2 + \text{HO}_2$  pathway.

Thus, evidence suggests that the general  $\text{RO}_2 + \text{HO}_2$  reaction products are 0.22 MVK, 0-0.03 MACR, 0.22-0.25 OH, 0.22-0.25  $\text{CH}_2\text{O}$ , 0.22-0.25  $\text{NO}_2$ , and 0.75-0.78 INP. Assuming the midpoint of the MACR range forms, the kinetic mechanism matches experimental results reasonably well (Figure 3.4).

### Photooxidation of First-Generation Nitrates

Photooxidation was initiated after generating the first-generation nitrates to monitor their reaction with OH (Scheme 3). This chemistry is relevant in regions where  $\text{NO}_3$  reacts with isoprene during the day (under clouds and within forest canopies) or at sunrise when  $\text{NO}_3$  and OH chemistry regimes overlap.

### INHE Formation

We propose that INP reacts with OH to form INHE (Figure 3.3). INP and INHE are isobaric compounds. For naming INHE isomers, the first number corresponds to the hydroxy group, and the second number to the nitrate group.  $\text{C}_5$  dihydroxy nitrate (IDHN) is also isobaric with INP and INHE. IDHN was first proposed by Kwan et al. (2012) along with  $\text{C}_5$  hydroxy carbonyl nitrate (IHCN) and  $\text{C}_5$  hydroxy hydroperoxy nitrate (IHPN) to be a product of the 1,5 H-shift of trans-[1,4]-INO (Figure 3.12). Unfortunately, we suspect  $\delta$ -INHE and IDHN co-elute in the GC-ToF CIMS so individual quantification was not possible (see Section 3.9 for more details on peak assignments). When photooxidation was started, IHCN, a co-product with IDHN from  $\text{RO}_2 + \text{RO}_2$  reactions, increased initially but then leveled off, while the peak containing  $\delta$ -INHE and IDHN kept rising (Figure 3.13). We subtract the IHCN signal from the  $\delta$ -INHE and IDHN signal, and assume the remaining signal is  $\delta$ -INHE (Figure 3.5). Although this correction is sensitive to yields of these 1,5 H-shift products, IDHN should be less than IHCN, resulting in overcorrection;  $\delta$ -INHE can be observed to be clearly formed when photooxidation started after this correction (Figure 3.5). The peaks for the remaining products,  $\delta$ -INP,  $\beta$ -INP, and  $\beta$ -INHE, are distinct, and no correction is needed.

Figure 3.5 suggests that the kinetic mechanism may over-predict INHE formation, but this depends on many factors including, but not limited to, CIMS calibration factors, the  $\text{O}_3$  and OH reaction rates of  $\beta$ -INP, and  $\delta$ -INP, transmission through the 4 m GC column, the loss rate of INHE itself with OH and walls of the chamber, and the amount of IDHN formed. It is possible INHE has a higher wall loss than INP due to nitric acid acidifying the chamber walls. In the kinetic mechanism,

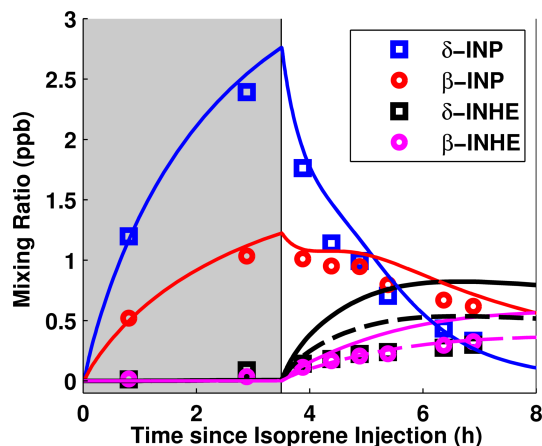


**Figure 3.5:** GC-ToF-CIMS data (markers) and kinetic mechanism results (lines) for  $\delta$ - and  $\beta$ -isomers of INP and INHE.  $\delta$ -INP GC-ToF-CIMS results are corrected for the low transmission rate through the 4m column (See Section 3.9). Solid lines indicate the base case of the mechanism, and dashed lines are results from reducing the INHE yield from INP + OH in the kinetic mechanism.

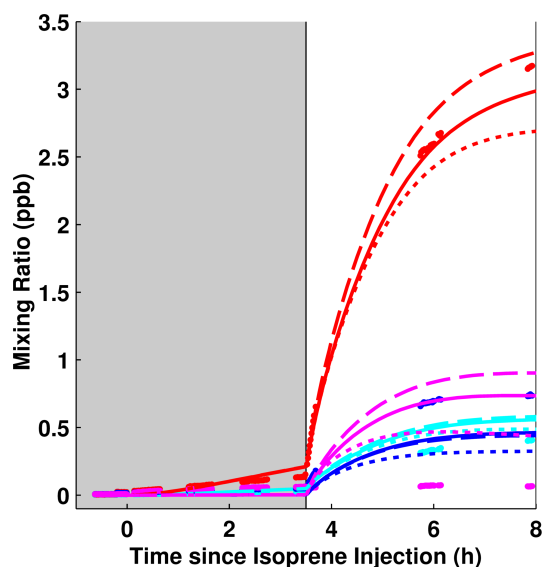
the INHE yields from the reaction of  $\delta$ -INP and  $\beta$ -INP with OH are assumed to be 0.37 and 0.78, respectively, based on the location of OH addition to standards similar to  $\delta$ -INP and  $\beta$ -INP (Teng et al., 2015; J. M. St. Clair et al., 2015) and the assumption that if the nascent alkyl radical is  $\beta$  to the hydroperoxide, INHE forms with unity yield. Due to the presence of the nitrooxy group, the lifetime of the alkyl radical before elimination of OH and formation of the epoxide may be longer than for ISOPOOH. If so, a larger fraction of the alkyl radicals may add  $O_2$  precluding INHE formation.

The yield of non-IEPOX products from OH addition to [1,2]-ISOPOOH and [4,3]-ISOPOOH has been measured to be  $\sim 0.13$  (J. M. St. Clair et al., 2015). Some of these products are likely from  $O_2$  addition prior to formation of IEPOX especially for [4,3]-ISOPOOH where OH is expected to add to the internal carbon minimally if OH addition is similar to MACR (0.035 for internal addition) (John D. Crounse, Knap, et al., 2012). For the dashed line, in Figure 3.5, a reduction of the  $\delta$ - and  $\beta$ -INHE yield in the kinetic mechanism by 36% for both isomers leads to a better match of  $\beta$ -INHE with experimental results. Given that  $\delta$ -INHE co-elutes with IDHN, we do not use the experimental results to optimize the yield of  $\delta$ -INHE, but it appears that a reduction  $> 36\%$  is necessary. Thus, results suggest that an INHE yield from the reaction of  $\delta$ -INP and  $\beta$ -INP with OH should be  $< 0.24$  and  $\sim 0.50$ , respectively. Figure 4 demonstrates that with this change PROPNN still reasonably aligns with experimental results.



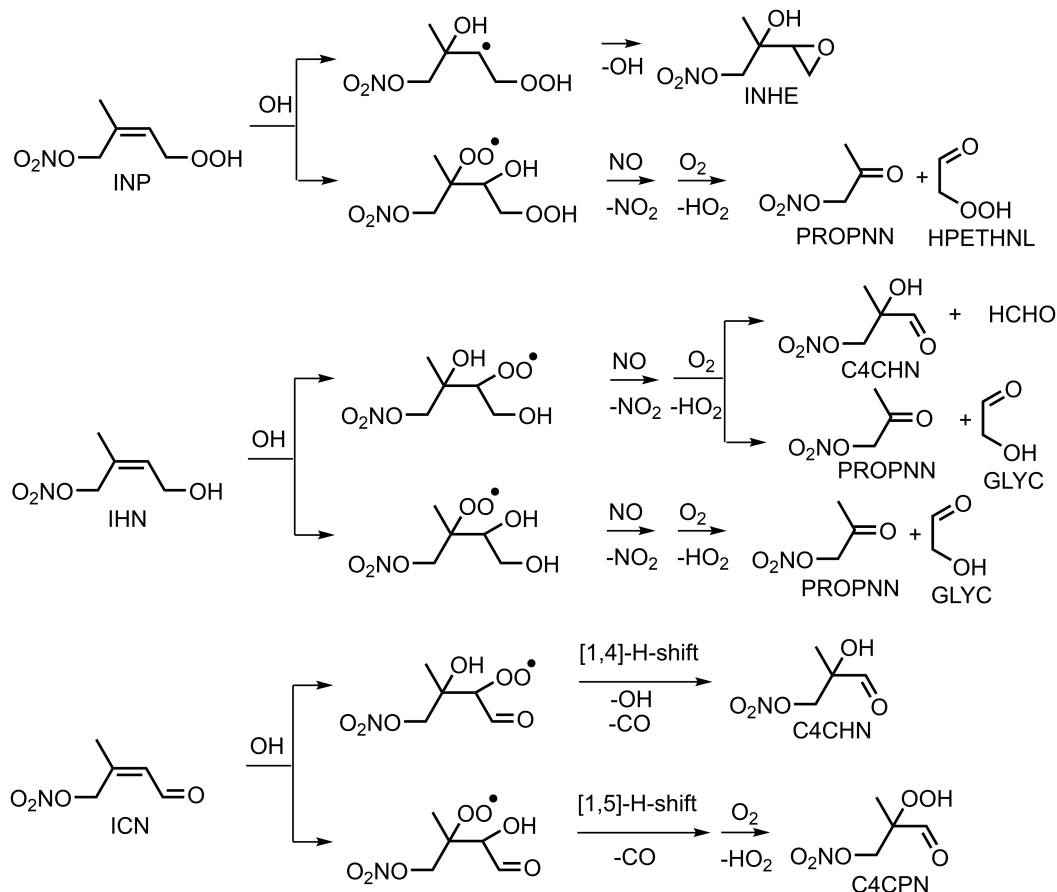
### Decomposition Products

Figure 4 and Scheme 3 show the primary nitrate decomposition products formed when INP, ICN, and IHN are photooxidized during experiment 8. Propanone nitrate (PROPNN) is observed with high yield. This is expected given that [1,4]-INO<sub>2</sub> is likely the dominant peroxy radical formed upon reaction of isoprene with OH. This chemistry has important atmospheric consequences because PROPNN has a fairly long photochemical lifetime in the atmosphere ( $\sim 7.1$  h including loss due to OH and photolysis) (Muller et al., 2014), although its dry deposition velocity is significant ( $\sim 2$  cm s<sup>-1</sup>) (T. B. Nguyen, J. D. Crounse, Teng, et al., 2015).



**Figure 3.6:** Experimental results (markers, 1 min averages) and kinetic mechanism results (lines) for propanone nitrate (red), ethanal nitrate (cyan), C<sub>4</sub> carbonyl hydroxynitrate (blue), and C<sub>4</sub> carbonyl hydroperoxynitrate (magenta) from experiment 8. Solid lines are for the base case, dashed lines are for revised IHNE yield (Section 3.9), and dotted lines are for the revised photolysis reactions (this section).

ICN, IHN, and INP are assumed to react with OH and O<sub>3</sub> similarly to the only standards that have been measured, [1,4N]-IHN and [4,3N]-IHN (see Figure 3.7 and Section 3.9 for more details) (Lance Lee et al., 2014; Jacobs, Burke, et al., 2014). The kinetic mechanism over-predicts ethanal nitrate (ETHLN) and C<sub>4</sub> carbonyl hydroperoxynitrate (C<sub>4</sub>CPN), but under-predicts C<sub>4</sub> carbonyl hydroxynitrate (C<sub>4</sub>CHN) (Figure 4). C<sub>4</sub>CPN is assumed to form from the peroxy radical, formed from ICN reacting with OH, undergoing a [1,5]-H shift (Figure 3.7 and Section 3.9) similar to the chemistry proposed by John D. Crounse, Knap, et al. (2012) for MACR. C<sub>4</sub>CPN is barely detected, but we expect this [1,5]-H-shift to be quite



**Figure 3.7:** The dominant decomposition products from the reaction of INP, IHN, and ICN with OH. For brevity, reactions for only the dominant isomer ([1,4]) and only major products are shown. See Section 3.9 for more details on additional products, branching ratios, and rates used in the kinetic mechanism. Acronyms not yet defined are glycolaldehyde (GLYC) and hydroperoxyethanal (HPETHNL).

fast because the [1,4]-H-shift for MACR64 occurs at  $0.5 \text{ s}^{-1}$ , and the [1,5]-H shift should be much faster. Possibly, the [1,5]-H shift leads to further decomposition forming PROPNN instead of C4CPN. Additionally, C4CPN might fragment while being ionized by  $\text{CF}_3\text{O}^-$ . For example,  $\beta$ -[1,2]-INP fragments by  $\sim 20\%$  (this work) and 3-hydroperoxy-4-hydroxybutan-2-one has been identified to fragment by 78% (Praske et al., 2015). Owing to the number of compounds present during photooxidation it is difficult to determine the fragmentation pattern of C4CPN. In the kinetic mechanism, C4CPN is assumed to photolyze to  $\text{MGLYX} + \text{OH} + \text{NO}_2 + \text{CH}_2\text{O}$ . No instrumentation was available to detect MGLYX to confirm that this process occurred.

We use the kinetic mechanism to test the extent to which loss due to photolysis can

explain the under-prediction of C4CPN. Theoretical (J. Peeters and Muller, 2010) and experimental (Wolfe et al., 2012) studies have found that hydroperoxyenals photolyze with a quantum yield of  $\sim 1$ , and Muller et al. (2014) proposed that many of the  $\alpha$ -nitrooxy aldehydes and ketones derived from isoprene also photolyze with a quantum yield of  $\sim 1$ . We revised the default MCM v3.2 quantum yield for PROPNN and ETHLN from 0.22 to 1, and for ICN from 0.00195 to 1. Although Wolfe et al. (2012) only verified that hydroperoxyenals photolyze with a quantum yield of  $\sim 1$ , we also assume that a similar effect occurs for  $\alpha$ -hydroperoxy carbonyls (e.g., C4CPN). As shown in Figure 3.6 (dotted lines), adding photolysis losses to the base case of the kinetic mechanism lowers the predicted amount of nitrates formed, but not outside of expected uncertainty (instrumental and kinetic mechanism assumptions). Even after increasing the rate of photolysis, C4CPN is still over-predicted by the kinetic mechanism, suggesting that the absorption cross sections could be larger than estimated due to the combined presence of a carbonyl, hydroperoxy, and nitrate group. Alternatively, the low signal may arise because either C4CPN does not form or C4CPN is fragmented during ionization.

Beyond the first-generation products, differences between the kinetic simulations and the experimental data cannot be securely tied to any particular uncertainty in the mechanism, owing to the complexity of the system. Nevertheless, the kinetic mechanism developed here suggests that using current understanding of how OH reacts with isoprene nitrates enables at least qualitatively correct simulations of the formation of the major nitrate decomposition products.

### **INHE Uptake onto Aerosols.**

INHE, similar to IEPOX (Fabien Paulot et al., 2009a; Surratt, Chan, et al., 2010), efficiently undergoes reactive uptake to highly acidified aerosol (Section 3.9 (Supplemental Information)). The INHE/IDHN-derived fragments in the AMS are identical to IEPOX ( $C_4H_5^+$ ,  $C_5H_6O^+$ ,  $C_3H_7O_2^+$ , and  $C_5H_8O_2^+$ ) (Lin et al., 2012) for highly acidic seed (likely due to the hydrolysis of the nitrate group). Thus, in the atmosphere under acidic conditions, INHE and IDHN likely add to the AMS tracer fragments that are generally assigned solely to IEPOX.

We would expect INHE, like IEPOX (T. B. Nguyen, Coggon, et al., 2014), to undergo reactive uptake to aqueous ammonium sulfate aerosol. There is an increase in the total organic mass measured by the AMS for hydrated ammonium sulfate aerosol compared to dry ammonium sulfate aerosol, but our results are inconclusive as this

could be due to INHE or other nitrates partitioning. From this work we find that a large fraction of the nitrates produced from  $\text{NO}_3$  oxidation are in the  $\delta$ -state (Table 3.3). If other  $\delta$ -nitrates hydrolyze as quickly as  $\delta$ -[1,4N]-IHN (neutral hydrolysis lifetime of 2.46 min) (Jacobs, Burke, et al., 2014), then the nitrates produced from  $\text{NO}_3$  oxidation might be an important sink for  $\text{NO}_3$  in humid locations. Further chamber studies run at a full range of relative humidities using synthetic standards of INHE and other nitrates are needed to better understand the influence isoprene  $\text{NO}_3$  oxidation has on SOA formed under humid conditions.

### 3.6 Atmospheric Relevance

During the SOAS field campaign (June-July 2013 in Brent, AL), products from  $\text{NO}_3$  oxidation of isoprene were detected in the ambient atmosphere (Figure 3.8). Consistent with the chemistry described here, ICN and INP/IDHN/INHE generally exhibit a nighttime peaking diurnal pattern, while IHN has a less clear diurnal pattern because it is produced from both the OH- and  $\text{NO}_3$ -initiated oxidation of isoprene. Interestingly, when ICN and INP/IDHN/INHE formed at night, their combined magnitude was similar to the amount of IHN formed during the day. INP/IDHN/INHE and ICN were observed in similar amounts, highlighting the importance of  $\text{RO}_2 + \text{HO}_2$  chemistry. ICN and INP/IDHN/INHE concentrations at night were quite variable during the campaign, likely reflecting changes in atmospheric conditions ( $\text{O}_3$ ,  $\text{NO}_2$ , temperature, isoprene).

On several days when ICN and INP/IDHN/INHE were detected at night, the main decomposition nitrates (PROPNN, ETHLN, and C4CHN) increased after sunrise, but this effect was not seen for all instances when ICN and INP/IDHN/INHE formed at night. It is difficult to attribute the formation of PROPNN, ETHLN, and C4CHN solely to chemical production given the large change in boundary layer dynamics forced by the increased surface heating. On some days, PROPNN, ETHLN, and/or C4CHN increased at sunrise even when ICN and INP/IDHN/INHE were not detected the night before. This does not necessarily suggest these products cannot be used as tracers for the nitrates derived from isoprene +  $\text{NO}_3$  because only measurements in the planetary boundary layer were made during SOAS by Caltech. It is possible that ICN and INP/IDHN/INHE were produced in the residual layer at night, and in the morning the photooxidation products were detected at the surface due to the rapid mixing that occurs at sunrise. Field studies measuring the formation of compounds in both the planetary boundary layer and residual layer at sunrise would be useful to better understand how PROPNN, ETHLN, and C4CHN form in the atmosphere.

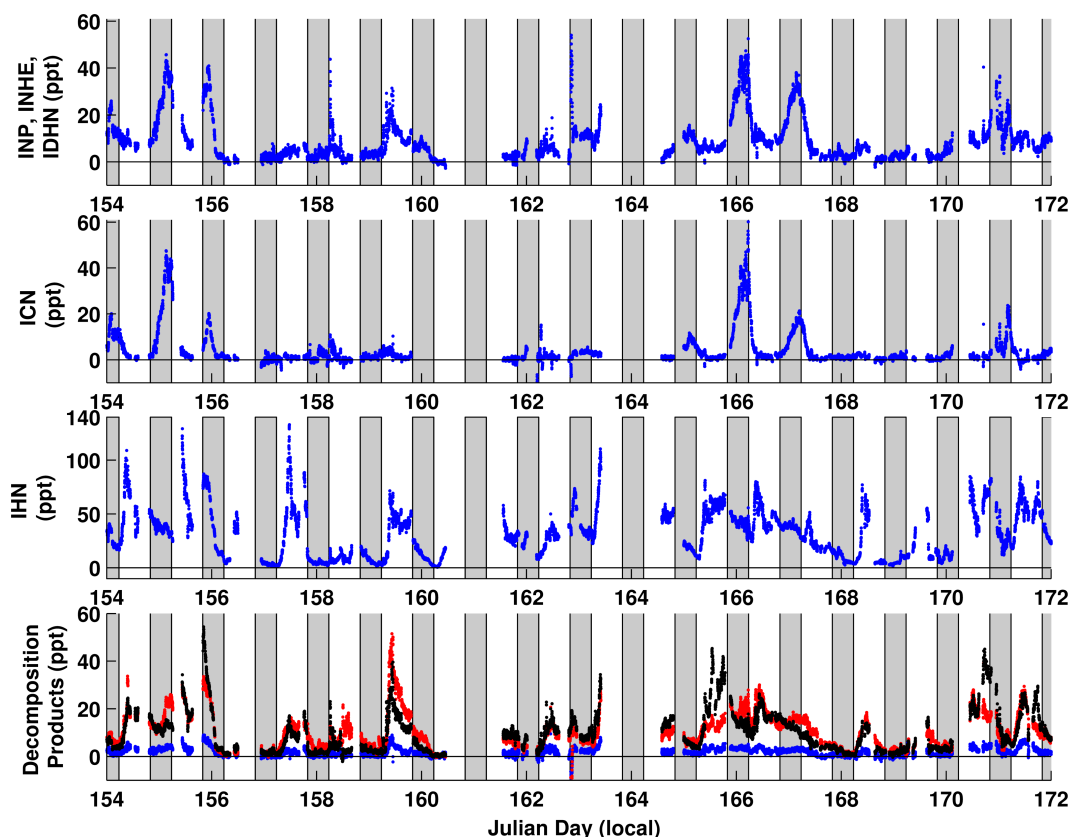


**Figure 3.8:** C<sub>5</sub> nitrooxy hydroperoxide (INP) + C<sub>5</sub> nitrooxy hydroxyepoxide (INHE) + C<sub>5</sub> dihydroxy nitrate (IDHN) [1<sup>st</sup> panel]; C<sub>5</sub> carbonyl nitrate (ICN) [2<sup>nd</sup> panel], C<sub>5</sub> hydroxy nitrate (IHN) [3<sup>rd</sup> panel], and primary decomposition products (ethanal nitrate (ETHLN) [blue], propanone nitrate (PROPNN) [red], and C<sub>4</sub> carbonyl hydroxynitrate (C<sub>4</sub>CHN) [black]) for several weeks during the SOAS 2013 field campaign. The shaded area represents nighttime. No fragmentation correction was applied for INP (Section 3.0), which may bias results low.

### 3.7 Conclusions

In this work, the alkylperoxy radical isomer distribution and product yields in the reaction of NO<sub>3</sub> with isoprene were determined at an RO<sub>2</sub> lifetime of ~30 s.  $\delta$ -nitrooxy alkylperoxy radicals are slightly more abundant than their  $\beta$  counterparts suggesting the alkylperoxy radical kinetics and thermodynamics are quite different for NO<sub>3</sub> vs OH derived peroxy radicals. The nitrate yield (i.e., isoprene nitrooxy hydroperoxide (INP) yield) from the RO<sub>2</sub> + HO<sub>2</sub> pathway is high (~0.78). Additionally, we find an OH yield (~0.22) from the INO<sub>2</sub> + HO<sub>2</sub> pathway. Updating the products for the INO<sub>2</sub> + HO<sub>2</sub> reaction into mechanisms will lead to more accurate predictions of atmospheric NO<sub>x</sub> and O<sub>3</sub> levels.

A large fraction of the nitrates produced from NO<sub>3</sub>-initiated oxidation of isoprene

are  $\delta$ -isomers. Since  $\delta$ -[1,4N]-IHN has been shown to hydrolyze quickly in neutral liquid water (Jacobs, Burke, et al., 2014), isoprene  $\text{NO}_3$  oxidation could be important as a terminal sink for  $\text{NO}_x$  in humid locations.

Because the lifetimes of isoprene nitrates with respect to oxidation by ozone ( $\text{O}_3$ ) and  $\text{NO}_3$  are quite long, most of the nitrates formed from isoprene oxidation by  $\text{NO}_3$  will remain in the atmosphere until sunrise when OH begins to form. Qualitatively, the decomposition products from the photooxidation of the major  $\text{NO}_3$  first-generation nitrates can be predicted using the isomer distributions determined by this study and current literature understanding, but to make further progress, synthetic standards are needed. Because  $\delta$ -[1,4]-nitrates are the dominant products, PROPNN is the major nitrate decomposition product.

Results from these chamber experiments suggest that OH will react with INP to form INHE, a newly identified product, which appears to have similar heterogeneous fates to IEPOX. INHE has a lower yield from INP than IEPOX has from ISOPOOH and is limited by the amount of INP remaining in the atmosphere at sunrise, so the impact of INHE on SOA formation is likely to be far less than that of IEPOX. Future studies measuring the INHE reaction rate with OH and its uptake potential to hydrated aerosol (specifically chamber studies using a synthetic standard of INHE and higher relative humidity) will be useful to elucidate the full impact of INHE on SOA.

### 3.8 Acknowledgments

The authors thank the National Science Foundation (AGS-1240604) and the Electric Power Research Institute for their support of this work. TBN acknowledges support from NSF PRF award AGS-1331360. Development of the GC-ToF-CIMS is supported by an award from the National Science Foundation's Major Research Instrumentation Program (AGS-1428482).

### 3.9 Supporting Information

#### Kinetic Mechanism Development

A kinetic mechanism is formulated to simulate the reaction conditions of these experiments. The reactions included are listed in the Appendix (Table A2, A3, and A4). Table A5 contains a list of the abbreviations used. Rate constants for most of the reactions included in the mechanism are based on recommendations from JPL (Sander et al., 2011), IUPAC (Atkinson, Baulch, Cox, J. N. Crowley, Hampson, Hynes, M. E. Jenkin, Rossi, Troe, and Subcommittee, 2006; Atkinson, Baulch, Cox, J. N. Crowley, Hampson, Hynes, M. E. Jenkin, Rossi, and Troe, 2004), or

MCM v3.2 (Saunders et al., 2003). However, some rate constants and branching ratios are not known. For these, we use our best judgment based on available data; explanations of the assumptions on which these estimates are based are included in this section. Some branching ratios and rate constants are estimated based on the experimental results presented here. Many of these branching ratios depend on the fraction of  $\delta$ - and  $\beta$ -isomers that form (Table 3.3 and 3.5), which will likely depend on the lifetime of the  $\text{RO}_2$  radical. Thus, the reaction products and rates presented here are most consistent with the experimental results for this study in which the overall  $\text{RO}_2$  lifetime was  $\sim 30$  s. The kinetic mechanism developed here represents our current level of understanding, and deviations from the experimental results highlight areas for future study.

### Basic Reactions in Kinetic Mechanism

$\text{HO}_2$  was constrained in the kinetic mechanism by the measured  $\text{H}_2\text{O}_2$  production rate. Prior to photooxidation,  $\text{H}_2\text{O}_2$  is predominantly formed from  $\text{HO}_2 + \text{HO}_2$  reactions. To match the observed  $\text{H}_2\text{O}_2$  production rate in experiments 5, 6, and 8, we arbitrarily increased the reaction rate constant for  $\text{CH}_2\text{O} + \text{NO}_3$  by a factor of 2.5-3 in the kinetic mechanism above that recommended by IUPAC. Although not perfect when correcting for the missing  $\text{HO}_2$  in this manner, the  $\text{H}_2\text{O}_2$  curves for the kinetic mechanism and the experimental results were fairly consistent. Under-prediction of  $\text{HO}_2$  could be caused by other missing chemistry including unaccounted for surface chemistry, later generation chemistry not incorporated into the kinetic mechanism, or many other possibilities. Here, we are confident that there is a missing source of  $\text{HO}_2$ , but are agnostic about the mechanism responsible.

Because the predominant loss of isoprene is due to reaction with  $\text{NO}_3$ , the measured isoprene decay rate was used to constrain the amount of  $\text{NO}_3$  present. Cantrell et al. (1985) proposed that  $\text{N}_2\text{O}_5$  would react with water present on the wall surface to form nitric acid even under dry conditions. We included a wall loss rate for  $\text{N}_2\text{O}_5$  (i.e.,  $\text{NO}_3$  loss rate) such that the isoprene decay in the kinetic mechanism matched with experimental results. This rate constant is chamber/experiment specific. For experiment 5 ( $24 \text{ m}^3$ , 2.2 ppm  $\text{CH}_2\text{O}$ ), 6 ( $24 \text{ m}^3$ , 4.7 ppm  $\text{CH}_2\text{O}$ ), 7 ( $1 \text{ m}^3$ , 2 ppm  $\text{CH}_2\text{O}$ ) and 8 ( $1 \text{ m}^3$ , 4 ppm  $\text{CH}_2\text{O}$ ),  $\text{N}_2\text{O}_5$  wall loss rate constants that best fit experimental conditions were  $1.5 \times 10^{-4}$ ,  $12 \times 10^{-4}$ ,  $6 \times 10^{-4}$  and  $12 \times 10^{-4} \text{ s}^{-1}$ , respectively. We observe that the  $\text{N}_2\text{O}_5$  loss rate appears to be sensitive to both the mixing ratio of  $\text{CH}_2\text{O}$  and the chamber. However, it should be noted that in

calculating these  $\text{N}_2\text{O}_5$  wall loss rate constants,  $\text{N}_2\text{O}_5$  wall loss is assumed to be the only missing sink of  $\text{NO}_3$ . Possibly there are other unknown  $\text{NO}_3$  sinks as well, and this will impact the relative differences between the wall loss rate constants calculated above.

For experiment 10, methyl nitrite, isoprene,  $\text{NO}_2$ , and  $\text{H}_2\text{O}_2$  were injected into the chamber, and photooxidation was initiated. Isoprene reacted with OH, and  $\text{HO}_2$  was generated. The formation rate of  $\text{HO}_2$  was adjusted in the kinetic mechanism so that the ratio of isoprene hydroxy hydroperoxide (ISOPPOOH) to isoprene hydroxy nitrate matched experimental results.  $\text{N}_2\text{O}_5$  loss to the walls was not needed in the kinetic mechanism for this experiment consistent with the hypothesis that the  $\text{N}_2\text{O}_5$  loss in the other experiments was enhanced by the presence of  $\text{CH}_2\text{O}$ .

### First-Generation Chemistry

The isoprene related reactions included in the kinetic mechanism are listed in Table A3. The  $\text{RO}_2 + \text{RO}_2$  proposed reaction rates and  $\text{RO}_2 + \text{HO}_2$  proposed products are addressed in Section 3.5. Not all isomers are included separately in the kinetic mechanism:  $\beta$ - and  $\delta$ -isomers are grouped together using the results from Tables 3.3 and 3.5. The generalized reaction rate constant determined in Section 3.5 is used in the kinetic mechanism for  $\text{INO}_2 + \text{INO}_2$ . The ToF-CIMS has been directly calibrated using IHN standards (Lance Lee et al., 2014), so the sensitivity for IHN is well constrained. When the maximum branching ratio reported by Kwan et al. (2012) for the  $\text{R}'\text{CHO} + \text{ROH}$  pathway (0.77), the median value for the ROOR pathway (0.035), and the remainder for the 2RO pathway (0.195) are used in the kinetic mechanism, experimental and predicted results for IHN agree well (Figure 3.4). All further oxidized isoprene nitrooxyperoxy radicals are assumed to react at the same rate and product distribution as  $\text{INO}_2 + \text{INO}_2$ . For  $\text{INO}_2$  reactions with other  $\text{RO}_2$  species, the reaction rate constants are estimated by taking the geometric mean of the respective self-reaction rate constants. The products formed are assumed to be the same as the self-reactions (see Table A3). This is clearly an approximation, but the exact product distributions are unknown.

In Section 3.5, we discussed that uncertainty in hydroxy methy peroxy (HMP) formation and reaction could influence the C5 nitrooxy peroxy ( $\text{INO}_2$ ) +  $\text{INO}_2$  reaction rate constants estimated by this study. To test this, we alter the following in the kinetic mechanism: use the  $\text{HMP} + \text{CH}_2\text{O}$  equilibrium rate constant measured by Zabel et al. (1987) and increase the  $\text{HMP} + \text{HMP}$  reaction rate constant to the acetyl



peroxy radical self-reaction rate constant ( $1.6 \times 10^{-11} \text{ cm}^3 \text{ molec}^{-1} \text{ s}^{-1}$ ) (Atkinson, Baulch, Cox, J. N. Crowley, Hampson, Hynes, M. E. Jenkin, Rossi, Troe, and Subcommittee, 2006). Now the  $\text{INO}_2 + \text{INO}_2$  rate constant that best fits the data is  $\sim 3.5 \times 10^{-12} \text{ cm}^3 \text{ molec}^{-1} \text{ s}^{-1}$ . Formic acid is greatly underpredicted by the kinetic mechanism without these changes ( $\sim 95\%$  missing prior to photooxidation and  $\sim 85\%$  3.5 h after photooxidation). With these adjustments, predicted formic acid is more consistent with experimental results ( $\sim 50\%$  missing prior to photooxidation and  $\sim 20\%$  3.5 h after photooxidation) although there are still significant differences. The magnitude of formic acid produced ( $\sim 10$  times the amount of isoprene reacted) is so large that it is highly likely a by-product of  $\text{CH}_2\text{O}$  chemistry. We also test whether uncertainty in the  $\text{H}_2\text{O}_2$  concentration affects the estimation of  $k_{\text{INO}_2+\text{INO}_2}$ . Even if  $\text{H}_2\text{O}_2$  were 20% lower, the kinetic mechanism still predicts  $k_{\text{INO}_2+\text{INO}_2}$  to be  $\sim 4 \times 10^{-12} \text{ cm}^3 \text{ molec}^{-1} \text{ s}^{-1}$ .

## Second-Generation Chemistry Rate Constants

Lance Lee et al. (2014) determined the OH addition rate constants for  $\delta$ -[1,4N]-IHN (average between *cis*- and *trans*-) and  $\beta$ -[4,3N]-IHN to be  $1.1 \times 10^{-10}$  and  $4.2 \times 10^{-11} \text{ cm}^3 \text{ molec}^{-1} \text{ s}^{-1}$ , respectively. Because no other studies have directly measured OH rate constants for isoprene nitrates,  $k_{\text{OH}} = 1.1 \times 10^{-10} \text{ cm}^3 \text{ molec}^{-1} \text{ s}^{-1}$  is used for  $\delta$ -INP,  $\delta$ -IHN, and ICN and  $k_{\text{OH}} = 4.2 \times 10^{-11} \text{ cm}^3 \text{ molec}^{-1} \text{ s}^{-1}$  is used for  $\beta$ -[1,2]-INP,  $\beta$ -[4,3]-INP, and  $\beta$ -IHN. (J. M. St. Clair et al., 2015) determined that OH abstracts a hydrogen from the hydroperoxide group of [1,2]-ISOPOOH and [4,3]-ISOPOOH with the following rate constants,  $9.0 \times 10^{-12}$  and  $4.7 \times 10^{-12} \text{ cm}^3 \text{ molec}^{-1} \text{ s}^{-1}$ , respectively. For lack of more information, it is assumed that both the  $\beta$ - and  $\delta$ -INP undergo hydrogen abstraction from the hydroperoxide group at the average of these two rate constants. The hydrogen  $\alpha$  to the carbonyl group on ICN is also extractable. A rate constant ( $1.7 \times 10^{-11} \text{ cm}^3 \text{ molec}^{-1} \text{ s}^{-1}$ ) based on the SAR method10 is used in the kinetic mechanism. The hydrogen abstraction rate is  $\sim 15\%$  of the expected OH addition rate.

The  $\text{O}_3$  addition rate constant for  $\delta$ -[1,4]-IHN (average between *cis*- and *trans*-) and  $\beta$ -[4,3]-IHN was measured by Lance Lee et al. (2014) to be  $2.8 \times 10^{-17}$  and  $2.6 \times 10^{-19} \text{ cm}^3 \text{ molec}^{-1} \text{ s}^{-1}$ , respectively. Lockwood et al. (2010) measured the  $\text{O}_3$  addition rate constant for  $\delta$ -[1,4]-trans-IHN,  $\beta$ -[1,2]-IHN, and  $\beta$ -[2,1]-IHN to be  $5.3 \times 10^{-17}$ ,  $1.06 \times 10^{-16}$ , and  $3.4 \times 10^{-16} \text{ cm}^3 \text{ molec}^{-1} \text{ s}^{-1}$ , respectively. The values measured by Lockwood et al. (2010) are too fast to be consistent with the observed

loss rate of IHN during the nighttime at SOAS, so the rate constants measured by Lance Lee et al. (2014) are incorporated into the kinetic mechanism, but this is an area for future research given the discrepancy between these two studies.  $k_{O_3}$  for  $\delta$ -IHN was assigned the value of  $2.8 \times 10^{-17} \text{ cm}^3 \text{ molec}^{-1} \text{ s}^{-1}$ , and  $k_{O_3}$  for  $\beta$ -[1,2]-INP,  $\beta$ -[4,3]-INP, and  $\beta$ -IHN is assigned to  $3.8 \times 10^{-19} \text{ cm}^3 \text{ molec}^{-1} \text{ s}^{-1}$ .

After most of the  $O_3$  had reacted away in experiment 6 (measured  $O_3 < 16$  ppb and modeled  $NO_3 < 6$  ppt), the stability of the main isoprene nitrates was monitored over 3.5 h to assess wall loss under the conditions of this study. The wall loss for INP, IHN, and ICN was measured to be  $9 \times 10^{-6}$ ,  $7 \times 10^{-6}$ , and  $6 \times 10^{-6} \text{ s}^{-1}$ , respectively. These wall loss rates are similar to the wall loss rates measured under different conditions for compounds of similar structure in the same chamber ( $24 \text{ m}^3$ ) (Zhang et al., 2015) and in the  $1 \text{ m}^3$  chamber (Lance Lee et al., 2014). These wall loss rates were incorporated into the kinetic mechanism.

Also in experiment 6, sequential amounts of  $O_3$  were added to the chamber to monitor the formation of later generation chemistry. The last  $O_3$  injection occurred after all isoprene had reacted. There was little loss of ICN, while IHN decayed the most. The nitrates were lost in many different ways (e.g., reaction with  $O_3$ , reaction with  $NO_3$ , and wall loss). The distribution of these losses is likely specific to the nitrate compound and isomer. Exact decay rates cannot be inferred from the kinetic mechanism because there are too many possible avenues. However, because ICN and INP decay slower than IHN, general  $O_3$  and  $NO_3$  rate constants were estimated based on the relative decay in experiment 6. The great differences in the decay curves alone suggest that  $O_3$  and/or  $NO_3$  reaction rates with ICN, INP, and IHN vary substantially. The relative  $O_3$  and  $NO_3$  reaction rate constants for ICN, INP, and IHN are assumed to be consistent. Rate constants for ICN and  $\delta$ -INP reaction with  $O_3$  were approximated by using the measured  $k_{O_3}$  for  $\delta$ -IHN (Lance Lee et al., 2014) and the ratio of the lifetimes determined from the decay curve in experiment 6 corrected for the wall loss rates.  $k_{O_3}$  for ICN is an upper bound as  $m/z = (-) 248$  (INP) fragments in the Triple-CIMS to form products at  $m/z = (-) 230$  (same  $m/z$  as ICN) (See Section 3.9).

For  $NO_3$ , Rollins, Kiendler-Scharr, et al. (2009) measured a combined isoprene nitrate rate constant of  $7 \times 10^{-14} \text{ cm}^3 \text{ molec}^{-1} \text{ s}^{-1}$  by fitting parameters to match experimental results in a kinetic mechanism largely based on MCM v3.1. This combined rate constant was based on total alkyl nitrate measurements made by Thermal Dissociation-Laser Induced Fluorescence and a variety of instruments

that measured  $\text{NO}_3$  and  $\text{N}_2\text{O}_5$ . Incorporation of this rate constant for IHN, ICN, and INP into the kinetic mechanism produced a rate of decay of the products that exceeded the experimental results. Thus,  $k_{\text{NO}_3+\text{IHN}}$  is assumed to be  $7 \times 10^{-14} \text{ cm}^3 \text{ molec}^{-1} \text{ s}^{-1}$  and  $k_{\text{NO}_3+\text{ICN}}$  is estimated ( $8.1 \times 10^{-15} \text{ cm}^3 \text{ molec}^{-1} \text{ s}^{-1}$ ) based on the ratio of lifetimes in experiment 6 with a correction for wall loss. A lower reaction rate constant for ICN is expected. Other studies have measured low reaction rate constants for reaction of  $\text{NO}_3$  with unsaturated aldehydes (e.g.,  $k_{\text{NO}_3+\text{trans-2-hexenal}} = 4.7 \times 10^{-15} \text{ cm}^3 \text{ molec}^{-1} \text{ s}^{-1}$ ) (Kerdouci et al., 2012). The influence of a hydroperoxy group on  $\text{NO}_3$  reaction rate constants is unknown. The approach used to estimate  $k_{\text{NO}_3+\text{ICN}}$  over-estimated  $k_{\text{NO}_3+\text{INP}}$ , so a different approach was used based on the formation of isoprene dinitrooxyepoxide (IDNE), which Kwan et al. (2012) proposed formed with a yield of 0.35. This yield is consistent with this study as well. IDNE forms from  $\text{NO}_3$  adding to the least substituted carbon of  $\beta$ -[1,2]-INP and  $\delta$ -[4,1]-INP, which make up 0.37 of all INP (Table 3.3). Predicted IDNE matches experimentally detected IDNE for experiment 5 (more  $\text{NO}_3$  oxidation of INP occurs in this experiment than experiment 8) when  $k_{\text{NO}_3+\text{INP}}$  is  $5 \times 10^{-15} \text{ cm}^3 \text{ molec}^{-1} \text{ s}^{-1}$ . This rate constant is substantially lower than that Rollins, Kiendler-Scharr, et al. (2009) predicted for the general rate constant. In the current system, IDNE could have a higher wall loss rate due to more nitric acid present in the chamber, which would cause  $k_{\text{NO}_3+\text{INP}}$  to be underpredicted.

The rate constants of  $\text{NO}_3$  with isoprene derived nitrates require further study with synthetic standards. Understanding the  $\text{NO}_3$  reaction rate constants for the main nitrates from  $\text{NO}_3$  oxidation is important, as without this knowledge models will not accurately depict which and how many of the nitrates survive through the night to react with OH at sunrise.

## Second Generation Chemistry Product Distribution

Product distributions and rate constants were incorporated based on the isomer distribution determined in this study (Table 3.3) and current literature understanding, but the kinetic mechanism was not further optimized. Given the complexity and the large number of unknowns, optimizing the kinetic mechanism for later-generation products has too many degrees of freedom. Standards for all of the primary products will need to be synthesized to understand fully the later generation chemistry.

Lance Lee et al. (2014) and Jacobs, Burke, et al. (2014) have both studied the products from the oxidation of isoprene hydroxy nitrates shown in Figure 3.9.

From the limited sample size available, it appears that the subsequent fragmentation following oxidation of the hydroxy nitrate is less likely to break the carbon bond next to a nitrate group than the carbon bond next to an OH group. Since all of the nitrates produced from  $\text{NO}_3$  oxidation will contain a nitrate group on either the  $\text{C}_1$  or  $\text{C}_4$  carbon, the products formed are assumed to be similar to the distribution of products from [1,4N]-IHN. Lance Lee et al. (2014) did not detect a  $\text{C}_4$  product without a nitrate group, so if there was a nitrate group  $\alpha$  to the peroxy group, it was assumed no  $\text{C}_4$  products formed. Additionally, all the  $\text{C}_4$  product detected by B. H. Lee et al. (2014) from [1,4N]-IHN + OH was assumed to come from the second peroxy radical (Figure 3.9).

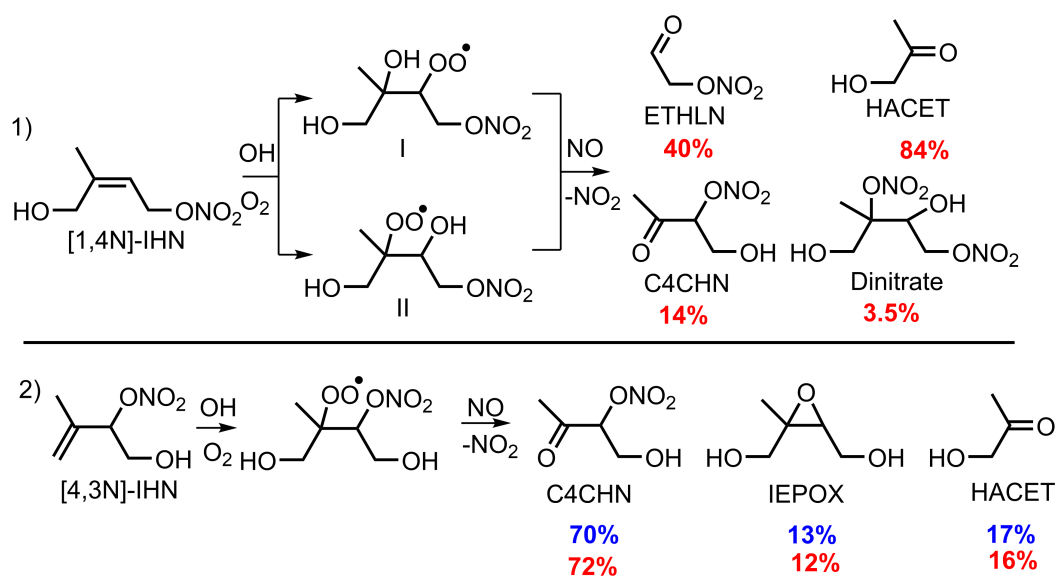


**Figure 3.9:** Isoprene nitrates reaction products that have been studied by Lance Lee et al. (2014) with adjusted HACET and IEPOX yields (L. Lee, 2014) in red and Jacobs, Burke, et al. (2014) in blue.

OH was assumed to add to the less substituted carbon. The branching ratios were determined based on compounds with a similar carbon backbone. Teng et al. (2015) determined that OH added to the least substituted carbon 69% of the time for 2-methyl-2-butene, which has the same carbon backbone as the  $\delta$ -nitrates. For  $\beta$ -[1,2]-nitrates and  $\beta$ -[4,3]-nitrates, OH is assumed to add to the least substituted carbon similar to MVK (Praske et al., 2015) (76%) and MACR (John D. Crounse, Knap, et al., 2012) (96.5%), respectively. An epoxide, like IEPOX, is assumed to form only if there is a nitrate group available to form an epoxide, otherwise the epoxide yield is distributed by weight to the other products. For INP, if OH adds in a position such that formation of an epoxide is possible, INHE is assumed to form

in 100% yield. Lance Lee et al. (2014) had NO levels higher than the atmosphere and the present study, which led to an unequal yield of hydroxyacetone (HACET) and ethanal nitrate (ETHLN). In this study (and in the atmosphere), these yields should be equivalent; 3.5% of dinitrates are assumed to form from NO reacting with any of the peroxy radicals formed from ICN, IHN, or INP (Lance Lee et al., 2014). Using results from Lance Lee et al. (2014) with revised HACET and IEPOX yields (L. Lee, 2014), 27% of hydroperoxides are assumed to form from HO<sub>2</sub> reacting with all peroxy radicals formed from the isoprene nitrates. Results from Table 3.3 with the assumptions stated above are used to predict the distribution of products for the  $\beta$ - and  $\delta$ -isomers of IHN, ICN, and INP (see Table A3).

Figure 4 illustrates that with the above assumptions the kinetic mechanism over-predicts ETHLN to a small degree, and under-predicts C<sub>4</sub>CHN by a large fraction. It is possible that the carbonyl is a better leaving group than the hydroxy. In the kinetic mechanism, if we assume that when OH reacts with ICN, the bond next to the carbonyl group fragments forming C<sub>4</sub>CHN and CO (rather than breaking the bond connecting C<sub>2</sub> and C<sub>3</sub> of isoprene), the simulated C<sub>4</sub>CHN is increased and ETHLN is reduced. However, C<sub>4</sub>CHN is still underpredicted by the kinetic mechanism, suggesting that there is another reason for C<sub>4</sub>CHN under-prediction.

Several studies have determined that hydrogen shifts can occur fast enough to be relevant in the atmosphere (John D. Crounse, Knap, et al., 2012; J. D. Crounse et al., 2011; John D. Crounse, Nielsen, et al., 2013). Most chamber studies run at low RO<sub>2</sub> lifetimes do not detect this chemistry, even though this pathway is likely to be important in the atmosphere. In this study, when photooxidation was initiated, the kinetic mechanism estimates an overall RO<sub>2</sub> lifetime of ~0.4 s and ~1 s for experiments 5 and 8, respectively. These lifetimes are fairly short, but when OH reacts with ICN, likely both the [1,4]- and [1,5]-H-shifts are competitive (Figure 3.10), as John D. Crounse, Knap, et al. (2012) inferred a rate constant of 0.5 s<sup>-1</sup> for a similar [1,4]-H-shift for MACR, and the [1,5]-H-shift should be even faster.

The rate constants for peroxy radical shifts will depend on many factors, including neighboring substituents, degree of substitution, and type of hydrogen shift. Currently, a comparison of all of these factors has not been well constrained for peroxy radical shifts, but the influence of all of these factors has been summarized by Carter et al. (1985) for alkoxy radical shifts. In order to estimate the relevance of peroxy radical shifts in these experiments, the relative rate constant differences for the degree of substitution and type of hydrogen shift is assumed to be similar for alkoxy

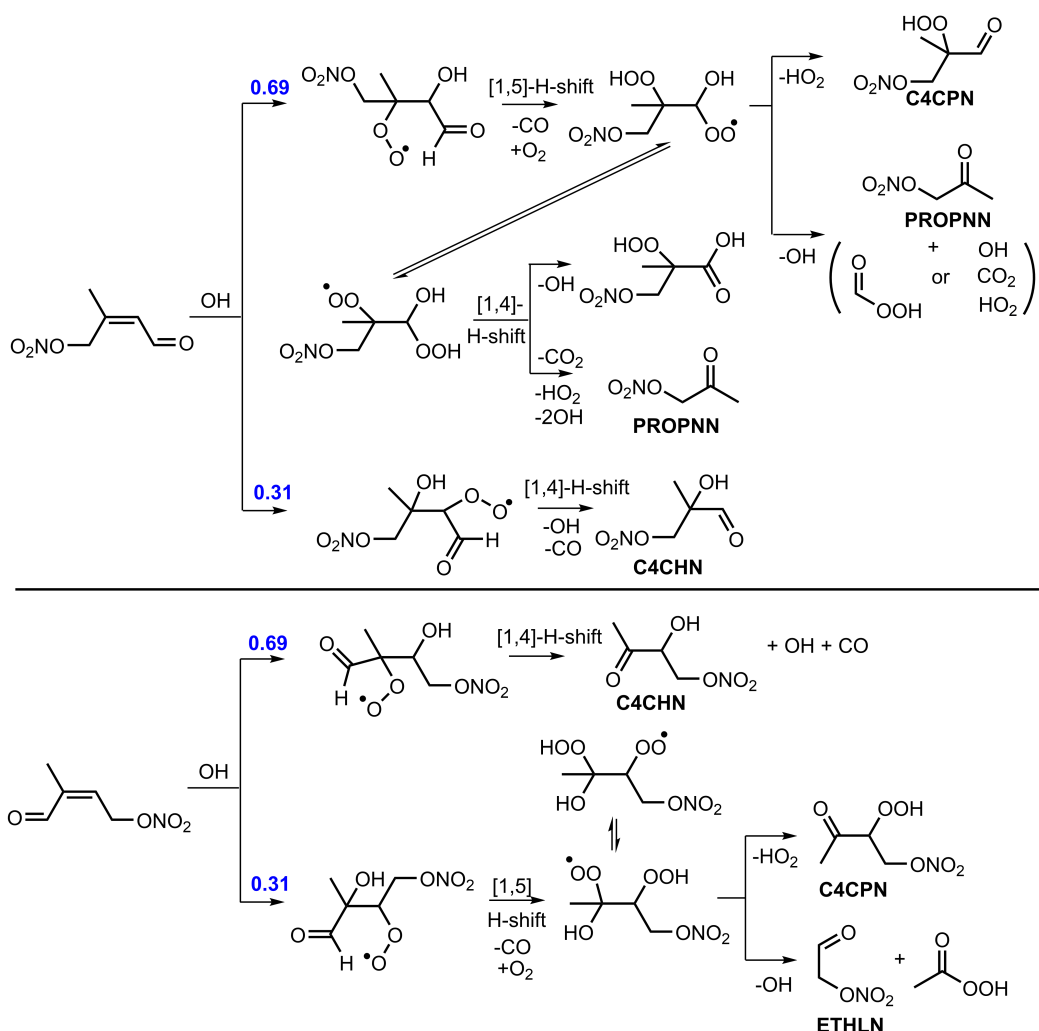


**Figure 3.10:** Possible H-shifts from OH oxidation of ICN.

and peroxy radicals. For example, if the [1,4]-H shift for ICN oxidation by OH is assumed to be similar to that of MVK ( $\sim 0.5 \text{ s}^{-1}$ ), (John D. Crounse, Knap, et al., 2012) then the [1,5]-H shifts will occur at  $\sim 2 \times 10^3 \text{ s}^{-1}$  if peroxy and alkoxy radicals act similarly. Since the [1,5]-H shift occurs so quickly, reaction with NO/NO<sub>3</sub>/HO<sub>2</sub> is not incorporated as an option for this peroxy radical. Because the [1,4]-H-shift is slower, both the possibility of a shift and reaction with NO/NO<sub>3</sub>/HO<sub>2</sub> are included in the kinetic mechanism. In the atmosphere both the [1,4]- and the [1,5]-H-shifts are expected to be important.

Given that a hydrogen  $\alpha$  to a nitrate group is  $\sim 200$  times less abstractable according to the SAR method (Kwok et al., 1995), shifts are not considered for this hydrogen. H-shifts for peroxy radicals with an  $\alpha$ -hydroxy/hydroperoxy group will be much slower

than those with an  $\alpha$ -carbonyl group. For example, John D. Crounse, Nielsen, et al. (2013) determined a minimum rate constant of  $0.1 \text{ s}^{-1}$  for a secondary [1,5]-H-shift from a carbon containing a hydroperoxy group. Since primary hydrogen shifts occur slower than secondary hydrogen shifts for alkoxy radicals (Carter et al., 1985) and this effect is likely similar for peroxy radicals, H-shifts for peroxy radicals with an  $\alpha$ -hydroxy/hydroperoxy group are assumed not to occur under the conditions of the current study. These hydrogen shifts are still likely relevant in the atmosphere and deserve further attention, but the conditions in the current study are not optimal for identifying them.

The products from the  $\text{O}_3$  oxidation of ICN, IHN, and INP are more complicated to predict based on currently available data than those from OH oxidation. The products from  $\beta$ -IHN or  $\beta$ -INP +  $\text{O}_3$  were not included as  $k_{\text{O}_3}$  for  $\beta$ -isomers is expected to be quite low.

The product yields from 2-methyl-2-butene have been quantified by many studies. The  $\text{C}_3$  and  $\text{C}_2$  Criegee distribution is  $\sim 0.3$  and  $\sim 0.7$  (Grosjean et al., 1996; Tuazon et al., 1997), respectively, and the OH yield is 0.88 (Atkinson et al., 2006). Lance Lee et al. (2014), the only current study to measure how  $\text{O}_3$  product yields are affected by nitrate or hydroxy groups, found *trans*-[1,4N]-IHN and *cis*-[1,4N]-IHN produced much less OH (0.2 and 0.48, respectively) than 2-methyl-2-butene. With the corrected HACET yields (L. Lee, 2014), ETHLN and HACET yields were 0.50 and 0.48 for *trans*-[1,4N]-IHN and 0.55 and 0.93 for *cis*-[1,4N]-IHN, respectively. The non-unity yield of the carbonyl species suggests that something quenches the Criegee for the *cis*-isomer. Possibly acetone was interfering, as between 0.5-2 ppm of acetone was present and acetone reacts with formaldehyde oxide with a rate constant of  $2.3 \times 10^{-13} \text{ cm}^3 \text{ molec}^{-1} \text{ s}^{-1}$  (or  $\tau_{\text{acetone}} = 0.1\text{-}0.4 \text{ s}$ ) (Taatjes et al., 2012). Since we are unsure why a non-unity yield of carbonyl species formed for the *cis*-isomer, all nitrates in this work are assumed to react like *trans*-[1,4N]-IHN.

The concentrations of CO, NO (during photooxidation), and  $\text{NO}_2$  were sufficient to quickly react with all of the Criegees that form. The  $\text{O}_3$  reactions that have been included in the kinetic mechanism are based on the following assumptions: (1) all of the nitrates react with  $\text{O}_3$  to form an equal number of  $\text{C}_2$  and  $\text{C}_3$  Criegees, (2) all  $\text{C}_2$  Criegees are stabilized by CO, NO, or  $\text{NO}_2$ , and (3) all  $\text{C}_3$  Criegees form 0.4 OH and the rest is stabilized by CO, NO, or  $\text{NO}_2$ .

A full set of products for the reaction of IHN, INP and ICN with  $\text{NO}_3$  is not estimated in the kinetic mechanism as there are no direct studies of these reactions. In total,

the kinetic mechanism predicts that 0.05 ppb of these second generation NO<sub>3</sub> products form for experiments 8, so this simplification is not expected to influence the decomposition product results. IDNE and OH are included with a yield of 0.35 as products for  $\delta$  and  $\beta$ -INP + NO<sub>3</sub> reactions (Kwan et al., 2012). Additionally, an epoxide could form from NO<sub>3</sub> adding to the least substituted carbon of [1,4] -IHN, -INP, and -ICN with release of a nitrate group (similar to OH addition to IHN to form IEPOX (Jacobs, Burke, et al., 2014)). This is incorporated into the kinetic mechanism with a product yield of 0.13 (Jacobs, Burke, et al., 2014) for the isomer that will produce an epoxide (e.g., 0.11 for all  $\delta$ -INP using the distribution in Table 3.3). The exact epoxide yield from isoprene nitrates reaction with NO<sub>3</sub> should be measured, as studies have found that organic nitrate SOA growth at night forms largely from multigenerational chemistry (Rollins, Browne, et al., 2012).

The rate constants and products of INHE + OH were predicted based on two IEPOX + OH product studies (Bates et al., 2014; Jacobs, A. I. Darer, et al., 2013). Jacobs, A. I. Darer, et al. (2013) measured much higher rate constants ( $\delta$ 4-IEPOX:  $3.52 \times 10^{-11}$ ,  $\beta$ -IEPOX:  $3.6 \times 10^{-11}$ ) then Bates et al. (2014) ( $\delta$ 1-IEPOX:  $8.4 \times 10^{-12}$ , *cis*- $\beta$ -IEPOX  $1.52 \times 10^{-11}$ , *trans*- $\beta$ -IEPOX:  $9.8 \times 10^{-12}$ ). The reaction rate constants measured by Bates et al. (2014) are used in the kinetic mechanism for  $\delta$ -INHE and  $\beta$ -INHE (average of the *trans* and *cis*). The products included in the kinetic mechanism for INHE reacting with OH are based on the products formed from OH reacting with  $\beta$ -IEPOX (Bates et al., 2014) and  $\delta$ 4-IEPOX (Jacobs, A. I. Darer, et al., 2013). The hydrogen  $\alpha$  to a nitrate group is assumed not to be abstractable, and the distribution of the INHE isomers was determined from results in Table 3.3 assuming OH adds to INP in the ratios described above.

## Photolysis

The photolysis reactions included in the kinetic mechanism are outlined in Table A4. Most are based on recommendations from JPL (Sander et al., 2011) or MCM v3.2(Saunders et al., 2003). ISOPOOH and INP were assumed to photolyze at the same rate as methyl hydroperoxide like MCM v3.2(Saunders et al., 2003) suggests. Preliminary evidence from a side experiment suggests that the photolysis rate for INP is much faster than the rate for methyl hydroperoxide. The absorption spectrum and quantum yields for INP deserve further attention as photolysis could be a competitive sink for INP in the atmosphere.



### Peak Assignments for GC-ToF-CIMS

Because peak shapes were not perfect Gaussians, when compounds eluted fully separated from other isomers or when peak separation was not necessary, the area under the peak was determined by adding up all data points and multiplying by the sampling frequency. With co-eluting isomers, peaks were fit assuming an exponentially broadened Gaussian peak shape. The time constant, peak position, width, and height were selected based on minimization of the root mean square fitting error. In all cases, the distribution of isomers was determined by the areas measured for the first GC run in any given experiment to avoid the influence of second generation chemistry and wall loss. Peak percentages determined by subsequent GC results were within 7%, 4%, and 12% of the first GC results for INP, ICN, and IHN, respectively.

Several of the GC-ToF-CIMS chromatographs for IHN during experiment 8 are shown in Figure 3.11. Synthesized standards were available for all of the IHN compounds formed in this work except [4N,3]-IHN (Lance Lee et al., 2014; T. B. Nguyen, J. D. Crounse, Schwantes, et al., 2014). Given the elution times of compounds with similar structures, we expect [4N,3]-IHN to elute right after [1N,2]-IHN, so we assign [4N,3]-IHN to peak 1.

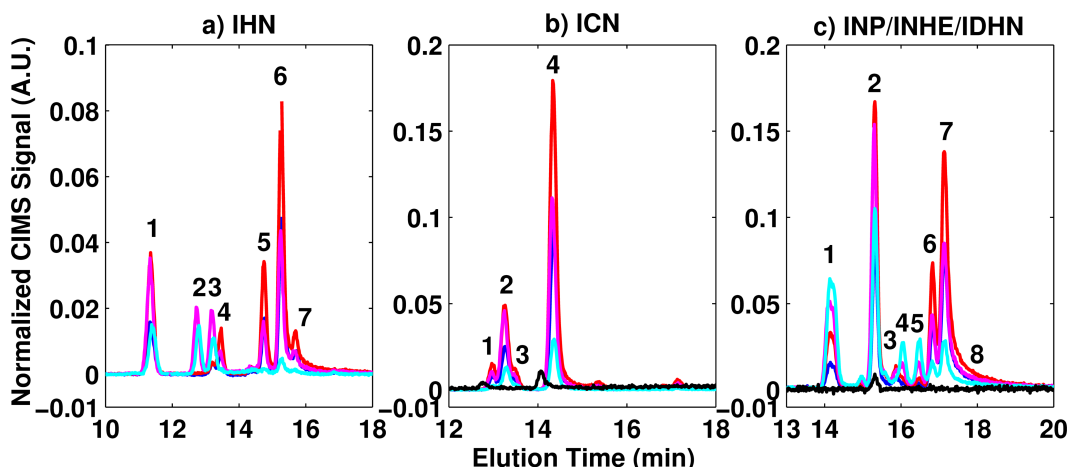


**Figure 3.11:** GC-ToF-CIMS chromatographs for experiment 8 as a function of time following the initiation of the photochemistry: -2.7h (blue), -0.6h (red), +0.9h (magenta), +2.9h (cyan), for panel b, 2 x  $m/z$  = (-)185 at +2.9h (black) and for panel c, 2 x  $m/z$  = (-)63 at -2.7h (black). See Table 3.6 for a list of isomers assigned to each peak.

The *trans*-[1N,4]-IHN and *cis*-[4N,1]-IHN isomers co-elute and so differentiating between these isomers is not possible. The distribution of the areas for peaks 5,

**Table 3.6:** List of isomers assigned to each peak labeled in Figure 3.11.

| peak # | a) IHN                                    | b) ICN                         | c) INP/INHE                                 |
|--------|---|--------------------------------|---|
| 1      | [4N,3]                                    | <i>cis</i> - $\delta$ -[4,1]   | $\delta$ -INHE + IDHN                       |
| 2      | [1,2N]                                    | <i>trans</i> - $\delta$ -[4,1] | $\beta$ -[1,2]-INP                          |
| 3      | [4,3N]                                    | <i>cis</i> - $\delta$ -[1,4]   | $\beta$ -[4,3]-INP                          |
| 4      | Unknown                                   | <i>trans</i> - $\delta$ -[1,4] | <i>cis/trans</i> - $\beta$ -[4,1]-INHE      |
| 5      | <i>cis</i> -[1N,4]                        | NA                             | <i>cis/trans</i> - $\beta$ -[4,1]-INHE      |
| 6      | <i>trans</i> -[1N,4] + <i>cis</i> -[4N,1] | NA                             | <i>cis</i> -[1,4]-INP                       |
| 7      | <i>trans</i> -[4N,1]                      | NA                             | <i>trans</i> -[1,4] + <i>cis</i> -[4,1]-INP |
| 8      | NA  | NA                             | <i>trans</i> -[4,1]-INP                     |

6, and 7 at 49 minutes after the start of NO<sub>3</sub> oxidation are 22%, 67%, and 11%, respectively. If there exists an equal amount of *cis*- and *trans*-isomers, the area under peaks 5 and 7 should equal the area under peak 6. This is clearly not the case, suggesting that either the *cis* and *trans* INO<sub>2</sub> species are not present in equal amounts or the RO<sub>2</sub> + RO<sub>2</sub> rates are quite different for the *cis* and *trans* peroxy radicals. Since the INO<sub>2</sub> distribution favors C<sub>1</sub> addition and the relative rates of  $\delta$ -[1,4]-INO<sub>2</sub> and  $\delta$ -[4,1]-INO<sub>2</sub> with RO<sub>2</sub> are expected to be similar to what Michael E. Jenkin, Boyd, et al. (1998) predicted, the *trans*-INO<sub>2</sub> fraction or *trans*-INO<sub>2</sub> + RO<sub>2</sub> rate constant must be ~3 times larger than those of the *cis*-isomer. Assuming that C<sub>1</sub> and C<sub>4</sub> addition products have the same ratio of *cis*- and *trans*-products, [4N,1]-IHN and [1N,4]-IHN make up 86% and 14% of  $\delta$ -IHN, respectively.

Several GC-ToF-CIMS chromatographs for ICN (*m/z* = (-) 230) are shown in Figure 3.11b. The only possible  $\beta$ -ICN is  $\beta$ -[4,3]-ICN. The  $\beta$ -[4N,3]-IHN standard elutes at least 3 min prior to any of the  $\delta$ -IHN isomers (Figure 3.11a) and isoprene hydroxy carbonyl species, which are both  $\delta$ -isomers (*m/z* = (-) 185), elute at nearly the same time as ICN, which suggests that none of the peaks at *m/z* = (-) 230 are  $\beta$ -ICN. The distribution of areas for peaks 1, 2, 3, and 4 at 49 minutes into photooxidation are 6%, 20%, 5%, and 69%, respectively. Because peak 4 represents most of the signal, and many studies have already determined that C<sub>1</sub> addition is favored over C<sub>4</sub> addition (Skov et al., 1992; Berndt et al., 1997; Suh et al., 2001), we assign peak 4 to be either *trans*- and/or *cis*-[1,4]-ICN. This demonstrates that ICN behaves differently on the GC column than IHN (Table 3.6). Based on peak area we suspect peak 1 is *cis*-[4,1]-ICN and peak 2 is *trans*-[4,1]-ICN. We tentatively assign peak 3 to *cis*-[1,4]-ICN, but it is also quite possible that *cis*-[1,4]-ICN co-elutes with

*trans*-[1,4]-ICN (peak 4). With these assumptions, 74% is [1,4]-ICN and 26% is [4,1]-ICN. These results compare well with a previous report, based predominantly on the isomer distribution of ICN (Skov et al., 1992), that estimated C<sub>1</sub> addition (78%) to be favored over C<sub>4</sub> addition (22%). Because ICN peak assignments are largely based on area and other studies suggesting C<sub>1</sub> addition occurs more favorably than C<sub>4</sub> addition, the isomer distribution determined is more speculative than IHN and INP.

The chromatographs for *m/z* = (-) 248 (representing INP, C<sub>5</sub> dihydroxy nitrate (IDHN), and C<sub>5</sub> nitrooxy hydroxyepoxide (INHE)) are shown in Figure 3.11c. The combined presence of INHE, IDHN, and INP adds uncertainty in peak assignment. In addition, the GC transmission for *m/z* = (-) 248 through the 4 m column was only ~0% before the initiation of photooxidation unlike IHN and ICN, which was ~100%.  $\delta$ -INP in all chromatographs formed a large right-handed tail which adds uncertainty to peak fitting even assuming an exponentially broadened Gaussian peak shape. Because of this, GC results for experiment 10 (first GC, ~40 min into NO<sub>3</sub> oxidation) were used to determine the isomer distribution of INP. In this experiment, a shorter column (1m) and lower sample loading decreased the tailing and increased the transmission (~100%).

Additionally, the influence of RO<sub>2</sub> + RO<sub>2</sub> chemistry on INP formation was lower in experiment 10 compared to the other experiments (see Section 3.0). Prior to the start of photooxidation the  $\beta$ - and  $\delta$ -isomer fractions were similar in experiment 7 (0.35 & 0.65), 8 (0.30 & 0.70 -assuming some loss of the  $\delta$ -isomers), and 10 (0.30 & 0.70). The  $\beta$ -isomers might be more favored in experiment 7 due to differential isomer loss to the walls or reaction with O<sub>3</sub>/NO<sub>3</sub> because the first GC-ToF-CIMS was taken nearly 5 h after the start of NO<sub>3</sub> oxidation.

Based on  $\beta$ -ISOPOOH standards (Bates et al., 2014) and the known ratio of C<sub>1</sub> to C<sub>4</sub> addition (~3.5- 7.4) (Skov et al., 1992; Berndt et al., 1997) we suspect  $\beta$ -[1,2]-INP and  $\beta$ -[4,3]-INP to be peaks 2 and 3, respectively. The ratio of peak 2 to peak 3 decreases, in experiments 7, 8, and 10, as the influence of RO<sub>2</sub> + RO<sub>2</sub> chemistry declines. This is consistent with the peak assignment order, since  $\beta$ -[4,3]-INO<sub>2</sub> is expected to have the highest RO<sub>2</sub> rate constant of all the isomers. Additionally, using MS/MS with the GC-Triple-CIMS we observe the (-) 63 product ion characteristic of hydroperoxide fragments (Fabien Paulot et al., 2009a) for both  $\beta$ -INP (peaks 2 and 3). In fact, even the  $\delta$ -INP (peaks 6-8) forms a small amount of the (-) 63 daughter, but the fraction is much lower than for  $\beta$ -INP.

We suspect that  $\delta$ -INP has the same elution order as  $\delta$ -IHN (Table 3.6). The distribution of areas for peaks 6, 7, and 8 at 40 min into photooxidation in experiment 10 is 31%, 59%, and 10% respectively. Similar to IHN, assuming  $C_1$  and  $C_4$  addition products produce the same ratio of *cis*- and *trans*-products, *trans* is favored 1.7 times over *cis*, and [1,4]-INP and [4,1]-INP make up 84% and 16% of  $\delta$ -INP.

Peaks 1, 4, and 5 in Figure 3.11c are assigned to INHE isomers. Based on the elution time of  $\delta$ - and  $\beta$ -IEPOX, (Bates et al., 2014) and the relative amounts of  $\beta$ -[1,2]-INP to  $\beta$ -[4,3]-INP, we assign peak 1 to be all  $\delta$ -INHE isomers, and peak 4 and 5 to be *trans*- and *cis*- $\beta$ -[4,1]-INHE, which is formed from  $\beta$ -[1,2]-INP + OH. The *trans*- and *cis*- $\beta$ -[1,4]-INHE (produced from  $\beta$ -[4,3]-INP + OH) probably also forms, but likely the peaks are small and have the same elution time as peaks 6-8.

In experiment 8, chamber conditions were specifically altered to limit second-generation chemistry and OH formation in the dark. As expected, very little ISOPOOH (<100 ppt as an OH tracer) formed in the dark during this experiment, but peak 1 still represents approximately ~8% of the  $m/z = (-) 248$  signal. Very little INHE is predicted to form under dark conditions with low OH (Figure 3.4). Some of the  $\delta$ -INHE signal formed in the dark could be from  $NO_3$  reacting with IHN, but the reaction is slow and the yield is low (~13% if the chemistry is similar to what Jacobs, Burke, et al. (2014) found for  $\beta$ -[4,3]-IHN + OH). The data suggests a first-generation product co-elutes with  $\delta$ -INHE.

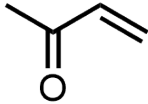
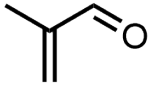
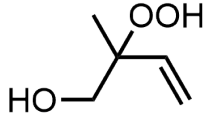
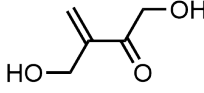
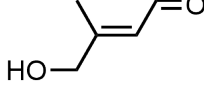
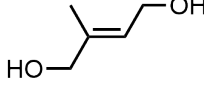
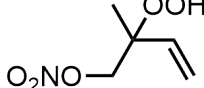
Isoprene dihydroxy nitrate (IDHN), a product of the 1,5 H-shift of *trans*-[1,4]-INO (Figure 3.12), is the most likely candidate for this first-generation product based on both its structure and expectation that it should form in relatively high yield. Furthermore, the percentage of IDHN and  $\delta$ -INHE to the entire  $m/z = (-) 248$  signal (18%, 6%, and 1%, in experiment 7, 8, and 10) decreased as the contribution of  $RO_2 + RO_2$  reactions decreased and other tracers for the [1,5]-H-shift reaction (IHCN and IHPN) decreased.

### Products Formed From $NO_3$ Oxidation

Section 3.0 of the main work described the dominant products that form in the dark in experiment 8. The product yields for experiments 3-5 are included in Table 3.7 for comparison. Results from experiment 9 where the ToF-CIMS and the triple-CIMS were run together were used to estimate sensitivities for the triple-CIMS. As for the ToF-CIMS, the sensitivities for the triple-CIMS for all large nitrates ( $m/z \geq (-) 230$  except  $(-) 232$  and  $(-) 234$ , for which the ToF-CIMS sensitivity has been measured)

are assumed to be the same as the triple-CIMS sensitivity for IHN. The sensitivities for the triple-CIMS changed over time depending on impurities in the system and other factors. A calibration system containing formic acid was used to account for changing sensitivities, so that experiments run at different times of the year could be compared. The sensitivities used in this study for the ToF-CIMS and triple-CIMS are listed in Table A1.

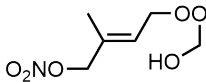
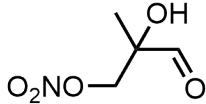
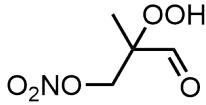
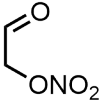
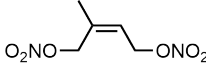
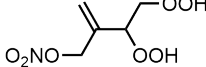
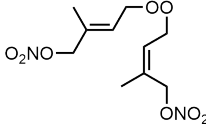
**Table 3.7:** Yields for products formed during experiments 3-5 and experiment 8.

| Name                                  | Abbrev. | Possible Structure   | m/z (-) | avg yield expts 3-5 (%) | Yield expt 8 (%) |
|---------------------------------------|---------|--|---------|-------------------------|------------------|
| Non-Nitrates                          |         |  |         |                         |                  |
| Methyl Vinyl Ketone                   | MVK     |    | NA      | 0.090 <sup>A</sup>      | not measured     |
| Methacrolein                          | MACR    |    | NA      | 0.042 <sup>A</sup>      | not measured     |
| C <sub>5</sub> Hydroxy Hydroperoxide  | ISOPOOH |    | (-) 203 | 0.02                    | 0.007            |
| C <sub>5</sub> Dihydroxy Carbonyl *   | IDHC    |    | (-) 201 | 0.019                   | 0.032            |
| C <sub>5</sub> Hydroxy Carbonyl       | IHC     |  | (-) 185 | 0.01                    | 0.008            |
| C <sub>5</sub> Dihydroxy              | IDH     |  | (-) 187 | 0.006                   | 0.006            |
| C <sub>5</sub> Nitrooxy Hydroperoxide | INP     |  | (-) 248 | 0.32                    | 0.41             |

**Table 3.7:** Yields for products formed during experiments 3-5 and experiment 8.

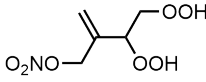
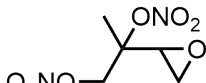
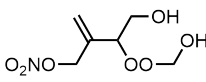
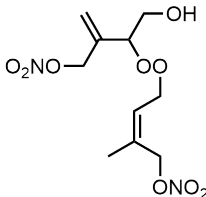
| Name   | Abbrev. | Possible Structure | m/z (-) | avg yield expts 3-5 (%) | Yield expt 8 (%) |
|--|---------|--------------------|---------|-------------------------|------------------|
| C <sub>5</sub> Nitrooxy Hydroxyepoxide       | INHE    |                    | (-) 248 |                         |                  |
| C <sub>5</sub> Dihydroxy Nitrate             | IDHN    |                    | (-) 248 |                         |                  |
| C <sub>5</sub> Carbonylnitrate               | ICN     |                    | (-) 230 | 0.26                    | 0.12             |
| C <sub>5</sub> Hydroxynitrate                | IHN     |                    | (-) 232 | 0.13                    | 0.12             |
| Propanone Nitrate                            | PROPNN  |                    | (-) 204 | 0.045                   | 0.011            |
| C <sub>5</sub> Hydroxy Carbonyl Nitrate      | IHCN    |                    | (-) 246 | 0.029                   | 0.021            |
| C <sub>5</sub> Hydroxy Hydroperoxide Nitrate | IHPN    |                    | (-) 264 | 0.028                   | 0.032            |
| Isoprene Dicarboxyl Nitrate*                 | IDCN    |                    | (-) 244 | 0.015                   | 0.008            |
| Unknown                                      |         |                    | (-) 261 | 0.015                   | 0.005            |

**Table 3.7:** Yields for products formed during experiments 3-5 and experiment 8.

| Name  | Abbrev. | Possible Structure   | m/z (-) | avg yield expts 3-5 (%) | Yield expt 8 (%) |
|---|---------|--|---------|-------------------------|------------------|
| ROOR from $\text{INO}_2$ and HMP* <i>B</i>  | INO2HM  |    | (-) 278 | 0.01                    | 0.017            |
| C <sub>4</sub> Carbonyl Hydroxy Nitrate     | C4CHN   |    | (-) 234 | 0.009                   | 0.004            |
| C <sub>4</sub> Carbonyl Hydroperoxy Nitrate | C4CPN   |    | (-) 250 | 0.006                   | 0.005            |
| Ethanal Nitrate                             | ETHLN   |    | (-) 190 | 0.005                   | 0.002            |
| C <sub>5</sub> Dinitrate                    | IDN     |    | (-) 277 | 0.004                   | ~ 0              |
| C <sub>5</sub> Carbonyl Hydroperoxy Nitrate | ICPN    |  | (-) 262 | 0.003                   | 0.001            |
| ROOR from $\text{INO}_2$ and $\text{INO}_2$ | INO2IN  |  | (-) 377 | 0.002                   | ~0               |



**Table 3.7:** Yields for products formed during experiments 3-5 and experiment 8.

| Name   | Abbrev. | Possible Structure   | m/z (-) | avg yield expts 3-5 (%) | Yield expt 8 (%)  |
|--|---------|--|---------|-------------------------|-------------------|
| C <sub>5</sub> Dihydroperoxy Nitrate             | IDPN    |  | (-) 280 | 0.002                   | 0.002             |
| C <sub>5</sub> Dinitrooxy Epoxide                | IDNE    |  | (-) 293 | 0.002                   | 0.001             |
| ROOR from IHNO <sub>2</sub> and HMP <sup>B</sup> | IHNO2HM |  | (-) 294 | 0.001                   | 0.002             |
| ROOR from INO <sub>2</sub> and IHNO <sub>2</sub> | INO2IHN |  | (-) 393 | 0.001                   | ~ 0               |
|  |         |  |         | totals                  |                   |
| Non-nitrate sum                                  |         |  |         | 0.19                    | 0.05 <sup>C</sup> |
| Nitrate sum                                      |         |  |         | 0.89                    | 0.76              |
| Total sum  |         |  |         | 1.08                    | 0.81 <sup>C</sup> |

**Table 3.7:** Yields for products formed during experiments 3-5 and experiment 8.

| Name | Abbrev. | Possible Structure | m/z (-) | avg yield expts 3-5 (%) | Yield expt 8 (%) |
|------|---------|--------------------|---------|-------------------------|------------------|
|------|---------|--------------------|---------|-------------------------|------------------|

<sup>A</sup> A cold trap was only used for experiments 4-5, so MVK and MACR yields are only based on these experiments.<sup>B</sup> and/or CIMS complex btw IHPN and CH<sub>2</sub>O. <sup>C</sup> These yields do not include the yield for MVK and MACR as it was not measured for experiment 8. Abbreviation used are INO<sub>2</sub> (Isoprene nitrooxy peroxy radical), IHNO<sub>2</sub> (Isoprene hydroxy nitrooxy peroxy radical from 1,5 H shift), and HMP (hydroxy methyl peroxy). Yields for experiments 3-5 and experiment 8 were calculated 4 h and 2.5h after isoprene injection, respectively. \* Assignment of this compound is less certain. A compound with a different/unknown structure could also be present.

Based on the GC-ToF-CIMS results, INP is fragmenting in the  $\text{CF}_3\text{O}^-$  CIMS to a number of products detected at  $m/z = (-)$  59,  $(-)$  63,  $(-)$  81,  $(-)$  118,  $(-)$  202,  $(-)$  209,  $(-)$  225,  $(-)$  228, and  $(-)$  230. Results for experiment 7, which had the highest amount of INP formed, were used to calculate the degree of fragmentation for all fragments except for  $m/z = (-)$  230. Experiment 8, which had higher resolution results, was used to calculate the fragmentation for  $m/z = (-)$  230. Only products with a transmission less than  $\sim 100\%$  and elution time similar to INP were included.  $\beta$ -INP ( $\sim 20\%$ ) fragmented more than  $\delta$ -INP ( $\sim 9\%$ ). The degree of fragmentation was used to correct the overall  $\beta$  to  $\delta$  ratio determined by the GC-CIMS. If the ratio of  $\beta$ - to  $\delta$ -INP is similar to this study,  $\sim 12\%$  of INP fragments.

Some products had much higher transmissions, but they were not included because fragmentation could be occurring in the CIMS or on the column. It is also possible that INP fragments into products we cannot detect (e.g., MVK and MACR). Additionally,  $m/z = (-)$  278 could be a complex of INP and  $\text{CH}_2\text{O}$  in the  $\text{CF}_3\text{O}^-$  CIMS, but the transmission of  $m/z = (-)$  278 through the 1m and 4m columns is only  $\sim 70\%$  and  $\sim 40\%$ , respectively. We would expect the transmission to be zero if  $m/z = (-)$  278 is all a complex on the CIMS. We do not include a correction for this, but if all of the  $m/z = (-)$  278 not transmitting through the column is a complex of INP and  $\text{CH}_2\text{O}$ , this would increase the INP signal in experiment 8 by  $\sim 2\%$ . Part of the  $(-)$  278 signal is likely the ROOR product from  $\text{INO}_2 + \text{hydroxy methyl peroxy radical (HMP)}$ . However, the  $m/z = (-)$  278 signal is too high to be explained entirely by the two pathways above, suggesting there is another pathway for its formation as well (see Section 3.9 for more possibilities).

$\sim 5\%$  of INP fragments in the ToF-CIMS to form  $m/z = (-)$  230. We know from experiment 9 that  $\sim 16\%$  of INP fragments in the triple-CIMS to form  $m/z = (-)$  230. The experimental data in Table 3.7 for INP and ICN were corrected based on this fragmentation. A GC is not attached to the triple-CIMS used in experiments 1-6, so INP should be taken as a lower limit for these experiments, as other fragmentation products likely form, but a correction cannot be measured.

The estimated sensitivities are the largest source of error for these experiments. The estimated total error for the triple-CIMS, a combination of the error in ToF-sensitivities ( $\pm 20\%$ ) and the non-direct triple calibration ( $\pm 15\%$ ), is approximately  $\pm 35\%$  for compounds in which the ToF sensitivities are understood ( $m/z < (-)$  230 and  $(-)$  232, and  $(-)$  234). For the large nitrates ( $m/z \geq (-)$  230 except  $(-)$  234 and  $(-)$  232) the errors could be larger because no synthetic standards are available to

calibrate the instruments, but we do not expect the errors to be much greater than  $\pm 35\%$ .

Two compounds at  $m/z = (-) 201$  and  $(-) 244$  form in the dark, but we are not able to define a chemical mechanism consistent with the production of compounds at these masses. During the BEARPEX field campaign  $m/z = (-) 244$  formed at night, so this product is likely atmospherically relevant (Beaver et al., 2012). Both products may form in a minor yield from reactions of  $\text{INO}_2$ ,  $\text{IHNO}_2$  or  $\text{IPNO}_2$  with  $\text{HO}_2$  or  $\text{RO}_2$ .

### Proposed RO [1-5] Hydrogen Shift Products

Kwan et al. (2012) and Ng et al. (2008) proposed the formation of products from the [1,5]-H-shift of *trans*-[1,4]-INO and *cis*-[1,4]-INO, respectively (Figure 3.12). We expect that the peroxy radical ( $\text{IHNO}_2$ ) that forms from the [1,5]-H-shift of the *trans*-[1,4]-INO will react with  $\text{HO}_2$  and form only the  $\text{C}_5$  hydroxy hydroperoxy nitrate (IHPN) given that only acetylperoxy radicals and  $\alpha$ -carbonyl peroxy radicals have been shown to produce OH (Orlando et al., 2012). Both resonance structures of IHPN have the nitrate group further removed from the peroxy radical. However, more studies measuring OH yields from functionalized nitrooxy peroxy radicals need to be conducted to confirm this assumption.  $\text{C}_5$  hydroxy carbonyl will form from the [1,5]-H-shift of *cis*-[1,4]-INO radical (Figure 3.12) and isoprene + OH chemistry, so we do not try to estimate a rate constant for this [1,5]-H-shift. However, we expect the H-shift of the *cis*-[1,4]-INO radical to be slower because hydrogen abstraction occurs more slowly for carbons adjacent to a nitrate group (Kwok et al., 1995).

IDHN and  $\delta$ -INHE co-elute. In order to estimate the amount of IDHN present in the experiments we have included the [1,5]-H-shift of the *trans*-[1,4]-INO into the kinetic mechanism. A general  $k_{[1,5]\text{-H-shift}} = \sim 2 \times 10^5 \text{ s}^{-1}$  and increasing all  $k_{\text{IHNO}_2 + \text{RO}_2}$  (except  $\text{IHO}_2$ ) by 2-fold best fit the experimental data for experiment 5. Jozef Peeters et al. (2014) found that  $\text{C}_5$  carbonyl alkoxy radicals (produced from the photolysis of  $\text{C}_5$  hydroperoxy aldehydes (HPALDs)) rapidly interconvert between the *cis* and *trans* states. Assuming a similar interconversion occurs for the nitrooxy alkoxy radicals and that most of the INO in this study comes from  $\text{RO}_2 + \text{RO}_2$  chemistry, we use the  $\delta$ -[1,4] distribution (0.73) in Table 3.4, Column 2 to adjust the rate constant to account for only the [1,4]-INO undergoing the shift ( $\sim 3 \times 10^5 \text{ s}^{-1}$ ). Not many [1,5]-H-shift rate constants have been measured. The isomerization rate constants for *n*-butoxy ( $2.4 \times 10^5 \text{ s}^{-1}$ ) and 2-pentoxy radicals ( $3.0 \times 10^5 \text{ s}^{-1}$ )

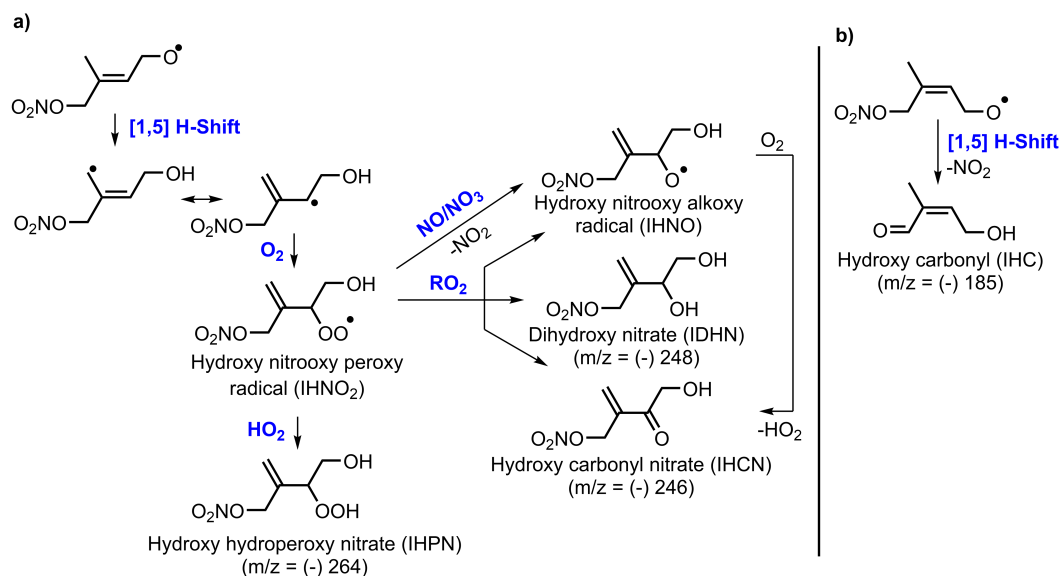


**Figure 3.12:** Main products proposed for the [1,5]-H-shift of (a) *trans*-[1,4]-INO, and (b) *cis*-[1,4]-INO (Ng et al., 2008). For brevity, products from only the dominant resonance structure are shown.

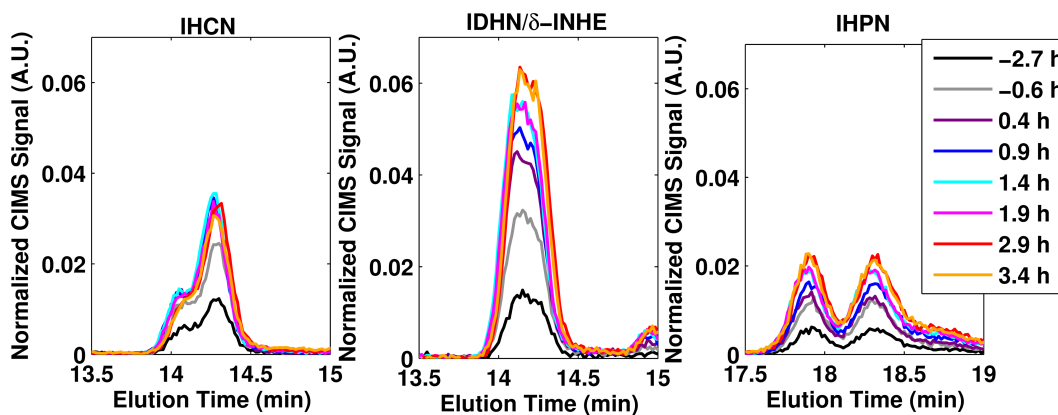


**Figure 3.13:** GC-ToF-CIMS chromatographs for C<sub>5</sub> hydroxy carbonyl nitrate (IHCN), C<sub>5</sub> dihydroxy nitrate (IDHN)/ $\delta$ -INHE, and C<sub>5</sub> hydroxy hydroperoxy nitrate (IHPN) as a function of time since photochemistry initiation. Signals for IHPN were increased by 25% to account for low transmission in the 4m column.

(Sprague et al., 2012) are close to the adjusted rate constant.

Although the oxidation of IHPN by OH might be expected to form an epoxide, there is no clear evidence suggesting this occurs. In experiment 7, there was 100% transmission of m/z = (-) 264 throughout the experiment, and no new peak formed after photooxidation. It is possible that the epoxide formed, but quick wall and lines losses prevented detection by the CIMS.

### Proposed RO<sub>2</sub> [1-6] Hydrogen Shift Products

Given the formation in the dark of ICPN ( $m/z = (-) 262$ ) and IDPN ( $m/z = (-) 280$ ), we suspect that the *trans*-[1,4]-INO<sub>2</sub> isomer will undergo a [1,6]-hydrogen shift (Figure 3.14). Both of these signals increased only when isoprene was present in the chamber, suggesting they are first-generation products. We inferred rate constants using the kinetic mechanism and results for experiment 5. There are two pathways in this system to form isoprene carbonyl hydroperoxy nitrate (ICPN). For simplicity,  $k_{\text{IPNO}_2 + \text{RO}_2}$  (except IHO<sub>2</sub>) was increased by the same factor (2) as  $k_{\text{IHNO}_2 + \text{RO}_2}$  (except IHO<sub>2</sub>), and the rest of the ICPN signal was assumed to be from the [1,4]-H shift.

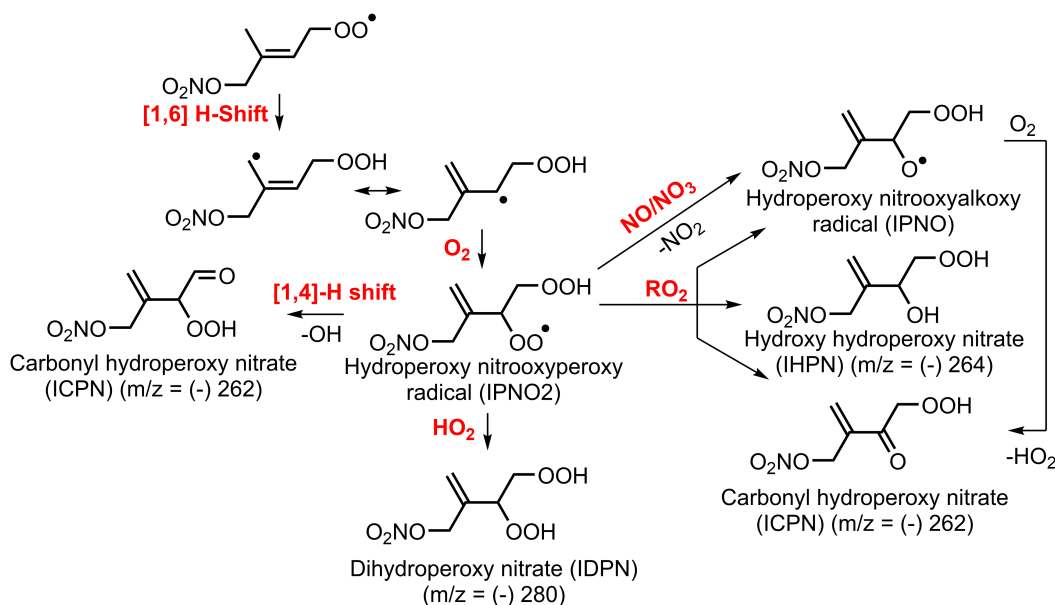


**Figure 3.14:** Main products formed from the [1,6]-H-shift of *trans*-[1,4]-INO<sub>2</sub>. For simplicity, products from only the dominant resonance structure are shown.

The [1,6]-H-shift rate constant that best fits with the experimental results is  $\sim 4 \times 10^{-4} \text{ s}^{-1}$ . To account for only one isomer isomerizing, the INO<sub>2</sub> distribution determined in Table 3.5 is used together with the assumption that an equal amount of *trans* and *cis* isomers form, to scale the [1,6]-H-shift rate constant to  $\sim 2 \times 10^{-3} \text{ s}^{-1}$ . The  $k_{[1,4]\text{-H-shift}}$  that best fit experimental results is  $\sim 2 \times 10^{-2} \text{ s}^{-1}$  which, as expected, is less than the  $k_{[1,5]\text{-H-shift}}$  ( $> 0.1 \text{ s}^{-1}$ ) determined by John D. Crounse, Nielsen, et al. (2013) for a similar compound. Recall, however, that all of the ICPN product may be explained by a greater  $k_{\text{IPNO}_2 + \text{RO}_2}$ . It is also possible to form ICPN and IDPN by other means (e.g., the [1,4]-H-shift of IHNO<sub>2</sub> also could form ICPN), so the above

rate constant and subsequent branching ratios are only upper limits/rough estimates and need to be verified using a simpler system. Nevertheless, the RO<sub>2</sub> lifetime at night is often much longer than that during the day, so this chemistry could be quite important in the ambient atmosphere and deserves further study.

## Aerosol Uptake

### INHE Uptake into Highly-Acidified Seed

After INHE formation in experiments 3, we injected highly-acidified seed particles under low RH conditions (particle pH <0, particle water content ~10-30% by volume due to H<sub>2</sub>SO<sub>4</sub> hygroscopicity (Xiong et al., 1998)) to more-clearly demonstrate uptake. We note that this was done to diagnose that INHE is surface active; it is not meant to be representative of atmospheric heterogeneous chemistry.

When highly acidic MgSO<sub>4</sub> + H<sub>2</sub>SO<sub>4</sub> seed was atomized into the chamber, INHE declined in the gas phase (Figure 3.15a) and the total organic increased in the particle phase (Figure 3.15b). The particle growth demonstrates that, like other epoxides (Fabien Paulot et al., 2009a; Surratt, Chan, et al., 2010), INHE efficiently undergoes reactive uptake to wet acidified aerosol. The gas-phase loss is likely due to the combination of uptake onto wet acidic seeds and irreversible losses to acidic chamber walls.

At the time of seed injection for experiments 1-5, most of the CIMS signal at m/z = (-) 248 is carried by INHE. The kinetic mechanism predicts that INP, IDHN, and INHE make up 1%, 15%, and 83%, respectively, of the m/z = (-) 248 signal. The (-) 63 daughter characteristic of organic peroxides is no longer being produced in MS/MS mode from m/z = (-) 248. Although only  $\beta$ -INP isomers efficiently produce the (-) 63 daughter in MS/MS mode, we expect that concentrations of  $\delta$ -INP are also minimal as they react with OH faster than  $\beta$ -INP.

Lin et al. (2012) identified the following AMS tracers for IEPOX: C<sub>4</sub>H<sub>5</sub><sup>+</sup>, C<sub>5</sub>H<sub>6</sub>O<sup>+</sup>, C<sub>3</sub>H<sub>7</sub>O<sub>2</sub><sup>+</sup>, and C<sub>5</sub>H<sub>8</sub>O<sub>2</sub><sup>+</sup>. These same tracers increase significantly when highly acidic seed is injected into the chamber both during experiment 3 and 6 (Figure 3.16 and 3.17), but not for the other seed types. When particles were injected in these experiments, there was only ~0.3 and ~0.1 ppb of IEPOX, so IEPOX was not the main source of these ions. The main source of these fragments is likely INHE for experiment 3 and IDHN for experiment 6.

We verify that lingering IEPOX, ~0.3 ppb (experiment 3) and ~0.1 ppb (experiment 6), present during seed injection, contributes to these signals only to a small degree.

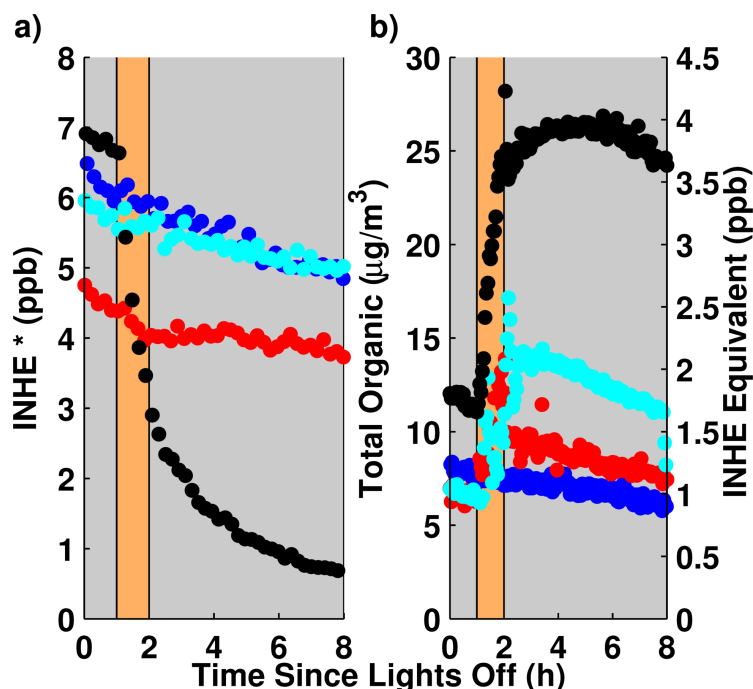


**Figure 3.15:** (a) INHE gas phase loss detected by CIMS and (b) total organic mass growth detected by the AMS for dry and no seed (blue), dry (NH<sub>4</sub>)<sub>2</sub>SO<sub>4</sub> (red), hydrated (NH<sub>4</sub>)<sub>2</sub>SO<sub>4</sub> (cyan), and hydrated MgSO<sub>4</sub>·H<sub>2</sub>SO<sub>4</sub> (black). \*This signal also includes a small fraction IDHN and INP. The tan region indicates when seed was injected. On the right hand axis of panel b, total organic is converted to INHE (ppb) for clarity.

In experiment 3 where IEPOX had the highest concentration, INHE declined on the CIMS by  $\sim 40 \mu\text{g}/\text{m}^3$ . Other compounds also declined including hydroxy methyl hydroperoxide, C<sub>5</sub> carbonyl hydroxy epoxide, IEPOX, C<sub>5</sub> hydroxy hydroperoxy epoxide, C<sub>4</sub> nitrooxycarbonyl hydroperoxide, and C<sub>5</sub> hydroxy hydroperoxide nitrate. These other compounds made up an additional  $\sim 30 \mu\text{g}/\text{m}^3$  as determined by the decline in the CIMS signal. We assume IEPOX fragments on the AMS as measured by *cis*- and *trans*-IEPOX standards by T. B. Nguyen, Coggon, et al. (2014), and that the ratio of *cis* and *trans*-IEPOX formed is similar to that measured by Bates et al. (2014). After seed injection, the AMS signal increased by  $\sim 15 \mu\text{g}/\text{m}^3$ , so the worst case the adjusted  $f_{\text{C}_5\text{H}_6\text{O}+}$  fragment becomes 1.0% and best case 1.3%. Both cases are well above what is considered background signal for  $f_{\text{C}_5\text{H}_6\text{O}+}$  (W. W. Hu et al., 2015).

There are two possibilities for why AMS tracers for heterogeneous uptake of INHE and IDHN are similar to those for IEPOX. In the MgSO<sub>4</sub> + H<sub>2</sub>SO<sub>4</sub> seeds, the nitrate group is known to be easily hydrolyzed (Jacobs, Burke, et al., 2014; Adam I. Darer



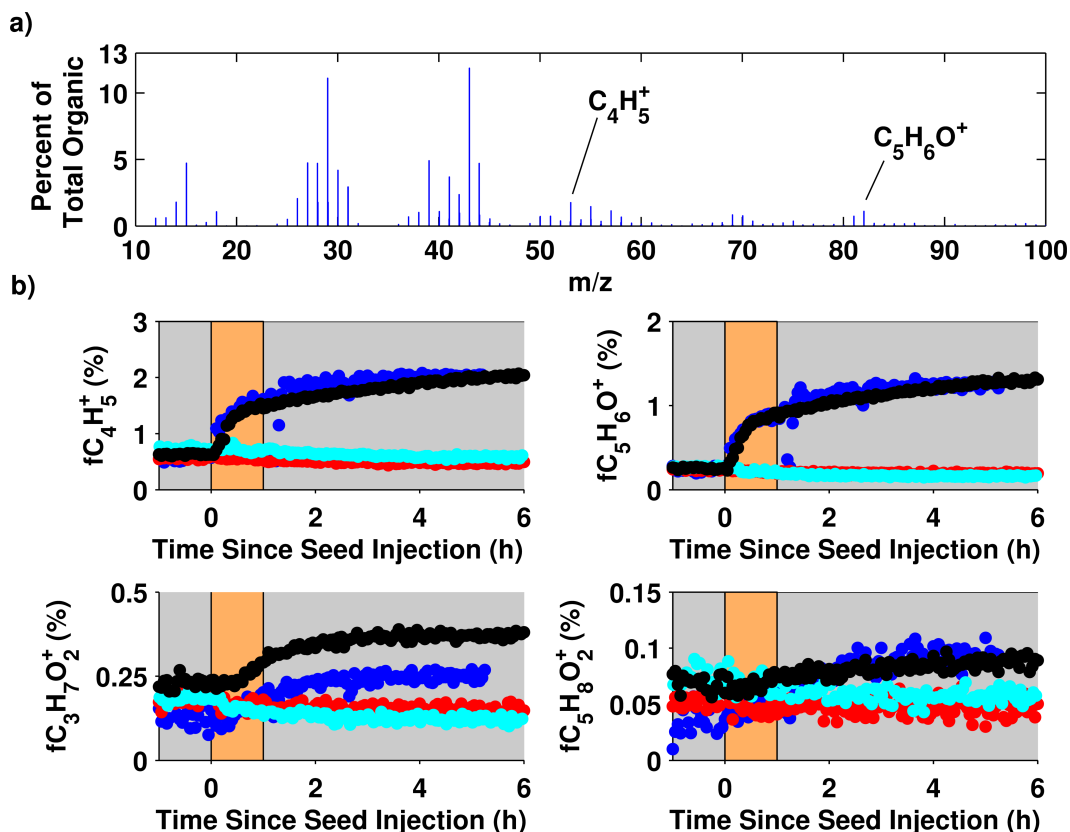


**Figure 3.16:** (a) AMS spectrum (percent of total organic) for hydrated  $MgSO_4:H_2SO_4$  (1:1) seed at peak growth. (b) AMS fragments (percent of total organic) proposed to be tracers for IEPOX (Lin et al., 2012) for hydrated  $MgSO_4:H_2SO_4$  seed before photooxidation (blue), dry  $(NH_4)_2SO_4$  seed (red), hydrated  $(NH_4)_2SO_4$  seed (cyan), and hydrated  $MgSO_4:H_2SO_4$  seed after photooxidation (black). Tan region indicates when seed was injected.

et al., 2011; K. S. Hu et al., 2011) yielding tetrols and organic sulfates identical to those produced from IEPOX (Surratt, Chan, et al., 2010) (Figure 3.18). If correct, these AMS tracers will only reflect INHE/IDHN uptake when the nitrate groups are hydrolyzed. Under less acidic conditions, reactive uptake of INHE may still occur, but different products are formed, which would have different fragmentation patterns on the AMS (e.g., INHE-derived dinitrate if nitric acid also partitions as is the case here). This implies that INHE undergoes reactive uptake to both hydrated  $(NH_4)_2SO_4$  and acidic sulfate, similarly to IEPOX (Fabien Paulot et al., 2009a; Surratt, Chan, et al., 2010; T. B. Nguyen, Coggon, et al., 2014). Alternatively, it is possible that the AMS fragments INHE/IDHN-derived compounds in a similar manner to IEPOX-derived compounds (i.e., the nitrate group does not greatly impact the fractionation pattern). If this is true, it implies that INHE does not undergo

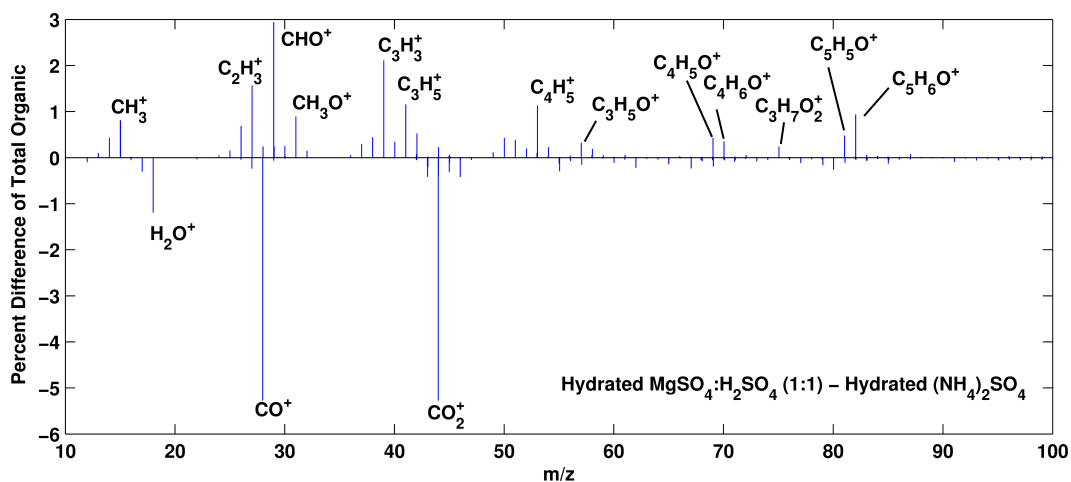


**Figure 3.17:** AMS difference spectrum (percent of total organic) between hydrated  $\text{MgSO}_4\text{:H}_2\text{SO}_4$  (1:1) and hydrated  $(\text{NH}_4)_2\text{SO}_4$  seed.

reactive uptake to seed types less acidic than  $\text{MgSO}_4\text{:H}_2\text{SO}_4$  seed because IEPOX AMS tracers do not increase for the dry or hydrated  $(\text{NH}_4)_2\text{SO}_4$  seeds.

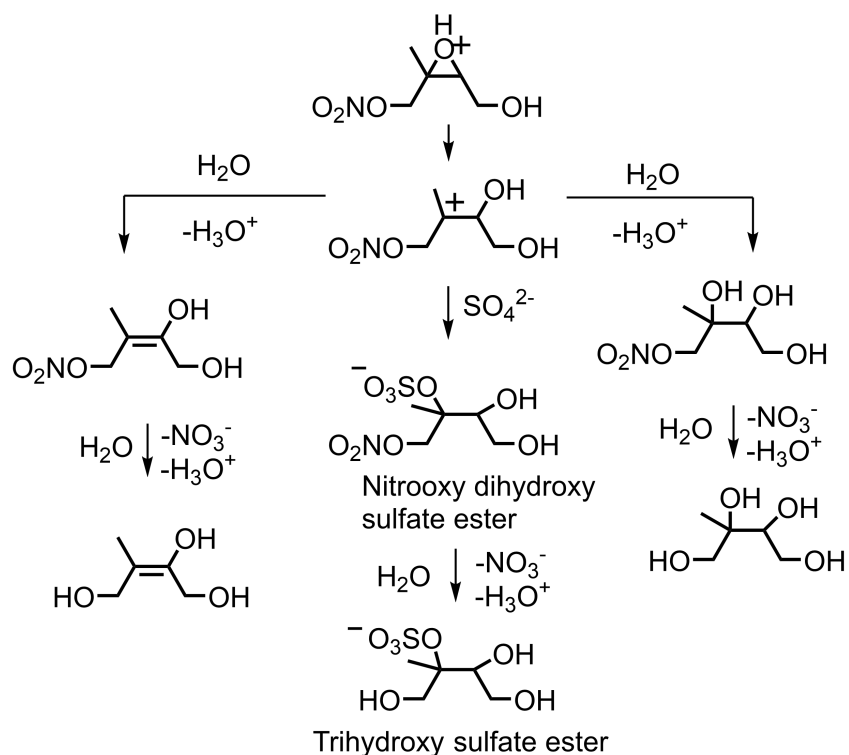


**Figure 3.18:** Proposed products of  $\beta$ -[4,1]-INHE that form in the particle phase under hydrated acidic conditions.

From this study, we conclude that in acidic atmospheric aerosols, uptake of INHE/IDHN

will yield the AMS tracers  $C_4H_5^+$ ,  $C_5H_6O^+$ ,  $C_3H_7O_2^+$ , and  $C_5H_8O_2^+$  that are clearly not unique to IEPOX. Indeed, Ng et al. (2008) using UPLC/(-)ESI-TOFMS detected trihydroxy sulfate ester and nitrooxy dihydroxy sulfate ester (Figure 3.18) in SOA generated during isoprene  $NO_3$  oxidation chamber experiments with highly acidic seed. Ng et al. (2008) note that these products have been previously detected in field studies as organosulfates produced from isoprene photooxidation (Surratt, Kroll, et al., 2007; Gomez-Gonzalez et al., 2008).

Hatch et al. (2011) using ATOFMS during the ANARChE and AMIGAS field campaigns found that trihydroxy sulfate ester increased at night and is well correlated with  $NO_x$  emissions. It is possible that in this study, some of the trihydroxy sulfate ester attributed to IEPOX reflected uptake of INHE/IDHN instead. The chemistry described in the present study could be a direct link for nighttime SOA formation from isoprene.

### Potential INHE Uptake into Hydrated $(NH_4)_2SO_4$ Seed

T. B. Nguyen, Coggon, et al. (2014) found that *cis* and *trans*- $\beta$ -IEPOX undergoes reactive uptake to hydrated  $(NH_4)_2SO_4$  seed aerosol. By analogy, IHNE should also undergo reactive uptake to aqueous seeds, but our results are inconclusive, and further work is needed as hydrated  $(NH_4)_2SO_4$  seeds are expected to be important in the lower troposphere. There is an increase in the total organic mass for hydrated  $(NH_4)_2SO_4$  (RH ~42% at seed injection) versus dry  $(NH_4)_2SO_4$  (Figure 3.15b, cyan markers) that equals ~ half the organic mass of the experiment using highly-acidified seeds (Figure 3.15b, black markers). Thus, hydrated  $(NH_4)_2SO_4$  seeds clearly produce SOA from the partitioning of organic compounds in this reaction. However, the CIMS signal for INHE for dry and hydrated  $(NH_4)_2SO_4$  experiments looks similar, and without a corresponding net decay of the INHE signal, it is not possible to implicate this epoxide in the reactive uptake. Even though  $\sim 300 \mu g m^{-3}$  of seed was added, the surface area of the chamber walls is still  $\sim 200$  times greater than the surface area of the particles. Unless the particles represent a very different surface chemically than the walls (e.g., highly acidic seeds), the decline in the gas phase from any seed addition will be masked by wall deposition, so the CIMS signal is unlikely to change substantially when seed is injected.

The O:C and N:C ratios of the nucleated aerosol prior to seed injection for all of the experiments are fairly similar (red markers in 3.19). The O:C ratio decreased rapidly for the highly acidic seed, and increased slightly for the dry and hydrated

(NH<sub>4</sub>)<sub>2</sub>SO<sub>4</sub> seeds. One possible explanation for why the O:C ratio decreases for the acidic seed case is that after injection, gas-phase products undergo reactive uptake to the acidic seed. The O:C ratio of these gas-phase products is likely lower than that of the organic aerosol formed prior to seed addition. The N:C ratio grew appreciably for only the hydrated (NH<sub>4</sub>)<sub>2</sub>SO<sub>4</sub> seeds. There are three possible explanations. The CIMS signal for nitric acid dropped significantly (~90 ppb), only when hydrated (NH<sub>4</sub>)<sub>2</sub>SO<sub>4</sub> seed was injected into the chamber. This nitric acid can react with organic species in the particle phase to form organonitrates, reactive uptake of nitrates present in the gas phase can occur, or there may be organic amine formation from the epoxide (T. B. Nguyen, Coggon, et al., 2014). In the present system it is not possible to determine which scenario is dominant. Figure 3.19 demonstrates that the chemical nature of the particles depends greatly on the relative humidity and seed type.

Hydrolysis of primary  $\delta$ -hydroxy nitrates was thought to be slow in neutral solutions ( $\tau > 2500$  h) (Adam I. Darer et al., 2011). Very acidic conditions (55 wt% D<sub>2</sub>SO<sub>4</sub>) were needed for the loss rate to be reasonably fast ( $\tau = 1.7$ -2.5 h) (K. S. Hu et al., 2011), and such high acidities are unlikely to occur in the ambient atmosphere. Jacobs, Burke, et al. (2014), however, measured the neutral hydrolysis lifetimes of  $\delta$ -[1,4N]-IHN and  $\beta$ -[4,3N]-IHN to be 2.46 min and 17.5 h, respectively, and suggested the neutral hydrolysis lifetimes of these nitrates are much faster than equivalent saturated hydroxy nitrates because of the allylic character of their transition states. Many of the isomers of INP, IHN, and ICN also have transition states of an allylic nature, so we anticipate that their hydrolysis rates may also be fast (although the influence of a carbonyl or hydroperoxide substituent on hydrolysis rate constants is unknown). Thus, hydrolysis of the  $\delta$  isomers produced in the NO<sub>3</sub> chemistry may be important in the atmosphere, especially for regions with high RH.

After seed injection, products partitioning to the gas phase from the particle phase are quite different depending on whether hydrated non-acidified seed or hydrated highly acidic seed is injected, implying that there is very different chemistry occurring in the two conditions. Some of the chemistry is likely similar between the two cases. For example, for both seed types, glycolaldehyde was produced in the particle phase in sufficient quantities to partition to the gas phase several hours after seed injection. There are also differences as well. For instance, several hours after hydrated (NH<sub>4</sub>)<sub>2</sub>SO<sub>4</sub> was injected into the chamber the signal for H<sub>2</sub>O<sub>2</sub> increased, but this did not happen during the high RH no seed experiment or for any other

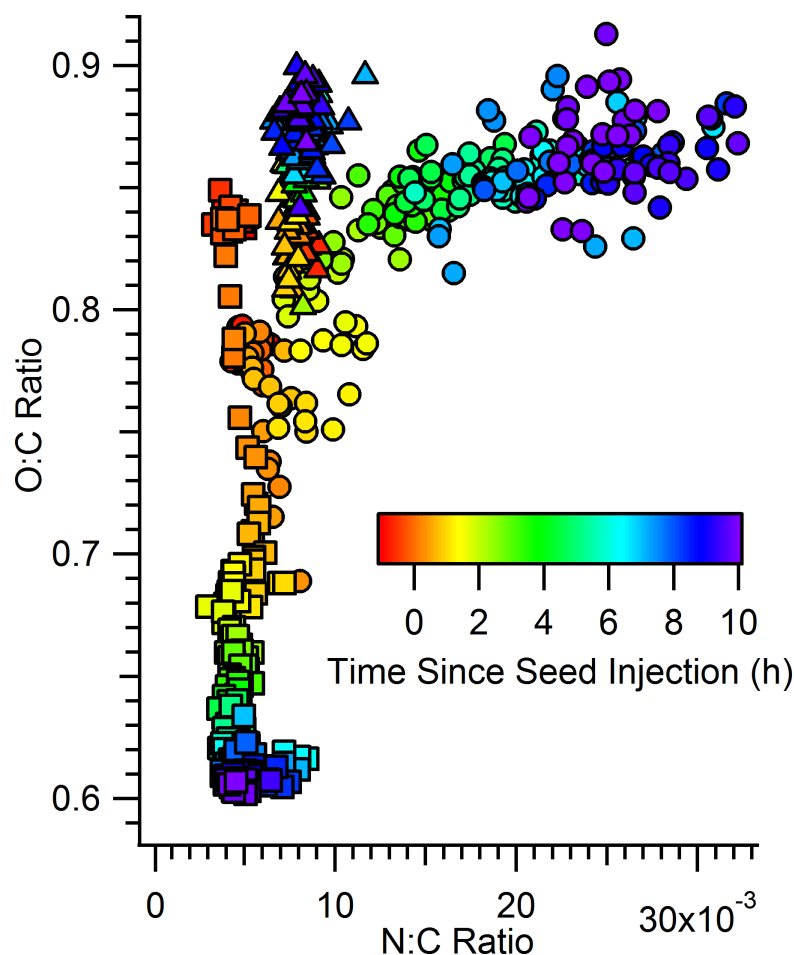


**Figure 3.19:** Change in N:C and O:C ratios for hydrated  $(\text{NH}_4)_2\text{SO}_4$  seeds (circles), hydrated  $\text{MgSO}_4 + \text{H}_2\text{SO}_4$  seeds (squares), and dry  $(\text{NH}_4)_2\text{SO}_4$  seeds (triangles).

seed types. This suggests that either  $\text{H}_2\text{O}_2$  or precursors to  $\text{H}_2\text{O}_2$  (i.e.,  $\text{HO}_2$  or  $\text{OH}$ ) formed in the particle phase and partitioned to the gas phase. Understanding this chemistry may be important for accurately simulating the  $\text{HO}_x$  cycle in atmospheric models.  $\text{H}_2\text{O}_2$  has unique chemistry in the hydrated  $(\text{NH}_4)_2\text{SO}_4$  case, which is the most atmospherically relevant, and highlights the importance of running chamber experiments under high RH conditions.

Jacobs, Burke, et al. (2014) found that [4,3N]-IHN oxidation by  $\text{OH}$  produced a 13% yield of IEPOX at 760 torr and proposed that this chemistry likely occurs for many compounds where an alkyl radical is adjacent to a nitrate group. In these experiments, there was a slight increase in the mass signals for these epoxides when photooxidation began and  $\text{OH}$  added to the double bond in ICN and INP. Like

other epoxides, these signals decline when hydrated highly acidic seed particles are injected into the chamber, but not when  $(\text{NH}_4)_2\text{SO}_4$  seed particles are injected at low RH.

During the high RH experiments, wall deposition of hydroxyl methylperoxyl radical (HMP) and IHPN was sufficiently high that none of the products remained in the gas phase by the time seed was injected into the chamber. HMP and IHPN also decayed quickly when hydrated highly acidic seed was injected in experiments 3 and 6.

### Potential Influence of $\text{CH}_2\text{O}$ .

Because  $\text{CH}_2\text{O}$  was used in high quantities in these experiments, it is important to determine its influence on the particle phase chemistry. The products that form can also help determine the types of reactions expected to occur in the atmosphere.  $\text{CH}_2\text{O}$  in aqueous solution exists mostly in the hydrated form (i.e.,  $\text{CH}_2(\text{OH})_2$ ). In experiments 1 and 2 when the RH is  $\sim 40\%$ ,  $\text{CH}_2(\text{OH})_2$  ( $m/z = 133$ ) increased as soon as  $\text{CH}_2\text{O}$  was injected into the chamber.  $\text{CH}_2\text{O}$  likely reacted with water present on the walls and some of the  $\text{CH}_2(\text{OH})_2$  partitioned back to the gas phase.  $\text{CH}_2(\text{OH})_2$  also formed in the low RH experiments, but with a much smaller yield. The following equilibria have been identified for  $\text{CH}_2(\text{OH})_2$  in the aqueous phase (Marklund, 1971), where BHMP is  $\text{HOCH}_2\text{O}_2\text{CH}_2\text{OH}$ :



Immediately after seed injection, HMHP declined in both experiments 3 and 6, but BHMP and  $\text{CH}_2(\text{OH})_2$  increased only in experiment 6. This implies that for the conditions of experiment 6,  $\text{CH}_2\text{O}$  partitions to the particle phase.  $\text{MgSO}_4$  &  $\text{H}_2\text{SO}_4$  seed is acidic enough to attract water, and  $\text{CH}_2(\text{OH})_2$  reacts with HMHP in the particle phase to form BHMP, some of which partitioned to the gas phase.

Since Marklund (1971) found that HMHP reacts with  $\text{CH}_2(\text{OH})_2$ , it is possible that other hydroperoxides will react with  $\text{CH}_2(\text{OH})_2$  in a similar manner. In experiment 6, when  $\text{MgSO}_4$  &  $\text{H}_2\text{SO}_4$  seed aerosol was added to the chamber, a small amount of  $m/z = (-) 233$ ,  $(-) 278$  and  $(-) 294$  was produced slowly. These signals are potentially the ROOR formed from ISOPPOOH, INP and IHPN reacting with  $\text{CH}_2(\text{OH})_2$  in the particle-phase. We see  $m/z = (-) 278$  rising much more than we would expect due

to ROOR formation from  $\text{RO}_2 + \text{RO}_2$  gas-phase reactions. It is possible that these ROOR form on the walls and repartition in a small degree back to the gas-phase. In experiment 3,  $m/z = (-) 233$  and  $(-) 278$  also grew when  $\text{MgSO}_4$  &  $\text{H}_2\text{SO}_4$  seed was added, but ISOPOOH and INP are not expected to undergo reactive uptake to the  $\text{MgSO}_4$  &  $\text{H}_2\text{SO}_4$ . Possibly  $m/z = (-) 233$  and  $(-) 278$  are IEPOX and INHE ring opening in acidic conditions and reacting with  $\text{CH}_2\text{O}$  to form diaxolane-type compounds (Yadav et al., 2013). This chemistry is highly speculative, but deserves further study.

The formation of these  $\text{CH}_2\text{O}$  and nitrate dimers seems to be acid catalyzed since these products are not detected in the gas phase when other seed types were added into the chamber. However, our understanding is limited to the products that partition back to the gas-phase. These dimer species could also have been present in the hydrated  $(\text{NH}_4)_2\text{SO}_4$  seed, but the larger activity of water prevented them from partitioning out of the particle phase or the dimers formed more slowly and never accumulated sufficiently in the gas phase in order to be detected by the CIMS. Understanding this effect will be important for future aerosol yield studies if  $\text{CH}_2\text{O}$  is used to generate  $\text{HO}_2$ . However, if these dimer products form under all conditions, they are unlikely to alter the yield significantly since  $\text{CH}_2\text{O}$  has such a low mass. Because we see these dimers form only under highly acidic conditions, the yields determined from dry or hydrated  $(\text{NH}_4)_2\text{SO}_4$  seeds will likely not be affected by this chemistry.

## References

- Atkinson, R., D. L. Baulch, R. A. Cox, J. N. Crowley, R. F. Hampson, R. G. Hynes, M. E. Jenkin, M. J. Rossi, and J. Troe (2004). "Evaluated Kinetic and Photochemical Data for Atmospheric Chemistry: Volume I - Gas Phase Reactions of  $\text{O}_x$ ,  $\text{HO}_x$ ,  $\text{NO}_x$  and  $\text{SO}_x$  Species". In: *Atmos. Chem. Phys.* 4, pp. 1461–1738.
- Atkinson, R., D. L. Baulch, R. A. Cox, J. N. Crowley, R. F. Hampson, R. G. Hynes, M. E. Jenkin, M. J. Rossi, J. Troe, and IUPAC Subcommittee (2006). "Evaluated Kinetic and Photochemical Data for Atmospheric Chemistry: Volume II – Gas Phase Reactions of Organic Species". In: *Atmos. Chem. Phys.* 6, pp. 3625–4055.
- Barnes, Ian et al. (1990). "Kinetics and Products of the Reactions of  $\text{NO}_3$  with Monoalkenes, Dialkenes, and Monoterpenes". In: *J. Phys. Chem.* 94, pp. 2413–2419.
- Bates, Kelvin H. et al. (2014). "Gas Phase Production and Loss of Isoprene Epoxydiols". In: *J. Phys. Chem. A*. 118.7, pp. 1237–1246. doi: 10.1021/jp4107958.

- Beaver, M. R. et al. (2012). “Importance of Biogenic Precursors to the Budget of Organic Nitrates: Observations of Multifunctional Organic Nitrates by CIMS and TD-LIF during BEARPEX 2009”. In: *Atmos. Chem. Phys.* 12, pp. 5773–5785. doi: 10.5194/acp-12-5773-2012.
- Berndt, Torsten and Olaf Boge (1997). “Gas-Phase Reaction of NO<sub>3</sub> Radicals with Isoprene : A Kinetic and Mechanistic Study”. In: *Int. J. Chem. Kinet.* 29, pp. 755–765.
- Bouvier-Brown, N. C. et al. (2009). “In-situ Ambient Quantification of Monoterpenes, Sesquiterpenes, and Related Oxygenated Compounds during BEARPEX 2007: Implications for Gas- and Particle-Phase Chemistry”. In: *Atmos. Chem. Phys.* 9, pp. 5505–5518.
- Brown, S. S., J. A. DeGouw, et al. (2009a). “Nocturnal Isoprene Oxidation over the Northeast United States in Summer and Its Impact on Reactive Nitrogen Partitioning and Secondary Organic Aerosol”. In: *Atmos. Chem. Phys.* 9, pp. 3027–3042.
- Brown, S. S., T. B. Ryerson, et al. (2006). “Variability in Nocturnal Nitrogen Oxide Processing and Its Role in Regional Air Quality”. In: *Science* 311, pp. 67–70. doi: 10.1126/science.1120120.
- Brown, Steven S. and Jochen Stutz (2012). “Nighttime Radical Observations and Chemistry”. In: *Chem. Soc. Rev.* 41, pp. 6405–6447. doi: 10.1039/c2cs35181a.
- Canagaratna, M. R. et al. (2015). “Elemental Ratio Measurements of Organic Compounds Using Aerosol Mass Spectrometry: Characterization, Improved Calibration, and Implications”. In: *Atmos. Chem. Phys.* 15, pp. 253–272.
- Cantrell, Christopher A. et al. (1985). “Kinetic Study of the NO<sub>3</sub>-CH<sub>2</sub>O Reaction and Its Possible Role in Nighttime Tropospheric Chemistry”. In: *J. Phys. Chem.* 89, pp. 139–146.
- Carter, W. P. L. and R. Atkinson (1985). “Atmospheric Chemistry of Alkanes”. In: *J. Atmos. Chem.* 3, pp. 377–405.
- Chen, X., D. Hulbert, and P. B. Shepson (1998). “Measurement of the Organic Nitrate Yield from OH Reaction with Isoprene”. In: *J. Geophys. Res.* 103.25, pp. 563–568.
- Compernelle, S., K. Ceulemans, and J. F. Muller (2011). “EVAPORATION: A New Vapour Pressure Estimation Method for Organic Molecules Including Non-Additivity and Intramolecular Interactions”. In: *Atmos. Chem. Phys.* 11, pp. 9431–9450.
- Crounse, J. D. et al. (2011). “Peroxy Radical Isomerization in the Oxidation of Isoprene”. In: *Phys. Chem. Chem. Phys.* 13, pp. 13607–13613. doi: 10.1039/c1cp21330j.



- Crounse, John D., Hasse C. Knap, et al. (2012). “Atmospheric Fate of Methacrolein. 1. Peroxy Radical Isomerization Following Addition of OH and O<sub>2</sub>”. In: *J. Phys. Chem. A*. 116, pp. 5756–5762. DOI: 10.1021/jp211560u.
- Crounse, John D., Karna A. McKinney, et al. (2006). “Measurement of Gas-Phase Hydroperoxides by Chemical Ionization Mass Spectrometry”. In: *Anal. Chem.* 78, pp. 6726–6732.
- Crounse, John D., Lasse B. Nielsen, et al. (2013). “Autoxidation of Organic Compounds in the Atmosphere”. In: *J. Phys. Chem. Lett.* 4, pp. 3513–3520. DOI: 10.1021/jz4019207.
- Crowley, John N. and Geert K. Moortgat (1992). “2-Bromoethylperoxy and 2-Bromo-1-Methylpropylperoxy Radicals : Ultraviolet Absorption Spectra and Self-Reaction Rate Constants at 298 K”. In: *J. Chem. Soc., Faraday Trans.* 88.17, pp. 2437–2444.
- Darer, Adam I. et al. (2011). “Formation and Stability of Atmospherically Relevant Isoprene-Derived Organosulfates and Organonitrates”. In: *Environ. Sci. Technol.* 45, pp. 1895–1902.
- DeCarlo, P. F. et al. (2006). “Field-Deployable, High-Resolution, Time-of-Flight Aerosol Mass Spectrometer.” In: *Anal. Chem.* 78.24, pp. 8281–8289.
- Dillon, T. J. and J. N. Crowley (2008). “Direct Detection of OH Formation in the Reactions of HO<sub>2</sub> with CH<sub>3</sub>C(O)O<sub>2</sub> and Other Substituted Peroxy Radicals”. In: *Atmos. Chem. Phys.* 8, pp. 4877–4889.
- Drewnick, F. et al. (2005). “A New Time-of-Flight Aerosol Mass Spectrometer (TOF-AMS)—Instrument Description and First Field Deployment”. In: *Aerosol Sci. Tech.* 39, pp. 637–658.
- Gomez-Gonzalez, Y. et al. (2008). “Characterization of Organosulfates from the Photooxidation of Isoprene and Unsaturated Fatty Acids in Ambient Aerosol Using Liquid Chromatography/(-) Electrospray Ionization Mass Spectrometry”. In: *J. Mass Spectrom.* 43, pp. 371–382. DOI: 10.1002/jms.
- Grosjean, E., J. B. de Andrade, and D. Grosjean (1996). “Carbonyl Products of the Gas-Phase Reaction of Ozone with Simple Alkenes”. In: *Environ. Sci. Technol.* 30.975, p. 983.
- Hasson, A. S., G. S. Tyndall, and J. J. Orlando (2004). “A Product Yield Study of the Reaction of HO<sub>2</sub> Radicals with Ethyl Peroxy (C<sub>2</sub>H<sub>5</sub>O<sub>2</sub>), Acetyl Peroxy (CH<sub>3</sub>C(O)O<sub>2</sub>), and Acetonyl Peroxy (CH<sub>3</sub>C(O)CH<sub>2</sub>O<sub>2</sub>) Radicals”. In: *J. Phys. Chem. A*. 108, pp. 5979–5989.
- Hasson, Alan S. et al. (2012). “Branching Ratios for the Reaction of Selected Carbonyl-Containing Peroxy Radicals with Hydroperoxy Radicals”. In: *J. Phys. Chem. A*. 116, pp. 6264–6281. DOI: 10.1021/jp211799c.

- Hatch, Lindsay E. et al. (2011). “Measurements of Isoprene-Derived Organosulfates in Ambient Aerosols by Aerosol Time-of-Flight Mass Spectrometry-Part 2: Temporal Variability and Formation Mechanisms”. In: *Environ. Sci. Technol.* 45, pp. 8648–8655.
- Horowitz, Larry W. et al. (2007). “Observational Constraints on the Chemistry of Isoprene Nitrates over the Eastern United States”. In: *J. Geophys. Res.* 112, pp. 1–13. DOI: 10.1029/2006JD007747.
- Hou, Hua, Lizhi Deng, et al. (2005). “A Systematic Computational Study of the Reactions of HO<sub>2</sub> with RO<sub>2</sub>: The HO<sub>2</sub> + CH<sub>2</sub>ClO<sub>2</sub>, CHCl<sub>2</sub>O<sub>2</sub>, and CCl<sub>3</sub>O<sub>2</sub> Reactions”. In: *J. Phys. Chem. A.* 109, pp. 9299–9309.
- Hou, Hua and Baoshan Wang (2005). “A Systematic Computational Study on the Reactions of HO<sub>2</sub> with RO<sub>2</sub>: The HO<sub>2</sub> + CH<sub>3</sub>O<sub>2</sub>(CD<sub>3</sub>O<sub>2</sub>) and HO<sub>2</sub> + CH<sub>2</sub>FO<sub>2</sub> Reactions”. In: *J. Phys. Chem. A.* 109, pp. 451–460.
- Hu, K. S., A. I. Darer, and M. J. Elrod (2011). “Thermodynamics and Kinetics of the Hydrolysis of Atmospherically Relevant Organonitrates and Organosulfates”. In: *Atmos. Chem. Phys.* 11, pp. 8307–8320. DOI: 10.5194/acp-11-8307-2011.
- Hu, W. W. et al. (2015). “Characterization of a Real-Time Tracer for Isoprene Epoxydiols-Derived Secondary Organic Aerosol (IEPOX-SOA) from Aerosol Mass Spectrometer Measurements”. In: *Atmos. Chem. Phys. Discuss.* 15, pp. 11223–11276.
- Hurley, M. D. et al. (2006). “Atmospheric Chemistry of n-C<sub>x</sub>F<sub>2x+1</sub>CHO (x = 1, 2, 3, 4): Fate of n-C<sub>x</sub>F<sub>2x+1</sub>C(O) Radicals”. In: *J. Phys. Chem. A.* 110, pp. 12443–12447.
- Jacobs, M. I., W. J. Burke, and M. J. Elrod (2014). “Kinetics of the Reactions of Isoprene-Derived Hydroxynitrates: Gas Phase Epoxide Formation and Solution Phase Hydrolysis”. In: *Atmos. Chem. Phys.* 14, pp. 8933–8946. ISSN: 1489332014. DOI: 10.5194/acp-14-8933-2014.
- Jacobs, M. I., A. I. Darer, and M. J. Elrod (2013). “Rate Constants and Products of the OH Reaction with Isoprene-Derived Epoxides”. In: *Environ. Sci. Technol.* 47, pp. 12868–12876.
- Jenkin, M. E., M. D. Hurley, and T. J. Wallington (2007). “Investigation of the Radical Product Channel of the CH<sub>3</sub>COO<sub>2</sub> + HO<sub>2</sub> Reaction in the Gas Phase”. In: *Phys. Chem. Chem. Phys.* 9, pp. 3149–3162. DOI: 10.1039/b702757e.
- (2010). “Investigation of the Radical Product Channel of the CH<sub>3</sub>OCH<sub>2</sub>O<sub>2</sub> + HO<sub>2</sub> Reaction in the Gas Phase”. In: *J. Phys. Chem. A.* 114, pp. 408–416. DOI: 10.1021/jp908158w.
- Jenkin, Michael E., Andrew A. Boyd, and Robert Lesclaux (1998). “Peroxy Radical Kinetics Resulting from the OH-Initiated Oxidation of 1, 3-Butadiene, 2, 3-Dimethyl-1, 3-Butadiene and Isoprene”. In: *J. Atmos. Chem.* 29, pp. 267–298. DOI: 10.1023/A:1005940332441.

- Jenkin, Michael E. and Garry D. Hayman (1995). "Kinetics of Reactions of Primary, Secondary and Tertiary Beta-Hydroxy Peroxyl Radicals: Application to Isoprene Degradation". In: *J. Chem. Soc., Faraday Trans.* 91.13, pp. 1911–1922.
- Kerdouci, J. et al. (2012). "An Experimental Study of the Gas-Phase Reactions of NO<sub>3</sub> Radicals with a Series of Unsaturated Aldehydes: trans-2-Hexenal, trans-2-Heptenal, and trans-2-Octenal". In: *J. Phys. Chem. A*. 116, pp. 10135–10142.
- Kwan, A. J. et al. (2012). "Peroxy Radical Chemistry and OH Radical Production during the NO<sub>3</sub>-Initiated Oxidation of Isoprene". In: *Atmos. Chem. Phys.* 12, pp. 7499–7515. DOI: 10.5194/acp-12-7499-2012.
- Kwok, E. S. C. and R. Atkinson (1995). "Estimation of Hydroxyl Radical Reaction Rate Constants for Gas-Phase Organic Compounds Using a Structure-Reactivity Relationship: An Update". In: *Atmos. Environ.* 29.14, pp. 1685–1695.
- Lee, B. H. et al. (2014). "An Iodide-Adduct High-Resolution Time-of-Flight Chemical-Ionization Mass Spectrometer: Application to Atmospheric Inorganic and Organic Compounds". In: *Environ. Sci. Technol.* 48.11, pp. 6309–6317.
- Lee, L. (2014). "Interactive Comment on "Kinetics of the Reactions of Isoprene-Derived Hydroxynitrates: Gas Phase Epoxide Formation and Solution Phase Hydrolysis" by M. I. Jacobs et al." In: *Atmos. Chem. Phys. Discuss.* 14, pp. 3249–3251.
- Lee, Lance et al. (2014). "On Rates and Mechanisms of OH and O<sub>3</sub> Reactions with Isoprene-Derived Hydroxy Nitrates". In: *J. Phys. Chem. A*. 118, pp. 1622–1637. DOI: 10.1021/jp4107603.
- Lin, Ying-Hsuan et al. (2012). "Isoprene Epoxydiols as Precursors to Secondary Organic Aerosol Formation: Acid-Catalyzed Reactive Uptake Studies with Authentic Compounds". In: *Environ. Sci. Technol.* 46, pp. 250–258. DOI: 10.1021/es202554c.
- Liu, Y. J. et al. (2013). "Production of Methyl Vinyl Ketone and Methacrolein via the Hydroperoxyl Pathway of Isoprene Oxidation". In: *Atmos. Chem. Phys.* 13, pp. 5715–5730. DOI: 10.5194/acp-13-5715-2013.
- Lockwood, A. L. et al. (2010). "Isoprene Nitrates: Preparation, Separation, Identification, Yields, and Atmospheric Chemistry". In: *Atmos. Chem. Phys.* 10, pp. 6169–6178.
- Loreto, Francesco and Thomas D. Sharkey (1990). "A Gas-Exchange Study of Photosynthesis and Isoprene Emission in *Quercus Rubra* L". In: *Planta* 182, pp. 523–531.
- Mao, J., F. Paulot, et al. (2013). "Ozone and Organic Nitrates over the Eastern United States: Sensitivity to Isoprene Chemistry". In: *J. Geophys. Res. : Atmos.* 118, pp. 11256–11258.

- Mao, J., X. Ren, et al. (2012). "Insights into Hydroxyl Measurements and Atmospheric Oxidation in a California Forest". In: *Atmos. Chem. Phys.* 12, pp. 8009–8020.
- Marklund, Stefan (1971). "The Simultaneous Determination of Bis(hydroxymethyl)-Peroxide (BHMP), Hydroxymethylhydroperoxide (HMP), and  $\text{H}_2\text{O}_2$  with Titanium(IV). Equilibria Between the Peroxides and the Stabilities of HMP and BHMP at Physiological Conditions". In: *Acta Chem. Scand.* 25, pp. 3517–3531.
- Monson, R. K. and R. Fall (1989). "Isoprene Emission from Aspen Leaves: Influence of Environment and Relation to Photosynthesis and Photorespiration". In: *Plant Physiol.* 90, pp. 267–274.
- Muller, J. F., J. Peeters, and T. Stavrakou (2014). "Fast Photolysis of Carbonyl Nitrates from Isoprene". In: *Atmos. Chem. Phys.* 14, pp. 2497–2508.
- Murrells, Timothy P. et al. (1991). "Laser Flash Photolysis Study of the UV Spectrum and Kinetics of Reactions of  $\text{HOCH}_2\text{CH}_2\text{O}_2$  Radicals". In: *J. Chem. Soc., Faraday Trans.* 87.15, pp. 2351–2360.
- Ng, N. L. et al. (2008). "Secondary Organic Aerosol (SOA) Formation from Reaction of Isoprene with Nitrate Radicals ( $\text{NO}_3$ )". In: *Atmos. Chem. Phys.* 8, pp. 4117–4140. DOI: 10.5194/acpd-8-3163-2008.
- Nguyen, T. B., M. M. Coggon, et al. (2014). "Organic Aerosol Formation from the Reactive Uptake of Isoprene Epoxydiols (IEPOX) onto Non-Acidified Inorganic Seeds". In: *Atmos. Chem. Phys.* 14, pp. 3497–3510. DOI: 10.5194/acp-14-3497-2014.
- Nguyen, T. B., J. D. Crounse, R. H. Schwantes, et al. (2014). "Overview of the Focused Isoprene eXperiment at the California Institute of Technology (FIXCIT): Mechanistic Chamber Studies on the Oxidation of Biogenic Compounds". In: *Atmos. Chem. Phys.* 14, pp. 13531–13549. DOI: 10.5194/acp-14-13531-2014.
- Nguyen, T. B., J. D. Crounse, A. P. Teng, et al. (2015). "Rapid Deposition of Oxidized Biogenic Compounds to a Temperate Forest". In: *Proc. Natl. Acad. Sci. U. S. A.* 112, E392–E401.
- Orlando, John J. and Geoffrey S. Tyndall (2012). "Laboratory Studies of Organic Peroxy Radical Chemistry: An Overview with Emphasis on Recent Issues of Atmospheric Significance". In: *Chem. Soc. Rev.* 41.19, pp. 6294–317. DOI: 10.1039/c2cs35166h.
- Paulot, Fabien et al. (2009a). "Unexpected Epoxide Formation in the Gas-Phase Photooxidation of Isoprene". In: *Science* 325, pp. 730–733. DOI: 10.1126/science.1172910.
- Paulot, F. et al. (2009b). "Isoprene Photooxidation: New Insights into the Production of Acids and Organic Nitrates". In: *Atmos. Chem. Phys.* 9, pp. 1479–1501.

- Peeters, J. and J. F. Muller (2010). “HO<sub>x</sub> Radical Regeneration in Isoprene Oxidation via Peroxy Radical Isomerizations. II: Experimental Evidence and Global Impact.” In: *Phys. Chem. Chem. Phys.* 12, pp. 14227–14235.
- Peeters, J., T. L. Nguyen, and L. Vereecken (2009). “HO<sub>x</sub> Radical Regeneration in the Oxidation of Isoprene”. In: *Phys. Chem. Chem. Phys.* 11, pp. 5935–5939. doi: 10.1039/b908511d.
- Peeters, Jozef et al. (2014). “Hydroxyl Radical Recycling in Isoprene Oxidation Driven by Hydrogen Bonding and Hydrogen Tunneling: The Upgraded LIM1 Mechanism”. In: *J. Phys. Chem. A* 118, pp. 8625–8643. doi: 10.1021/jp5033146.
- Perring, A. E. et al. (2009). “A Product Study of the Isoprene + NO<sub>3</sub> Reaction”. In: *Atmos. Chem. Phys.* 9, pp. 4945–4956.
- Praske, E. et al. (2015). “Atmospheric Fate of Methyl Vinyl Ketone: Peroxy Radical Reactions with NO and HO<sub>2</sub>”. In: *J. Phys. Chem. A* 119, pp. 4562–4572.
- Rivera-Rios, J. C. et al. (2014). “Conversion of Hydroperoxides to Carbonyls in Field and Laboratory Instrumentation: Observational Bias in Diagnosing Pristine versus Anthropogenically Controlled Atmospheric Chemistry”. In: *Geophys. Res. Lett.* 41.23, pp. 8645–8651.
- Rollins, A. W., E. C. Browne, et al. (2012). “Evidence for NO<sub>x</sub> Control over Night-time SOA Formation”. In: *Science* 337, pp. 1210–1212. doi: 10.1126/science.1221520.
- Rollins, A. W., A. Kiendler-Scharr, et al. (2009). “Isoprene Oxidation by Nitrate Radical: Alkyl Nitrate and Secondary Organic Aerosol Yields”. In: *Atmos. Chem. Phys.* 9, pp. 6685–6703.
- Sander, S. P. et al. (2011). *Chemical Kinetics and Photochemical Data for Use in Atmospheric Studies, Evaluation No. 17*. Jet Propulsion Laboratory, Pasadena: JPL Publication 10-6.
- Saunders, S. M. et al. (2003). “Protocol for the Development of the Master Chemical Mechanism, MCMv3 (Part A): Tropospheric Degradation of Non-Aromatic Volatile Organic Compounds”. In: *Atmos. Chem. Phys.* 3, pp. 161–180.
- Skov, H. et al. (1992). “Products and Mechanisms of the Reactions of the Nitrate Radical (NO<sub>3</sub>) with Isoprene, 1,3-Butadiene and 2,3-Dimethyl-1,3-Butadiene in Air”. In: *Atmos. Environ.* 26A.15, pp. 2771–2783.
- Sprague, Matthew K. et al. (2012). “Kinetics of n-Butoxy and 2-Pentoxo Isomerization and Detection of Primary Products by Infrared Cavity Ringdown Spectroscopy”. In: *J. Phys. Chem. A* 116, pp. 6327–6340. doi: 10.1021/jp212136r.
- Sprengnether, M. et al. (2002). “Product Analysis of the OH Oxidation of Isoprene and 1,3-Butadiene in the Presence of NO”. In: *J. Geophys. Res.* 107.D15, p. 4268.

- St. Clair, J. M. et al. (2015). “Kinetics and Products of the Reaction of the First-Generation Isoprene Hydroxy Hydroperoxide (ISOPOOH) with OH”. In: *J. Phys. Chem. A*. 120, pp. 1441–1451.
- St. Clair, Jason M. et al. (2010). “Chemical Ionization Tandem Mass Spectrometer for the in Situ Measurement of Methyl Hydrogen Peroxide”. In: *Rev. Sci. Instrum.* 81, pp. 094102–094102. DOI: 10.1063/1.3480552.
- Starn, T. K. et al. (1998). “Nighttime Isoprene Chemistry at an Urban-Impacted Forest Site”. In: *J. Geophys. Res.* 103.D17, pp. 22437–22447.
- Steinbacher, M. et al. (2005). “Volatile Organic Compounds in the Po Basin. Part B: Biogenic VOCs”. In: *J. Atmos. Chem.* 51, pp. 293–315. DOI: 10.1007/s10874-005-3577-0.
- Stone, D., L. K. Whalley, and D. E. Heard (2012). “Tropospheric OH and HO<sub>2</sub> Radicals: Field Measurements and Model Comparisons”. In: *Chem. Soc. Rev.* 41, pp. 6348–6404.
- Stroud, C. A. et al. (2002). “Nighttime Isoprene Trends at an Urban Forested Site during the 1999 Southern Oxidant Study”. In: *J. Geophys. Res.* 107.D16, pp. 1–14.
- Suh, Inseon, Wenfang Lei, and Renyi Zhang (2001). “Experimental and Theoretical Studies of Isoprene Reaction with NO<sub>3</sub>”. In: *J. Phys. Chem. A*. 105, pp. 6471–6478. DOI: 10.1021/jp0105950.
- Sulbaek Andersen, M. P. et al. (2003). “Atmospheric Chemistry of C<sub>2</sub>F<sub>5</sub>CHO: Mechanism of the C<sub>2</sub>F<sub>5</sub>C(O)O<sub>2</sub>+HO<sub>2</sub> Reaction”. In: *Chem. Phys. Lett.* 381, pp. 14–21. DOI: 10.1016/j.cplett.2003.09.085.
- Surratt, J. D., a W. H. Chan, et al. (2010). “Reactive Intermediates Revealed in Secondary Organic Aerosol Formation from Isoprene”. In: *Proc. Natl. Acad. Sci. U. S. A.* 107.15, pp. 6640–6645. DOI: 10.1073/pnas.0911114107.
- Surratt, J. D., J. H. Kroll, et al. (2007). “Evidence for Organosulfate in Secondary Organic Aerosol”. In: *Environ. Sci. Technol.* 41, pp. 517–527.
- Taatjes, C. A. et al. (2012). “Direct Measurement of Criegee Intermediate (CH<sub>2</sub>OO) Reactions with Acetone, Acetaldehyde, and Hexafluoroacetone”. In: *Phys. Chem. Chem. Phys.* 14, pp. 10391–10400.
- Teng, A. P. et al. (2015). “Hydroxy Nitrate Production in the OH-Initiated Oxidation of Alkenes”. In: *Atmos. Chem. Phys.* 15, pp. 4297–4316.
- Tuazon, E. C. et al. (1997). “Products of the Gas-Phase Reactions of O<sub>3</sub> with a Series of Methyl-Substituted Ethenes”. In: *Environ. Sci. Technol.* 31, pp. 3004–3009.
- Warneke, C. et al. (2004). “Comparison of Daytime and Nighttime Oxidation of Biogenic and Anthropogenic VOCs along the New England Coast in Summer during New England Air Quality Study 2002”. In: *J. Geophys. Res.* 109, pp. D10309–D10309. DOI: 10.1029/2003JD004424.

- Wolfe, G. M. et al. (2012). “Photolysis, OH Reactivity and Ozone Reactivity of a Proxy for Isoprene-Derived Hydroperoxyenals (HPALDs)”. In: *Phys. Chem. Chem. Phys.* 14, pp. 7276–7286.
- Xie, Y. et al. (2013). “Understanding the Impact of Recent Advances in Isoprene Photooxidation on Simulations of Regional Air Quality”. In: *Atmos. Chem. Phys.* 13, pp. 8439–8455. DOI: 10.5194/acp-13-8439-2013.
- Xiong, J. Q. et al. (1998). “Influence of Organic Films on the Hygroscopicity of Ultrafine Sulfuric Acid Aerosol”. In: *Environ. Sci. Technol.* 32, pp. 3536–3541.
- Yadav, Ganapati D. and Prasad S. Surve (2013). “Atom Economical Green Synthesis of Chloromethyl-1,3-dioxolanes from Epichlorohydrin Using Supported Heteropolyacids”. In: *Ind. Eng. Chem. Res.* 52, pp. 6129–6137.
- Zabel, F., K. A. Sahetchian, and C. Chachaty (1987). “ESR Spectra of Free Radicals Formed During the Gas-Phase Photo-Oxidation of Formaldehyde: Thermal Stability of the HOCH<sub>2</sub>OO Radical”. In: *Chem. Phys. Lett.* 134.5, pp. 433–437.
- Zhang, X. et al. (2015). “Vapor Wall Deposition in Teflon Chambers”. In: *Atmos. Chem. Phys.* 15, pp. 4197–4214. DOI: 10.5194/acp-15-4197-2015.
- Zhao, Jun and Renyi Zhang (2008). “A Theoretical Investigation of Nitrooxyalkyl Peroxy Radicals from NO<sub>3</sub>-Initiated Oxidation of Isoprene”. In: *Atmos. Environ.* 42, pp. 5849–5858. DOI: 10.1016/j.atmosenv.2007.09.023.

*Chapter 4*FORMATION OF HIGHLY OXYGENATED LOW-VOLATILITY  
PRODUCTS FROM CRESOL OXIDATION

Schwantes, R. H. et al. (2016). “Formation of Highly Oxygenated Low-Volatility Products from Cresol Oxidation”. In: *Atmos. Chem. Phys. Disc.* DOI: 10.5194/acp-2016-887.

**4.1 Abstract**

Hydroxyl radical (OH) oxidation of toluene produces ring-retaining products (cresol and benzaldehyde) and ring-opening products (bicyclic intermediate compounds and epoxides). Here, first- and later-generation OH oxidation products from cresol and benzaldehyde are identified in laboratory chamber experiments. For benzaldehyde, first-generation ring-retaining products are identified, but later-generation products are not detected. For cresol, low-volatility (saturation mass concentration,  $C^* \sim 3.5 \times 10^4 - 7.7 \times 10^{-3} \mu\text{g m}^{-3}$ ) first- and later-generation ring-retaining products are identified. Subsequent OH addition to the aromatic ring of *o*-cresol leads to compounds such as hydroxy, dihydroxy, and trihydroxy methyl benzoquinones and dihydroxy, trihydroxy, tetrahydroxy, and pentahydroxy toluenes. These products are detected in the gas phase by chemical ionization mass spectrometry (CIMS) and in the particle phase using offline direct analysis in real time mass spectrometry (DART-MS). Our data suggest that the yield of trihydroxy toluene from dihydroxy toluene is substantial. While an exact yield cannot be reported, as authentic standards are unavailable, we find that a yield for trihydroxy toluene from dihydroxy toluene of  $\sim 0.7$  (equal to the yield of dihydroxy toluene from *o*-cresol), is consistent with experimental results for *o*-cresol oxidation under low-NO conditions. These results suggest that even though the cresol pathway accounts for only  $\sim 20\%$  of the oxidation products of toluene, it is the source of a significant fraction ( $\sim 20\text{--}40\%$ ) of toluene secondary organic aerosol (SOA) due to the formation of low-volatility products.

**4.2 Introduction**

Aromatic compounds are emitted from both anthropogenic (e.g., solvent use and motor vehicle exhaust) and natural (e.g., wildfires) processes. Oxidation of aromatic compounds leads to the formation of ozone ( $\text{O}_3$ ) and secondary organic



aerosol (SOA) (Calvert et al., 2002, and references therein). Despite the number of studies performed, the spectrum of gas-phase aromatic oxidation products remains incomplete, especially those of later generation and those responsible for producing secondary organic aerosol. Toluene, one of the principal aromatic compounds present in the atmosphere, is emitted from both anthropogenic processes (~60%) and biofuel/biomass burning (~40%) (Henze et al., 2008). Chamber studies have measured particularly high SOA mass yields (0.9-1.6  $\mu\text{g}/\mu\text{g}$ ) from toluene (Zhang et al., 2014) when correcting for vapor wall loss using the Statistical Oxidation Model. Modeling studies, using SOA yields that do not account for vapor wall loss (e.g., 0.1-0.3  $\mu\text{g}/\mu\text{g}$ , (Ng et al., 2007)), estimated that toluene SOA contributes ~4% of the total SOA produced globally (Henze et al., 2008). Incorporation of the updated SOA yields is expected to increase the significance of toluene to the global SOA budget.

Hydroxyl radical (OH) oxidation of toluene takes place via four pathways, yielding benzaldehyde, cresol, bicyclic intermediates, and epoxides (Figure 4.1). Identification of subsequent gas-phase oxidation products from the benzaldehyde and cresol pathways is the focus of this work. These pathways lead to high yields of ring-retaining products. If sustained during subsequent oxidation, these ring-retaining compounds are likely to lead to SOA. Since OH addition to the aromatic ring of toluene increases the reaction rate constant for subsequent OH addition (Calvert et al., 2002), continued addition of OH to the aromatic ring has the potential to accelerate the path to highly oxidized products.

Benzaldehyde forms as a result of hydrogen abstraction from the methyl group of toluene. Reported benzaldehyde yields from toluene oxidation are relatively consistent in the range of 0.053-0.12 (Calvert et al., 2002, and references therein). MCM v3.3.1 recommends a yield of 0.07, which is in the middle of this range (Jenkin et al., 2003; Bloss et al., 2005).

Cresol is produced from OH addition to the aromatic ring of toluene with subsequent  $\text{O}_2$  addition and  $\text{HO}_2$  elimination. Measured yields of cresol from toluene oxidation range from 0.03 to 0.385 (Calvert et al., 2002, and references therein) with several studies converging to a yield of 0.18 (Klotz et al., 1998; Smith et al., 1998). A recent theoretical study suggests a cresol yield of 0.32 (Wu et al., 2014). Cresol yields from OH oxidation of toluene are difficult to measure quantitatively because cresol is prone to losses (e.g., to sampling tubing) that are dependent on the measurement technique (Klotz et al., 1998). Once formed, cresol ( $k_{\text{OH}} \sim 5 \times 10^{-11} \text{ cm}^3 \text{ molec}^{-1}$

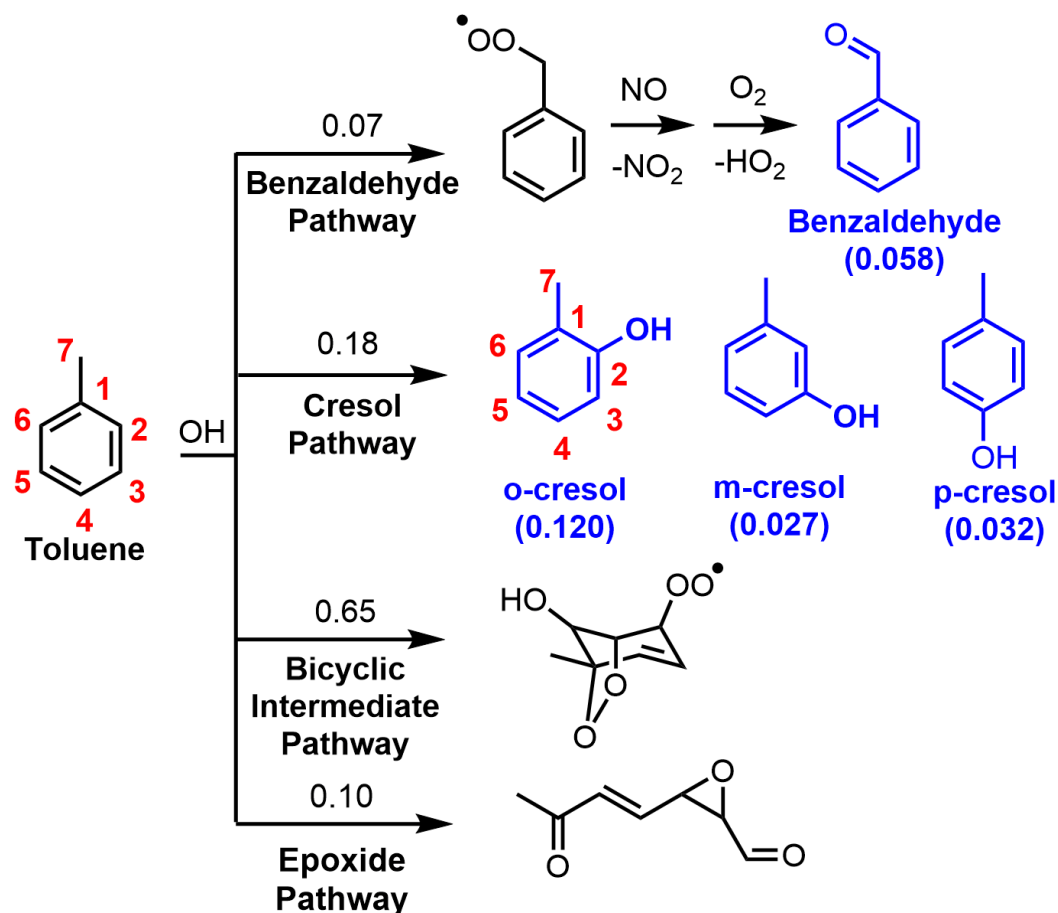


**Figure 4.1:** Toluene photooxidation pathways as exemplified by the Master Chemical Mechanism (MCM) v3.3.1 including cresol isomer distribution (Klotz et al., 1998). Ring-retaining products are shown in blue. Carbons on the toluene and *o*-cresol ring structure are labeled in red from 1-7 to facilitate identification of isomers throughout the text.

$s^{-1}$ ) reacts much faster with OH than its precursor toluene ( $k_{OH} = 6 \times 10^{-12} \text{ cm}^3 \text{ molec}^{-1} \text{ s}^{-1}$ ) (Calvert et al., 2002). Nakao, Liu, et al. (2012) detected products in the particle phase indicative of successive OH addition to the aromatic ring of *o*-cresol (i.e.,  $C_7H_8O_4$  and  $C_7H_8O_5$ ) and phenol and estimated that the cresol pathway contributes ~20% of SOA produced from toluene. Most studies (Olariu, Klotz, et al., 2002; Caralp et al., 1999) have focused on monitoring first-generation products from cresol and benzaldehyde in the gas-phase, but not second- and third-generation products. The goal of this work is to identify gas-phase pathways and specific oxidization products important for toluene SOA formation by monitoring later-generation products in the gas phase and linking these products to those detected in the particle phase.

### 4.3 Methods

Chamber experiments were performed to study products from toluene OH oxidation under both low- and high-NO conditions. In order to explore later-generation chemistry and identify important precursors for SOA, later-generation ring-retaining products were also used as the initial precursor.

#### Experimental Design

All experiments were performed in the 24 m<sup>3</sup> Teflon chambers at the Caltech dual chamber facility. Low- and high-NO experiments were carried out in separate chambers to avoid contamination of NO and related compounds in the low-NO chamber. The chambers were flushed with purified air for 24 h prior to each experiment. Purified air is generated by removing volatile organic carbon, ozone, nitrogen oxides, and water vapor from compressed air. Experiments oxidizing toluene, *o*-cresol, 3-methyl catechol, and benzaldehyde under low- and high-NO conditions were performed (Table 4.1). For all experiments, hydrogen peroxide (H<sub>2</sub>O<sub>2</sub>) as an OH source was injected first by flowing purified air through a glass bulb heated to 36°C; 2 ppm of H<sub>2</sub>O<sub>2</sub> was used for all gas-phase and high-NO particle-phase experiments, and 4 ppm H<sub>2</sub>O<sub>2</sub> was used for low-NO particle-phase experiments.

**Table 4.1:** Description of Experiments

| Expt.<br>#                                    | VOC               | VOC<br>(ppb) | Oxidant<br>Precursor               | Initial NO<br>(ppb) | Continuous NO Injection<br>(ppb h <sup>-1</sup> ) <sup>a</sup> | Temp. (K)/<br>RH (%) <sup>b</sup> |
|---|-------------------|--------------|------------------------------------|---------------------|--|-----------------------------------|
| <b>Gas-Phase Experiments<sup>c</sup></b>      |                   |              |                                    |                     |  |                                   |
| 1   | Toluene           | 98           | H <sub>2</sub> O <sub>2</sub> + NO | 72                  | 98 (149); 61 (223); 30 (UE)                                    | 301 / <3-7                        |
| 2   | Toluene           | 91           | H <sub>2</sub> O <sub>2</sub>      | NA                  | NA   | 301 / <3-5                        |
| 3   | Toluene           | 49           | H <sub>2</sub> O <sub>2</sub> + NO | 74                  | 98 (120); 61 (204); 30 (UE)                                    | 301 / <3-5                        |
| 4   | Toluene           | 46           | H <sub>2</sub> O <sub>2</sub>      | NA                  | NA   | 301 / ≤3                          |
| 5   | <i>o</i> -cresol  | 40           | H <sub>2</sub> O <sub>2</sub> + NO | 79                  | 98 (120); 61 (20); 30 (UE)                                     | 301 / 4-9                         |
| 6   | <i>o</i> -cresol  | 36           | H <sub>2</sub> O <sub>2</sub>      | NA                  | NA   | 301 / <3-4                        |
| 7   | 3-methyl catechol | 69           | H <sub>2</sub> O <sub>2</sub> + NO | 74                  | 98 (123); 30 (UE)  | 301 / 3-7                         |
| 8   | 3-methyl catechol | 97           | H <sub>2</sub> O <sub>2</sub>      | NA                  | NA   | 301 / ≤3                          |
| 9   | 3-methyl catechol | 59           | H <sub>2</sub> O <sub>2</sub>      | NA                  | NA   | 289-315/ <14                      |
| 10  | 3-methyl catechol | 65           | H <sub>2</sub> O <sub>2</sub>      | NA                  | NA   | 302 / <3                          |
| 11  | Benzaldehyde      | ~50          | H <sub>2</sub> O <sub>2</sub>      | NA                  | NA   | 301 / ≤3                          |
| 12  | Benzaldehyde      | ~50          | H <sub>2</sub> O <sub>2</sub> + NO | 72                  | 98 (68); 61 (35); 30 (329); 22 (UE)                            | 301 / ≤3                          |
| <b>Particle-Phase Experiments<sup>c</sup></b> |                   |              |                                    |                     |  |                                   |
| 13  | Toluene           | 286          | H <sub>2</sub> O <sub>2</sub>      | NA                  | NA   | 301 / 3-6                         |
| 14  | Toluene           | 313          | H <sub>2</sub> O <sub>2</sub> + NO | 78                  | 146 (263); 53 (734); 15 (UE)                                   | 300 / <3-7                        |
| 15  | <i>o</i> -cresol  | 143          | H <sub>2</sub> O <sub>2</sub> + NO | 84                  | 146 (262); 53 (182); 15 (UE)                                   | 301 / 9-12                        |

<sup>a</sup> NO was continuously injected. The rate of NO injection decreased over the course of the experiment. The following format is used: rate in ppb h<sup>-1</sup> (number of minutes injected at that rate). “UE” indicates that the rate was used until the end of the experiment. <sup>b</sup> RH = Relative Humidity. <sup>c</sup> Seed aerosol was injected into the chamber for all particle-phase experiments, but not for gas-phase experiments.

After addition of the oxidant, the volatile organic compound (VOC) was injected. Toluene (99.8% purity) and benzaldehyde ( $\geq 99\%$  purity) were injected into a glass bulb using a gas-tight syringe. Purified air was passed into the glass bulb and subsequently injected into the chamber at  $5 \text{ L min}^{-1}$ . A weighed amount of *o*-cresol (99.5% purity) was heated to  $49^\circ\text{C}$ , and an excess amount of 3-methyl catechol (98% purity) was heated to  $36^\circ\text{C}$  while purified air was passed into a glass bulb. A water bath was used to provide consistent heating.

For high-NO experiments, NO (501 ppm in  $\text{N}_2$ , Scott Specialty Gases) was injected into the chamber using a calibrated mass flow controller at the start of the experiment, and continuously throughout the experiment. The goal of the continuous NO injection was to control the amount of NO present during the experiment, such that the level of  $\text{NO}_x$  remained as low as possible. A kinetic model is used to verify that these experimental conditions are relevant to the atmosphere (see Section 4.3).

For experiments in which particle-phase sampling was performed, the last step included atomization of 0.06 M ammonium sulfate through a  $^{210}\text{Po}$  neutralizer and into the chamber. Photooxidation ( $j_{\text{NO}_2} = 4.4 \times 10^{-3} \text{ s}^{-1}$ ) was initiated at least 1 h after all injections were complete to ensure adequate mixing. Because  $\text{NO}_3$  forms in the chamber and reacts rapidly with a number of compounds present, lights remained on to ensure photolysis of  $\text{NO}_3$  until all filters had been collected.

Some studies (Tan et al., 2009; Lim et al., 2010) have implicated glyoxal, an OH oxidation product of toluene, in SOA formation under humid conditions, and one study suggested that glyoxal leads to enhanced SOA growth by increasing OH concentrations rather than directly forming aerosol (Nakao, Liu, et al., 2012). In the present study, all experiments were carried out under dry conditions ( $\text{RH} < 10\%$ ) to simplify gas-phase measurements and to focus on the later-generation low-volatility products that form in the gas phase and partition to the particle phase.

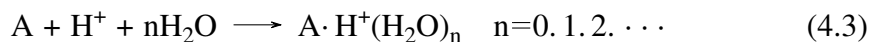
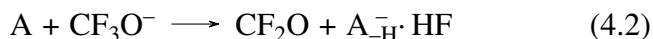
In experiment 9, all procedures were the same as described in the preceding paragraphs, but after 1.5 h of photooxidation, lights were turned off. While lights were off, the decay of 3-methyl catechol oxidation products due to wall deposition was measured. In experiment 10, all procedures were the same as described above, but lights were turned on for only 3.2 h. Once an adequate level of oxidation products from 3-methyl catechol oxidation were generated, the chamber experiment was ended and purified air was sampled by the CIMS to monitor the desorption of 3-methyl catechol oxidation products off the CIMS walls.

### Chamber Instrumentation

Commercial instruments were used to monitor toluene, nitrogen oxides ( $\text{NO}_x$ ), ozone ( $\text{O}_3$ ), relative humidity (RH), and temperature. Toluene was monitored by a gas chromatograph with a flame ionization detector (GC-FID, Agilent 6890N, HP-5 column).  $\text{NO}_x$  and  $\text{O}_3$  were monitored by a Teledyne T200  $\text{NO}_x$  monitor and Horiba APOA-360  $\text{O}_3$  monitor, respectively. A Vaisala HMM211 probe was used to monitor temperature and RH. Gas-phase oxidized compounds were detected via a  $\text{CF}_3\text{O}^-$  Chemical Ionization Mass Spectrometer (CIMS) (Section 4.3). Particle-phase compounds were monitored using high-resolution direct analysis in real time mass spectrometry (DART-MS) from filters collected at the end of each experiment (Section 4.3).

### CIMS Description and Calibration

A chemical ionization mass spectrometer (CIMS) was used to monitor oxidized organic compounds in the gas-phase. The CIMS uses a custom-modified triple quadrupole mass analyzer (Varian 1200) (St. Clair et al., 2010). The instrument was operated in both negative and positive mode using  $\text{CF}_3\text{O}^-$  and  $\text{H}^+$ , respectively, as the reagent ions. A compound (A) with an affinity for fluorine interacts with  $\text{CF}_3\text{O}^-$  either to form a complex (R4.1) or a  $\text{F}^-$  transfer reaction (typically acidic compounds, R4.2). A compound is detected at its molecular weight + 85 for the complex and + 19 for the  $\text{F}^-$  transfer. In positive mode,  $\text{H}^+$  typically interacts with a compound along with  $0 - n$  water molecules to form a complex at the molecular weight +  $(18n + 1)$  (R4.3). Other ions (e.g.,  $\text{NO}^+$ ) also cluster in positive mode complicating interpretation of signals. The reactions are:



More detail about the ion chemistry of the CIMS is provided in St. Clair et al. (2010), Crounse et al. (2006), and Paulot et al. (2009a). Positive mode was used to monitor the decay of benzaldehyde, which is not detected in negative mode. Negative mode was normalized by the total number of reagent ions. Signals were not normalized for positive mode, because the total reagent ions cannot be monitored.

MS/MS mode was used to confirm the identity of certain products and to separate isobaric compounds. In MS/MS mode, only complex interactions will produce a  $\text{CF}_3\text{O}^-$  daughter ( $m/z = (-)85$ ). Transfer reactions produce an  $\text{A}_{(-\text{H})}^-$  daughter ( $m/z = \text{molecular weight of the analyte} - 1$ ). Detection of the  $\text{A}_{(-\text{H})}^-$  daughter and not the  $\text{CF}_3\text{O}^-$  daughter confirms the ion is correctly assigned as a  $\text{F}^-$  transfer and the analyte is acidic. The structural information provided by MS/MS mode helps correctly identify compounds.

The CIMS was calibrated using *o*-cresol. An excess amount of *o*-cresol was heated at  $46^\circ\text{C}$  in a glass bulb.  $\text{N}_2$  was blown into this glass bulb and then directed into a Teflon pillow bag to produce a concentrated mixture containing  $\sim 80$  ppm of *o*-cresol. A 500 mL glass bulb was filled from this concentrated bag and Fourier transform infrared absorption (FT-IR) spectroscopy (pathlength 19 cm) was used to determine the concentration. After confirmation with FT-IR each time, the remaining *o*-cresol contained in the glass bulb was used to create a dilute pillow bag ( $\sim 200$  ppb). The dilute pillow bag was filled with either dry  $\text{N}_2$  or the same purified air used to fill the large  $24\text{ m}^3$  Teflon chambers. This dilute pillow bag was then sampled by the CIMS.

The *o*-cresol integrated cross section for region  $3145\text{--}2824\text{ cm}^{-1}$  measured by Etzkorn et al. (1999) was used for quantification. To our knowledge there are no other reported FT-IR quantifications of *o*-cresol. *m*-Cresol has been quantified at Pacific Northwest National Laboratory (PNNL) using FT-IR (Sharpe et al., 2004). As verification of the Etzkorn et al. (1999) calibration, the integrated cross section for the region  $3178\text{--}2706\text{ cm}^{-1}$  of *m*-cresol was used to evaluate the PNNL spectrum. The PNNL calibration (1 ppm) is 28% lower than the Etzkorn et al. (1999) calibration (1.39 ppm). The absorption spectra for *o*-cresol and *m*-cresol in this region only partially align, but the integrated cross sections measured by Etzkorn et al. (1999) are similar ( $12.7 \times 10^{-18}$  and  $12.6 \times 10^{-18}\text{ cm molec}^{-1}$ , respectively).

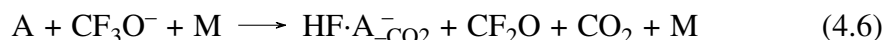
Sequential FT-IR runs confirmed loss of *o*-cresol to the glass cell ( $\sim 8\%$  in the first 10 min and  $\sim 24\%$  after  $\sim 1$  h). Within 10 min of the FT-IR sample collection, the glass bulb was flushed into the dilute pillow bag. If wall deposition of *o*-cresol is reversible, the *o*-cresol that deposited on the wall would be flushed into the pillow bag. Because the extent of reversibility of *o*-cresol wall loss is unknown, a correction for wall loss was not applied, but instead added as uncertainty (8%). Thus, the uncertainty for the *o*-cresol sensitivity is estimated as 36%, a combination of the uncertainty in the FT-IR quantification and loss of *o*-cresol during the calibration.

Traditionally, an analyte (A) is either detected at the  $F^-$  transfer reaction ( $A+19$ ) or complex formation ( $A+85$ ). However, fragmentation products have also been detected (Praske et al., 2015). *o*-cresol predominantly forms a complex with  $CF_3O^-$ . The proportion of *o*-cresol that undergoes a transfer reaction versus fragmenting is dependent on the water mixing ratio. Fragmentation is higher in the purified air versus the drier nitrogen (Table 4.2). Likely the presence of water destabilizes the molecular ion formed from  $CF_3O^-$  ionization leading to more fragmentation.

**Table 4.2:** Fraction of CIMS signal detected from the transfer reaction, complex formation, or fragmentation

| VOC               | Gas                | Fraction of Signal |         |           |
|-------------------|--------------------|--------------------|---------|-----------|
|                   |                    | Transfer           | Complex | Fragments |
| <i>o</i> -cresol  | purified air       | 0.12               | 0.77    | 0.11      |
| <i>o</i> -cresol  | dry N <sub>2</sub> | 0.19               | 0.75    | 0.05      |
| 3-methyl catechol | purified air       | 0.78               | 0.02    | 0.20      |
| 3-methyl catechol | dry N <sub>2</sub> | 0.90               | <0.01   | 0.10      |

Many of the fragmentation products are small and not uniquely formed from one  $m/z$ , and so cannot be used to determine the concentration of an individual compound. Instead all possible unique fragments were considered in determining the concentration of a compound. This includes reactions R1, R2 and the following:



Because the small fragment signals cannot be uniquely assigned to a specific compound, the fraction of these signals to the total needs to be known for all water levels used in the experiments. The influence of water on the fraction of the *o*-cresol signal produced from unique signals was determined by sampling a sustained amount of *o*-cresol and sequentially adding more water to the CIMS sampling inlet. For *o*-cresol, the sum of all signals (unique and small fragmentation products) is relatively consistent for the relative humidities used in these experiments (Table 4.1). The CIMS sensitivity determined from the FT-IR dry N<sub>2</sub> calibration was corrected for the influence of water in the purified air. The FT-IR purified air calibration was within 10% of this approach. The water correction for *o*-cresol is minor. The CIMS



sensitivity (including only unique signals) decreases by  $< 1\%$  due to the slight RH change over the course of the experiments.

3-methyl catechol calibration was attempted using the same FT-IR method as *o*-cresol. However, because the vapor pressure of 3-methyl catechol ( $6.8 \times 10^{-6}$  atm) is much lower than that of *o*-cresol ( $3.9 \times 10^{-4}$  atm) (Table 4.3), preparation of a sufficiently concentrated pillow bag for FT-IR quantification was not possible. Instead the sensitivities of *o*-cresol and 3-methyl catechol were assumed to be the same in dry N<sub>2</sub> when including the sum of all detected signals (i.e., transfer, complex, and fragments) with a correction for the difference in the ion-molecule collision rate for the compounds. The ion-molecule collision rate (dependent on the molecular weight, dipole moment, and polarizability of two colliding molecules) was estimated using the technique explained in Su et al. (1982) (see Section 3.9 and Tables 3.6 and 3.7 of the supplemental information for more details).

**Table 4.3:** Estimated vapor pressures and saturation mass concentrations for main products detected by CIMS from toluene oxidation

| VOC                                     | Estimated Vapor Pressure <sup>a</sup> |                                 | Saturation Mass Concentration <sup>b</sup> |                      |
|---|---------------------------------------|---------------------------------|--|----------------------|
|   | (atm, 298K)                           |                                 | (C*) ( $\mu\text{g m}^{-3}$ )              |                      |
|   | EVAP                                  | Nann                            | Evap                                       | Nann                 |
| Toluene                                 | $3.7 \times 10^{-2} \text{ }^c$       | $3.7 \times 10^{-2} \text{ }^c$ | $1.4 \times 10^8$                          | $1.4 \times 10^8$    |
| <i>o</i> -cresol                        | $3.9 \times 10^{-4} \text{ }^c$       | $3.9 \times 10^{-4} \text{ }^c$ | $1.7 \times 10^6$                          | $1.7 \times 10^6$    |
| Acetyl acrylic acid                     | $6.6 \times 10^{-6}$                  | $1.7 \times 10^{-5}$            | $3.1 \times 10^4$                          | $7.9 \times 10^4$    |
| Hydroxy methyl hydroperoxy benzoquinone | $1.9 \times 10^{-9}$                  | U                               | $1.3 \times 10^1$                          | NA                   |
| Hydroxy methyl trioxo cyclohexene       | $8.2 \times 10^{-7}$                  | U                               | $5.2 \times 10^3$                          | NA                   |
| 3-methyl catechol                       | $2.3 \times 10^{-6}$                  | $6.8 \times 10^{-6}$            | $1.2 \times 10^4$                          | $3.5 \times 10^4$    |
| Hydroxy methyl benzoquinone             | $5.3 \times 10^{-7}$                  | U                               | $3.0 \times 10^3$                          | NA                   |
| Trihydroxy toluene                      | $1.1 \times 10^{-8}$                  | $6.0 \times 10^{-8}$            | $6.3 \times 10^1$                          | $3.4 \times 10^2$    |
| Dihydroxy methyl benzoquinone           | $8.3 \times 10^{-9}$                  | U                               | $5.2 \times 10^1$                          | NA                   |
| Tetrahydroxy toluene                    | $2.4 \times 10^{-11}$                 | $3.3 \times 10^{-10}$           | $1.5 \times 10^{-1}$                       | 2.1                  |
| Trihydroxy methyl benzoquinone          | $9.5 \times 10^{-11}$                 | U                               | $6.6 \times 10^{-1}$                       | NA                   |
| Pentahydroxy toluene                    | $9.0 \times 10^{-14}$                 | $1.1 \times 10^{-12}$           | $6.3 \times 10^{-4}$                       | $7.7 \times 10^{-3}$ |
| Hydroxy nitrotoluene                    | U                                     | $1.8 \times 10^{-5}$            | NA   | $1.1 \times 10^5$    |
| Hydroxy tricarbonyl pentane             | $3.1 \times 10^{-4}$                  | U                               | $1.7 \times 10^6$                          | NA                   |
| Dihydroxy nitrotoluene                  | U                                     | $2.0 \times 10^{-7}$            | NA   | $1.4 \times 10^3$    |
| Glyoxylic acid                          | $1.9 \times 10^{-3}$                  | U                               | $5.5 \times 10^5$                          | NA                   |
| Benzoic acid                            | $1.1 \times 10^{-5}$                  | $8.2 \times 10^{-6}$            | $5.5 \times 10^4$                          | $4.1 \times 10^4$    |

**Table 4.3:** Estimated vapor pressures and saturation mass concentrations for main products detected by CIMS from toluene oxidation

| VOC  | Estimated Vapor Pressure <sup>a</sup> |                      | Saturation Mass Concentration <sup>b</sup> |                   |
|--|---------------------------------------|----------------------|--|-------------------|
|  | (atm, 298K)                           |                      | (C*) ( $\mu\text{g m}^{-3}$ )              |                   |
|  | EVAP                                  | Nann                 | Evap                                       | Nann              |
| Peroxybenzoic acid                             | $8.8 \times 10^{-5}$                  | U                    | $5.0 \times 10^5$                          | NA                |
| Nitrophenol                                    | U                                     | $8.7 \times 10^{-5}$ | NA   | $5.0 \times 10^5$ |
| Dinitrophenol                                  | U                                     | $3.3 \times 10^{-7}$ | NA   | $2.5 \times 10^3$ |
| Hydroxy methyl dicarbonyl butene               | $1.4 \times 10^{-4}$                  | U                    | $6.5 \times 10^5$                          | NA                |
| Methyl glyoxylic acid                          | $6.1 \times 10^{-4}$                  | U                    | $2.2 \times 10^6$                          | NA                |
| Carbonyl methyl butene carboxylic acid         | $6.6 \times 10^{-6}$                  | $1.9 \times 10^{-5}$ | $3.1 \times 10^4$                          | $8.9 \times 10^4$ |
| Carbonyl butene carboxylic acid                | $2.0 \times 10^{-5}$                  | $3.0 \times 10^{-5}$ | $8.2 \times 10^4$                          | $1.2 \times 10^5$ |
| Carbonyl hydroxy methyl butene carboxylic acid | $1.1 \times 10^{-7}$                  | U                    | $5.9 \times 10^2$                          | NA                |
| Hydroxy glyoxylic acid                         | $2.9 \times 10^{-7}$                  | U                    | $1.1 \times 10^3$                          | NA                |
| Dicarbonyl dihydroxy pentene                   | $5.8 \times 10^{-6}$                  | U                    | $3.1 \times 10^4$                          | NA                |
| Carbonyl hydroxy butene carboxylic acid        | $3.3 \times 10^{-7}$                  | U                    | $1.6 \times 10^3$                          | NA                |
| Carbonyl dihydroxy butene carboxylic acid      | $7.6 \times 10^{-9}$                  | U                    | $4.1 \times 10^1$                          | NA                |
| Carbonyl methyl hydroxy butene carboxylic acid | $1.1 \times 10^{-7}$                  | U                    | $5.9 \times 10^2$                          | NA                |
| Carbonyl dihydroxy pentene carboxylic acid     | $2.4 \times 10^{-9}$                  | U                    | $1.4 \times 10^1$                          | NA                |

<sup>a</sup> U = Unable to estimate, EVAP = EVAPORATION and Naan = Nannoolal. <sup>b</sup> Here  $C^* = MW \cdot P^0 / (RT)$  where MW = molecular weight,  $P^0$  = liquid vapor pressure,  $R$  = gas constant, and  $T$  = temperature. <sup>c</sup> The values reported are the measured values (Yaws, 1994).

The additional OH group on 3-methyl catechol increases the acidity such that it dominantly undergoes a  $F^-$  transfer reaction (Table 4.2). Unlike complex interactions,  $F^-$  transfer reactions are increasingly likely to decompose into smaller fragments as the mixing ratio of water increases (Table 4.2). The influence of water vapor on the sensitivity of 3-methyl catechol was measured in the same manner as that of *o*-cresol. Unlike *o*-cresol the sum of all unique signals and small fragmentation products for 3-methyl catechol are not consistent for the relative humidities used in these experiments. Likely at higher water concentrations, more fragmentation products with an  $m/z < 50$  (the lower limit of the CIMS scanning range) are produced. The sensitivity (including only unique signals) decreased over the course of the experiments more for 3-methyl catechol (9-15%) than for *o*-cresol (<1%).

Because the  $CF_3O^-$  chemical ionization process for 3-methyl catechol exhibits more fragmentation and dependence on water than *o*-cresol, extrapolating the sensitivities to other more oxidized compounds (e.g., trihydroxy toluene), has a high degree of uncertainty. The fragmentation and water dependence could exceed that for 3-methyl catechol. No authentic standards for trihydroxy toluene are currently available. However, two isomers (5-methyl-benzene-1,2,3-triol and 2,4,6-trihydroxytoluene) of trihydroxy toluene from Sigma's "collection of rare and unique chemicals" are available. Because Sigma does not validate the identity and purity of these compounds, these compounds were used only to examine the ion chemistry on the CIMS. Purified air was flowed through a heated ( $\sim 60$ - $150^\circ\text{C}$ ) glass bulb containing each compound into a Teflon pillow bag. Due to the low volatility (saturation mass concentration,  $C^* \sim 340 \mu\text{g m}^{-3}$ ) of these compounds, introducing detectable amounts into the gas-phase without decomposition was extremely difficult. 2,4,6-trihydroxy toluene seemed to be more stable and a higher signal was achieved compared to 5-methyl-benzene-1,2,3-triol. Enough sample of 2,4,6-trihydroxy toluene was introduced to confirm that  $m/z (-)159$  produced the  $m/z (-)139$  daughter but not the  $m/z (-)115$  daughter in MS/MS mode. Additionally,  $m/z (-)225$  produced the  $m/z (-)205$  daughter. The 5-methyl-benzene-1,2,3-triol signal was too low to monitor the compound in MS/MS mode, which is less sensitive than MS mode. In MS mode, 2,4,6-trihydroxy toluene produced the following signals  $m/z (-)225 > 205 > 159 > 139 > 115$  as well as many signals attributed to decomposition products or impurities (e.g., acetic acid). In MS mode, 5-methyl-benzene-1,2,3-triol produced the following signals  $m/z (-)205 > 159$  and also produced many decomposition products or impurities (e.g., formic acid). Possibly,  $m/z (-)115$  and  $m/z (-)225$  also formed from 5-methyl-benzene-1,2,3-triol, but the signal to noise ratio was too low to confirm.

There was a large array of additional signals measured by the CIMS from these standards. These signals are caused by impurities in the standards, decomposition outside of the CIMS due to heating, and fragmentation inside the CIMS during chemical ionization. When the standards were introduced into the pillow bag at different temperatures, the ratio of these compounds to the  $m/z$  (-)159 (trihydroxy toluene) signal was not consistent, suggesting these signals are largely due to impurities or decomposition outside of the CIMS. Fragmentation inside the CIMS during ionization would produce relatively consistent product fractions. Further understanding of the fragmentation occurring inside the instrument for trihydroxy toluene was unattainable owing to the high signals of impurities and decomposition products.

The sensitivity (all unique signals) determined for *o*-cresol was assumed to extend directly to the following compounds methyl hydroxy benzoquinone, methyl nitrophenol, benzoic acid, peroxy benzoic acid, phenyl hydroperoxide, nitrophenol, and dinitrophenol with a correction for the ion-molecule collision rate (Table 4.4). Similarly, the sensitivity (all unique signals) determined for 3-methyl catechol was assumed to extend directly to trihydroxy toluene, tetrahydroxy toluene, dihydroxy methyl benzoquinone, and dihydroxy nitrotoluene with a correction for the ion-molecule collision rate (Table 4.4). To the extent possible, all signals (transfer, complex, and potential unique fragmentation products (R1, R2, R4, R5, and R6)) for these compounds were used to determine their mixing ratio.

During toluene oxidation, *m*-cresol and *p*-cresol also form. *o*-, *m*-, and *p*-cresol all produce similar amounts of non-unique fragmentation products in purified air (89-91%). Therefore, the slight difference in the ion-molecule collision rate (Table 4.4) and the isomer distribution produced during toluene oxidation (Klotz et al., 1998) was used to calculate a general cresol sensitivity.

### DART-MS Description

SOA was collected during the final 4 h of experiments at  $24 \text{ L min}^{-1}$  on a Teflon membrane filter (47 mm,  $1.0 \mu\text{m}$  pore size, Pall Life Sciences). The filters were analyzed by high-resolution direct analysis in real time mass spectrometry (DART-MS, JEOL, Inc.). A DART source is a low-temperature He plasma that generates primarily  $[\text{A}+\text{H}]^+$  ions through proton transfer reactions between the analyte, A, and ionized ambient water vapor ( $\text{H}_3\text{O}^+$ ) (Cody et al., 2005; Cody, 2009). Samples are introduced directly into the DART stream, between the end of the DART source and

the mass spectrometer inlet. A portion of the filter membrane was cut free from the support ring using a stainless steel scalpel and wrapped in a spiral around the barrel of a glass Pasteur pipet. The pipet was rotated slowly in the DART stream to warm the glass and desorb organic material gently from the Teflon filter. Each sample was cut and analyzed in triplicate. The final data are an average of these three replicates. Additional analysis details and interpreted mass spectral data corrected to remove background ions are provided in Section 4.6 (Supplemental Information).

With such a broad spectrum of compounds and the absence of synthetic standards, only ions with signals well above the background were selected for analysis. Ions with signals  $> 10\%$  of the maximum ion signal (experiments 14 and 15) or second maximum ion signal (experiment 13) were selected. In experiment 13, the signal of one ion dominated the mass spectrum (i.e.,  $>6$  times any other ion signal), so this signal was not used for ion selection. The accurate  $m/z$  of each selected ion was assigned a chemical formula using ChemCalc (Patiny et al., 2013). This chemical formula was adjusted to its neutral form, and given a proposed structure based on the Master Chemical Mechanism (MCM) v3.3.1 (Jenkin et al., 2003; Bloss et al., 2005) toluene photooxidation mechanism, previously reported components of toluene SOA (Calvert et al., 2002; Olariu, Klotz, et al., 2002; Sato et al., 2007; Jang et al., 2001; Nakao, Clark, et al., 2011), and gas-phase photooxidation products detected here by the CIMS.

DART-generated signal intensity for a given compound is proportional to the product of its vapor pressure, proton affinity, and concentration (Nilles et al., 2009; Schilling Fahnestock et al., 2015; Chan et al., 2013). Because the ion intensity is proportional to the vapor pressure, the vapor pressure of each compound needs to be known or estimated. Estimates of vapor pressures for low-volatility compounds have higher uncertainty due to lower availability and accuracy of experimental data (Barley et al., 2010; O'Meara et al., 2014; Kurten et al., 2016). Thus, the results presented for the DART-MS analysis should be interpreted only qualitatively.

Two vapor pressure estimation methods are used here: 1) the Estimation of Vapor Pressure of Organics, Accounting for Temperature, Intramolecular, and Non-additivity Effects (EVAPORATION) method (Compernelle et al., 2011) and; 2) the method of Nannoolal, Rarey, Ramjugernath, and Cordes (2004) and Nannoolal, Rarey, and Ramjugernath (2008). Both methods have online tools available for estimating the vapor pressure at [http://tropo.aeronomie.be/models/evaporation\\_run.htm](http://tropo.aeronomie.be/models/evaporation_run.htm) and [http://www.aim.env.uea.ac.uk/aim/ddbst/pcalc\\_](http://www.aim.env.uea.ac.uk/aim/ddbst/pcalc_)

main.php, respectively. The EVAPORATION and Nannoolal methods are compatible with molecules containing oxygen-based functional groups and nitrates. Unlike the Nannoolal method, the EVAPORATION method has not been optimized for aromatic compounds, while the Nannoolal method cannot be used for diketones. Thus, EVAPORATION is used for all non-aromatic compounds and Nannoolal is used for all aromatics.

### Kinetic Model

The chamber experiments were simulated with a kinetic model containing all reactions related to toluene from MCM v3.3.1 (Jenkin et al., 2003; Bloss et al., 2005), via <http://mcm.leeds.ac.uk/MCM>. Version 1 of the kinetic model includes all MCM v3.3.1 reactions relevant to toluene oxidation and inorganic chemistry, as well as experimentally measured wall deposition rates of *o*-cresol and dihydroxy toluene. Version 2 includes all reactions in Version 1 as well as photolysis of hydroxy nitrotoluene and dihydroxy nitrotoluene. Version 3 includes all reactions in Version 2 as well as additional oxidation reactions for dihydroxy toluene and benzaldehyde. Additional discussion of the kinetic model, including a list of reactions, is provided in Section 4.6 of the Supplemental information.

The kinetic model was used to evaluate the extent to which chamber conditions are representative of those in the atmosphere. The two main concerns in chamber studies performed under high-NO conditions are high NO<sub>2</sub> and NO<sub>3</sub> levels. Upon reaction with OH, a VOC forms an OH-VOC adduct, that will react with either NO<sub>2</sub> or O<sub>2</sub>. Under atmospherically relevant conditions, the OH-VOC adduct reacts predominantly with O<sub>2</sub>. The NO<sub>2</sub> reading on the NO<sub>x</sub> monitor used in this study includes all NO<sub>y</sub> products (e.g., organic nitrates, HNO<sub>3</sub>, HONO, and NO<sub>2</sub>). Instead of using the NO<sub>x</sub> monitor, the kinetic model was used to predict the maximum NO<sub>2</sub> concentration. OH-*o*-cresol and OH-3-methyl catechol adducts are assumed to react at the same rate with NO<sub>2</sub> and O<sub>2</sub> as OH-*m*-cresol adduct (Koch et al., 2007), and the OH-benzaldehyde adduct was assumed to react with NO<sub>2</sub> and O<sub>2</sub> at the same rate as the OH-toluene adduct (Koch et al., 2007). The percent of OH-VOC adduct reacting with NO<sub>2</sub> versus O<sub>2</sub> for each experiment is presented in Table A5. For gas-phase experiments, the percentage of the OH-VOC adduct reacting with NO<sub>2</sub> was <6%. The higher loading necessary for the filter analysis required larger amounts of NO<sub>x</sub> for the particle-phase experiments, for which the percentage of OH-VOC reacting with NO<sub>2</sub> was <10%.

Both *o*-cresol ( $1.4 \times 10^{-11} \text{ cm}^3 \text{ molec}^{-1} \text{ s}^{-1}$ , (Atkinson et al., 1992)) and 3-methyl catechol ( $1.7 \times 10^{-10} \text{ cm}^3 \text{ molec}^{-1} \text{ s}^{-1}$ , (Olariu, Bejan, et al., 2004)) react rapidly with  $\text{NO}_3$ . For the toluene high-NO experiments, a substantial amount of 3-methyl catechol and *o*-cresol is predicted to react with  $\text{NO}_3$  (e.g., as much as 80% for the particle-phase experiments, Table 4.8). Caution is needed when interpreting results for high-NO oxidation conditions as both  $\text{NO}_3$  and OH oxidation occur. In the present work, when starting with *o*-cresol or 3-methyl catechol, the percentage reacting with  $\text{NO}_3$  was minor (e.g., < 4% for *o*-cresol for Experiment 5, Table 4.8). The kinetic model was also used to verify that  $\text{RO}_2 + \text{RO}_2$  reactions were minimized for all experiments (Table 4.8). For example, in the toluene low-NO experiments,  $\text{RO}_2 + \text{RO}_2$  reactions for the gas-phase and particle-phase experiments were estimated to be <12% and <18%, respectively, of all  $\text{RO}_2$  pathways.

#### 4.4 Results

Toluene reacts with OH to form both ring-retaining products (cresol and benzaldehyde) and ring-opening products (bicyclic intermediate compounds and epoxides) (Figure 4.1). Later generation gas-phase oxidation products from the ring-retaining pathways are identified. These oxidation products have a range of volatilities ( $C^* \sim 5 \times 10^5 - 7.7 \times 10^{-3} \mu\text{g m}^{-3}$ ). The lower volatilities of which are detected in the particle-phase, implying that the ring-retaining pathways are important for SOA formation. In order to monitor later generation products and constrain the pathways from which products emerge, oxidation of first-generation products (*o*-cresol and benzaldehyde) and second-generation products (3-methyl catechol) was performed under both high- and low-NO conditions.

##### *o*-Cresol Oxidation

Previous studies generally recommend a ~0.18 yield of cresol (total of all isomers) from the toluene + OH pathway (Klotz et al., 1998; Smith et al., 1998) (Figure 4.1). The kinetic model (Version 1) assuming a 0.18 yield predicts cresol levels within the uncertainties of the CIMS measurements under both low- and high-NO conditions (Figure 4.2). As noted, version 1 of the kinetic model includes all MCM v3.3.1 reactions related to toluene and wall deposition (see Section 4.5) of *o*-cresol and dihydroxy toluene. An approximate cresol yield (~0.2) was calculated using the equation of Olariu, Klotz, et al. (2002) and the decay of toluene, rise in cresol, and accounting for losses of cresol from wall deposition and reaction with OH. The yield was calculated only under low-NO conditions. Under high-NO conditions, the



correction for *o*-cresol reaction with  $\text{NO}_3$  adds more uncertainty (Figure 4.2). The yield determined here is similar to that of other studies (Klotz et al., 1998; Smith et al., 1998).

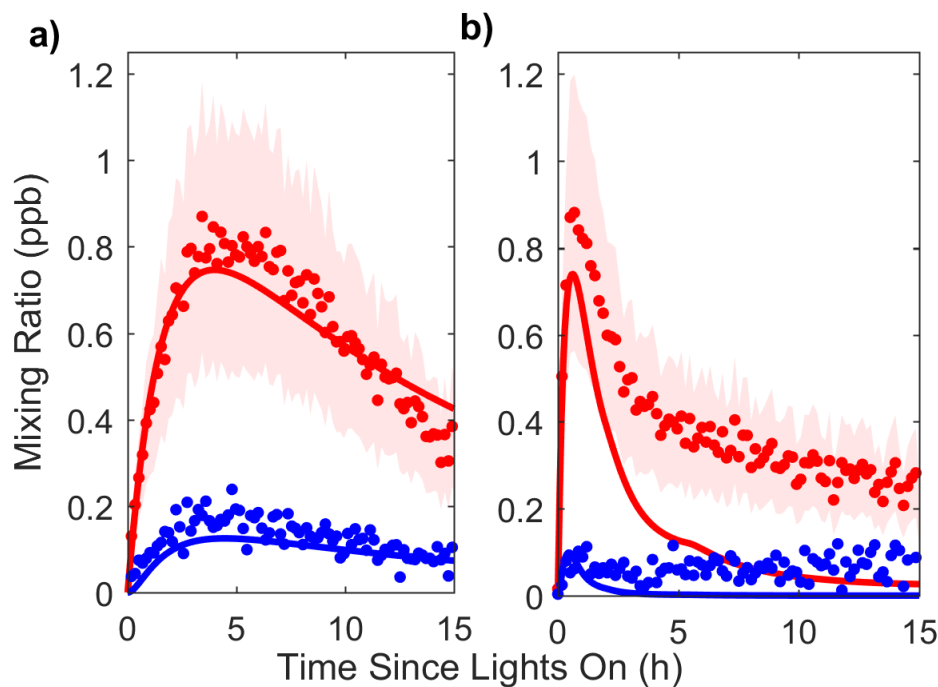


**Figure 4.2:** Kinetic model predictions (Version 1 solid lines) compared to CIMS measurements (markers) under low-NO (a, experiment 4) and high-NO (b, experiment 3) oxidation of toluene for cresol (red) and dihydroxy toluene (blue). The uncertainty in the CIMS measurements for cresol is shown in red shading.

The *o*-cresol oxidation mechanism in MCM v3.3.1, based on Olariu, Klotz, et al. (2002), is shown in black in Figure 4.3 for low-NO conditions and in Figure 4.4 for high-NO conditions. OH reacts with *o*-cresol via hydrogen abstraction to form a methyl phenoxy radical or addition to form either a bicyclic intermediate product or dihydroxy toluene (the dominant isomer being 3-methyl catechol). In experiment 4, when starting with 46 ppb of toluene, the maximum detected mixing ratio of dihydroxy toluene was only ~0.2 ppb (Figure 4.2), emphasizing the importance of starting with later-generation products in order to determine the subsequent chemistry. Photooxidation of *o*-cresol produces dihydroxy toluene ( $m/z$  (-) 143) in agreement with Olariu, Klotz, et al. (2002). Under high-NO conditions, the methyl phenoxy radical reacts with  $\text{NO}_2$  to form hydroxy nitrotoluene ( $m/z$  (-) 172,  $\text{F}^-$  transfer and  $m/z$  (-) 152, fragment).

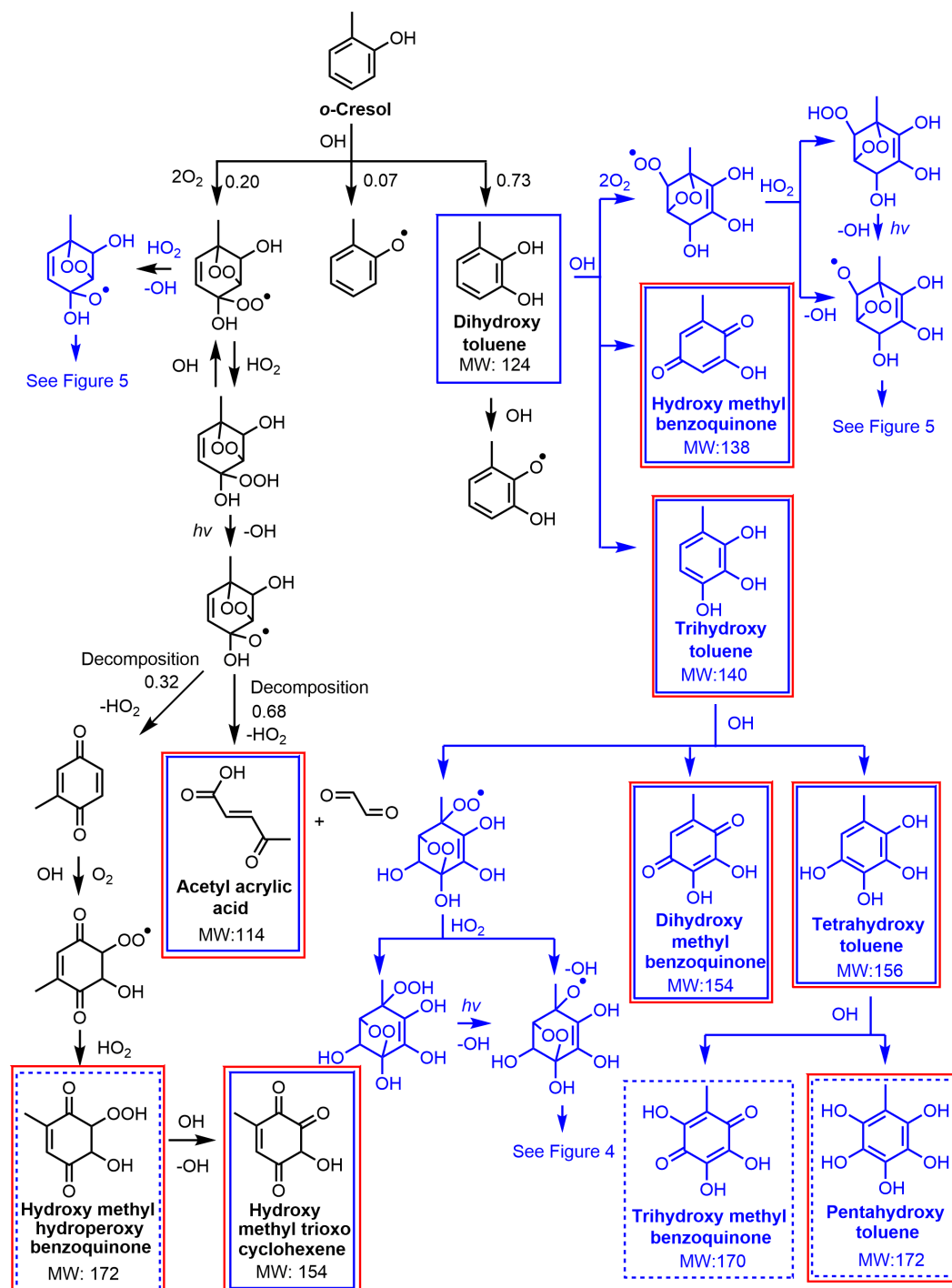


**Figure 4.3:** Gas-phase chemical mechanism for *o*-cresol photooxidation under low-NO conditions. Recommended pathways by MCM v3.3.1 are shown in black. The proposed mechanism from the present study is shown in blue. Products detected in this study by the CIMS and DART-MS are outlined in blue and red boxes, respectively, with dashed lines indicating compounds detected at only a minimal level.

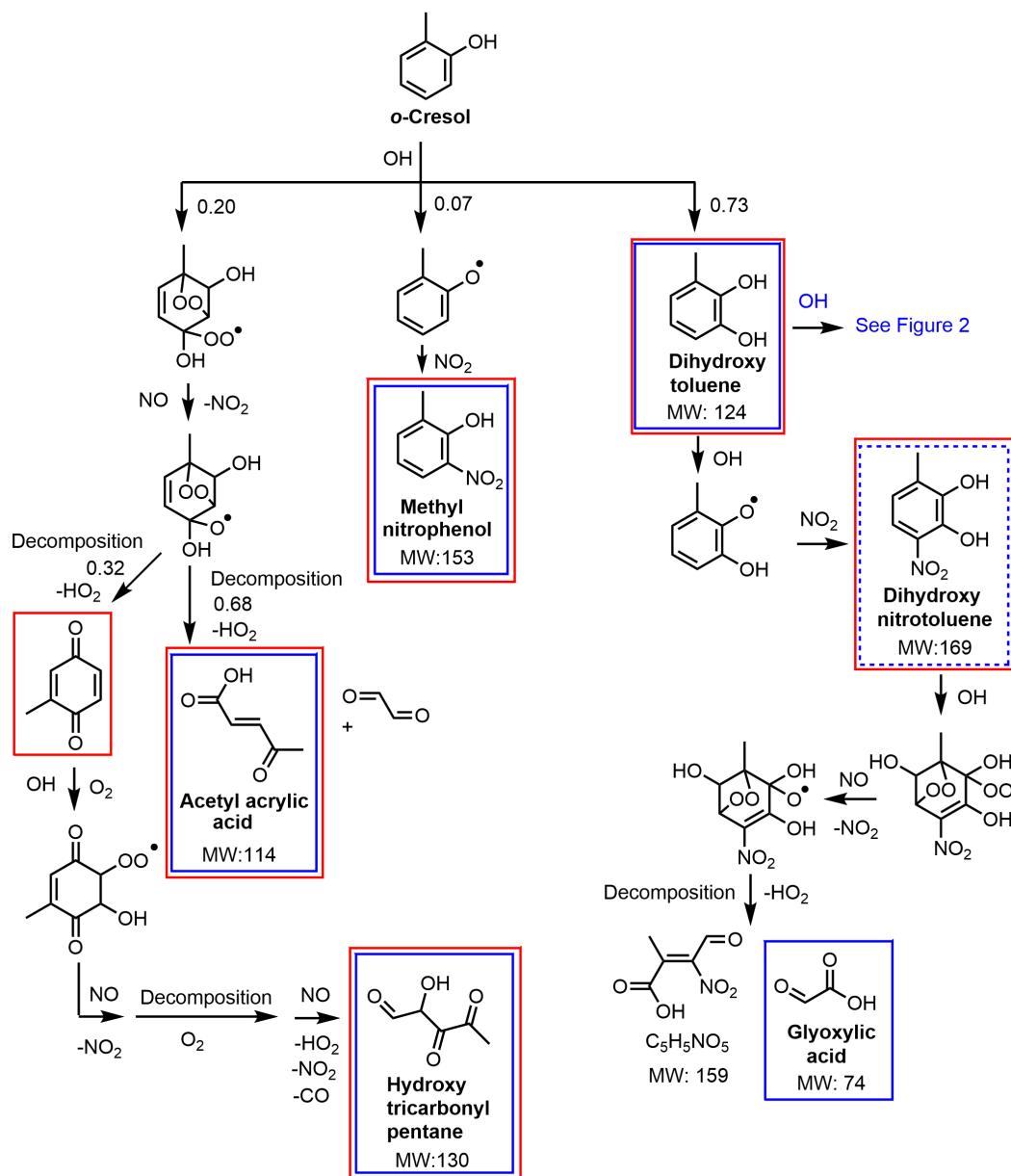


**Figure 4.4:** Gas-phase chemical mechanism for *o*-cresol photooxidation under high-NO conditions. The MCM v3.3.1 scheme is shown in black. Products outlined in blue were detected in the present study by the CIMS with dashed lines indicating only a minor amount was detected. Red boxed compounds were detected in the present study by the DART-MS.

3-Methyl catechol oxidation leads to the following products (Figure 4.3): trihydroxy toluene, hydroxy methyl benzoquinone, and various decomposition products presumably from the bicyclic intermediate pathway. These products likely result from OH addition to the ring of 3-methyl catechol. This pathway is not included in MCM

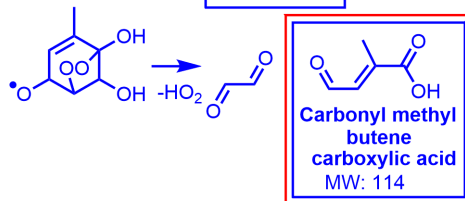
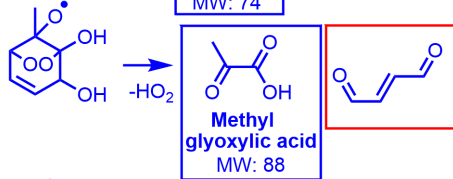
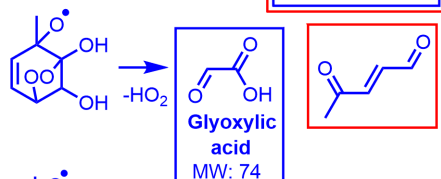
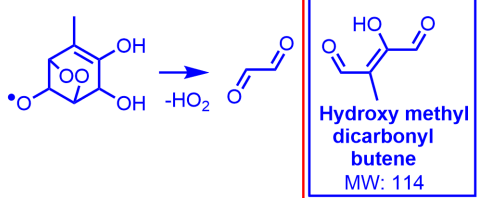
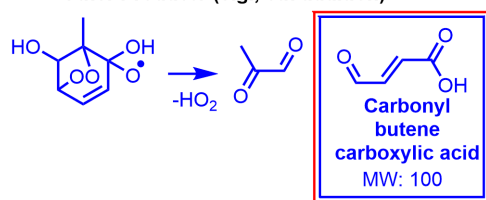
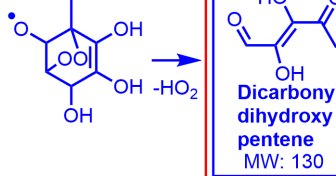
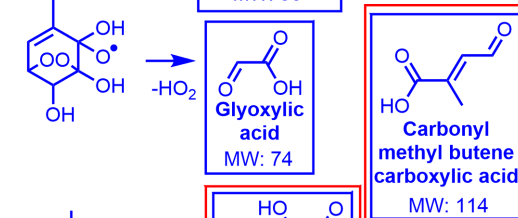
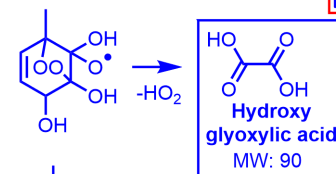
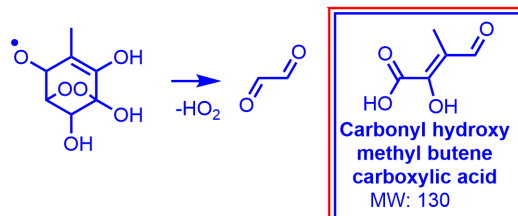
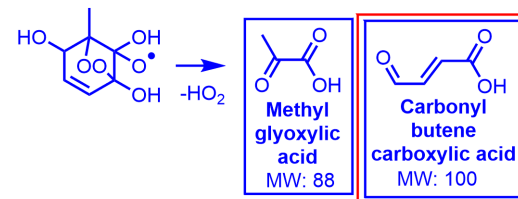
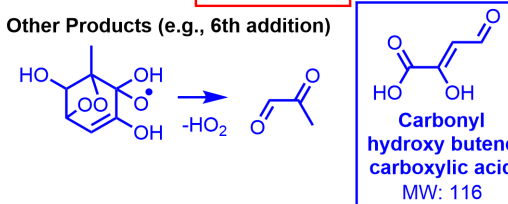
v3.3.1, which assumes that hydrogen abstraction is the sole OH oxidation pathway for 3-methyl catechol. Dihydroxy nitrotoluene ( $m/z$  (-)188,  $F^-$  transfer and  $m/z$  (-)168, fragment), the expected product of hydrogen abstraction of 3-methyl catechol, is detected minimally ( $< 0.5$  ppb) by the CIMS. This suggests that hydrogen abstraction is not the dominant pathway for OH oxidation.

Without authentic standards for trihydroxy toluene and hydroxy methyl benzoquinone, quantification cannot be achieved (Section 4.3). Exact yields are not reported, but the experimental results are compared to the kinetic model (Section 4.5). Trihydroxy toluene is detected at several different signals in MS mode on the  $CF_3O^-$  CIMS:  $m/z$  (-)159 ( $F^-$  transfer),  $m/z$  (-)225 (complex),  $m/z$  (-)115 (fragment, possibly loss of  $CO_2$ ),  $m/z$  (-) 205 (loss of HF from complex), and  $m/z$  (-) 139 (loss of HF from transfer). Three daughters are detected in MS/MS mode from  $m/z$  (-)159:  $m/z$  (-)139 (loss of HF),  $m/z$  (-)115 (possibly loss of  $CO_2$ ), and  $m/z$  (-)85 ( $CF_3O^-$ ). The presence of the  $m/z$  (-)85 daughter implies two compounds are detected at  $m/z$  (-)159: trihydroxy toluene and another compound that forms a  $CF_3O^-$  complex (e.g., hydroxyacetone). Here MS/MS mode is used to separate the trihydroxy toluene signal from the interfering compound. Hydroxy methyl benzoquinone is detected at  $m/z$  (-)223 (complex),  $m/z$  (-)157 ( $F^-$  transfer), and  $m/z$  (-)137 (fragment).

Several products from photooxidation of trihydroxy toluene are also detected by the CIMS in the 3-methyl catechol oxidation experiments, including tetrahydroxy toluene, dihydroxy methyl benzoquinone, and various decomposition products from the bicyclic intermediate pathway (Figure 4.3). Tetrahydroxy toluene, like trihydroxy toluene, is detected at  $m/z$  (-)175 ( $F^-$  transfer),  $m/z$  (-)241 (complex), and  $m/z$  (-)131 (fragment, possibly loss of  $CO_2$ ). Dihydroxy methyl benzoquinone is detected at  $m/z$  (-)239 (complex),  $m/z$  (-)173 ( $F^-$  transfer), and  $m/z$  (-)153 (fragment). Trihydroxy methyl benzoquinone ( $m/z$  (-)189) and pentahydroxy toluene ( $m/z$  (-)191), likely oxidation products from tetrahydroxy toluene, are also detected by the CIMS, but the signals are close to background. As shown in Figure 4.3, OH oxidation of methyl benzoquinone possibly also forms products detected at the same mass as pentahydroxy toluene and dihydroxy methyl benzoquinone. However, these products are detected from 3-methyl catechol oxidation consistent with the proposed mechanism (Figure 4.3).

An array of decomposition products presumably from the bicyclic intermediate oxidation pathway of *o*-cresol, 3-methyl catechol, trihydroxy toluene, and tetrahydroxy

toluene is detected (Figures 4.5 and 4.6). These decomposition products vary greatly in volatility ( $C^* \sim 2.2 \times 10^6$  to  $14 \mu\text{g m}^{-3}$ ). The highly oxygenated products such as  $\text{C}_4\text{H}_4\text{O}_5$  and  $\text{C}_5\text{H}_6\text{O}_5$  ( $C^* \sim 14$  to  $41 \mu\text{g m}^{-3}$ ) are likely to result only from trihydroxy toluene and tetrahydroxy toluene oxidation, and are sufficiently low in volatility to partition in some degree to the particle phase. Because theoretical (PengZhen et al., 2012; Xu et al., 2013; Jorgensen, 2012) and experimental (Olariu, Klotz, et al., 2002) studies of OH addition to phenol and *o*-cresol all suggest *ortho*-addition is dominant, OH is presumed to also add to the *ortho*-position in Figures 4.5 and 4.6. OH addition to the other positions of the ring produces similar products. For *o*-cresol and 3-methyl catechol, all possibilities of OH addition are enumerated and the additional products appear at the bottom of Figure 4.5.

**O-Cresol****Addition to 3rd Position****Other Products (e.g., 6th addition)****3-Methyl Catechol****Addition to 4th Position****Other Products (e.g., 6th addition)**

**Figure 4.5:** Proposed decomposition pathways for bicyclic intermediate compounds formed from OH oxidation of *o*-cresol and 3-methyl catechol. Blue and red boxed compounds were detected by CIMS and DART-MS, respectively.

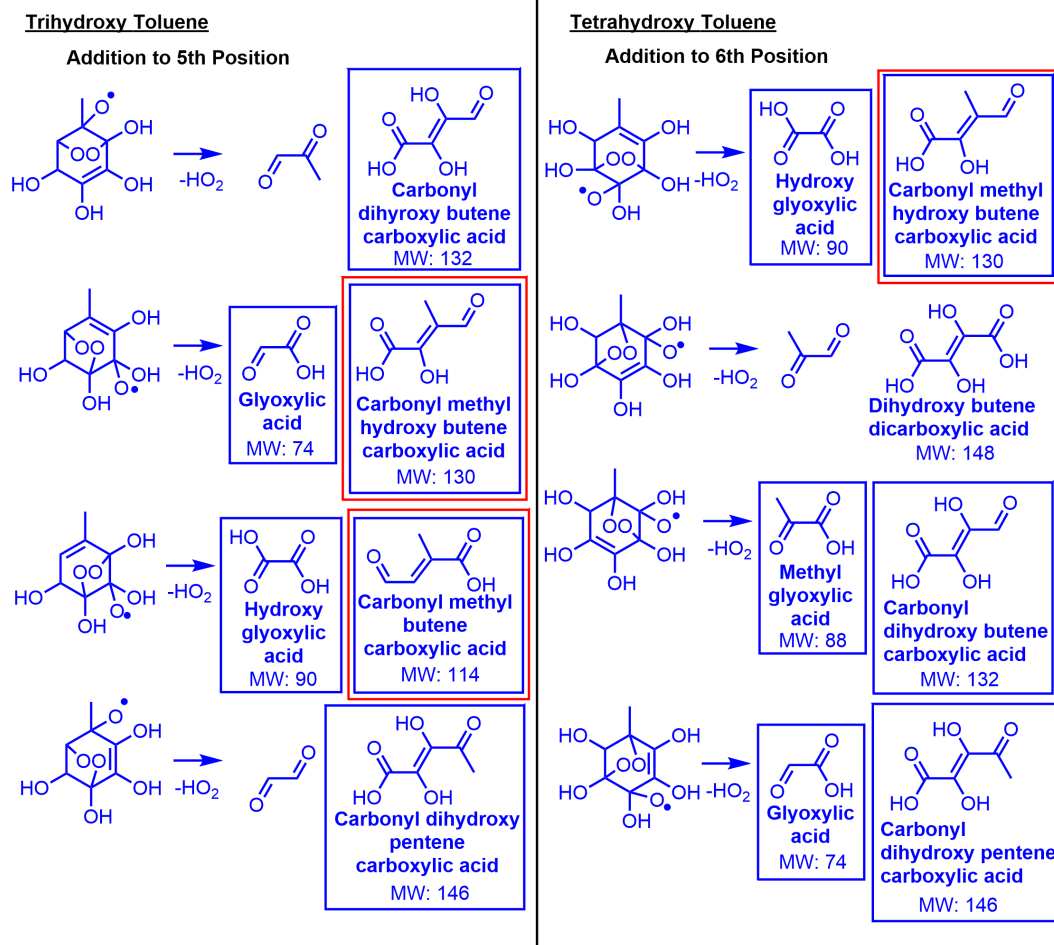


**Figure 4.6:** Proposed decomposition pathways for bicyclic intermediate compounds formed from OH oxidation of trihydroxytoluene and tetrahydroxytoluene. Blue and red boxed compounds were detected by CIMS and DART-MS, respectively.

### Benzaldehyde Oxidation

MCM v3.3.1 recommendations for OH oxidation of benzaldehyde are generally in agreement with the products detected by the CIMS (Figure 4.7). OH oxidation of benzaldehyde occurs via hydrogen abstraction of the formyl group followed by  $O_2$  addition to form a peroxy radical. This peroxy radical reacts with  $HO_2$  under low-NO conditions to form benzoic acid, peroxybenzoic acid, and phenyl hydroperoxide. Benzoic acid ( $m/z$  (-) 141) and peroxybenzoic acid ( $m/z$  (-) 223) are the dominant first-generation products detected. Phenyl hydroperoxide ( $m/z$  (-) 129) is minimally detected (<0.2 ppb) either due to a low yield or instability in the CIMS (Hydroperoxides have been known to fragment in the  $CF_3O^-$  CIMS (Praske et al., 2015)). As a result of the relatively large  $RO_2 + RO_2$  rate constant for the peroxy

radical of benzaldehyde ( $1.1 \times 10^{-11} \text{ cm}^3 \text{ molec}^{-1} \text{ s}^{-1}$ ), the benzaldehyde low-NO experiment was characterized by the kinetic model as having a higher fraction of  $\text{RO}_2 + \text{RO}_2$  reactions than other experiments (Table 4.8). The proportions of benzoic acid and peroxybenzoic acid measured by the CIMS differ from those predicted by MCM v3.3.1 (see Section 4.6 and Figure 4.12 for more details).

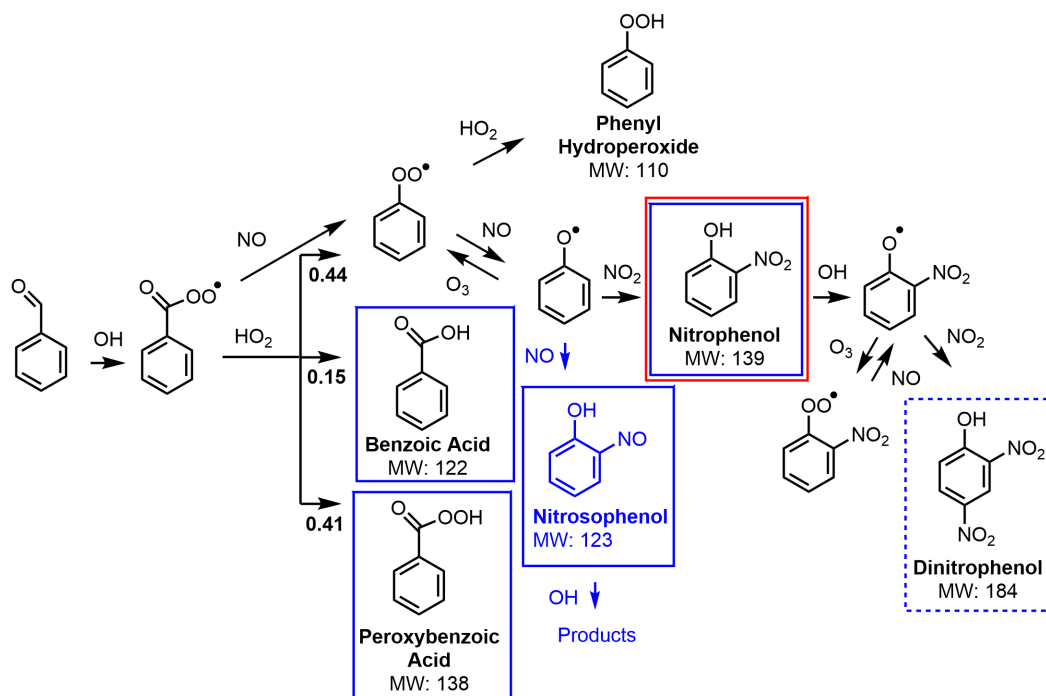


**Figure 4.7:** Gas-phase chemical mechanism for benzaldehyde photooxidation under low- and high-NO conditions. MCM v3.3.1 pathways are shown in black. Products detected by the CIMS are boxed in blue, with dashed lines indicating only a minor amount forms.

Other first-generation products are also detected, including signals at  $m/z$  (-)155, (-)175, and (-)179. These minor signals comprise only 6%, 3%, and 5%, respectively, of the signals produced from benzoic and peroxybenzoic acids. Phenol is likely  $m/z$  (-)179. Compounds forming signals at  $m/z$  (-)155 and (-)175 rise with the other first-generation products, suggesting they are minor first-generation products from the  $\text{RO}_2 + \text{RO}_2$  or  $\text{RO}_2 + \text{HO}_2$  pathways.

The dominant first-generation product detected from benzaldehyde oxidation under high-NO conditions is nitrophenol ( $m/z$  (-)158,  $\text{F}^-$  transfer and  $m/z$  (-)138, fragment) (Figure 4.7). Dinitrophenol ( $m/z$  (-)203,  $\text{F}^-$  transfer and  $m/z$  (-)183, fragment), an OH oxidation product of nitrophenol, was also detected. Predictions of both products



are over-predicted by MCM v3.3.1 using the kinetic model (Section 4.5 and Figure 4.13) compared to the CIMS measurements.

OH addition to the aromatic ring of benzaldehyde or benzoic acid is not expected to occur. The rate of OH addition to an aromatic ring is proportional to the electrophilic nature of the substituents around the ring; unlike methyl and hydroxy groups, carboxy and formyl groups are not electrophilic (Calvert et al., 2002). OH addition to the ring of benzaldehyde would form hydroxy benzaldehyde, which is isobaric to benzoic acid. Only the transfer signal ( $m/z$  (-)141), not the complex ( $m/z$  (-)207), is detected, indicative that the product is highly acidic, like a carboxylic acid. That hydroxy benzoic acid does not form cannot be explicitly confirmed because this compound is isobaric to peroxybenzoic acid. However, dihydroxy benzoic acid ( $m/z$  (-)173) as expected does not form.

Oxidation of benzaldehyde under high- and low-NO conditions does not yield many later generation products detectable by the  $\text{CF}_3\text{O}^-$  CIMS. The CIMS is expected to be sensitive to later generation products from the benzaldehyde pathway that retain the aromatic ring. Likely the main later generation products from benzaldehyde are ring-opening decomposition products, to which the CIMS is not sensitive (e.g., unfunctionalized ketones and aldehydes). Thus, we conclude that the cresol pathway is more important for SOA formation compared to the benzaldehyde pathway, based on the detectable products of the  $\text{CF}_3\text{O}^-$  CIMS and their expected volatilities (Table 4.3).

### **Products Detected in the Particle Phase by DART-MS**

Products detected in the gas phase are compared to those detected in the particle phase to further understand the mechanism for toluene SOA formation. Filters, collected at the end of each experiment, were analyzed using high-resolution direct analysis in real time mass spectrometry (DART-MS). As expected, a number of compounds (e.g., trihydroxy toluene, tetrahydroxy toluene, and pentahydroxy toluene) measured in the gas-phase were also detected in the particle-phase by the DART-MS.

The intensity of the DART signal for a given compound is proportional to the product of the proton affinity, vapor pressure, and concentration of the compound. The proton affinity of each compound is assumed to be similar, due to shared ionizable functional groups. To compare the relative amounts of each product detected, the measured intensity is normalized by the compound's estimated vapor pressure to

produce a normalized intensity ( $I_n$ ). The relative fraction ( $R_f$ ) of each compound is then calculated by dividing each compound's normalized intensity by the sum of the normalized intensities of all compounds in a given experiment.  $R_f$  values for each compound detected are reported in Tables 4.9-4.11 in the Supplemental Information.

Vapor pressures for the compounds detected in this study have been estimated using both EVAPORATION and Nannoolal methods (Compernelle et al., 2011; Nannoolal, Rarey, Ramjugernath, and Cordes, 2004; Nannoolal, Rarey, and Ramjugernath, 2008). As noted earlier (Section 4.3), due to limitations in the methods, Nannoolal is used for all aromatics and EVAPORATION is used for all non-aromatic compounds. As demonstrated in Table 4.3, as the volatility of an aromatic compound decreases, the EVAPORATION method increasingly underestimates vapor pressures as compared to Nannoolal. Owing to the uncertainty in these vapor pressure estimates, the reported  $R_f$  values should be considered only qualitatively.

The same *o*-cresol oxidation products, detected by the CIMS in the gas phase and expected to be low in volatility, are detected in the particle phase by the DART-MS. The corroborative analyses by CIMS and DART-MS support the proposed mechanism that OH subsequently adds to the ring of *o*-cresol forming low volatility products. For example, the following are dominant products detected in the particle-phase under low-NO oxidation of toluene (Figure 4.8a): polyols including trihydroxy toluene ( $C_7H_8O_3$ ), tetrahydroxy toluene ( $C_7H_8O_4$ ), and pentahydroxytoluene ( $C_7H_8O_5$ ); benzoquinones including hydroxy methyl benzoquinone ( $C_7H_6O_3$ ) and dihydroxymethyl benzoquinone ( $C_7H_6O_4$ ); and various products from the bicyclic intermediate pathway including  $C_4H_4O_2$ ,  $C_5H_6O_2$ , and  $C_5H_6O_3$ . Nakao, Liu, et al. (2012) also detected  $C_7H_8O_4$  and  $C_7H_8O_5$  in the particle-phase from *o*-cresol oxidation under low-NO conditions using a Particle-into-Liquid Sampler coupled with a Time-of-Flight Mass Spectrometer. Nakao, Liu, et al. (2012) suspected these signals were due to successive OH addition to the aromatic ring; the combined CIMS and DART-MS analysis corroborates their conjecture.

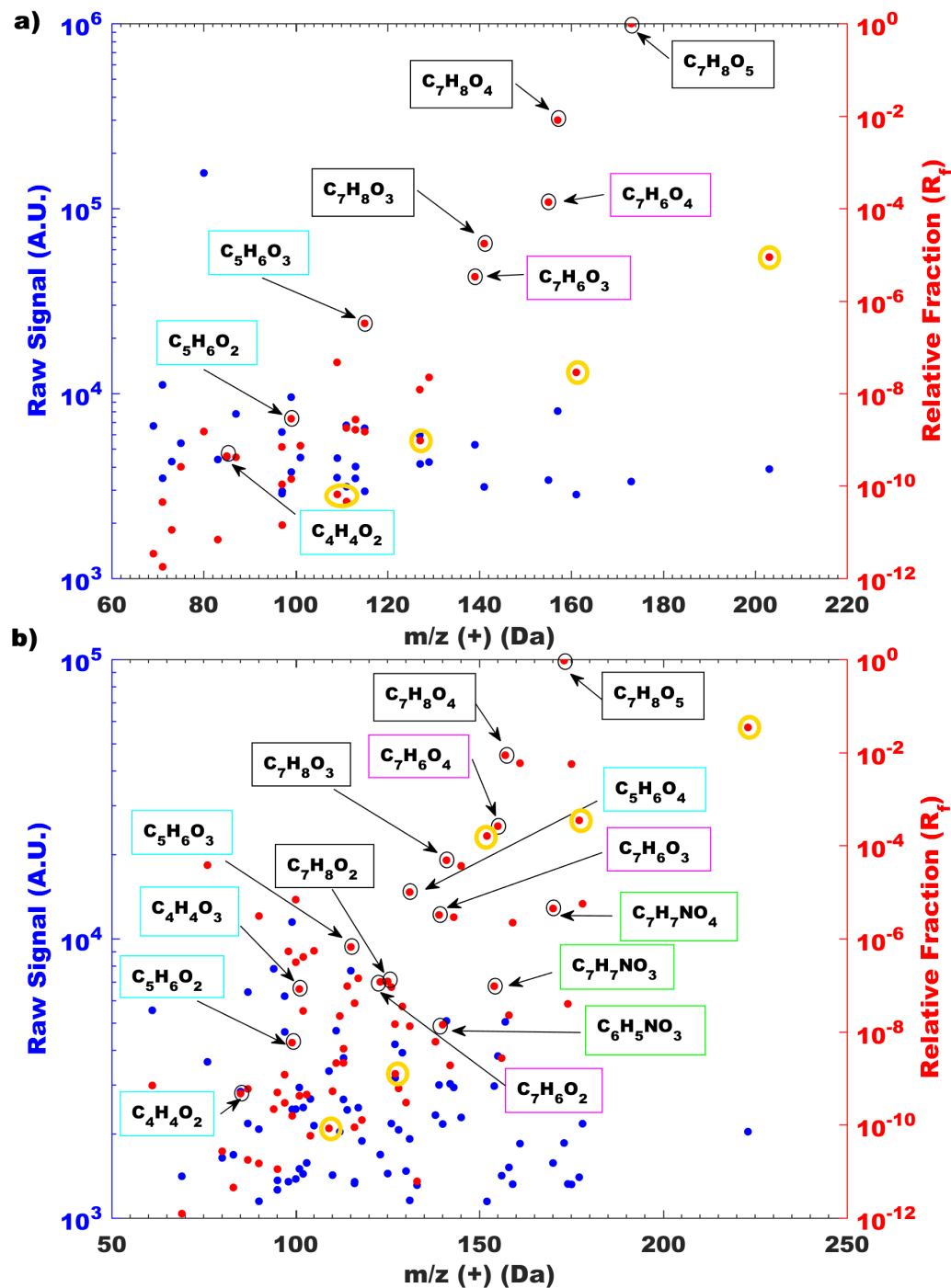


**Figure 4.8:** Particle-phase products detected by DART-MS during oxidation of toluene under low-NO conditions (a, experiment 13) and high-NO conditions (b, experiment 14) with boxes identifying the following types of compounds: polyols (black), methyl benzoquinone type compounds (magenta), decomposition products from the bicyclic intermediate pathway (cyan), nitro compounds (green), and presumed oligomerization products (i.e., those with >7 carbons, gold).

As shown in Figure 4.8b, similar products were detected under toluene high-NO oxidation. Under high-NO conditions, methyl nitrophenol and dihydroxy nitro-toluene were also detected in the particle phase, albeit at lower relative fractions than many of the polyols and benzoquinone compounds (Figure 4.8b). At the end of the toluene high-NO experiment, estimated  $\text{NO}_3$  oxidation of *o*-cresol (80%) and 3-methyl catechol (66%) was quite high compared to OH oxidation (Table 4.8). Part of the methyl nitrophenol signal could be influenced by  $\text{NO}_3$  oxidation.

Some of the compounds (e.g., tetrahydroxy toluene and pentahydroxy toluene) are structural isomers of those produced from the epoxide pathway of toluene oxidation under low-NO conditions; under high-NO conditions, the products from the epoxide channel largely decompose (Figure 4.16). Signals assigned to tetrahydroxy toluene and pentahydroxy toluene are dominant in the particle phase from toluene oxidation under both high- and low-NO conditions (Figure 4.8). This is consistent with the products forming from the *o*-cresol oxidation mechanism proposed in Figure 4.3 rather than the epoxide mechanism. Hydroxy methyl hydroperoxy benzoquinone, a product of OH oxidation of benzoquinone under low-NO conditions, and pentahydroxy toluene are structural isomers (Figure 4.3). Because the signal assigned to pentahydroxy toluene is detected under both low- and high-NO conditions, the product is more likely to be generated from tetrahydroxy toluene than benzoquinone.

Nitrophenol from benzaldehyde oxidation is also detected in the particle-phase. Part of the signal for  $\text{C}_7\text{H}_6\text{O}_3$  may represent peroxybenzoic acid, as this compound is isobaric to hydroxy methyl benzoquinone. In general, products from cresol oxidation dominate over products from benzaldehyde oxidation in the particle phase. This is consistent with the gas-phase chemistry discussed in Section 4.4, in which few ring-retaining later generation products are detected from benzaldehyde oxidation.

### Estimating the Contribution of Cresol to Toluene SOA

Considering that many products produced by the cresol pathway in the gas phase are also detected in the particle phase, the contribution of these products to toluene SOA is estimated. Chamber studies have recently reported toluene SOA mass yields to be between 0.9-1.6  $\mu\text{g}/\mu\text{g}$  when using the Statistical Oxidation Model to correct for vapor wall loss (Zhang et al., 2014). Without the model corrections for vapor wall loss, Zhang et al. (2014) measured the toluene SOA mass yields to be 0.5-0.65  $\mu\text{g}/\mu\text{g}$  for the experiments at maximum seed aerosol surface area (i.e., the experiments that minimized vapor wall loss as much as possible).

Under low-NO conditions the toluene SOA yield with the model corrections for vapor wall loss ( $1.6 \mu\text{g}/\mu\text{g}$ ) implies a near unity carbon yield (Zhang et al., 2014), so at the lower bound the cresol pathway contributes to  $\sim 20\%$  of toluene SOA. For an upper bound estimate, we assume that trihydroxy toluene and hydroxy methyl benzoquinone and all oxidation products from these compounds partition to the particle phase and that the average molecular weight of all compounds in the aerosol is equal to that of pentahydroxy toluene. With these assumptions and using the toluene SOA mass yield of 0.5 (the lowest yield explained above), the cresol pathway is estimated to contribute  $\sim 40\%$  of toluene SOA. Based on this, the contribution of the cresol pathway to toluene SOA is estimated as  $\sim 20\text{-}40\%$ .

## 4.5 Discussion

Gas- and particle-phase measurements by the CIMS and DART-MS confirm that OH oxidation of dihydroxy toluene leads to low-volatility products that partition to the particle phase. For example, the following three products, which form from subsequently adding OH to the aromatic ring, are detected in the gas and particle phases: trihydroxy toluene ( $C^* \sim 340 \mu\text{g m}^{-3}$ ), tetrahydroxy toluene ( $C^* \sim 2.1 \mu\text{g m}^{-3}$ ) and pentahydroxy toluene ( $C^* \sim 7.7 \times 10^{-3} \mu\text{g m}^{-3}$ ). Here we discuss other theory and experimental work pertaining to OH addition to the aromatic ring, and use the kinetic model to further interpret the CIMS results.

### OH Addition to an Aromatic Ring

The chemical mechanism proposed in Figure 4.3 is consistent with previous observations of aromatic chemistry. As OH groups add to an aromatic ring, the aromatic ring becomes more activated, and the OH addition rate constant increases (Calvert et al., 2002). For example, the OH reaction rate constants for toluene, *o*-cresol, and 3-methyl catechol are  $6 \times 10^{-12}$ ,  $4 \times 10^{-11} \text{ cm}^3$ , and  $2 \times 10^{-10} \text{ cm}^3 \text{ molec}^{-1} \text{ s}^{-1}$ , respectively (Calvert et al., 2002; Olariu, Barnes, et al., 2000).

In the atmosphere, once OH adds to the aromatic ring,  $\text{O}_2$  also adds, and one of the following four processes occurs:  $\text{O}_2$  elimination,  $\text{HO}_2$  elimination, bicyclic intermediate formation, or reaction with NO,  $\text{HO}_2$  or  $\text{RO}_2$ . For the toluene system,  $\text{HO}_2$  elimination to re-form the aromatic ring or cyclization to form a bicyclic intermediate are the most commonly expected processes. Experiment and theory both suggest that  $\text{HO}_2$  elimination occurs more rapidly than bicyclic intermediate formation for products with more hydroxy functional groups around the aromatic ring. Experimental studies report the cresol yield from toluene to be  $\sim 0.2$  (Klotz

et al., 1998; Smith et al., 1998), while the 3-methyl catechol yield from *o*-cresol is  $\sim 0.7$  (Olariu, Klotz, et al., 2002). By analogy, the yield of trihydroxy toluene, the OH addition product from 3-methyl catechol, is also expected to be substantial. Theoretical calculations for phenol suggest that the elimination of HO<sub>2</sub> after O<sub>2</sub> addition occurs faster than the formation of a bicyclic intermediate (Xu et al., 2013). The O<sub>2</sub> addition reaction rate constant for the phenol-OH adduct at 323 K ( $300 \times 10^{-16} \text{ cm}^3 \text{ molec}^{-1} \text{ s}^{-1}$  (Koch et al., 2007)) is suggested by Xu et al. (2013) to be large due to the rapid elimination of HO<sub>2</sub>. In contrast, the O<sub>2</sub> addition rate constant for the toluene-OH adduct at 321K ( $5.6 \times 10^{-16} \text{ cm}^3 \text{ molec}^{-1} \text{ s}^{-1}$  (Koch et al., 2007)) is much lower. Similarly, HO<sub>2</sub> elimination may pull the O<sub>2</sub> reaction channel forward in the cresol system as the O<sub>2</sub> addition rate constant for *m*-cresol-OH adduct ( $800 \times 10^{-16} \text{ cm}^3 \text{ molec}^{-1} \text{ s}^{-1}$  (Zetzsch et al., 1997)) is even larger than that of phenol.

### Comparing CIMS Measurements with Kinetic Model Predictions

In order to evaluate the products detected by the CIMS, the mechanism outlined in Figures 3-7 is incorporated into the kinetic model. Version 2 of the kinetic model includes photolysis of hydroxy nitrotoluene and dihydroxy nitrotoluene. Version 3 of the kinetic model includes additional products for 3-methyl catechol and benzaldehyde oxidation (see Section 4.6 for more details).

### Vapor Wall Deposition

In order to compare the CIMS results to the kinetic model predictions, all loss processes need to be constrained for the compounds of interest. This includes reaction with OH/NO<sub>3</sub> and vapor wall deposition. Considering the reaction rate constant for 3-methyl catechol + OH is already fast ( $2.0 \times 10^{-10} \text{ cm}^3 \text{ molec}^{-1} \text{ s}^{-1}$ ) (Olariu, Barnes, et al., 2000), the hard sphere collision rate limit ( $2.5 \times 10^{-10} \text{ cm}^3 \text{ molec}^{-1} \text{ s}^{-1}$ ) is assumed for OH reaction with trihydroxy and tetrahydroxy toluene. The approximations for NO<sub>3</sub> oxidation are more speculative than those for OH oxidation, so more focus is given to comparing the CIMS measurements and the kinetic model results under low-NO conditions.

In experiment 9 (Table 4.1), lights were turned on to generate oxidation products of 3-methyl catechol. After 1.5 h, lights were turned off, and wall deposition rates of the following five compounds were measured: 3-methyl catechol, trihydroxy toluene, tetrahydroxy toluene, hydroxy methyl benzoquinone, and dihydroxy methyl benzoquinone. After 9 h of lights off at 28°C, the chamber was heated to 42°C for

4 h, then cooled to 16°C for 3 h, and finally heated back to 28°C for 3 h (Figure 4.9). An equilibrium is established for each compound between the gas phase and chamber wall. Heating and cooling the chamber disrupts this equilibrium. Most of the compounds did not significantly re-partition back into the gas phase when heating the chamber from 28°C to 42°C. This implies the absence of a large reversible reservoir on the chamber walls, so measuring the decay after 1.5 h of photooxidation is reasonable for these compounds. All of the compounds were lost to the walls faster at 16°C than at 28°C. As the chamber was heated from 16 to 28°C, some of the products slightly re-partitioned back to the gas phase, but not to the level expected if the chamber had not been cooled, suggesting that some loss was irreversible.

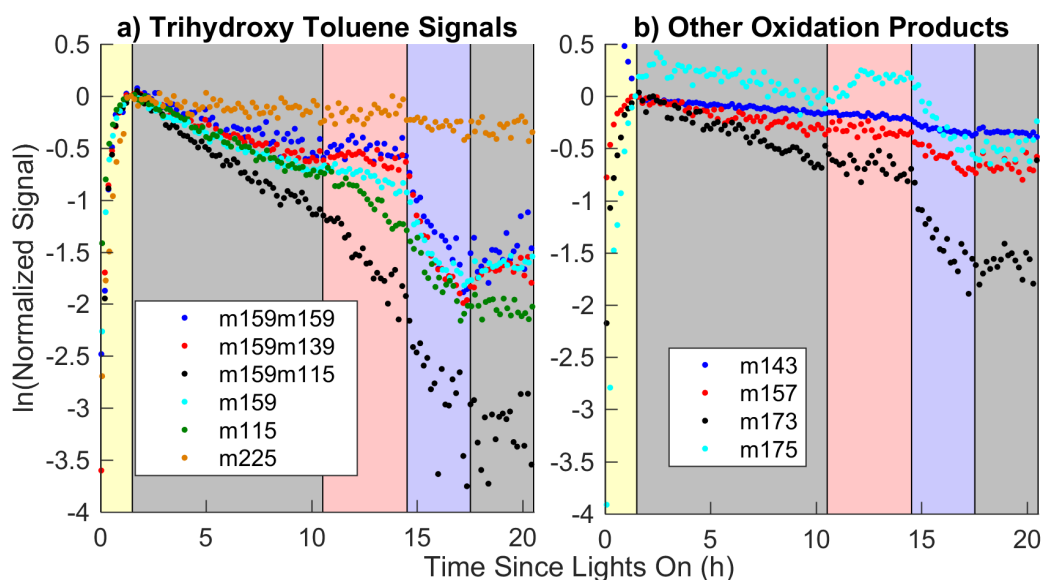


**Figure 4.9:** CIMS signals for trihydroxy toluene (panel a) and the following compounds (panel b): 3-methyl catechol (blue), hydroxy methyl benzoquinone (red), dihydroxy methyl benzoquinone (black), and tetrahydroxy toluene (cyan) during experiment 9. During this experiment, lights were turned on to generate 3-methyl catechol oxidation products (yellow shading). Then lights were turned off to measure the decay of these products to the chamber walls at 28°C (gray shading). Then the chamber was heated to 42°C (red shading), cooled to 16°C (blue shading), and finally heated back to 28°C (gray shading).

In experiment 10 (Table 4.1), photooxidation products from 3-methyl catechol were generated in the chamber. After 3.2 h of oxidation, purified air was sampled on the CIMS to monitor desorption of these oxidation products off the walls of the instrument. Desorption was minimal (i.e., within two scans, the signal was <0.08

of the original signal) for all of the five compounds measured except tetrahydroxy toluene (Figure 4.11). The signals for tetrahydroxy toluene dropped to  $\sim 1/2$  their original value after sampling purified air, and slowly decayed from this point onward. Therefore, this compound is lost reversibly to the walls of the CIMS such that accurate quantification and wall loss determination is not possible. This was the only compound that rose nearly to its original signal after heating the chamber to  $42^{\circ}\text{C}$  (Figure 4.9b, cyan), suggesting a possible large reversible reservoir of this compound on the wall as well.

For 3-methyl catechol ( $m/z$  (-)143), hydroxy methyl benzoquinone ( $m/z$  (-)157), and dihydroxy methyl benzoquinone ( $m/z$  173), MS mode was used to determine the wall deposition rate constants (Figure 4.9b) (MS/MS mode produced similar results). The MS and MS/MS results for trihydroxy toluene (Figure 4.9a) imply that multiple isomers, with different wall loss rates and fragmentation patterns on the CIMS, are forming. For example, the wall loss rate determined from the MS signal  $m/z$  (-) 159 ( $2.3 \times 10^{-5} \text{ s}^{-1}$ ) is different from those determined from the MS/MS daughters of  $m/z$  (-)159:  $1.8 \times 10^{-5} \text{ s}^{-1}$  ( $m/z$  (-) 159),  $1.9 \times 10^{-5} \text{ s}^{-1}$  ( $m/z$  (-)139), and  $3.6 \times 10^{-5} \text{ s}^{-1}$  ( $m/z$  (-)115).

The  $\text{pK}_a$  values of compounds similar to trihydroxy toluene demonstrate that aromatic compounds with an OH group *ortho* to another OH group are more acidic than those with an OH group *meta* or *para* to another OH group. For example, 1,2 dihydroxy benzene, 1,3 dihydroxy benzene, and 1,4 dihydroxy benzene have the following  $\text{pK}_a$  values 9.36, 9.44, and 9.91, respectively (Dean, 1992). Likely the arrangement of the OH groups on trihydroxy toluene influences the acidity, which then influences both the wall deposition and the CIMS fragmentation patterns. The two standards of trihydroxy toluene monitored on the CIMS (Section 4.3) also demonstrate this effect. The isomer with the hydroxy groups spread out among the ring (2,4,6-trihydroxytoluene) was detected more at the complex than 5-methyl-benzene-1,2,3-triol, implying it is less acidic than 5-methyl-benzene-1,2,3-triol.

For simplicity, the wall deposition rate determined for  $m/z$  (-)159 is used in the kinetic model to represent the wall deposition of all trihydroxy toluene isomers, but in order to understand more fully the yield of this product, the isomer distribution and wall deposition for each isomer would need to be known. The water curve correction was applied in calculating the wall deposition rate constants for *o*-cresol, 3-methyl catechol, and trihydroxy toluene, but not for hydroxy methyl benzoquinone or dihydroxy methyl benzoquinone as the influence of water on benzoquinones is



unknown. The *o*-cresol and 3-methyl catechol water curve corrections add  $2 \times 10^{-8}$  and  $1.6 \times 10^{-6} \text{ s}^{-1}$  uncertainty, respectively, to the measured wall deposition rate constants. The wall deposition for tetrahydroxy toluene was approximated in the kinetic model since it cannot be measured. A plot of the natural log of  $C^*$  versus the natural log of the wall deposition rate constant produces a fairly linear fit for the compounds measured in this work (Figure 4.15). This fit is used to approximate the wall loss of tetrahydroxy toluene, pentahydroxy toluene, and trihydroxy methyl benzoquinone. There is more uncertainty in the wall deposition rates for these compounds due to the necessity of extrapolation.

### Formation and Loss of Nitro and Nitroso Compounds

MCM v3.3.1 does not include the photolysis of many nitro compounds, even though recent studies have measured fast photolysis rates (Bardini, 2006; Bejan, Barnes, et al., 2007; Bejan, Abd El Aal, et al., 2006). For example, hydroxy nitrotoluene has an atmospheric lifetime with respect to photolysis of  $< 1 \text{ h}$  (Bejan, Barnes, et al., 2007). No studies thus far have reported the photolysis rate constants of dihydroxy nitrotoluene. In version 2 of the kinetic model, the photolysis rate constant for 6-methyl-2-nitrophenol (Bejan, Barnes, et al., 2007) was used for hydroxy nitrotoluene and dihydroxy nitrotoluene with a correction for the difference in the  $\text{NO}_2$  photolysis rate constants between the Caltech chamber and that used by Bejan, Barnes, et al. (2007).

Under high- $\text{NO}$  conditions during 3-methyl catechol oxidation, dihydroxy nitrotoluene is detected only minimally ( $< 0.5 \text{ ppb}$ ) even though the MCM v3.3.1 chemical mechanism predicts a peak value of  $\sim 60 \text{ ppb}$  (Figure 4.3 and Figure 4.10). Even after accounting for possible photolysis of dihydroxy nitrotoluene, the kinetic model (Version 2) still predicts a peak value of  $\sim 45 \text{ ppb}$ . Other nitro compounds are detected quite well by the CIMS (e.g., hydroxy nitrotoluene (Section 4.4) and nitrophenol (Section 4.4)), so this is unlikely caused by a sensitivity issue. Dihydroxy nitrotoluene has a lower estimated vapor pressure than the other nitro compounds detected (Table 4.3), so this compound is possibly lost to chamber walls and Teflon tubing to a higher degree. Considering the estimated photolysis rate constant ( $1.73 \times 10^{-4} \text{ s}^{-1}$ ) is nearly an order of magnitude larger than the predicted wall deposition rate constant ( $1 \times 10^{-5} \text{ s}^{-1}$ , Figure 4.15), losses to chamber walls and Teflon tubing are unlikely the explanation for minimal detection of this compound. More likely, dihydroxy nitrotoluene, the expected product of hydrogen abstraction of 3-methyl

catechol, is not, in fact, a main product. Contrary to the recommendations of MCM v3.3.1, hydrogen abstraction contributes only a small degree to OH oxidation of 3-methyl catechol.

MCM v3.3.1 predictions of nitrophenol, a product of benzaldehyde oxidation, exceed the CIMS measurements (Figure 4.13). An estimated photolysis rate constant was added to the kinetic model based on that for 2-nitrophenol measured by Bardini (2006) and reported by Chen et al. (2011). This photolysis rate constant was corrected for the difference in the photolysis of NO<sub>2</sub> between the Caltech chamber and the atmosphere when/where Bardini made the measurement. With this adjustment (Figure 4.13), nitrophenol is under-predicted by the kinetic model compared to the CIMS measurements, but within uncertainties in the CIMS sensitivity and the photolysis approximation.

### ***o*-Cresol Oxidation Products**

During *o*-cresol oxidation, theory suggests that OH addition occurs dominantly *ipso* (position 2) or *ortho* (position 1 and 3) to the OH substituent due to hydrogen bonding (Jorgensen, 2012). Only OH addition to position 3 will form a dihydroxy toluene as positions 1 and 2 do not have an abstractable hydrogen to undergo HO<sub>2</sub> elimination. Consistent with these theory calculations, Olariu, Klotz, et al. (2002) detected only 3-methyl catechol from *o*-cresol oxidation. Here, results suggest that 3-methyl catechol is not the only isomer of dihydroxy toluene that forms from *o*-cresol oxidation. 3-methyl catechol is detected mostly at the F<sup>-</sup> transfer (97%) and only minimally at the cluster (3%). However, dihydroxy toluene produced from *o*-cresol oxidation under low- and high-NO conditions is detected more at the complex (~12%) than 3-methyl catechol. This suggests that *o*-cresol oxidation produces an additional isomer or isomers. These isomer(s) are likely less acidic than 3-methyl catechol (i.e., the OH substituents are not on adjacent carbons).

In the kinetic model (Version 3), dihydroxy, trihydroxy, and tetrahydroxy toluene oxidation products are inferred from the products recommended by MCM v3.3.1 (Jenkin et al., 2003; Bloss et al., 2005) and Olariu, Klotz, et al. (2002) for *o*-cresol oxidation (Figure 4.3, Section 4.6). The hydrogen abstraction pathway is assumed to produce 6-methyl-2-nitrophenol and the bicyclic intermediate pathway is assumed to produce the unidentified products. Thus, dihydroxy, trihydroxy, and tetrahydroxy toluene are assumed to produce the following: a benzoquinone (0.07), a polyol (0.73), a product from the hydrogen abstraction pathway (0.07),

and a product from the bicyclic intermediate pathway (0.13). Isomers are not treated separately in the kinetic model. With these additional reactions, when oxidizing *o*-cresol under low-NO conditions, the kinetic model results are similar to the CIMS measurements for first-generation products (dihydroxy toluene) and second-generation products (hydroxy methyl benzoquinone and trihydroxy toluene) (Figure 4.10a). Although exact yields cannot be reported owing to the lack of availability of authentic standards, yields of  $\sim 0.7$  for trihydroxy toluene and  $\sim 0.1$  for hydroxy methyl benzoquinone from dihydroxy toluene oxidation appear to be reasonable. Additionally, the CIMS sensitivity (i.e., the ion-molecule collision rate correction, Section 4.6) for dihydroxy toluene and trihydroxy toluene is dependent on the isomers that form. The suspected dominant isomers of dihydroxy toluene (3-methyl catechol) and trihydroxy toluene (2,3,4-trihydroxy toluene) both have a higher sensitivity correction than their other isomer counterparts (Table 4.4). Thus, dihydroxy toluene and trihydroxytoluene may be underestimated by the CIMS if other isomers form to a large degree.

For 3-methyl catechol oxidation, like *o*-cresol oxidation, OH addition is assumed to occur at the *ortho* position forming 2,3,4-trihydroxy toluene as the dominant isomer. The wall deposition results (Section 4.5) imply that multiple isomers of trihydroxy toluene with different wall loss rates and fragmentation patterns on the CIMS are produced from 3-methyl catechol oxidation. Likely (as theory suggests), 2,3,4-trihydroxy toluene is the dominant isomer, but other isomers also form. Results suggest that the trihydroxy toluene isomers produced during *o*-cresol oxidation versus 3-methyl catechol oxidation are different. The distribution of the complex ( $m/z$  (-)225),  $F^-$  transfer ( $m/z$  (-)159), and fragment ( $m/z$  (-)115) signals for trihydroxy toluene is different during *o*-cresol oxidation (0.38, 0.42, 0.2, respectively) versus 3-methyl catechol oxidation (0.04, 0.42, 0.54, respectively). Likely the distribution of trihydroxy toluene isomers is different between the two cases because 3-methyl catechol is not the sole isomer of dihydroxy toluene produced from *o*-cresol oxidation. The isomers of trihydroxy toluene from *o*-cresol oxidation are detected more at the complex (likely less acidic), while the isomers from 3-methyl catechol oxidation fragment more (likely more acidic).

When 3-methyl catechol is oxidized under low-NO conditions, trihydroxy toluene is over-predicted by the kinetic model compared to the CIMS measurements (Figure 4.10c). Likely, the trihydroxy toluene isomers produced from 3-methyl catechol have a lower yield or CIMS sensitivity compared to those produced from *o*-cresol. In

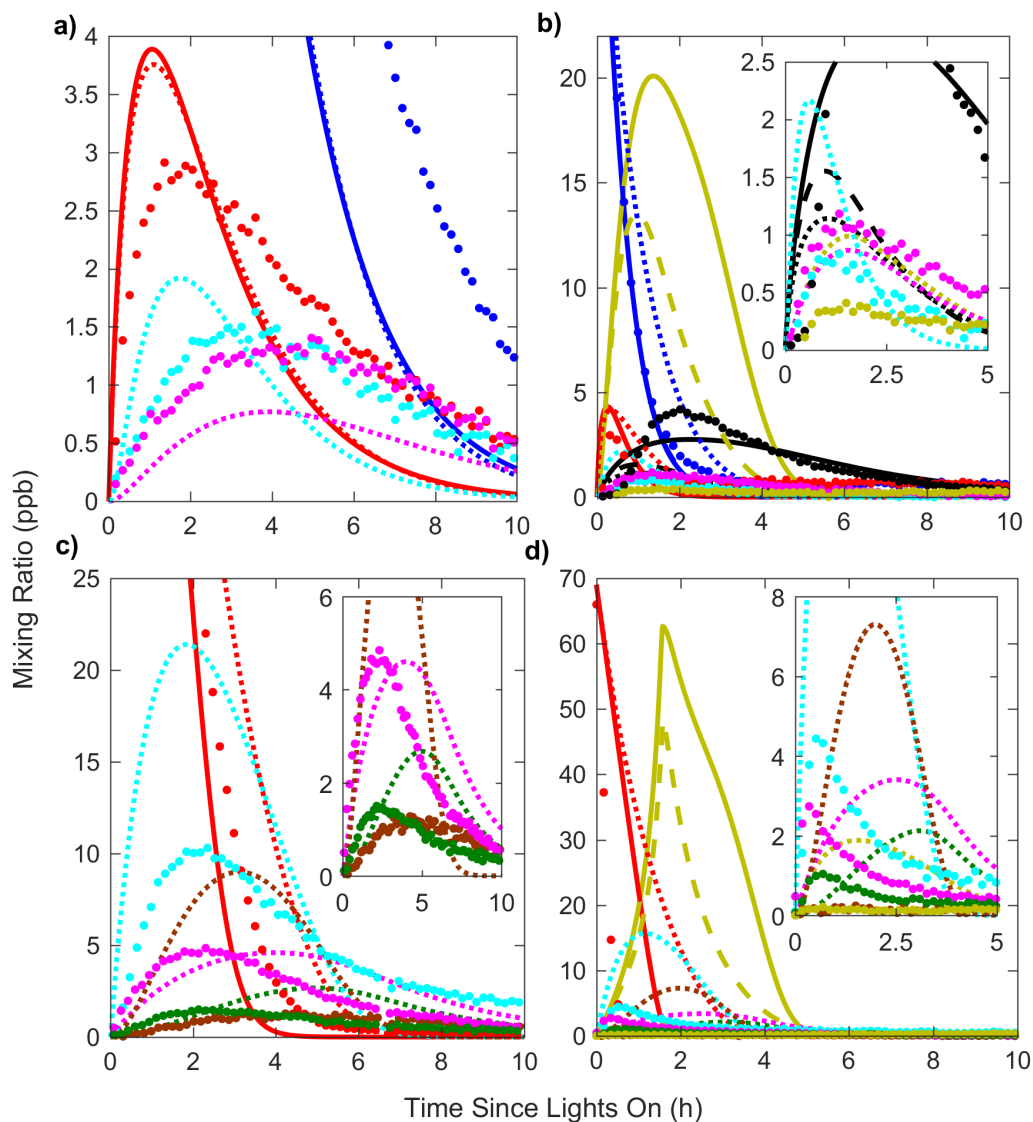


**Figure 4.10:** Kinetic model predictions (Version 1 solid lines, Version 2 dashed lines, Version 3 dotted lines) versus CIMS measurements (markers) for *o*-cresol oxidation under low-NO (a) and high-NO (b) conditions and 3-methyl catechol oxidation under low-NO (c) and high-NO (d) conditions. When necessary, a finer detail plot of selected compounds with lower signal is shown in the upper right corner. Colors for all graphs are *o*-cresol (blue), 3-methyl catechol (red), trihydroxy toluene (cyan), tetrahydroxy toluene (brown), hydroxy methyl benzoquinone (magenta), dihydroxy methyl benzoquinone (green), hydroxy nitrotoluene (black), and dihydroxy nitrotoluene (gold).

order to constrain the exact yield of trihydroxy toluene from dihydroxy toluene, the isomer distribution and wall deposition rate for each isomer need to be understood.

Under high-NO conditions, the kinetic model over-predicts trihydroxy toluene forma-

tion compared to the CIMS measurements for both *o*-cresol and 3-methyl catechol oxidation (Figure 4.10).  $\text{NO}_3$  oxidation is potentially more significant in the experiments than the kinetic model predicts because the kinetic model under-predicts methyl nitrophenol, a product from OH and  $\text{NO}_3$  oxidation of *o*-cresol. Under-predicting the occurrence of  $\text{NO}_3$  oxidation would lead to an over-prediction of OH oxidation products such as trihydroxy toluene.

Tetrahydroxy toluene and dihydroxy methyl benzoquinone are both over-predicted by the kinetic model as compared to experimental results (Figure 4.10c). Because desorption of tetrahydroxy toluene from the instrument walls occurs and chamber wall deposition of this compound was approximated instead of directly measured, this low yield does not necessarily indicate a low yield of the product.

### **Formation of Decomposition Products From Bicyclic Intermediate Pathway**

A bicyclic intermediate peroxy radical forms from: 1) OH addition to the ring of an aromatic compound, 2) subsequent  $\text{O}_2$  addition, 3) cyclization, and 4) another  $\text{O}_2$  addition. In MCM v3.3.1, this peroxy radical reacts either with NO producing an alkoxy radical that decomposes or with  $\text{HO}_2$  producing a hydroperoxide. This hydroperoxide will either react with OH to reform the original  $\text{RO}_2$  or photolyze to form decomposition products (Figure 4.3). Here, results suggest that either this hydroperoxide photolyzes more rapidly than MCM v3.3.1 assumes or the initial reaction with  $\text{HO}_2$  proceeds through two reaction channels: 1) formation of a hydroperoxide and, 2) formation of OH and an alkoxy radical, which rapidly decomposes. Under low-NO conditions, the kinetic mechanism (Version 1) predicts most of the bicyclic intermediate products are in the form of the bicyclic intermediate hydroperoxide. Conversely, the CIMS measurements imply that most of the bicyclic intermediate products are in the form of decomposition products. *o*-Cresol and 3-methyl catechol oxidation under low- and high-NO conditions produce the same decomposition products rapidly and in high concentration. More specifically, for *o*-cresol oxidation under low-NO conditions, the CIMS detects acetyl acrylic acid, a decomposition product from the bicyclic intermediate pathway, at a peak of  $\sim 1.5$  ppb, while the kinetic mechanism predicts much less acetyl acrylic acid forms (peak  $\sim 0.1$  ppb). The  $\text{CF}_3\text{O}^-$  CIMS does not detect the bicyclic intermediate hydroperoxide. Either the signal is below the detection limit or the compound is not stable under  $\text{CF}_3\text{O}^-$  ion chemistry. Birdsall et al. (2010) similarly proposed that some of the bicyclic intermediate peroxy radical from toluene reacts with  $\text{HO}_2$  to

form an alkoxy radical and OH. Additionally, recent studies have identified various peroxy radicals that upon reaction with HO<sub>2</sub> do not form a hydroperoxide in unity yield (Orlando et al., 2012, and references therein). The additional OH produced from the bicyclic intermediate pathway would help explain why Version 3 of the kinetic model under-predicts the decay of the precursor (Figure 4.10).

A variety of decomposition products suspected to arise from the bicyclic intermediate pathway were detected by the CIMS (Figures 4.5 and 4.6). However, not all products formed from this pathway are detected as the CIMS is not sensitive to unfunctionalized ketones and aldehydes. OH oxidation of *o*-cresol and 3-methyl catechol through the bicyclic intermediate pathway yields two products, only one of which is typically detected by the CIMS. For trihydroxy toluene and tetrahydroxy toluene, often both products are detected. Many basic simplifications/assumptions are made to compare the CIMS and kinetic model results. All products are estimated to have the same CIMS sensitivity as glycolaldehyde. In the kinetic mechanism (version 3), *o*-cresol, 3-methyl catechol, trihydroxy toluene, and tetrahydroxy toluene are assumed to form a 0.13 yield of bicyclic intermediate products (Section 4.5). The OH reaction rate constant for all bicyclic intermediate compounds is assumed to be the same as that for acetyl acrylic acid (MCM v3.3.1).

With these additional reactions, the bicyclic intermediate decomposition products formed from 3-methyl catechol oxidation under low- (Figure 4.14) and high-NO conditions are well represented by the kinetic model compared to the CIMS measurements. These same products from *o*-cresol oxidation under low- and high-NO conditions are under-predicted by the kinetic model, but still within reasonable uncertainty. Most of the products detected are not unique to one of the precursors (Figures 4.5 and 4.6). However, C<sub>4</sub>H<sub>4</sub>O<sub>5</sub> and C<sub>5</sub>H<sub>6</sub>O<sub>5</sub> are expected to form only from trihydroxy toluene and tetrahydroxy toluene. The CIMS measurements confirm C<sub>4</sub>H<sub>4</sub>O<sub>5</sub> and C<sub>5</sub>H<sub>6</sub>O<sub>5</sub> are produced later in the experiment, as expected for second- or third-generation products (Figure 4.14).

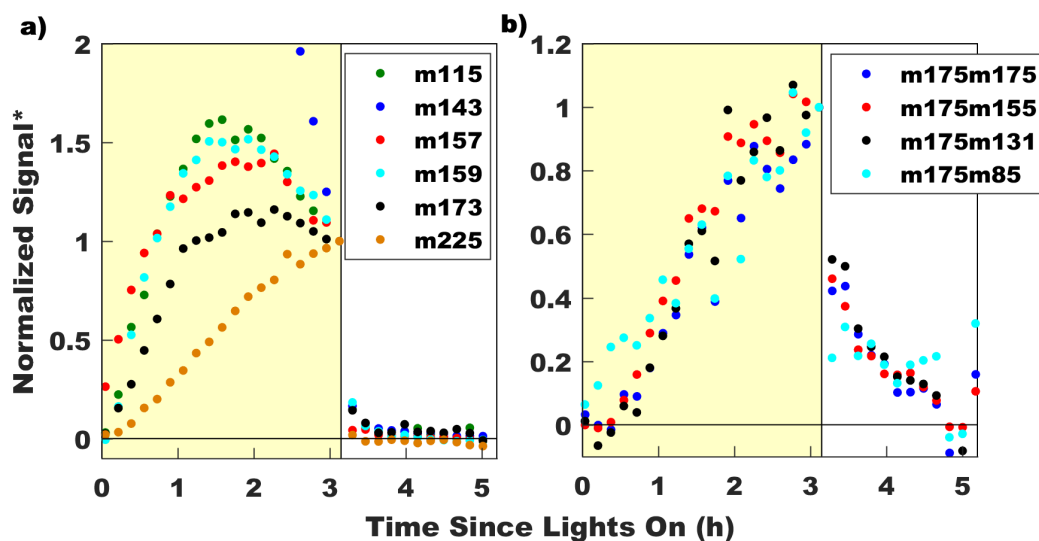
## Conclusions

OH oxidation of 3-methyl catechol (the dominant OH oxidation product from *o*-cresol) produces the following first-generation products: trihydroxy toluene, hydroxy methyl benzoquinone, and various decomposition products likely from the bicyclic intermediate pathway. Second- and third-generation products from 3-methyl catechol include tetrahydroxy toluene, dihydroxy methyl benzoquinone, pentahy-

droxy toluene, and trihydroxy methyl benzoquinone. Detection of these products implies that subsequent OH addition to the aromatic ring occurs during *o*-cresol oxidation. Many of these products are expected to be relatively low in volatility ( $C^* \sim 3.0 \times 10^3 - 7.7 \times 10^{-3} \mu\text{g m}^{-3}$ ) and are detected in the particle phase by the DART-MS. Although the gas-phase cresol pathway is relatively minor ( $\sim 20\%$ ), oxidation products from this pathway are estimated to contribute significantly ( $\sim 20\text{-}40\%$ ) to toluene SOA. Thus, a simple and direct pathway for toluene SOA formation has been identified. Oxidation products from the phenolic pathway of other aromatic compounds are also likely to be important for SOA formation.

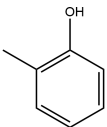
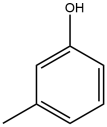
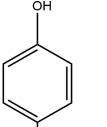
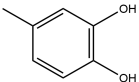
#### 4.6 Supporting Information

##### Further Details on $\text{CF}_3\text{O}^-$ CIMS Analysis



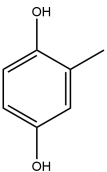
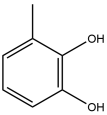
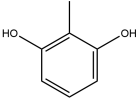
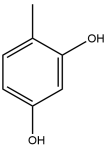
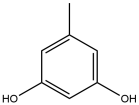
**Figure 4.11:** CIMS MS signals of 3-methyl catechol oxidation products (panel a) and MS/MS signals of tetrahydroxy toluene (panel b) for experiment 10. Desorption of compounds from instrument walls was measured by sampling photooxidation products generated in the chamber (yellow) and then immediately switching to purified air (white). \*CIMS signal is normalized to time right before lights off.

**Table 4.4:** Estimated CIMS sensitivity factors

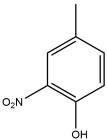
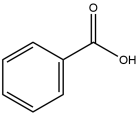
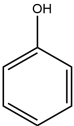
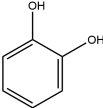
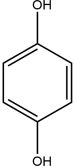
| Compound                  | Structure   | Polarizability<br>$(\text{\AA}^3)^a$ | Dipole Mo-<br>ment (D) <sup>b</sup> | Sensitivity<br>Factor <sup>c</sup> | Notes |
|---------------------------|---|--------------------------------------|-------------------------------------|------------------------------------|-------|
| Toluene Related Compounds |   |                                      |                                     |                                    |       |
| <i>o</i> -Cresol          |    | 11.8                                 | 1.42                                | 1                                  |       |
| <i>m</i> -Cresol          |    | 13.1                                 | 1.53                                | 1.07                               |       |
| <i>p</i> -Cresol          |   | 13                                   | 1.53                                | 1.06                               |       |
| 4-Methylcatechol          |  | 13.7                                 | 2.7                                 | 1.44                               |       |



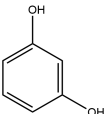
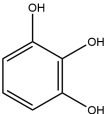
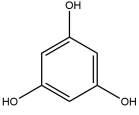
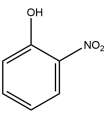
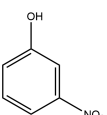
**Table 4.4:** Estimated CIMS sensitivity factors

| Compound             | Structure   | Polarizability<br>( $\text{\AA}^3$ ) <sup>a</sup> | Dipole Mo-<br>ment (D) <sup>b</sup> | Sensitivity<br>Factor <sup>c</sup> | Notes   |
|----------------------|---|---|-------------------------------------|------------------------------------|---|
| Methyl hydro-quinone |    | 13.7  | 2.05                                | 1.21                               | Assume same polarizability as 4-methyl catechol |
| 3-Methylcatechol     |    | 13.7  | 2.42                                | 1.34                               | Assume same polarizability as 4-methyl catechol |
| 2-Methyl resorcinol  |    | 13.7  | 2                                   | 1.19                               | Assume same polarizability as 4-methyl catechol |
| 4-Methyl resorcinol  |   | 13.7  | 1.81                                | 1.13                               | Assume same polarizability as 4-methyl catechol |
| 5-Methyl resorcinol  |  | 13.7  | 2.1                                 | 1.23                               | Assume same polarizability as 4-methyl catechol |

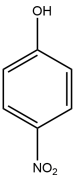
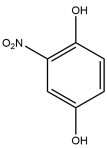
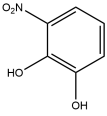
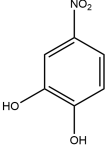
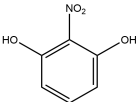
**Table 4.4:** Estimated CIMS sensitivity factors

| Compound                  | Structure   | Polarizability<br>( $\text{\AA}^3$ ) <sup>a</sup> | Dipole Mo-<br>ment (D) <sup>b</sup> | Sensitivity<br>Factor <sup>c</sup> | Notes                                   |
|---------------------------|---|---|-------------------------------------|------------------------------------|---|
| 4-Methyl-2-nitrophenol    |    | 16.2  | 3.49                                | 1.69                               |   |
| Benzoic acid              |    | 11.3  | 1.26                                | 0.92                               |   |
| Benzene Related Compounds |   |   |                                     |                                    |   |
| Phenol                    |    | 11.1  | 1.54                                | 1                                  |   |
| Catechol                  |  | 13.1  | 2.64                                | 1.37                               |   |
| Hydroquinone              |  | 13.1  | 1.78                                | 1.08                               | Assume polarizability same as catechol. |

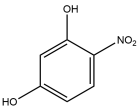
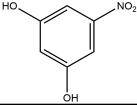
**Table 4.4:** Estimated CIMS sensitivity factors

| Compound                    | Structure   | Polarizability<br>( $\text{\AA}^3$ ) <sup>a</sup> | Dipole Mo-<br>ment (D) <sup>b</sup> | Sensitivity<br>Factor <sup>c</sup> | Notes   |
|-----------------------------|---|---|-------------------------------------|------------------------------------|---|
| Resorcinol                  |    | 13.1  | 2.04                                | 1.16                               | Assume polarizability same as catechol.             |
| 1,2,3-Benzene triol         |    | 11.1  | 3.17                                | 1.47                               |   |
| 1,3,5-Trihydroxy<br>benzene |    | 11.1  | 2.7                                 | 1.32                               | Assume polarizability same as 1,2,3-benzene triol   |
| <i>o</i> -Nitrophenol       |   | 14  | 3.12                                | 1.48                               |   |
| <i>m</i> -Nitrophenol       |  | 14  | 3.89                                | 1.73                               | Assume polarizability same as <i>o</i> -nitrophenol |

**Table 4.4:** Estimated CIMS sensitivity factors

| Compound              | Structure   | Polarizability<br>( $\text{\AA}^3$ ) <sup>a</sup> | Dipole Mo-<br>ment (D) <sup>b</sup> | Sensitivity<br>Factor <sup>c</sup> | Notes  |
|-----------------------|---|---|-------------------------------------|------------------------------------|--|
| <i>p</i> -Nitrophenol |    | 14  | 4.9                                 | 2.06                               | Assume polarizability same as <i>o</i> -nitrophenol            |
| Nitrohydroquinone     |    | 14  | 3.5                                 | 1.60                               | Assume polarizability same as <i>o</i> -nitrophenol            |
| 3-Nitrocatechol       |   | 16.5  | 2.1                                 | 1.16                               | Assume polarity increases by same factor as phenol to catechol |
| 4-Nitrocatechol       |  | 16.5  | 4.95                                | 2.07                               | Assume polarity increases by same factor as phenol to catechol |
| 2-Nitroresorcinol     |  | 16.5  | 2.18                                | 1.19                               | Assume polarity increases by same factor as phenol to catechol |

**Table 4.4:** Estimated CIMS sensitivity factors

| Compound          | Structure   | Polarizability<br>( $\text{\AA}^3$ ) <sup>a</sup> | Dipole Mo-<br>ment (D) <sup>b</sup> | Sensitivity<br>Factor <sup>c</sup> | Notes  |
|-------------------|---|---|-------------------------------------|------------------------------------|--|
| 4-Nitroresorcinol |  | 16.5  | 4.44                                | 1.91                               | Assume polarity increases by same factor as phenol to catechol |
| 5-nitroresorcinol |  | 16.5  | 3.9                                 | 1.74                               | Assume polarity increases by same factor as phenol to catechol |

<sup>a</sup> Polarizability was estimated using the refractive index of each compound reported in Lide (2001) as done by Dewar et al. (1984). <sup>b</sup> The reported dipole moment is the average of all values reported in McClellan (1974) for experiments using benzene as a solvent and taken between 20-30 °C. <sup>c</sup> The sensitivity factor equals the ion-molecule collision rate of the compound / ion-molecule collision rate of *o*-cresol for toluene related compounds or phenol for benzene related compounds.

**Table 4.5:** Water curve correction and sensitivity factors applied to each compound of interest

| Compound                      | Water Curve Correction | Compound Sensitivity Factor Based on <sup>a</sup>                |
|-------------------------------|------------------------|--|
| Cresol                        | <i>o</i> -cresol       | Weighted <i>o</i> -, <i>m</i> -, & <i>p</i> -cresol <sup>b</sup> |
| Dihydroxy toluene             | 3-methyl catechol      | 3-methyl catechol  |
| Trihydroxy toluene            | 3-methyl catechol      | 1,2,3 benzene triol  |
| Tetrahydroxy toluene          | 3-methyl catechol      | 1,2,3 benzene triol  |
| Hydroxy methyl benzoquinone   | <i>o</i> -cresol       | <i>o</i> -cresol   |
| Dihydroxy methyl benzoquinone | 3-methyl catechol      | 3-methyl catechol  |
| Methyl nitrophenol            | <i>o</i> -cresol       | 4-methyl-2-nitrophenol   |
| Dihydroxy nitrotoluene        | 3-methyl catechol      | 3-nitrocatechol  |
| Benzoic acid                  | <i>o</i> -cresol       | benzoic acid   |
| Peroxy benzoic acid           | <i>o</i> -cresol       | benzoic acid   |
| Phenyl hydroperoxide          | <i>o</i> -cresol       | benzoic acid   |
| Nitrosophenol                 | <i>o</i> -cresol       | <i>o</i> -nitrophenol  |
| Nitrophenol                   | <i>o</i> -cresol       | <i>o</i> -nitrophenol  |
| Dinitrophenol                 | <i>o</i> -cresol       | <i>o</i> -nitrophenol  |

<sup>a</sup> The sensitivity factors are listed in Table 4.4. <sup>b</sup> The photooxidation isomer distribution reported by Klotz et al. (1998) was used to create a generalized cresol sensitivity factor.

As done by Dewar et al. (1984), polarizability was estimated using the refractive index reported in (Lide, 2001) and the formula:  $\bar{P} = (3/4\pi N)(M/d)[(n^2 - 1)/(n^2 + 2)] * 10^{24}$  where  $\bar{P}$  is the average polarizability,  $n$  is the refractive index,  $N$  is Avogadro's number,  $M$  is the molecular weight, and  $d$  is the density.

As noted in Table 4.4 when refractive index was unavailable, the polarizability for the closest related compound was used. The ion-molecule collision rate for each compound was estimated using the polarizabilities and dipole moments reported in Table 4.4 and the technique described in Su et al. (1982). The sensitivity is expected to be proportional to the ion-molecule collision rate. The sensitivity factor reported in Table 4.4 is the ratio of the ion-molecule collision rate for the compound to that of *o*-cresol for toluene related compounds and phenol for benzene related compounds.

As stated in the main text, the *o*-cresol or 3-methyl catechol water curve was used to determine the sensitivity of a compound with a correction for the ion-molecule collision rate. In Table 4.5, the water curve correction and the sensitivity factor used for each compound is reported. In some cases, as specified in Table 4.5 the polarizability and dipole moments were not available for toluene related compounds, so the benzene counterpart was used instead. Note that depending on the fraction of

isomers of dihydroxy toluene that form from *o*-cresol oxidation, dihydroxy toluene may be underestimated. 3-methyl catechol has the highest sensitivity of all the isomers that could form from *o*-cresol oxidation (3-methyl catechol, 2-methyl resorcinol, 4-methyl resorcinol, and methyl hydroquinone). Similarly, depending on the exact isomer distribution that forms from dihydroxy toluene oxidation, trihydroxy toluene may be underestimated. 1,3,5-trihydroxy benzene has a lower sensitivity factor (1.32) compared to that for 1,2,3 benzene triol (1.47). Polarizability and dipole moment measurements are not available for hydroxy methyl benzoquinone or dihydroxy methyl benzoquinone. Thus, we assume that hydroxy methyl benzoquinone behaves like *o*-cresol and dihydroxy methyl benzoquinone behaves like 3-methyl catechol.

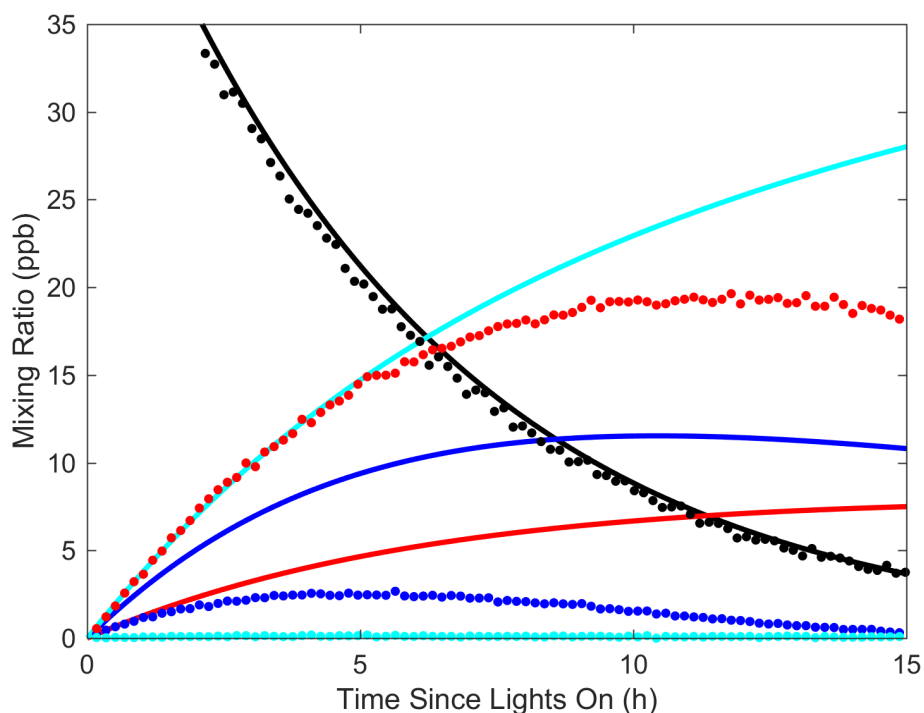


**Figure 4.12:** CIMS measurements (markers) compared to predictions from version 1 of kinetic model (lines) for benzaldehyde low-NO oxidation (experiment 10) for the following compounds benzaldehyde (black), peroxybenzoic acid (blue), benzoic acid (red), and phenyl hydroperoxide (cyan).

CIMS measurements and kinetic model results for products from low-NO oxidation of benzaldehyde are displayed in Figure 4.12. Benzoic acid is under-predicted by the kinetic model, suggesting it is formed in a higher yield from  $\text{RO}_2 + \text{RO}_2$  reactions,  $\text{RO}_2 + \text{HO}_2$  reactions, or both. The low yield measured by the CIMS

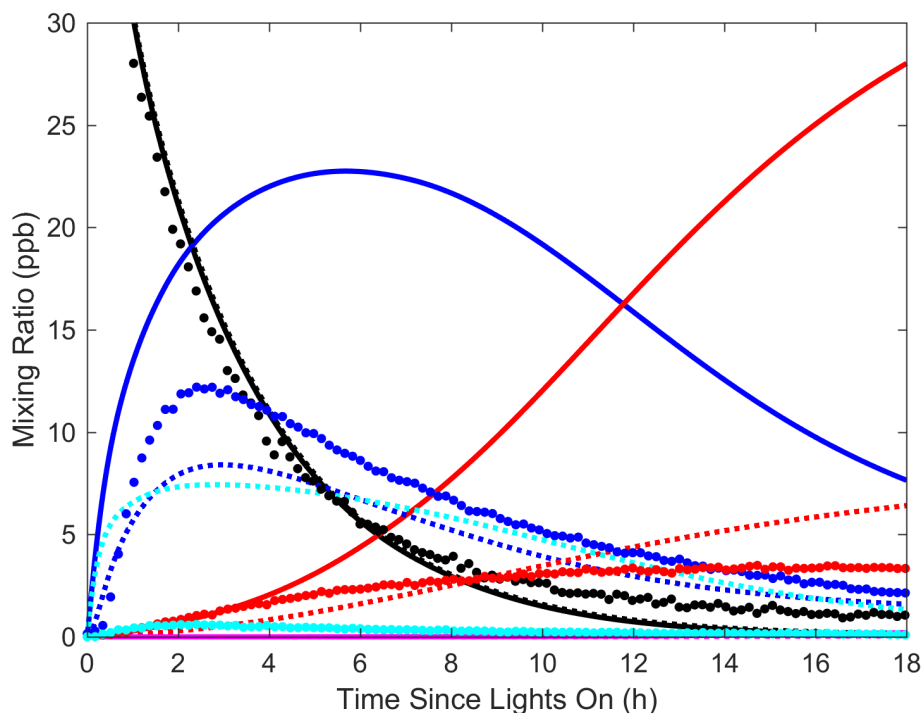


**Figure 4.13:** CIMS measurements (markers) compared to predictions from the kinetic model (solid lines version 1 and dotted lines version 3) for benzaldehyde oxidation under high-NO conditions (experiment 11) for the following compounds benzaldehyde (black), nitrophenol (blue), nitrosophenol (cyan), dinitrophenol (red), and maleic anhydride (magenta).

of peroxybenzoic acid, a product from only  $\text{RO}_2 + \text{HO}_2$  reaction, could be caused by a variety of factors. For example, if the  $\text{RO}_2 + \text{RO}_2$  reaction rate constant used in MCM v3.3.1 is too low, more  $\text{RO}_2 + \text{HO}_2$  reactions would occur in the kinetic model producing an over-prediction of peroxybenzoic acid. Another possibility is that the branching ratio for the  $\text{RO}_2 + \text{HO}_2$  reaction favors formation of benzoic acid more so than recommended by MCM v3.3.1. Because benzoic acid is a product from both  $\text{RO}_2 + \text{RO}_2$  and  $\text{RO}_2 + \text{HO}_2$  reactions further constraint is not possible.

Nitrosophenol is detected from benzaldehyde oxidation under high NO conditions (Figure 4.13). Previous studies have detected a product ( $\text{C}_6\text{H}_5\text{O}(\text{NO})$ ) from the reaction of phenoxy with NO (Tao et al., 1999). The exact isomer that forms has not been experimentally confirmed. Based on theory, nitrosophenol is the most stable isomer (Yu et al., 1995). Two kinetic studies (Berho et al., 1998; Yu et al., 1995) proposed that phenyl nitrite is the dominant isomer given that nitrosophenol, which requires rearrangement, would not form at the timescales of their studies.



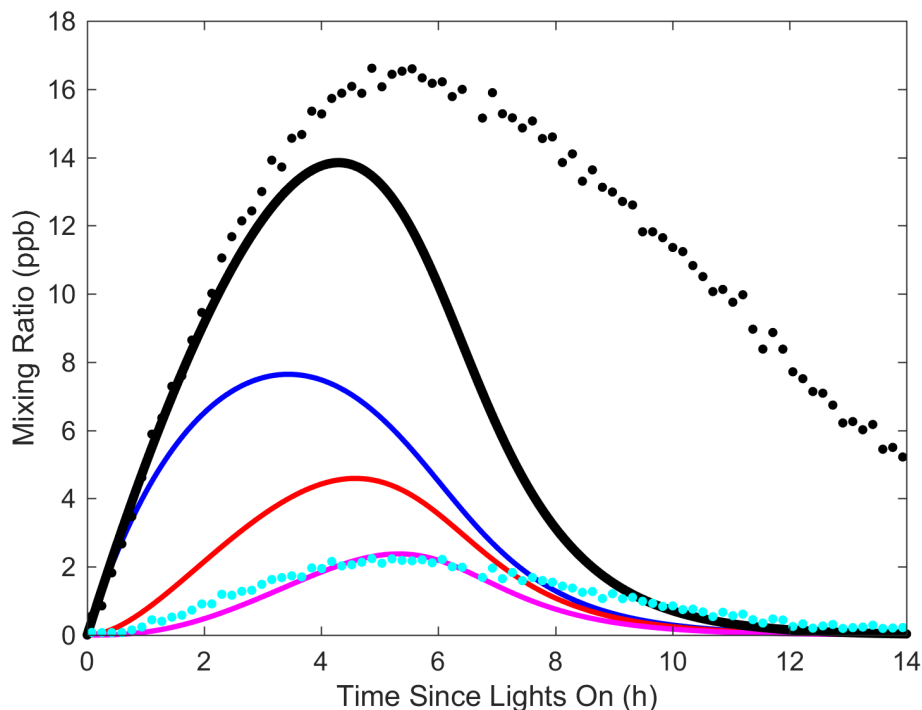


**Figure 4.14:** CIMS measurements (markers) compared to predictions from version 3 of the kinetic model (lines) for 3-methyl catechol oxidation under low-NO conditions for bicyclic intermediate products from all precursors (black), 3-methyl catechol (blue), trihydroxy toluene (red), tetrahydroxy toluene (magenta), and trihydroxy toluene or tetrahydroxy toluene tracers (cyan).

$\text{C}_6\text{H}_5\text{O}(\text{NO})$  was detected at the fluorine transfer at  $m/z$  (-) 142, implying that it is acidic like nitrosophenol. Possibly, nitrosophenol is over-predicted by version 3 of the kinetic model (Figure 4.13) because two isomers (nitrosophenol and phenyl nitrite) form and the CIMS is only sensitive to nitrosophenol. The reaction rate constant for  $\text{C}_6\text{H}_5\text{O} + \text{NO}$  measured by Berho et al. (1998) ( $1.65 \times 10^{-12} \text{ cm}^3 \text{ molec}^{-1} \text{ s}^{-1}$ ) is used in the revised mechanism. The reaction of  $\text{C}_6\text{H}_5\text{O} + \text{NO}$  has been shown to be reversible, but not at temperatures relevant to this study (Berho et al., 1998; Yu et al., 1995).

$m/z$  (-) 183, assumed to be a fragment of dinitrophenol, is possibly also maleic anhydride (cluster). Maleic anhydride is a decomposition product from dinitrophenol in MCM v3.3.1. However, the predicted amount of maleic anhydride formed in the kinetic mechanism (version 1 and 3) is  $\sim 0.2$  ppb after 18 hours of oxidation (Figure 4.13). Additionally, all nitro products detected by the CIMS have a corresponding fragment at the the  $\text{F}^-$  transfer minus 20 (hydroxy nitrotoluene, di-

hydroxy nitrotoluene, and nitrophenol). Thus, the  $m/z$  (-) 183 signal is attributed to dinitrophenol.

### Further Details on Kinetic Model

The initial conditions specified in Table 1 of the main text were used as input in the kinetic model. The kinetic model was run with 3 different versions. Version 1, the base case of the kinetic model, included reactions from MCM v3.3.1 for toluene and inorganic gas-phase chemistry and experimentally derived wall loss rates of *o*-cresol and 3-methyl catechol. Version 2 includes all reactions in Version 1 and photolysis of hydroxy nitrotoluene and dihydroxy nitrotoluene. Version 3 includes all reactions in Version 2 and oxidation products for 3-methyl catechol and benzaldehyde. The reactions and rate constants are listed in Table 4.6 and abbreviations are defined in Table 4.7. These reactions were included to test the chemistry proposed in the main text. Exact branching ratios and reaction rates for these reactions are unknown. Estimates based on known reactions of similar compounds were used.

Hydrogen abstraction from the hydroxy group of 3-methyl catechol, OH3TOL, and OH4TOL is assumed to form an intermediate that then reacts with NO<sub>2</sub> to form a nitro compound. Under low-NO conditions, there is no loss process for this intermediate in the kinetic model or MCM v3.1.1. In experiments 1 and 2, after all injections were complete, lights on was delayed for 2.5 h to estimate the wall loss of *o*-cresol. Wall loss of all other compounds is explained in section 4.2.1 in the main text.

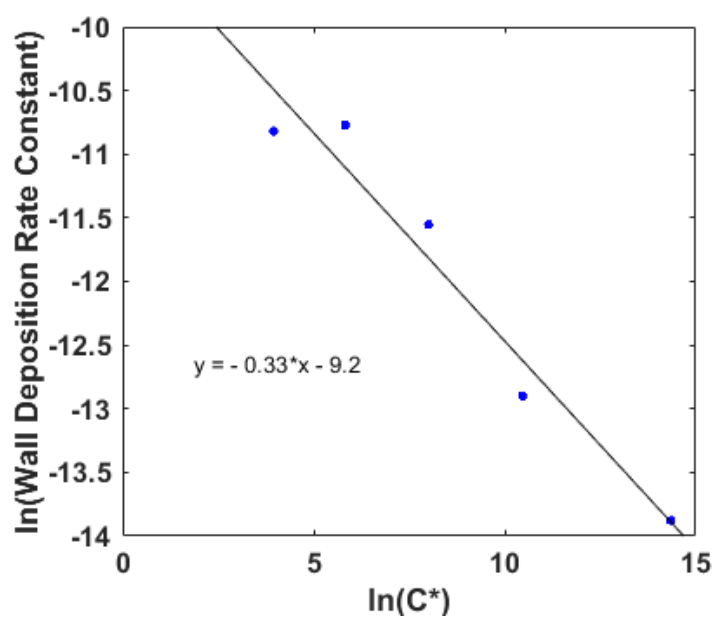


**Figure 4.15:** Linear fit to natural log of wall deposition rate constant versus natural log of  $C^*$  used to estimate wall deposition of compounds that cannot be directly measured.

**Table 4.6:** Reactions and reaction rate constants added to chemistry in MCM v3.3.1 to test proposed chemistry.

| New Reaction  | New Reaction Rate <sup>a</sup>       | Assumptions  |
|---|--------------------------------------|--|
| <b>Version 1</b> – All reactions in MCM v 3.3.1 and those listed below. |                                      |  |
| CRESOL → wall   | $9.4 \times 10^{-7} \text{ s}^{-1}$  | Measured in this study   |
| MCATECHOL → wall  | $2.5 \times 10^{-6} \text{ s}^{-1}$  | Measured in this study   |
| <b>Version 2</b> – All reactions in Version 1 and those listed below.   |                                      |  |
| TOL1OHNO2 + hv → products   | $1.73 \times 10^{-4} \text{ s}^{-1}$ | Assume similar to  |
| MNCATECH + hv → products  | $1.73 \times 10^{-4} \text{ s}^{-1}$ | 6-methyl-2-nitrophenol (Bejan, Barnes, et al., 2007)                             |
| <b>Version 3</b> – All reactions in Version 2 and those listed below.   |                                      |  |
| CRESOL + OH → BCRESOL   | $4.65 \times 10^{-11} * 0.2 * 0.65$  | Assume missing products from Olariu, Klotz, et al. (2002) from bicyclic pathway. |
| MCATECHOL + OH → MCATEC1O   | $2.0 \times 10^{-10} * 0.07$         | Assume same as <i>o</i> -cresol  |
| MCATECHOL + OH → OHMBQN   | $2.0 \times 10^{-10} * 0.07$         | oxidation from MCM v3.3.1  |
| MCATECHOL + OH → OH3TOL   | $2.0 \times 10^{-10} * 0.73$         | and (Olariu, Klotz, et al., 2002)  |
| MCATECHOL + OH → BMCATECHOL   | $2.0 \times 10^{-10} * 0.13$         |  |
| OH3TOL + OH → OH3TOL1O  | $2.5 \times 10^{-10} * 0.07$         | Assume same as <i>o</i> -cresol oxidation  |
| OH3TOL + OH → OH2MBQN   | $2.5 \times 10^{-10} * 0.07$         | from MCM v3.3.1 and Olariu 2002,2000.  |
| OH3TOL + OH → OH4TOL  | $2.5 \times 10^{-10} * 0.73$         | Increased reaction rate constant due to additional                               |
| OH3TOL + OH → BOH3TOL   | $2.5 \times 10^{-10} * 0.13$         | OH group to hard sphere collision rate limit.                                    |
| OH4TOL + OH → OH4TOL1O  | $2.5 \times 10^{-10} * 0.07$         | Assume same as <i>o</i> -cresol oxidation  |
| OH4TOL + OH → OH3MBQN   | $2.5 \times 10^{-10} * 0.07$         | from MCM v3.3.1 and Olariu 2002,2000.  |

**Table 4.6:** Reactions and reaction rate constants added to chemistry in MCM v3.3.1 to test proposed chemistry.

| New Reaction                           | New Reaction Rate <sup>a</sup>       | Assumptions  |
|--|--------------------------------------|--|
| OH4TOL + OH → OH5TOL                   | $2.5 \times 10^{-10} * 0.73$         | Increased reaction rate constant due to additional OH group to hard sphere collision rate limit. |
| OH4TOL + OH → BOH4TOL                  | $2.5 \times 10^{-10} * 0.13$         |  |
| BCRESOL + OH → products                | $5.44 \times 10^{-11}$               | Assume same as C5CO14OH from MCM v 3.3.1   |
| BMCATECHOL + OH → products             | $5.44 \times 10^{-11}$               |  |
| BOH3TOL + OH → products                | $5.44 \times 10^{-11}$               |  |
| BOH4TOL + OH → products                | $5.44 \times 10^{-11}$               |  |
| OHMBQN + OH → products                 | $2.3 \times 10^{-11}$                | Assume same as PTLQONE from MCM v 3.3.1  |
| OH2MBQN + OH → products                | $2.3 \times 10^{-11}$                |  |
| OH3TOL1O + NO <sub>2</sub> → products  | $2.08 \times 10^{-12}$               | Assume same as MCATEC1O from MCM v3.3.1  |
| OH4TOL1O + NO <sub>2</sub> → products  | $2.08 \times 10^{-12}$               |  |
| HOC6H4NO2 + <i>hν</i> → products       | $6.13 \times 10^{-5} \text{ s}^{-1}$ | Based on 2-nitrophenol measured by Bardini (2006) reported by Chen et al. (2011)                 |
| C6H5O + NO → C6H5O(NO)                 | $1.65 \times 10^{-12}$               | Berho et al. (1998)  |
| C6H5O(NO) + OH → products              | $9.0 \times 10^{-13}$                | Assume same as HOC6H4NO2 from MCM v3.3.1   |
| C6H5O(NO) + NO <sub>3</sub> → products | $9.0 \times 10^{-14}$                |  |
| OH3TOL → wall                          | $2.1 \times 10^{-5} \text{ s}^{-1}$  | Measured in this study   |
| OH4TOL → wall                          | $7.9 \times 10^{-5} \text{ s}^{-1}$  | Estimated in this study  |
| OH5TOL → wall                          | $5.0 \times 10^{-4} \text{ s}^{-1}$  | Estimated in this study  |

**Table 4.6:** Reactions and reaction rate constants added to chemistry in MCM v3.3.1 to test proposed chemistry.

| New Reaction   | New Reaction Rate <sup>a</sup>      | Assumptions             |
|----------------|-------------------------------------|-------------------------|
| OHMBQN → wall  | $9.6 \times 10^{-6} \text{ s}^{-1}$ | Measured in this study  |
| OH2MBQN → wall | $2.0 \times 10^{-5} \text{ s}^{-1}$ | Measured in this study  |
| OH3MBQN → wall | $1.2 \times 10^{-4} \text{ s}^{-1}$ | Estimated in this study |

<sup>a</sup> Reaction rate units are  $\text{cm}^3 \text{ molec}^{-1} \text{ s}^{-1}$  unless otherwise noted.

**Table 4.7:** Abbreviations used in Table 4.6

| Abbreviation | Description   |
|--------------|---|
| BCRESOL      | Tracer for products from the bicyclic intermediate pathway from cresol oxidation.                       |
| BMCATECHOL   | Tracer for products from the bicyclic intermediate pathway from methyl catechol.                        |
| BOH3TOL      | Tracer for products from the bicyclic intermediate pathway from trihydroxy toluene.                     |
| BOH4TOL      | Tracer for products from the bicyclic intermediate pathway from tetrahydroxy toluene.                   |
| C5CO14OH     | Acetyl acrylic acid (one of the bicyclic intermediate pathway products from o-cresol oxidation in MCM). |
| CRESOL       | Cresol  |
| HOC6H4NO2    | Nitrophenol   |
| MCATEC1O     | Product from H-abstraction of OH group of methyl catechol   |
| MCATECHOL    | Methyl catechol   |
| MNCATECH     | Nitro dihydroxy toluene   |
| OH2MBQN      | Dihydroxy methyl benzoquinone   |
| OH3MBQN      | Trihydroxy methyl benzoquinone  |
| OH3TOL       | Trihydroxy toluene  |
| OH3TOL1O     | Product from H-abstraction of OH group of trihydroxy toluene  |
| OH3TOL1O     | Product from H-abstraction of OH group of tetrahydroxy toluene  |
| OH4TOL       | Tetrahydroxy toluene  |
| OH5TOL       | Pentahydroxy toluene  |
| OHMBQN       | Hydroxy methyl benzoquinone   |
| PTLQONE      | Methyl benzoquinone (one of the bicyclic intermediate pathway products from cresol oxidation in MCM)    |
| TOL1OHNO2    | Nitro hydroxy toluene   |

**Table 4.8:** Chamber conditions based on kinetic model (Version 1)

| Expt<br># | VOC-OH adduct rxn (%) |                 | <i>o</i> -cresol rxn (%) |                 | 3-methyl catechol rxn (%) |                 | RO <sub>2</sub> Reaction Partner (%)  |                  |                 |
|-----------|-----------------------|-----------------|--------------------------|-----------------|---------------------------|-----------------|---|------------------|-----------------|
|           | O <sub>2</sub>        | NO <sub>2</sub> | OH                       | NO <sub>3</sub> | OH                        | NO <sub>3</sub> | RO <sub>2</sub>   | HO <sub>2</sub>  | NO              |
| 1         | 94                    | 6               | >31                      | <69             | >41                       | <59             | ~0  | <1               | >99             |
| 2         | 100                   | 0               | 100                      | 0               | 100                       | 0               | <12   | >88              | ~0              |
| 3         | 94                    | 6               | >44                      | <56             | >44                       | <56             | ~0  | <1               | >99             |
| 4         | 100                   | 0               | 100                      | 0               | 100                       | 0               | <6  | >94              | ~0              |
| 5         | >99.9                 | <0.1            | >96                      | <4              | >91                       | <9              | ~0  | <1               | >99             |
| 6         | 100                   | 0               | 100                      | 0               | 100                       | 0               | <1  | >99              | ~0              |
| 7         | >99.9                 | <0.1            | NA                       | NA              | ~100                      | ~0              | ~0  | <2               | >98             |
| 8         | 100                   | 0               | NA                       | NA              | 100                       | 0               | No RO <sub>2</sub> forms in MCM<br>from low NO oxidation<br>of methyl catechol. |                  |                 |
| 9         | 100                   | 0               | NA                       | NA              | 100                       | 0               |   |                  |                 |
| 10        | 100                   | 0               | NA                       | NA              | 100                       | 0               |   |                  |                 |
| 11        | 100                   | 0               | NA                       | NA              | NA                        | NA              | ~16 <sup>a</sup>  | ~84 <sup>a</sup> | ~0 <sup>a</sup> |
| 12        | 97                    | 3               | NA                       | NA              | NA                        | NA              | ~0  | <4               | >96             |
| 13        | 100                   | 0               | 100                      | 0               | 100                       | 0               | <18   | >82              | ~0              |
| 14        | 90                    | 10              | >20                      | <80             | >34                       | <66             | ~0  | <1               | >99             |
| 15        | >99.9                 | <0.1            | >98                      | <2              | >94                       | <6              | ~0  | <1               | >99             |

<sup>a</sup> Throughout most of the experiment, the peroxy radical distribution was that stated. However, over the first hour there was exponential convergence to these steady state values from RO<sub>2</sub> + RO<sub>2</sub> = 100% and RO<sub>2</sub> + HO<sub>2</sub> = 0%.



## **DART-MS Analysis Details and Product Identification**

### **DART-MS Analysis Details**

A mass calibrant and an independent quality assurance/quality control (QA/QC) compound were run with each sample set to ensure mass accuracy to within 5 mDa. The mass calibrant used for positive mode was polyethylene glycol (average molecular weight of 600 amu, PEG-600; Acros Organics, Geel, Belgium), which was dissolved in methanol. The independent QA/QC compound used is reserpine, which was purchased from Sigma-Aldrich and diluted in methanol.

Tweezers were used to introduce the samples into the DART gas stream. Before analysis, the tweezers were rinsed with acetone, and were introduced into the gas stream to vaporize any contaminants. A strip (~1 cm) was cut from each sample substrate for testing. The cutting was tested in triplicate, with each sampling being from a different area of the substrate.

In these studies, a solution of PEG-600 (50  $\mu\text{L}$  in 10 mL of methanol) was used to calibrate (61-679 Da) the mass spectrometer for each run. Acceptable calibration was determined if the calibration Mass Center software produced a residual value of  $>9 \times 10^{-12}$ . To ensure proper calibration, a solution of reserpine (5 mg in 10 mL of methanol) was analyzed subsequent to the PEG-600 in every sample run. Calibration was deemed sufficient if the  $m/z$  of reserpine fell within  $\pm 0.005$  Da of the theoretical value (609.281 Da).

The instrument used was a JEOL (Tokyo, Japan) AccuTOF™ mass spectrometer (JMS-T100LC) coupled with an IonSense (Saugus, MA, USA) DART® source. Ultra-pure helium was used as the ionizing gas with a flow rate of  $1.75 \text{ L min}^{-1}$ . For all analyses, the DART® source was set to a needle voltage of  $\pm 3.5 \text{ kV}$ . Electrode 1 and electrode 2 voltages were both set to  $\pm 150 \text{ V}$ . Mass spectrometer settings include: an orifice 1 voltage of  $\pm 20 \text{ V}$ , orifice 2 voltage of  $\pm 5 \text{ V}$ , a ring lens voltage of  $\pm 5 \text{ V}$ , a peak voltage of  $1500 \text{ V}$ , a mass range of  $50 - 1500 \text{ m/z}$  at 0.5 seconds per scan. A helium gas stream temperature of  $325^\circ\text{C}$  was also employed.

### **DART-MS Product Identification**

Best available knowledge was used to assign the compounds displayed in Tables 4.9, 4.10, and 4.11. The smaller compounds could be fragmentation products.  $\text{C}_x\text{H}_y\text{NO}$  and  $\text{C}_x\text{H}_y\text{NO}_2$  were assumed to be amines. These products could also be small nitro or nitroso compounds or fragmentation products of nitrates. Products that appeared to be fragmentation products (i.e., reasonable structures could not be

drawn) were excluded from the list. The structure of each compound was necessary to estimate the vapor pressure. The most probable dominant isomer was selected in all cases, but there are likely many additional structural isomers that form as well. The abundances reported in Tables 4.9, 4.10, and 4.11 are not meant to be used quantitatively due to uncertainties in the vapor pressure estimation methods and centroid fitting algorithm. Often each  $m/z$  contained many over-lapping peaks and corrections were not made for isotope effects.

**Table 4.9:** DART-MS data from low NO toluene oxidation (experiment 13).

| m/z (+) (Da) | Intensity (A.U.) | C | H  | N | O | $\Delta$ (mDa) <sup>a</sup> | Smiles                        | Est. VP (atm) <sup>b</sup> | Abundance ( $R_f$ ) |
|--------------|------------------|---|----|---|---|-----------------------------|-------------------------------|----------------------------|---------------------|
| 69.067377    | 6671.45          | 5 | 8  | 0 | 0 | 3.05                        | <chem>C=CC=CC</chem>          | 6.49E-01 (E)               | 3.42E-12            |
| 71.046739    | 11123.71         | 4 | 6  | 0 | 1 | 2.95                        | <chem>CC=CC=O</chem>          | 8.30E-02 (E)               | 4.46E-11            |
| 71.081281    | 3477.48          | 5 | 10 | 0 | 0 | 4.79                        | <chem>C=CCCC</chem>           | 6.49E-01 (E)               | 1.78E-12            |
| 73.064072    | 4280.44          | 4 | 8  | 0 | 1 | 1.27                        | <chem>CCCC=O</chem>           | 1.27E-01 (E)               | 1.12E-11            |
| 75.04371     | 5382.00          | 3 | 6  | 0 | 2 | 0.89                        | <chem>CC(CO)=O</chem>         | 6.92E-03 (E)               | 2.59E-10            |
| 80.048339    | 155429.63        | 5 | 5  | 1 | 0 | 1.69                        | <chem>C1=CC=CC=N1</chem>      | 3.46E-02 (N)               | 1.50E-09            |
| 83.082762    | 4393.36          | 6 | 10 | 0 | 0 | 3.31                        | <chem>C=CCCC=C</chem>         | 2.12E-01 (E)               | 6.89E-12            |
| 85.025484    | 4539.76          | 4 | 4  | 0 | 2 | 3.47                        | <chem>O=CC=CC=O</chem>        | 3.42E-03 (E)               | 4.41E-10            |
| 87.039802    | 7748.51          | 4 | 6  | 0 | 2 | 4.80                        | <chem>O=CCCC=O</chem>         | 6.19E-03 (E)               | 4.16E-10            |
| 97.026419    | 6180.71          | 5 | 4  | 0 | 2 | 2.53                        | <chem>O=CC1=CC=CO1</chem>     | 2.96E-03 (N)               | 6.95E-10            |
| 97.055251    | 2871.86          | 6 | 8  | 0 | 1 | 10.09                       | <chem>CC(C=CC=C)=O</chem>     | 8.87E-03 (E)               | 1.08E-10            |
| 97.101391    | 2954.88          | 7 | 12 | 0 | 0 | 0.33                        | <chem>CC1C=CCCC1</chem>       | 6.93E-02 (E)               | 1.42E-11            |
| 99.043366    | 9545.71          | 5 | 6  | 0 | 2 | 1.24                        | <chem>O=C(C)C=CC=O</chem>     | 1.12E-03 (E)               | 2.84E-09            |
| 99.072496    | 3758.17          | 6 | 10 | 0 | 1 | 8.49                        | <chem>CC(C=CCC)=O</chem>      | 8.87E-03 (E)               | 1.41E-10            |
| 101.057523   | 4501.87          | 5 | 8  | 0 | 2 | 2.73                        | <chem>O=C(C)CCC=O</chem>      | 2.02E-03 (E)               | 7.40E-10            |
| 109.035545   | 3507.03          | 6 | 4  | 0 | 2 | -6.59                       | <chem>O=C1C=CC(C=C1)=O</chem> | 2.48E-05 (E)               | 4.69E-08            |
| 109.096678   | 4467.03          | 8 | 12 | 0 | 0 | 5.05                        | <chem>C=CC=CC=CCC</chem>      | 2.27E-02 (E)               | 6.55E-11            |
| 111.043476   | 6721.86          | 6 | 6  | 0 | 2 | 1.13                        | <chem>O=CC1=CC=C(O1)C</chem>  | 1.25E-03 (N)               | 1.79E-09            |
| 111.11751    | 3129.72          | 8 | 14 | 0 | 0 | -0.13                       | <chem>CCC=CC=CCC</chem>       | 2.27E-02 (E)               | 4.59E-11            |

**Table 4.9:** DART-MS data from low NO toluene oxidation (experiment 13).

| m/z (+) (Da) | Intensity (A.U.) | C  | H  | N | O | $\Delta$ (mDa) <sup>a</sup> | Smiles                                 | Est. VP (atm) <sup>b</sup> | Abundance (R <sub>f</sub> ) |
|--------------|------------------|----|----|---|---|-----------------------------|--|----------------------------|-----------------------------|
| 113.019938   | 3471.30          | 5  | 4  | 0 | 3 | 3.93                        | <chem>O=C1C(C)=CC(O1)=O</chem>         | 7.03E-04 (E)               | 1.64E-09                    |
| 113.05728    | 4021.97          | 6  | 8  | 0 | 2 | 2.97                        | <chem>O=CCCC=CC=O</chem>               | 4.92E-04 (E)               | 2.72E-09                    |
| 115.038947   | 6483.21          | 5  | 6  | 0 | 3 | 0.57                        | <chem>O=C(C)C=CC(O)=O</chem>           | 6.57E-06 (E)               | 3.28E-07                    |
| 115.064062   | 2955.96          | 6  | 10 | 0 | 2 | 11.84                       | <chem>O=CCCCC=O</chem>                 | 6.62E-04 (E)               | 1.49E-09                    |
| 127.039667   | 5945.22          | 6  | 6  | 0 | 3 | -0.15                       | <chem>O=C(C)C=CC(C=O)=O</chem>         | 1.64E-04 (E)               | 1.21E-08                    |
| 127.112254   | 4155.67          | 8  | 14 | 0 | 1 | 0.04                        | <chem>O=CCCCC=CC</chem>                | 1.45E-03 (E)               | 9.55E-10                    |
| 129.053327   | 4254.59          | 6  | 8  | 0 | 3 | 1.84                        | <chem>O=C(C=CC(O)C=O)C</chem>          | 6.36E-05 (E)               | 2.22E-08                    |
| 139.034538   | 5275.37          | 7  | 6  | 0 | 3 | 4.98                        | <chem>CC1=CC(C=C(O)C1=O)=O</chem>      | 5.26E-07 (E)               | 3.34E-06                    |
| 141.050361   | 3122.55          | 7  | 8  | 0 | 3 | 4.81                        | <chem>CC1=CC=C(O)C(O)=C1O</chem>       | 5.97E-08 (N)               | 1.74E-05                    |
| 155.034837   | 3399.08          | 7  | 6  | 0 | 4 | -0.40                       | <chem>CC1=CC(C(O)=C(O)C1=O)=O</chem>   | 8.26E-09 (E)               | 1.37E-04                    |
| 157.045695   | 8025.67          | 7  | 8  | 0 | 4 | 4.39                        | <chem>CC1=CC(O)=C(O)C(O)=C1O</chem>    | 3.28E-10 (N)               | 8.13E-03                    |
| 161.091424   | 2838.46          | 11 | 12 | 0 | 1 | 5.22                        | <chem>O=CC=CC=CC=CC=C</chem>           | 3.32E-05 (E)               | 2.85E-08                    |
| 173.044149   | 3338.73          | 7  | 8  | 0 | 5 | 0.85                        | <chem>CC1=C(O)C(O)=C(C(O)=C1O)O</chem> | 1.12E-12 (N)               | 9.92E-01                    |
| 203.10019    | 3898.22          | 13 | 14 | 0 | 2 | 7.01                        | <chem>O=CC=CC=CC=CC=CC(C)=O</chem>     | 1.46E-07 (E)               | 8.87E-06                    |

<sup>a</sup> The difference between the measured and proposed compound exact mass. <sup>b</sup> Est. VP = Estimated vapor pressure. Estimation Method in parenthesis: E = EVAPORATION method and N = Nannoolal method.

**Table 4.10:** DART-MS data from high NO *o*-cresol oxidation (experiment 15).

| m/z (+) (Da) | Intensity <sup>a</sup> | C | H  | N | O | $\Delta$ <sup>b</sup> (mDa) | Smiles                    | Est. VP (atm) <sup>c</sup> | Abundance ( $R_f$ ) |
|--------------|------------------------|---|----|---|---|-----------------------------|---------------------------|----------------------------|---------------------|
| 69.06738     | 4799.51                | 5 | 8  | 0 | 0 | 3.05                        | <chem>C=CC=CC</chem>      | 6.49E-01 (E)               | 1.17E-11            |
| 71.04674     | 7360.97                | 4 | 6  | 0 | 1 | 2.95                        | <chem>CC=CC=O</chem>      | 8.30E-02 (E)               | 1.40E-10            |
| 73.06407     | 3055.72                | 4 | 8  | 0 | 1 | 1.27                        | <chem>CCCC=O</chem>       | 1.27E-01 (E)               | 3.82E-11            |
| 75.04371     | 3495.06                | 3 | 6  | 0 | 2 | 0.89                        | <chem>CC(CO)=O</chem>     | 6.92E-03 (E)               | 7.99E-10            |
| 76.0358      | 2830.61                | 2 | 5  | 1 | 2 | 4.06                        | <chem>OCC(N)=O</chem>     | 5.43E-08 (N)               | 8.25E-05            |
| 80.04834     | 2555.95                | 5 | 5  | 1 | 0 | 1.69                        | <chem>C1=CC=CC=N1</chem>  | 3.46E-02 (N)               | 1.17E-10            |
| 81.0676      | 2116.91                | 6 | 8  | 0 | 0 | 2.83                        | <chem>C=CC=CC=C</chem>    | 2.12E-01 (E)               | 1.58E-11            |
| 83.08276     | 2977.45                | 6 | 10 | 0 | 0 | 3.31                        | <chem>C=CCCC=C</chem>     | 2.12E-01 (E)               | 2.22E-11            |
| 85.02548     | 2862.51                | 4 | 4  | 0 | 2 | 3.47                        | <chem>O=CC=CC=O</chem>    | 3.42E-03 (E)               | 1.32E-09            |
| 85.06327     | 2015.80                | 5 | 8  | 0 | 1 | 2.07                        | <chem>CC(C=CC)=O</chem>   | 2.71E-02 (E)               | 1.17E-10            |
| 87.04526     | 4217.44                | 4 | 6  | 0 | 2 | -0.66                       | <chem>O=CCCC=O</chem>     | 6.19E-03 (E)               | 1.08E-09            |
| 94.06261     | 2373.32                | 6 | 7  | 1 | 0 | 3.06                        | <chem>N1C=CC=CC=C1</chem> | 2.04E-02 (N)               | 1.84E-10            |
| 95.08159     | 1934.09                | 7 | 10 | 0 | 0 | 4.49                        | <chem>CC1C=CCC=C1</chem>  | 6.93E-02 (E)               | 4.41E-11            |
| 97.02642     | 4443.40                | 5 | 4  | 0 | 2 | 2.53                        | <chem>O=CC1=CC=CO1</chem> | 2.96E-03 (N)               | 2.38E-09            |
| 97.06102     | 3408.60                | 6 | 8  | 0 | 1 | 4.32                        | <chem>CC(C=CC=C)=O</chem> | 8.87E-03 (E)               | 6.08E-10            |
| 97.09562     | 2367.86                | 7 | 12 | 0 | 0 | 6.10                        | <chem>CC1C=CCCC1</chem>   | 6.93E-02 (E)               | 5.40E-11            |
| 98.06128     | 2115.28                | 5 | 7  | 1 | 1 | -0.69                       | <chem>NC(C=CC=C)=O</chem> | 1.44E-06 (N)               | 2.33E-06            |
| 99.04337     | 5939.65                | 5 | 6  | 0 | 2 | 1.24                        | <chem>O=C(C)C=CC=O</chem> | 1.12E-03 (E)               | 8.40E-09            |
| 99.07832     | 3689.73                | 6 | 10 | 0 | 1 | 2.67                        | <chem>CC(C=CCC)=O</chem>  | 8.87E-03 (E)               | 6.58E-10            |

**Table 4.10:** DART-MS data from high NO *o*-cresol oxidation (experiment 15).

| m/z (+) (Da) | Intensity <sup>a</sup> | C | H  | N | O | $\Delta$ <sup>b</sup> (mDa) | Smiles                          | Est. VP (atm) <sup>c</sup> | Abundance (R <sub>f</sub> ) |
|--------------|------------------------|---|----|---|---|-----------------------------|---------------------------------|----------------------------|-----------------------------|
| 100.0362     | 2821.45                | 4 | 5  | 1 | 2 | 3.65                        | <chem>O=CC=CC(N)=O</chem>       | 2.02E-07 (N)               | 2.21E-05                    |
| 101.0222     | 2194.10                | 4 | 4  | 0 | 3 | 1.65                        | <chem>O=CC=CC(O)=O</chem>       | 2.01E-05 (E)               | 1.73E-07                    |
| 101.0575     | 3823.68                | 5 | 8  | 0 | 2 | 2.73                        | <chem>O=C(C)CCC=O</chem>        | 2.02E-03 (E)               | 2.99E-09                    |
| 102.0545     | 2971.25                | 4 | 7  | 1 | 2 | 1.54                        | <chem>NCC=CC(O)=O</chem>        | 2.92E-05 (N)               | 1.61E-07                    |
| 104.0332     | 5611.42                | 3 | 5  | 1 | 3 | 1.60                        | <chem>CC=CON(=O)=O</chem>       | 2.60E-02 (E)               | 3.42E-10                    |
| 109.1028     | 3360.34                | 8 | 12 | 0 | 0 | -1.07                       | <chem>C=CC=CC=CCC</chem>        | 2.27E-02 (E)               | 2.34E-10                    |
| 111.0435     | 4461.87                | 6 | 6  | 0 | 2 | 1.13                        | <chem>O=CC1=CC=C(O1)C</chem>    | 1.25E-03 (N)               | 5.64E-09                    |
| 111.1175     | 2507.94                | 8 | 14 | 0 | 0 | -0.13                       | <chem>CCC=CC=CCC</chem>         | 2.27E-02 (E)               | 1.75E-10                    |
| 113.0262     | 1862.29                | 5 | 4  | 0 | 3 | -2.29                       | <chem>O=C1C(C)=CC(O1)=O</chem>  | 7.03E-04 (E)               | 4.19E-09                    |
| 113.0573     | 3145.91                | 6 | 8  | 0 | 2 | 2.97                        | <chem>O=CCCC=CC=O</chem>        | 4.92E-04 (E)               | 1.01E-08                    |
| 114.0553     | 2382.57                | 5 | 7  | 1 | 2 | 0.17                        | <chem>C=C(C=CC(O)=O)N</chem>    | 1.45E-05 (N)               | 2.59E-07                    |
| 115.0389     | 3284.56                | 5 | 6  | 0 | 3 | 0.57                        | <chem>O=C(C)C=CC(O)=O</chem>    | 6.57E-06 (E)               | 7.90E-07                    |
| 115.0703     | 2005.33                | 6 | 10 | 0 | 2 | 5.56                        | <chem>O=CCCCC=O</chem>          | 6.62E-04 (E)               | 4.79E-09                    |
| 118.0469     | 2527.17                | 4 | 7  | 1 | 3 | 3.51                        | <chem>CCC=CON(=O)=O</chem>      | 8.50E-03 (E)               | 4.71E-10                    |
| 120.0524     | 3185.49                | 4 | 9  | 1 | 3 | 13.66                       | <chem>CCCCON(=O)=O</chem>       | 8.50E-03 (E)               | 5.93E-10                    |
| 126.0519     | 1896.52                | 6 | 7  | 1 | 2 | 3.58                        | <chem>OC1=CN=C(C)C(O)=C1</chem> | 1.36E-05 (N)               | 2.20E-07                    |
| 127.0397     | 3814.74                | 6 | 6  | 0 | 3 | -0.15                       | <chem>O=C(C)C=CC(C=O)=O</chem>  | 1.64E-04 (E)               | 3.68E-08                    |
| 127.0661     | 2199.51                | 7 | 10 | 0 | 2 | 9.84                        | <chem>O=C(C)CC=CCC=O</chem>     | 2.16E-04 (E)               | 1.61E-08                    |
| 127.1123     | 3306.85                | 8 | 14 | 0 | 1 | 0.04                        | <chem>O=CCCCC=CC</chem>         | 1.45E-03 (E)               | 3.61E-09                    |

**Table 4.10:** DART-MS data from high NO *o*-cresol oxidation (experiment 15).

| m/z (+) (Da) | Intensity <sup>a</sup> | C  | H  | N | O | $\Delta$ <sup>b</sup> (mDa) | Smiles   | Est. VP (atm) <sup>c</sup> | Abundance (R <sub>f</sub> ) |
|--------------|------------------------|----|----|---|---|-----------------------------|--|----------------------------|-----------------------------|
| 128.071      | 1864.39                | 6  | 9  | 1 | 2 | 0.14                        | <chem>O=C(C=CC=CCN)O</chem>                              | 3.46E-06 (N)               | 8.52E-07                    |
| 129.0533     | 2463.10                | 6  | 8  | 0 | 3 | 1.84                        | <chem>O=C(C=CC(O)C=O)C</chem>                            | 6.36E-05 (E)               | 6.12E-08                    |
| 130.0527     | 1871.23                | 5  | 7  | 1 | 3 | -2.32                       | <chem>O=N(OC=CC=CC)=O</chem>                             | 2.78E-03 (E)               | 1.07E-09                    |
| 139.0414     | 2114.31                | 7  | 6  | 0 | 3 | -1.92                       | <chem>CC1=CC(C=C(O)C1=O)=O</chem>                        | 5.26E-07 (E)               | 6.36E-06                    |
| 142.0463     | 2154.17                | 6  | 7  | 1 | 3 | 4.15                        | <chem>C=CC=CC(ON(=O)=O)=C</chem>                         | 9.08E-04 (E)               | 3.75E-09                    |
| 154.0524     | 1956.21                | 7  | 7  | 1 | 3 | -2.01                       | <chem>OC1=C(N(=O)=O)C=CC=C1C</chem>                      | 1.77E-05 (N)               | 1.75E-07                    |
| 155.0348     | 3607.35                | 7  | 6  | 0 | 4 | -0.40                       | <chem>CC1=CC(C(O)=C(O)C1=O)=O</chem>                     | 8.26E-09 (E)               | 6.91E-04                    |
| 157.0457     | 1941.16                | 7  | 8  | 0 | 4 | 4.39                        | <chem>CC1=CC(O)=C(O)C(O)=C1O</chem>                      | 3.28E-10 (N)               | 9.36E-03                    |
| 267.1658     | 2870.33                | 15 | 22 | 0 | 4 | -6.13                       | <chem>OC(OC1=C(O)C(O)=CC=C1C)CCCC=CC</chem> <sup>c</sup> | 4.59E-12 (N)               | 9.90E-01                    |

<sup>a</sup> (A.U.) <sup>b</sup> The difference between the measured and proposed compound exact mass. <sup>c</sup> Est. VP = Estimated vapor pressure. Estimation Method in parenthesis: E = EVAPORATION method, and N = Nannoolal method. <sup>c</sup> Smiles in table is that of the structure predicted to form. Vapor pressure method could not estimate the vapor pressure of this structure so a very similar structure was used instead (OC(C(O)=CC=C1C)=C1OCC(O)CCCC=CC).

**Table 4.11:** DART-MS data from high NO toluene oxidation (experiment 14).

| m/z (+) (Da) | Intensity <sup>a</sup> | C | H  | N | O | $\Delta$ <sup>b</sup> (mDa) | Smiles       | Est. VP (atm) <sup>c</sup> | Abundance ( $R_f$ ) |
|--------------|------------------------|---|----|---|---|-----------------------------|--------------|----------------------------|---------------------|
| 61.026497    | 5540.57                | 2 | 4  | 0 | 2 | 2.46                        | CC(O)=O      | 4.49E-03 (E)               | 7.02E-10            |
| 69.067377    | 1410.70                | 5 | 8  | 0 | 0 | 3.05                        | C=CC=CC      | 6.49E-01 (E)               | 1.24E-12            |
| 76.035796    | 3623.11                | 2 | 5  | 1 | 2 | 4.06                        | OCC(N)=O     | 5.43E-08 (N)               | 3.80E-05            |
| 80.048339    | 1641.73                | 5 | 5  | 1 | 0 | 1.69                        | C1=CC=CC=N1  | 3.46E-02 (N)               | 2.71E-11            |
| 83.082762    | 1684.25                | 6 | 10 | 0 | 0 | 3.31                        | C=CCCC=C     | 2.12E-01 (E)               | 4.52E-12            |
| 85.025484    | 2836.08                | 4 | 4  | 0 | 2 | 3.47                        | O=CC=CC=O    | 3.42E-03 (E)               | 4.72E-10            |
| 87.007038    | 2179.84                | 3 | 2  | 0 | 3 | 1.18                        | O=CC(C=O)=O  | 7.03E-02 (E)               | 1.77E-11            |
| 87.039802    | 6440.08                | 4 | 6  | 0 | 2 | 4.80                        | O=CCCC=O     | 6.19E-03 (E)               | 5.93E-10            |
| 90.013837    | 2080.44                | 2 | 3  | 1 | 3 | 5.28                        | C=CON(=O)=O  | 7.95E-02 (E)               | 1.49E-11            |
| 90.047162    | 1148.22                | 3 | 7  | 1 | 2 | 8.34                        | OC(C)C(N)=O  | 2.13E-07 (N)               | 3.07E-06            |
| 94.06261     | 7800.17                | 6 | 7  | 1 | 0 | 3.06                        | N1C=CC=CC=C1 | 2.04E-02 (N)               | 2.18E-10            |
| 95.053048    | 1261.49                | 6 | 6  | 0 | 1 | -3.36                       | OC1=CC=CC=C1 | 1.44E-03 (N)               | 4.98E-10            |
| 95.081585    | 1364.08                | 7 | 10 | 0 | 0 | 4.49                        | CC1C=CCC=C1  | 6.93E-02 (E)               | 1.12E-11            |
| 97.026419    | 6227.32                | 5 | 4  | 0 | 2 | 2.53                        | O=CC1=CC=CO1 | 2.96E-03 (N)               | 1.20E-09            |
| 97.061018    | 4637.55                | 6 | 8  | 0 | 1 | 4.32                        | CC(C=CC=C)=O | 8.87E-03 (E)               | 2.98E-10            |
| 98.06128     | 1349.16                | 5 | 7  | 1 | 1 | -0.69                       | NC(C=CC=C)=O | 1.44E-06 (N)               | 5.35E-07            |
| 99.043366    | 11466.81               | 5 | 6  | 0 | 2 | 1.24                        | O=C(C)C=CC=O | 1.12E-03 (E)               | 5.84E-09            |
| 99.089977    | 2449.13                | 6 | 10 | 0 | 1 | -8.99                       | CC(C=CCC)=O  | 8.87E-03 (E)               | 1.57E-10            |
| 100.042055   | 2453.04                | 4 | 5  | 1 | 2 | -2.20                       | O=CC=CC(N)=O | 2.02E-07 (N)               | 6.91E-06            |



**Table 4.11:** DART-MS data from high NO toluene oxidation (experiment 14).

| m/z (+) (Da) | Intensity <sup>a</sup> | C | H  | N | O | $\Delta$ <sup>b</sup> (mDa) | Smiles            | Est. VP (atm) <sup>c</sup> | Abundance (R <sub>f</sub> ) |
|--------------|------------------------|---|----|---|---|-----------------------------|-------------------|----------------------------|-----------------------------|
| 100.071332   | 1379.97                | 5 | 9  | 1 | 1 | 4.91                        | NC(C=CCC)=O       | 2.52E-06 (N)               | 3.12E-07                    |
| 101.022218   | 2932.23                | 4 | 4  | 0 | 3 | 1.65                        | O=CC=CC(O)=O      | 2.01E-05 (E)               | 8.30E-08                    |
| 101.051638   | 1499.95                | 5 | 8  | 0 | 2 | 8.62                        | O=C(C)CCC=O       | 2.02E-03 (E)               | 4.22E-10                    |
| 102.054463   | 1439.00                | 4 | 7  | 1 | 2 | 1.54                        | NCC=CC(O)=O       | 2.92E-05 (N)               | 2.81E-08                    |
| 102.089947   | 2487.60                | 5 | 11 | 1 | 1 | 1.94                        | NC(CCCC)=O        | 3.50E-06 (N)               | 4.05E-07                    |
| 103.03847    | 1574.86                | 4 | 6  | 0 | 3 | 1.05                        | CC(C(C=O)O)=O     | 2.00E-03 (E)               | 4.48E-10                    |
| 104.033168   | 2667.65                | 3 | 5  | 1 | 3 | 1.60                        | CC=CON(=O)=O      | 2.60E-02 (E)               | 5.85E-11                    |
| 105.014648   | 2141.85                | 3 | 4  | 0 | 4 | 4.14                        | O=C(O)C(CO)=O     | 2.22E-06 (E)               | 5.49E-07                    |
| 109.096678   | 3357.59                | 8 | 12 | 0 | 0 | 5.05                        | C=CC=CC=CCC       | 2.27E-02 (E)               | 8.44E-11                    |
| 110.058713   | 1424.19                | 6 | 7  | 1 | 1 | 1.88                        | OC1=CC=CN=C1C     | 1.53E-03 (N)               | 5.29E-10                    |
| 111.043476   | 4684.00                | 6 | 6  | 0 | 2 | 1.13                        | O=CC1=CC=C(O1)C   | 1.25E-03 (N)               | 2.13E-09                    |
| 112.038821   | 2037.51                | 5 | 5  | 1 | 2 | 1.03                        | OC1=CC(O)=CN=C1   | 5.32E-05 (N)               | 2.18E-08                    |
| 113.026161   | 2657.15                | 5 | 4  | 0 | 3 | -2.29                       | O=C1C(C)=CC(O1)=O | 7.03E-04 (E)               | 2.15E-09                    |
| 113.05728    | 3740.34                | 6 | 8  | 0 | 2 | 2.97                        | O=CCCC=CC=O       | 4.92E-04 (E)               | 4.33E-09                    |
| 114.055338   | 2438.47                | 5 | 7  | 1 | 2 | 0.17                        | C=C(C=CC(O)=O)N   | 1.45E-05 (N)               | 9.56E-08                    |
| 115.038947   | 7677.84                | 5 | 6  | 0 | 3 | 0.57                        | O=C(C)C=CC(O)=O   | 6.57E-06 (E)               | 6.65E-07                    |
| 116.033084   | 1330.37                | 4 | 5  | 1 | 3 | 1.68                        | C=CC=CON(=O)=O    | 8.50E-03 (E)               | 8.92E-11                    |
| 116.064614   | 1348.08                | 5 | 9  | 1 | 2 | 6.54                        | CC(N)C=CC(O)=O    | 1.87E-05 (N)               | 4.12E-08                    |
| 117.050497   | 2483.76                | 5 | 8  | 0 | 3 | 4.67                        | O=C(C)CCC(O)=O    | 1.00E-05 (E)               | 1.41E-07                    |

**Table 4.11:** DART-MS data from high NO toluene oxidation (experiment 14).

| m/z (+) (Da) | Intensity <sup>a</sup> | C | H  | N | O | $\Delta$ <sup>b</sup> (mDa) | Smiles                             | Est. VP (atm) <sup>c</sup> | Abundance ( $R_f$ ) |
|--------------|------------------------|---|----|---|---|-----------------------------|------------------------------------|----------------------------|---------------------|
| 118.046909   | 1887.46                | 4 | 7  | 1 | 3 | 3.51                        | <chem>CCC=CON(=O)=O</chem>         | 8.50E-03 (E)               | 1.27E-10            |
| 123.046863   | 1686.79                | 7 | 6  | 0 | 2 | -2.26                       | <chem>CC1=CC(C=CC1=O)=O</chem>     | 8.12E-06 (E)               | 1.18E-07            |
| 125.06148    | 1442.25                | 7 | 8  | 0 | 2 | -1.23                       | <chem>CC1=CC=CC(O)=C1O</chem>      | 6.77E-06 (N)               | 1.21E-07            |
| 126.051919   | 2178.90                | 6 | 7  | 1 | 2 | 3.58                        | <chem>OC1=CN=C(C)C(O)=C1</chem>    | 1.36E-05 (N)               | 9.10E-08            |
| 127.039667   | 4187.31                | 6 | 6  | 0 | 3 | -0.15                       | <chem>O=C(C)C=CC(C=O)=O</chem>     | 1.64E-04 (E)               | 1.46E-08            |
| 127.112254   | 3174.50                | 8 | 14 | 0 | 1 | 0.04                        | <chem>O=CCCCC=CC</chem>            | 1.45E-03 (E)               | 1.25E-09            |
| 128.03127    | 2068.51                | 5 | 5  | 1 | 3 | 3.50                        | <chem>O=N(C1=CC=C(C)O1)=O</chem>   | 1.93E-03 (N)               | 6.09E-10            |
| 129.053327   | 3905.59                | 6 | 8  | 0 | 3 | 1.84                        | <chem>O=C(C=CC(O)C=O)C</chem>      | 6.36E-05 (E)               | 3.50E-08            |
| 130.052743   | 1472.64                | 5 | 7  | 1 | 3 | -2.32                       | <chem>O=N(OC=CC=CC)=O</chem>       | 2.78E-03 (E)               | 3.02E-10            |
| 131.035911   | 1919.85                | 5 | 6  | 0 | 4 | -1.48                       | <chem>OC(C(O)=C(C=O)C)=O</chem>    | 1.09E-07 (E)               | 1.00E-05            |
| 131.062715   | 1156.33                | 6 | 10 | 0 | 3 | 8.10                        | <chem>O=C(C)CCC(C=O)O</chem>       | 4.99E-05 (E)               | 1.32E-08            |
| 133.047111   | 1311.02                | 5 | 8  | 0 | 4 | 2.97                        | <chem>OC(C(C(C)C=O)O)=O</chem>     | 1.22E-01 (E)               | 6.13E-12            |
| 138.049261   | 2335.43                | 7 | 7  | 1 | 2 | 6.24                        | <chem>CC1=C(N(=O)=O)C=CC=C1</chem> | 2.18E-04 (N)               | 6.12E-09            |
| 139.034538   | 2994.57                | 7 | 6  | 0 | 3 | 4.98                        | <chem>CC1=CC(C=C(O)C1=O)=O</chem>  | 5.26E-07 (E)               | 3.24E-06            |
| 140.030245   | 2170.62                | 6 | 5  | 1 | 3 | 4.52                        | <chem>OC1=CC=CC=C1N(=O)=O</chem>   | 8.71E-05 (N)               | 1.42E-08            |
| 141.050361   | 5078.50                | 7 | 8  | 0 | 3 | 4.81                        | <chem>CC1=CC=C(O)C(O)=C1O</chem>   | 5.97E-08 (N)               | 4.85E-05            |
| 142.046271   | 3022.13                | 6 | 7  | 1 | 3 | 4.15                        | <chem>C=CC=CC(ON(=O)=O)=C</chem>   | 9.08E-04 (E)               | 1.90E-09            |
| 143.031682   | 2933.82                | 6 | 6  | 0 | 4 | 2.75                        | <chem>O=C(C)C=CC(C(O)=O)=O</chem>  | 5.77E-07 (E)               | 2.90E-06            |
| 145.047972   | 2291.30                | 6 | 8  | 0 | 4 | 2.11                        | <chem>O=C(C=CC(O)C(O)=O)C</chem>   | 3.56E-08 (E)               | 3.66E-05            |

**Table 4.11:** DART-MS data from high NO toluene oxidation (experiment 14).

| m/z (+) (Da) | Intensity <sup>a</sup> | C  | H  | N | O | $\Delta$ <sup>b</sup> (mDa) | Smiles                                     | Est. VP (atm) <sup>c</sup> | Abundance ( $R_f$ ) |
|--------------|------------------------|----|----|---|---|-----------------------------|--|----------------------------|---------------------|
| 152.068107   | 1146.80                | 8  | 9  | 1 | 2 | 3.05                        | <chem>NC(C=CC=CC=CC=O)=O</chem>            | 4.05E-09 (N)               | 1.61E-04            |
| 154.045164   | 2966.87                | 7  | 7  | 1 | 3 | 5.25                        | <chem>OC1=C(N(=O)=O)C=CC=C1C</chem>        | 1.77E-05 (N)               | 9.55E-08            |
| 155.034837   | 3800.38                | 7  | 6  | 0 | 4 | -0.40                       | <chem>CC1=CC(C(O)=C(O)C1=O)=O</chem>       | 8.26E-09 (E)               | 2.62E-04            |
| 156.06424    | 1417.63                | 7  | 9  | 1 | 3 | 1.83                        | <chem>CC=CC=CC=CON(=O)=O</chem>            | 2.97E-04 (E)               | 2.72E-09            |
| 157.045695   | 5036.75                | 7  | 8  | 0 | 4 | 4.39                        | <chem>CC1=CC(O)=C(O)C(O)=C1O</chem>        | 3.28E-10 (N)               | 8.74E-03            |
| 158.044945   | 1517.74                | 6  | 7  | 1 | 4 | 0.39                        | <chem>O=N(OC=CC(CC=C)=O)=O</chem>          | 3.80E-05 (E)               | 2.27E-08            |
| 159.062128   | 1321.64                | 7  | 10 | 0 | 4 | 3.61                        | <chem>CC(C=CC(C(O)C=O)O)=O</chem>          | 3.41E-07 (E)               | 2.21E-06            |
| 161.046849   | 1846.47                | 6  | 8  | 0 | 5 | -1.85                       | <chem>O=C(CO)C=CC(C(O)=O)O</chem>          | 1.79E-10 (E)               | 5.89E-03            |
| 170.046401   | 1573.59                | 7  | 7  | 1 | 4 | -1.07                       | <chem>OC1=C(O)C(N(=O)=O)=CC=C1C</chem>     | 2.01E-07 (N)               | 4.46E-06            |
| 173.044149   | 1855.62                | 7  | 8  | 0 | 5 | 0.85                        | <chem>CC1=C(O)C(O)=C(C(O)=C1O)O</chem>     | 1.12E-12 (N)               | 9.44E-01            |
| 174.069813   | 1324.07                | 7  | 11 | 1 | 4 | 6.82                        | <chem>O=N(OC=CCCCC=O)=O</chem>             | 1.90E-05 (E)               | 3.98E-08            |
| 175.059781   | 1319.16                | 7  | 10 | 0 | 5 | 0.87                        | <chem>O=C(C)C=CC(O)C(O)C(O)=O</chem>       | 1.33E-10 (E)               | 5.64E-03            |
| 177.157199   | 1399.51                | 9  | 20 | 0 | 3 | -8.13                       | <chem>CCCCC(O)C(O)CCCO</chem>              | 2.29E-09 (E)               | 3.49E-04            |
| 178.069959   | 2175.62                | 6  | 11 | 1 | 5 | 1.59                        | <chem>O=N(OCCCCC(O)=O)=O</chem>            | 2.20E-07 (E)               | 5.63E-06            |
| 223.064145   | 2037.80                | 11 | 10 | 0 | 5 | -3.50                       | <chem>O=C(O)C=CC=CC=CC=CC(C(O)=O)=O</chem> | 3.35E-11 (E)               | 3.46E-02            |

**Table 4.11:** DART-MS data from high NO toluene oxidation (experiment 14).

| m/z (+) (Da) | Intensity <sup>a</sup> | C | H | N | O | $\Delta$ <sup>b</sup> (mDa) | Smiles | Est. VP (atm) <sup>c</sup> | Abundance (R <sub>f</sub> ) |
|--------------|------------------------|---|---|---|---|-----------------------------|--------|----------------------------|-----------------------------|
|--------------|------------------------|---|---|---|---|-----------------------------|--------|----------------------------|-----------------------------|

<sup>a</sup> (A.U.) <sup>b</sup> The difference between the measured and proposed compound exact mass. <sup>b</sup> Est. VP = Estimated vapor pressure.

Estimation Method in parenthesis: E = EVAPORATION method, and N = Nannoolal method.

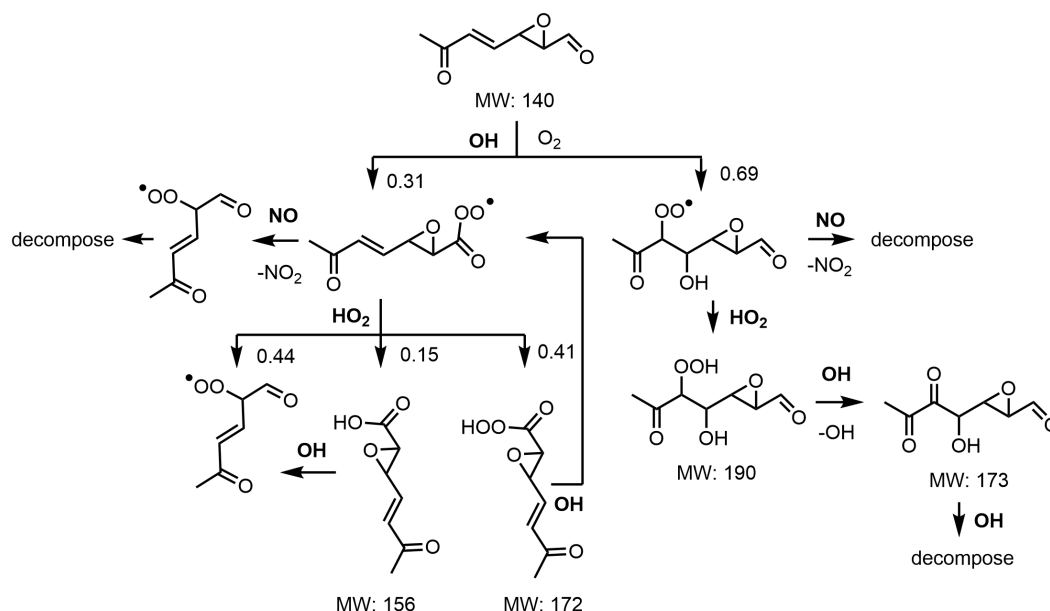


**Figure 4.16:** Epoxide pathway oxidation mechanism under both low- and high-NO conditions as recommended by MCM v3.3.1

Other studies have reported structural isomers of the compounds listed in Tables 4.9, 4.10, and 4.11 in the gas-phase and particle-phase from toluene SOA (Jang et al., 2001; Sato et al., 2007). As here, peaks for C<sub>7</sub>H<sub>8</sub>O<sub>4</sub> and C<sub>7</sub>H<sub>8</sub>O<sub>5</sub> had the largest intensity in the particle-phase measurements in the study by Sato et al. (2007), but it should be noted that only 1% of the SOA constituents were quantified in that study. Both of these studies suggest that the compounds are ring-opening products not produced from the cresol pathway. Given the new evidence from the CF<sub>3</sub>O<sup>-</sup> CIMS in this study, it is clear that these compounds are produced from the cresol pathway.

Products detected in the particle-phase by the DART-MS under *o*-cresol high NO conditions are shown in Figure 4.17. An oligomer product, C<sub>15</sub>H<sub>22</sub>O<sub>4</sub>, is detected as one of the dominant products in *o*-cresol oxidation under high-NO conditions (Figure 4.17). It is possible this product forms from oligomerization of trihydroxy toluene and C<sub>8</sub>H<sub>14</sub>O to form a hemiacetal.

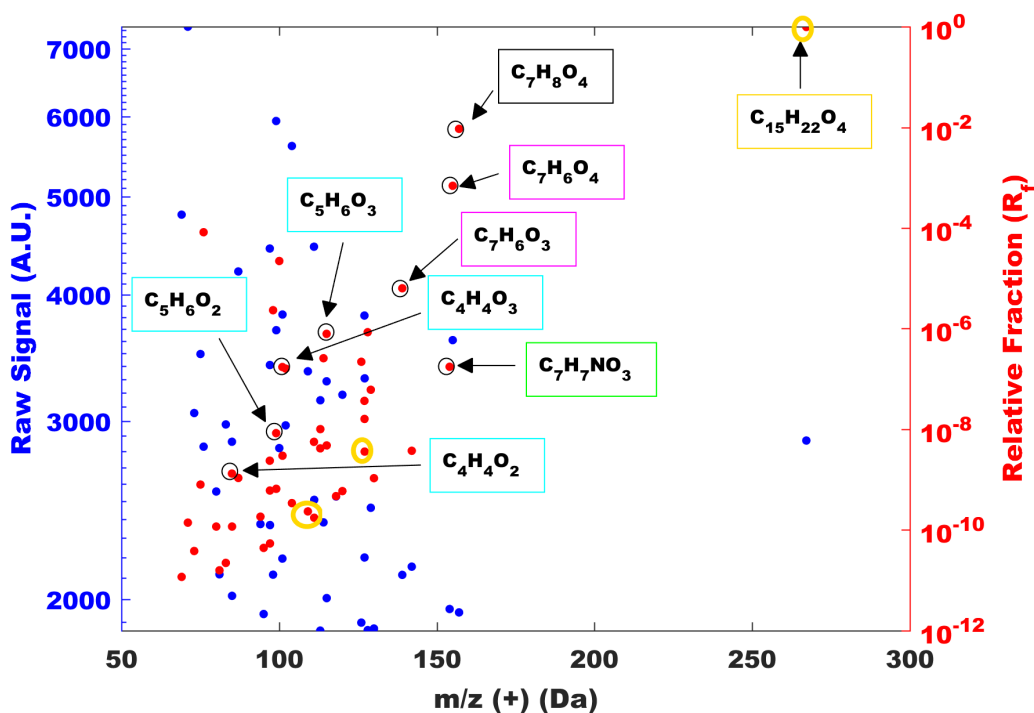


**Figure 4.17:** Products detected by DART-MS in the particle phase during oxidation of *o*-cresol under high NO conditions (experiment 15) with boxes identifying the following types of compounds: polyols (black), methyl benzoquinone type compounds (magenta), decomposition products from the bicyclic intermediate pathway (cyan), products with more than 7 carbons (gold), and nitro compounds (green).

## References

- Atkinson, R., S. M. Aschmann, and J. Arey (1992). "Reactions of OH and NO<sub>3</sub> radicals with phenol, cresols, and 2-nitrophenol at 296 ± 2 K". In: *Environ. Sci. Technol.* 26, pp. 1397–1403.
- Bardini, P. (2006). "Atmospheric Chemistry of Dimethylphenols and Nitrophenols, Ph.D. Thesis". Thesis.
- Barley, M. H. and G. McFiggans (2010). "The critical assessment of vapour pressure estimation methods for use in modelling the formation of atmospheric organic aerosol". In: *Atmos. Chem. Phys.* 10, pp. 749–767.
- Bejan, I., Y. Abd El Aal, et al. (2006). "The Photolysis of ortho-Nitrophenols: A New Gas Phase Source of HONO". In: *Phys. Chem. Chem. Phys.* 8, pp. 2028–2035.
- Bejan, I., I. Barnes, et al. (2007). "Investigations on the Gas-Phase Photolysis and OH Radical Kinetics of Methyl-2-Nitrophenols". In: *Phys. Chem. Chem. Phys.* 9, pp. 5686–5692.

- Berho, F. et al. (1998). "Kinetics and Thermochemistry of the Reversible Combination Reaction of the Phenoxy Radical with NO". In: *J. Phys. Chem. A*. 102.1, pp. 1–8.
- Birdsall, A. W., J. F. Andreoni, and M. J. Elrod (2010). "Investigation of the Role of Bicyclic Peroxy Radicals in the Oxidation Mechanism of Toluene". In: *J. Phys. Chem. A*. 114, pp. 10655–10663.
- Bloss, C. et al. (2005). "Development of a detailed chemical mechanism (MCMv3.1) for the atmospheric oxidation of aromatic hydrocarbons". In: *Atmos. Chem. Phys.* 5, pp. 641–664.
- Calvert, J. et al. (2002). *The Mechanisms of Atmospheric Oxidation of Aromatic Hydrocarbons*. New York: Oxford University Press, Inc.
- Caralp, F. et al. (1999). "Atmospheric chemistry of benzaldehyde: UV absorption spectrum and reaction kinetics and mechanisms of the  $\text{C}_6\text{H}_5\text{C}(\text{O})\text{O}_2$  radical". In: *Phys. Chem. Chem. Phys.* 1, pp. 3509–3517.
- Chan, M. N., T. Nah, and K. R. Wilson (2013). "Real Time In Situ Chemical Characterization of Sub-Micron Organic Aerosols using Direct Analysis in Real Time Mass Spectrometry (DART-MS): The Effect of Aerosol Size and Volatility". In: *Analyst* 138, pp. 3749–3757.
- Chen, J., J. C. Wenger, and D. S. Venables (2011). "Near-Ultraviolet Absorption Cross Sections of Nitrophenols and Their Potential Influence on Tropospheric Oxidation Capacity". In: *J. Phys. Chem. A*. 115, pp. 12235–12242.
- Cody, R. B. (2009). "Observation of Molecular Ions and Analysis of Nonpolar Compounds with the Direct Analysis in Real Time Ion Source". In: *Anal. Chem.* 81, pp. 1101–1107.
- Cody, R. B., J. A. Laramée, and H. D. Durst (2005). "Versatile New Ion Source for the Analysis of Materials in Open Air under Ambient Conditions". In: *Anal. Chem.* 77, pp. 2297–2302.
- Compernelle, S., K. Ceulemans, and J. F. Muller (2011). "EVAPORATION: A New Vapour Pressure Estimation Method for Organic Molecules Including Non-Additivity and Intramolecular Interactions". In: *Atmos. Chem. Phys.* 11, pp. 9431–9450.
- Crounse, John D. et al. (2006). "Measurement of Gas-Phase Hydroperoxides by Chemical Ionization Mass Spectrometry". In: *Anal. Chem.* 78, pp. 6726–6732.
- Dean, J. A. (1992). *Lange's Handbook of Chemistry 14th Ed.* New York: McGraw-Hill, Inc.
- Dewar, M. J. S. and J. J. P. Stewart (1984). "A new procedure for calculating molecular polarizabilities; Applications using MNDO." In: *Chem. Phys. Lett.* 111.4.5, pp. 416–420.

- Etzkorn, T. et al. (1999). "Gas-phase absorption cross sections of 24 monocyclic aromatic hydrocarbons in the UV and IR spectral ranges". In: *Atmos. Environ.* 33, pp. 525–540.
- Henze, D. K. et al. (2008). "Global modeling of secondary organic aerosol formation from aromatic hydrocarbons: high- vs. low-yield pathways". In: *Atmos. Chem. Phys.* 8, pp. 2405–2421.
- Jang, M. and R. M. Kamens (2001). "Characterization of Secondary Aerosol from the Photooxidation of Toluene in the Presence of  $\text{NO}_x$  and 1-Propene". In: *Environ. Sci. Technol.* 35, pp. 3626–3639.
- Jenkin, M. E. et al. (2003). "Protocol for the development of the Master Chemical Mechanism, MCM v3 (Part B): tropospheric degradation of aromatic volatile organic compounds". In: *Atmos. Chem. Phys.* 3, pp. 181–193.
- Jorgensen, S. (2012). "Gas-phase oxidation of cresol isomers initiated by OH or  $\text{NO}_3$  radicals in the presence of  $\text{NO}_2$ ". In: *Int. J. Chem. Kinet.* 44.3, pp. 165–178.
- Klotz, B. et al. (1998). "Atmospheric oxidation of toluene in a large-volume outdoor photoreactor: in situ determination of ring-retaining product yields". In: *J. Phys. Chem. A* 102.10289-10299.
- Koch, R. et al. (2007). "Consecutive reactions of aromatic-OH adducts with  $\text{NO}$ ,  $\text{NO}_2$  and  $\text{O}_2$ : benzene, naphthalene, toluene, *m*- and *p*-xylene, hexamethylbenzene, phenol, *m*-cresol and aniline". In: *Atmos. Chem. Phys.* 7, pp. 2057–2071.
- Kurten, T. et al. (2016). " $\alpha$ -Pinene autoxidation products may not have extremely low saturation vapor pressures despite high O:C ratios". In: *J. Phys. Chem. A* 120, pp. 2569–2582.
- Lide, D. R. (2001). *CRC Handbook of Chemistry and Physics*. Vol. 82. Boca Raton, Florida: CRC Press LLC.
- Lim, Y. B. et al. (2010). "Aqueous chemistry and its role in secondary organic aerosol (SOA) formation". In: *Atmos. Chem. Phys.* 10, pp. 10521–10539.
- McClellan, A. L. (1974). *Table of Experimental Dipole Moments*. Vol. 2. El Cerrito, Ca: Rahara Enterprises.
- Nakao, S., C. Clark, et al. (2011). "Secondary organic aerosol formation from phenolic compounds in the absence of  $\text{NO}_x$ ". In: *Atmos. Chem. Phys.* 11, pp. 10649–10660.
- Nakao, S., Y. Liu, et al. (2012). "Chamber studies of SOA formation from aromatic hydrocarbons: observation of limited glyoxal uptake". In: *Atmos. Chem. Phys.* 12, pp. 3927–3937.
- Nannoolal, Y., J. Rarey, and D. Ramjugernath (2008). "Estimation of Pure Component Properties Part 3. Estimation of the Vapor Pressure of Non-Electrolyte Organic Compounds Via Group Contributions and Group Interactions". In: *Fluid Phase Equilibria* 269, pp. 117–133.



- Nannoolal, Y., J. Rarey, D. Ramjugernath, and W. Cordes (2004). "Estimation of Pure Component Properties Part 1. Estimation of the Normal Boiling Point of Non-Electrolyte Organic Compounds Via Group Contributions and Group Interactions". In: *Fluid Phase Equilibria* 226, pp. 45–63.
- Ng, N. L. et al. (2007). "Secondary organic aerosol formation from *m*-Xylene, toluene, and benzene". In: *Atmos. Chem. Phys.* 7, pp. 3909–3922.
- Nilles, J. M., T. R. Connell, and H. D. Durst (2009). "Quantitation of Chemical Warfare Agents Using the Direct Analysis in Real Time (DART) Technique". In: *Anal. Chem.* 81, pp. 6744–6749.
- Olariu, R. I., I. Barnes, et al. (2000). "Rate coefficients for the gas-phase reaction of OH radicals with selected dihydroxybenzenes and benzoquinones". In: *Int. J. Chem. Kinet.* 32.11, pp. 696–702.
- Olariu, R. I., I. Bejan, et al. (2004). "Rate coefficients for the gas-phase reaction of NO<sub>3</sub> radicals with selected dihydroxybenzenes". In: *Int. J. Chem. Kinet.* 36.11, pp. 577–583.
- Olariu, R. I., B. Klotz, et al. (2002). "FT-IR study of the ring-retaining products from the reaction of OH radicals with phenol, *o*-, *m*-, and *p*-cresol". In: *Atmos. Environ.* 36, pp. 3685–3697.
- O'Meara, S. et al. (2014). "An assessment of vapour pressure estimation methods". In: *Phys. Chem. Chem. Phys.* 16, pp. 19453–19469.
- Orlando, John J. and Geoffrey S. Tyndall (2012). "Laboratory Studies of Organic Peroxy Radical Chemistry: An Overview with Emphasis on Recent Issues of Atmospheric Significance". In: *Chem. Soc. Rev.* 41.19, pp. 6294–317. DOI: 10.1039/c2cs35166h.
- Patiny, L. and A. Borel (2013). "ChemCalc: A Building Block for Tomorrow's Chemical Infrastructure". In: *J. Chem. Inf. Model.* 53, pp. 1223–1228.
- Paulot, Fabien et al. (2009a). "Unexpected Epoxide Formation in the Gas-Phase Photooxidation of Isoprene". In: *Science* 325, pp. 730–733. doi: 10.1126/science.1172910.
- PengZhen, W. U. et al. (2012). "Theoretical study of mechanism and kinetics for the addition of hydroxyl radical to phenol". In: *Sci China Chem* 55.2, pp. 270–276.
- Praske, E. et al. (2015). "Atmospheric Fate of Methyl Vinyl Ketone: Peroxy Radical Reactions with NO and HO<sub>2</sub>". In: *J. Phys. Chem. A.* 119, pp. 4562–4572.
- Sato, K., S. Hatakeyama, and T. Imamura (2007). "Secondary Organic Aerosol Formation during the Photooxidation of Toluene: NO<sub>x</sub> Dependence of Chemical Composition". In: *J. Phys. Chem. A.* 111, pp. 9796–9808.
- Schilling Fahnestock, K. A. et al. (2015). "Secondary Organic Aerosol Composition from C<sub>12</sub> Alkanes". In: *J. Phys. Chem. A.* 119, pp. 4281–4297.

- Sharpe, S. W. et al. (2004). "Gas-Phase Databases for Quantitative Infrared Spectroscopy, Composite Spectrum for MCRESOL\_25T, Version 1.0, July, 03". In: *Applied Spectroscopy* 58.12, pp. 1452–1461.
- Smith, D. F., C. D. McIver, and T. E. Kleindienst (1998). "Primary Product Distribution from the Reaction of Hydroxyl Radicals with Toluene at ppb NO<sub>x</sub> Mixing Ratios". In: *J. Atmos. Chem.* 30, pp. 209–228.
- St. Clair, Jason M. et al. (2010). "Chemical Ionization Tandem Mass Spectrometer for the in Situ Measurement of Methyl Hydrogen Peroxide". In: *Rev. Sci. Instrum.* 81, pp. 094102–094102. DOI: 10.1063/1.3480552.
- Su, T and W. J. Chesnavich (1982). "Parametrization of the ion-polar molecule collision rate constant by trajectory calculations". In: *J. Chem. Phys.* 76.10, pp. 5183–5185.
- Tan, Y. et al. (2009). "Effects of precursor concentration and acidic sulfate in aqueous glyoxal-OH radical oxidation and implications for secondary organic aerosol". In: *Environ. Sci. Technol.* 43, pp. 8105–8112.
- Tao, Z. and Z. Li (1999). "A Kinetics Study on Reactions of C<sub>6</sub>H<sub>5</sub>O with C<sub>6</sub>H<sub>5</sub>O and O<sub>3</sub> at 298 K". In: *Int. J. Chem. Kinet.* 31.1, pp. 65–72.
- Wu, R. et al. (2014). "Atmospheric oxidation mechanism of toluene". In: *J. Phys. Chem. A* 118, pp. 4533–4547.
- Xu, C. and L. Wang (2013). "Atmospheric oxidation mechanism of phenol initiated by OH radical". In: *J. Phys. Chem. A* 117, pp. 2358–2364.
- Yaws, C. L. (1994). *Handbook of Vapor Pressures: C<sub>5</sub> to C<sub>7</sub> Compounds*. Vol. 2. Houston, Texas: Gulf Publishing Company.
- Yu, T., A. M. Mebel, and M. C. Lin (1995). "Reaction of Phenoxy Radical with Nitric Oxide". In: *J. Phys. Org. Chem.* 8.1, pp. 47–53.
- Zetzsch, C. et al. (1997). "Adduct formation of OH with aromatics and unsaturated hydrocarbons and consecutive reactions with O<sub>2</sub> and NO<sub>x</sub> to regenerate OH". In: *Chemical Processes in Atmospheric Oxidation*. Ed. by G. LeBras. Berlin: Springer-Verlag, pp. 247–256.
- Zhang, X. et al. (2014). "Influence of Vapor Wall Loss in Laboratory Chambers on Yields of Secondary Organic Aerosol". In: *P. Natl. Acad. Sci. USA* 111.16, pp. 5802–5807.

*Chapter 5*

## CONCLUSIONS AND FUTURE WORK

This work discusses how laboratory atmospheric chamber experiments were performed in order to better understand secondary organic aerosol (SOA) and ozone formation in the atmosphere. First the new Caltech chamber facility was characterized (chapter 2). These characterization experiments facilitated the design and execution of future experiments (e.g., Chapters 3 & 4 Appendices B, C & D).

In chapter 3, the gas-phase chemical mechanism for a novel SOA precursor (nitrooxy hydroxy epoxide) from isoprene  $\text{NO}_3$  oxidation was identified. In order to fully understand the impact of nitrooxy hydroxy epoxide on SOA more studies are needed. Experiments using standards of nitrooxy hydroxy epoxide to measure both the OH reaction rate constant and uptake to aqueous aerosol would be particularly useful. Additionally, the current work measured mostly  $\delta$ -organic nitrates from isoprene  $\text{NO}_3$  oxidation. Jacobs et al. (2014) measured the hydrolysis of  $\delta$ -[1,4]-isoprene hydroxy nitrate to be quite high even under neutral conditions. More studies examining the hydrolysis rate constants of organic nitrates are needed. The results from Jacobs et al. (2014) suggest that the  $\delta$ -organic nitrates formed from  $\text{NO}_3$  oxidation could potentially be terminal sinks for  $\text{NO}_x$  in humid locations like the southeastern United States.

In chapter 4, low-volatility products from cresol oxidation including (trihydroxy toluene, tetrahydroxy toluene, and pentahydroxy toluene) were detected in the gas-phase by the chemical ionization mass spectrometer (CIMS) and in the particle-phase by offline filter analysis using direct analysis in real time mass spectrometry (DART-MS). This chapter identifies a simple and direct chemical mechanism for toluene SOA formation via the cresol pathway. Even though the cresol channel is relatively minor in the gas-phase ( $\sim 20\%$ ), based on the low-volatility products detected in the gas-phase, the cresol pathway is estimated to produce a significant fraction ( $\sim 20$ - $40\%$ ) of toluene SOA. Although this study only examined SOA formation from toluene, likely the phenolic pathway is important for generating SOA from other aromatic compounds as well. Results from this work will likely motivate future studies to further examine gas-phase oxidation products and SOA formation from the phenolic pathway of aromatic compounds.

In chapter 3, the isomer distribution of organic nitrates produced from  $\text{NO}_3$  oxidation of isoprene was identified. The isomer distribution influences the fate of these organic nitrates. Now that the fate of the organic nitrates produced from  $\text{NO}_3$  oxidation is better understood, this chemistry can be included in large global chemical transport models. Updating this chemistry will improve the ability of these models to predict the formation of ozone.

A large challenge in atmospheric chemistry today is to better understand how  $\text{O}_3$  is produced. The EPA has recently strengthened regulations on  $\text{O}_3$  in order to protect human health (USEPA, 2015). Thus, global models need to accurately simulate ozone, so that mitigation strategies can be developed for regions out of compliance. My next research goal is to incorporate the chemical mechanism knowledge I have gained from performing atmospheric chamber studies into CAM-Chem (Community Atmosphere Model with chemistry, which is a component of the Community Earth System Model (CESM)). CAM-Chem is a global chemical transport model maintained by the National Center for Atmospheric Research (NCAR) and used throughout the atmospheric science community.

Currently, many global chemical transport models including CAM-Chem consistently over-predict  $\text{O}_3$  during the summer in the eastern United States (Fiore et al., 2009). It is believed this is caused by not understanding properly how  $\text{NO}_x$ , an anthropogenic pollutant, is recycled from biogenic VOCs. For this reason, I am planning on updating the isoprene and monoterpene parts of the chemical mechanism in CAM-Chem. Hopefully, by improving how this chemistry is described in the model,  $\text{O}_3$  will be better predicted and  $\text{NO}_x$  recycling/ $\text{O}_3$  production in this region will be better understood.

Models are routinely used to predict future air quality. In the future, emissions of biogenic VOCs are expected to increase due to the overall warming climate. Additionally,  $\text{NO}_x$  emissions are expected to decrease due to regulations designed to improve air quality. If models do not match observations in the present day for regions highly influenced by biogenic emissions, then we cannot trust future predictions of  $\text{O}_3$ . This leaves us uncertain as to how climate change will impact air quality. Furthermore, Knote et al. (2015) found that different chemical mechanisms used today in global and regional chemical transport models produce results that would recommend opposite policy regulations to decrease  $\text{O}_3$  production (i.e., reduce VOC emissions versus reduce  $\text{NO}_x$  emissions).

Thus, more research needs to be done to better understand  $\text{O}_3$  production from

biogenic VOCs influenced by anthropogenic pollutants like  $\text{NO}_x$ . Inclusive in this is:

- (1) Performing laboratory experiments including atmospheric chamber experiments in order to better understand the exact chemical processes that occur;
- (2) Updating and optimizing the chemical mechanisms in global chemical transport models to represent the most current understanding of chemistry associated with the most significant VOCs in the atmosphere;
- (3) Carefully developing chemical mechanisms that make assumptions and simplifications to reduce the computational cost, but not at the expense of accurately simulating tropospheric chemistry;
- (4) Comparing the predictions from global models to results from field studies to better understand where uncertainties exist;
- (5) and better constraining the uncertainties discovered in step 4 by designing and performing future laboratory chamber experiments or future field missions.

This thesis describes research efforts conducted to expand knowledge about the formation of ozone through step 1. Laboratory atmospheric chamber experiments were conducted in order to better understand organic nitrate formation and fate in the atmosphere. My next step is to incorporate these results and the results of other recent laboratory studies into a chemical mechanism for CAM-Chem that simplifies the chemistry in consideration of computational cost, but still accurately simulates tropospheric ozone (steps 3-4).

## References

- Fiore, A. M. et al. (2009). "Multimodel Estimates of Intercontinental Source-Receptor relationships for Ozone Pollution". In: *J. Geophys. Res.* 114, p. D04301.
- Jacobs, M. I., W. J. Burke, and M. J. Elrod (2014). "Kinetics of the Reactions of Isoprene-Derived Hydroxynitrates: Gas Phase Epoxide Formation and Solution Phase Hydrolysis". In: *Atmos. Chem. Phys.* 14, pp. 8933–8946. ISSN: 1489332014. DOI: 10.5194/acp-14-8933-2014.
- Knote, C. et al. (2015). "Influence of the Choice of Gas-Phase Mechanism on Predictions of Key Gaseous Pollutants During the AQMEII Phase-2 Intercomparison". In: *Atmos. Environ.* 115, pp. 553–568.
- USEPA (2015). *National Ambient Air Quality Standards for Ozone: Final Rule*. Vol. 206, pp. 65292–65468.

*Appendix A*

CIMS SENSITIVITIES AND REACTIONS INCLUDED IN THE  
KINETIC MECHANISM DEVELOPED TO BETTER  
UNDERSTAND ISOPRENE NO<sub>3</sub> OXIDATION

Schwantes, R. H. et al. (2015). “Isoprene NO<sub>3</sub> Oxidation Products from the RO<sub>2</sub> + HO<sub>2</sub> Pathway”. In: *J. Phys. Chem. A*. 119.40, pp. 10158–10171. DOI: 10.1021/acs.jpca.5b06355.

**Table A.1:** Sensitivities used in this study for the triple-CIMS (experiments 3-5) and ToF-CIMS.

| name   | CIMS<br>m/z | Triple-CIMS<br>sensitivity<br>(normcts/pppt) | ToF-CIMS<br>sensitivity<br>(normcts/pppt) |
|--|-------------|--|---|
| Formic Acid  | (-) 65      | $2.0 \times 10^{-5}{}^A$                     | $1.0 \times 10^{-4}{}^A$                  |
| Nitric Acid  | (-) 82      | $9.1 \times 10^{-5}{}^A$                     | $3.9 \times 10^{-4}{}^A$                  |
| H <sub>2</sub> O <sub>2</sub>  | (-) 119     | $1.1 \times 10^{-4}{}^A$                     | $1.5 \times 10^{-4}{}^A$                  |
| Hydroxy Methyl Hydroperoxide   | (-) 149     | $4.5 \times 10^{-5}$                         | NA  |
| C <sub>5</sub> Hydroxy Carbonyl  | (-) 185     | $9.5 \times 10^{-5}$                         | $2.0 \times 10^{-4}$                      |
| C <sub>5</sub> Dihydroxy   | (-) 187     | $9.5 \times 10^{-5}$                         | $2.0 \times 10^{-4}$                      |
| C <sub>5</sub> Dihydroxy Carbonyl  | (-) 201     | $8.9 \times 10^{-5}$                         | $1.4 \times 10^{-4}$                      |
| C <sub>5</sub> Carbonyl Hydroxy Epoxide  | (-) 201     | <sup>B</sup>                                 | NA  |
| ISOPOOH/IEPOX  | (-) 203     | $1.1 \times 10^{-4}{}^A$                     | $1.6 \times 10^{-4}$                      |
| Ethanal Nitrate  | (-) 190     | $2.2 \times 10^{-4}$                         | $3.6 \times 10^{-4}$                      |
| Propanone Nitrate  | (-) 204     | $1.9 \times 10^{-4}$                         | $3.1 \times 10^{-4}$                      |
| C <sub>5</sub> Hydroxy Hydroperoxy Epoxide                                     | (-) 217     | <sup>B</sup>                                 | NA  |
| IHN  | (-) 232     | $2.6 \times 10^{-4}$                         | $3.6 \times 10^{-4}$                      |
| C <sub>4</sub> Carbonyl Hydroxy Nitrate  | (-) 234     | $2.2 \times 10^{-4}$                         | $3.3 \times 10^{-4}$                      |
| INP/INHE   | (-) 248     |  |   |
| ICN  | (-) 230     |  |   |
| C <sub>5</sub> Dicarboxyl Nitrate  | (-) 244     |  |   |
| C <sub>5</sub> Hydroxy Carbonyl Nitrate  | (-) 246     |  |   |
| C <sub>4</sub> Nitrooxycarbonyl Hydroperoxide                                  | (-) 250     |  |   |
| Unknown  | (-) 261     |  |   |
| C <sub>5</sub> Carbonyl Hydroperoxide Nitrate                                  | (-) 262     |  |   |
| C <sub>5</sub> Hydroxy Hydroperoxide Nitrate                                   | (-) 264     |  |   |
| C <sub>5</sub> Dinitrate   | (-) 277     | $2.6 \times 10^{-4}$                         | $3.6 \times 10^{-4}$                      |
| ROOR from INO <sub>2</sub> and HMP<br>or complex btw INP and CH <sub>2</sub> O | (-) 278     |  |   |
| C <sub>5</sub> Dihydroperoxide Nitrate   | (-) 280     |  |   |
| C <sub>5</sub> Dinitrooxy Epoxide  | (-) 293     |  |   |
| ROOR from IHNO <sub>2</sub> & HMP  | (-) 294     |  |   |
| ROOR from INO <sub>2</sub> & INO <sub>2</sub>                                  | (-) 377     |  |   |
| ROOR from INO <sub>2</sub> & IHNO <sub>2</sub>                                 | (-) 393     |  |   |

<sup>A</sup> Sensitivities are dependent on Relative Humidity.<sup>B</sup> Assume same as IEPOX.

**Table A.2:** List of the general reactions in the kinetic mechanism.

| Reaction  | Rate Constant <sup>A</sup>                         | Rate Source               | Rxn Source    |
|---|--|---------------------------|---------------|
| CH <sub>2</sub> O Reactions   |  |                           |               |
| CH <sub>2</sub> O + NO <sub>3</sub> → HNO <sub>3</sub> + HO <sub>2</sub> + CO   | $2 \times 10^{-12} e^{-2440/T} \text{ *(2.5-3.0)}$ | IUPAC*2.9 <sup>B</sup>    | IUPAC         |
| CH <sub>2</sub> O + OH → H <sub>2</sub> O + HO <sub>2</sub> + CO  | $5.4 \times 10^{-12} e^{135/T}$                    | IUPAC                     | IUPAC         |
| HO <sub>2</sub> + CH <sub>2</sub> O → HMP   | $9.7 \times 10^{-15} e^{625/T}$                    | IUPAC                     | IUPAC         |
| HMP → CH <sub>2</sub> O + HO <sub>2</sub>   | $2.4 \times 10^{12} e^{-7000/T} \text{ s}^{-1}$    | IUPAC                     | IUPAC         |
| HMP + HO <sub>2</sub> → 0.5 (HMHP + O <sub>2</sub> ) + 0.3 (HCOOH + H <sub>2</sub> O + O <sub>2</sub> )<br>+ 0.2 (HCOOH + HO <sub>2</sub> + OH + O <sub>2</sub> ) | $5.6 \times 10^{-15} e^{2300/T}$                   | IUPAC                     | Jenkin (2007) |
| HMP + HMP → HCOOH + CH <sub>2</sub> (OH) <sub>2</sub> ≡O <sub>2</sub>   | $7.0 \times 10^{-13}$                              | IUPAC                     | IUPAC         |
| HMP + HMP → 2 HCOOH + 2 HO <sub>2</sub> + O <sub>2</sub>  | $5.5 \times 10^{-12}$                              | IUPAC                     | IUPAC         |
| HMP + NO → HO <sub>2</sub> + HCOOH + NO <sub>2</sub>  | $5.6 \times 10^{-12}$                              | IUPAC                     | IUPAC         |
| HMP≡NO <sub>3</sub> → HO <sub>2</sub> + HCOOH + NO <sub>2</sub>   | $1.2 \times 10^{-12} \text{ IUPAC } ^C$            | IUPAC                     |               |
| OH + HCOOH → CO <sub>2</sub> + HO <sub>2</sub> + H <sub>2</sub> O   | $4.5 \times 10^{-13}$                              | IUPAC                     | IUPAC         |
| HMHP + OH → 0.12 (HMP + H <sub>2</sub> O)   | $3.1 \times 10^{-11}$                              | Jenkin(2007) <sup>D</sup> | Jenkin(2007)  |



| Reaction   | Rate Constant <sup>A</sup>   | Rate Source | Rxn Source |
|--|--|-------------|------------|
| + 0.88 (HCOOH + OH + H <sub>2</sub> O)   |  |             |            |
| CO + OH $\longrightarrow$ HO <sub>2</sub> + CO <sub>2</sub>  | $k_0 = 5.9 \times 10^{-33} (T/300)^{-1.4};$<br>$k_\infty = 1.1 \times 10^{-12} (T/300)^{1.3}; F_c = 0.6$                                     | JPL         | JPL        |
| CO + OH $\longrightarrow$ HO <sub>2</sub> + CO <sub>2</sub>  | $k_0 = 1.5 \times 10^{-13} (T/300)^{0.6};$<br>$k_\infty = 2.1 \times 10^9 (T/300)^{6.1}; F_c = 0.6$  | JPL         | JPL        |
| HO <sub>x</sub> Reactions  |  |             |            |
| HO <sub>2</sub> + HO <sub>2</sub> $\longrightarrow$ H <sub>2</sub> O <sub>2</sub> + O <sub>2</sub> | $(3.0 \times 10^{-13} e^{460/T} + 2.1 \times 10^{-33} e^{920/T} \text{ M})$<br>$* (1 + 1.4 \times 10^{-21} [\text{H}_2\text{O}] e^{2200/T})$ | JPL         | JPL        |
| OH + OH $\longrightarrow$ H <sub>2</sub> O <sub>2</sub>  | $k_0 = 6.9 \times 10^{-31} (T/300)^{-1};$<br>$k_\infty = 2.6 \times 10^{-11} (T/300)^0; F_c = 0.6$   | JPL         | JPL        |
| OH + OH $\longrightarrow$ H <sub>2</sub> O + O   | $1.8 \times 10^{-12}$  | JPL         | JPL        |
| OH + H <sub>2</sub> O <sub>2</sub> $\longrightarrow$ HO <sub>2</sub> + H <sub>2</sub> O            | $1.8 \times 10^{-12}$  | JPL         | JPL        |
| OH + HO <sub>2</sub> $\longrightarrow$ H <sub>2</sub> O + O <sub>2</sub>                           | $4.8 \times 10^{-11} e^{250/T}$  | JPL         | JPL        |
| O <sub>3</sub> Reactions   |  |             |            |
| O <sub>3</sub> + HO <sub>2</sub> $\longrightarrow$ OH + 2 O <sub>2</sub>                           | $2.03 \times 10^{-16} (T/300)^{4.57} e^{693/T}$  | IUPAC       | IUPAC      |

| Reaction  | Rate Constant <sup>A</sup>  | Rate Source | Rxn Source |
|---|---|-------------|------------|
| $\text{O}_3 + \text{OH} \longrightarrow \text{HO}_2 + \text{O}_2$         | $1.7 \times 10^{-12} \text{ e}^{-940/T}$  | JPL         | JPL        |
| $\text{O}(^1\text{D}) + \text{H}_2\text{O} \longrightarrow {}_2\text{OH}$ | $1.63 \times 10^{-10} \text{ e}^{60/T}$   | JPL         | JPL        |
| $\text{O}(^1\text{D}) \longrightarrow \text{O}$                           | $3.3 \times 10^{-11} \text{ e}^{55/T} \text{ 0.21 M} +$<br>$2.15 \times 10^{-11} \text{ e}^{110/T} \text{ 0.78 M s}^{-1}$ | JPL         | JPL        |
| $\text{O} + \text{O}_3 \longrightarrow 2 \text{O}_2$                      | $8.0 \times 10^{-12} \text{ e}^{-2060/T}$   | JPL         | JPL        |
| $\text{O} + \text{OH} \longrightarrow \text{O}_2 + \text{HO}_2$           | $1.8 \times 10^{-11} \text{ e}^{180/T}$   | JPL         | JPL        |
| $\text{O} + \text{HO}_2 \longrightarrow \text{OH} + \text{O}_2$           | $3.0 \times 10^{-11} \text{ e}^{200/T}$   | JPL         | JPL        |
| $\text{O} + \text{H}_2\text{O}_2 \longrightarrow \text{OH} + \text{HO}_2$ | $1.4 \times 10^{-12} \text{ e}^{-2000/T}$   | JPL         | JPL        |
| $\text{O} + \text{O}_2 \longrightarrow \text{O}_3$                        | $6.0 \times 10^{-34} (\text{T}/300)^{-2.4} \text{ M}$   | JPL         | JPL        |
| <b>NO<sub>x</sub> Reactions</b>   |   |             |            |
| $\text{O} + \text{NO} \longrightarrow \text{NO}_2$                        | $k_0 = 9.0 \times 10^{-32} (\text{T}/300)^{-1.5}; k_\infty = 3.0 \times 10^{-11} (\text{T}/300)^0; F_c = 0.6$             | JPL         | JPL        |
| $\text{O} + \text{NO}_2 \longrightarrow \text{NO}_3$                      | $k_0 = 2.5 \times 10^{-31} (\text{T}/300)^{-1.8}; k_\infty = 2.2 \times 10^{-11} (\text{T}/300)^{-0.7}; F_c = 0.6$        | JPL         | JPL        |
| $\text{O} + \text{NO}_2 \longrightarrow \text{NO} + \text{O}_2$           | $5.1 \times 10^{-12} \text{ e}^{210/T}$   | JPL         | JPL        |
| $\text{O} + \text{NO}_3 \longrightarrow \text{O}_2 + \text{NO}_2$         | $1.0 \times 10^{-11}$   | JPL         | JPL        |
| $\text{O}_3 + \text{NO} \longrightarrow \text{O}_2 + \text{NO}_2$         | $3 \times 10^{-12} \text{ e}^{-1500/T}$   | JPL         | JPL        |

| Reaction  | Rate Constant <sup>A</sup>   | Rate Source     | Rxn Source      |
|---|--|-----------------|-----------------|
| $\text{O}_3 + \text{NO}_2 \longrightarrow \text{NO}_3 + \text{O}_2$                         | $1.2 \times 10^{-13} \text{ e}^{-2450/T}$  | JPL             | JPL             |
| $\text{O}_3 + \text{NO}_2 \longrightarrow \text{NO} + 2 \text{O}_2$                         | $9.7 \times 10^{-19}$  | Cantrell (1985) | Cantrell (1985) |
| $\text{NO}_2 + \text{NO}_3 \longrightarrow \text{NO} + \text{NO}_2 + \text{O}_2$            | $4.5 \times 10^{-14} \text{ e}^{-1260/T}$  | JPL             | JPL             |
| $\text{NO}_3 + \text{NO}_2 + \text{M} \rightleftharpoons \text{N}_2\text{O}_5 + \text{M}$   | $k_0 = 2.0 \times 10^{-30} (\text{T}/300)^{-4.4}; k_\infty = 1.4 \times 10^{-12} (\text{T}/300)^{-0.7};$<br>$k_{eq} = 2.7 \times 10^{-27} \text{ e}^{11000/T}; F_c = 0.6$      | JPL             | JPL             |
| $\text{N}_2\text{O}_5 + \text{H}_2\text{O} + \text{wall} \longrightarrow 2 \text{HNO}_3$    | Varied <sup>E</sup>  | NA              | Cantrell (1985) |
| $\text{NO}_3 + \text{NO} \longrightarrow 2 \text{NO}_2$                                     | $1.5 \times 10^{-11} \text{ e}^{170/T}$  | JPL             | JPL             |
| $\text{NO}_3 + \text{NO}_3 \longrightarrow 2 \text{NO}_2 + \text{O}_2$                      | $8.5 \times 10^{-13} \text{ e}^{-2450/T}$  | JPL             | JPL             |
| $\text{NO}_3 + \text{HO}_2 \longrightarrow \text{OH} + \text{O}_2 + \text{NO}_2$            | $4.0 \times 10^{-12}$  | IUPAC           | IUPAC           |
| $\text{NO} + \text{HO}_2 \longrightarrow \text{NO}_2 + \text{OH}$                           | $3.3 \times 10^{-12} \text{ e}^{270/T}$  | JPL             | JPL             |
| $\text{NO}_2 + \text{HO}_2 \longrightarrow \text{HONO} + \text{O}_2$                        | $5.0 \times 10^{-16}$  | JPL             | JPL             |
| $\text{NO}_2 + \text{HO}_2 + \text{M} \rightleftharpoons \text{HO}_2\text{NO}_2 + \text{M}$ | $k_0 = 2.0 \times 10^{-31} (\text{T}/300)^{-3.4};$<br>$k_\infty = 2.9 \times 10^{-12} (\text{T}/300)^{-1.1};$<br>$k_{eq} = 2.1 \times 10^{-27} \text{ e}^{10900/T}; F_c = 0.6$ | JPL             | JPL             |
| $\text{NO} + \text{OH} + \text{M} \longrightarrow \text{HONO} + \text{M}$                   | $k_0 = 7.0 \times 10^{-31} (\text{T}/300)^{-2.6};$   | JPL             | JPL             |

| Reaction   | Rate Constant <sup>A</sup>  | Rate Source     | Rxn Source      |
|--|---|-----------------|-----------------|
|  | $k_{\infty} = 3.6 \times 10^{-11} (T/300)^{-0.1}$ ; $F_c = 0.6$                   |                 |                 |
| $\text{NO}_2 + \text{OH} + \text{M} \longrightarrow \text{HNO}_3 + \text{M}$                       | $k_0 = 1.8 \times 10^{-30} (T/300)^{-3.0}$ ;                                      | JPL             | JPL             |
|  | $k_{\infty} = 2.8 \times 10^{-11} (T/300)^0$ ; $F_c = 0.6$                        |                 |                 |
| $\text{NO}_2 + \text{OH} + \text{M} \rightleftharpoons \text{HOONO} + \text{M}$                    | $k_0 = 9.1 \times 10^{-32} (T/300)^{-3.9}$ ;                                      | JPL             | JPL             |
|  | $k_{\infty} = 4.2 \times 10^{-11} (T/300)^{-0.5}$ ;                               |                 |                 |
|  | $k_{eq} = 3.5 \times 10^{-27} e^{10135/T}$ ; $F_c = 0.6$                          |                 |                 |
| $\text{NO}_3 + \text{OH} \longrightarrow \text{NO}_2 + \text{HO}_2$                                | $2.0 \times 10^{-11}$   | IUPAC           | IUPAC           |
| $\text{HONO} + \text{OH} \longrightarrow \text{NO}_2 + \text{H}_2\text{O}$                         | $1.8 \times 10^{-11} e^{-390/T}$  | JPL             | JPL             |
| $\text{HNO}_3 + \text{OH} \longrightarrow \text{H}_2\text{O} + \text{NO}_3$                        | $k_0 = 2.4 \times 10^{-14} e^{460/T}$ ;   | JPL             | JPL             |
|  | $k_2 = 2.7 \times 10^{-17} e^{2199/T}$ ; $k_3 = 6.5 \times 10^{-34} e^{1335/T}$ ; |                 |                 |
|  | $k = k_0 + k_3 M / (1 + k_3 M / k_2)$   |                 |                 |
| $\text{HO}_2\text{NO}_2 + \text{OH} \longrightarrow \text{H}_2\text{O} + \text{O}_2 + \text{NO}_2$ | $3.2 \times 10^{-13} e^{690/T}$   | IUPAC           | IUPAC           |
| $\text{HONO} + \text{HNO}_3 \longrightarrow 2 \text{NO}_2 + \text{H}_2\text{O}$                    | $2.71 \times 10^{-17}$  | Cantrell (1985) | Cantrell (1985) |

<sup>A</sup> Rate constant units are  $\text{cm}^3 \text{ molec}^{-1} \text{ s}^{-1}$  unless noted otherwise. <sup>B</sup> Increased IUPAC rate constant by a factor such that the experimental results for  $\text{H}_2\text{O}_2$  matched the kinetic mechanism results. <sup>C</sup> Specific rate unknown used IUPAC rate constant/products

| Reaction  | Rate Constant <sup>A</sup> | Rate Source | Rxn Source |
|---|----------------------------|-------------|------------|
| for CH <sub>3</sub> O <sub>2</sub> + NO <sub>3</sub> . <sup>D</sup> Rate constant estimated by Jenkin (2007) by SAR method. <sup>E</sup> Varied based on chamber/experiment. See Table A5 for full names of the abbreviations used above. |                            |             |            |

**Table A.3:** List of isoprene related reactions in the kinetic mechanism.

| Reaction  | Rate Constant <sup>A</sup>       | Rxn Source                   | Rate Source                     |
|---|----------------------------------|------------------------------|---------------------------------|
| <b>Isoprene + OH/O<sub>3</sub> Reactions</b>  |                                  |                              |                                 |
| ISOP + OH $\xrightarrow{\text{O}_2}$ IHO <sub>2</sub>   | $2.7 \times 10^{-11} e^{390/T}$  | MCM v3.2                     | IUPAC                           |
| IHO <sub>2</sub> + NO $\xrightarrow{\text{O}_2}$ 0.22 IHC + 0.88 HO <sub>2</sub> + 0.39 MVK +<br>0.27 MACR + 0.66 CH <sub>2</sub> O + 0.88 NO <sub>2</sub> + 0.12 ISOPN | $2.7 \times 10^{-12} e^{360/T}$  | Paulot (2009,b),<br>MCM v3.2 | MCM v3.24                       |
| IHO <sub>2</sub> + NO <sub>3</sub> $\xrightarrow{\text{O}_2}$ 0.25 IHC + HO <sub>2</sub> + 0.444 MVK +<br>0.306 MACR + 0.75 CH <sub>2</sub> O + NO <sub>2</sub>         | $2.3 \times 10^{-12}$            | MCM v3.2                     | MCM v3.2                        |
| IHO $\xrightarrow{\text{O}_2}$ + 0.45 IHC + 0.55 MACR + 0.55 CH <sub>2</sub> O + HO <sub>2</sub>  | $1.0 \times 10^6 \text{ s}^{-1}$ | MCM v3.2                     | MCM v3.2                        |
| IHO <sub>2</sub> + IHO <sub>2</sub> $\rightarrow$ 0.18 IHC + 0.22 MACR + 0.4 IDH<br>+ 1.2 IHO   | $2.6 \times 10^{-12}$            | MCM v3.2,<br>Jenkin (1997)   | Jenkin (1998) <sup>B</sup>      |
| IHO <sub>2</sub> + INO <sub>2</sub> $\rightarrow$ 0.09 IHC + 0.11 MACR + 0.2 IDH + 0.6 IHO +  | $3.6 \times 10^{-12}$            | MCM v3.2, Kwan (2012),       | geometric mean IHO <sub>2</sub> |

| Reaction  | Rate Constant <sup>A</sup>                       | Rxn Source  | Rate Source  |
|---|--|---|--|
| 0.23 INO + 0.308 IHN $\delta$ + 0.077 IHN $\beta$ + 0.385 ICN   |  | Jenkin (1997), This work                              | and INO <sub>2</sub> self-reaction                       |
| IHO <sub>2</sub> + IHNO <sub>2</sub> $\longrightarrow$ 0.09 IHC + 0.11 MACR + 0.2 IDH + 0.6 IHO +<br>0.23 IHNO + 0.385 IHCN + 0.385 IDHN                    | 3.6 x 10 <sup>-12</sup>                          | MCM v3.2, Kwan (2012),<br>Jenkin (1997)               | this work  |
| IPNO <sub>2</sub> + IHO <sub>2</sub> $\longrightarrow$ 0.23 IPNO + 0.385 ICPN + 0.385 IHPN<br>+ 0.6 IHO + 0.09 IHC + 0.11 MACR + 0.2 IDH                    | 3.6 x 10 <sup>-12</sup>                          | assume same as<br>INO <sub>2</sub> + IHO <sub>2</sub> | this work  |
| IHO <sub>2</sub> + HMP $\longrightarrow$ 0.09 IHC + 0.11 MACR + 0.2 IDH<br>+ 0.6 IHO + HCOOH + HO <sub>2</sub>  | 3.8 x 10 <sup>-12</sup>                          | MCM v3.2/<br>IUPAC/Jenkin (1997)                      | geometric mean HMP<br>and IHO <sub>2</sub> self-reaction |
| IHO <sub>2</sub> + HO <sub>2</sub> $\longrightarrow$ 0.937 ISOPOOH + 0.063 OH + 0.025 MACR<br>+ 0.038 MVK + 0.063 HO <sub>2</sub> + 0.063 CH <sub>2</sub> O | 2.91 x 10 <sup>-13</sup><br>$e^{1300/T} * 0.706$ | Liu (2013)  | Saunders (2003)  |
| ISOPOOH + OH $\longrightarrow$ 0.7 IO <sub>2</sub> + 0.3 IHC + 0.3 OH   | 3.8 x 10 <sup>-12</sup> $e^{200/T}$              | Paulot (2009,a)                                       | Paulot (2009,a)  |
| ISOPOOH + OH $\longrightarrow$ IEPOX + OH   | 1.9 x 10 <sup>-11</sup> $e^{390/T}$              | Paulot (2009,a)                                       | Paulot (2009,a)  |
| IEPOX + OH $\longrightarrow$ 0.07 GLYC + 0.09 HACET + Products  | 1.15 x 10 <sup>-11</sup>                         | Bates (2014), (high NO)                               | Bates (2014) <sup>C</sup>                                |
| ISOP + O <sub>3</sub> $\longrightarrow$ 0.41 MACR + 0.16 MVK + 0.26 OH<br>+ 0.26 HO <sub>2</sub> + Products   | 1.03 x 10 <sup>-14</sup><br>$e^{-1995/T}$        | see notes <sup>D</sup>                                | IUPAC  |
| IHC + OH $\xrightarrow{O_2} \xrightarrow[-NO_2]{NO}$ HO <sub>2</sub> + 0.59 HACET<br>+ 0.59 GLYX + 0.41 MGLYX + 0.41 GLYC                                   | 4.52 x 10 <sup>-11</sup>                         | MCM v3.2 (include<br>only main products)              | MCM v3.2   |

| Reaction   | Rate Constant <sup>A</sup>  | Rxn Source     | Rate Source                |
|--|---|----------------|----------------------------|
| $\text{IDH} + \text{OH} \xrightarrow{\text{O}_2} \text{IHC} + \text{HO}_2$   | $9.3 \times 10^{-11}$   | MCM v3.2       | MCM v3.2                   |
| <b>NO<sub>2</sub> reactions (included as verification that high [NO<sub>2</sub>] has only a minor impact on the chemistry)</b>   |   |                |                            |
| $\text{ISOP} + \text{NO}_2 \longrightarrow \text{Products}$  | $1.10 \times 10^{-19}$  | Bernard (2013) | Bernard (2013)             |
| $\text{INO} + \text{NO}_2 \longrightarrow \text{INO}_3\text{N}$  | $2.8 \times 10^{-11}$   | IUPAC          | IUPAC <sup>E</sup>         |
| $\text{INO}_2 + \text{NO}_2 + \text{M} \longrightarrow \text{INO}_4\text{N}$   | $k_0 = 1.3 \times 10^{-29} (\text{T}/300)^{-6.2};$<br>$k_\infty = 8.8 \times 10^{-12}; F_c = 0.31$                              | IUPAC          | IUPAC <sup>F</sup>         |
| $\text{INO}_4\text{N} + \text{M} \longrightarrow \text{INO}_2 + \text{NO}_2 + \text{M}$  | $k_0 = 4.8 \times 10^{-4} \text{e}^{-9285/\text{T}};$<br>$k_\infty = 8.8 \times 10^{15} \text{e}^{-10440/\text{T}}; F_c = 0.31$ | IUPAC          | IUPAC <sup>G</sup>         |
| $\text{IN}^\bullet + \text{NO}_2 \longrightarrow \text{INO}_2\text{N}$   | $2.37 \times 10^{-12}$  | Canosa (1979)  | Canosa (1979) <sup>H</sup> |
| <b>Isoprene + NO<sub>3</sub> (first generation) reactions</b>  |   |                |                            |
| $\text{ISOP} + \text{NO}_3 \longrightarrow \text{IN}^\bullet$  | $3.15 \times 10^{-12} \text{e}^{-450/\text{T}}$   | IUPAC          | IUPAC                      |
| $\text{IN}^\bullet + \text{O}_2 \longrightarrow \text{INO}_2$  | $k_0 = 5.9 \times 10^{-29} (\text{T}/300)^{-3.8};$<br>$k_\infty = 7.8 \times 10^{-12}; F_c = 0.54$                              | IUPAC          | IUPAC                      |
| $\text{INO}_2 + \text{HO}_2 \longrightarrow 0.22 \text{MVK} + 0.015 \text{MACR} + 0.235 \text{OH}$<br>$+ 0.235 \text{NO}_2 + 0.235 \text{CH}_2\text{O} + 0.54 \text{INP}\delta + 0.23 \text{INP}\beta$ | $2.91 \times 10^{-13} \text{e}^{1300/\text{T}} * 0.706$   | this work      | Saunders (2003)            |
| $\text{INO}_2 + \text{INO}_2 \longrightarrow 0.39 \text{INO} + 0.67 \text{ICN} + 0.10 \text{MACR}$   | $5.0 \times 10^{-12}$   | this work      | this work                  |

| Reaction   | Rate Constant <sup>A</sup>              | Rxn Source  | Rate Source  |
|--|---|---|--|
| $+ 0.616 \text{IHN}\delta + 0.154 \text{IHN}\beta + 0.035 \text{INO}_2\text{IN}$<br>$\text{INO}_2 + \text{MHP} \longrightarrow 0.195 \text{INO} + 0.34 \text{ICN} + 0.05 \text{MACR}$<br>$+ 0.308 \text{IHN}\delta + 0.077 \text{IHN}\delta + 0.965 \text{HO}_2$<br>$+ 0.965 \text{HCOOH} + 0.035 \text{INO}_2\text{HM}$ | $5.2 \times 10^{-12}$                   | IUPAC/this work                                   | geometric mean of<br>INO <sub>2</sub> and HMP<br>self-reaction |
| $\text{INO}_2 + \text{NO}_3 \longrightarrow 0.42 \text{MVK} + 0.04 \text{MACR} + 0.46 \text{CH}_2\text{O}$<br>$+ 1.46 \text{NO}_2 + 0.54 \text{ICN} + 0.54 \text{HO}_2$  | $2.3 \times 10^{-12}$                   | MCM v3.2, this work                               | MCM v3.2   |
| $\text{INO}_2 + \text{NO} \longrightarrow 0.12 \text{IDN} + 0.47 \text{ICN} + 0.47 \text{HO}_2$<br>$+ 1.29 \text{NO}_2 + 0.37 \text{MVK} + 0.04 \text{MACR} + 0.41 \text{CH}_2\text{O}$  | $2.7 \times 10^{-12} \text{e}^{360/T}$  | assume same as<br>IHO <sub>2</sub> + NO           | MCM v3.2   |
| $\text{INO} + \text{O}_2 \longrightarrow 0.88 \text{ICN} + 0.88 \text{HO}_2 + 0.12 \text{MACR}$<br>$+ 0.12 \text{CH}_2\text{O} + 0.12 \text{NO}_2$   | $2.5 \times 10^{-14} \text{e}^{-300/T}$ | MCM v3.2, this work                               | MCM v3.24  |
| <b>[1,5]-H-Shift of trans-[1,4]-INO reactions</b>  |   |   |  |
| $\text{INO} \xrightarrow{\text{O}_2} \text{IHNO}_2$  | $2 \times 10^5 \text{ s}^{-1}$          | Kwan (2012)                                       | this work  |
| $\text{IHNO}_2 + \text{NO}_3 \longrightarrow \text{IHNO} + \text{NO}_2$  | $2.3 \times 10^{-12}$                   | assume same as INO <sub>2</sub> + NO <sub>3</sub> | assume same as INO <sub>2</sub> + NO <sub>3</sub>              |
| $\text{IHNO}_2 + \text{NO} \longrightarrow \text{IHNO} + \text{NO}_2$  | $2.7 \times 10^{-12} \text{e}^{360/T}$  | assume same as INO <sub>2</sub> + NO              | assume same as INO <sub>2</sub> + NO                           |
| $\text{IHNO} + \text{O}_2 \longrightarrow \text{IHCN} + \text{HO}_2$   | $2.5 \times 10^{-14} \text{e}^{-300/T}$ | assume same as INO + O <sub>2</sub>               | assume same as INO + O <sub>2</sub>                            |



| Reaction   | Rate Constant <sup>A</sup>                     | Rxn Source                                | Rate Source                              |
|--|--|---|--|
| $\text{IHNO}_2 + \text{HO}_2 \longrightarrow \text{IHPN}$  | $2.91 \times 10^{-13}$<br>$e^{1300/T} * 0.706$ | assume IHPN only product                  | Saunders (2003)                          |
| $\text{IHNO}_2 + \text{IHNO}_2 \longrightarrow 0.46 \text{ IHNO} + 0.77 \text{ IHCN}$<br>$+ 0.77 \text{ IDHN}$   | $2 * 5.0 \times 10^{-12}$                      | assume same $\text{INO}_2 + \text{INO}_2$ | this work                                |
| $\text{IHNO}_2 + \text{INO}_2 \longrightarrow 0.195 \text{ INO} + 0.385 \text{ ICN} + 0.308 \text{ IHN}\delta$<br>$+ 0.077 \text{ IHN}\beta + 0.385 \text{ IHCN} + 0.385 \text{ IDHN}$<br>$+ 0.035 \text{ INO}_2\text{IHN} + 0.195 \text{ IHNO}$ | $2 * 5.0 \times 10^{-12}$                      | assume same $\text{INO}_2 + \text{INO}_2$ | this work                                |
| $\text{IHNO}_2 + \text{HMP} \longrightarrow 0.195 \text{ IHNO} + 0.385 \text{ IHCN} + 0.385 \text{ IDHN}$<br>$+ 0.965 \text{ HO}_2 + 0.965 \text{ HCOOH} + 0.035 \text{ IHNO}_2\text{HM}$  | $2 * 5.2 \times 10^{-12}$                      | assume same $\text{INO}_2 + \text{HMP}$   | this work                                |
| <b>[1,6]-H shift of trans-[1,4]-INO<sub>2</sub> reactions</b>  |  |   |  |
| $\text{INO}_2 \xrightarrow{\text{O}_2} \text{IPNO}_2$  | $4 \times 10^{-4} \text{ s}^{-1}$              | this work                                 | this work                                |
| $\text{IPNO}_2 \xrightarrow{1,4\text{-Hshift}} \text{ICPN} + \text{OH}$  | $2 \times 10^{-2} \text{ s}^{-1}$              | this work                                 | this work                                |
| $\text{IPNO}_2 + \text{NO} \longrightarrow \text{IPNO} + \text{NO}_2$  | $2.7 \times 10^{-12} e^{360/T}$                | assume same $\text{INO}_2 + \text{NO}$    | assume same $\text{INO}_2 + \text{NO}$   |
| $\text{IPNO}_2 + \text{NO}_3 \longrightarrow \text{IPNO} + \text{NO}_2$  | $2.3 \times 10^{-12}$                          | assume same $\text{INO}_2 + \text{NO}_3$  | assume same $\text{INO}_2 + \text{NO}_3$ |
| $\text{IPNO} + \text{O}_2 \longrightarrow \text{ICPN} + \text{HO}_2$   | $2.5 \times 10^{-14} e^{-300/T}$               | assume same $\text{INO} + \text{O}_2$     | assume same $\text{INO} + \text{O}_2$    |

| Reaction   | Rate Constant <sup>A</sup>                             | Rxn Source   | Rate Source     |
|--|--|--|-----------------|
| IPNO <sub>2</sub> + HO <sub>2</sub> → IDPN   | 2.91 x 10 <sup>-13</sup><br>e <sup>1300/T</sup> *0.706 | assume same IHNO <sub>2</sub> + HO <sub>2</sub>    | Saunders (2003) |
| IPNO <sub>2</sub> + IPNO <sub>2</sub> → 0.46 IPNO + 0.77 ICPN + 0.77 IHPN  | 2*5.0 x 10 <sup>-12</sup>                              | assume same as INO <sub>2</sub> + INO <sub>2</sub> | this work       |
| IPNO <sub>2</sub> + INO <sub>2</sub> → 0.23 IPNO + 0.385 ICPN + 0.385 IHPN<br>+ 0.23 INO + 0.308 IHNδ + 0.077 IHNβ + 0.385 ICN | 2*5.0 x 10 <sup>-12</sup>                              | assume same as INO <sub>2</sub> + INO <sub>2</sub> | this work       |
| IPNO <sub>2</sub> + HMP → 0.23 IPNO + 0.385 ICPN + 0.385 IHPN<br>+ HCOOH + HO <sub>2</sub>                                     | 2*5.2 x 10 <sup>-12</sup>                              | assume same as INO <sub>2</sub> + MHP              | this work       |
| IPNO <sub>2</sub> + IHNO <sub>2</sub> → 0.23 IPNO + 0.385 ICPN + 0.385 IHPN<br>+ 0.23 IHNO + 0.385 IDHN + 0.385 IHCN           | 2*5.0 x 10 <sup>-12</sup>                              | assume same as INO <sub>2</sub> + INO <sub>2</sub> | this work       |
| <b>INP Reactions</b>   |  |  |                 |
| INPδ + wall → Products   | 9 x 10 <sup>-6</sup> s <sup>-1</sup>                   | NA   | this work       |
| INPβ + wall → Products   | 9 x 10 <sup>-6</sup> s <sup>-1</sup>                   | NA   | this work       |
| INHEβ + wall → Products  | 9 x 10 <sup>-6</sup> s <sup>-1</sup>                   | NA   | this work       |
| INHEδ + wall → Products  | 9 x 10 <sup>-6</sup> s <sup>-1</sup>                   | NA   | this work       |
| INHEδ <sub>2</sub> + wall → Products   | 9 x 10 <sup>-6</sup> s <sup>-1</sup>                   | NA   | this work       |
| INPδ + OH → 0.37 INHEδ + 0.37 OH + 0.08 IHPE +   | 1.1 x 10 <sup>-10</sup>                                | this work  | Lee (2014) *    |

| Reaction   | Rate Constant <sup>A</sup>                             | Rxn Source | Rate Source                                       |
|--|--|------------|---|
| + 0.08 NO <sub>2</sub> + 0.55 INPHO <sub>2</sub> δ   |  |            |   |
| INPδ + OH → INO <sub>2</sub> + HO <sub>2</sub>   | 6.9 x 10 <sup>-12</sup>                                | this work  | estimated from St. Clair (2015)                   |
| INPβ + OH → 0.78 INHEβ + 0.78 OH + 0.22 INPHO <sub>2</sub> β   | 4.2 x 10 <sup>-11</sup>                                | this work  | Lee (2014) *                                      |
| INPβ + OH → INO <sub>2</sub> + HO <sub>2</sub>   | 6.9 x 10 <sup>-12</sup>                                | this work  | estimated from St. Clair (2015)                   |
| INPHO <sub>2</sub> β + HO <sub>2</sub> → 0.27 IHDPN + 0.73 OH + 0.73 HO <sub>2</sub> + 0.73 CH <sub>2</sub> O<br>+ 0.72 C <sub>4</sub> CPN <sub>A</sub> + 0.01 C <sub>4</sub> CPN <sub>K</sub> | 2.91 x 10 <sup>-13</sup><br>e <sup>1300/T</sup> *0.706 | this work  | Saunders (2003)                                   |
| INPHO <sub>2</sub> β + NO <sub>3</sub> → NO <sub>2</sub> + HO <sub>2</sub> + CH <sub>2</sub> O + 0.98 C <sub>4</sub> CPN <sub>A</sub> + 0.02 C <sub>4</sub> CPN <sub>K</sub>                   | 2.3 x 10 <sup>-12</sup>                                | this work  | assume same as INO <sub>2</sub> + NO <sub>3</sub> |
| INPHO <sub>2</sub> β + NO → 0.04 IHDPN + 0.96 NO <sub>2</sub> + 0.96 HO <sub>2</sub> + 0.02 C <sub>4</sub> CPN <sub>K</sub><br>+ 0.94 C <sub>4</sub> CPN <sub>A</sub> + 0.96 CH <sub>2</sub> O | 2.7 x 10 <sup>-12</sup> e <sup>360/T</sup>             | this work  | assume same as INO <sub>2</sub> + NO              |
| INPHO <sub>2</sub> δ + HO <sub>2</sub> → 0.27 IHDPN + 0.06 ETHLN + 0.73 OH + 0.73 HO <sub>2</sub><br>+ 0.67 PROPNN + 0.67 HPETHNL + 0.06 HPAC  | 2.91 x 10 <sup>-13</sup><br>e <sup>1300/T</sup> *0.706 | this work  | Saunders (2003)                                   |
| INPHO <sub>2</sub> δ + NO <sub>3</sub> → HO <sub>2</sub> + NO <sub>2</sub> + 0.92 PROPNN + 0.92 HPETHNL<br>+ 0.08 HPAC + 0.08 ETHLN  | 2.3 x 10 <sup>-12</sup>                                | this work  | assume same as INO <sub>2</sub> + NO <sub>3</sub> |
| INPHO <sub>2</sub> δ + NO → 0.04 IHDPN + 0.96 HO <sub>2</sub> + 0.96 NO <sub>2</sub><br>+ 0.88 PROPNN + 0.08 ETHLN + 0.88 HPETHNL + 0.08 HPAC  | 2.7 x 10 <sup>-12</sup> e <sup>360/T</sup>             | this work  | assume same as INO <sub>2</sub> + NO              |
| INHEδ + OH → 0.1 INCE + 0.27 HACET + 0.73 CO + 0.27 NO <sub>2</sub> +  | 8.4 x 10 <sup>-12</sup>                                | this work  | assumed same as δ-IEPOX,                          |

| Reaction  | Rate Constant <sup>A</sup>           | Rxn Source             | Rate Source  |
|---|--------------------------------------|------------------------|--|
| + 0.27 CH <sub>2</sub> O + 0.17 PROPNN + 0.17 GLYX + 0.46 C <sub>4</sub> CHN <sub>A</sub>   |                                      | Bates (2014)           |  |
| INHE $\beta$ + OH $\longrightarrow$ 0.08 INCE + 0.31 GLYC + 0.43 NO <sub>2</sub> + 0.31 MGLYX<br>+ 0.20 PROPNN + 0.20 GLYX + 0.12 C <sub>4</sub> DCH + 0.41 CH <sub>2</sub> O + 0.26 C <sub>4</sub> CHN <sub>A</sub><br>+ 0.02 C <sub>4</sub> DCN + 0.01 HACET + 0.01 ETHLN | 1.25 x 10 <sup>-11</sup>             | this work              | assumed same as<br>$\beta$ -IEPOX (avg <i>cis</i><br>& <i>trans</i> ) Bates (2014) |
| INHE $\delta_2$ + OH $\longrightarrow$ 0.1 INCE + 0.9 MGLYX + 0.9 GLYC + 0.9 NO <sub>2</sub>  | 8.4 x 10 <sup>-12</sup>              | this work              | assumed same INHE $\delta$ + OH  |
| INP $\delta$ + NO <sub>3</sub> $\longrightarrow$ 0.35 IDNE + 0.35 OH + 0.11 INPE + 0.11 NO <sub>2</sub> + Products  | 5 x 10 <sup>-15</sup>                | Kwan (2012)            | this work  |
| INP $\beta$ + NO <sub>3</sub> $\longrightarrow$ 0.35 IDNE + 0.35 OH + Products  | 5 x 10 <sup>-15</sup>                | Kwan (2012)            | this work  |
| INP $\delta$ + O <sub>3</sub> $\longrightarrow$ 0.2 OH + 0.17 C <sub>3</sub> CNO <sub>2</sub> + 0.03 C <sub>3</sub> CPO <sub>2</sub><br>+ 0.67 PROPNN + 0.13 HPAC + 0.84 HPETHNL + 0.16 ETHLN   | 1.3 x 10 <sup>-17</sup>              | this work <sup>I</sup> | this work  |
| INP $\beta$ + O <sub>3</sub> $\longrightarrow$ Products   | 3.8 x 10 <sup>-19</sup>              | NA                     | Lee (2014) *   |
| <b>ICN Reactions</b>  |                                      |                        |  |
| ICN + wall $\longrightarrow$ Products   | 6 x 10 <sup>-6</sup> s <sup>-1</sup> | NA                     | this work  |
| ICN + OH $\xrightarrow{\text{O}_2}$ 0.51 ICHNO <sub>2</sub> I <sub>5</sub> + 0.08 NO <sub>2</sub> + 0.41 ICHNO <sub>2</sub> I <sub>4</sub> + 0.08 ICHE  | 1.1 x 10 <sup>-10</sup>              | this work see          | Lee (2014) *   |
| ICN + OH $\xrightarrow{\text{H-abstraction}}$ Products  | 2.0 x 10 <sup>-11</sup>              | NA                     | MCM v3.2   |
| ICHNO <sub>2</sub> I <sub>5</sub> $\longrightarrow$ 0.86 C <sub>4</sub> CPN <sub>A</sub> + CO + HO <sub>2</sub> + 0.14 C <sub>4</sub> CPN <sub>K</sub>  | > 0.5 s <sup>-1</sup>                | this work              | assumed > [1,4]-H shift<br>Crounse (2012)  |

| Reaction  | Rate Constant <sup>A</sup>                            | Rxn Source             | Rate Source                                     |
|---|---|------------------------|---|
| $\text{ICHNO}_2\text{I}_4 \longrightarrow 0.56 \text{C}_4\text{CHN}_\text{A} + 0.44 \text{C}_4\text{CHN}_\text{K} + \text{OH} + \text{CO}$  | $0.5 \text{ s}^{-1}$                                  | this work              | assumed same as [1,4]-H shift in Crounse (2012) |
| $\text{ICHNO}_2\text{I}_4 + \text{HO}_2 \longrightarrow 0.27 \text{ICHPN} + 0.73 \text{OH} + 0.73 \text{HO}_2 + 0.32 \text{PROPNN}$<br>$+ 0.32 \text{GLYX} + 0.25 \text{MGLYX} + 0.25 \text{ETHLN} + 0.08 \text{C}_4\text{CHN}_\text{A} + 0.07 \text{C}_4\text{CHN}_\text{K}$<br>$+ 0.15 \text{CO}$ | $2.91 \times 10^{-13}$<br>$\text{e}^{1300/T} * 0.706$ | this work              | Saunders (2003)                                 |
| $\text{ICHNO}_2\text{I}_4 + \text{NO}_3 \longrightarrow \text{NO}_2 + 0.44 \text{PROPNN} + 0.44 \text{GLYX} + 0.21 \text{CO}$<br>$+ 0.35 \text{MGLYX} + 0.35 \text{ETHLN} + \text{HO}_2 + 0.12 \text{C}_4\text{CHN}_\text{A} + 0.09 \text{C}_4\text{CHN}_\text{K}$                                  | $2.3 \times 10^{-12}$                                 | this work              | assume same $\text{INO}_2 + \text{NO}_3$        |
| $\text{ICHNO}_2\text{I}_4 + \text{NO} \longrightarrow 0.04 \text{IHCDN} + 0.96 \text{NO}_2 + 0.96 \text{HO}_2 + 0.43 \text{PROPNN}$<br>$+ 0.43 \text{GLYX} + 0.34 \text{MGLYX} + 0.34 \text{ETHLN} + 0.11 \text{C}_4\text{CHN}_\text{A} + 0.09 \text{C}_4\text{CHN}_\text{K}$<br>$+ 0.2 \text{CO}$  | $2.7 \times 10^{-12} \text{e}^{360/T}$                | this work              | assume same $\text{INO}_2 + \text{NO}$          |
| $\text{ICN} + \text{NO}_3 \longrightarrow 0.1 \text{INCE} + 0.1 \text{NO}_2 + \text{Products}$  | $8.1 \times 10^{-15}$                                 | this work              | assumed same $\text{INP} + \text{NO}_3$         |
| $\text{ICN} + \text{O}_3 \longrightarrow 0.2 \text{OH} + 0.15 \text{C}_3\text{CNO}_2 + 0.05 \text{C}_3\text{DCO}_2 + 0.59 \text{PROPNN}$<br>$+ 0.21 \text{MGLYX} + 0.74 \text{GLYX} + 0.26 \text{ETHLN}$  | $3.2 \times 10^{-18}$                                 | this work <sup>J</sup> | this work                                       |
| <b>IHN Reactions</b>  |   |                        |   |
| $\text{IHN}\delta + \text{wall} \longrightarrow \text{Products}$  | $7 \times 10^{-6} \text{ s}^{-1}$                     | NA                     | this work                                       |
| $\text{IHN}\beta + \text{wall} \longrightarrow \text{Products}$   | $7 \times 10^{-6} \text{ s}^{-1}$                     | NA                     | this work                                       |

| Reaction  | Rate Constant <sup>A</sup>                     | Rxn Source | Rate Source                                    |
|---|--|------------|--|
| $\text{IHN}\delta + \text{OH} \longrightarrow 0.92 \text{IDHNO}_2\delta + 0.08 \text{IEPOX} + 0.08 \text{NO}_2$   | $1.1 \times 10^{-10}$                          | this work  | Lee (2014) *                                   |
| $\text{IHN}\beta + \text{OH} \longrightarrow \text{IDHNO}_2\beta$   | $4.2 \times 10^{-11}$                          | this work  | Lee (2014) *                                   |
| $\text{IDHNO}_2\delta + \text{HO}_2 \longrightarrow 0.27 \text{IDHPN} + 0.73 \text{OH} + 0.73 \text{HO}_2$<br>+ 0.09 HACET + 0.09 ETHLN + 0.58 PROPNN + 0.58 GLYC<br>+ 0.04 C <sub>4</sub> CHN <sub>A</sub> + 0.02 C <sub>4</sub> CHN <sub>K</sub> + 0.06 CH <sub>2</sub> O | $2.91 \times 10^{-13}$<br>$e^{1300/T} * 0.706$ | this work  | Saunders (2003)                                |
| $\text{IDHNO}_2\delta + \text{NO} \longrightarrow 0.04 \text{IDHDN} + 0.96 \text{HO}_2 + 0.96 \text{NO}_2$<br>+ 0.12 HACET + 0.12 ETHLN + 0.77 PROPNN + 0.77 GLYC<br>+ 0.06 C <sub>4</sub> CHN <sub>A</sub> + 0.02 C <sub>4</sub> CHN <sub>K</sub> + 0.08 CH <sub>2</sub> O | $2.7 \times 10^{-12} e^{360/T}$                | this work  | assume same INO <sub>2</sub> + NO              |
| $\text{IDHNO}_2\delta + \text{NO}_3 \longrightarrow \text{HO}_2 + \text{NO}_2 + 0.12 \text{HACET} + 0.12 \text{ETHLN}$<br>+ 0.80 GLYC + 0.80 PROPNN + 0.06 C <sub>4</sub> CHN <sub>A</sub> + 0.02 C <sub>4</sub> CHN <sub>K</sub><br>+ 0.08 CH <sub>2</sub> O               | $2.3 \times 10^{-12}$                          | this work  | assume same INO <sub>2</sub> + NO <sub>3</sub> |
| $\text{IDHNO}_2\beta + \text{HO}_2 \longrightarrow 0.27 \text{IDHPN} + 0.73 \text{OH} + 0.73 \text{HO}_2$<br>+ 0.56 HACET + 0.17 CH <sub>2</sub> O + 0.56 ETHLN + 0.17 C <sub>4</sub> CHN <sub>K</sub>  | $2.91 \times 10^{-13} e^{1300/T} * 0.706$      | this work  | Saunders (2003)                                |
| $\text{IDHNO}_2\beta + \text{NO} \longrightarrow 0.04 \text{IDHDN} + 0.96 \text{HO}_2 + 0.96 \text{NO}_2$<br>+ 0.74 HACET + 0.74 ETHLN + 0.23 C <sub>4</sub> CHN <sub>K</sub> + 0.23 CH <sub>2</sub> O  | $2.7 \times 10^{-12} e^{360/T}$                | this work  | assume same INO <sub>2</sub> + NO              |
| $\text{IDHNO}_2\beta + \text{NO}_3 \longrightarrow \text{HO}_2 + \text{NO}_2 + 0.76 \text{HACET} + 0.76 \text{ETHLN}$   | $2.3 \times 10^{-12}$                          | this work  | assume same INO <sub>2</sub> + NO <sub>3</sub> |

| Reaction  | Rate Constant <sup>A</sup>                              | Rxn Source   | Rate Source  |
|---|---|--|--|
| + 0.23 C <sub>4</sub> CHN <sub>K</sub> + 0.23 CH <sub>2</sub> O   |   |  |  |
| IHN $\delta$ + NO <sub>3</sub> $\longrightarrow$ 0.11 INHE $\delta_2$ + 0.11 NO <sub>2</sub> + Products   | 7 x 10 <sup>-14</sup>                                   | this work  | Rollins (2009)                                     |
| IHN $\beta$ + NO <sub>3</sub> $\longrightarrow$ Products  | 7 x 10 <sup>-14</sup>                                   | this work  | Rollins (2009)                                     |
| IHN $\delta$ + O <sub>3</sub> $\longrightarrow$ 0.2 OH + 0.17 C <sub>3</sub> CNO <sub>2</sub> + 0.03 C <sub>3</sub> CHO <sub>2</sub><br>+ 0.69 PROPNN + 0.11 HACET + 0.86 GLYC + 0.14 ETHLN | 2.8 x 10 <sup>-17</sup>                                 | this work <sup>K</sup>   | Lee (2014) *                                       |
| IHN $\beta$ + O <sub>3</sub> $\longrightarrow$ Products   | 3.8 x 10 <sup>-19</sup>                                 | NA   | Lee (2014) 6 *                                     |
| <b>MACR Reactions</b>   |   |  |  |
| MACR + O <sub>3</sub> $\longrightarrow$ Products  | 1.4 x 10 <sup>-15</sup> e <sup>-2100/T</sup>            | NA   | MCM v3.2   |
| MACR + OH $\longrightarrow$ 0.45 MACRO <sub>2</sub> + 0.55 MACRHO <sub>2</sub>  | 8.0 x 10 <sup>-12</sup> e <sup>380/T</sup>              | Orlando (1999)   | MCM v3.2/IUPAC                                     |
| MACRO <sub>2</sub> + HO <sub>2</sub> $\longrightarrow$ 0.4 MPAA + 0.4 CO <sub>2</sub> + 0.4 OH + 0.4 PENYLO <sub>2</sub><br>+ 0.2 MAA + 0.2 O <sub>3</sub>                                  | 5.2 x 10 <sup>-13</sup> e <sup>980/T</sup>              | assume ~ acetylperoxy<br>+ HO <sub>2</sub> , Hasson (2004) <sup>L</sup>                                | assume ~ acetylperoxy<br>+ HO <sub>2</sub> , IUPAC |
| MACRO <sub>2</sub> + NO $\longrightarrow$ 0.03 C <sub>4</sub> CN + 0.967 CO <sub>2</sub> + 0.96 PENYLO <sub>2</sub> + NO <sub>2</sub>   | 8.7 x 10 <sup>-12</sup> e <sup>290/T</sup>              | MCM v3.2 <sup>M</sup>  | MCM v3.2   |
| MACRO <sub>2</sub> + NO <sub>3</sub> $\longrightarrow$ CO <sub>2</sub> + PENYLO <sub>2</sub> + NO <sub>2</sub>  | 2.3 x 10 <sup>-12</sup> *1.74                           | MCM v3.2 <sup>N</sup>  | MCM v3.2   |
| MACRHO <sub>2</sub> $\xrightarrow{[1,4]\text{-Hshift}}$ HACET + CO + OH   | 0.5 s <sup>-1</sup>                                     | Crounse (2012)   | Crounse (2012)                                     |
| MACRHO <sub>2</sub> + HO <sub>2</sub> $\longrightarrow$ 0.42 C <sub>4</sub> CHP + 0.58 OH + 0.58 HACET<br>+ 0.58 CO + 0.58 HO <sub>2</sub>  | 2.91 x 10 <sup>-13</sup> 5<br>e <sup>1300/T</sup> *0.62 | assume ~ CH <sub>3</sub> C(O)CH-<br>(O <sub>2</sub> )CH <sub>3</sub> + HO <sub>2</sub> , Hasson (2012) | Saunders (2003)                                    |

| Reaction   | Rate Constant <sup>A</sup>                             | Rxn Source                    | Rate Source                                    |
|--|--|-------------------------------|--|
| MACRHO <sub>2</sub> + NO → 0.03 C <sub>4</sub> CHN + 0.97 NO <sub>2</sub> + 0.97 HACET<br>+ 0.97 CO + 0.97 HO <sub>2</sub>   | 2.7 x 10 <sup>-12</sup> e <sup>360/T</sup>             | Crounse (2012) <sup>O</sup>   | MCM v3.2                                       |
| MACRHO <sub>2</sub> + NO <sub>3</sub> → NO <sub>2</sub> + HACET + CO + HO <sub>2</sub>   | 2.3 x 10 <sup>-12</sup>                                | est. MACRHO <sub>2</sub> + NO | MCM v3.2                                       |
| <b>MVK Reactions</b>   |  |                               |  |
| MVK + OH → MVKHO <sub>2</sub>  | 2.6 x 10 <sup>-12</sup> e <sup>610/T</sup>             | MCM v3.2                      | MCM v3.2                                       |
| MVK + O <sub>3</sub> → Products  | 8.5 x 10 <sup>-16</sup> e <sup>-1520/T</sup>           | NA                            | MCM v3.2                                       |
| MVKHO <sub>2</sub> + HO <sub>2</sub> → 0.04 MGLYX + 0.18 HO <sub>2</sub> + 0.36 GLYC<br>+ 0.36 C <sub>2</sub> CO <sub>2</sub> + 0.04 CH <sub>2</sub> O + 0.54 OH + 0.46 C <sub>4</sub> CHP + 0.14 C <sub>4</sub> DCH | 2.91 x 10 <sup>-13</sup><br>e <sup>1300/T</sup> *0.625 | Praske (2015) <sup>P</sup>    | Saunders (2003)                                |
| MVKHO <sub>2</sub> + NO → 0.04 C <sub>4</sub> CHN + 0.74 GLYC + 0.74 C <sub>2</sub> CO <sub>2</sub><br>+ 0.96 NO <sub>2</sub> + 0.22 CH <sub>2</sub> O + 0.22 MGLYX + 0.22 HO <sub>2</sub>                           | 2.7 x 10 <sup>-12</sup> e <sup>360/T</sup>             | Praske (2015)                 | assume same INO <sub>2</sub> + NO              |
| MVKHO <sub>2</sub> + NO <sub>3</sub> → 0.76 GLYC + 0.76 C <sub>2</sub> CO <sub>2</sub> + NO <sub>2</sub> + 0.24 CH <sub>2</sub> O<br>+ 0.24 MGLYX + 0.24 HO <sub>2</sub>   | 2.3 x 10 <sup>-12</sup>                                | est. MVKHO <sub>2</sub> + NO  | assume same INO <sub>2</sub> + NO <sub>3</sub> |
| <b>Miscellaneous Reactions</b>   |  |                               |  |
| GLYC + OH → Products   | 1.1 x 10 <sup>-11</sup>                                | NA                            | JPL  |
| HPETHNL + OH → Products  | 1.1 x 10 <sup>-11</sup>                                | NA                            | assume ~ to GLYC + OH                          |
| PROPNN + OH → MGLYX + NO <sub>2</sub>  | 1.0 x 10 <sup>-12</sup>                                | MCM v3.2                      | MCM v3.2                                       |



| Reaction   | Rate Constant <sup>A</sup>                | Rxn Source   | Rate Source                                       |
|--|---|--------------|---|
| ETHLN + OH $\longrightarrow$ Products  | $3.4 \times 10^{-12}$                     | NA           | MCM v3.2  |
| IHCN + OH $\longrightarrow$ Products   | $1 \times 10^{-11}$                       | NA           | match expt decay                                  |
| IHPN + OH $\longrightarrow$ Products   | $1 \times 10^{-11}$                       | NA           | match expt decay                                  |
| IDHN + OH $\longrightarrow$ Products   | $1 \times 10^{-11}$                       | NA           | match expt decay                                  |
| C <sub>4</sub> CHN <sub>A</sub> + OH $\longrightarrow$ PROPNN + HO <sub>2</sub> + CO   | $1.7 \times 10^{-11}$                     | Kwok (1995)  | Kwok (1995)                                       |
| C <sub>4</sub> CPN <sub>A</sub> + OH $\longrightarrow$ PROPNN + OH + CO  | $1.7 \times 10^{-11}$                     | Kwok (1995)  | Kwok (1995)                                       |
| <b>Reactions included to test different decomposition branching ratios for ICHNO<sub>2</sub>I<sub>4</sub> <sup>Q</sup></b>   |   |              |   |
| ICHNO <sub>2</sub> I <sub>4</sub> + HO <sub>2</sub> $\longrightarrow$ 0.27 ICHPN + 0.73 OH + 0.73 HO <sub>2</sub><br>+ 0.41 C <sub>4</sub> CHN <sub>A</sub> + 0.32 C <sub>4</sub> CHN <sub>K</sub> + 0.73 CO | $2.91 \times 10^{-13} e^{1300/T} * 0.706$ | this work    | Saunders (2003)                                   |
| ICHNO <sub>2</sub> I <sub>4</sub> + NO <sub>3</sub> $\longrightarrow$ NO <sub>2</sub> + HO <sub>2</sub> + 0.56 C <sub>4</sub> CHN <sub>A</sub><br>+ 0.44 C <sub>4</sub> CHN <sub>K</sub> + CO                | $2.3 \times 10^{-12}$                     | this work    | assume same as INO <sub>2</sub> + NO <sub>3</sub> |
| ICHNO <sub>2</sub> I <sub>4</sub> + NO $\longrightarrow$ 0.04 IHCDN + 0.96 NO <sub>2</sub> + 0.96 HO <sub>2</sub><br>+ 0.54 C <sub>4</sub> CHN <sub>A</sub> + 0.42 C <sub>4</sub> CHN <sub>K</sub> + 0.96 CO | $2.7 \times 10^{-12} e^{360/T}$           | this work    | assume same INO <sub>2</sub> + NO                 |
| <b>Reactions included to test reduced INHE yield from INP + OH (Section 4.4.1) <sup>Q</sup></b>  |   |              |   |
| INP $\delta$ + OH $\longrightarrow$ 0.24 INHE $\delta$ + 0.24 OH<br>+ 0.08 IHPE + 0.08 NO <sub>2</sub> + 0.68 INPHO <sub>2</sub> $\delta$  | $1.1 \times 10^{-10}$<br>this work        | Lee (2014) * |   |

| Reaction   | Rate Constant <sup>A</sup> | Rxn Source | Rate Source  |
|--|----------------------------|------------|--------------|
| INP $\beta$ + OH $\longrightarrow$ 0.50 INHE $\beta$ + 0.50 OH<br>+ 0.50 INPHO $_2\beta$ | 4.2 x 10 <sup>-11</sup>    | this work  | Lee (2014) * |

\*Because actual rate constant is unknown assumed OH rate constant is the same as the OH rate constant for hydroxynitrates produced from high NO<sub>x</sub> OH isoprene oxidation. \*\* Branching ratios only estimated to verify probability of chemistry occurring through this pathway. Branching ratios need to be experimentally verified with synthetic standards. <sup>A</sup> Rate constant units are in cm<sup>3</sup> molec<sup>-1</sup>s<sup>-1</sup> unless noted otherwise. <sup>B</sup> Rate constant calculated using a weighted average of the distribution fractions and the rate constants for all the IHO<sub>2</sub> isomers reported by Jenkin (1998). <sup>C</sup> Calculated assuming *cis: trans*  $\beta$ -IEPOX ratio is 1:2.13 and no  $\delta$ -IEPOX forms. <sup>D</sup> MVK/MACR Aschmann (1995) & Grosjean (1993); OH Atkinson (1992), Paulson (1992), & Neeb (1999); HO<sub>2</sub> Malkin (2010). <sup>E</sup> Based on C<sub>2</sub>H<sub>5</sub>O + NO<sub>2</sub> rate constant. <sup>F</sup> Based on C<sub>2</sub>H<sub>5</sub>O<sub>2</sub> + NO<sub>2</sub> rate constant. <sup>G</sup> Based on C<sub>2</sub>H<sub>5</sub>O<sub>2</sub>NO<sub>2</sub> decomposition rate constant. <sup>H</sup> Based on CH<sub>3</sub> + NO<sub>2</sub> rate constant. <sup>I</sup> Products for C<sub>3</sub>CNO<sub>2</sub> and C<sub>3</sub>CPO<sub>2</sub> were not included in the kinetic mechanism. <sup>J</sup> Products for C<sub>3</sub>CNO<sub>2</sub> and C<sub>3</sub>DCO<sub>2</sub> were not included in the kinetic mechanism. <sup>K</sup> Products for C<sub>3</sub>CNO<sub>2</sub> and C<sub>3</sub>CHO<sub>2</sub> were not included in the kinetic mechanism. <sup>L</sup> Products for PENYLO<sub>2</sub> were not included in the kinetic mechanism. <sup>M</sup> Nitrate yield from secondary RO<sub>2</sub> of MVK, Praske (2015). <sup>N</sup> Products for PENYLO<sub>2</sub> were not included in the kinetic mechanism. <sup>O</sup> Assume nitrate yield similar to secondary RO<sub>2</sub> from MVK, Praske (2015). <sup>P</sup> Products for C<sub>2</sub>CO<sub>2</sub> are not included in the kinetic mechanism. <sup>Q</sup> Reactions replaced old reactions in base case of kinetic mechanism. See Table A5 for full names of the abbreviations used above.

**Table A.4:** List of photolysis reactions in the kinetic mechanism.

| Reaction   | source of cross section | source of quantum yield | source of reaction |
|--|-------------------------|-------------------------|--------------------|
| Basic Reactions  |                         |                         |                    |
| $\text{H}_2\text{O}_2 + h\nu \longrightarrow 2 \text{OH}$                            | Kahan (2012)            | JPL                     | JPL                |
| $\text{O}_3 + h\nu \longrightarrow \text{O}(^1\text{D}) + \text{O}_2$                | JPL                     | JPL                     | JPL                |
| $\text{O}_3 + h\nu \longrightarrow \text{O} + \text{O}_2$                            | JPL                     | JPL                     | JPL                |
| $\text{NO}_2 + h\nu \longrightarrow \text{O} + \text{NO}$                            | JPL                     | JPL                     | JPL                |
| $\text{NO}_3 + h\nu \longrightarrow \text{NO} + \text{O}_2$                          | JPL                     | JPL                     | JPL                |
| $\text{NO}_3 + h\nu \longrightarrow \text{NO}_2 + \text{O}$                          | JPL                     | JPL                     | JPL                |
| $\text{HONO} + h\nu \longrightarrow \text{OH} + \text{NO}$                           | JPL                     | JPL                     | JPL                |
| $\text{HNO}_3 + h\nu \longrightarrow \text{OH} + \text{NO}_2$                        | JPL                     | JPL                     | JPL                |
| $\text{N}_2\text{O}_5 + h\nu \longrightarrow \text{NO}_2 + \text{NO}_3$              | JPL                     | JPL                     | JPL                |
| Non-nitrate Hydrocarbon Reactions  |                         |                         |                    |
| $\text{CH}_2\text{O} + h\nu \longrightarrow 2 \text{HO}_2 + \text{CO}$               | JPL                     | JPL                     | JPL                |
| $\text{CH}_2\text{O} + h\nu \longrightarrow \text{H}_2 + \text{CO}$                  | JPL                     | JPL                     | JPL                |
| $\text{GLYC} + h\nu \longrightarrow 2 \text{HO}_2 + \text{CO} + \text{CH}_2\text{O}$ | JPL                     | JPL                     | JPL                |

| Reaction  | source of cross section | source of quantum yield | source of reaction |
|---|-------------------------|-------------------------|--------------------|
| GLYC + hv $\longrightarrow$ CH <sub>3</sub> OH + CO                                 | JPL                     | JPL                     | JPL                |
| GLYC + hv $\longrightarrow$ OH + CH <sub>2</sub> CHO                                | JPL                     | JPL                     | JPL                |
| HPETHNL + hv $\longrightarrow$ Products   | assume ~ GLYC           | assume ~ GLYC           | assume ~ GLYC      |
| GLYX + hv $\longrightarrow$ 2 HO <sub>2</sub> + 2 CO                                | JPL                     | JPL                     | JPL                |
| GLYX + hv $\longrightarrow$ H <sub>2</sub> + 2 CO                                   | JPL                     | JPL                     | JPL                |
| GLYX + hv $\longrightarrow$ CH <sub>2</sub> O + CO                                  | JPL                     | JPL                     | JPL                |
| MGLYX + hv $\longrightarrow$ CH <sub>3</sub> CO + HO <sub>2</sub> + CO              | JPL                     | JPL                     | JPL                |
| MACR + hv $\longrightarrow$ CH <sub>2</sub> CCH <sub>3</sub> + HO <sub>2</sub> + CO | MCM v3.2                | MCM v3.2                | MCM v. 3.2         |
| MACR + hv $\longrightarrow$ CH <sub>2</sub> CCH <sub>3</sub> CO + HO <sub>2</sub>   | MCM v3.2                | MCM v3.2                | MCM v. 3.2         |
| MVK + hv $\longrightarrow$ CH <sub>3</sub> CHCH <sub>2</sub> + CO                   | MCM v3.2                | MCM v3.2                | MCM v. 3.2         |
| MVK + hv $\longrightarrow$ CH <sub>3</sub> CO + CH <sub>2</sub> CH                  | MCM v3.2                | MCM v3.2                | MCM v. 3.2         |
| ISOPOOH + hv $\longrightarrow$ IHO + OH   | MCM v3.2                | MCM v3.2                | MCM v. 3.2         |
| Nitrate Hydrocarbon Reactions   |                         |                         |                    |
| CH <sub>3</sub> ONO + hv $\longrightarrow$ NO + HO <sub>2</sub> + CH <sub>2</sub> O | JPL                     | JPL                     | JPL                |
| INP + hv $\longrightarrow$ INO + OH   | MCM v3.2                | MCM v3.2                | MCM v. 3.2         |
| IHPN + hv $\longrightarrow$ IHNO + OH   | assume same INP         | assume same INP         | assume same INP    |

| Reaction  | source of cross section                                    | source of quantum yield                       | source of reaction              |
|---|--|---|---------------------------------|
| $\text{ICN} + h\nu \longrightarrow \text{PROPNN} + 2 \text{CO} + 2 \text{HO}_2$                                     | MCM v3.2   | 0.00195, MCM v3.2                             | MCM v. 3.2                      |
| $\text{IHN} + h\nu \longrightarrow \text{IO} + \text{NO}_2$   | MCM v3.2   | MCM v3.2                                      | MCM v. 3.2                      |
| $\text{IHCN} + h\nu \longrightarrow \text{NO}_2 + \text{Products}$  | assume same MVK  | assume same MVK                               | assume O-NO <sub>2</sub> breaks |
| $\text{IDHN} + h\nu \longrightarrow \text{NO}_2 + \text{Products}$  | assume same IHN  | assume same IHN                               | assume same IHN                 |
| $\text{C}_4\text{DCN} + h\nu \longrightarrow \text{NO}_2 + \text{Products}$   | assume same MGLYX  | assume same MGLYX                             | assume O-NO <sub>2</sub> breaks |
| $\text{C}_4\text{CHN}_\text{A} + h\nu \longrightarrow \text{NO}_2 + \text{Products}$                                | assume same C <sub>3</sub> H <sub>7</sub> CHO <sup>A</sup> | assume same C <sub>3</sub> H <sub>7</sub> CHO | assume O-NO <sub>2</sub> breaks |
| $\text{C}_4\text{CPN}_\text{A} + h\nu \longrightarrow \text{OH} + \text{MGLYX} + \text{CH}_2\text{O} + \text{NO}_2$ | assume same INP  | assume same INP                               | assume same INP                 |
| $\text{C}_4\text{CHN}_\text{K} + h\nu \longrightarrow \text{NO}_2 + \text{Products}$                                | assume same MEK <sup>B</sup>                               | assume same MEK                               | assume O-NO <sub>2</sub> breaks |
| $\text{C}_4\text{CPN}_\text{K} + h\nu \longrightarrow \text{OH} + \text{MGLYX} + \text{CH}_2\text{O} + \text{NO}_2$ | assume same INP  | assume same INP                               | assume same INP                 |
| $\text{PROPNN} + h\nu \longrightarrow \text{CH}_3\text{COCH}_2\text{O} + \text{NO}_2$                               | MCM v3.2   | MCM v3.2                                      | MCM v3.2                        |
| $\text{PROPNN} + h\nu \longrightarrow \text{CH}_3\text{CO} + \text{CH}_2\text{O} + \text{NO}_2$                     | MCM v3.2   | MCM v3.2                                      | MCM v3.2                        |
| $\text{ETHLN} + h\nu \longrightarrow \text{CH}_2\text{O} + \text{CO} + \text{HO}_2 + \text{NO}_2$                   | MCM v3.2   | MCM v3.2                                      | MCM v3.2                        |
| $\text{ETHLN} + h\nu \longrightarrow \text{CH}_2\text{O} + \text{CO} + \text{HO}_2 + \text{NO}_2$                   | MCM v3.2   | MCM v3.2                                      | MCM v3.2                        |
| Revised photolysis reactions  |  |   |                                 |
| $\text{ICN} + h\nu \longrightarrow \text{PROPNN} + 2 \text{CO} + 2 \text{HO}_2^*$                                   | assume same MACR   | 1, Muller (2014)                              | MCM v. 3.2                      |
| $\text{C}_4\text{DCN} + h\nu \longrightarrow \text{NO}_2 + \text{Products}^*$                                       | assume same MGLYX  | 1, Muller (2014)                              | assume O-NO <sub>2</sub> breaks |

| Reaction  | source of cross section | source of quantum yield        | source of reaction |
|---|-------------------------|--------------------------------|--------------------|
| $C_4CPN_A + h\nu \longrightarrow OH + MGLYX + CH_2O + NO_2$ | assume same $C_3H_7CHO$ | 1, Muller (2014), Wolfe (2012) | assume same as INP |
| $C_4CPN_K + h\nu \longrightarrow OH + MGLYX + CH_2O + NO_2$ | assume same MEK         | 1, Muller (2014), Wolfe (2012) | assume same INP    |
| $PROPNN + h\nu \longrightarrow CH_3COCH_2O + NO_2^*$        | MCM v3.2                | Muller (2014)                  | MCM v. 3.2         |
| $PROPNN + h\nu \longrightarrow CH_3CO + CH_2O + NO_2^*$     | MCM v3.2                | Muller (2014)                  | MCM v. 3.2         |
| $ETHLN + h\nu \longrightarrow CH_2O + CO + HO_2 + NO_2^*$   | MCM v3.2                | Muller (2014)                  | MCM v. 3.2         |
| $ETHLN + h\nu \longrightarrow CH_2O + CO + HO_2 + NO_2^*$   | MCM v3.2                | Muller (2014)                  | MCM v. 3.2         |

Notes: See Table A5 for full names of the abbreviations used above. \* Reactions replaced old reactions in kinetic mechanism. <sup>A</sup> In MCM v3.2  $MACRNO_3$  photolysis is also based on  $C_3H_7CHO$ . <sup>B</sup> Backbone structure is similar to MEK so like MCM v3.2 does for functionalized nitrates we assumed this compound photolyzed like MEK.

**Table A.5:** Full name of abbreviations used in the kinetic mechanism.

| Abbreviation  | Name  |
|---------------|---|
| $C_2CO_2$     | ethanal peroxy radical                      |
| $C_3CHO_2$    | hydroxy acetone peroxy radical              |
| $C_3CNO_2$    | propanone nitrate peroxy radical            |
| $C_3CPO_2$    | hydroperoxy acetone peroxy radical          |
| $C_3DCO_2$    | methyl glyoxal peroxy radical               |
| $C_3H_7CHO$   | 2-methylpropanal                            |
| $C_4CHN$      | $C_4$ carbonyl hydroxynitrate               |
| $C_4CHP$      | $C_4$ carbonyl hydroxy hydroperoxide        |
| $C_4CN$       | $C_4$ carbonyl nitrate with one double bond |
| $C_4CPN$      | $C_4$ nitrooxycarbonyl hydroperoxide        |
| $C_4DCH$      | $C_4$ hydroxy dicarbonyl                    |
| $C_4DCN$      | $C_4$ dicarbonyl nitrate                    |
| $CH_2(OH)_2$  | methanediol                                 |
| $CH_2CCH_3$   | $CH_2C^{\bullet}CH_3$                       |
| $CH_2CCH_3CO$ | $CH_2CCH_3C^{\bullet}O$                     |
| $CH_2CH$      | $CH_2C^{\bullet}H$                          |
| $CH_2CHO$     | $C^{\bullet}H_2CHO$                         |
| $CH_2O$       | formaldehyde                                |
| $CH_3CHCH_2$  | $CH_3CHCH_2$                                |
| $CH_3CO$      | $CH_3C^{\bullet}O$                          |
| $CH_3OH$      | methanol                                    |
| $CO$          | carbon monoxide                             |
| $CO_2$        | carbon dioxide                              |
| $ETHLN$       | ethanal nitrate                             |
| $GLYC$        | glycolaldehyde                              |

| Abbreviation                      | Name  |
|-----------------------------------|---|
| GLYX                              | glyoxal   |
| H <sub>2</sub>                    | dihydrogen  |
| H <sub>2</sub> O                  | water   |
| H <sub>2</sub> O <sub>2</sub>     | hydrogen peroxide   |
| HACET                             | hydroxyacetone  |
| HCOOH                             | formic acid   |
| HMHP                              | hydroxymethyl hydroperoxide   |
| HMP                               | hydroxymethyl peroxy radical (HOCH <sub>2</sub> O <sub>2</sub> )                            |
| HNO <sub>3</sub>                  | nitric acid   |
| HO <sub>2</sub>                   | hydroperoxyl radical  |
| HO <sub>2</sub> NO <sub>2</sub>   | peroxynitric acid   |
| HONO                              | nitrous acid  |
| HOONO                             | peroxynitrous acid  |
| HPAC                              | hydroperoxy acetone   |
| HPETHNL                           | hydroperoxyethanal (not peracetic acid)   |
| ICHE                              | C <sub>5</sub> carbonyl hydroxy epoxide   |
| ICHNO <sub>2</sub> I <sub>4</sub> | C <sub>5</sub> carbonyl hydroxy nitrooxyperoxy radical (Capable of 1,4 H shift)             |
| ICHNO <sub>2</sub> I <sub>5</sub> | C <sub>5</sub> carbonyl hydroxy nitrooxyperoxy radical (Capable of 1,5 H shift)             |
| ICHPN                             | C <sub>5</sub> carbonyl hydroxy nitrooxy hydroperoxide                                      |
| ICN                               | C <sub>5</sub> carbonyl nitrate   |
| ICPDNAH                           | C <sub>5</sub> dinitrooxy peroxyacid hydroxide  |
| ICPN                              | C <sub>5</sub> carbonylhydroperoxide nitrate  |
| IDH                               | C <sub>5</sub> dihydroxy  |
| IDHDN                             | C <sub>5</sub> dinitrate from IDHNO <sub>2</sub> $\delta$ / IDHNO <sub>2</sub> $\beta$ + NO |
| IDHN                              | C <sub>5</sub> dihydroxy nitrate  |
| IDHNO <sub>2</sub> $\beta$        | C <sub>5</sub> dihydroxy nitrooxyperoxy radical– $\beta$ isomer                             |
| IDHNO <sub>2</sub> $\delta$       | C <sub>5</sub> dihydroxy nitrooxyperoxy radical – $\delta$ isomer                           |



| Abbreviation               | Name   |
|----------------------------|--|
| IDHPN                      | C <sub>5</sub> dihydroxy nitrooxy hydroperoxide  |
| IDN                        | C <sub>5</sub> dinitrate   |
| IDNE                       | C <sub>5</sub> dinitrooxy epoxide  |
| IDPN                       | C <sub>5</sub> dihydroperoxide nitrate   |
| IEPOX                      | C <sub>5</sub> hydroxy epoxide   |
| IHC                        | C <sub>5</sub> hydroxy carbonyl  |
| IHCDN                      | C <sub>5</sub> dinitrate from ICHNO <sub>2</sub> I <sub>4</sub> + NO                       |
| IHCN                       | C <sub>5</sub> hydroxy carbonyl nitrate  |
| IHDPN                      | C <sub>5</sub> hydroxy nitrooxy dihydroperoxide  |
| IHNO                       | C <sub>5</sub> hydroxy nitrooxyalkoxy radical  |
| IHNO <sub>2</sub>          | C <sub>5</sub> hydroxy nitrooxyperoxy radical (1,5 H shift product)                        |
| IHNO <sub>2</sub> HM       | ROOR product from IHNO <sub>2</sub> and HMP  |
| IHN $\beta$                | C <sub>5</sub> hydroxy nitrate – $\beta$ isomer  |
| IHN $\delta$               | C <sub>5</sub> hydroxy nitrate – $\delta$ isomer   |
| IHO                        | C <sub>5</sub> hydroxy alkoxy radical  |
| IHO <sub>2</sub>           | C <sub>5</sub> hydroxy peroxy radical  |
| IHPDN                      | C <sub>5</sub> dinitrate from INPHO <sub>2</sub> $\beta$ /INPHO <sub>2</sub> $\delta$ + NO |
| IHPE                       | C <sub>5</sub> hydroxy hydroperoxy epoxide   |
| IHPN                       | C <sub>5</sub> hydroxy hydroperoxide nitrate   |
| IN                         | C <sub>5</sub> nitrooxy radical  |
| INCE                       | C <sub>5</sub> nitrooxy carbonyl epoxide   |
| INHE $\beta$               | C <sub>5</sub> nitrooxy hydroxy epoxide – $\beta$ isomer                                   |
| INHE $\delta$              | C <sub>5</sub> nitrooxy hydroxy epoxide – $\delta$ isomer                                  |
| INHE $\delta$ <sub>2</sub> | C <sub>5</sub> nitrooxy hydroxyl epoxide from NO <sub>3</sub> oxidation of IHN             |
| INO                        | C <sub>5</sub> nitrooxyalkoxy radical  |
| INO <sub>2</sub>           | C <sub>5</sub> nitrooxyperoxy radical  |
| INO <sub>2</sub> HM        | ROOR product from INO <sub>2</sub> and HMP   |

| Abbreviation                  | Name  |
|-------------------------------|---|
| INO <sub>2</sub> IHN          | ROOR product from INO <sub>2</sub> and IHNO <sub>2</sub>                    |
| INO <sub>2</sub> IN           | ROOR product from INO <sub>2</sub> and INO <sub>2</sub>                     |
| INO <sub>2</sub> N            | C <sub>5</sub> nitrooxy nitrite   |
| INO <sub>3</sub> N            | C <sub>5</sub> dinitrate  |
| INO <sub>4</sub> N            | C <sub>5</sub> nitrooxy peroxy nirate                                       |
| INPE                          | C <sub>5</sub> nitrooxy hydroperoxy epoxide                                 |
| INPHO <sub>2</sub> β          | C <sub>5</sub> nitrooxy hydroperoxy hydroxy peroxy radical (From β isomers) |
| INPHO <sub>2</sub> δ          | C <sub>5</sub> nitrooxy hydroperoxy hydroxy peroxy radical (From δ isomers) |
| INPβ                          | C <sub>5</sub> nitrooxy hydroperoxide – β isomer                            |
| INPδ                          | C <sub>5</sub> nitrooxy hydroperoxide – δ isomer                            |
| IPNO                          | C <sub>5</sub> hydroperoxide nitrooxyalkoxy radical                         |
| IPNO <sub>2</sub>             | C <sub>5</sub> hydroperoxide nitrooxyperoxy radical                         |
| ISOP                          | isoprene  |
| ISOPN                         | C <sub>5</sub> hydroxynitrate from OH oxidation chemistry                   |
| ISOPOOH                       | C <sub>5</sub> hydroxy hydroperoxide  |
| MAA                           | methacrylic acid  |
| MACR                          | methacrolein  |
| MACRHO <sub>2</sub>           | peroxy radical from OH addition to MACR                                     |
| MACRO <sub>2</sub>            | peroxy radical from H-abstraction of MACR                                   |
| MGLYX                         | methylglyoxal   |
| MHP                           | methyl hydroperoxide  |
| MPAA                          | methacrylicperoxy acid  |
| MVK                           | methyl vinyl ketone   |
| MVKHO <sub>2</sub>            | peroxy radical from OH addition to MVK                                      |
| N <sub>2</sub> O <sub>5</sub> | dinitrogen pentoxide  |
| NO                            | nitrogen monoxide   |
| NO <sub>2</sub>               | nitrogen dioxide  |

| Abbreviation        | Name                                   |
|---------------------|--|
| NO <sub>3</sub>     | nitrate Radical                        |
| O                   | oxygen radical ( <sup>3</sup> P state) |
| O( <sup>1</sup> D)  | oxygen radical ( <sup>1</sup> D state) |
| O <sub>2</sub>      | molecular oxygen                       |
| O <sub>3</sub>      | ozone                                  |
| OH                  | hydroxyl radical                       |
| PENYLO <sub>2</sub> | propenyl peroxy radical                |
| PROPNN              | propanone nitrate                      |

### References

- Atkinson, R., D. L. Baulch, R. A. Cox, J. N. Crowley, R. F. Hampson, R. G. Hynes, M. E. Jenkin, M. J. Rossi, and J. Troe (2004). "Evaluated Kinetic and Photochemical Data for Atmospheric Chemistry: Volume I - Gas Phase Reactions of O<sub>x</sub>, HO<sub>x</sub>, NO<sub>x</sub> and SO<sub>x</sub> Species". In: *Atmos. Chem. Phys.* 4, pp. 1461–1738.
- Atkinson, R., D. L. Baulch, R. A. Cox, J. N. Crowley, R. F. Hampson, R. G. Hynes, M. E. Jenkin, M. J. Rossi, J. Troe, and IUPAC Subcommittee (2006). "Evaluated Kinetic and Photochemical Data for Atmospheric Chemistry: Volume II – Gas Phase Reactions of Organic Species". In: *Atmos. Chem. Phys.* 6, pp. 3625–4055.
- Bates, Kelvin H. et al. (2014). "Gas Phase Production and Loss of Isoprene Epoxydiols". In: *J. Phys. Chem. A* 118.7, pp. 1237–1246. DOI: 10.1021/jp4107958.
- Bernard, Francois et al. (2013). "Reaction of NO<sub>2</sub> with Selected Conjugated Alkenes". In: *J. Phys. Chem. A* 117.51, pp. 14132–14140.
- Canosa, C., R. D. Penzhorn, and C. Von. Sonntag (1979). "Product Quantum Yields from the Photolysis of NO<sub>2</sub> at 366 nm in the Presence of Ethylene. – The Role of NO<sub>3</sub>\*". In: *Ber. Bunsenges. Phys. Chem.* 83, pp. 217–225.
- Cantrell, Christopher A. et al. (1985). "Kinetic Study of the NO<sub>3</sub>-CH<sub>2</sub>O Reaction and Its Possible Role in Nighttime Tropospheric Chemistry". In: *J. Phys. Chem.* 89, pp. 139–146.
- Crounse, John D. et al. (2012). "Atmospheric Fate of Methacrolein. 1. Peroxy Radical Isomerization Following Addition of OH and O<sub>2</sub>". In: *J. Phys. Chem. A* 116, pp. 5756–5762. DOI: 10.1021/jp211560u.
- Jenkin, M. E., M. D. Hurley, and T. J. Wallington (2007). "Investigation of the Radical Product Channel of the CH<sub>3</sub>COO<sub>2</sub> + HO<sub>2</sub> Reaction in the Gas Phase". In: *Phys. Chem. Chem. Phys.* 9, pp. 3149–3162. DOI: 10.1039/b702757e.

- Jenkin, M. E., S. M. Saunders, and M. J. Pilling (1997). "The Tropospheric Degradation of Volatile Organic Compounds: A Protocol for Mechanism Development". In: *Atmos. Environ.* 31.1, pp. 81–104.
- Jenkin, Michael E., Andrew A. Boyd, and Robert Lesclaux (1998). "Peroxy Radical Kinetics Resulting from the OH-Initiated Oxidation of 1, 3-Butadiene, 2, 3-Dimethyl-1, 3-Butadiene and Isoprene". In: *J. Atmos. Chem.* 29, pp. 267–298. DOI: 10.1023/A:1005940332441.
- Kahan, Tara F. et al. (2012). "Cavity-Enhanced Measurements of Hydrogen Peroxide Absorption Cross Sections from 353 to 410 nm". In: *J. Phys. Chem. A.* 116, pp. 5941–5947. DOI: 10.1021/jp2104616.
- Kwan, A. J. et al. (2012). "Peroxy Radical Chemistry and OH Radical Production during the NO<sub>3</sub>-Initiated Oxidation of Isoprene". In: *Atmos. Chem. Phys.* 12, pp. 7499–7515. DOI: 10.5194/acp-12-7499-2012.
- Kwok, E. S. C. and R. Atkinson (1995). "Estimation of Hydroxyl Radical Reaction Rate Constants for Gas-Phase Organic Compounds Using a Structure-Reactivity Relationship: An Update". In: *Atmos. Environ.* 29.14, pp. 1685–1695.
- Lee, B. H. et al. (2014). "An Iodide-Adduct High-Resolution Time-of-Flight Chemical-Ionization Mass Spectrometer: Application to Atmospheric Inorganic and Organic Compounds". In: *Environ. Sci. Technol.* 48.11, pp. 6309–6317.
- Muller, J. F., J. Peeters, and T. Stavrakou (2014). "Fast Photolysis of Carbonyl Nitrates from Isoprene". In: *Atmos. Chem. Phys.* 14, pp. 2497–2508.
- Paulot, Fabien et al. (2009a). "Unexpected Epoxide Formation in the Gas-Phase Photooxidation of Isoprene". In: *Science* 325, pp. 730–733. DOI: 10.1126/science.1172910.
- Paulot, F. et al. (2009b). "Isoprene Photooxidation: New Insights into the Production of Acids and Organic Nitrates". In: *Atmos. Chem. Phys.* 9, pp. 1479–1501.
- Praske, E. et al. (2015). "Atmospheric Fate of Methyl Vinyl Ketone: Peroxy Radical Reactions with NO and HO<sub>2</sub>". In: *J. Phys. Chem. A.* 119, pp. 4562–4572.
- Rollins, A. W. et al. (2009). "Isoprene Oxidation by Nitrate Radical: Alkyl Nitrate and Secondary Organic Aerosol Yields". In: *Atmos. Chem. Phys.* 9, pp. 6685–6703.
- Sander, S. P. et al. (2011). *Chemical Kinetics and Photochemical Data for Use in Atmospheric Studies, Evaluation No. 17*. Jet Propulsion Laboratory, Pasadena: JPL Publication 10-6.
- Saunders, S. M. et al. (2003). "Protocol for the Development of the Master Chemical Mechanism, MCMv3 (Part A): Tropospheric Degradation of Non-Aromatic Volatile Organic Compounds". In: *Atmos. Chem. Phys.* 3, pp. 161–180.

- St. Clair, J. M. et al. (2015). “Kinetics and Products of the Reaction of the First-Generation Isoprene Hydroxy Hydroperoxide (ISOPOOH) with OH”. In: *J. Phys. Chem. A*. 120, pp. 1441–1451.
- Wolfe, G. M. et al. (2012). “Photolysis, OH Reactivity and Ozone Reactivity of a Proxy for Isoprene-Derived Hydroperoxyenals (HPALDs)”. In: *Phys. Chem. Chem. Phys.* 14, pp. 7276–7286.

*Appendix B*

OVERVIEW OF THE FOCUSED ISOPRENE EXPERIMENT AT  
THE CALIFORNIA INSTITUTE OF TECHNOLOGY (FIXCIT):  
MECHANISTIC CHAMBER STUDIES ON THE OXIDATION OF  
BIOGENIC COMPOUNDS

Nguyen, T. B. et al. (2014). “Overview of the Focused Isoprene eXperiment at the California Institute of Technology (FIXCIT): Mechanistic Chamber Studies on the Oxidation of Biogenic Compounds”. In: *Atmos. Chem. Phys.* 14, pp. 13531–13549. DOI: 10.5194/acp-14-13531-2014.



## Overview of the Focused Isoprene eXperiment at the California Institute of Technology (FIXCIT): mechanistic chamber studies on the oxidation of biogenic compounds

T. B. Nguyen<sup>1</sup>, J. D. Crounse<sup>1</sup>, R. H. Schwantes<sup>1</sup>, A. P. Teng<sup>1</sup>, K. H. Bates<sup>2</sup>, X. Zhang<sup>1</sup>, J. M. St. Clair<sup>1</sup>, W. H. Brune<sup>3</sup>, G. S. Tyndall<sup>4</sup>, F. N. Keutsch<sup>5</sup>, J. H. Seinfeld<sup>2,6</sup>, and P. O. Wennberg<sup>1,6</sup>

<sup>1</sup>Division of Geological and Planetary Sciences, California Institute of Technology, Pasadena, California, USA

<sup>2</sup>Division of Chemistry and Chemical Engineering, California Institute of Technology, Pasadena, California, USA

<sup>3</sup>Department of Meteorology, Pennsylvania State University, University Park, Pennsylvania, USA

<sup>4</sup>Atmospheric Chemistry Division, National Center for Atmospheric Research, Boulder, Colorado, USA

<sup>5</sup>Department of Chemistry, University of Wisconsin – Madison, Madison, Wisconsin, USA

<sup>6</sup>Division of Engineering and Applied Science, California Institute of Technology, Pasadena, California, USA

Correspondence to: T. B. Nguyen (tbn@caltech.edu)

Received: 27 July 2014 – Published in Atmos. Chem. Phys. Discuss.: 25 August 2014

Revised: 10 November 2014 – Accepted: 20 November 2014 – Published: 19 December 2014

**Abstract.** The Focused Isoprene eXperiment at the California Institute of Technology (FIXCIT) was a collaborative atmospheric chamber campaign that occurred during January 2014. FIXCIT is the laboratory component of a synergistic field and laboratory effort aimed toward (1) better understanding the chemical details behind ambient observations relevant to the southeastern United States, (2) advancing the knowledge of atmospheric oxidation mechanisms of important biogenic hydrocarbons, and (3) characterizing the behavior of field instrumentation using authentic standards. Approximately 20 principal scientists from 14 academic and government institutions performed parallel measurements at a forested site in Alabama and at the atmospheric chambers at Caltech. During the 4 week campaign period, a series of chamber experiments was conducted to investigate the dark- and photo-induced oxidation of isoprene,  $\alpha$ -pinene, methacrolein, pinonaldehyde, acylperoxy nitrates, isoprene hydroxy nitrates (ISOPN), isoprene hydroxy hydroperoxides (ISOPOOH), and isoprene epoxydiols (IEPOX) in a highly controlled and atmospherically relevant manner. Pinonaldehyde and isomer-specific standards of ISOPN, ISOPOOH, and IEPOX were synthesized and contributed by campaign participants, which enabled explicit exploration into the oxidation mechanisms and instrument responses for these important atmospheric compounds. The present overview de-

scribes the goals, experimental design, instrumental techniques, and preliminary observations from the campaign. This work provides context for forthcoming publications affiliated with the FIXCIT campaign. Insights from FIXCIT are anticipated to aid significantly in interpretation of field data and the revision of mechanisms currently implemented in regional and global atmospheric models.

### 1 Introduction

#### 1.1 Background

Biogenically produced isoprenoids (hydrocarbons comprised of  $C_5H_8$  units) have global emission rates into the atmosphere surpassing those of anthropogenic hydrocarbons and methane (Guenther et al., 1995, 2012). The biogenic carbon emission flux is dominated by isoprene ( $C_5H_8$ ) and monoterpenes ( $C_{10}H_{16}$ ), which account for approximately 50 and 30 % of the OH reactivity over land, respectively (Fuentes et al., 2000). Furthermore, it has been suggested that the atmospheric oxidation of isoprene, in particular, can buffer the oxidative capacity of forested regions by maintaining levels of the hydroxyl radical (OH) under lower nitric oxide (NO) conditions (Lelieveld et al., 2008). Due to their large abundances,

isoprene and monoterpenes also dominate the global budget of secondary organic aerosol (SOA) (Henze et al., 2008). Thus, the accurate representation of detailed chemistry for isoprene and monoterpene is necessary for meaningful simulations of atmospheric  $\text{HO}_x$  ( $\text{OH} + \text{HO}_2$ ),  $\text{NO}_x$  ( $\text{NO} + \text{NO}_2$ ), surface ozone ( $\text{O}_3$ ), trace gas lifetimes, and SOA.

Unsaturated hydrocarbons like isoprene and monoterpenes are primarily oxidized by OH,  $\text{O}_3$ , and the nitrate ( $\text{NO}_3$ ) radical in the atmosphere. OH oxidation is the dominant fate for isoprene, but  $\text{O}_3$  and  $\text{NO}_3$  oxidation can dominate reactivity for monoterpenes and sesquiterpenes. Our understanding of the OH-initiated isoprene oxidation mechanism has significantly improved during the last decade, following the first suggestion of the capacity of isoprene to produce SOA (Claeys et al., 2004). The mechanistic developments have been propelled by technological advancements in instrumentation (Hansel et al., 1995; Crounse et al., 2006; Jordan et al., 2009; Junninen et al., 2010), enabling the detection of more complex oxidation products derived from isoprene and other biogenic hydrocarbons. However, the scientific understanding of these biogenic oxidation mechanisms is far from complete. It is outside the scope of this overview to describe comprehensively the isoprene and monoterpene oxidation mechanisms. Rather, we provide a brief background of the oxidation of biogenic hydrocarbons, which includes “state-of-the-science” knowledge, to motivate the study. The mechanisms described here are illustrated in Scheme 1.

### 1.1.1 OH oxidation

OH predominantly adds to either of the double bonds of isoprene, followed by the reversible addition of  $\text{O}_2$  (Peeters et al., 2009) to produce several isomers of alkylperoxy radicals ( $\text{RO}_2$ ). In the atmosphere, these  $\text{RO}_2$  react mainly with  $\text{HO}_2$  and NO to form stable products, although self-reaction can be non-negligible under certain conditions. The stable products are often termed oxidized volatile organic compounds (OVOCs). In urban-influenced areas, the “high-NO” pathway is more important and in more pristine environments, the “low-NO” or  $\text{HO}_2$ -dominated pathway is more important. The high-NO pathway generates isoprene hydroxy nitrates (ISOPN) that act as reservoirs for  $\text{NO}_x$ , as well as other products such as methyl vinyl ketone (MVK), methacrolein (MAC), and hydroxyacetone (HAC) (Paulot et al., 2009a). For conditions with sufficiently high  $\text{NO}_2$ -to-NO ratios, as is mainly the case in the atmospheric boundary layer outside of cities, methacryloyl peroxyxynitrate (MPAN) is formed from the photooxidation of MAC. Further oxidation of MPAN can generate SOA (Chan et al., 2010; Surratt et al., 2010). The low-NO pathway generates isoprene hydroxy hydroperoxides (ISOPOOH) in almost quantitative yields, and further OH oxidation of ISOPOOH produces the epoxydiols in an OH-conserving mechanism (Paulot et al., 2009b). In unpolluted atmospheres, when the  $\text{RO}_2$  lifetimes are sufficiently long ( $\sim 100$  s in a forest), isomerization of the  $\text{RO}_2$  followed

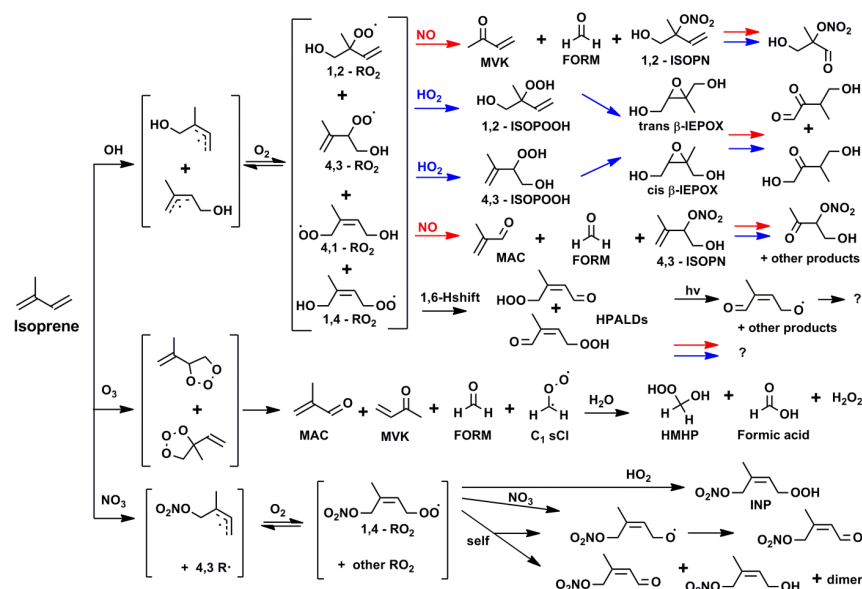
by reaction with  $\text{O}_2$  becomes an important fate, producing the isoprene hydroperoxy aldehydes (HPALDs) and other products (Peeters et al., 2009; Crounse et al., 2011). These  $\text{RO}_2$  isomerization reactions are a type of rapid oxygen incorporation chemistry (Vereecken et al., 2007; Crounse et al., 2013; Ehn et al., 2014) that is thought to be responsible for the prompt generation of low-volatility SOA components. Further generations of OH oxidation in isoprene are currently being explored owing to recent success with chemical syntheses of important OVOCs (Wolfe et al., 2012; Jacobs et al., 2013; Bates et al., 2014; L. Lee et al., 2014). It has been found that the OH oxidation of IEPOX and ISOPN, surprisingly under both low-NO and high-NO conditions, results primarily in fragmentation of the  $\text{C}_5$  skeleton.

Despite extensive work on the isoprene + OH mechanism, large uncertainties persist, some of which directly translate into uncertainties in atmospheric model predictions. These uncertainties stem from, for example, the large range in reported yields for isoprene nitrates (4–15 %) (Paulot et al., 2009a), disagreements up to 90 % in reported MAC and MVK yields from the low-NO pathway (Liu et al., 2013, and references therein), various proposed sources of SOA from the high-NO pathway (Chan et al., 2010; Kjaergaard et al., 2012; Lin et al., 2013), missing contributions to SOA mass from the low-NO pathway (Surratt et al., 2010), uncharacterized fates of oxidized species like HPALDs (which may have isomer dependence), incomplete understanding of oxygen incorporation (Peeters et al., 2009; Crounse et al., 2013), and under-characterized impact of  $\text{RO}_2$  lifetimes on chamber results (Wolfe et al., 2012). The OH oxidation of  $\alpha$ -pinene (Eddingsaas et al., 2012) and other monoterpenes is less well characterized than that of isoprene, but, in general, proceeds through analogous steps.

### 1.1.2 Ozone oxidation

Ozonolysis is a significant sink for unsaturated hydrocarbons and a large nighttime source of OH, particularly in urban-influenced areas. Reaction with ozone is more important for monoterpenes than isoprene, due to the faster rate coefficients (Atkinson and Carter, 1984) and the nighttime emission profile for the monoterpenes. Furthermore, monoterpene ozonolysis is highly efficient at converting VOC mass to SOA (Hoffmann et al., 1997; Griffin et al., 1999). There is a general consensus that ozonolysis occurs via the Criegee mechanism (Criegee, 1975), wherein ozone adds to a hydrocarbon double bond to form a five-member primary ozonide that quickly decomposes to a stable carbonyl product and an energy-rich Criegee intermediate (CI). In  $\alpha$ -pinene oxidation, ozonolysis,  $\text{NO}_3$ -initiated, and OH-initiated reactions all produce pinonaldehyde ( $\text{C}_{10}\text{H}_{16}\text{O}_2$ ) as a major product (Wängberg et al., 1997; Atkinson and Arey, 2003), whereas major first-generation products from isoprene ozonolysis include MAC, MVK, and formaldehyde. The “hot” Criegee can promptly lose OH (Kroll et al., 2001) while ejecting an





**Scheme 1.** Representative mechanism from the OH-, O<sub>3</sub>- and NO<sub>3</sub>-initiated oxidation of isoprene. The most abundant isomers of a particular pathway are shown. Red and blue arrows in the OH-oxidation scheme denote the NO-dominated and HO<sub>2</sub>-dominated RO<sub>2</sub> reactions, respectively. For the ozonolysis reaction, only the C<sub>1</sub> sCI and its reaction with water are shown as further-generation chemistry. For the NO<sub>3</sub>-oxidation pathway, only one isomer each of R and RO<sub>2</sub> radicals is shown for brevity. Abbreviations are defined in the text.

alkyl radical, or become stabilized by collision with atmospheric gases to form a stabilized Criegee intermediate (sCI) with long enough lifetimes to react bimolecularly. The subsequent reactions of sCIs produce both carbonyl products and non-carbonyl products such as hydroperoxides. The *syn* and *anti* conformers of CIs and sCI can have substantially different reactivities (Kuwata et al., 2010; Anglada et al., 2011), with *syn* conformers more likely to decompose unimolecularly, possibly through a vinyl hydroperoxide intermediate (Donahue et al., 2011).

It has been suggested that reaction with water molecules is a major (if not dominant) bimolecular fate of sCI in the atmosphere due to the overwhelming abundance of atmospheric water (Fenske et al., 2000). This suggestion is supported by observations of high mixing ratios (up to 5 ppbv) of hydroxymethyl hydroperoxide (HMHP), a characteristic product of reactions of the smallest sCI (CH<sub>2</sub>OO) with water (Neeb et al., 1997), over forested regions and in biomass burning plumes (Gäb et al., 1985; Lee et al., 1993, 2000; Valverde-Canossa et al., 2006). Although HMHP and other hydroperoxides produced from ozonolysis are important atmospheric compounds, their yield estimates are highly uncertain (Becker et al., 1990; Neeb et al., 1997; Sauer et al., 1999; Hasson et al., 2001; Huang et al., 2013). This may be attributable to the fact that hydroperoxide yields have mainly

been determined by offline methods or under conditions with highly elevated hydrocarbon loadings. Furthermore, few empirical data exist on the humidity dependence of product branching in this reaction. Lastly, the rate coefficients for the sCI + H<sub>2</sub>O reaction, and other sCI reactions, are still uncertain by several orders of magnitude (Johnson and Marston, 2008; Welz et al., 2012), precluding the assessment of their atmospheric importance.

### 1.1.3 Nitrate oxidation

NO<sub>3</sub> oxidation also produces RO<sub>2</sub> radicals by addition to alkenes in the presence of O<sub>2</sub>. Owing to its high reaction rate coefficient coupled to atmospheric abundance, α-pinene is expected to be an important sink for NO<sub>3</sub> in many areas. The NO<sub>3</sub>-derived RO<sub>2</sub> radicals react with (a) NO<sub>3</sub> to form alkoxy radicals (RO) that lead primarily to the production of nitrooxy carbonyls (b); with other RO<sub>2</sub> radicals to form RO radicals, nitrooxy carbonyls, hydroxy nitrates, and nitrooxy peroxy dimers; and (c) with HO<sub>2</sub> to form nitrooxy hydroperoxides. Further generation NO<sub>3</sub>-oxidation produces dinitrates, amongst other products. As the NO<sub>3</sub> addition initiates the reaction, the thermodynamically preferred organic hydroxy nitrates produced through nighttime oxidation may be structurally different than those produced in the daytime through OH oxidation. During nighttime oxidation, tropo-

spheric HO<sub>2</sub> mixing ratios often surpass those of NO<sub>3</sub> (Mao et al., 2012), implying HO<sub>2</sub> reaction to be a common fate for NO<sub>3</sub>-derived RO<sub>2</sub>. However, previous studies of this reaction have maintained conditions where minimal HO<sub>2</sub> + RO<sub>2</sub> chemistry occurs and the dominant fate of RO<sub>2</sub> is reaction with NO<sub>3</sub> and RO<sub>2</sub> (Ng et al., 2008; Perring et al., 2009; Rollins et al., 2009; Kwan et al., 2012). This may be one of the reasons why nitrooxy hydroperoxides (the RO<sub>2</sub> + HO<sub>2</sub> product) are observed with much higher relative abundances in ambient air (Beaver et al., 2012) than in chamber studies.

## 1.2 Scientific goals

The 2014 Focused Isoprene eXperiment at the California Institute of Technology (FIXCIT) is a collaborative atmospheric chamber campaign focused on advancing the understanding of biogenic hydrocarbon oxidation in the atmosphere. The campaign was motivated by the communal need for a tight coupling of field and laboratory efforts toward understanding the mechanistic details responsible for ambient observations, exploring explicit chemistry as driven by the fate of RO<sub>2</sub> radicals through well-controlled experiments, and fully characterizing instrumental response to important trace gases using authentic standards to guide data interpretation. To accomplish these goals, a suite of instruments typically deployed for field missions was used to perform parallel measurements at a forested site in Alabama and then in the atmospheric chambers at Caltech. This overview provides an account of the goals and conditions for the experiments performed during the campaign. A key component of FIXCIT is the re-design of “typical chamber experiments” to recreate the ambient atmosphere with higher fidelity so that results from laboratory studies can be implemented in models and used to interpret ambient observations with higher confidence.

### 1.2.1 Understanding ambient observations

FIXCIT was designed as a sister investigation to the 2013 Southern Oxidant and Aerosol Study (SOAS). During SOAS (June–July 2013), a select sub-suite of instruments recorded ambient observations above the forest canopy on top of a metal walk-up tower 20 m in height. The sampling site, located in Brent, Alabama at the Centreville (CTR) SEARCH location managed by the Electric Power Research Institute (CTR, latitude 32.90289 longitude −87.24968), was surrounded by a temperate mixed forest (part of the Talladega National Forest) that was occasionally impacted by anthropogenic emission. CTR was characterized by high atmospheric water content (2.4–3 vol. % typically), elevated temperatures (28–30 °C during the day), high SOA loadings (particulate organics ∼4–10 μg m<sup>−3</sup>; sulfate ∼2 μg m<sup>−3</sup>), high isoprene mixing ratios (4–10 ppbv), high ozone (40–60 ppbv), low-to-moderate nitrogen oxides ([NO] ∼0.3–1.5 ppbv, [NO<sub>2</sub>] ∼1–5 ppbv), occasional plumes of SO<sub>2</sub> from

nearby power plants, and occasional biomass burning events during the SOAS campaign.

The first goal of the chamber campaign was to further investigate the more interesting observations at SOAS. Due to the ability of laboratory experiments to study the chemistry of a single reactive hydrocarbon in a controlled setting, it was possible to test hypotheses during FIXCIT in a systematic manner. Below we list some relevant questions from the SOAS campaign that were explored during FIXCIT.

1. Which reactions or environmental conditions control the formation and destruction of OVOCs in the southeastern US?
2. Are RO<sub>2</sub> isomerization and other rapid oxygen incorporation mechanisms of key hydrocarbons important during SOAS?
3. How do anthropogenic influences, e.g., NO<sub>x</sub>, O<sub>3</sub>, and (NH<sub>4</sub>)<sub>2</sub>SO<sub>4</sub>, impact atmospheric chemistry over the forest?
4. How much does the NO<sub>3</sub>-initiated reaction control nighttime chemistry during SOAS?
5. How do environmental conditions in the southeastern US affect ozonolysis end products, which are known to be water sensitive?
6. Which reactions or environmental conditions most significantly impact SOA mass and composition?

### 1.2.2 Updating the isoprene and monoterpene mechanisms

Several experiments were designed to “fill in the gaps” of the isoprene oxidation mechanisms by leveraging the comprehensive collection of sophisticated instrumentation at FIXCIT. We targeted the following acknowledged open questions.

7. What are the products of the photochemical reactions stemming from OVOCs like ISOPOOH, IEPOX, ISOPN, and pinonaldehyde?
8. What is the impact of photolysis vs. photooxidation for photolabile compounds?
9. What is the true yield of isoprene nitrates from the high-NO photooxidation pathway?
10. What is the product distribution and true yield of nitrooxy hydroperoxides from the NO<sub>3</sub> oxidation reaction of isoprene and monoterpenes under typical atmospheric conditions?
11. How do products and yields change as RO<sub>2</sub> lifetimes in chamber studies approach values estimated to be prevalent in the troposphere?

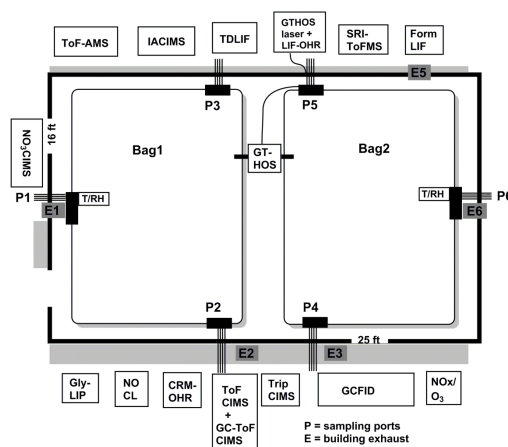


**Figure 2.** Arrangement of instruments at the Caltech Atmospheric Chamber Facility during the campaign. Instrument IDs are in Table 1.

### 1.2.3 Instrument characterization

A final goal of FIXCIT was to evaluate, compare, and identify biases in field instrumentation by isolating one variable at a time. We focused on the following objectives.

12. Identify the causal factor(s) producing the “OH interference” (Mao et al., 2012) that has been observed in various biogenically impacted regions by some gas-expansion laser-induced fluorescence (LIF) techniques.
13. Characterize the performance of newly commercially available CIMS instrumentation with respect to the detection of OVOCs by using authentic standards.
14. Compare similar measurements (e.g., OH reactivity, hydrocarbons, OVOCs) made with different techniques.

## 2 Scope of the campaign

### 2.1 Facilities

Experiments were performed in the Caltech Atmospheric Chamber Facility within a 1 month period in January 2014. The facility contains several in-house gas- and aerosol-phase instruments and an  $8 \times 5$  m insulated enclosure, housing two side-by-side Teflon atmospheric chambers that are suspended from the ceiling. The chambers were manufactured from fluorinated ethylene propylene (FEP) Teflon. The chamber volume was measured regularly by quantitative transfer of highly volatile organics such as isoprene by an externally calibrated GC-FID. Quantitative transfer was checked via

injections of a measured quantity of isoprene (checked by gravimetric, volumetric, and FT-IR methods) into a pillow bag with known volume by timing a calibrated mass flow of air into the pillow bag. For most experiments, the chamber volume was between 23 and 24 m<sup>3</sup>. The spatial configuration of instruments in the chamber facility during FIXCIT is shown in Fig. 1. The instruments, contributors, and identifying abbreviations used in this work are described in Table 1. A total of 320 UV black lamps (broadband  $\lambda_{\text{max}} \sim 350$  nm) are mounted on the walls of the enclosure. The lamps are located behind Teflon films so that the heat produced from the operation of the lamps can be removed by recirculating cool air. The interior of the enclosure is covered with reflective aluminum sheets. Light intensities can be tuned to 100, 50, 10, and 1 %.  $J_{\text{NO}_2}$  was measured to be  $7 \times 10^{-3} \text{ s}^{-1}$  at 100 % light intensity. Light fluxes at several locations within the chamber (e.g., center, corner, right, left, high, low) did not vary more than 15 %. Temperature controls in the chamber enclosure are tunable from 10 to 50 °C (typically set at 25 °C) and did not fluctuate more than 1 °C, except during periods when the temperature was explicitly changed or during a 30 min period immediately following a change in the light intensities (up to 2 °C increase was observed from switching on 100 % lights.)

The chamber experiments were operated in batch mode throughout the campaign. Temperature and RH were monitored continuously inside the chamber by a Vaisala HMM211 probe calibrated with saturated salt solutions in the RH range of 11–95 %. In the range  $\text{RH} < 11$  %, water vapor measurements were provided by the TripCIMS. The chambers were flushed at least 24 h before each use with ultra-purified air (purified in-house via a series of molecular sieves, activated carbon, Purafil™ media, and particulate filters), at elevated temperature when needed ( $\sim 40$  °C), so that the backgrounds on gas- and particle-phase instrumentation are at baseline levels. As a reference, NO levels before each run were typically less than 100 pptv (from NO-CL measurements) and particle concentrations were less than  $0.01 \mu\text{g m}^{-3}$ . Flushing rates, as balanced by exhaust rates, were typically  $250 \text{ SD L min}^{-1}$  (SLM) or  $\sim 0.6$  chamber volumes per hour. Chambers were mixed on the timescale of minutes by injecting high-pressure pulses of air during the beginning of experiments.

Chamber 1 was reserved for low-NO experiments, so that the walls did not contact elevated levels of nitric acid and organic nitrates during the lifetime of the chamber, while Chamber 2 was reserved for moderate- to high-NO experiments. Experiments were carried out daily in alternating chambers to allow for the full flushing period of the previously used chamber. Each chamber was characterized separately prior to the campaign for vapor and particle wall loss rates. Typically, wall loss rates for gas-phase species are slightly higher in the high-NO chamber than the low-NO chamber due to the greater acidity of the walls. Particle wall loss rates were not significantly different between chambers.

**Table 1.** List of participating instruments, principle investigators (PIs), and institutions. Key acronyms: laser-induced fluorescence (LIF), laser-induced phosphorescence (LIP), high-resolution time-of-flight (HRTof), compact time-of-flight (CTof), MS (mass spectrometer), and CIMS (chemical ionization mass spectrometer).

| Instrument   | Instr. ID               | PI(s)   | Institutions   | Measurements   | Ref.   |
|--|-------------------------|---|--|--|--|
| Ground-based hydrogen oxide sensor   | GTHOS                   | W. H. Brune                                     | Pennsylvania State University (PSU)                                  | OH, HO <sub>2</sub> , RO <sub>2</sub>  | Brune et al. (1995)                              |
| LIF OH reactivity monitor  | LIF-OHR                 | W. H. Brune                                     | PSU  | OH reactivity by decay of OH   | Mao et al. (2009)                                |
| Thermal dissociation LIF NO <sub>2</sub> monitor   | TDLIF                   | R. C. Cohen                                     | University of California, Berkeley (UCB)                             | NO <sub>2</sub> , sum of organic nitrates (ΣANs), sum of peroxy nitrates (ΣPNs), particulate organic nitrates (pANs) | Day et al. (2002)                                |
| Switchable iodide and acetate ion HRTof-CIMS   | IACIMS                  | D. K. Farmer                                    | Colorado State University (CSU)                                      | Oxidized VOCs (organic nitrates, organic acids, etc.)  | Lee et al. (2014a)                               |
| NO <sub>3</sub> <sup>-</sup> HRTof-CIMS  | NO <sub>3</sub> CIMS    | M. R. Canagaratna, D. R. Worsnop, J. L. Jimenez | Aerodyne Research, Inc. (ARI) and Univ. of Colorado, Boulder (CUB)   | Low-volatility organic compounds   | Junninen et al. (2010)                           |
| LIP glyoxal monitor  | GlyLIP                  | F. N. Keutsch                                   | University of Wisconsin, Madison (UWM)                               | Glyoxal  | Huisman et al. (2008)                            |
| LIF formaldehyde monitor   | FormLIF                 | F. N. Keutsch                                   | UWM  | Formaldehyde   | Hottle et al. (2008); DiGangi et al. (2011)      |
| Comparative rate method OH reactivity monitor  | CRM-OHR                 | S. Kim, A. B. Guenther                          | Univ. of California, Irvine (UCI) and Pacific NW National Lab (PNNL) | OH reactivity by decay of hydrocarbons   | Sinha et al. (2008)                              |
| Switchable reagent ion (H <sub>3</sub> O <sup>+</sup> /NO <sup>+</sup> /O <sub>2</sub> <sup>+</sup> ) HRTof-MS | SRI-ToFMS               | A. B. Guenther, J. E. Mak, A. H. Goldstein      | PNNL, SUNY Stonybrook (SUNY), and UCB                                | Hydrocarbons, carbonyls, alcohols, etc.  | Jordan et al., 2009                              |
| Chemical luminescence NO monitor   | NO-CL                   | G. S. Tyndall, D. D. Montzka, A. J. Weinheimer  | National Center for Atmospheric Research (NCAR)                      | NO (> 25 pptv)   | Ridley and Grahek (1990)                         |
| CF <sub>3</sub> O <sup>-</sup> triple quadrupole CIMS  | TripCIMS                | P. O. Wennberg                                  | California Institute of Technology (Caltech)                         | ISOPOOH, IEPOX, glycolaldehyde, acetic acid, methyl hydroperoxide  | St. Clair et al. (2010)                          |
| CF <sub>3</sub> O <sup>-</sup> CTof-CIMS   | ToFCIMS                 | P. O. Wennberg                                  | Caltech  | Oxygenated VOCs (hydroperoxides, organic nitrates, multi-functional compounds)                                       | Crounse et al. (2006)                            |
| Gas chromatograph with ToFCIMS   | GC-ToFCIMS              | P. O. Wennberg                                  | Caltech  | Isomers for oxygenated VOCs  | Bates et al. (2014)                              |
| HRTof-aerosol mass spectrometer  | ToF-AMS                 | J. H. Seinfeld                                  | Caltech  | Aerosol composition and size distribution  | DeCarlo et al. (2006); Canagaratna et al. (2007) |
| Gas chromatograph with flame-ionization detector   | GCFID                   | J. H. Seinfeld                                  | Caltech  | Isoprene, methacrolein, methyl vinyl ketone, cyclohexane   | N/A  |
| Thermocouple and membrane probe  | <i>T</i> / RH probe     | J. H. Seinfeld                                  | Caltech  | Temperature and relative humidity  | N/A  |
| UV-absorption ozone monitor  | O <sub>3</sub> monitor  | J. H. Seinfeld                                  | Caltech  | O <sub>3</sub> (> 1000 pptv)   | N/A  |
| Chemical luminescence NO <sub>x</sub> detector   | NO <sub>x</sub> monitor | J. H. Seinfeld                                  | Caltech  | NO (> 500 pptv), and NO <sub>2</sub> (catalytic conversion to NO)  | N/A  |

Measurements of the particle wall loss rates were performed by injecting ammonium sulfate (AS) seed aerosols into the chamber and monitoring the decay over the course of 10–24 h. Particles were injected via atomization of dilute salt solutions (e.g., AS 0.06 M) through a <sup>210</sup>Po neutralizer and water trap. Measurements of vapor wall loss rates were per-

formed by injecting OVOC standards (e.g., IEPOX, HMHP, etc.) into the chamber. Both particle and vapor wall loss characterizations were performed at several RH conditions (4–85 % RH). These characterizations have been described in more detail previously (Loza et al., 2010; Nguyen et al., 2014).

Organic compounds were injected into the chamber by two methods. (1) For volatile compounds, a measured volume was injected with a micro-syringe through a septum into a clean glass bulb, and the evaporated standard was quantitatively transferred into the chamber by dry purified air. Gas introduction of VOCs (done for isoprene and methacrolein) by filling an evacuated bulb with the chemical vapor, backfilling with nitrogen gas, and characterizing with Fourier transform infrared spectrometry before injecting did not produce significantly different results than volume injection. (2) For semi-volatile compounds, the solid or liquid standard was placed inside a two-neck flask, which was heated by a water bath (35–65 °C), and the headspace was carried into the chamber by dry purified air. The ToFCIMS or TripCIMS instruments measured the gas-phase mixing ratio of the semi-volatiles in real time as the compounds entered the chamber, and injection was halted when a satisfactory quantity was introduced. OVOCs were calibrated by the ToFCIMS and TripCIMS by methods described earlier (Paulot et al., 2009a). The desired RH inside the chamber was achieved by flowing dry purified air through a water-permeable (Nafion) membrane humidifier (FC200, Permapure LLC), kept moist by recirculating 27 °C ultra-purified (18 M $\Omega$ , 3 ppb TOC) water (Milli-Q, Millipore Corp). Particles were atomized into the chamber as described for particle wall loss experiments. When hydrated particles were needed for experiments, particles were injected via an in-line, heated, wet-wall denuder into a chamber that has RH above the efflorescence point of the particular salt (Martin, 2000).

## 2.2 Instrumentation and sampling modifications

Instruments were connected via sampling lines to both chambers through port holes in the enclosure as shown in Fig. 1. Sampling lines were capped when not in use. Inlet and tubing material were instrument specific, and included stainless steel (GTHOS and ToF-AMS), heated stainless steel and quartz (TDLIF), electro-polished steel and FEP Teflon (NO<sub>3</sub>CIMS), polyetheretherketone (PEEK) and Teflon (SRI-ToFMS), and perfluoroalkoxy polymer (PFA) Teflon (other instruments).

The duration of each experiment (i.e., the level of oxidation that can be probed) was critically dependent on the net sampling flow rates at which air was withdrawn from the chamber. Sampling strategies were developed to minimize the effective sampling flow rate from each instrument, in such a way that instrument responses were not significantly different than during field campaigns. In many cases, a common high-flow Teflon sampling line was used to minimize the residence time of gases through tubing, and smaller flows were sampled orthogonally by each instrument. In some cases, a duty cycle was used as needed.

Several modifications from field designs were utilized for chamber sampling. The modifications were that (1) the GTHOS detection system was located between the cham-

bers inside of the enclosure to minimize the residence time of HO<sub>x</sub> inside the instrument (Fig. 1). The detection system was connected to the laser on the outside of the enclosure via a 3 m fiber optic cable fed through the side port hole. The sampling flow rate was similar to field flows (6 SLM); however, the fast-flow inlet was situated horizontally (~2 m in height) instead of vertically. The inlet was adapted to each bag directly, by attaching it to a Teflon plate that was in turn secured to the chamber walls via a large o-ring. The GTHOS inlet switched from Chamber 1 to Chamber 2 as needed. Chemical zeroing was performed by releasing hexafluoropropene (C<sub>3</sub>F<sub>6</sub>) into the inlet as an OH scrubber, and dark zeroing by measuring the difference between online and offline signals. Chemical and dark zeroing methods were used to distinguish between OH present in the chamber or atmosphere (chemical OH) and OH that may have been produced after the gas stream enters the instrument, which is additional to the chemical OH signal; (2) LIF-OHR was diluted a factor of 10 with nitrogen gas (effective flow 6 SLM); (3) NO<sub>3</sub>CIMS was diluted a factor of 5 with scrubbed zero air (effective flow 2 SLM); (4) GlyLIP and FormLIF both operated at 5 SLM instead of the usual 17 and 10 SLM, respectively; and (5) SRI-ToFMS (1.5 SLM) and GCFID (0.1 SLM) occasionally sampled through a 0.125–0.25" OD PFA Teflon tube that was submerged in a cold bath kept at –40 °C in order to remove interferences from certain OVOC (see Sect. 2.3).

GC-ToFCIMS, first described in Bates et al. (2014), is an extension of the ToFCIMS. Analyte gas samples were focused with a cold trap onto the head of a RTX 1701 column (Restek) and eluted with a temperature ramping program (30–130 °C) in the oven before reaching the ToFCIMS for mass spectrometry detection. GC-ToFCIMS recorded data only when isomer separation was needed, because its operation took the standard scanning mode of the ToFCIMS offline. All other instruments operated normally with the following sampling flows: TDLIF (4 SLM), ToFCIMS and TripCIMS (2 SLM), CRM-OHR (0.5 SLM), NO-CL (1 SLM), and IACIMS (2 SLM). Frequencies of zeroing (with dry N<sub>2</sub> or ultrazero air) and calibration (various methods) were instrument specific, with some instruments zeroing once per hour and calibrating once every few hours and others performing zeroing/calibration between experiments.

## 2.3 Experimental design

The experiments performed at FIXCIT can be divided into several categories, each probing one or more specific science questions outlined in Sect. 1.2. Every experiment included successful elements from past studies, but with a special focus on extending to atmospheric conditions. One example is reducing the occurrence of RO<sub>2</sub> + RO<sub>2</sub> side reactions in chamber experiments, which can lead to yields of atmospherically relevant products that are biased low. Enabled by the high sensitivity of field instruments, photooxidation was per-

**Table 2.** Formal experiments and reaction conditions during the campaign. Chemical abbreviations are defined in Table 3. Other abbreviations are C1 = Chamber 1, C2 = Chamber 2, ISOP = isoprene,  $\alpha$ -PIN =  $\alpha$ -pinene, HP = hydrogen peroxide, MN = methyl nitrite, CHX = cyclohexane, HCHO = formaldehyde, AS = ammonium sulfate seeds. Exp. types are defined in the text. Exp. no. corresponds to the date in January 2014 when the experiment was performed.

| No. | Exp. type | HC precursor                | [HC] (ppb) | O <sub>x</sub>  | O <sub>x</sub> source            | [OH] <sub>ss</sub> (# cm <sup>-3</sup> )  | [O <sub>3</sub> ] <sub>i</sub> (ppb) | [NO] <sub>i</sub> (ppb) | [NO <sub>2</sub> ] <sub>i</sub> (ppb) | [NO]/[HO <sub>2</sub> ] | Add'l inj.     | Rxn T (°C) | RH (%) |
|-----|-----------|-----------------------------|------------|-----------------|----------------------------------|---|--------------------------------------|-------------------------|---------------------------------------|-------------------------|----------------|------------|--------|
| 2   | b         | ISOP                        | 45         | OH              | HP + <i>hν</i>                   | $1.5 \times 10^6$                         | <5                                   | <0.04                   | <2                                    | 1/7                     | –              | 27         | <5     |
| 3   | c         | ISOP                        | 100        | OH              | HP + <i>hν</i>                   | $2.4 \times 10^6$                         | <5                                   | 500                     | 15                                    | >100                    | –              | 26         | <5     |
| 4a  | i         | ISOPOOHs                    | 250        | –               | –                                | –   | –                                    | –                       | –                                     | –                       | –              | 24         | <3     |
| 4b  | a         | Blank C1                    | 0          | OH              | HP + <i>hν</i>                   | $2.0 \times 10^6$                         | <5                                   | <0.04                   | <3                                    | 1/6                     | –              | 27–33      | <5     |
| 5a  | i         | ISOPNs                      | <13        | –               | –                                | –   | –                                    | –                       | –                                     | –                       | –              | 24         | <3     |
| 5b  | a         | Blank C2                    | 0          | OH              | HP + <i>hν</i>                   | $2.0 \times 10^6$                         | <5                                   | <0.04                   | <2                                    | 1/5                     | –              | 27         | <5     |
| 6   | e         | ISOP                        | 91         | O <sub>3</sub>  | O <sub>3</sub> rxn               | [OH] <sub>i</sub><br>~<br>$1 \times 10^6$ | 615                                  | <0.04                   | <3                                    | –                       | –              | 25         | <5     |
| 7*  | d         | ISOP                        | 30         | OH              | MN + <i>hν</i>                   | $4.1 \times 10^4$ ,<br>$4.8 \times 10^6$  | <5                                   | 0.08                    | 45                                    | 2, 6                    | –              | 40, 40     | <5     |
| 9   | f         | ISOP                        | 18         | NO <sub>3</sub> | NO <sub>2</sub> / O <sub>3</sub> | $3.8 \times 10^8$                         | 55                                   | 0.10                    | 100                                   | 2–3                     | HCHO           | 26         | <5     |
| 10  | b         | $\alpha$ -PIN               | 30         | OH              | HP + <i>hν</i>                   | $2.0 \times 10^6$                         | <5                                   | <0.04                   | <2                                    | 1/10                    | –              | 27         | <5     |
| 11  | c         | $\alpha$ -PIN               | 30         | OH              | HP + <i>hν</i>                   | $2.5 \times 10^6$                         | <5                                   | 85                      | 10                                    | >100                    | –              | 26         | <5     |
| 13  | f         | $\alpha$ -PIN               | 30         | NO <sub>3</sub> | NO <sub>2</sub> / O <sub>3</sub> | $4 \times 10^8$                           | 75                                   | 0.17                    | 150                                   | 1.5–8                   | HCHO           | 25         | <5     |
| 14  | e         | ISOP                        | 100        | O <sub>3</sub>  | O <sub>3</sub> rxn               | [OH] <sub>i</sub><br>~0                   | 605                                  | <0.04                   | <3                                    | –                       | CHX            | 25         | <5     |
| 16* | d         | $\alpha$ -PIN               | 30         | OH              | MN + <i>hν</i>                   | $6 \times 10^4$<br>$4 \times 10^6$        | <5                                   | 0.08                    | <3                                    | 2–3,<br>10              | –              | 40, 40     | <5     |
| 17  | b, i      | 4,3-ISOPOOH                 | 60         | OH              | HP + <i>hν</i>                   | $1.2 \times 10^6$                         | <5                                   | <0.04                   | <3                                    | 1/5                     | –              | 26         | <5     |
| 18* | d         | ISOP                        | 28         | OH              | MN + <i>hν</i>                   | $1.0 \times 10^5$ ,<br>$4.3 \times 10^6$  | <5                                   | 0.08                    | <3                                    | 2–3,<br>>100            | –              | 25, 26     | <5     |
| 19  | b, h      | ISOP                        | 60         | OH              | HP + <i>hν</i>                   | $1.0 \times 10^6$                         | <5                                   | <0.04                   | <4                                    | 1/5                     | wet AS         | 28         | 51     |
| 21  | b         | ISOP                        | 22         | OH              | HP + <i>hν</i>                   | $2.0 \times 10^6$                         | <5                                   | <0.04                   | <2                                    | 1/10                    | –              | 27         | <5     |
| 22  | c         | ISOP                        | 100        | OH              | HP + <i>hν</i>                   | $2.3 \times 10^6$                         | <5                                   | 430                     | 15                                    | >100                    | –              | 27         | <5     |
| 23  | e         | ISOP                        | 90         | O <sub>3</sub>  | O <sub>3</sub> rxn               | [OH] <sub>i</sub><br>~<br>$1 \times 10^6$ | 600                                  | <0.04                   | <3                                    | –                       | –              | 25         | 50     |
| 24  | c, h, i   | 4,3-ISOPN                   | 12         | OH              | HP + <i>hν</i>                   | $3 \times 10^6$                           | 7                                    | 115                     | 55                                    | >100                    | wet AS         | 26         | 52     |
| 25  | b         | MAC                         | 43         | OH              | HP + <i>hν</i>                   | $3 \times 10^6$                           | <5                                   | <0.03                   | <3                                    | 1/10                    | –              | 28         | <5     |
| 26  | g, h      | MAC                         | 45         | OH              | MN + <i>hν</i>                   | $2 \times 10^7$                           | <5                                   | 3.5                     | 50                                    | 10–20                   | MAE,<br>wet AS | 26         | <5, 40 |
| 27  | d, i      | <i>trans</i> $\beta$ -IEPOX | 60         | OH              | MN + <i>hν</i>                   | $7.3 \times 10^6$                         | <5                                   | 0.25                    | <3                                    | 2–5                     | –              | 25         | <5     |
| 29  | e         | ISOP                        | 91         | O <sub>3</sub>  | O <sub>3</sub> rxn               | [OH] <sub>i</sub><br>~0                   | 610                                  | <0.04                   | <4                                    | –                       | CHX            | 25         | 38     |
| 30  | g, h, i   | Pinonald.                   | 15         | OH              | MN + <i>hν</i>                   | $3.5 \times 10^6$                         | <5                                   | 0.50                    | <3                                    | 4–8                     | –              | 26         | <5     |

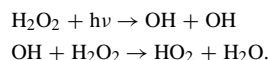
\* 1 % lights, 20 % lights, then 100 % lights.

formed with precursor mixing ratios as low as 12 ppbv. Certain instruments that required extensive dilution in a chamber setting, e.g., LIF-OHR, had poorer-quality data for low-loading experiments. Experimental durations were typically 4–6 h, with the exception of overnight runs where the majority of instruments sampled briefly to establish starting con-

ditions, then were taken offline during the nighttime and resumed sampling in the morning. The typical reaction time for an overnight experiment was ~15 h. Experimental details are reported in Table 2. OH concentrations were derived from hydrocarbon decay data from GC/FID, SRI-ToFMS, or ToFCIMS, when available, using published rate coefficients

(Atkinson et al., 2006; L. Lee et al., 2014; Bates et al., 2014). Otherwise, preliminary GTHOS chemical-zeroing data were used. The following types of experiments were included in the study:

- a. Blank (Exp. 4b and 5b): blank experiments were designed to investigate background signals present in experiments that may have sources other than gas-phase chemistry of the injected hydrocarbon, e.g., from heterogeneous oxidation of residual organics on the chamber walls. OH precursors, such as hydrogen peroxide, were added to each chamber, the UV lamps were turned on, and sampling occurred as usual. Furthermore, the temperatures inside the chambers were ramped from 25 to 35 °C to explore the extent to which elevated temperatures change the chamber background signals due to increased volatilization of organics. Blank experiments were performed under dry conditions. Common background compounds produced from heterogeneous wall reactions are formic acid and acetic acid.
- b. Low-NO photooxidation (Exp. 2, 10, 17, 19, and 25): the low-NO experiments that have been extensively investigated in atmospheric chamber studies were designed to be relevant to the pristine troposphere, and certain conditions at SOAS, where HO<sub>2</sub> reactions dominate the RO<sub>2</sub> fate. Experiments were initiated by H<sub>2</sub>O<sub>2</sub> photolysis as a NO<sub>x</sub>-free source of OH and HO<sub>2</sub>:



The execution of these experiments requires precise engineering to simulate the troposphere closely. One outstanding challenge of low-NO experiments is the variation in initial NO levels across different chamber settings and on different days. Because typical HO<sub>2</sub> levels in a chamber environment do not typically exceed ~200 pptv from the self-limiting HO<sub>2</sub> recombination, NO should be ~40 pptv during the reaction (a factor of 5 less abundant) in order for the C<sub>5</sub> RO<sub>2</sub> reactions to be dominated by HO<sub>2</sub> by a factor of 10 ( $k_{\text{RO}_2+\text{HO}_2} \sim 1.6 \times 10^{-11}$  and  $k_{\text{RO}_2+\text{NO}} \sim 8.5 \times 10^{-12} \text{ cm}^3 \text{ molec}^{-1} \text{ s}^{-1}$  at 298K (Atkinson et al., 2006)). Thus, experimental variations in NO that can lead to discrepancies in low-NO kinetics typically elude quantification by commercially available NO chemiluminescence instruments, owing to their high limits of detection (~500 pptv).

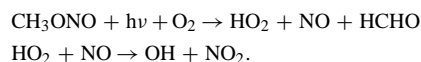
NO levels in the Caltech chambers were suppressed by continually flushing with filtered air on the inside and outside the chamber walls. Initial NO levels of <40 pptv were typically achieved during experiments. The NO-CL instrument available during FIXCIT (Table 1) has a limit of detection better than 25 pptv, and the

GTHOS instrument provided online HO<sub>2</sub> quantification at the pptv level. Another common challenge for low-NO experiments (even when [NO] is less than [HO<sub>2</sub>]) is that homogeneous or cross RO<sub>2</sub> + RO<sub>2</sub> reactions may dominate the RO<sub>2</sub> reactivity ( $k_{\text{RO}_2+\text{RO}_2} \sim 10^{-15} - 10^{-11} \text{ cm}^3 \text{ molec}^{-1} \text{ s}^{-1}$  at 298 K; Atkinson et al., 2006). These experiments may be more correctly characterized as “low-NO, high-RO<sub>2</sub>”. For experiments using [H<sub>2</sub>O<sub>2</sub>] as an OH precursor, RO<sub>2</sub> + RO<sub>2</sub> reactions were largely minimized by using reaction conditions that ensure [HO<sub>2</sub>] greater than [RO<sub>2</sub>] (e.g.,  $[\text{H}_2\text{O}_2]_0 / [\text{ISOP}]_0 \sim 10^2$  and  $J[\text{H}_2\text{O}_2] \sim 4-5 \times 10^{-6} \text{ s}^{-1}$ ). Thus, the peroxy radical self-reaction channels are minor compared to RO<sub>2</sub> + HO<sub>2</sub> chemistry. We estimate that the low-NO experiments were HO<sub>2</sub>-dominated by at least a factor of 10 in RO<sub>2</sub> reactivity by monitoring tracers of chemistry stemming from high-NO (isoprene nitrates), high-RO<sub>2</sub> (C<sub>5</sub> diols and other products), and low-NO (ISOPOOH and IEPOX) pathways. The molar yield of the low-NO products ISOPOOH + IEPOX (measured within the first 15 min of reaction) was estimated at 95 %, supporting the dominance of RO<sub>2</sub> + HO<sub>2</sub> chemistry over other channels. The structurally isomeric ISOPOOH and IEPOX that were formed from the HO<sub>2</sub>-dominated isoprene photooxidation were distinguished by TripCIMS, and the sum was measured by ToFCIMS, IACIMS, and NO<sub>3</sub>CIMS. These experiments were performed with isoprene,  $\alpha$ -pinene, 4,3-ISOPOOH and MAC precursors.

- c. High-NO photooxidation (Exp. 3, 11, 22, and 24): high-NO experiments are also commonly performed in chamber studies. These experiments were designed to be relevant to the urban-influenced troposphere, such as some cases at SOAS, where NO can dominate RO<sub>2</sub> reactions. Experiments were typically initiated by H<sub>2</sub>O<sub>2</sub> with added NO during FIXCIT, but have been performed using HONO or other precursors elsewhere. It is easier to ensure that reaction with NO is the main fate of RO<sub>2</sub>, even with higher hydrocarbon loadings, because NO mixing ratios are typically in excess of both HO<sub>2</sub> and RO<sub>2</sub> by hundreds of ppbv. Hydroxy nitrate products were measured by TDLIF, IACIMS, ToFCIMS, and GC-ToFCIMS. Functionalized carbonyl products were measured by SRI-ToFMS and ToFCIMS. Glyoxal and formaldehyde, also important high-NO products, were measured by the GlyLIP and FormLIF, respectively. This well-studied experiment was important for multiple reasons, including calibration, diagnostics, and for determining the hydroxy nitrate yields from alkenes within the first few minutes of photooxidation. However, it should be noted that the experimental result represents a boundary condition that may not fully represent NO-influenced reactions in the atmosphere due to the extremely short RO<sub>2</sub> lifetimes (<0.01 s at 500 ppbv

NO). These experiments were performed with isoprene,  $\alpha$ -pinene, and the 4,3-ISOPN standard synthesized by the Caltech group.

- d. Slow chemistry photooxidation (Exp. 7, 16, 18, and 27): the slow chemistry experiment is designed to extend RO<sub>2</sub> lifetimes closer to atmospheric values when both NO and HO<sub>2</sub> impact RO<sub>2</sub> reactivity ( $\sim 3$ –30 s, assuming 1500–100 pptv NO and 40 pptv HO<sub>2</sub>). This was achieved by employing low radical mixing ratios. With relevant RO<sub>2</sub> lifetimes, the RO<sub>2</sub> isomers may be closer to their equilibrium distribution because of the reversible addition of oxygen (Peeters et al., 2009). Figure 2 shows the progress of a representative slow chemistry experiment. The “slow” portion of experiments was performed under a low light flux ( $J_{\text{NO}_2} \sim 4 \times 10^{-5} \text{ s}^{-1}$ ) with methyl nitrite as the OH precursor (Atkinson et al., 1981):



These reactions produce a steady-state OH concentration of  $[\text{OH}]_{\text{ss}} \sim 0.4\text{--}1 \times 10^5 \text{ molec cm}^{-3}$  and an atmospherically relevant ratio of NO / HO<sub>2</sub> (2–3) that is stable throughout the majority of the experiment. Furthermore, we aimed to simulate the summer conditions at SOAS, where RO<sub>2</sub> isomerization is competitive with RO<sub>2</sub> + HO<sub>2</sub> and RO<sub>2</sub> + NO chemistry. Thus, most experiments of this type were performed at elevated temperatures ( $T \sim 40$ –45 °C) to facilitate the isoprene RO<sub>2</sub> isomerization to HPALDs (Crounse et al., 2011), as measured by ToFCIMS. The atmospheric RO<sub>2</sub> fates were qualitatively deduced by observations of their respective products during SOAS (forthcoming papers) and during other campaigns (Paulot et al., 2009b; Wolfe et al., 2011; Beaver et al., 2012).

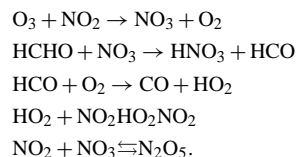
The fate of HPALDs is not known, but has been suggested as being strongly influenced by photolysis based on reactions of chemical analogs (Wolfe et al., 2012). After the slow chemistry period, 20–100 % lights were turned on in order to diagnose the effects of direct photolysis and OH oxidation on the product compounds, which is especially instructive when coupled with photochemical modeling. Table 2 reports conditions only for the  $\leq 1$  % light period and the 20 % light period due to availability of hydrocarbon decay data. When CH<sub>3</sub>ONO experiments were performed with higher light flux from the start, the NO-to-HO<sub>2</sub> reactivities were still competitive, but the OH mixing ratios were higher. These experiments were performed with isoprene,  $\alpha$ -pinene, and *trans*  $\beta$ -IEPOX precursors.

- e. Ozonolysis (Exp. 6, 14, 23, and 29): ozonolysis reactions were performed in the dark, with and

without the use of excess cyclohexane (50 ppmv) as a scavenger for OH (Atkinson, 1995). Ozone reacts with isoprene and  $\alpha$ -pinene with rate coefficients of  $k_{\text{ISO}+\text{O}_3} = 1.3 \times 10^{-17} \text{ molec cm}^{-3}$  and  $k_{\alpha\text{-PIN}+\text{O}_3} = 9.0 \times 10^{-17} \text{ molec cm}^{-3}$  at 298 K, respectively (Atkinson et al., 2006). After the first few steps of the reaction, however, little agreement exists in the literature for product yields, product distribution, or rate coefficients stemming from reactions of stabilized Criegee intermediates (sCI). This may be due to the large differences among studies in the hydrocarbon loadings ( $[\text{ISO}]_i = 40$ –10 000 ppbv), ozone-to-isoprene ratios ( $< 0.5$  to  $> 100$ ), water vapor content ( $< 10$ –20 000 ppmv), reaction pressures (4–760 torr), analytical methods used for product analysis (GC, HPLC, FTIR, direct OH vs. scavenging, etc.), and methods used to generate sCI ( $\text{CH}_2\text{I}_2 + h\nu$  vs. gas-phase ozonolysis) (Simonaitis et al., 1991; Neeb et al., 1997; Sauer et al., 1999; Hasson et al., 2001; Kroll et al., 2002; Johnson and Marston, 2008; Drozd and Donahue, 2011; Welz et al., 2012; Huang et al., 2013).

We designed the ozonolysis experiments to have similar ozone-to-isoprene ratios to those observed during SOAS ( $\sim 5$ –7), and performed the experiments under dry (RH  $\sim 4$  %) and moderately humid (RH  $\sim 50$  %) conditions. The ozonolysis experiments at FIXCIT primarily focused on studying unimolecular and bimolecular chemistry of sCI that affects the yields of OH, hydroperoxides, organic acids, aldehydes and ketones under humid vs. dry conditions. These experiments represent the first coupling between direct OH observations from GTHOS, aldehyde/ketone measurements from GCFID and SRI-ToFMS, online formaldehyde measurements from FormLIF, and online hydroperoxide measurements from the various CIMS instruments present to provide the most comprehensive picture thus far on the humidity-dependent ozonolysis of isoprene.

- f. Competitive HO<sub>2</sub> nitrate (NO<sub>3</sub>) oxidation (Exp. 9 and 13): the NO<sub>3</sub>-initiated experiments during the campaign were performed in the dark, under dry conditions. Excess formaldehyde ( $[\text{HCHO}]_i \sim 4$ –8 ppmv) was used as a dark HO<sub>2</sub> precursor in order to elevate the contributions of RO<sub>2</sub> + HO<sub>2</sub> reactions in the NO<sub>3</sub> chemistry:



This process produces an HO<sub>2</sub> / NO<sub>3</sub> ratio of approximately 2 (determined by photochemical modeling from the mechanism described in Paulot et al., 2009), a ratio more relevant to the troposphere during nighttime



oxidation. As  $\alpha$ -pinene has a higher  $\text{NO}_3$  loss rate compared to isoprene, a factor of 2 greater mixing ratio of initial formaldehyde was used. The consequence of the experimental design is that the isoprene nitrooxy hydroperoxide (INP) and monoterpene nitrooxy hydroperoxide (MTNP) are major products, in contrast to experiments performed under  $\text{RO}_2 + \text{RO}_2$  or  $\text{RO}_2 + \text{NO}_3$  dominated conditions (Ng et al., 2008; Perring et al., 2009; Kwan et al., 2012). The focus of these experiments was the quantification of INP and MTNP with the various CIMS and with TDLIF, and further exploration of their loss channels to OH oxidation (simulating sunrise) or to dry AS seed particles by measuring organic aerosol growth on the ToF-AMS. These experiments were performed with isoprene and  $\alpha$ -pinene precursors.

- g. High  $\text{NO}_2/\text{NO}$  photooxidation (Exp. 26 and 30): the high  $\text{NO}_2$ -to- $\text{NO}$  ratios in the lower troposphere in most regions of the globe favor the production of acylperoxy nitrates (APNs) from the OH-initiated reaction of aldehydes like methacrolein and pinonaldehyde (Bertman and Roberts, 1991; Nozière and Barnes, 1998). Unlike the APN from methacrolein (MPAN), the APN from pinonaldehyde has never been measured in the atmosphere (Nouaime et al., 1998; Roberts et al., 1998; Wolfe et al., 2009). The OH oxidations of aldehydes were performed with an  $\text{NO}_2/\text{NO}$  ratio greater than 10, and  $\text{NO}_2$  was replenished as it was reacted away. These reactions were initiated by  $\text{CH}_3\text{ONO}$  photolysis under higher light flux, producing  $[\text{OH}]$  greater than  $3 \times 10^6 \text{ molec cm}^{-3}$ . Certain APNs were monitored with ToFCIMS, and total peroxy nitrates ( $\Sigma\text{PNs}$ ) were monitored with TDLIF. A major focus of the high- $\text{NO}_2$  experiments was to investigate the SOA-formation potential and mechanisms from atmospherically relevant APNs, which is expanded in h.
- h. SOA-formation chemistry (Exp. 19, 24, 26, and 30): experiments aimed specifically at studying chemistry leading to SOA formation have overlapping goals with those described above. One focus was the evaluation of the SOA-formation route from APNs by the proposed dioxo ketone, lactone, and epoxide mechanisms (Chan et al., 2010; Kjaergaard et al., 2012; Lin et al., 2013), none of which has yet been validated by independent studies. However, the proposed epoxide chemistry has been integrated into some studies published soon after the proposal by Lin et al. (2013) (Worton et al., 2013; Pye et al., 2013). After MPAN was formed from the high- $\text{NO}_2$  reaction of  $\text{MAC} + \text{OH}$ , a synthesized standard of methacrylic acid epoxide (MAE, provided by the UNC group), the proposed epoxide intermediate, was added to discern the SOA-forming potential of MAE vs. other reactive intermediates in the MPAN reaction. Following the injection and stabilization of MAE, water vapor was added until the reaction mixture reached  $\sim 40\%$  RH. Then wet AS seeds were injected to investigate any SOA mass growth, as quantified by ToF-AMS.
- SOA formation from ISOPN high- $\text{NO}$  photooxidation and isoprene low- $\text{NO}$  photooxidation products were investigated in the presence of wet AS seeds (40–50 % particle liquid water by volume), meant to simulate the high particle liquid water and sulfate quantities during SOAS. For these experiments, the chambers were humidified to 40–50 % RH, and hydrated AS particles were injected through a wet-wall denuder so that the seed particles retain liquid water above the efflorescence point of AS (Biskos et al., 2006). In the ISOPN high- $\text{NO}$  photooxidation, the potential for forming organics that will likely condense onto seed particles, e.g., dinitrates and IEPOX, was recently suggested (L. Lee et al., 2014; Jacobs et al., 2014). The dinitrate pathway was investigated as a potential source of particle-phase organic nitrogen. In the low- $\text{NO}$  isoprene photooxidation, IEPOX reactive uptake onto acidic  $\text{Mg}_2\text{SO}_4$  particles (Lin et al., 2012) and non-acidified AS particles (Nguyen et al., 2014), both with non-zero liquid water content, were recently demonstrated. We focused on AS particles with no added acid. The impact of the partitioning of IEPOX on the gas-phase mixing ratios was examined as a potential reason for the differences in observed IEPOX in dry and humid regions.
- i. Cross-calibrations (Exp. 4a, 5a, 24, 27, and 30): newly commercially available negative-ion CIMS (Junninen et al., 2010; B. H. Lee et al., 2014) may become common tools for monitoring complex OVOCs in the atmosphere, similarly to the widespread adoption of positive ion CIMS (PTR-MS-based instruments). Some of the new negative ion CIMS instruments were deployed for the first time in field campaigns occurring in recent years. During FIXCIT, synthesized standards of eight isomer-specific compounds were available for cross calibrations with different CIMS in order to better understand the chemical sources of ambient signals during SOAS and in other field campaigns. Table 3 shows the structures, abbreviations, and contributors of the synthesized chemicals. The TripCIMS and the GC-ToFCIMS separated structural isomers through collision-induced dissociation (CID) and through chromatography, respectively. Figure 3 shows a GC-ToFCIMS separation of isomers of the ISOPN synthesized standards, as well as ISOPNs present in a complex photooxidation mixture. SRI-ToFMS and IACIMS tested the switchable reagent ion sources for preferential detection of one or more isomers of compounds with the same molecular formula.

For certain cross-calibration experiments, standards were injected into an inflatable pillow bag ( $\sim 0.2$ – $0.3\text{ m}^3$ ) that was filled with dry  $\text{N}_2$  to a known volume. The purities of the standards were quantified by nuclear magnetic resonance (NMR) or Fourier transform infrared spectrometry (FT-IR). The injected material was measured by vapor pressure, quantitative volume transfer, or by ToFCIMS and TripCIMS that were calibrated using techniques described elsewhere (Garden et al., 2009; Paulot et al., 2009a; L. Lee et al., 2014; Bates et al., 2014). Some experiments, such as the IEPOX photooxidation experiment, also served a dual purpose for cross-calibration. For example, *trans*- $\beta$ -IEPOX was injected into a clean chamber and instruments were allowed to sample for  $\sim 1\text{ h}$  to cross-calibrate before an oxidant precursor was injected. Both LIF-OHR and CRM-OHR were able to measure the OH reactivity of these OVOC compounds individually, which aids in determining the known and unknown OH reactivity in ambient environments.

- j. GTHOS test experiments: the OH interference in GTHOS, and possibly other gas-expansion LIF techniques, has been shown to bias OH measurements systematically high in some biogenically influenced areas unless chemical zeroing was performed (Mao et al., 2012). The excess OH was demonstrated not to be produced by the GTHOS laser itself (308 nm), but rather, more likely, in the low-pressure flow zone within the nozzle of the instrument. During FIXCIT, several hypotheses proposed by Mao et al. (2012), and some original proposals based on field observations, were tested. The interference precursor candidates were: (i) ozonolysis intermediates – tested with ozonolysis experiments and with ozone injection into the GTHOS inlet; (ii) biogenic peroxides like ISOPOOH or HMHP – tested with synthesized standards; (iii) background chemistry such as  $\text{NO}_2 + \text{O}_3$  – tested by the nitrate-oxidation experiment and by sequential injection of  $\text{NO}_2$  and  $\text{O}_3$  separately; (iv) dry and humid  $\text{HO}_2 + \text{O}_3$  reaction – tested by formaldehyde photolysis with ozone injection during a separate experiment (01/02/2014, not shown in Table 2); (v) beta-hydroxy  $\text{RO}_2$  radicals formed from  $\text{OH} + \text{alkene}$  – tested with the photooxidation of 2-methyl-2-butanol and compared with 2,2-dimethylbutane (02/02/2014 and 31/01/2014, not shown in Table 2); and (vi) heat-mediated decomposition of thermally unstable species – tested by temperature ramping to 35–40 °C inside the chamber. Often, single variables (like ozone or heat) were isolated by incremental additions toward the end of an experiment.

The experiments not described in Table 2 (to test iv and v) were performed after the formal experiments; thus, not all investigators were present. Only GTHOS, ToFCIMS, TripCIMS, ToF-AMS, GCFID,  $\text{O}_3$  monitor

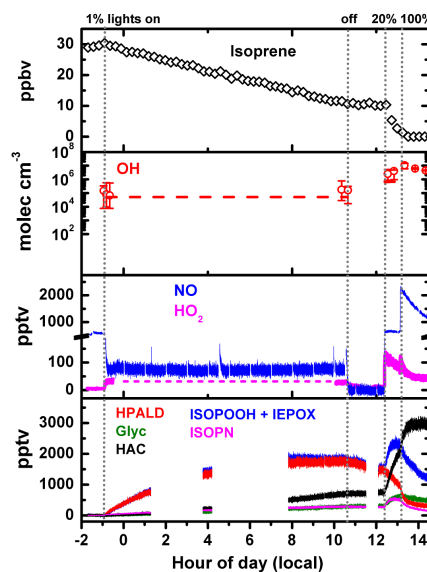


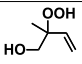
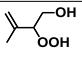
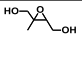
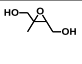
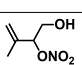
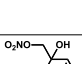
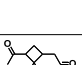
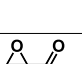
**Figure 3.** Progress of the slow chemistry experiment performed on 01/07/2014. Isoprene data were provided by GCFID. The red dashed line in the OH plot is the steady-state OH concentration derived from the decay of isoprene as monitored by GCFID. OH and  $\text{HO}_2$  preliminary data were provided by GTHOS, using chemical zeroing, although the steady-state value of  $(0.4\text{--}1) \times 10^5\text{ molec cm}^{-3}$  was below the detection limit of GTHOS. OH preliminary data were averaged to reduce noise. NO data were provided by NO-CL and OVOC data were provided by ToFCIMS.

and  $\text{NO}_x$  monitor were collecting data. The  $\text{HO}_2 + \text{O}_3$  test experiment (01/02/2014) was performed by injecting  $\sim 600\text{ ppbv}$  of ozone, then  $\sim 50\text{ ppbv}$  of cyclohexane as an OH tracer for CIMS (monitored by the formation of cyclohexyl hydroperoxide). UV lights were turned on and then  $4\text{ ppmv}$  of formaldehyde was injected, which photolyzed to produce  $550\text{ pptv}$  of  $\text{HO}_2$ . The  $\text{HO}_2$  reaction with formaldehyde produced a small yield of HMHP (Niki et al., 1980). Water vapor was injected to diagnose the effect of humidity. Experiments to test the effects of  $\text{RO}_2$  structure utilized  $\text{CH}_3\text{ONO}$  to oxidize  $\sim 50\text{ ppbv}$  of either 2-methyl-2-butanol and 2,2-dimethylbutane with OH. Ozone ( $\sim 600\text{ ppbv}$ ), water vapor (until RH  $\sim 30$ – $40\%$ ), and  $\text{NO}_2$  ( $400\text{ ppbv}$ ) were added sequentially at toward the end of the photooxidation. Finally severally hundred ppb of NO was added to titrate away the ozone.

## 2.4 Analytical challenges

Throughout the campaign, several sources of analytical interferences or systematic biases were discovered. Some chal-

**Table 3.** List of contributed synthesized chemical standards for experiments and calibration.

| Synthesized standard   | PIs  | Institutions                                      | Molecular structure   | Atmos. relevance  | Synthesis ref.          |
|--|--|---|---|---|-------------------------|
| Isoprene 1-hydroxy 2-hydroperoxide (1,2-ISOPOOH)                 | F. N. Keutsch  | UWM   |    | Major first-gen. low-NO isoprene + OH product                                     | Rivera et al. (2014)    |
| Isoprene 3-hydroxy 4-hydroperoxide (3,4-ISOPOOH)                 | F. N. Keutsch  | UWM   |    | Major first-gen. low-NO isoprene + OH product                                     | Rivera et al. (2014)    |
| <i>Trans</i> isoprene 2-epoxydiol ( <i>trans</i> $\beta$ -IEPOX) | P. O. Wennberg and J. H. Seinfeld                            | Caltech   |    | Major second-gen. low-NO isoprene + OH product                                    | Bates et al. (2014)     |
| <i>Cis</i> isoprene 2-epoxydiol ( <i>cis</i> $\beta$ -IEPOX)     | P. O. Wennberg and J. H. Seinfeld                            | Caltech   |    | Major second-gen. low-NO isoprene + OH product                                    | Bates et al. (2014)     |
| Isoprene 4-hydroxy 3-nitrate (4,3-ISOPN)                         | R. C. Cohen, P. B. Shepson, A. S. Hasson, and P. O. Wennberg | UCB, Purdue Univ., CSU Fresno (CSUF), and Caltech |    | Major first-gen. high-NO isoprene + OH product                                    | Lee et al. (2014b)      |
| Isoprene 2-hydroxy 1-nitrate (2,1-ISOPN)                         | A. S. Hasson   | CSUF  |    | Minor first-gen. high-NO isoprene + OH product                                    | N/A                     |
| Pinonaldehyde  | P. O. Wennberg and J. H. Seinfeld                            | Caltech   |   | Major first-gen. $\alpha$ -Pinene + OH and O <sub>3</sub> product                 | Griesbaum et al. (1997) |
| Methacrylic acid epoxide (MAE)                                   | J. D. Surratt and A. Gold                                    | Univ. of NC Chapel Hill (UNC)                     |  | Minor product and possible SOA precursor from MAC + OH + NO <sub>2</sub> reaction | Lin et al. (2013)       |

lenges resulted from the integration of field instruments to a chamber setting, where high concentrations of certain chemicals were used to engineer extremely specific conditions. Thus, these issues do not affect ambient sampling. For example, (1) high NO<sub>2</sub> levels in some experiments affected the normal operation of TDLIF because the  $\Sigma$ ANs and  $\Sigma$ PNs measurements were determined by subtraction of NO<sub>2</sub>. When NO<sub>2</sub> is much higher than  $\Sigma$ ANs and  $\Sigma$ PNs, the measurement by difference contains large uncertainties; (2) high H<sub>2</sub>O<sub>2</sub> for low-NO conditions affected the operation of some CIMS instruments because the ppmv mixing ratios of H<sub>2</sub>O<sub>2</sub> depleted a non-negligible quantity of reagent ions. In order to correct for this, the CIMS instruments needed to calibrate as a function of H<sub>2</sub>O<sub>2</sub> in addition to traditional methods, or account for the true reagent ion signal (which was anti-correlated with H<sub>2</sub>O<sub>2</sub> concentration). High H<sub>2</sub>O<sub>2</sub> also affected GTHOS due to photolysis-derived OH production by the laser. GTHOS corrected for this effect by removing the OH background that was determined by sampling

when only H<sub>2</sub>O<sub>2</sub> was present; (3) High formaldehyde, cyclohexane, or H<sub>2</sub>O<sub>2</sub> dominated the OH reactivity for certain experiments. In experiments where ppmv levels of volatile compounds were used, LIF-OHR and CRM-OHR did not operate. In contrast, high ozone and NO levels did not appear to affect the operation of any instruments. Temperature and humidity effects on ion sensitivities have been corrected for by ToFCIMS and TripCIMS as standard procedure. Other CIMS are actively characterizing these effects for analytes of interest.

However, other analytical challenges were not unique to laboratory studies. It was found that chemical artifacts were produced from the decomposition of multifunctional OVOC (e.g., ISOPN, ISOPOOH, IEPOX, and pinonaldehyde) under normal operating conditions in some instruments; thus, possibly affecting ambient sampling and field data interpretation. Scheme 2 shows the proposed decomposition pathways of certain isomers of isoprene-derived OVOC to form MAC and MVK. We are aware of MAC and MVK interfer-

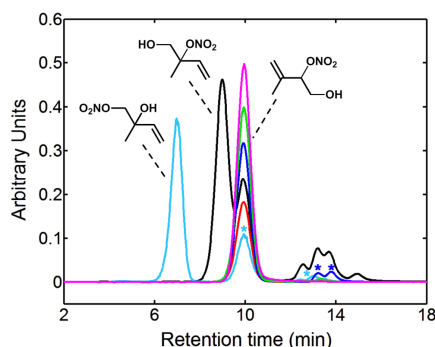
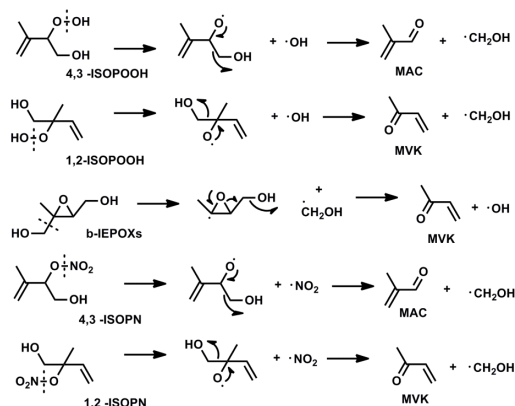


**Figure 4.** GC-ToFCIMS chromatogram of ISOPNs from an isoprene high-NO photooxidation experiment (black), and from the introduction of 2,1-ISOPN standard synthesized by CSUF (cyan) and 4,3-ISOPN standards synthesized by Caltech (magenta), CSUF (green), UCB (blue), and Purdue (red). The rightmost four peaks apparent in the photooxidation chromatogram are preliminarily identified as the *cis* and *trans* 1,4-ISOPN and *cis* and *trans* 4,1-ISOPN, although the elution order is not clear. Asterisks (\*) denote impurities in synthesized samples of corresponding color.



**Scheme 2.** Select proposed mechanism for the decomposition of OVOCs to carbonyls on contact with metal surfaces or high ionization energies within instrumentation. Other decomposition pathways likely exist and the branching ratios are dependent on instrument operation conditions. Cleavage sites are indicated by dashed lines.

ence only from the 1,2- and 4,3- isomers of ISOPN, the 1,2- and 4,3- isomers and ISOPN, and the beta isomers of IEPOX (i.e., the peroxide, nitrate, and epoxide groups are secondary or tertiary). Unfortunately, these isomers are expected to be the most abundant in the atmosphere, e.g., the beta IEPOXs are estimated to represent more than 97 % of atmospheric IEPOX (Bates et al., 2014). The extent of decom-

position and product distribution may also vary based on the operating conditions of the particular analytical method. In general, the decomposition was exacerbated by instruments with harsher sampling conditions, i.e., high ionization energy (e.g., the standard  $\text{H}_3\text{O}^+$  mode of SRI-ToFMS), high temperatures, and/or materials incompatible with organics (e.g., the hot stainless steel sample loop and inlet of GCFID). OVOCs from the low-NO isoprene photooxidation have been shown to decompose to MAC and MVK in commercial PTRMS instruments (Liu et al., 2013), but the exact identities of the compounds were unclear. During FIXCIT, it was observed that ISOPOOH, IEPOX, and pinonaldehyde were detected at  $m/z$  71.050 in the SRI-ToFMS in PTR mode (the sum of MAC + MVK). Switchable reagent ions show promise for removing certain biases, but more work is needed to characterize the chemistry that forms interfering ions. Furthermore, we observed that the decomposition interference also affected GCFID, the other commonly used detection method for MAC and MVK in ambient samples. ISOPOOH, IEPOX, and ISOPN were detected as either MAC or MVK in the GCFID, depending on the specific isomer. The interferences may not be localized to this particular GCFID, and a more detailed account is forthcoming (Rivera et al., 2014). Conversion efficiencies of OVOCs to the  $\text{C}_4$  carbonyls in the Caltech GCFID range in order of ISOPOOH > IEPOX > ISOPN, and can be almost quantitative for ISOPOOH because of the facile cleavage of the weak O–O bond. Lastly, ISOPN were found to be converted to NO with a small yield in the NO–CL and a larger yield in commercial  $\text{NO}_x$  analyzers.

All decomposition-derived artifacts can be avoided by collecting the air sample through a length of tubing submerged in a cold bath ( $-40^\circ\text{C}$ ), which trapped OVOCs that are less volatile than authentic MAC and MVK. Liu et al. (2013) implemented this technique successfully in their laboratory study using SRI-ToFMS, resulting in a lower yield than previously reported for MAC and MVK in the low-NO oxidation of isoprene. Field application may prove more challenging, however, as the trapping is labor intensive and requires careful humidity control to avoid ice buildup and blockage. During FIXCIT, both GCFID and SRI-ToFMS employed trapping techniques at various times to avoid biases in the detection and interpretation of MAC and MVK data.

### 3 Preliminary results and atmospheric implications

Forthcoming papers will discuss campaign results in detail. Here, we summarize a few interesting observations that appeared to be robust, based on preliminary data analysis of the laboratory and field work.

- Nighttime chemistry of alkenes, as controlled by the  $\text{NO}_3$  radical, leads to several organic nitrates that are unique compared to daytime high-NO photooxidation. A significant product is the nitrooxy hydroperoxide, the atmospheric importance of which has likely been sig-

nificantly underestimated in past chamber studies. The nitrooxy hydroperoxide reacts further in the daytime through a currently unknown mechanism.

- The high-NO hydroxy nitrate yield from isoprene is closer to the high end of the spectrum (range 4–15 %), important for the accurate simulations of volatile nitrogen in the atmosphere.
- Observed mixing ratios of isoprene low-NO photooxidation products are impacted by heterogeneous chemistry that appears to be mediated by aqueous processes, which has implications for the interpretation of IEPOX observations in dry vs. humid areas of the world.
- Environmental conditions in many locations, including within a biomass burning plume, are favorable for the H-shift RO<sub>2</sub> isomerization chemistry that produces compounds like HPALDs and very low-volatility oxygenates. The atmospheric fate of HPALDs is highly impacted by direct photolysis that recycles OH, as well as other complex chemistry and physical processes.
- The ozonolysis reaction of isoprene produces a high yield of C<sub>1</sub> compounds that are also observed with considerable abundance during ambient sampling. The hydroperoxide and acid yields appear to be underestimated by previous studies that detected these compounds via offline techniques. The OH yield may not follow the same trend with RH as the hydroperoxide and acid yields.
- APNs are efficient SOA precursors. SOA formation was prompt, and organic mass growth occurred quickly without the addition of inorganic seeds, i.e., the SOA intermediate(s) from APN + OH condensed onto predominantly organic SOA material. Injections of the MAE standard did not increase the SOA mass growth.
- Several experiments produced significant amounts of excess OH, as measured by the GTHOS instrument, providing further avenues for investigation. These experiments also ruled out several candidates for the OH interference. More work is underway to characterize the phenomenon comprehensively.
- Calibrations with several synthesized standards of OVOC (Table 3) significantly aid in data interpretation from OHR and new CIMS instruments. Sampling these OVOC through standard instrumentation may interfere with some routine field and chamber measurements (depends on the run conditions and instrument setup), but may be mediated by cold-trapping methods. This is likely a contributing factor in the high discrepancies in MAC and MVK yields from low-NO isoprene photooxidation previously reported. For example, we find the preliminary low-NO yields of MVK ( $6 \pm 3\%$ ) and

MAC ( $4 \pm 2\%$ ), determined by GC-FID, from photooxidation of isoprene are consistent with Liu et al. (2013) when cold-trapping methods were employed (Exp. 21). However, the low-NO “yields” of MVK and MAC are each greater than 40 % when sampled directly by the GC-FID from the chamber (Exp. 2) due to interferences by isomers of ISOPOOH (Rivera et al., 2014) and possibly other OVOCs.

Final data from the FIXCIT campaign will be made publicly available on archives hosted by the US National Oceanic and Atmospheric Administration (NOAA, <http://esrl.noaa.gov>) in January 2016. Data will be submitted in the ICARTT format, standardized by the US National Aeronautics and Space Administration (NASA, <http://www-air.larc.nasa.gov/missions/etc/IcarttDataFormat.htm>).

#### 4 Summary

Although data analysis is ongoing, the goals of the FIXCIT campaign appear to have been met during the campaign period. The insights gained from experimental observations under well-controlled laboratory conditions have already proved valuable for understanding ambient observations from SOAS. The community effort to pursue atmospherically important chemistry with sensitive ambient techniques and custom-synthesized chemicals has elevated our understanding of atmospheric oxidation for a number of biogenic compounds. Novel mechanistic information obtained during FIXCIT will be helpful to update chemical mechanisms currently implemented in large-scale chemistry-coupled transport models. Instrumental inter-comparisons, an important aspect of the campaign, have demonstrated that a thorough characterization of new and standard ambient sampling techniques using authentic standards is necessary for accurate data interpretation.

Chamber experiments are clearly invaluable to the field of atmospheric chemistry, as the results feed directly into models that are used to ascertain regional and global climate and chemistry feedbacks. Furthermore, chamber data aid in the interpretation of complex results obtained from field studies. However, it can be difficult to decipher the conditions under which chamber experiments are most relevant, and a standard protocol for data reporting may be needed. For example, best estimates of oxidation conditions in chambers (i.e., if reactions are HO<sub>2</sub>-dominated, low-NO but RO<sub>2</sub>-dominated, high-NO, high-NO<sub>x</sub> but low-NO, and so on) would greatly aid in comparisons of these experiments and others. The experiments in this campaign were fundamentally focused on the fate of the RO<sub>2</sub> radical as a delineation between chemical regimes. FIXCIT experiments (Table 2) can be further improved or tailored to the specific needs of the scientist. It has been demonstrated, here and elsewhere, that chamber studies that include chemistry representative of the atmosphere and well-characterized instrumental methods can accurately

reproduce observations in the ambient environment. The results from FIXCIT make a case for future synergistic integration of laboratory studies with field campaigns, which maximizes the level of mechanistic understanding and data confidence obtained from the combination of both types of studies.

**Acknowledgements.** We acknowledge the collaborative efforts of FIXCIT participants (Tables 2 and 3), as well as the organizers and logistics personnel for SOAS 2013. FIXCIT was made possible by the support from multiple agencies: the US National Science Foundation (NSF) under grants AGS-1240604 (Caltech), AGS-1246918 (PSU), AGS-1247421 (UWM), AGS-1243354 (CU/ARI), AGS-1240611 (CSU), and AGS-1120076 (UCB); the US Department of Energy under grant DE-SC0006626 (Caltech); and the US Environmental Protection Agency (EPA) under STAR grant 835407 (PNNL/UCB/SUNY). T. B. Nguyen (Caltech) was supported by the NSF Postdoctoral Research Fellowship program, award AGS-1331360. NCAR is operated under the sponsorship of the NSF.

Edited by: N. L. Ng

## References

- Anglada, J. M., Gonzalez, J., and Torrent-Sucarrat, M.: Effects of the substituents on the reactivity of carbonyl oxides. A theoretical study on the reaction of substituted carbonyl oxides with water, *Phys. Chem. Chem. Phys.*, 13, 13034–13045, doi:10.1039/c1cp20872a, 2011.
- Atkinson, R. and Carter, W. P. L.: Kinetics and mechanisms of the gas-phase reactions of ozone with organic compounds under atmospheric conditions, *Chem. Rev.*, 84, 437–470, 1984.
- Atkinson, R. and Arey, J.: Gas-phase tropospheric chemistry of biogenic volatile organic compounds: A review, *Atmospheric Environment*, 37, 197–219, 2003.
- Atkinson, R., Carter, W. P., Winer, A. M., and Pitts Jr, J. N.: An experimental protocol for the determination of OH radical rate constants with organics using methyl nitrite photolysis as an OH radical source, *J. Air Pollut. Contr. Assoc.*, 31, 1090–1092, 1981.
- Atkinson, R., Tuazon, E. C., and Aschmann, S. M.: Products of the gas-phase reactions of O<sub>3</sub> with alkenes *Environ. Sci. Technol.*, 29, 1860–1866, 1995.
- Atkinson, R., Baulch, D. L., Cox, R. A., Crowley, J. N., Hampson, R. F., Hynes, R. G., Jenkin, M. E., Rossi, M. J., Troe, J., and Subcommittee, I.: Evaluated kinetic and photochemical data for atmospheric chemistry: Volume II – gas phase reactions of organic species, *Atmos. Chem. Phys.*, 6, 3625–4055, doi:10.5194/acp-6-3625-2006, 2006.
- Bates, K. H., Crounse, J. D., St. Clair, J. M., Bennett, N. B., Nguyen, T. B., Seinfeld, J. H., Stoltz, B. M., and Wennberg, P. O.: Gas phase production and loss of isoprene epoxydiols, *J. Phys. Chem. A*, 118, 1237–1246, doi:10.1021/jp4107958, 2014.
- Beaver, M. R., Clair, J. M. S., Paulot, F., Spencer, K. M., Crounse, J. D., LaFranchi, B. W., Min, K. E., Pusede, S. E., Wooldridge, P. J., Schade, G. W., Park, C., Cohen, R. C., and Wennberg, P. O.: Importance of biogenic precursors to the budget of organic nitrates: Observations of multifunctional organic nitrates by cims and TD-LIF during BEARPEX 2009, *Atmos. Chem. Phys.*, 12, 5773–5785, doi:10.5194/acp-12-5773-2012, 2012.
- Becker, K. H., Brockmann, K. J., and Bechara, J.: Production of hydrogen peroxide in forest air by reaction of ozone with terpenes, *Nature*, 346, 256–258, 1990.
- Bertman, S. B. and Roberts, J. M.: A PAN analog from isoprene photooxidation, *Geophys. Res. Lett.*, 18, 1461–1464, 1991.
- Biskos, G., Paulsen, D., Russell, L. M., Buseck, P. R., and Martin, S. T.: Prompt deliquescence and efflorescence of aerosol nanoparticles, *Atmos. Chem. Phys.*, 6, 4633–4642, doi:10.5194/acp-6-4633-2006, 2006.
- Brune, W. H., Stevens, P. S., and Mather, J. H.: Measuring OH and HO<sub>2</sub> in the troposphere by laser-induced fluorescence at low pressure, *J. Atmos. Sci.*, 52, 3328–3336, doi:10.1175/1520-0469(1995)052<3328:moahit>2.0.co;2, 1995.
- Canagaratna, M. R., Jayne, J. T., Jimenez, J. L., Allan, J. D., Alfarra, M. R., Zhang, Q., Onasch, T. B., Drewnick, F., Coe, H., Middlebrook, A., Delia, A., Williams, L. R., Trimborn, A. M., Northway, M. J., DeCarlo, P. F., Kolb, C. E., Davidovits, P., and Worsnop, D. R.: Chemical and microphysical characterization of ambient aerosols with the aerodyne aerosol mass spectrometer, *Mass Spectrom. Rev.*, 26, 185–222, doi:10.1002/mas.20115, 2007.
- Chan, A. W. H., Chan, M. N., Surratt, J. D., Chhabra, P. S., Loza, C. L., Crounse, J. D., Yee, L. D., Flagan, R. C., Wennberg, P. O., and Seinfeld, J. H.: Role of aldehyde chemistry and NO<sub>x</sub> concentrations in secondary organic aerosol formation, *Atmos. Chem. Phys.*, 10, 7169–7188, doi:10.5194/acp-10-7169-2010, 2010.
- Claeys, M., Wang, W., Ion, A. C., Kourichev, I., Gelencser, A., and Maenhaut, W.: Formation of secondary organic aerosols from isoprene and its gas-phase oxidation products through reaction with hydrogen peroxide, *Atmos. Environ.*, 38, 4093–4098, doi:10.1016/j.atmosenv.2004.06.001, 2004.
- Criegee, R.: Mechanism of ozonolysis, *Angew. Chem.*, 87, 765–771, 1975.
- Crounse, J. D., McKinney, K. A., Kwan, A. J., and Wennberg, P. O.: Measurement of gas-phase hydroperoxides by chemical ionization mass spectrometry, *Anal. Chem.*, 78, 6726–6732, doi:10.1021/ac0604235, 2006.
- Crounse, J. D., Paulot, F., Kjaergaard, H. G., and Wennberg, P. O.: Peroxy radical isomerization in the oxidation of isoprene, *Phys. Chem. Chem. Phys.*, 13, 13607–13613, 2011.
- Crounse, J. D., Nielsen, L. B., Jørgensen, S., Kjaergaard, H. G., and Wennberg, P. O.: Autooxidation of organic compounds in the atmosphere, *J. Phys. Chem. Lett.*, 4, 3513–3520, doi:10.1021/jz4019207, 2013.
- Day, D. A., Wooldridge, P. J., Dillon, M. B., Thornton, J. A., and Cohen, R. C.: A thermal dissociation laser-induced fluorescence instrument for in situ detection of NO<sub>2</sub>, peroxy nitrates, alkyl nitrates, and HNO<sub>3</sub>, *J. Geophys. Res.*, 107, 4046, doi:10.1029/2001jd000779, 2002.
- DeCarlo, P. F., Kimmel, J. R., Trimborn, A., Northway, M. J., Jayne, J. T., Aiken, A. C., Gonin, M., Fuhrer, K., Horvath, T., Docherty, K., Worsnop, D. R., and Jimenez, J. L. Field-Deployable, High-Resolution, Time-of-Flight Aerosol Mass Spectrometer, *Anal. Chem.*, 78, 8281–8289, 2006.
- DiGangi, J., Boyle, E., Karl, T., Harley, P., Turnipseed, A., Kim, S., Cantrell, C., Maudlin Iii, R., Zheng, W., and Flocke, F.: First

- direct measurements of formaldehyde flux via eddy covariance: Implications for missing in-canopy formaldehyde sources, *Atmos. Chem. Phys.*, 11, 10565–10578, doi:10.5194/acp-11-10565-2011, 2011.
- Donahue, N. M., Drozd, G. T., Epstein, S. A., Presto, A. A., and Kroll, J. H.: Adventures in ozoneland: Down the rabbit-hole, *Phys. Chem. Chem. Phys.*, 13, 10848–10857, 2011.
- Drozd, G. T. and Donahue, N. M.: Pressure dependence of stabilized Criegee intermediate formation from a sequence of alkenes, *J. Phys. Chem. A*, 115, 4381–4387, doi:10.1021/jp2001089, 2011.
- Eddingsaas, N. C., Loza, C. L., Yee, L. D., Seinfeld, J. H., and Wennberg, P. O.:  $\alpha$ -pinene photooxidation under controlled chemical conditions – Part 1: Gas-phase composition in low- and high-NO<sub>x</sub> environments, *Atmos. Chem. Phys.*, 12, 6489–6504, doi:10.5194/acp-12-6489-2012, 2012.
- Ehn, M., Thornton, J. A., Kleist, E., Sipila, M., Junninen, H., Pullinen, I., Springer, M., Rubach, F., Tillmann, R., Lee, B., Lopez-Hilfiker, F., Andres, S., Acir, I.-H., Rissanen, M., Jokinen, T., Schobesberger, S., Kangasluoma, J., Kontkanen, J., Nieminen, T., Kurten, T., Nielsen, L. B., Jorgensen, S., Kjaergaard, H. G., Canagaratna, M., Maso, M. D., Berndt, T., Petaja, T., Wahner, A., Kerminen, V.-M., Kulmala, M., Worsnop, D. R., Wildt, J., and Mentel, T. F.: A large source of low-volatility secondary organic aerosol, *Nature*, 506, 476–479, doi:10.1038/nature13032, 2014.
- Fenske, J. D., Hasson, A. S., Ho, A. W., and Paulson, S. E.: Measurement of absolute unimolecular and bimolecular rate constants for CH<sub>3</sub>CHO generated by the trans-2-butene reaction with ozone in the gas phase, *J. Phys. Chem. A*, 104, 9921–9932, 2000.
- Fuentes, J. D., Lerdau, M., Atkinson, R., Baldocchi, D., Bottenheim, J. W., Ciccioli, P., Lamb, B., Geron, C., Gu, L., Guenther, A., Sharkey, T. D., and Stockwell, W.: Biogenic hydrocarbons in the atmospheric boundary layer: A review, *B. Am. Meteorol. Soc.*, 81, 1537–1575, 2000.
- Gäb, S., Hellpointner, E., Turner, W. V., and Korte, F.: Hydroxymethyl hydroperoxide and bis(hydroxymethyl) peroxide from gas-phase ozonolysis of naturally occurring alkenes, *Nature*, 316, 535–536, 1985.
- Garden, A. L., Paulot, F., Crounse, J. D., Maxwell-Cameron, I. J., Wennberg, P. O., and Kjaergaard, H. G.: Calculation of conformationally weighted dipole moments useful in ion–molecule collision rate estimates, *Chem. Phys. Lett.*, 474, 45–50, 2009.
- Griesbaum, K., Dong, Y., and McCullough, K. J.: Ozonolyses of acetylenes: Trapping of  $\alpha$ -oxo carbonyl oxides by carbonyl compounds and stabilization of  $\alpha$ -oxo ozonides by derivatizations, *J. Org. Chem.*, 62, 6129–6136, 1997.
- Griffin, R. J., Cocker, D. R., III, Flagan, R. C., and Seinfeld, J. H.: Organic aerosol formation from the oxidation of biogenic hydrocarbons, *J. Geophys. Res.*, 104, 3555–3567, 1999.
- Guenther, A., Hewitt, C. N., Erickson, D., Fall, R., Geron, C., Graedel, T., Harley, P., Klinger, L., Lerdau, M., McKay, W. A., Scholes, B., Steinbrecher, R., Tallamraju, R., Taylor, J., and Zimmerman, P.: A global model of natural volatile organic compound emissions, *J. Geophys. Res.*, 100, 8873–8892, 1995.
- Guenther, A. B., Jiang, X., Heald, C. L., Sakulyanontvittaya, T., Duhl, T., Emmons, L. K., and Wang, X.: The model of emissions of gases and aerosols from nature version 2.1 (MEGAN2.1): An extended and updated framework for modeling biogenic emissions, *Geosci. Model Dev.*, 5, 1471–1492, doi:10.5194/gmd-5-1471-2012, 2012.
- Hansel, A., Jordan, A., Holzinger, R., Prazeller, P., Vogel, W., and Lindinger, W.: Proton transfer reaction mass spectrometry: On-line trace gas analysis at the ppb level, *Int. J. Mass. Spectrom. Ion Proc.*, 149–150, 609–619, 1995.
- Hasson, A. S., Ho, A. W., Kuwata, K. T., and Paulson, S. E.: Production of stabilized Criegee intermediates and peroxides in the gas phase ozonolysis of alkenes 2. Asymmetric and biogenic alkenes, *J. Geophys. Res.*, 106, 34143–34153, 2001.
- Henze, D. K., Seinfeld, J. H., Ng, N. L., Kroll, J. H., Fu, T. M., Jacob, D. J., and Heald, C. L.: Global modeling of secondary organic aerosol formation from aromatic hydrocarbons: High- vs. Low-yield pathways, *Atmos. Chem. Phys.*, 8, 2405–2420, doi:10.5194/acp-8-2405-2008, 2008.
- Hoffmann, T., Odum, J. R., Bowman, F., Collins, D., Klockow, D., Flagan, R. C., and Seinfeld, J. H.: Formation of organic aerosols from the oxidation of biogenic hydrocarbons, *J. Atmos. Chem.*, 26, 189–222, 1997.
- Hottle, J. R., Huisman, A. J., DiGangi, J. P., Kammrath, A., Galloway, M. M., Coens, K. L., and Keutsch, F. N.: A laser induced fluorescence-based instrument for in-situ measurements of atmospheric formaldehyde, *Environ. Sci. Technol.*, 43, 790–795, doi:10.1021/es801621f, 2008.
- Huang, D., Chen, Z., Zhao, Y., and Liang, H.: Newly observed peroxides and the water effect on the formation and removal of hydroxyalkyl hydroperoxides in the ozonolysis of isoprene, *Atmos. Chem. Phys.*, 13, 5671–5683, doi:10.5194/acp-13-5671-2013, 2013.
- Huisman, A. J., Hottle, J. R., Coens, K. L., DiGangi, J. P., Galloway, M. M., Kammrath, A., and Keutsch, F. N.: Laser-induced phosphorescence for the in situ detection of glyoxal at part per trillion mixing ratios, *Anal. Chem.*, 80, 5884–5891, 2008.
- Jacobs, M. I., Darer, A. I., and Elrod, M. J.: Rate constants and products of the OH reaction with isoprene-derived epoxides, *Environ. Sci. Technol.*, 47, 12868–12876, 2013.
- Jacobs, M. I., Burke, W. J., and Elrod, M. J.: Kinetics of the reactions of isoprene-derived hydroxynitrates: gas phase epoxide formation and solution phase hydrolysis, *Atmos. Chem. Phys.*, 14, 8933–8946, doi:10.5194/acp-14-8933-2014, 2014.
- Johnson, D., and Marston, G.: The gas-phase ozonolysis of unsaturated volatile organic compounds in the troposphere, *Chem. Soc. Rev.*, 37, 699–716, 2008.
- Jordan, A., Haidacher, S., Hanel, G., Hartungen, E., Herbig, J., Märk, L., Schottkowsky, R., Seehauser, H., Sulzer, P., and Märk, T.: An online ultra-high sensitivity proton-transfer-reaction mass-spectrometer combined with switchable reagent ion capability (PTR+ SRI–MS), *Int. J. Mass Spectrom.*, 286, 32–38, 2009.
- Junninen, H., Ehn, M., Petäjä, T., Luosujärvi, L., Kotiaho, T., Koskiainen, R., Rohner, U., Gonin, M., Fuhrer, K., Kulmala, M., and Worsnop, D. R.: A high-resolution mass spectrometer to measure atmospheric ion composition, *Atmos. Meas. Tech.*, 3, 1039–1053, doi:10.5194/amt-3-1039-2010, 2010.
- Kjaergaard, H. G., Knap, H. C., Ørnsø, K. B., Jørgensen, S., Crounse, J. D., Paulot, F., and Wennberg, P. O.: Atmospheric fate of methacrolein. 2. Formation of lactone and implications for or-

- ganic aerosol production, *J. Phys. Chem. A*, 116, 5763–5768, doi:10.1021/jp210853h, 2012.
- Kroll, J. H., Clarke, J. S., Donahue, N. M., Anderson, J. G., and Demerjian, K. L.: Mechanism of  $\text{HO}_x$  formation in the gas-phase ozone-alkene reaction. 1. Direct, pressure-dependent measurements of prompt OH yields, *J. Phys. Chem. A*, 105, 1554–1560, 2001.
- Kroll, J. H., Donahue, N. M., Cee, V. J., Demerjian, K. L., and Anderson, J. G.: Gas-phase ozonolysis of alkenes: Formation of OH from *anti* carbonyl oxides, *J. Amer. Chem. Soc.*, 124, 8518–8519, 2002.
- Kuwata, K. T., Hermes, M. R., Carlson, M. J., and Zogg, C. K.: Computational studies of the isomerization and hydration reactions of acetaldehyde oxide and methyl vinyl carbonyl oxide, *J. Phys. Chem. A*, 114, 9192–9204, doi:10.1021/jp105358v, 2010.
- Kwan, A. J., Chan, A. W. H., Ng, N. L., Kjaergaard, H. G., Seinfeld, J. H., and Wennberg, P. O.: Peroxy radical chemistry and OH radical production during the  $\text{NO}_3$ -initiated oxidation of isoprene, *Atmos. Chem. Phys.*, 12, 7499–7515, doi:10.5194/acp-12-7499-2012, 2012.
- Lee, B. H., Lopez-Hilfiker, F. D., Mohr, C., Kurtén, T., Worsnop, D. R., and Thornton, J. A.: An iodide-adduct high-resolution time-of-flight chemical-ionization mass spectrometer: Application to atmospheric inorganic and organic compounds, *Environ. Sci. Technol.*, 48, 6309–6317, doi:10.1021/es500362a, 2014.
- Lee, J. H., Leahy, D. F., Tang, I. N., and Newman, L.: Measurement and speciation of gas phase peroxides in the atmosphere, *J. Geophys. Res.*, 98, 2911–2915, doi:10.1029/92jd02514, 1993.
- Lee, L., Teng, A. P., Wennberg, P. O., Crounse, J. D., and Cohen, R. C.: On rates and mechanisms of OH and  $\text{O}_3$  reactions with isoprene-derived hydroxy nitrates, *J. Phys. Chem. A*, 118, 1622–1637, doi:10.1021/jp4107603, 2014.
- Lee, M., Heikes, B. G., and O'Sullivan, D. W.: Hydrogen peroxide and organic hydroperoxide in the troposphere: A review, *Atmos. Environ.*, 34, 3475–3494, doi:10.1016/S1352-2310(99)00432-X, 2000.
- Lelieveld, J., Butler, T. M., Crowley, J. N., Dillon, T. J., Fischer, H., Ganzeveld, L., Harder, H., Lawrence, M. G., Martinez, M., Taraborrelli, D., and Williams, J.: Atmospheric oxidation capacity sustained by a tropical forest, *Nature*, 452, 737–740, doi:10.1038/nature06870, 2008.
- Lin, Y.-H., Zhang, Z., Docherty, K. S., Zhang, H., Budisulistiorini, S. H., Rubitschun, C. L., Shaw, S. L., Knipping, E. M., Edgerton, E. S., Kleindienst, T. E., Gold, A., and Surratt, J. D.: Isoprene epoxydiols as precursors to secondary organic aerosol formation: Acid-catalyzed reactive uptake studies with authentic compounds, *Environ. Sci. Technol.*, 46, 250–258, doi:10.1021/es202554c, 2012.
- Lin, Y.-H., Zhang, H., Pye, H. O. T., Zhang, Z., Marth, W. J., Park, S., Arashiro, M., Cui, T., Budisulistiorini, S. H., Sexton, K. G., Vizuete, W., Xie, Y., Luecken, D. J., Piletic, I. R., Edney, E. O., Bartolotti, L. J., Gold, A., and Surratt, J. D.: Epoxide as a precursor to secondary organic aerosol formation from isoprene photooxidation in the presence of nitrogen oxides, *Proc. Nat. Acad. Sci.*, 110, 6718–6723, doi:10.1073/pnas.1221150110, 2013.
- Liu, Y. J., Herdinger-Blatt, I., McKinney, K. A., and Martin, S. T.: Production of methyl vinyl ketone and methacrolein via the hydroperoxyl pathway of isoprene oxidation, *Atmos. Chem. Phys.*, 13, 5715–5730, doi:10.5194/acp-13-5715-2013, 2013.
- Loza, C. L., Chan, A. W. H., Galloway, M. M., Keutsch, F. N., Flagan, R. C., and Seinfeld, J. H.: Characterization of vapor wall loss in laboratory chambers, *Environ. Sci. Technol.*, 44, 5074–5078, doi:10.1021/es100727v, 2010.
- Mao, J., Ren, X., Brune, W. H., Olson, J. R., Crawford, J. H., Fried, A., Huey, L. G., Cohen, R. C., Heikes, B., Singh, H. B., Blake, D. R., Sachse, G. W., Diskin, G. S., Hall, S. R., and Shetter, R. E.: Airborne measurement of OH reactivity during INTEX-B, *Atmos. Chem. Phys.*, 9, 163–173, doi:10.5194/acp-9-163-2009, 2009.
- Mao, J., Ren, X., Zhang, L., Van Duin, D. M., Cohen, R. C., Park, J. H., Goldstein, A. H., Paulot, F., Beaver, M. R., Crounse, J. D., Wennberg, P. O., DiGangi, J. P., Henry, S. B., Keutsch, F. N., Park, C., Schade, G. W., Wolfe, G. M., Thornton, J. A., and Brune, W. H.: Insights into hydroxyl measurements and atmospheric oxidation in a California forest, *Atmos. Chem. Phys.*, 12, 8009–8020, doi:10.5194/acp-12-8009-2012, 2012.
- Martin, S. T.: Phase transitions of aqueous atmospheric particles, *Chem. Rev.*, 100, 3403–3453, 2000.
- Neeb, P., Sauer, F., Horie, O., and Moortgat, G. K.: Formation of hydroxymethyl hydroperoxide and formic acid in alkene ozonolysis in the presence of water vapor, *Atmos. Environ.*, 31, 1417–1423, 1997.
- Ng, N. L., Kwan, A. J., Surratt, J. D., Chan, A. W. H., Chhabra, P. S., Sorooshian, A., Pye, H. O. T., Crounse, J. D., Wennberg, P. O., Flagan, R. C., and Seinfeld, J. H.: Secondary organic aerosol (SOA) formation from reaction of isoprene with nitrate radicals ( $\text{NO}_3$ ), *Atmos. Chem. Phys.*, 8, 4117–4140, doi:10.5194/acp-8-4117-2008, 2008.
- Nguyen, T. B., Coggon, M. M., Bates, K. H., Zhang, X., Schwantes, R. H., Schilling, K. A., Loza, C. L., Flagan, R. C., Wennberg, P. O., and Seinfeld, J. H.: Organic aerosol formation from the reactive uptake of isoprene epoxydiols (IEPOX) onto non-acidified inorganic seeds, *Atmos. Chem. Phys.*, 14, 3497–3510, doi:10.5194/acp-14-3497-2014, 2014.
- Niki, H., Maker, P. D., Savage, C. M., and Breitenbach, L. P.: Further spectroscopic evidence for the formation of hydroperoxy-hydroxymethane in the gas phase reaction of hydroperoxy radical with formaldehyde, *Chem. Phys. Lett.*, 75, 533–535, 1980.
- Nouaime, G., Bertman, S., Seaver, C., Elyea, D., Huang, H., Shepson, P., Starn, T., Riener, D., Zika, R., and Olszyna, K.: Sequential oxidation products from tropospheric isoprene chemistry: MACR and MPAN at a  $\text{NO}_x$ -rich forest environment in the southeastern United States, *J. Geophys. Res.*, 103, 22463–22471, 1998.
- Nozière, B. and Barnes, I.: Evidence for formation of a PAN analogue of pinonic structure and investigation of its thermal stability, *J. Geophys. Res.*, 103, 25587–25597, 1998.
- Paulot, F., Crounse, J. D., Kjaergaard, H. G., Kroll, J. H., Seinfeld, J. H., and Wennberg, P. O.: Isoprene photooxidation: New insights into the production of acids and organic nitrates, *Atmos. Chem. Phys.*, 9, 1479–1501, doi:10.5194/acp-9-1479-2009, 2009a.
- Paulot, F., Crounse, J. D., Kjaergaard, H. G., Kurten, A., St. Clair, J. M., Seinfeld, J. H., and Wennberg, P. O.: Unexpected epoxide formation in the gas-phase photooxidation of isoprene, *Science*, 325, 730–733, doi:10.1126/science.1172910, 2009b.
- Peeters, J., Nguyen, T. L., and Vereecken, L.:  $\text{HO}_x$  radical regeneration in the oxidation of isoprene, *Phys. Chem. Chem. Phys.*, 11, 5935–5939, 2009.



- Perring, A. E., Wisthaler, A., Graus, M., Wooldridge, P. J., Lockwood, A. L., Mielke, L. H., Shepson, P. B., Hansel, A., and Cohen, R. C.: A product study of the isoprene + NO<sub>3</sub> reaction, *Atmos. Chem. Phys.*, 9, 4945–4956, doi:10.5194/acp-9-4945-2009, 2009.
- Pye, H. O. T., Pinder, R. W., Piletic, I. R., Xie, Y., Capps, S. L., Lin, Y.-H., Surratt, J. D., Zhang, Z., Gold, A., Luecken, D. J., Hutzell, W. T., Jaoui, M., Offenberg, J. H., Kleindienst, T. E., Lewandowski, M., and Edney, E. O.: Epoxide pathways improve model predictions of isoprene markers and reveal key role of acidity in aerosol formation, *Environ. Sci. Technol.*, 47, 11056–11064, doi:10.1021/es402106h, 2013.
- Ridley, B. and Grahek, F.: A small, low flow, high sensitivity reaction vessel for NO chemiluminescence detectors, *J. Atmos. Ocean. Tech.*, 7, 307–311, 1990.
- Rivera-Rios, J. C., Nguyen, T. B., Crounse, J. D., Jud, W., St. Clair, J. M., Mikoviny, T., Gilman, J. B., Lerner, B. M., Kaiser, J. B., de Gouw, J., Wisthaler, A., Hansel, A., Wennberg, P. O., Seinfeld, J. H., and Keutsch, F. N.: Conversion of hydroperoxides to carbonyls in field and laboratory instrumentation: Observational bias in diagnosing pristine versus anthropogenically controlled atmospheric chemistry, *Geophys. Res. Lett.*, 41, doi:10.1002/2014GL061919, 2014.
- Roberts, J. M., Williams, J., Baumann, K., Buhr, M. P., Goldan, P. D., Holloway, J., Hübler, G., Kuster, W. C., McKeen, S. A., and Ryerson, T. B.: Measurements of PAN, PPN, and MPAN made during the 1994 and 1995 Nashville intensives of the southern oxidant study: Implications for regional ozone production from biogenic hydrocarbons, *J. Geophys. Res.*, 103, 22473–22490, 1998.
- Rollins, A. W., Kiendler-Scharr, A., Fry, J. L., Brauers, T., Brown, S. S., Dorn, H. P., Dubé, W. P., Fuchs, H., Mensah, A., Mentel, T. F., Rohrer, F., Tillmann, R., Wegener, R., Wooldridge, P. J., and Cohen, R. C.: Isoprene oxidation by nitrate radical: Alkyl nitrate and secondary organic aerosol yields, *Atmos. Chem. Phys.*, 9, 6685–6703, doi:10.5194/acp-9-6685-2009, 2009.
- Sauer, F., Schäfer, C., Neeb, P., Horie, O., and Moortgat, G. K.: Formation of hydrogen peroxide in the ozonolysis of isoprene and simple alkenes under humid conditions, *Atmos. Environ.*, 33, 229–241, 1999.
- Simonaitis, R., Olszyna, K., and Meagher, J.: Production of hydrogen peroxide and organic peroxides in the gas phase reactions of ozone with natural alkenes, *Geophys. Res. Lett.*, 18, 9–12, 1991.
- Sinha, V., Williams, J., Crowley, J., and Lelieveld, J.: The comparative reactivity method—a new tool to measure total OH reactivity in ambient air, *Atmos. Chem. Phys.*, 8, 2213–2227, doi:10.5194/acp-8-2213-2008, 2008.
- St. Clair, J. M., McCabe, D. C., Crounse, J. D., Steiner, U., and Wennberg, P. O.: Chemical ionization tandem mass spectrometer for the in situ measurement of methyl hydrogen peroxide, *Rev. Sci. Instrum.*, 81, 094102–094106, 2010.
- Surratt, J., Chan, A. W. H., Eddingsaas, N. C., Chan, M., Loza, C. L., Kwan, A. J., Hersey, S. P., Flagan, R. C., Wennberg, P. O., and Seinfeld, J. H.: Reactive intermediates revealed in secondary organic aerosol formation from isoprene, *P. Natl. Acad. Sci.*, 107, 6640–6645, 2010.
- Valverde-Canossa, J., Ganzeveld, L., Rappenglück, B., Steinbrecher, R., Klemm, O., Schuster, G., and Moortgat, G.: First measurements of H<sub>2</sub>O<sub>2</sub> and organic peroxides surface fluxes by the relaxed eddy-accumulation technique, *Atmos. Environ.*, 40, 55–67, 2006.
- Vereecken, L., Müller, J.-F., and Peeters, J.: Low-volatility polyoxygenates in the OH-initiated atmospheric oxidation of  $\alpha$ -pinene: Impact of non-traditional peroxy radical chemistry, *Phys. Chem. Chem. Phys.*, 9, 5241–5248, 2007.
- Welz, O., Savee, J. D., Osborn, D. L., Vasu, S. S., Percival, C. J., Shallcross, D. E., and Taatjes, C. A.: Direct kinetic measurements of Criegee intermediate (CH<sub>2</sub>OO) formed by reaction of CH<sub>2</sub>I with O<sub>2</sub>, *Science*, 335, 204–207, doi:10.1126/science.1213229, 2012.
- Wängberg, I., Barnes, I., and Becker, K. H.: Product and mechanistic study of the reaction of NO<sub>3</sub> radicals with  $\alpha$ -pinene, *Environ. Sci. Technol.*, 31, 2130–2135, doi:10.1021/es960958n, 1997.
- Wolfe, G. M., Thornton, J. A., Yatavelli, R. L. N., McKay, M., Goldstein, A. H., LaFranchi, B., Min, K. E., and Cohen, R. C.: Eddy covariance fluxes of acyl peroxy nitrates (PAN, PPN and MPAN) above a ponderosa pine forest, *Atmos. Chem. Phys.*, 9, 615–634, doi:10.5194/acp-9-615-2009, 2009.
- Wolfe, G. M., Thornton, J. A., Bouvier-Brown, N. C., Goldstein, A. H., Park, J.-H., McKay, M., Matross, D. M., Mao, J., Brune, W. H., LaFranchi, B. W., Browne, E. C., Min, K.-E., Wooldridge, P. J., Cohen, R. C., Crounse, J. D., Faloona, I. C., Gilman, J. B., Kuster, W. C., de Gouw, J. A., Huisman, A., and Keutsch, F. N.: The Chemistry of Atmosphere-Forest Exchange (CAFE) Model – Part 2: Application to BEARPEX-2007 observations, *Atmos. Chem. Phys.*, 11, 1269–1294, doi:10.5194/acp-11-1269-2011, 2011.
- Wolfe, G. M., Crounse, J. D., Parrish, J. D., Clair, J. M. S., Beaver, M. R., Paulot, F., Yoon, T. P., Wennberg, P. O., and Keutsch, F. N.: Photolysis, OH reactivity and ozone reactivity of a proxy for isoprene-derived hydroperoxyenals (HPALDs), *Phys. Chem. Chem. Phys.*, 14, 7276–7286, 2012.
- Worton, D. R., Surratt, J. D., LaFranchi, B. W., Chan, A. W. H., Zhao, Y., Weber, R. J., Park, J.-H., Gilman, J. B., de Gouw, J., Park, C., Schade, G., Beaver, M., Clair, J. M. S., Crounse, J., Wennberg, P., Wolfe, G. M., Harrold, S., Thornton, J. A., Farmer, D. K., Docherty, K. S., Cubison, M. J., Jimenez, J.-L., Frossard, A. A., Russell, L. M., Kristensen, K., Glasius, M., Mao, J., Ren, X., Brune, W., Browne, E. C., Pusede, S. E., Cohen, R. C., Seinfeld, J. H., and Goldstein, A. H.: Observational insights into aerosol formation from isoprene, *Environ. Sci. Technol.*, 47, 11403–11413, doi:10.1021/es4011064, 2013.

*Appendix C*

## VAPOR WALL DEPOSITION IN TEFLON CHAMBERS

Zhang, X. et al. (2015). “Vapor Wall Deposition in Teflon Chambers”. In: *Atmos. Chem. Phys.* 15, pp. 4197–4214. doi: 10.5194/acp-15-4197-2015.



## Vapor wall deposition in Teflon chambers

X. Zhang<sup>1</sup>, R. H. Schwantes<sup>1</sup>, R. C. McVay<sup>2</sup>, H. Lignell<sup>2</sup>, M. M. Coggon<sup>2</sup>, R. C. Flagan<sup>1,2</sup>, and J. H. Seinfeld<sup>1,2</sup>

<sup>1</sup>Division of Engineering and Applied Science, California Institute of Technology, Pasadena, CA, USA

<sup>2</sup>Division of Chemistry and Chemical Engineering, California Institute of Technology, Pasadena, CA, USA

Correspondence to: J. H. Seinfeld (seinfeld@caltech.edu)

Received: 23 September 2014 – Published in Atmos. Chem. Phys. Discuss.: 24 October 2014

Revised: 7 February 2015 – Accepted: 25 March 2015 – Published: 23 April 2015

**Abstract.** Teflon chambers are ubiquitous in studies of atmospheric chemistry. Secondary organic aerosol (SOA) formation can be underestimated, owing to deposition of SOA-forming vapors to the chamber wall. We present here an experimental protocol and a model framework to constrain the vapor–wall interactions in Teflon chambers. We measured the wall deposition rates of 25 oxidized organic compounds generated from the photooxidation of isoprene, toluene,  $\alpha$ -pinene, and dodecane in two chambers that had been extensively used and in two new unused chambers. We found that the extent of prior use of the chamber did not significantly affect the sorption behavior of the Teflon films. Among the 25 compounds studied, the maximum wall deposition rate is exhibited by the most highly oxygenated and least volatile compounds. By optimizing the model output to the observed vapor decay profiles, we identified that the dominant parameter governing the extent of wall deposition of a compound is its wall accommodation coefficient ( $\alpha_{w,i}$ ), which can be correlated through its volatility with the number of carbons and oxygens in the molecule. By doing so, the wall-induced deposition rate of intermediate/semi-volatile organic vapors can be reasonably predicted based on their molecular constituency. The extent to which vapor wall deposition impacts measured SOA yields depends on the competition between uptake of organic vapors by suspended particles and the chamber wall. The timescale associated with vapor wall deposition can vary from minutes to hours depending on the value of  $\alpha_{w,i}$ . For volatile and intermediate volatility organic compounds (small  $\alpha_{w,i}$ ), gas-particle partitioning will dominate wall deposition for typical particle number concentrations in chamber experiments. For compounds characterized by relatively large  $\alpha_{w,i}$ , vapor transport to particles is suppressed by competition with the chamber wall even with perfect particle accommodation.

### 1 Introduction

Understanding of the mechanism and extent of secondary organic aerosol (SOA) formation from oxidation of volatile organic compounds (VOCs) has been derived largely from experiments in Teflon chambers. Chamber-measured SOA yields (mass of SOA formed per mass of VOC reacted) have been widely parameterized into regional/global atmospheric models, and chemical mechanisms leading to SOA formation and aging have been derived based on the gas/particle-phase identification of intermediate/semi/low-volatility compounds generated in controlled chamber experiments. An unavoidable consequence of the use of an environmental chamber is interaction of vapors and particles with the chamber wall. It has been recently established that SOA formation can be substantially underestimated due to deposition of SOA-forming vapors to the chamber wall rather than growing particles (Zhang et al., 2014a).

Chamber-wall-induced decay of organic vapors was reported 30 years ago. Grosjean (1985) and McMurry and Grosjean (1985) measured wall deposition rates of several volatile organic compounds in a chamber constructed from Fluorinated ethylene propylene (FEP) Teflon film. The lifetime of the VOCs, with respect to wall deposition, was found generally to exceed  $\sim 15$  h. Loza et al. (2010) found that deposition of the isoprene oxidation product surrogate, 2,3-epoxy-1,4-butanediol (BEPOX), and glyoxal to the FEP Teflon chamber wall is reversible on sufficiently long timescales. On the contrary, rapid reversible gas–wall partitioning of  $n$ -alkanes, 1-alkenes, 2-alcohols, 2-ketones, monoacids, and 1,2-diols was universally observed by Matsunaga and Ziemann (2010) and Yeh and Ziemann (2014). Following the same experimental protocol, Kokkola et al. (2014) measured that the equilibrium fractions of

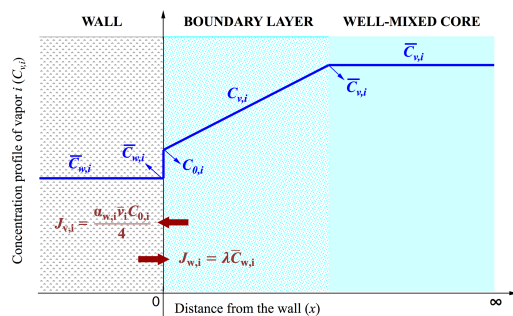


**Figure 1.** Theoretical framework representing the vapor–wall interactions. Concentrations of organic vapor  $i$  in the well-mixed core, in the boundary layer, over the surface of the chamber wall, and in the chamber wall are denoted by  $\bar{C}_{v,i}$ ,  $C_{v,i}$ ,  $C_{0,i}$ ,  $\bar{C}_{w,i}$ , respectively. Vapor fluxes at the gas–wall interface are denoted by  $J_{v,i}$  and  $J_{w,i}$ .

nopinone and pinanediol on the wall of a 4 m<sup>3</sup> FEP Teflon chamber are on average 0.4 and 0.8, respectively.

The extent to which vapors and the chamber wall interact is reflected by properties such as the gas-phase transport rate of organic molecules, affinity of the wall for various organic molecules, the degree of reversibility of the vapor–wall partitioning, and the equilibrium solubility of organic vapors in the wall. Organic materials generated in chamber experiments can deposit on the chamber wall to form a coating that can act as the primary absorbing medium, or the Teflon film itself could act as the absorbing medium, in a process akin to the sorption of small molecules by organic polymers. While measurement of vapor wall deposition rates for the thousands of organic molecules that are produced from the oxidation of SOA precursor VOCs is not presently possible, empirical expressions that represent the deposition rates of organic vapors as a function of general molecular properties would be highly useful.

A prime goal of characterizing vapor wall deposition in a chamber is to understand its impact on SOA formation and evolution. We present here an experimental protocol to constrain the nature of organic vapor wall deposition in Teflon chambers. We measured wall-induced dark decay rates of 25 intermediate/semi-volatility organic vapors, which span a range of volatilities and oxidation states, in both unused and previously used chambers constructed with FEP Teflon film. A temperature ramping program (298–318 K) was implemented to study the reversibility of vapor–wall partitioning. A model framework is developed to describe interactions between organic vapors and the chamber wall following the theories for particle wall deposition and gas-particle partitioning. We address the following questions in the present study. (1) What is the physicochemical nature of the chamber wall? (2) What are the key parameters that characterize the vapor–wall interactions and how can these values be de-

termined? (3) How can one predict the wall deposition rate of a specific compound based on its molecular properties?

## 2 Vapor wall deposition – theory

Figure 1 depicts the steady-state concentration profiles of an organic compound  $i$  in the well-mixed core of the chamber ( $\bar{C}_{v,i}$ ), in the boundary layer adjacent to the wall ( $C_{v,i}$ ), at the wall surface ( $C_{0,i}$ ), and in the chamber wall ( $\bar{C}_{w,i}$ ). Vapor molecules in the well-mixed core of a chamber are transported through a boundary layer adjacent to the wall by a combination of molecular and turbulent diffusion. The transport rate depends on both the molecular properties of the individual organic compound (as characterized by the molecular diffusion coefficient,  $D_i$ ), as well as the extent of turbulent mixing in the chamber (as characterized by the coefficient of eddy diffusion,  $K_e$ ). As vapor molecules encounter the chamber wall, the fraction of those encounters that lead to uptake is represented by the accommodation coefficient ( $\alpha_{w,i}$ ), and molecules rebound with a probability of  $1 - \alpha_{w,i}$ . The accommodation coefficient depends, in principle, on the nature of the wall surface as well as the compound chemical composition. It is worth emphasizing that  $\alpha_{w,i}$  characterizes imperfect wall accommodation of the gas–wall interface. Molecules deposited on the wall may re-evaporate at a rate that depends on their concentration in the wall. In order to represent this process, we note that, at equilibrium, the flux arriving from the gas phase ( $J_{v,i}$ ) and the evaporation flux from the wall ( $J_{w,i}$ ) are equal. Thus, the evaporative flux from the wall ( $J_{w,i}$ ) can be expressed as a function of the accommodation coefficient ( $\alpha_{w,i}$ ), as described in Eqs. (7)–(9) later.

A conservation balance on  $\bar{C}_{v,i}$ , the concentration of vapor  $i$  in the well-mixed core of a chamber that is subject only to the deposition process, is given by

$$\frac{d\bar{C}_{v,i}}{dt} = -k_{w,depo,i}\bar{C}_{v,i} + k_{w,evap,i}\bar{C}_{w,i}, \quad (1)$$

where  $k_{w,depo,i}$  (s<sup>−1</sup>) is the deposition rate coefficient to the wall,  $k_{w,evap,i}$  (s<sup>−1</sup>) is the evaporation rate coefficient from the wall, and  $\bar{C}_{w,i}$  is the concentration of vapor  $i$  that has accumulated on the chamber wall. The dynamic behavior of  $\bar{C}_{w,i}$  is described by a corresponding balance:

$$\frac{d\bar{C}_{w,i}}{dt} = -k_{w,evap,i}\bar{C}_{w,i} + k_{w,depo,i}\bar{C}_{v,i}. \quad (2)$$

Note that  $\bar{C}_{w,i}$  is assumed to be zero at the onset of vapor  $i$  generation, ultimately reaching equilibrium with  $\bar{C}_{v,i}$ .

### 2.1 Vapor flux arriving from the gas phase ( $J_{v,i}$ )

For a chamber that is relatively well mixed, transport to the wall occurs by molecular and turbulent diffusion across a thin boundary layer, of thickness  $\delta$ , adjacent to the chamber wall.

The flux due to molecular diffusion is given by  $-D_i \nabla C_{v,i}$ , where  $C_{v,i}$  is the local vapor  $i$  concentration in the boundary layer and  $D_i$  is its molecular diffusivity. The turbulent diffusion flux is expressed as  $-D_e \nabla C_{v,i}$ , where  $D_e$  is the eddy diffusivity. One can invoke the Prandtl mixing length expression near a wall,  $D_e = K_e x^2$ , where  $x$  is the distance from the wall, and  $K_e$  is the coefficient of eddy diffusion (Corner and Pendlebury, 1951; Crump and Seinfeld, 1981). Owing to the small value of  $\delta$ , a quasi-steady state condition exists in the boundary layer, and the concentration of vapor  $i$  within the boundary layer,  $0 \leq x \leq \delta$ , is governed by

$$\frac{d}{dx} \left[ (K_e x^2 + D_i) \frac{dC_{v,i}}{dx} \right] = 0. \quad (3)$$

Introducing the dimensionless variable  $z$  by setting  $x = (D_i/K_e)^{1/2} z$ , Eq. (3) becomes

$$(z^2 + 1) \frac{d^2 C_{v,i}}{dz^2} + 2z \frac{dC_{v,i}}{dz} = 0, \quad (4)$$

subject to the boundary conditions,

$$x = 0 (z = 0) \rightarrow C_{v,i} = C_{0,i},$$

$$x = \delta (z = (K_e/D_i)^{1/2} \delta) \rightarrow C_{v,i} = \bar{C}_{v,i},$$

where  $C_{0,i}$  and  $\bar{C}_{v,i}$  are concentrations of vapor  $i$  over the wall surface and in the well-mixed core of the chamber, respectively. Note that the accommodation coefficient for particles on the wall was assumed to be unity in previous theoretical studies (e.g., Crump and Seinfeld, 1981; McMurry and Grosjean, 1985), meaning that particles that encounter the wall will lead to 100 % uptake. This assumption is reasonable, especially if particles are in a quasi-liquid state. On the other hand, the accommodation coefficient for vapors on the wall ( $\alpha_{w,i}$ ) is likely less than unity, and the steady-state concentration is then nonzero at the chamber wall surface. The solution of Eq. (4) expressed in the original variables is

$$C_{v,i} = C_{0,i} + (\bar{C}_{v,i} - C_{0,i}) \frac{\tan^{-1} [(K_e/D_i)^{1/2} x]}{\tan^{-1} [(K_e/D_i)^{1/2} \delta]} \\ \approx C_{0,i} + (\bar{C}_{v,i} - C_{0,i}) \frac{\tan^{-1} [(K_e/D_i)^{1/2} x]}{\pi/2}. \quad (5)$$

Physically, turbulent diffusion dominates molecular diffusion at the outer edge of the boundary layer, so that  $(K_e/D_i)^{1/2} \delta \gg 1$ .

The vapor flux arriving from the gas phase to the wall surface ( $J_{v,i}$ ) is derived from the kinetic theory of gases:

$$J_{v,i} = \frac{\alpha_{w,i} \bar{v}_i C_{0,i}}{4}, \quad (6)$$

where  $\bar{v}_i$  is the species mean thermal speed.

## 2.2 Vapor flux leaving from the wall due to evaporation ( $J_{w,i}$ )

Without loss of generality, vapor wall deposition can be assumed to be reversible. The flux of molecules  $i$  that evaporate from the wall back to the gas phase ( $J_{w,i}$ ) depends on the concentration of  $i$  in the wall ( $\bar{C}_{w,i}$ ). So we can write  $J_{w,i}$  as a function of  $\bar{C}_{w,i}$ :

$$J_{w,i} \propto \bar{C}_{w,i} \text{ or } J_{w,i} = \lambda \bar{C}_{w,i}, \quad (7)$$

where  $\lambda$  is simply a quantity that reflects the positive correlation between  $J_{w,i}$  and  $\bar{C}_{w,i}$ . If the gas and wall phases are at equilibrium, then

$$J_{v,i,(\text{eq})} = J_{w,i,(\text{eq})}. \quad (8)$$

Therefore,

$$\lambda = \frac{\alpha_{w,i} \bar{v}_i C_{0,i,\text{eq}}}{4 \bar{C}_{w,i,\text{eq}}} = \frac{\alpha_{w,i} \bar{v}_i}{4 H_i}, \quad (9)$$

where  $H_i$  is the Henry's law constant of organic species  $i$ . Substitution of Eq. (9) into Eq. (7) gives

$$J_{w,i} = \frac{\alpha_{w,i} \bar{v}_i \bar{C}_{w,i}}{4 H_i}. \quad (10)$$

If applying vapor–particle partitioning theory here, Eq. (10) can be rewritten as

$$J_{w,i} = \frac{\alpha_{w,i} \bar{v}_i \bar{C}_{w,i}}{4 K_{w,i} C_w}, \quad (11)$$

where  $K_{w,i}$  is vapor–wall partition coefficient (Matsunaga and Ziemann, 2010):

$$K_{w,i} = \frac{RT}{p_{L,i}^0 \gamma_i \bar{M}_w}, \quad (12)$$

and where  $p_{L,i}^0$  is the vapor pressure of compound  $i$  as a liquid. We calculate  $p_{L,i}^0$  by the average of two group contribution methods, “SIMPOL.1” developed by Pankow and Asher (2008) and “EVAPORATION” developed by Compennolle et al. (2011).  $\gamma_i$ , the activity coefficient in the wall layer on a mole fraction basis, is assumed to be unity here,  $R$  is the gas constant,  $T$  is temperature, and  $\bar{M}_w$  is the average molecular weight of the absorbing organic material on the wall, which, following Matsunaga and Ziemann (2010), is assumed to be  $250 \text{ g mol}^{-1}$ .  $C_w$  ( $\text{g m}^{-3}$ ) is an assumed equivalent mass of absorbing organic material on the chamber wall (Matsunaga and Ziemann, 2010). It can be regarded as characterizing the equilibrium solubility of individual organic molecules in FEP Teflon polymer and, possibly, in other organic materials deposited on the wall. When  $C_w \rightarrow \infty$ , the wall presents essentially an absorbing medium of infinite extent, and vapor wall deposition is ultimately an irreversible process. Note,

however, that the concept of an “equivalent absorbing organic mass” does not necessarily imply that an actual layer of organic material exists on the chamber wall.  $C_w$  might well represent the accumulation of deposited organic material from previous chamber experiments, or it could reflect the absorption properties of FEP film itself. We will return to the nature of  $C_w$  shortly.

Since the gas–wall interface is presumed to have no thickness, the net flux across the interface results from the concentration gradient,

$$D_i \left. \frac{dC_{v,i}}{dx} \right|_{x=0} = J_{v,i} - J_{w,i} = \frac{\alpha_{w,i} \bar{v}_i C_{0,i}}{4} - \frac{\alpha_{w,i} \bar{v}_i \bar{C}_{w,i}}{4K_{w,i} C_w}. \quad (13)$$

Note that when equilibrium is established, the net flux becomes zero and the concentration gradient no longer exists at the gas–wall interface. The LHS of Eq. (13) is based on Fick’s law of diffusion and leads to Eq. (5). In this way, the quantity  $C_{0,i}$  is expressed as a function of  $\bar{C}_{v,i}$  and  $\bar{C}_{w,i}$ . Therefore, the conservation equation for the change in the concentration of vapor  $i$  in the well-mixed core of the chamber owing to wall deposition is given by

$$\frac{d\bar{C}_{v,i}}{dt} = \left( \frac{A}{V} \right) \left( \frac{\alpha_{w,i} \bar{v}_i / 4}{\pi \alpha_{w,i} \bar{v}_i / 8 (D_i K_e)^{1/2} + 1} \right) \left( \frac{\bar{C}_{w,i}}{K_{w,i} C_w} - \bar{C}_{v,i} \right), \quad (14)$$

where  $A$  and  $V$  are the surface area and volume of the chamber, respectively. A rewrite of Eq. (14) gives

$$k_{w,depo,i} = \left( \frac{A}{V} \right) \left( \frac{\alpha_{w,i} \bar{v}_i / 4}{\pi \alpha_{w,i} \bar{v}_i / 8 (D_i K_e)^{1/2} + 1} \right), \quad (15a)$$

$$k_{w,evap,i} = \frac{k_{w,depo,i}}{K_{w,i} C_w}. \quad (15b)$$

### 3 Vapor wall deposition – experiment

Experiments were conducted in the Caltech dual 24 m<sup>3</sup> Fluorinated ethylene propylene (FEP) Teflon chambers that are suitable for pristine (low-NO) and polluted (high-NO) conditions (Zhang and Seinfeld, 2013; Fehner et al., 2014; Loza et al., 2014). Figure 2 shows a schematic of the experimental protocol used to measure deposition of organic vapors to the chamber wall. Oxidized organic vapors were generated via photooxidation of four parent VOCs, isoprene, toluene,  $\alpha$ -pinene, and dodecane, in the absence of seed aerosol. Once a sufficient amount of oxidized products is formed with none or limited aerosol formation via nucleation, irradiation is ceased, and the ensuing wall-induced dark decay of the array of oxidation products is monitored by chemical ionization mass spectrometry (CIMS). Following this period, the chambers were heated to investigate the extent to which vapor–wall partitioning is reversible. These experiments were carried out in two chambers that had been used in past SOA

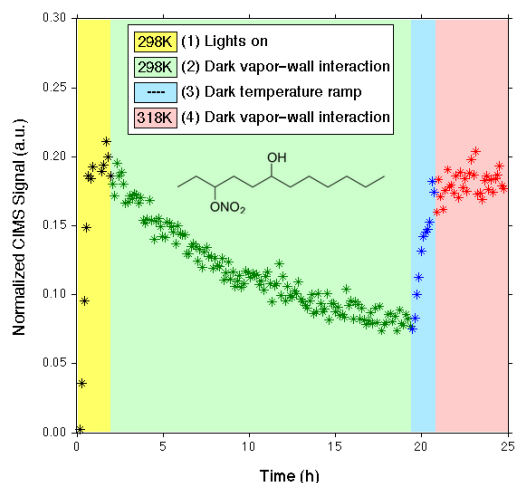


**Figure 2.** Example of the experimental procedure to assess vapor wall deposition using 3-nitrooxy-6-dodecanol ( $m/z = (-)332$ ): period (1) organic oxidation product generation; period (2) vapor wall deposition at 298 K in the dark; period (3) chamber temperature ramp from 298 to 318 K; and Period (4) temperature held at 318 K in the dark.

studies. Two control experiments were also conducted in two unused 24 m<sup>3</sup> Teflon chambers using identical experimental protocols, see Table 1.

Vapor molecules representing SOA products were generated directly via VOC photooxidation, as opposed to the external injection of commercially available chemical standards. In this manner, uncertainty in the initial vapor concentration due to filling and mixing is avoided. In order to generate a spectrum of oxidized compounds characterized by a combination of different carbon numbers and types of functional groups, isoprene, toluene,  $\alpha$ -pinene, and dodecane were chosen as the parent VOCs. Prior to each experiment, the Teflon chambers were flushed with purified dry air for 12 h at 45 °C, then “conditioned” by UV irradiation for 24 h in the presence of 2 ppm H<sub>2</sub>O<sub>2</sub>, followed by purging with purified dry air for ~4 days at 25 °C. Experiments were carried out under conditions in which the peroxy radicals formed from the initial OH reaction with the parent hydrocarbon react either primarily with NO (so-called high-NO) or HO<sub>2</sub> and RO<sub>2</sub> (so-called low-NO). For low-NO conditions, hydrogen peroxide (H<sub>2</sub>O<sub>2</sub>) was used as the OH source by evaporating 120  $\mu$ L of 50 % wt aqueous solution into the chamber with 5 L min<sup>-1</sup> of purified air for ~110 min, resulting in an approximate starting H<sub>2</sub>O<sub>2</sub> mixing ratio of 2.0 ppm. For high-NO conditions, nitrous acid (HONO) was used as the OH source by dropwise addition of 15 mL of 1 wt% NaNO<sub>2</sub> into 30 mL of 10 wt% H<sub>2</sub>SO<sub>4</sub> in a glass bulb and introduced into the chambers with 5 L min<sup>-1</sup> of purified air

**Table 1.** Experimental conditions for production of oxidized organic vapors.

|         | Exp.# | Lights<br>on (h) | Lights<br>off (h) | <i>T</i> program <sup>a</sup><br>(K [h–h]) | OH<br>source                  | VOC              | HC <sub>0</sub><br>(ppb) | (NO) <sub>0</sub><br>(ppb) | (NO <sub>2</sub> ) <sub>0</sub><br>(ppb) | Maximum<br>Particle conc.<br>(μg m <sup>−3</sup> ) | FEP Bag<br>condition |
|---------|-------|------------------|-------------------|--|-------------------------------|------------------|--------------------------|----------------------------|--|--|----------------------|
| high-NO | 1     | ~ 1              | ~ 24.2            | 298 [0–17.6]<br>318 [19.9–25.2]            | HONO                          | $\alpha$ -pinene | ~ 30                     | 242                        | 458                                      | ~ 0.4  | used                 |
|         | 2     | ~ 1              | ~ 24.2            | 298 [0–17.6]<br>318 [19.9–25.2]            | HONO                          | $\alpha$ -pinene | ~ 30                     | 229                        | 371                                      | ~ 0.3  | unused               |
|         | 3     | ~ 1              | ~ 23.8            | 298 [0–17.3]<br>318 [20.9–24.8]            | HONO                          | dodecane         | ~ 50                     | 275                        | 556                                      | ~ 2.1  | used                 |
|         | 4     | ~ 2              | ~ 23              | 298 [0–17.3]<br>318 [20.8–25]              | HONO                          | isoprene         | ~ 200                    | 243                        | 460                                      | ~ 0.2  | used                 |
| low-NO  | 5     | ~ 1              | ~ 24.2            | 298 [0–17.8]<br>318 [20.3–25.2]            | H <sub>2</sub> O <sub>2</sub> | $\alpha$ -pinene | ~ 30                     | < DL                       | < DL                                     | ~ 1.2  | used                 |
|         | 6     | ~ 1              | ~ 24.2            | 298 [0–17.8]<br>318 [20.3–25.2]            | H <sub>2</sub> O <sub>2</sub> | $\alpha$ -pinene | ~ 30                     | < DL                       | < DL                                     | ~ 1.1  | unused               |
|         | 7     | ~ 7              | ~ 21.6            | 298 [0–20.6]<br>318 [22–28.6]              | H <sub>2</sub> O <sub>2</sub> | dodecane         | ~ 50                     | < DL                       | < DL                                     | ~ 0.0  | used                 |
|         | 8     | ~ 5              | ~ 24.7            | 298 [0–21.3]<br>318 [24.7–29.7]            | H <sub>2</sub> O <sub>2</sub> | toluene          | ~ 100                    | < DL                       | < DL                                     | ~ 0.1  | used                 |

<sup>a</sup> The temperature is controlled at 298 K for the first ~ 20 h of the experiment, including ~ 1–7 h irradiation and ~ 13–16 h darkness, and then ramped up to 318 K within ~ 3 h and held for ~ 4–6 h.

for ~ 40 min. Ozone formation is substantially limited in the presence of a high concentration of HONO, and NO<sub>3</sub> formation is negligible. A measured volume of hydrocarbon (isoprene/toluene/ $\alpha$ -pinene/dodecane) was injected via a syringe into a glass bulb, which was connected to the Teflon chamber. Heated 5 L min<sup>−1</sup> of purified air flowed through the glass bulb into the chamber for 20 min, introducing 25–200 ppb of hydrocarbon into the chamber. After ~ 60 min mixing, photooxidation was initiated by irradiating the chamber with black lights with output wavelength ranging from 300 to 400 nm. Over the course of the irradiation period, the maximum particle mass concentration formed via nucleation ranged from 0.3 to 2 μg m<sup>−3</sup>, corresponding to a particle surface area to chamber wall area ratio of < 10<sup>−5</sup>. Under these conditions, the surface area of particles present in the chamber is sufficiently low that partitioning of organic vapors onto particles is negligible. After ~ 1–7 h of reaction, UV lights were turned off and the decay of oxidation products due to wall deposition was monitored for ~ 13–16 h at 25 °C. The chamber temperature was then ramped up to 45 °C during the remaining ~ 4–6 h of the experiment with other conditions held constant.

Gas-phase organic compounds were monitored using a custom-modified Varian 1200 triple-quadrupole CIMS (Crounse et al., 2006; Paulot et al., 2009). In negative-mode operation, CF<sub>3</sub>O<sup>−</sup> was used as the reagent ion to cluster with analytes [R] with strong fluorine affinity such as hydroperoxide, producing [R·CF<sub>3</sub>O]<sup>−</sup> or  $m/z = [M + 85]^-$ , where  $M$  is the molecular weight of the analyte. For more strongly acidic species [X], the transfer product, [X<sub>[H]</sub>·HF]<sup>−</sup> or  $m/z = [M + 19]^-$ , is formed during ionization. Carboxylic

acids tend to have contributions to both the transfer and cluster products, in which case the trace with higher signal-to-noise ratio is considered. Prior to each experiment, the purified air in the chamber was sampled, and this is subtracted off as the CIMS background signal. The background signal is fairly consistent between the masses and over time. However, this background subtraction does not guarantee that the background for every  $m/z$  signal is absolutely zero, as noted in Fig. 3 that the CIMS background for certain ions is hovering around zero. Identification of products by CIMS from the photooxidation of isoprene,  $\alpha$ -pinene, and dodecane in our laboratory has been previously reported (Paulot et al., 2009; Eddingsaas et al., 2012; Yee et al., 2012; Zhang et al., 2014b).

#### 4 Absorbing organic mass on the chamber wall ( $C_w$ )

Figure 3 shows the continuous dark decay of the 25 organic vapors generated from the photooxidation of isoprene, toluene,  $\alpha$ -pinene, and dodecane under high/low-NO conditions. In contrast to the behavior in Fig. 3, Matsunaga and Ziemann (2010) and Yeh and Ziemann (2014) observed rapid equilibrium established within less than an hour for vapor wall losses of  $n$ -alkanes, 1-alkenes, 2-alcohols, 2-ketones, monoacids, and 1,2-diols in both 1.7 and 5.9 m<sup>3</sup> Teflon chambers. The organic vapor generation period in the present study ranges from 1 to 7 h, thus precluding the possibility of observing more rapid partitioning that may have occurred. In view of this, we carried out one vapor wall deposition experiment in the  $\alpha$ -pinene+OH low-NO system, with the

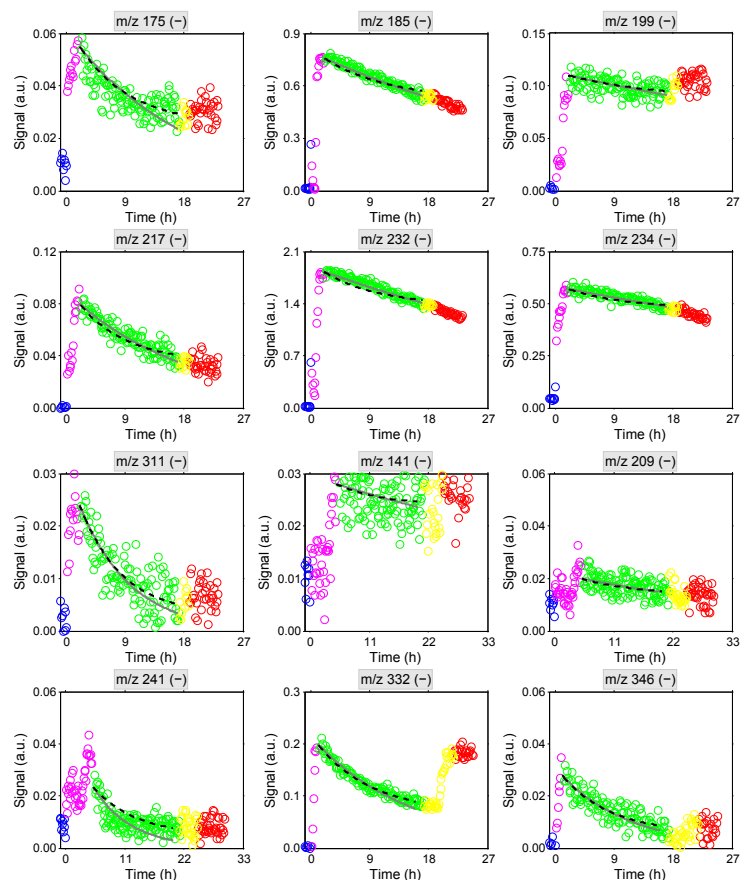
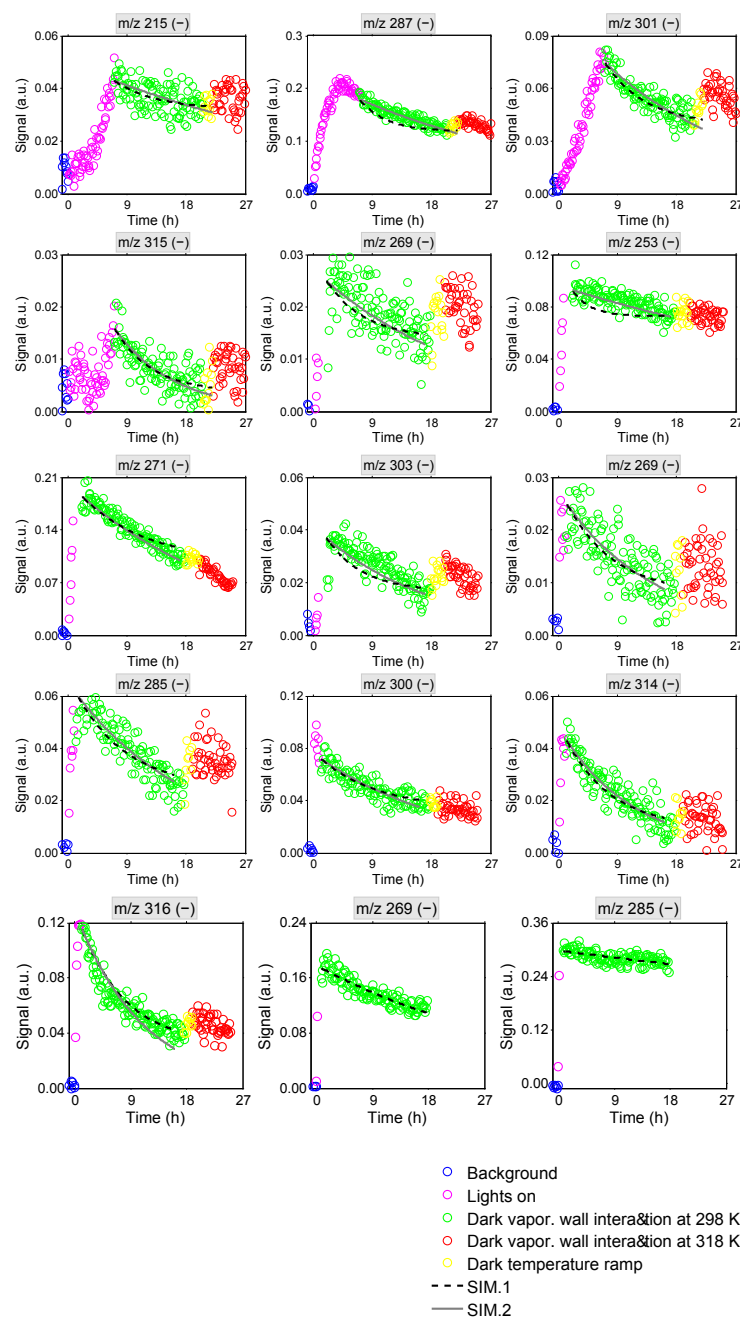


Figure 3.

experimental procedures identical to those in Sect. 3, but with lights on for only 10 min. We also increased the initial mixing ratios of  $\alpha$ -pinene and OH radical precursor  $\text{H}_2\text{O}_2$  to 1 and 4 ppm, respectively, in order to generate sufficient organic vapor CIMS signals during the short irradiation period. Prompt formation of two ions,  $m/z$  269 (–) and  $m/z$  285 (–), was observed on the CIMS after 10 min of photochemistry. These are assigned to be two first-generation products, pinonic acid ( $\text{C}_{10}\text{H}_{16}\text{O}_3$ ) and pinonic peroxy acid ( $\text{C}_{10}\text{H}_{16}\text{O}_4$ ), respectively (see Table 2 for the proposed chemical structures). Owing to the short photochemical reaction timescale, the other four possible products in Table 2 were not found in this experiment. Figure 3 (bottom panel) shows the wall induced dark decay of  $m/z$  269 (–) and  $m/z$  285 (–) at 298 K. The best-fit first-order decay rates lie within the same order of magnitude as those reported in Table 2, i.e.,  $7.61 \times 10^{-6} \text{ s}^{-1}$  vs.  $8.95 \times 10^{-6} \text{ s}^{-1}$  for  $m/z$  269 (–) and  $1.67 \times 10^{-6} \text{ s}^{-1}$

vs.  $2.98 \times 10^{-6} \text{ s}^{-1}$  for  $m/z$  285 (–). No rapid vapor wall loss was found immediately after lights off, and the deposition rates for both ions were pretty consistent over the course of  $\sim 15$  h dark decay. Note that  $m/z$  285 (–), although having a higher molecular weight, decays more slowly than  $m/z$  269 (–). We will demonstrate later that the wall-induced decay rate depends inversely on the vapor pressure, which is a function of the molecule size and functionalities. The addition of a carboxylic acid group, as in  $m/z$  269 (–), leads to a greater decrease in volatility than that resulting from the addition of a peroxy carboxylic acid group, as in  $m/z$  285 (–). Our observations for these two compounds are consistent with the observed behavior of the other 23 compounds. There are three considerations regarding equipment setup and experimental protocol that potentially contribute to the differences between the present study and Ziemann and co-worker's work: (1) chamber size and depletion rate; (2) mixing status, i.e.,





**Figure 3.** CIMS traces of oxidized organic vapors generated from the photooxidation of isoprene, toluene,  $\alpha$ -pinene and dodecane under high/low-NO conditions over the four chamber periods in Fig. 2. Colored circles represent CIMS measured normalized signals during background (blue), vapor generation (magenta), vapor wall deposition at 298 K (green), temperature ramp (yellow), and vapor re-evaporation at 318 K (red). Black dashed lines and gray solid lines represent the simulated deposition rates generated from SIM.1 and SIM.2, respectively.

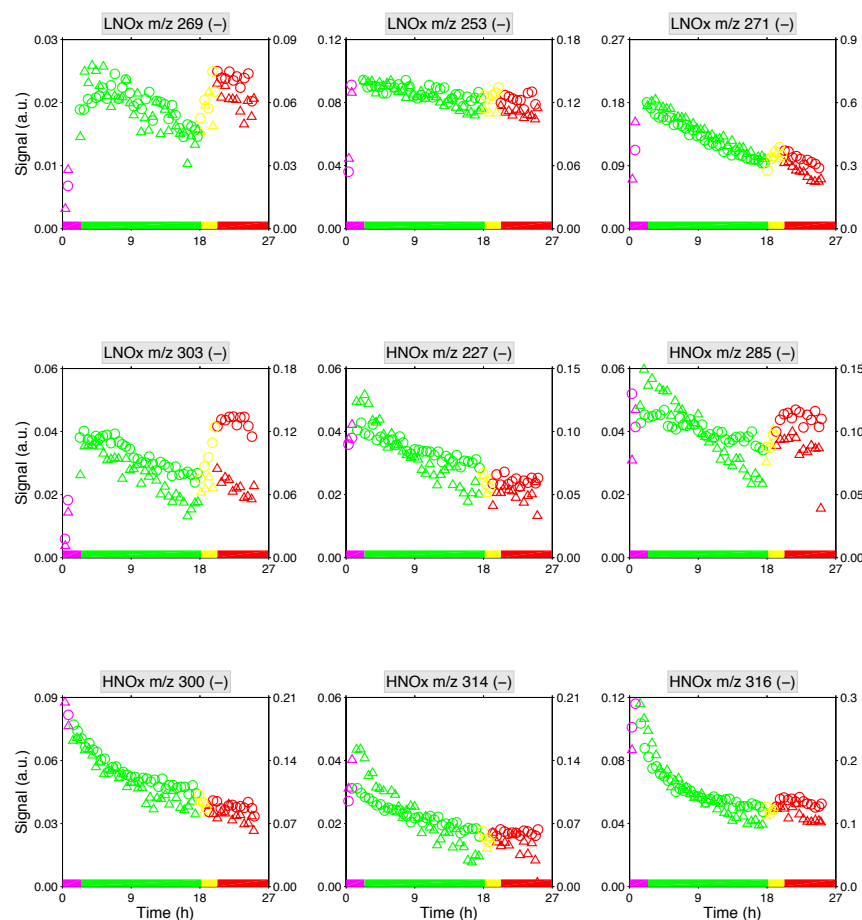


**Figure 4.** Comparison of vapor–wall interactions for  $\alpha$ -pinene + OH products under controlled experimental conditions in used (triangle) vs. unused (circle) Teflon chambers. 30-min averaged data are shown here for clarity. Colored bands denote successive experimental periods: vapor generation (magenta), vapor wall deposition at 298 K (green), temperature ramp (yellow), and vapor re-evaporation at 318 K (red).

actively mixed vs. static; and (3) definition of the starting point of the gas-phase vapor concentration.

When the chamber temperature was increased from 25 to 45 °C, with all the other experimental conditions held constant, the concentrations of most compounds in the chamber increased to a minor degree relative to the initial peak signal, reflecting modest desorption of vapors from the chamber wall. As noted earlier, the chamber wall (in the used chambers) might actually be coated with organic materials from previous experiments, or the FEP Teflon film itself may act as an absorbing medium. In view of the uncertain nature of the wall itself, two control experiments were also conducted in the unused dual 24 m<sup>3</sup> FEP Teflon chambers with identical protocols: see Table 1. Organic vapor deposition and evapo-

ration rates between unused and used chambers are compared in Fig. 4. For all the  $\alpha$ -pinene photooxidation products studied here, their interaction with the wall in the unused chambers is in general agreement with that in the used chambers, except for a few oxidation products generated under high-NO conditions. The fact that these particular compounds exhibit slightly higher deposition rates in used chambers might be due to the heterogeneous chemistry on the wall catalyzed by nitric acid, a product from the NO<sub>x</sub>-O<sub>3</sub> photochemical cycle. Overall, we conclude that the extent to which chambers have been previously used is not a significant factor in the sorption behavior of the FEP Teflon films.

The equivalent absorbing organic mass parameter ( $C_w/\text{g m}^{-3}$ ) is estimated using equilibrium partitioning

**Table 2.** Best-fit values of vapor–wall accommodation coefficient ( $\alpha_{w,i}$ ) and calculated equivalent absorbing organic mass ( $C_w$ ) on the chamber wall for vapors with structure proposed based on the CIMS measurement.

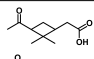
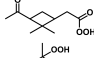
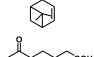
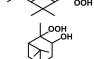
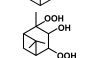
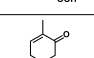
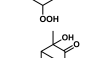
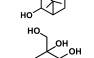
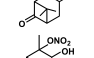
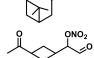
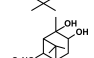
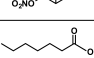
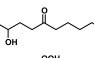
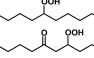
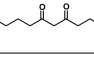
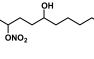
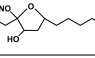


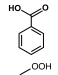
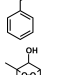
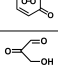
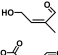
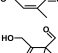
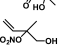
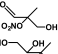
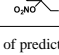
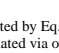
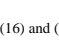
| Observed $m/z$ | Molecular weight | Chemical formula                                 | Proposed structure  | Vapor pressure (atm @ 298 K) <sup>a</sup> | Vapor wall deposition rate $k_{w,i}$ (s <sup>-1</sup> ) <sup>b</sup> | $\alpha_{w,i}^c$                 | $C_w$ (g m <sup>-3</sup> ) <sup>d</sup> | Formation mechanism  |
|----------------|------------------|--|---|---|--|----------------------------------|---|--|
| 269 (-)        | 184              | C <sub>10</sub> H <sub>16</sub> O <sub>3</sub>   |    | $9.64 \times 10^{-8}$                     | $(8.95 \pm 2.55) \times 10^{-6}$                                     | $(9.15 \pm 2.63) \times 10^{-8}$ | $(6.59 \pm 3.43) \times 10^{-4}$        | $\alpha$ -pinene + OH<br>(low-NO <sub>x</sub> )<br>Eddingsaas et al. (2012)  |
| 285 (-)        | 200              | C <sub>10</sub> H <sub>16</sub> O <sub>4</sub>   |    | $1.05 \times 10^{-6}$                     | $(2.98 \pm 1.14) \times 10^{-6}$                                     | $(3.24 \pm 1.20) \times 10^{-8}$ | $(5.90 \pm 3.65) \times 10^{-3}$        |  |
| 253 (-)        | 168              | C <sub>10</sub> H <sub>16</sub> O <sub>2</sub>   |    | $6.79 \times 10^{-6}$                     | $(4.40 \pm 0.70) \times 10^{-6}$                                     | $(4.31 \pm 0.68) \times 10^{-8}$ | $(4.57 \pm 2.45) \times 10^{-3}$        |  |
| 257 (-)        | 172              | C <sub>9</sub> H <sub>16</sub> O <sub>3</sub>    |    | $2.65 \times 10^{-6}$                     | $(3.19 \pm 3.13) \times 10^{-6}$                                     | $(3.12 \pm 3.07) \times 10^{-8}$ | $(6.31 \pm 4.98) \times 10^{-3}$        |  |
| 271 (-)        | 186              | C <sub>10</sub> H <sub>18</sub> O <sub>3</sub>   |    | $5.14 \times 10^{-8}$                     | $(1.09 \pm 0.06) \times 10^{-5}$                                     | $(1.15 \pm 0.07) \times 10^{-7}$ | $(5.56 \pm 3.86) \times 10^{-5}$        |  |
| 303 (-)        | 218              | C <sub>10</sub> H <sub>18</sub> O <sub>5</sub>   |    | $1.56 \times 10^{-10}$                    | $(1.32 \pm 0.19) \times 10^{-5}$                                     | $(1.49 \pm 0.22) \times 10^{-7}$ | $(1.12 \pm 1.19) \times 10^{-6}$        |  |
| 227 (-)        | 142              | C <sub>7</sub> H <sub>10</sub> O <sub>3</sub>    |   | $1.24 \times 10^{-5}$                     | $(1.63 \pm 0.50) \times 10^{-5}$                                     | $(1.52 \pm 0.15) \times 10^{-7}$ | $(1.01 \pm 0.91) \times 10^{-2}$        | $\alpha$ -pinene + OH<br>(high-NO <sub>x</sub> )<br>Eddingsaas et al. (2012) |
| 269 (-)        | 184              | C <sub>10</sub> H <sub>16</sub> O <sub>3</sub>   |  | $3.48 \times 10^{-9}$                     | $(1.94 \pm 0.30) \times 10^{-5}$                                     | $(1.97 \pm 0.32) \times 10^{-7}$ | $(2.80 \pm 1.02) \times 10^{-5}$        |  |
| 285 (-)        | 200              | C <sub>10</sub> H <sub>16</sub> O <sub>4</sub>   |  | $6.32 \times 10^{-11}$                    | $(1.51 \pm 0.15) \times 10^{-5}$                                     | $(1.62 \pm 0.16) \times 10^{-7}$ | $(3.83 \pm 3.11) \times 10^{-7}$        |  |
| 300 (-)        | 215              | C <sub>10</sub> H <sub>17</sub> O <sub>4</sub> N |  | $1.53 \times 10^{-7}$                     | $(1.19 \pm 0.13) \times 10^{-5}$                                     | $(1.34 \pm 0.14) \times 10^{-7}$ | $(1.79 \pm 0.06) \times 10^{-4}$        |  |
| 314 (-)        | 229              | C <sub>10</sub> H <sub>15</sub> O <sub>5</sub> N |  | $1.52 \times 10^{-7}$                     | $(2.31 \pm 0.21) \times 10^{-5}$                                     | $(2.94 \pm 0.26) \times 10^{-7}$ | $(1.14 \pm 0.10) \times 10^{-3}$        |  |
| 316 (-)        | 231              | C <sub>10</sub> H <sub>17</sub> O <sub>5</sub> N |  | $9.03 \times 10^{-10}$                    | $(1.85 \pm 0.14) \times 10^{-5}$                                     | $(2.19 \pm 0.17) \times 10^{-7}$ | $(5.36 \pm 9.85) \times 10^{-6}$        |  |
| 215 (-)        | 130              | C <sub>7</sub> H <sub>14</sub> O <sub>2</sub>    |  | $1.98 \times 10^{-5}$                     | $(5.27 \pm 1.74) \times 10^{-6}$                                     | $(4.50 \pm 1.49) \times 10^{-8}$ | $(3.10 \pm 0.55) \times 10^{-2}$        | Dodecane + OH<br>(low-NO <sub>x</sub> )<br>Yee et al. (2012)                 |
| 285 (-)        | 200              | C <sub>12</sub> H <sub>24</sub> O <sub>2</sub>   |  | $3.58 \times 10^{-7}$                     | $(1.32 \pm 0.44) \times 10^{-5}$                                     | $(1.42 \pm 0.46) \times 10^{-7}$ | $(3.50 \pm 0.81) \times 10^{-3}$        |  |
| 287 (-)        | 202              | C <sub>12</sub> H <sub>26</sub> O <sub>2</sub>   |  | $1.21 \times 10^{-6}$                     | $(8.25 \pm 0.67) \times 10^{-6}$                                     | $(8.79 \pm 0.73) \times 10^{-8}$ | $(2.81 \pm 1.92) \times 10^{-3}$        |  |
| 301 (-)        | 216              | C <sub>12</sub> H <sub>24</sub> O <sub>3</sub>   |  | $1.30 \times 10^{-7}$                     | $(1.19 \pm 0.13) \times 10^{-5}$                                     | $(1.35 \pm 0.15) \times 10^{-7}$ | $(8.39 \pm 7.24) \times 10^{-4}$        |  |
| 315 (-)        | 230              | C <sub>12</sub> H <sub>22</sub> O <sub>4</sub>   |  | $1.56 \times 10^{-8}$                     | $(2.68 \pm 0.49) \times 10^{-5}$                                     | $(3.17 \pm 0.61) \times 10^{-7}$ | $(1.79 \pm 2.15) \times 10^{-4}$        |  |
| 332 (-)        | 247              | C <sub>12</sub> H <sub>25</sub> O <sub>4</sub> N |  | $2.17 \times 10^{-8}$                     | $(1.55 \pm 0.07) \times 10^{-5}$                                     | $(1.86 \pm 0.09) \times 10^{-7}$ | $(3.93 \pm 0.46) \times 10^{-4}$        | Dodecane + OH<br>(high-NO <sub>x</sub> )<br>Zhang et al. (2014b)             |
| 346 (-)        | 261              | C <sub>12</sub> H <sub>23</sub> O <sub>5</sub> N |  | $4.46 \times 10^{-9}$                     | $(2.33 \pm 0.25) \times 10^{-5}$                                     | $(2.91 \pm 0.33) \times 10^{-7}$ | $(1.87 \pm 0.21) \times 10^{-5}$        |  |

Table 2. Continued.

| Observed $m/z$ | Molecular weight | Chemical formula   | Proposed structure   | Vapor pressure (atm @ 298 K) <sup>a</sup> | Vapor wall deposition rate $k_{w,i}$ (s <sup>-1</sup> ) <sup>b</sup> | $\alpha_{w,i}^c$                 | $C_w$ (g m <sup>-3</sup> ) <sup>d</sup> | Formation mechanism  |
|----------------|------------------|--|--|---|--|----------------------------------|---|--|
| 141 (-)        | 122              | C <sub>7</sub> H <sub>6</sub> O <sub>2</sub>                 |   | $5.30 \times 10^{-6}$                     | $(2.04 \pm 1.88) \times 10^{-6}$                                     | $(1.68 \pm 1.35) \times 10^{-8}$ | $(1.13 \pm 0.07) \times 10^{-2}$        | toluene + OH (low-NO <sub>x</sub> ) MCM v3.2               |
| 209 (-)        | 124              | C <sub>7</sub> H <sub>8</sub> O <sub>2</sub>                 |   | $4.89 \times 10^{-5}$                     | $(5.78 \pm 1.93) \times 10^{-6}$                                     | $(4.82 \pm 1.62) \times 10^{-8}$ | $(7.03 \pm 1.42) \times 10^{-2}$        |  |
| 241 (-)        | 156              | C <sub>7</sub> H <sub>8</sub> O <sub>4</sub>                 |   | $4.00 \times 10^{-6}$                     | $(2.04 \pm 0.40) \times 10^{-5}$                                     | $(1.95 \pm 0.39) \times 10^{-7}$ | $(2.66 \pm 0.71) \times 10^{-2}$        |  |
| 175 (-)        | 90               | C <sub>3</sub> H <sub>6</sub> O <sub>3</sub>                 |   | $2.21 \times 10^{-4}$                     | $(9.68 \pm 1.51) \times 10^{-6}$                                     | $(6.90 \pm 1.08) \times 10^{-8}$ | $(3.03 \pm 1.10) \times 10^{-1}$        | isoprene + OH (high-NO <sub>x</sub> ) Paulot et al. (2009) |
| 185 (-)        | 100              | C <sub>5</sub> H <sub>8</sub> O <sub>2</sub>                 |   | $1.73 \times 10^{-4}$                     | $(6.58 \pm 0.30) \times 10^{-6}$                                     | $(4.93 \pm 0.22) \times 10^{-8}$ | $(7.70 \pm 2.01) \times 10^{-2}$        |  |
| 199 (-)        | 114              | C <sub>5</sub> H <sub>6</sub> O <sub>3</sub>                 |   | $8.17 \times 10^{-6}$                     | $(2.46 \pm 0.81) \times 10^{-6}$                                     | $(1.96 \pm 0.64) \times 10^{-8}$ | $(1.23 \pm 0.31) \times 10^{-2}$        |  |
| 217 (-)        | 132              | C <sub>5</sub> H <sub>8</sub> O <sub>4</sub>                 |   | $2.70 \times 10^{-7}$                     | $(1.40 \pm 0.11) \times 10^{-5}$                                     | $(1.22 \pm 0.10) \times 10^{-7}$ | $(1.15 \pm 0.60) \times 10^{-4}$        |  |
| 232 (-)        | 147              | C <sub>5</sub> H <sub>9</sub> O <sub>4</sub> N               |   | $2.34 \times 10^{-5}$                     | $(5.24 \pm 0.24) \times 10^{-6}$                                     | $(4.76 \pm 0.22) \times 10^{-8}$ | $(1.78 \pm 0.42) \times 10^{-3}$        |  |
| 234 (-)        | 149              | C <sub>4</sub> H <sub>7</sub> O <sub>5</sub> N               |   | $3.93 \times 10^{-6}$                     | $(3.23 \pm 1.30) \times 10^{-6}$                                     | $(2.97 \pm 0.28) \times 10^{-8}$ | $(5.16 \pm 1.36) \times 10^{-4}$        |  |
| 311 (-)        | 226              | C <sub>5</sub> H <sub>10</sub> O <sub>8</sub> N <sub>2</sub> |  | $1.15 \times 10^{-9}$                     | $(3.10 \pm 0.45) \times 10^{-5}$                                     | $(3.66 \pm 0.54) \times 10^{-7}$ | $(8.27 \pm 1.24) \times 10^{-6}$        |  |

<sup>a</sup> Vapor pressures are estimated from the average of predictions from the two group contribution methods, “SIMPOL.1” (Pankow and Asher, 2008) and “EVAPORATION” (Compernelle et al., 2011).

<sup>b</sup> The vapor wall deposition rate ( $k_{w,i}$ ) is calculated by Eq. (22b).

<sup>c</sup> The accommodation coefficient ( $\alpha_{w,i}$ ) is calculated via optimal fitting of Eq. (22b) to the CIMS measured vapor decay rate assuming first-order kinetics and irreversible gas–wall partitioning.

<sup>d</sup>  $C_w$  is calculated from the combination of Eqs. (16) and (17) as an equation set.

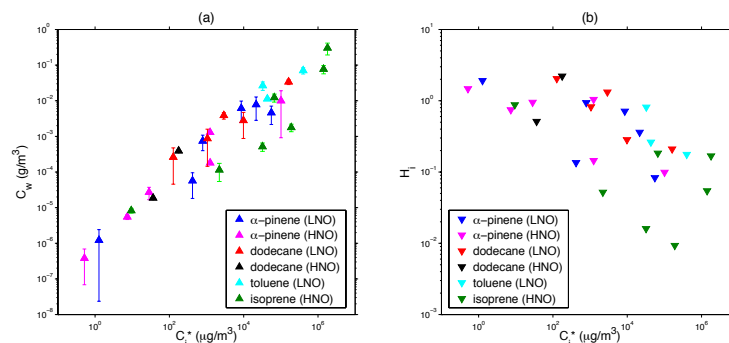


**Figure 5.** Inferred total amount of (a) equivalent absorbing organic mass on the chamber wall,  $C_w$  (g m<sup>-3</sup>), and (b) dimensionless Henry's law constants,  $H_i$ , as a function of saturation concentration,  $C_i^*$  (μg m<sup>-3</sup>). Estimated vapor pressures of organic compounds studied here are obtained from the average of predictions from the two group contribution methods, “SIMPOL.1” (Pankow and Asher, 2008) and “EVAPORATION” (Compernelle et al., 2011). The uncertainty bars give the upper and lower limits of  $C_w$  values derived from Eq. (12), together with Eqs. (16) and (17), when either “EVAPORATION” or “SIMPOL.1” is used to estimate vapor pressures.

theory. We show in the Supplementary Materials that this theory is suitable for  $C_w$  estimation after  $\sim 18$  h of wall-induced vapor decay. The ratio of the concentration of vapor  $i$  in the wall phase ( $\bar{C}_{w,i}$ ) to that in the gas phase ( $\bar{C}_{v,i}$ ) is expressed as a function of the corresponding gas–wall partitioning coefficient ( $K_{w,i}$ ) and the total amount of equivalent absorbing organic mass on the chamber wall ( $C_w$ ). Ideally,

$C_w$  can be obtained if the initial total concentration ( $\bar{C}_{\text{tot},i}$ ) and equilibrium gas-phase concentration ( $\bar{C}_{v,i}$ ) of vapor  $i$  can be measured by CIMS. However, since the fraction of organic compound  $i$  in the chamber wall at the onset of vapor wall deposition is unknown, we estimate  $C_w$  via the combination of equilibrium partitioning expressions at two

different temperatures, e.g., 298 and 318 K:

$$\frac{\bar{C}_{w,i@298\text{ K}}}{\bar{C}_{v,i@298\text{ K}}} = \frac{\bar{C}_{\text{tot},i} - \bar{C}_{v,i@298\text{ K}}}{\bar{C}_{v,i@298\text{ K}}} = K_{w,i@298\text{ K}} C_w, \quad (16)$$

$$\frac{\bar{C}_{w,i@318\text{ K}}}{\bar{C}_{v,i@318\text{ K}}} = \frac{\bar{C}_{\text{tot},i} - \bar{C}_{v,i@318\text{ K}}}{\bar{C}_{v,i@318\text{ K}}} = K_{w,i@318\text{ K}} C_w, \quad (17)$$

where  $\bar{C}_{\text{tot},i}$  is the total initial concentration of vapor  $i$ ,  $\bar{C}_{v,i@298/318\text{ K}}$  is the gas-phase concentration (as indicated by the normalized CIMS signal with unit “a.u.”) of vapor  $i$  at 298/318 K, and  $K_{w,i@T}$  is the corresponding partitioning coefficient at temperature  $T$ , see Eq. (12). In this manner, both  $\bar{C}_{\text{tot},i}$  and  $C_w$  can be calculated by solving the equation set (16) and (17). Note that the product  $K_{w,i@T} C_w$  is dimensionless, so that the normalized CIMS signal can be directly substituted into Eqs. (16) and (17) as the actual gas-phase concentration of organic vapor  $i$ . In the calculation,  $\bar{C}_{v,i@298\text{ K}}$  and  $\bar{C}_{v,i@318\text{ K}}$  were obtained by taking a 30 min average of the first-order extrapolation of the normalized CIMS signals at 298 and 318 K, respectively, during the temperature ramping period. The estimated  $C_w$  values vary by approximately 5 orders of magnitude and exhibit a strong dependence on the volatility of the organics, as shown in Table 2 and Fig. 5a. We will address subsequently why the  $C_w$  values span such a wide range.

## 5 Vapor sorption into FEP Teflon films

It is instructive to consider possible mechanisms of organic vapor interactions with Teflon films. Dual sorption mechanisms in glassy polymers have been identified: ordinary dissolution and microvoid-filling (Meares, 1954; Paul, 1979; Paterson et al., 1999; Tsujita, 2003; Kanehashi and Nagai, 2005). From the point of view of solubility behavior, organic polymers such as FEP Teflon may be idealized as high molecular weight organic liquids (Vieth et al., 1966). The polymer rubbery state is hypothesized to represent a thermodynamic equilibrium liquid state within which gas solubility obeys Henry's law. The glassy state, on the other hand, is considered to comprise two components: a hypothetical liquid state and a solid state, the latter containing a distribution of microvoids/holes that act to immobilize a portion of the penetrant molecules when the polymer is below its glass transition temperature ( $T_g = 339\text{ K}$  for FEP, Kim and Smith, 1990). The overall solubility of a gas molecule in a glassy polymer has been expressed by (Barrer et al., 1958; Michaels et al., 1963; Vieth et al., 1966; Kanehashi and Nagai, 2005):

$$C = C_H + C_L = k_H p + \frac{C'_L b p}{1 + b p}, \quad (18)$$

where  $C$  is the total vapor concentration in the glassy polymer,  $C_H$  is the concentration based on Henry's law dissolution,  $C_L$  is the concentration based on Langmuir sorption,  $k_H$  is the Henry's law constant,  $p$  is the partial pressure in the

gas phase,  $C'_L$  is the hole saturation constant, and  $b$  is the hole affinity constant. If  $b p \ll 1$ , Eq. (18) reduces to

$$C = (k_H + C'_L b) p. \quad (19)$$

The condition of  $b p \ll 1$  holds in the present situation because the partial pressures of organic vapors generated in the chamber are  $< 10^{-7}\text{ atm}$ , and the derived hole affinity constants for small organic molecules are  $< 1\text{ atm}^{-1}$  in glassy polymers (Vieth et al., 1966; Sada et al., 1988; Kanehashi and Nagai, 2005). If Eq. (18) holds for the equilibrium sorption behavior of organic vapors by FEP films, then the dimensionless form of the effective Henry's law constant ( $H_i$ ) can be expressed as a function of the partitioning coefficient of vapor  $i$  ( $K_{w,i}$ ) and total absorbing organic mass on the chamber wall ( $C_w$ ):

$$H_i = \frac{\bar{C}_{w,i}}{\bar{C}_{v,i}} = K_{w,i} C_w \propto (k_H + C'_L b). \quad (20)$$

As shown in Fig. 5b, the derived Henry's law constants ( $H_i$ ) for the organic oxidation products span approximately 2 orders of magnitude and depend inversely on saturation concentrations ( $C_i^*/\mu\text{g m}^{-3}$ ). This behavior suggests that organic vapor solubility in FEP films increases with decreasing volatility, i.e., increasing carbon number and functionalization. This behavior provides a qualitative explanation for the wide range of  $C_w$  values calculated for the 25 organic vapors studied here. Although the solubility of low volatility vapors in the FEP Teflon film is relatively high (large  $H_i$ ), the total equivalent absorbing organic mass on the wall required for gas-wall partitioning can still be low (small  $C_w$ ) because low volatility compounds tend to partition preferentially in the wall phase (large  $K_{w,i}$ ). As illustrated in Fig. 5b, the dimensionless Henry's law constant of  $m/z = (-)303$ , a product from  $\alpha$ -pinene low-NO photochemistry, is  $\sim 20$  times larger than that of  $m/z = (-)185$ , a product from isoprene + OH under high-NO conditions. The vapor pressure of  $m/z = (-)303$ , however, is  $\sim 6$  orders of magnitude lower than that of  $m/z = (-)185$ . As a result, the  $C_w$  value for  $m/z = (-)303$  is  $\sim 5$  orders of magnitude smaller than that for  $m/z = (-)185$ . One infers that the equivalent absorbing organic mass on the chamber wall derived earlier is not constant but specific to individual organic compounds, i.e., a function of volatility and solubility in FEP Teflon polymer. We will show that  $C_w$  is not the most dominant parameter, so the assumption of a single value for  $C_w$ , does not invalidate the usefulness of the theory.

## 6 Accommodation coefficient on the chamber wall ( $\alpha_{w,i}$ )

One key parameter that emerges from the theory of vapor wall deposition, the total equivalent absorbing organic mass ( $C_w$ ), can be calculated based on equilibrium gas-wall partitioning at two different temperatures. From this information,

we can estimate the other key parameter, the accommodation coefficient ( $\alpha_{w,i}$ ), by optimal fitting of the solution of Eq. (14) to CIMS measured organic vapor decay at 298 K:

$$\frac{d\bar{C}_{v,i}}{dt} = \left(\frac{A}{V}\right) \left( \frac{\alpha_{w,i} \bar{v}_i / 4}{\pi \alpha_{w,i} \bar{v}_i / 8(D_i K_e)^{1/2} + 1} \right) \cdot \left( \frac{\bar{C}_{\text{tot},i} - \bar{C}_{v,i}}{K_{w,i} C_w} - \bar{C}_{v,i} \right). \quad (21)$$

Note that Eq. (21) is simply Eq. (14) in which  $\bar{C}_{w,i}$  has been replaced with  $(\bar{C}_{\text{tot},i} - \bar{C}_{v,i})$ . Thus, Eq. (21) constitutes a linear ODE system with the one unknown (estimable) parameter,  $\alpha_{w,i}$ . The Levenberg–Marquardt method implemented in MATLAB’s “System Identification Toolbox” was used for the nonlinear minimization at each time step of its solution. The best-fit  $\alpha_{w,i}$  value obtained was then substituted into Eq. (21) to give the simulated temporal profile of the organic vapor  $i$ . Simulation results (SIM.1) are shown in Fig. 3.

The other limit of wall behavior is that of irreversible gas–wall partitioning ( $C_w \rightarrow \infty$ ). In this case, the accommodation coefficient  $\alpha_{w,i}$  is the sole governing parameter and Eq. (14) can be simplified as

$$\frac{d\bar{C}_{v,i}}{dt} = - \left(\frac{A}{V}\right) \left( \frac{\alpha_{w,i} \bar{v}_i / 4}{\pi \alpha_{w,i} \bar{v}_i / 8(D_i K_e)^{1/2} + 1} \right) \bar{C}_{v,i}. \quad (22a)$$

The overall wall loss rate of organic vapor  $i$  ( $k_{w,i}$ ) is therefore

$$k_{w,i} = \left(\frac{A}{V}\right) \left( \frac{\alpha_{w,i} \bar{v}_i / 4}{\pi \alpha_{w,i} \bar{v}_i / 8(D_i K_e)^{1/2} + 1} \right). \quad (22b)$$

Results for irreversible gas–wall partitioning (SIM.2) are shown in Fig. 3.

Simulations using both reversible (SIM.1) and irreversible (SIM.2) vapor wall deposition expressions match the experimental data. Outputs from SIM.1 tend to level off, whereas those from SIM.2 exhibit a continuous decreasing trend at the end of  $\sim 18$  h of vapor decay. The extent of agreement between observations and simulations depends on the nature of vapor wall deposition: most organic vapors in the Caltech Teflon chambers exhibit a continuous decay. The agreement between SIM.1 and SIM.2 indicates that the estimated  $C_w$  values are sufficiently large so that the wall-induced vapor deposition in the Caltech chamber can be treated as an irreversible process ( $C_w \rightarrow \infty$ ) within a relatively long timescale ( $< 18$  h).

Overall, results from the two simulations indicate that  $\alpha_{w,i}$  is the more influential parameter than  $C_w$  in describing the wall-induced deposition of semi-volatile organic vapors. The significance of  $\alpha_{w,i}$  is 2-fold: first, the accommodation coefficient for the desorption of organic molecules from the gas–wall interface equals that for the adsorption/uptake process, which together influence the time needed to establish equilibrium; and second, diffusion in the chamber wall is not considered in the theoretical framework; consequently, the best-fit  $\alpha_{w,i}$  will reflect the mass transfer resistance in both the

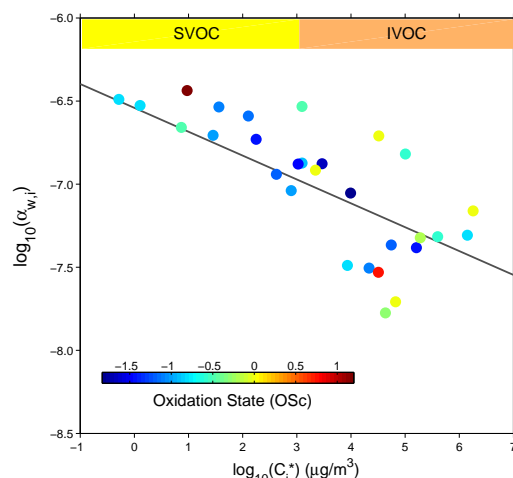


**Figure 6.** Inferred accommodation coefficients of organic oxidation products on the chamber wall ( $\log_{10}(\alpha_{w,i})$ ) as a function of saturation concentrations ( $\log_{10}(C_i^*)$ ) and average carbon oxidation state (OSc). Colored filled circles represent the best-fit  $\alpha_{w,i}$  assuming irreversible gas–wall partitioning. The black solid line represents the linear regression of  $\log_{10}(\alpha_{w,i})$  vs.  $\log_{10}(C_i^*)$  for all compounds.

gas–wall interface and the chamber wall layer. We suggest that the vapor wall deposition of individual compounds can be adequately parameterized through the accommodation coefficient  $\alpha_{w,i}$  as the single dominant variable. As shown in Table 2 and Fig. 6, for the compounds studied here, estimated values of  $\alpha_{w,i}$  span approximately 2 orders of magnitude ( $10^{-8}$ – $10^{-6}$ ) and depend inversely on volatility, implying that more highly functionalized compounds dissolve more easily in FEP Teflon film. The correlation of  $\alpha_{w,i}$  with the average carbon oxidation state (OSc), however, is not strong due to the fact that vapor pressures of molecules, although highly oxidized, are not necessarily low.

## 7 Characterizing chamber vapor wall deposition rate

The wall-induced deposition of the 25 organic compounds investigated in the present study can be sufficiently represented by a single parameter, the wall accommodation coefficient ( $\alpha_{w,i}$ ), which is observed to exhibit a strong inverse dependence on  $C_i^*$  (Fig. 6). It is possible to formulate an empirical expression for  $\alpha_{w,i}$  as a function of  $C_i^*$ , a parameter that can be estimated by vapor pressure prediction models.

Linear regression was performed on  $\log_{10}\alpha_{w,i}$  vs.  $\log_{10}C_i^*$  for the 25 organic vapors studied:

$$\log_{10}\alpha_{w,i} = -0.1919 \times \log_{10}C_i^* - 6.32. \quad (23)$$

We employ a group-contribution expression for  $\log_{10}C_i^*$  as a function of carbon number ( $n_C^i$ ) and oxygen number ( $n_O^i$ ) developed by Donahue et al. (2011):

$$\log_{10}C_i^* = (n_C^0 - n_C^i)b_C - n_O^i b_O - 2 \frac{n_C^i n_O^i}{n_C^i + n_O^i} b_{CO}, \quad (24)$$

where  $n_C^0$  is the carbon number of  $1 \mu\text{g m}^{-3}$  alkane ( $n_C^0 = 28.0483$ ),  $b_C$  is the carbon–carbon interaction term ( $b_C = 0.4015$ ),  $b_O$  is the oxygen–oxygen interaction term ( $b_O = 2.3335$ ), and  $b_{CO}$  is the carbon–oxygen nonideality term ( $b_{CO} = -0.4709$ ). Best-fit values of  $n_C^0$ ,  $b_C$ ,  $b_O$ , and  $b_{CO}$  are obtained by optimal fitting Eq. (24) to the saturation concentrations of 110 species, including C<sub>5</sub>–C<sub>14</sub> *n*-alkanes, C<sub>5</sub>–C<sub>14</sub> carbonyls, C<sub>5</sub>–C<sub>14</sub> di-carbonyls, C<sub>5</sub>–C<sub>14</sub> alcohols, C<sub>5</sub>–C<sub>14</sub> diols, C<sub>5</sub>–C<sub>14</sub> carboxylic acids, C<sub>5</sub>–C<sub>14</sub> di-carboxylic acids, C<sub>5</sub>–C<sub>14</sub> peroxides, C<sub>5</sub>–C<sub>14</sub> di-peroxides, C<sub>5</sub>–C<sub>14</sub> nitrates, and C<sub>5</sub>–C<sub>14</sub> di-nitrates. Vapor pressures of these species are estimated by taking the average of predictions from the two group contribution methods, “SIMPOL.1” and “EVAPORATION”.

Combining Eqs. (22), (23), and (24), the vapor wall deposition rate of any intermediate/semi/low-volatility compound ( $k_{w,i}/\text{s}^{-1}$ ) can be ultimately related to its carbon and oxygen numbers. This vapor wall loss rate estimation approach, although simplified, proves to be quite useful considering the limited knowledge of the chemical structures of the thousands of ions detected by mass spectrometry during an experiment. The proper guess of a molecular formula would be able to constrain the wall-induced decay rate of each ion, and thus provide information to better understand its formation and removal dynamics. In this way, one can reasonably constrain the wall-induced organic vapor deposition rate based on only two measurable or predictable properties, volatility and the extent of oxygenation.

As shown in Fig. 7, within a certain volatility range,  $k_{w,i}$  increases with decreasing  $C_i^*$ , implying that highly functionalized compounds tend to deposit on the chamber wall more efficiently. The maximum value of vapor wall deposition rate is eventually approached for highly oxygenated and extremely low-volatility compounds (which, of course, are precisely those compounds that are most prone to form SOA). Revisiting Eq. (22) reveals that the deposition rate of organic vapors is limited either by gas phase transport (molecular diffusion and turbulent mixing) or wall surface accommodation. For extremely small  $\alpha_{w,i}$  (large  $C_i^*$ ),  $k_{w,i}$  becomes

$$k_{w,i} = \left(\frac{A}{V}\right) \left(\frac{\alpha_{w,i} \bar{v}_i}{4}\right). \quad (25)$$

In this case, the organic vapor wall deposition rate is governed by the chamber wall accommodation process. On the other hand, if  $\alpha_{w,i}$  is sufficiently large (small  $C_i^*$ ),  $k_{w,i}$  is approximately given by

$$k_{w,i} = \frac{\pi}{2} \left(\frac{A}{V}\right) (D_i K_E)^{1/2}. \quad (26)$$

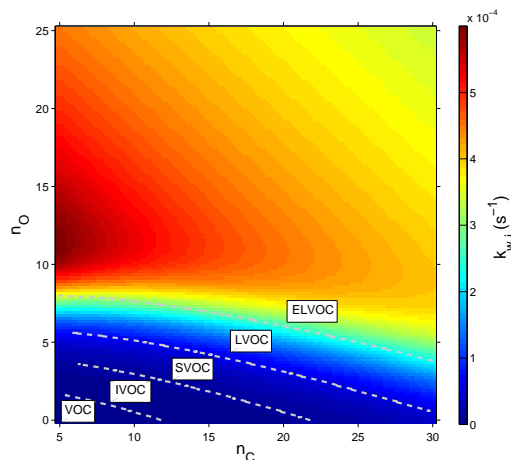


**Figure 7.** Predicted vapor wall deposition rate ( $k_{w,i}/\text{s}^{-1}$ ) of organic compounds in a Teflon chamber as a function of carbon number ( $n_C$ ) and oxygen number ( $n_O$ ).

In this case, the vapor wall deposition rate is ultimately controlled by the mixing state in the chamber. Equation (26) provides an expression for the upper limit of vapor wall deposition rate in a chamber, which is a manifestation of the extent of turbulent mixing in the chamber. One can determine which process is the limiting step in governing the overall wall deposition rate by referring to Eqs. (25) and (26). The threshold value of  $\alpha_{w,i}$ , at which gas phase transport (molecular diffusion and turbulence mixing) and wall surface accommodation contribute equally to the vapor wall deposition rate, is  $6.8 \times 10^{-6}$  in the Caltech chamber.

## 8 Impact of vapor wall deposition on SOA yields

The extent to which vapor wall deposition impacts measured SOA yields depends on the competition between uptake of organic vapors by suspended particles and the chamber wall. The timescale ( $\tau_{g/p,i}$ ) associated with establishing equilibrium gas-particle partitioning is governed by three transport processes: diffusion of vapor molecules from the bulk gas phase to the surface of the particle, uptake of vapor molecules by the particle surface, and diffusion of molecules in the bulk particle phase. Depending on a given situation, any of these three transport processes can be the limiting step in determining the overall equilibrium partitioning timescale. Here we represent the diffusional transport processes across the gas-particle interface and in the particle phase itself by a single parameter, the accommodation coefficient of organic vapors on the particle ( $\alpha_{p,i}$ ). In doing so, the mass transfer resistances at the gas-particle interface and in the particle phase are reflected by the single parameter  $\alpha_{p,i}$ , and the timescale

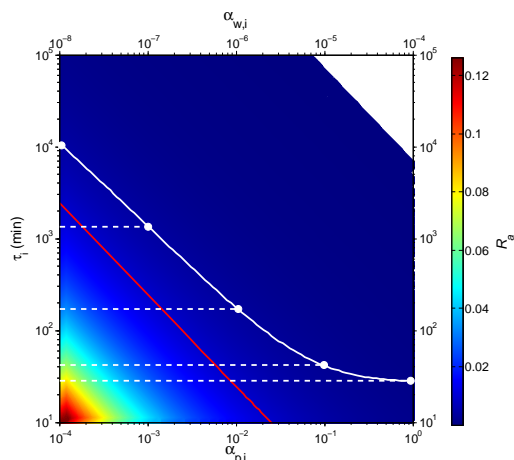


**Figure 8.** Comparison of estimated gas-particle equilibration timescale ( $\tau_{g/p,i}$ ) as a function of the gas-particle mass accommodation coefficient ( $\alpha_{p,i}$ , lower  $x$  axis) and the ratio of total particle surface area to the chamber wall area ( $R_a$ , color bar), and vapor wall deposition timescale ( $\tau_{g/w,i}$ ) as a function of gas–wall mass accommodation coefficient ( $\alpha_{w,i}$ , upper  $x$  axis). The red solid line represents the gas-particle equilibration time for a typical chamber experiment with seed surface area of  $\sim 1 \times 10^{-3} \mu\text{m}^2 \text{cm}^{-3}$ . White solid and dashed lines define the region where  $\tau_{g/p,i} \approx \tau_{g/w,i}$ . For example, the top dashed white line is a collection of data points for which the equality  $\tau_{g/p,i} = \tau_{g/w,i} = 1.3 \times 10^3 \text{ min}$  holds.  $\tau_{g/w,i}$  is calculated by substituting  $\alpha_{w,i} = 10^{-7}$  into Eqs. (22), (23), and (24).  $\tau_{g/p,i}$  is calculated from Eq. (27) by varying  $\alpha_{p,i}$  ( $10^{-4}$ – $10^{-3}$ ) and  $R_a$  (0.01–0.02).

to achieve gas-particle partitioning following a small perturbation of the condensing species in the gas phase is given by (Seinfeld and Pandis, 2006):

$$\tau_{g/p,i} = (2\pi N_p \bar{D}_p D_i f(Kn, \alpha_{p,i}))^{-1}, \quad (27)$$

where  $N_p$  is the total number concentration of suspended particles,  $\bar{D}_p$  is the number mean particle diameter,  $Kn (= 2\lambda/\bar{D}_p)$  is the Knudsen number, and  $f(Kn, \alpha_{p,i})$  is the correction factor for noncontinuum diffusion and imperfect accommodation (Seinfeld and Pandis, 2006).

Figure 8 shows the predicted  $\tau_{g/p,i}$  as a function of: (1) the ratio of total particle surface area to chamber wall area ( $R_a$ ) and (2)  $\alpha_{p,i}$ . The red solid line represents  $\tau_{g/p,i}$  for a typical chamber experiment with seed surface area of  $\sim 1000 \mu\text{m}^2 \text{cm}^{-3}$ . In this case, equilibrium vapor–particle partitioning is established within a few minutes in the presence of perfect accommodation of organic vapors onto particles ( $\alpha_{p,i} = 1$ ) or when a sufficiently large concentration of suspended particles is present (e.g.,  $C_{OA} > 10^5 \mu\text{g m}^{-3}$  when  $\alpha_{p,i} < 10^{-4}$ ).

By analogy with the treatment of gas-particle partitioning, the time scale associated with vapor–wall interactions is presumably governed by gas-phase diffusion of vapor molecules to the wall through a boundary layer adjacent to the wall, uptake of vapor molecules at the wall surface, and, potentially, diffusion of molecules in the wall. Again, a single parameter, the accommodation coefficient on the wall ( $\alpha_{w,i}$ ), is employed to represent the latter two processes. Thus, the vapor wall deposition timescale is given by

$$\tau_{g/w,i} = k_{w,i}^{-1}. \quad (28)$$

The white solid line in Fig. 8 represents the predicted  $\tau_{g/w,i}$ , covering a range of several minutes to several hours, as a function of the vapor accommodation coefficient on the chamber wall ( $\alpha_{w,i}$ ). The region to the left of the white solid line is that in which  $\tau_{g/w,i}$  and  $\tau_{g/p,i}$  are competitive. For low  $\alpha_{w,i}$  (e.g.,  $< 10^{-8}$ ),  $\tau_{g/w,i}$  is comparable to  $\tau_{g/p,i}$  only if the vapor has a low accommodation coefficient on the particles ( $\alpha_{p,i} < 10^{-4}$ ) or if a relatively small concentration of particles is present in the chamber ( $R_a < 10^{-4}$ ). For  $\alpha_{w,i} > 10^{-4}$ ,  $\tau_{g/w,i}$  is estimated to be of the order of several minutes and, as a result, vapor transport to particles is suppressed by competition with the chamber wall, even with perfect particle accommodation ( $\alpha_{p,i} = 1$ ) or high particle concentrations ( $R_a > 10^{-2}$ ).

Overall, in the region (confined by the white solid and dash lines in Fig. 8) where gas–wall partitioning is competitive with gas-particle partitioning, it is necessary to account for vapor wall deposition when deriving SOA yields from chamber experiments. The theoretical framework developed in this study suggests that the area of this region is ultimately controlled by the accommodation coefficient of organic vapors on particles ( $\alpha_{p,i}$ ) vs. the chamber wall ( $\alpha_{w,i}$ ).

## 9 Conclusions

The wall-induced decay of organic vapors is the result of coupled physical processes involving transport of organic vapors from the well-mixed core of a chamber to its wall by molecular and turbulent diffusion, uptake of organic molecules by the Teflon film, and re-evaporation from the wall. The wall-induced dark decay of 25 intermediate/semi-volatility organic compounds generated from the photochemistry of four parent hydrocarbons was monitored in the Caltech dual 24 m<sup>3</sup> FEP Teflon chambers. The extent to which organic vapors and the chamber wall interact was found to be similar in used vs. unused Teflon chambers. Based on this observation, one concludes that the Teflon film itself acts as an effective sorption medium, and organic materials deposited from past chamber experiments, if they indeed exist, do not significantly impact the sorption behavior of organic molecules. Reversibility in gas–wall partitioning was observed: evaporation of all 25 compounds that had deposited on the wall



during an 18 h deposition period occurred when the chamber temperature was increased from 25 to 45 °C.

Based on a derived model that describes the dynamics of vapor deposition on the chamber wall, a single parameter, the accommodation coefficient ( $\alpha_{w,i}$ ), emerges to govern the extent of the vapor–wall mass transfer process. Moreover,  $\alpha_{w,i}$  exhibits a strong dependence on the molecular properties, such as vapor pressure and oxidation state, of the 25 organics studied. We present an empirical expression for  $\alpha_{w,i}$  as a function of the compound vapor pressure, thus affording the possibility to predict the wall deposition rate of intermediate/semi/non-volatility compounds in a Teflon chamber based on their molecular constituency.

Previous studies have observed the chemical transformation of  $\delta$ -hydroxycarbonyls to substituted dihydrofurans on the chamber wall (Lim and Ziemann, 2005, 2009; Zhang et al., 2014b), suggesting the potential occurrence of heterogeneous reactions on the chamber wall surface. While the extent to which heterogeneous transformations proceed can be potentially represented through the accommodation coefficient, the occurrence of wall-induced chemistry adds another dimension of complexity in predicting vapor wall deposition rates.

Quantifying the impact of vapor wall deposition on the chamber-derived SOA yield is the next step in assessing the effect of vapor wall deposition of SOA formation and evolution. Future studies will be directed at (1) experiments to determine the accommodation coefficients of organic vapors on particles for a variety of SOA systems, and (2) state-of-art SOA predictive models that describe the dynamics of vapor–wall and vapor–particle interactions to estimate the fraction of organic vapor fluxes transported to the suspended particles vs. the chamber wall.

## Appendix A

|   |   |
|---|---|
| $A$ ( $\text{m}^2$ ):                                 | Total surface area of the chamber wall  |
| $\alpha_{\text{p},i}$ (dimensionless):                | Accommodation coefficient of organic vapor $i$ on particles                         |
| $\alpha_{\text{w},i}$ (dimensionless):                | Accommodation coefficient of organic vapor $i$ on the chamber wall                  |
| $C_{0,i}$ ( $\text{g m}^{-3}$ ):                      | Concentration of organic vapor $i$ over the gas–wall interface                      |
| $C_i^*$ ( $\text{g m}^{-3}$ ):                        | Saturation concentration of organic vapor $i$                                       |
| $\bar{C}_{\text{tot},i}$ ( $\text{g m}^{-3}$ ):       | Total concentration of organic vapor $i$ in the chamber                             |
| $\bar{C}_{\text{v},i}$ ( $\text{g m}^{-3}$ ):         | Concentration of organic vapor $i$ in the well-mixed core of the chamber            |
| $C_{\text{v},i}$ ( $\text{g m}^{-3}$ ):               | Local concentration of organic vapor $i$ in the boundary layer adjacent to the wall |
| $\bar{C}_{\text{w},i}$ ( $\text{g m}^{-3}$ ):         | Concentration of organic vapor $i$ that has accumulated on the chamber wall         |
| $C_{\text{w}}$ ( $\text{g m}^{-3}$ ):                 | Equivalent mass of absorbing organic material on the chamber wall                   |
| $\bar{D}_{\text{p}}$ (m):                             | Number mean particle diameter   |
| $D_{\text{e}}$ ( $\text{m}^2 \text{s}^{-1}$ ):        | Eddy diffusivity  |
| $D_i$ ( $\text{m}^2 \text{s}^{-1}$ ):                 | Molecular diffusivity of organic vapor $i$  |
| $\delta$ (m):   | Thickness of the boundary layer adjacent to the wall                                |
| $H_i$ (dimensionless):                                | Henry's law constant of organic compound $i$  |
| $J_{\text{v},i}$ ( $\text{g m}^{-2} \text{s}^{-1}$ ): | Vapor flux arriving at the gas–wall interface                                       |
| $J_{\text{w},i}$ ( $\text{g m}^{-2} \text{s}^{-1}$ ): | Vapor flux evaporating from the wall  |
| $K_{\text{e}}$ ( $\text{s}^{-1}$ ):                   | Eddy diffusion coefficient  |
| $K_{\text{w},i}$ ( $\text{m}^3 \text{g}^{-1}$ ):      | Gas–wall partitioning coefficient   |
| $k_{\text{w,depo},i}$ ( $\text{s}^{-1}$ ):            | Deposition rate coefficient to the wall   |
| $k_{\text{w,evap},i}$ ( $\text{s}^{-1}$ ):            | Evaporation rate coefficient from the wall  |
| $\bar{M}_{\text{w}}$ ( $\text{g mol}^{-1}$ ):         | Average molecular weight of the absorbing organic material on the wall              |
| $N_{\text{p}}$ ( $\text{m}^{-3}$ ):                   | Total number concentration of suspended particles                                   |
| $p_{\text{L},i}^0$ (atm):                             | Vapor pressure of organic compound $i$ as a liquid                                  |
| $\gamma_i$ (dimensionless):                           | Activity coefficient in the wall layer on a mole fraction basis                     |
| $\bar{v}_i$ ( $\text{m s}^{-1}$ ):                    | Mean thermal speed  |
| $V$ ( $\text{m}^3$ ):                                 | Total volume of the chamber   |

The Supplement related to this article is available online at doi:10.5194/acp-15-4197-2015-supplement.

**Acknowledgements.** This study was supported by NOAA Climate Program Office AC4 program, award # NA13OAR4310058 and State of California Air Resources Board agreement 13-321.

Edited by: V. F. McNeill

## References

- Barrer, R. M., Barrie, J. A., and Slater, J.: Sorption and diffusion in ethyl cellulose. Part III. Comparison between ethyl cellulose and rubber, *J. Polym. Sci.*, 27, 177–197, 1958.
- Compennolle, S., Ceulemans, K., and Müller, J.-F.: EVAPORATION: a new vapour pressure estimation method for organic molecules including non-additivity and intramolecular interactions, *Atmos. Chem. Phys.*, 11, 9431–9450, doi:10.5194/acp-11-9431-2011, 2011.
- Corner, J. and Pendlebury, E. D.: The coagulation and deposition of a stirred aerosol, *P. Phys. Soc. Lond. B.*, 64, 645–654, 1951.
- Crounse, J. D., McKinney, K. A., Kwan, A. J., and Wennberg, P. O.: Measurement of gas-phase hydroperoxides by chemical ionization mass spectrometry, *Anal. Chem.*, 78, 6726–6732, 2006.
- Crump, J. G. and Seinfeld, J. H.: Turbulent deposition and gravitational sedimentation of an aerosol in a vessel of arbitrary shape, *J. Aerosol. Sci.*, 12, 405–415, 1981.
- Donahue, N. M., Epstein, S. A., Pandis, S. N., and Robinson, A. L.: A two-dimensional volatility basis set: 1. organic-aerosol mixing thermodynamics, *Atmos. Chem. Phys.*, 11, 3303–3318, doi:10.5194/acp-11-3303-2011, 2011.
- Eddingsaas, N. C., Loza, C. L., Yee, L. D., Seinfeld, J. H., and Wennberg, P. O.:  $\alpha$ -pinene photooxidation under controlled chemical conditions – Part I: Gas-phase composition in low- and high- $\text{NO}_x$  environments, *Atmos. Chem. Phys.*, 12, 6489–6504, doi:10.5194/acp-12-6489-2012, 2012.
- Fahnestock, K. A. S., Yee, L. D., Loza, C. L., Coggon, M. M., Schwantes, R., Zhang, X., Dalleska, N. F., and Seinfeld, J. H.: Secondary Organic Aerosol Composition from  $\text{C}_{12}$  Alkanes, *J. Phys. Chem. A*, published online, doi:10.1021/jp501779w, 2014.
- Grosjean, D.: Wall loss of gaseous-pollutants in outdoor Teflon chambers, *Environ. Sci. Technol.*, 19, 1059–1065, 1985.
- Kanehashi, S. and Nagai, K.: Analysis of dual-mode model parameters for gas sorption in glassy polymers, *J. Membrane Sci.*, 253, 117–138, 2005.
- Kim, C. S. and Smith, T. L.: An improved method for measuring the thermal coefficient of linear expansion of flexible polymer-films, *J. Polym. Sci. Pol. Phys.*, 28, 2119–2126, 1990.
- Kokkola, H., Yli-Pirilä, P., Vesterinen, M., Korhonen, H., Keskinen, H., Romakkaniemi, S., Hao, L., Kortelainen, A., Joutsensaari, J., Worsnop, D. R., Virtanen, A., and Lehtinen, K. E. J.: The role of low volatile organics on secondary organic aerosol formation, *Atmos. Chem. Phys.*, 14, 1689–1700, doi:10.5194/acp-14-1689-2014, 2014.
- Lim, Y. B. and Ziemann, P. J.: Products and mechanism of secondary organic aerosol formation from reactions of  $n$ -alkanes with OH radicals in the presence of  $\text{NO}_x$ , *Environ. Sci. Technol.*, 39, 9229–9236, 2005.
- Lim, Y. B. and Ziemann, P. J.: Effects of molecular structure on aerosol yields from OH radical-initiated reactions of linear, branched, and cyclic alkanes in the presence of  $\text{NO}_x$ , *Environ. Sci. Technol.*, 43, 2328–2334, 2009.
- Loza, C. L., Chan, A. W. H., Galloway, M. M., Keutsch, F. N., Flagan, R. C., and Seinfeld, J. H.: Characterization of vapor wall loss in laboratory chambers, *Environ. Sci. Technol.*, 44, 5074–5078, 2010.
- Loza, C. L., Craven, J. S., Yee, L. D., Coggon, M. M., Schwantes, R. H., Shiraiwa, M., Zhang, X., Schilling, K. A., Ng, N. L., Canagaratna, M. R., Ziemann, P. J., Flagan, R. C., and Seinfeld, J. H.: Secondary organic aerosol yields of 12-carbon alkanes, *Atmos. Chem. Phys.*, 14, 1423–1439, doi:10.5194/acp-14-1423-2014, 2014.
- Matsunaga, A. and Ziemann, P. J.: Gas-wall partitioning of organic compounds in a Teflon film chamber and potential effects on reaction product and aerosol yield measurements, *Aerosol. Sci. Tech.*, 44, 881–892, 2010.
- McMurry, P. H. and Grosjean, D.: Gas and aerosol wall losses in Teflon film smog chambers, *Environ. Sci. Technol.*, 19, 1176–1182, 1985.
- Mearns, P.: The diffusion of gases through polyvinyl acetate, *J. Am. Chem. Soc.*, 76, 3415–3422, 1954.
- Michaels, A. S., Barrie, J. A., and Vieth, W. R.: Solution of gases in polyethylene terephthalate, *J. Appl. Phys.*, 34, 1–13, 1963.
- Pankow, J. F. and Asher, W. E.: SIMPOL.1: a simple group contribution method for predicting vapor pressures and enthalpies of vaporization of multifunctional organic compounds, *Atmos. Chem. Phys.*, 8, 2773–2796, doi:10.5194/acp-8-2773-2008, 2008.
- Paterson, R., Yampol'skii, Y., Fogg, P. G. T., Bokarev, A., Bondar, V., Ilinich, O., and Shishatskii, S.: IUPAC-NIST solubility data series 70. Solubility of gases in glassy polymers, *J. Phys. Chem. Ref. Data*, 28, 1255–1450, 1999.
- Paul, D. R.: Gas sorption and transport in glassy-polymers, *Ber. Bunsen. Phys. Chem.*, 83, 294–302, 1979.
- Paulot, F., Crounse, J. D., Kjaergaard, H. G., Kroll, J. H., Seinfeld, J. H., and Wennberg, P. O.: Isoprene photooxidation: new insights into the production of acids and organic nitrates, *Atmos. Chem. Phys.*, 9, 1479–1501, doi:10.5194/acp-9-1479-2009, 2009.
- Sada, E., Kumazawa, H., Xu, P., and Nishigaki, M.: Mechanism of gas permeation through glassy polymer-films, *J. Membrane Sci.*, 37, 165–179, 1988.
- Seinfeld, J. H. and Pandis, S. N.: Atmospheric chemistry and physics : from air pollution to climate change (2nd Edn.), John Wiley & Sons, Inc., Hoboken, NJ, 2006.
- Tsujita, Y.: Gas sorption and permeation of glassy polymers with microvoids, *Prog. Polym. Sci.*, 28, 1377–1401, 2003.
- Vieth, W. R., Tam, P. M., and Michaels, A. S.: Dual sorption mechanisms in glassy polystyrene, *J. Colloid. Interf. Sci.*, 22, 360–370, 1966.
- Yee, L. D., Craven, J. S., Loza, C. L., Schilling, K. A., Ng, N. L., Canagaratna, M. R., Ziemann, P. J., Flagan, R. C., and Seinfeld, J. H.: Secondary organic aerosol formation from low- $\text{NO}_x$  photooxidation of dodecane: Evolution of multigeneration gas-

- phase chemistry and aerosol composition, *J. Phys. Chem. A*, 116, 6211–6230, 2012.
- Yeh, G. K. and Ziemann, P. J.: Alkyl nitrate formation from the reactions of C8–C14 n-alkanes with OH radicals in the presence of NOx: measured yields with essential corrections for gas-wall partitioning, *J. Phys. Chem. A*, 118, 8147–8157, 2014.
- Zhang, X. and Seinfeld, J. H.: A functional group oxidation model (FGOM) for SOA formation and aging, *Atmos. Chem. Phys.*, 13, 5907–5926, doi:10.5194/acp-13-5907-2013, 2013.
- Zhang, X., Cappa, C. D., Jathar, S. H., McVay, R. C., Ensberg, J. J., Kleeman, M. J., and Seinfeld, J. H.: Influence of vapor wall loss in laboratory chambers on yields of secondary organic aerosol, *P. Natl. Acad. Sci. USA*, 111, 5802–5807, 2014a.
- Zhang, X., Schwantes, R. H., Coggon, M. M., Loza, C. L., Schilling, K. A., Flagan, R. C., and Seinfeld, J. H.: Role of ozone in SOA formation from alkane photooxidation, *Atmos. Chem. Phys.*, 14, 1733–1753, doi:10.5194/acp-14-1733-2014, 2014b.

Supplement of Atmos. Chem. Phys., 15, 4197–4214, 2015  
<http://www.atmos-chem-phys.net/15/4197/2015/>  
doi:10.5194/acp-15-4197-2015-supplement  
© Author(s) 2015. CC Attribution 3.0 License.



Atmospheric  
Chemistry  
and Physics  
Open Access



*Supplement of*

## **Vapor wall deposition in Teflon chambers**

**X. Zhang et al.**

*Correspondence to:* J. H. Seinfeld ([seinfeld@caltech.edu](mailto:seinfeld@caltech.edu))

### 1. Time-scale for gas-wall equilibrium partitioning

Eqs (S1) and (S2) describe the dynamic behavior of compound  $i$  in the gas phase ( $\bar{C}_{v,i}$ ) and on chamber walls ( $\bar{C}_{w,i}$ ), respectively.

$$\frac{d\bar{C}_{v,i}}{dt} = -k_{w,depo,i}\bar{C}_{v,i} + k_{w,evap,i}\bar{C}_{w,i} \quad (S1)$$

$$\frac{d\bar{C}_{w,i}}{dt} = -k_{w,evap,i}\bar{C}_{w,i} + k_{w,depo,i}\bar{C}_{v,i} \quad (S2)$$

where  $k_{w,depo,i}$  ( $s^{-1}$ ) is the deposition rate coefficient to the wall and  $k_{w,evap,i}$  ( $s^{-1}$ ) is the evaporation rate coefficient from the wall. The relationship between these two parameters is

$$k_{w,evap,i} = \frac{k_{w,depo,i}}{K_{w,i}C_w} \quad (S3)$$

where  $C_w$  is the total mass of equivalent absorbing organic material on the chamber walls, and  $K_{w,i}$  is the gas-wall partition coefficient, which depends on the vapor pressure of compound  $i$ ,

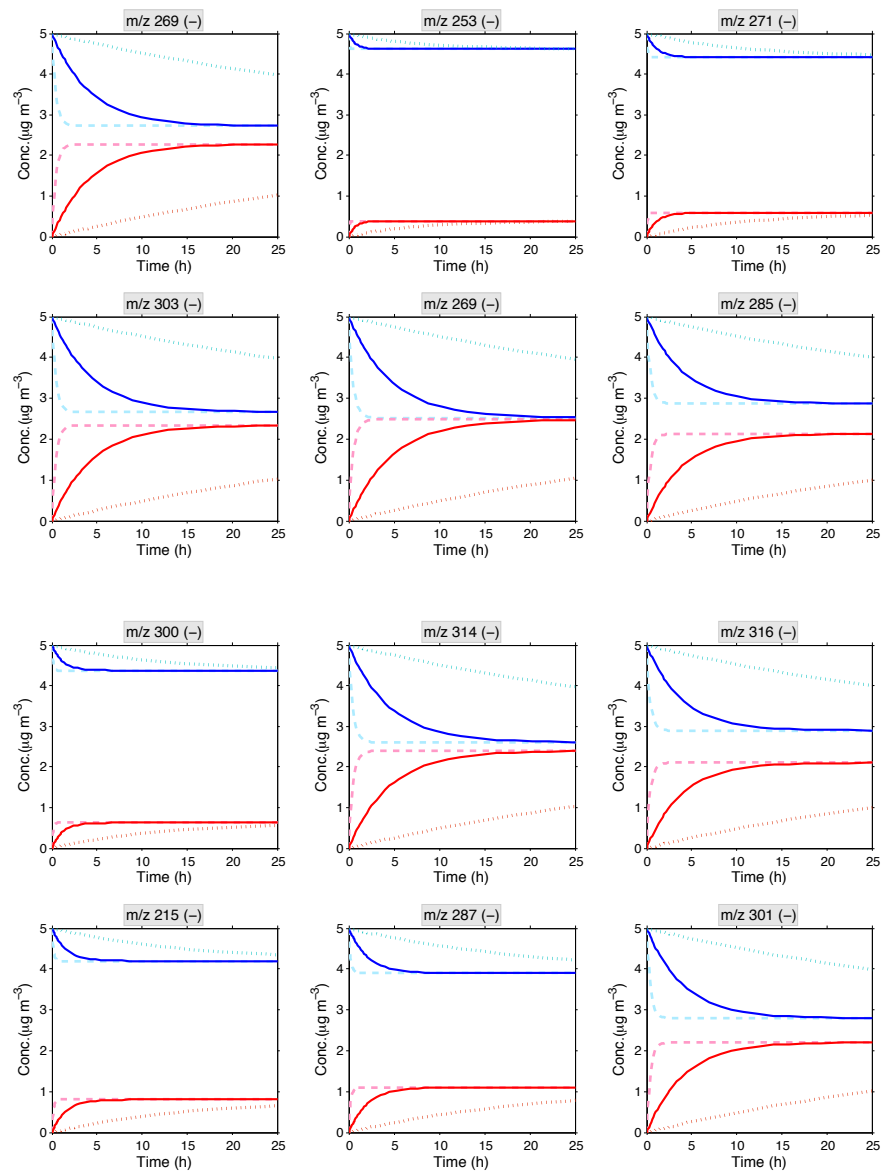
$$K_{w,i} = \frac{RT}{p_{L,i}^0 \gamma_i \bar{M}_w} \quad (S4)$$

where  $p_{L,i}^0$  is the vapor pressure of compound  $i$  as a liquid,  $\gamma_i$  is its activity coefficient on a mole fraction basis,  $R$  is the gas constant,  $T$  is temperature, and  $\bar{M}_w$  is the average molecular weight of the absorbing organic material on the wall.

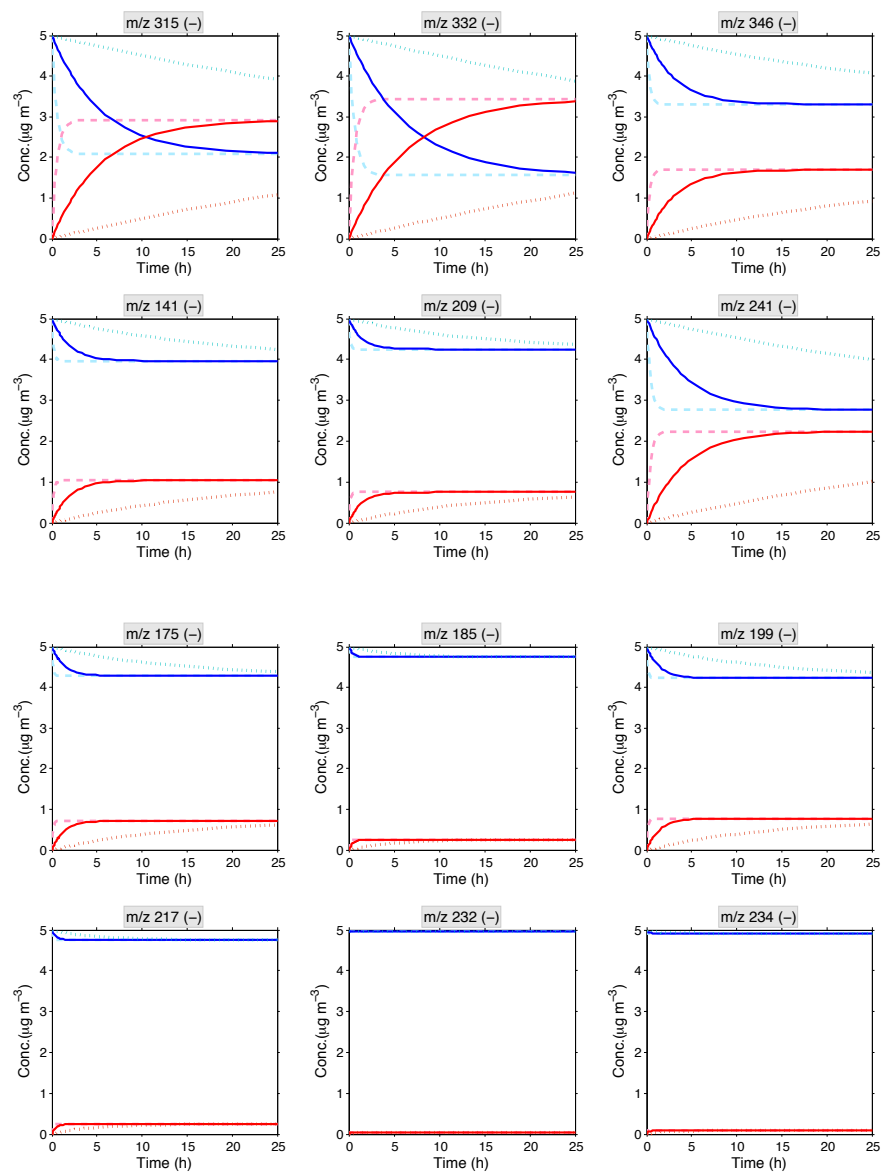
Simulations were performed to estimate timescales associated with gas-wall equilibrium partitioning for the 25 intermediate/semi-volatile organic vapors investigated. Although the deposition rate coefficient ( $k_{w,depo,i}$ ) for each organic vapor is unknown, upper and lower limits can be obtained. Note that CIMS measured overall decay rate of organic vapor  $i$  ( $k_{w,i}$ ) is a function of  $k_{w,depo,i}$  and  $k_{w,evap,i}$ . The upper limit ( $k_{w,depo,i} = 6 \times 10^{-4} s^{-1}$ ) is governed by the mixing status in the chamber,

$$k_{w,depo} = \frac{\pi}{2} \left( \frac{A}{V} \right) (D_v K_e)^{1/2} \quad (S5)$$

The lower limit ( $k_{w,depo,i} = 1 \times 10^{-6} \text{ s}^{-1}$ ) is chosen as the lowest dark decay rate among 25 organic vapors measured by CIMS. The middle value ( $k_{w,depo,i} = 3 \times 10^{-5} \text{ s}^{-1}$ ) is the average of upper and lower limits. The evaporation rates ( $k_{w,evap,i}$ ) can be obtained via Eq (S3) using the  $C_w$  values calculated from Section 4.2 in the main text. Predicted temporal profiles of  $\bar{C}_{v,i}$  and  $\bar{C}_{w,i}$  are shown in Figure S1. In general, vapors with lower volatilities tend to require a longer time to establish gas-wall equilibrium. For a specific compound, the equilibrium timescale is estimated to vary from a few minutes to over a day, depending on the deposition rate coefficients applied (upper limit  $k_{w,depo,i} = 6 \times 10^{-4} \text{ s}^{-1}$  vs. lower limit  $k_{w,depo,i} = 1 \times 10^{-6} \text{ s}^{-1}$ ). For the 25 vapors studied, gas-wall equilibrium partitioning is estimated to require > 20 min to < 25 h when the average deposition rate coefficient is employed ( $k_{w,depo,i} = 3 \times 10^{-5} \text{ s}^{-1}$ ) in the simulation. These results suggest that it is generally reasonable to estimate  $C_w$  assuming equilibrium partitioning after  $\sim 18$  h of wall-induced vapor decay.







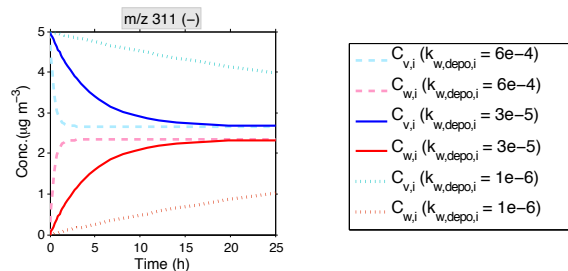


Figure S1. Timescales for gas-wall equilibrium partitioning of intermediate/semi-volatile organic vapors generated from photooxidation of isoprene, toluene,  $\alpha$ -pinene, and dodecane. Three values of  $k_{w,depo,i}$  are incorporated in the simulation here, representing the upper limit ( $k_{w,depo,i} = 6 \times 10^{-4} \text{ s}^{-1}$ ), average ( $k_{w,depo,i} = 3 \times 10^{-5} \text{ s}^{-1}$ ), and lower limit ( $k_{w,depo,i} = 1 \times 10^{-6} \text{ s}^{-1}$ ) of vapor deposition rate on chamber walls, respectively. The evaporation rates from chamber walls ( $k_{w,evap,i}$ ) are calculated using  $C_w$  derived from Eqs (12) and (13) in the main text (See Section 4 for more details). Initial concentrations of vapor  $i$  in the gas phase and on chamber walls are assumed to be 5 and 0  $\mu\text{g m}^{-3}$ , respectively.

*Appendix D*ROLE OF OZONE IN SOA FORMATION FROM ALKANE  
PHOTOOXIDATION

Zhang, X. et al. (2014). “Influence of Vapor Wall Loss in Laboratory Chambers on Yields of Secondary Organic Aerosol”. In: *P. Natl. Acad. Sci. USA* 111.16, pp. 5802–5807.



## Role of ozone in SOA formation from alkane photooxidation

X. Zhang<sup>1</sup>, R. H. Schwantes<sup>1</sup>, M. M. Coggon<sup>2</sup>, C. L. Loza<sup>2</sup>, K. A. Schilling<sup>2</sup>, R. C. Flagan<sup>1,2</sup>, and J. H. Seinfeld<sup>1,2</sup>

<sup>1</sup>Division of Engineering and Applied Science, California Institute of Technology, Pasadena, CA, USA

<sup>2</sup>Division of Chemistry and Chemical Engineering, California Institute of Technology, Pasadena, CA, USA

Correspondence to: J. H. Seinfeld (seinfeld@caltech.edu)

Received: 15 August 2013 – Published in Atmos. Chem. Phys. Discuss.: 24 September 2013

Revised: 2 January 2014 – Accepted: 9 January 2014 – Published: 14 February 2014

**Abstract.** Long-chain alkanes, which can be categorized as intermediate volatility organic compounds, are an important source of secondary organic aerosol (SOA). Mechanisms for the gas-phase OH-initiated oxidation of long-chain alkanes have been well documented; particle-phase chemistry, however, has received less attention. The  $\delta$ -hydroxycarbonyl, which is generated from the isomerization of alkoxy radicals, can undergo heterogeneous cyclization and dehydration to form substituted dihydrofuran. Due to the presence of C=C bonds, the substituted dihydrofuran is predicted to be highly reactive with OH, and even more so with O<sub>3</sub> and NO<sub>3</sub>, thereby opening a reaction pathway that is not usually accessible to alkanes. This work focuses on the role of substituted dihydrofuran formation and its subsequent reaction with OH, and more importantly ozone, in SOA formation from the photooxidation of long-chain alkanes. Experiments were carried out in the Caltech Environmental Chamber using dodecane as a representative alkane to investigate the difference in aerosol composition generated from “OH-oxidation-dominating” vs. “ozonolysis-dominating” environments. A detailed mechanism incorporating the specific gas-phase photochemistry, together with the heterogeneous formation of substituted dihydrofuran and its subsequent gas-phase OH/O<sub>3</sub> oxidation, is used to evaluate the importance of this reaction channel in dodecane SOA formation. We conclude that (1) the formation of  $\delta$ -hydroxycarbonyl and its subsequent heterogeneous conversion to substituted dihydrofuran is significant in the presence of NO<sub>x</sub>; (2) the ozonolysis of substituted dihydrofuran dominates over the OH-initiated oxidation under conditions prevalent in urban and rural air; and (3) a spectrum of highly oxygenated products with carboxylic acid, ester, and ether functional groups are produced from the substituted dihydrofuran chemistry, thereby affecting the average oxidation state of the SOA.

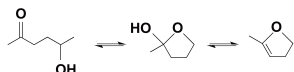
### 1 Introduction

Alkanes are important constituents of gasoline and vehicle emissions (Hoekman, 1992; Zielinska et al., 1996; Kirchstetter et al., 1999; Gentner et al., 2012; Jathar et al., 2013), accounting for ~50 % of volatile organic compounds (VOCs) in the urban atmosphere (Fraser et al., 1997; Schauer et al., 1999 and 2002). The unresolved complex mixture (UCM) of organics, which is potentially a significant source of secondary organic aerosol (SOA) formation in the atmosphere, has recently been shown to comprise many long-chain alkanes (Isaacman et al., 2012), which are expected to contribute to SOA formation (Robinson et al., 2007).

Laboratory chamber investigations of SOA formation from long-chain alkanes (Lim and Ziemann, 2005, 2009a, b, c; Presto et al., 2009, 2010; Miracolo et al., 2010, 2011; Craven et al., 2012; Lambe et al., 2012; Tkacik et al., 2012; Yee et al., 2012; Loza et al., 2013) provide a framework for understanding chemical mechanisms and determination of SOA yields (Jordan et al., 2008; Aumont et al., 2012 and 2013; Cappa et al., 2013; Zhang and Seinfeld, 2013). Particle-phase products from OH oxidation of alkanes contain a number of functional groups: organonitrate (–ONO<sub>2</sub>), hydroxyl (–OH), carbonyl (–C=O), ester (–C(O)O–), and hydroperoxide (–OOH). Ambient measurements of organic aerosol composition have shown, in addition, that the carboxylic acid functional group (–C(O)OH) is closely associated with products from fossil fuel combustion sources (Liu et al., 2011; Russell et al., 2011), of which alkanes are a principal component.

Atmospheric alkanes react in daytime exclusively with OH, producing an array of peroxy radicals (RO<sub>2</sub>). In the presence of sufficient NO, the alkoxy radical (RO) is the key product of the subsequent RO<sub>2</sub> reaction with NO. RONO<sub>2</sub>

is also produced, with a branching ratio of 0.1–0.3 (Arey et al., 2001). For alkanes with carbon number  $\geq 5$ , the 1,5-H shift isomerization is the dominant reaction pathway for RO, producing a  $\delta$ -hydroxycarbonyl, the primary fate of which is reaction with OH (Jenkin et al., 2003; Saunders et al., 2003; Bloss et al., 2005), with a lifetime of  $\sim 11.5$  h at room temperature and a typical ambient OH concentration of  $1 \times 10^6$  molecules  $\text{cm}^{-3}$ . One particular  $\delta$ -hydroxycarbonyl, 5-hydroxy-2-pentanone, was found to cyclize to form the cyclic hemiacetal. The cyclic hemiacetal can subsequently lose water to form 4,5-dihydro-2-methylfuran, with an overall lifetime as short as  $\sim 1.1$  h at 298 K (Cavalli et al., 2000; Martin et al., 2002). The presence of water vapor can, in principle, serve to convert the 4,5-dihydro-2-methylfuran back to 5-hydroxy-2-pentanone, leading to an equilibrium between these two species within several hours (Martin et al., 2002; Baker et al., 2005; Holt et al., 2005; Reisen et al., 2005):



This conversion to 4,5-dihydro-2-methylfuran is not unique to 5-hydroxy-2-pentanone and also occurs for other C<sub>5</sub>–C<sub>17</sub>  $\delta$ -hydroxycarbonyls (Lim and Ziemann, 2005, 2009a, b, c) at a rate that increases with the length of the carbon chain (Holt et al., 2005; Ziemann and Atkinson, 2012). The substituted dihydrofuran is highly reactive towards OH, O<sub>3</sub>, and NO<sub>3</sub> in the gas phase, owing to the presence of a C=C double bond. For typical ambient concentrations of OH, O<sub>3</sub>, and NO<sub>3</sub>, i.e.,  $2 \times 10^6$  molecules  $\text{cm}^{-3}$  (12 h average), 30 ppb (24 h average), and  $5 \times 10^8$  molecules  $\text{cm}^{-3}$  (12 h average), respectively, the lifetimes of the substituted dihydrofuran with respect to reactions with these oxidants in the gas phase are 1.3 h, 7 min, and 24 s, respectively (Martin et al., 2002; Ziemann and Atkinson, 2012). Based on these estimates, ozonolysis of substituted dihydrofurans may dominate OH oxidation during daytime in the urban atmosphere.

SOA formation from long-chain alkanes involves multiple generations of OH oxidation that include functionalization (O-atom addition in forms of a variety of moieties) and fragmentation of the parent carbon backbone. These two routes can eventually lead to highly oxygenated fragments that partition into the particle phase. Two recent modeling studies of C<sub>12</sub> alkanes suggest that particle-phase chemistry might play a potentially important role in the chemical composition of alkane SOA; this is inferred from the fact that simulations driven solely by gas-phase chemistry can successfully reproduce the chamber-measured SOA yield, but these fail to replicate the observed particulate O : C and H : C ratios in the absence of a particle-phase chemistry channel (Cappa et al., 2013; Zhang and Seinfeld, 2013). The extent to which particle-phase chemistry is important in alkane SOA formation has not been clearly established.

We address here the heterogeneous formation of substituted dihydrofurans and their subsequent gas-phase reaction

with ozone in SOA formation from alkanes. We present the results of a series of chamber dodecane photooxidation experiments under two reaction regimes, i.e., “OH-dominant”, in which over 70 % of substituted dihydrofurans are oxidized by OH, vs. “O<sub>3</sub>-dominant”, in which 80–90 % of substituted dihydrofurans react with O<sub>3</sub>. Gas-phase products that are unique to the substituted dihydrofuran chemistry are identified. The impact of ozonolysis of substituted dihydrofurans on the particle-phase product distribution from the photooxidation of dodecane is investigated by comparing intensities of certain ions that are indicative of ozonolysis chemistry. We also develop a detailed mechanism with the incorporation of substituted dihydrofuran chemistry and simulate the effect of this reaction channel on SOA yield from the photooxidation of dodecane.

## 2 Experimental

Experiments were conducted in the new Caltech dual 24-m<sup>3</sup> Environmental Chamber, in which the temperature (*T*) and relative humidity (RH) are automatically controlled. Prior to each experiment, the Teflon chambers were flushed with clean, dry air for 24 h until the particle number concentration was  $< 10 \text{ cm}^{-3}$  and volume concentration  $< 0.01 \mu\text{m}^3 \text{ cm}^{-3}$ . Seed aerosol was injected into the chamber by atomizing 0.015 M aqueous ammonium sulfate solution to provide sufficient surface area for the partition of semivolatile products. Hydrogen peroxide (H<sub>2</sub>O<sub>2</sub>) was used for the OH source by evaporating 85 and 226  $\mu\text{L}$  of 50 wt % aqueous solution into the chamber with 5 L min<sup>−1</sup> of purified air for  $\sim 110$  min, resulting in an approximate starting H<sub>2</sub>O<sub>2</sub> concentration of 1.5 and 4 ppm, respectively, under high- and low-NO<sub>x</sub> conditions. The 4 ppm H<sub>2</sub>O<sub>2</sub> concentration employed in low-NO<sub>x</sub> experiments creates a RO<sub>2</sub>+HO<sub>2</sub> dominant reaction regime. We replaced H<sub>2</sub>O<sub>2</sub> with nitrous acid (HONO) as the OH source for one experiment in order to minimize the formation of ozone. HONO was prepared by dropwise addition of 15 mL of 1 wt % NaNO<sub>2</sub> into 30 mL of 10 wt % H<sub>2</sub>SO<sub>4</sub> in a glass bulb and introduced into the chambers with 5 L min<sup>−1</sup> of purified air for  $\sim 40$  min. To minimize the vapor-phase wall loss along the injection line, 60  $\mu\text{L}$  of dodecane (Sigma-Aldrich, 98 % purity) was injected into a glass bulb, which was connected directly into the Teflon chamber via a 1/4 in. inside diameter (i.d.). Swagelock to NPT fitting located on a Teflon plate. Heated 5 L min<sup>−1</sup> of purified air flowed through the glass bulb into the chamber for 30 min, introducing  $\sim 200$  ppb dodecane into the chamber. After  $\sim 1$  h of mixing, photooxidation was initiated by irradiating the chamber with black lights with output wavelength ranging from 300 to 400 nm.

Experiments were carried out under conditions in which the peroxy radicals formed from the initial OH reaction with dodecane react either essentially exclusively with NO (so-called high NO<sub>x</sub>) (Exp. 1, 2, 3, 4, and 5) or essentially

**Table 1.** Experimental conditions for the photooxidation of dodecane.

|                                   | Exp. | $T_0$<br>(K) | RH <sub>0</sub><br>(%) | HC <sub>0</sub><br>(ppb) | (NO) <sub>0</sub><br>(ppb) | (NO <sub>2</sub> ) <sub>0</sub><br>(ppb) | (O <sub>3</sub> ) <sub>0</sub><br>(ppb) | Initial<br>seed vol.<br>( $\mu\text{m}^3 \text{m}^{-3}$ ) | Additional<br>NO inj.<br>(ppb h <sup>-1</sup> ) × (h) |
|-----------------------------------|------|--------------|------------------------|--------------------------|----------------------------|--|---|---|---|
| High NO <sub>x</sub> <sup>a</sup> | 1    | ~300         | ~3                     | 208                      | 430                        | 576                                      | < DL <sup>g</sup>                       | 18  | –   |
|                                   | 2    | ~300         | ~3                     | 208                      | 287                        | 12                                       | ~2                                      | 24  | Y <sup>c</sup>  |
|                                   | 3    | ~300         | ~11                    | 206                      | 45                         | 33                                       | ~2                                      | 30  | Y <sup>d</sup>  |
|                                   | 4    | ~300         | ~20                    | 178                      | 38                         | 156                                      | ~2                                      | 28  | Y <sup>e</sup>  |
|                                   | 5    | ~300         | ~55                    | 214                      | 69                         | 30                                       | ~2                                      | 43  | Y <sup>f</sup>  |
| Low NO <sub>x</sub> <sup>b</sup>  | 6    | ~300         | ~3                     | 208                      | < DL                       | < DL                                     | < DL                                    | 19  | –   |
|                                   | 7    | ~300         | ~3                     | 214                      | < DL                       | < DL                                     | 32.6                                    | 25  | –   |
|                                   | 8    | ~300         | ~55                    | 216                      | < DL                       | < DL                                     | < DL                                    | 58  | –   |

<sup>a</sup> Under high-NO<sub>x</sub> conditions, the simulated NO concentration (> 5 ppb) is at least 4 orders of magnitude higher than RO<sub>2</sub> (< 5 × 10<sup>7</sup> molecules cm<sup>-3</sup>). Over 99 % of RO<sub>2</sub> is predicted to react with NO.

<sup>b</sup> Under low-NO<sub>x</sub> conditions, the simulated HO<sub>2</sub> concentration (~ 1 × 10<sup>10</sup> molecules cm<sup>-3</sup>) is ~ 20 times higher than RO<sub>2</sub> (~ 5 × 10<sup>8</sup> molecules cm<sup>-3</sup>). RO<sub>2</sub> + HO<sub>2</sub> dominates the fate of RO<sub>2</sub>.

<sup>c</sup> NO source was controlled at 100 ppb h<sup>-1</sup> for the first 7 h of reaction and then 25 ppb h<sup>-1</sup> for the remainder of the reaction.

<sup>d</sup> NO source was controlled at 25 ppb h<sup>-1</sup> over the course of the experiment.

<sup>e</sup> NO source was controlled at 30 ppb h<sup>-1</sup> for the first 3 h of reaction and then 100 ppb h<sup>-1</sup> for the next 1 h of reaction and then back to 30 ppb h<sup>-1</sup> for the remainder of the reaction.

<sup>f</sup> NO source was controlled at 50 ppb h<sup>-1</sup> over the course of the experiment.

<sup>g</sup> Detection limits (DL) for O<sub>3</sub>, NO, and NO<sub>2</sub> are 0.5 ppb, 0.4 ppb, and 0.4 ppb, respectively. H<sub>2</sub>O<sub>2</sub> has an interference on the O<sub>3</sub> detection, increasing the O<sub>3</sub> monitor readout by ~ 2–3 ppb in the current study.

exclusively with HO<sub>2</sub> (so-called low NO<sub>x</sub>) (Exp. 6, 7, and 8). For each condition, O<sub>3</sub>-dominant vs. OH-dominant environments were generated by varying the OH source, initial NO, NO<sub>2</sub>, and O<sub>3</sub> concentrations, as well as the additional NO injection rate during the irradiation period (Table 1). The ozonolysis vs. OH oxidation of substituted dihydrofuran is calculated to be equally competitive when the ratio of O<sub>3</sub> to OH concentration is 6.3 × 10<sup>4</sup> : 1 (approximately 2.6 ppb O<sub>3</sub> vs. 1.0 × 10<sup>6</sup> molecules cm<sup>-3</sup> OH). Under low-NO<sub>x</sub> conditions, NO, NO<sub>2</sub>, NO<sub>x</sub>, and O<sub>3</sub> were below detection limits, and no ozone formation was observed over the course of 20 h experiments. OH oxidation of dihydrofuran is dominant with average OH concentrations of 1.8 × 10<sup>6</sup> and 1.5 × 10<sup>6</sup> molecules cm<sup>-3</sup>, respectively, in Exp. 6 and 8. OH concentration is calculated by optimal fitting of the exponential decay of the GC-FID (gas chromatograph with flame ionization detection)-measured dodecane temporal profile. In order to evaluate the effect of the ozonolysis of dihydrofuran chemistry on the dodecane SOA formation under low-NO<sub>x</sub> conditions, additional ~ 30 ppb of ozone was injected into the chamber before the onset of irradiation (Exp. 7). Under high-NO<sub>x</sub> conditions, HONO was used as the OH source for the OH-dominant environment (Exp. 1). Double HONO injection was carried out in order to fully consume dodecane (before the onset and after ~ 3 h of irradiation). The average OH concentration is ~ 5.0 × 10<sup>6</sup> molecules cm<sup>-3</sup>, whereas O<sub>3</sub> peaks at 8 ppb after 60 min of photooxidation and rapidly decays to ~ 0 ppb within 2 h. In this case, > 73 % of dihydrofuran is oxidized by OH over the course of Exp. 1. An O<sub>3</sub>-dominant environment was generated by injecting NO (38–287 ppb) and NO<sub>2</sub> (12–156 ppb) before the onset of irradiation.

Continuous NO injection with a certain flow rate (20–100 ppb h<sup>-1</sup>) was conducted over the course of experiments to reach a sufficient amount of O<sub>3</sub> and to maintain high-NO<sub>x</sub> levels. Under experimental conditions in Exp. 2, 3, 4, and 5, the average OH concentrations are calculated to be 1.7 × 10<sup>6</sup>, 2.0 × 10<sup>6</sup>, 1.4 × 10<sup>6</sup>, and 1.3 × 10<sup>6</sup> molecules cm<sup>-3</sup>, respectively, and the maximum O<sub>3</sub> mixing ratios are 20, 380, 150, and 250 ppb, respectively. As a result, ~ 82, ~ 96, ~ 97, and ~ 98 % of dihydrofuran reacts with O<sub>3</sub> when dihydrofuran peaks after ~ 3 h of photooxidation. High-humidity experiments were also carried out as a set of control experiments (Exp. 4, 5, and 8) addressing the role of water vapor in the heterogeneous interconversion between  $\delta$ -hydroxycarbonyls and substituted dihydrofurans.

A suite of instruments was used to investigate gas- and particle-phase chemistry. *T*, RH, NO, NO<sub>x</sub>, and O<sub>3</sub> were continuously monitored. Dodecane concentration was monitored by taking hourly samples at ~ 0.13 L min<sup>-1</sup> of chamber air for 3 min onto a Tenax adsorbent, which was loaded into the inlet of a GC-FID (Agilent 6890N), desorbed at 275 °C for 13 min, and then injected onto an HP-5 column (15 m × 0.53 mm i.d. × 1.5  $\mu\text{m}$  thickness, Hewlett-Packard) held at 30 °C. The oven was ramped from 30 to 275 °C at 10 °C min<sup>-1</sup> and held at 275 °C for 5 min. The retention time for dodecane is ~ 27.5 min. The gas-phase species were monitored using a custom-modified Varian 1200 triple-quadrupole chemical ionization mass spectrometer (CIMS) (Crounse et al., 2006; Paulot et al., 2009). In negative mode operation, CF<sub>3</sub>O<sup>-</sup> was used as the reagent ion to cluster with an analyte such as hydroperoxide or acid [*R*], producing [*R*-CF<sub>3</sub>O]<sup>-</sup> or *m/z* [*M* + 85]<sup>-</sup>, where *M* is the molecular

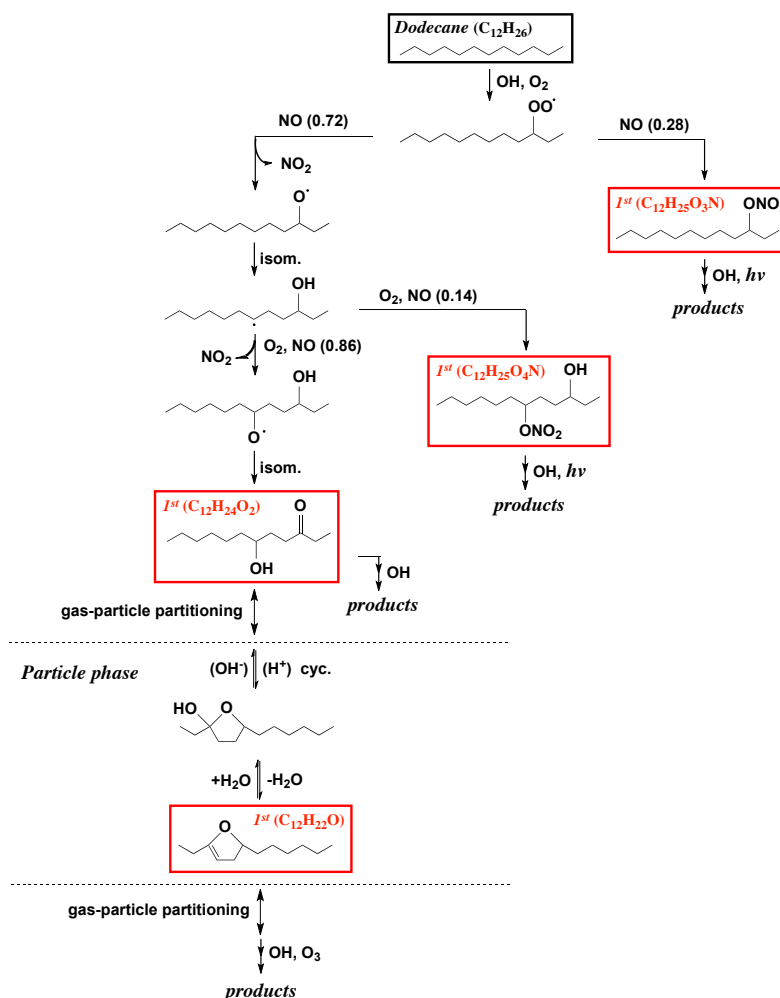


**Fig. 1a.** Schematic mechanism for the photooxidation of dodecane under high- $NO_x$  conditions. Note that only first-generation products are shown here. The boxes indicate compounds and associated reaction pathways incorporated in the model simulation.

weight of the analyte. For more strongly acidic species  $[H \cdot X]$ , the transfer product,  $[H \cdot X \cdot F]^-$  or  $m/z [M+19]^-$ , is formed during ionization. Carboxylic acids tend to have contributions to both the transfer and cluster product, in which case the overall signal of a compound is considered as the sum of the two product signals. In positive-mode operation, an analyte  $[R]$  can undergo proton transfer reaction, producing an ion in the form of  $[R \cdot H]^+$ , and/or react with  $n$  positively charged water clusters to form a cluster in the form of  $[(H_2O)_n \cdot R \cdot H]^+$ . Positive mode is employed in this study

for tracking less polar compounds, such as the substituted dihydrofuran.

Particle size distribution and number concentration were measured by a cylindrical differential mobility analyzer (DMA, TSI Model 3081) coupled to a condensation particle counter (TSI Model 3010). The protocol for applying particle wall loss correction to DMA measured SOA growth data is described in the Supplement. Real-time particle mass spectra were collected continuously by an Aerodyne high-resolution time-of-flight aerosol mass spectrometer (DeCarlo et al., 2006; Canagaratna et al., 2007). The AMS switched

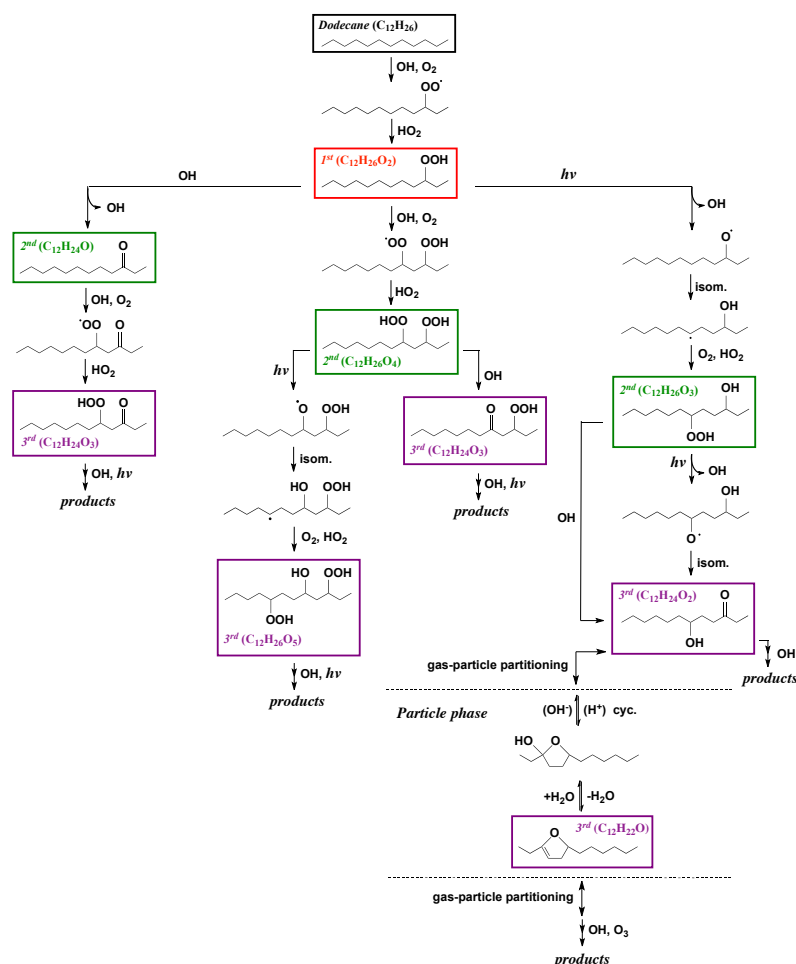


**Fig. 1b.** Schematic mechanism for the photooxidation of dodecane under low- $NO_x$  conditions. Note that only the first three generations of products are shown here. The boxes indicate compounds and associated reaction pathways incorporated in the model simulation.

once every minute between the high-resolution “W mode” and the lower resolution, higher sensitivity “V mode”. The V mode was utilized for quantification, as the higher  $m/z$  values exhibit a more favorable signal-to-noise ratio. The W mode was used for ion identification and clarification. Detailed AMS data analysis protocols can be found in the Supplement.

### 3 Chemical mechanism

A photochemical mechanism was used to simulate the gas-phase photochemistry of  $NO_x$ ,  $HO_x$ , and  $O_3$  corresponding

to the experimental conditions. Reactions and corresponding reaction rate constants are listed in Tables S1–S3 in the Supplement. Photolysis rate constants are calculated using the irradiance spectrum measured for the chamber UV lights as well as absorption cross sections and quantum yields from Sander et al. (2011).

The kinetic scheme for the gas-phase  $OH$ -initiated oxidation of dodecane and the further  $OH$  oxidation of multi-generational products was developed primarily based on the Master Chemical Mechanism v3.2 (MCM v3.2, <http://mcm.leeds.ac.uk/MCM/>). Products identified in Lim and Ziemann (2005; 2009 a, b, c) that are not in MCM are



also included here. The kinetic scheme was incorporated in the photochemical model to estimate yields of particle-phase products generated in the chamber. A simplified flow chart illustrating the mechanism for the multigeneration gas-phase chemistry is shown in Fig. 1a, b. In general, the OH-initiated oxidation of dodecane leads to RO<sub>2</sub>, the fate of which controls the distribution of further generation products. When sufficient NO<sub>x</sub> is present (the concentration of NO, i.e., >5 ppb, is at least 4 orders of magnitude higher than RO<sub>2</sub>, i.e., <5 × 10<sup>7</sup> molecules cm<sup>-3</sup>), over 99 % of RO<sub>2</sub> reacts with NO, leading to RO or alkyl nitrate (RONO<sub>2</sub>). The branching ratios for the production of RO and RONO<sub>2</sub> are obtained from Jordan et al. (2008). RO can isomerize through a 1,5-H-atom shift to a δ-hydroxyalkyl radical, react with O<sub>2</sub>, or undergo fragmentation. The alkyl nitrate formed either undergoes photolysis or reacts with OH via H-atom abstraction from a C atom or reacts with OH via H-atom abstraction from a C atom with a –ONO<sub>2</sub> group attached to produce a –C=O group. The δ-hydroxyalkyl radical reacts with O<sub>2</sub> and then NO and undergoes another isomerization to produce a δ-hydroxycarbonyl. At sufficiently low NO<sub>x</sub> concentrations, the simulated HO<sub>2</sub> concentration (~1 × 10<sup>10</sup> molecules cm<sup>-3</sup>) is ~20 times higher than RO<sub>2</sub> (~5 × 10<sup>8</sup> molecules cm<sup>-3</sup>). RO<sub>2</sub> + HO<sub>2</sub> dominates the fate of RO<sub>2</sub>, producing a hydroperoxide (ROOH). Further oxidation of ROOH involves the photolysis of the –OOH group, H-atom abstraction, and the OH oxidation of a C atom with a –OOH group attached to produce a –C=O group. Products through eight generations of oxidation are included in the mechanism, although only the formation of the first three generations of products is illustrated in Fig. 1. The reaction rate constants are obtained from MCM v3.2. In the absence of specific data, the photolysis rate constants of the –OOH, –C=O, and –ONO<sub>2</sub> groups on the carbon backbone are assumed to be the same as those for methyl peroxide (CH<sub>3</sub>OOH), 2-butanol (C<sub>3</sub>H<sub>7</sub>CHO), and *n*-propyl nitrate (*n*-CH<sub>3</sub>ONO<sub>2</sub>).

Cyclization and subsequent dehydration of δ-hydroxycarbonyl to substituted dihydrofuran is a heterogeneous process, including (1) gas-phase diffusion and reactive uptake of δ-hydroxycarbonyl to particles, (2) cyclization of δ-hydroxycarbonyl to cyclic hemiacetal, and (3) dehydration of cyclic hemiacetal to substituted dihydrofuran. (Atkinson et al., 2008; Lim and Ziemann, 2009c). The extent of this heterogeneous process occurring on/in particles has been predicted to predominate over chamber walls (Lim and Ziemann, 2009 c). In this study, we represent the individual steps of the conversion of δ-hydroxycarbonyl to substituted dihydrofuran by an overall first-order decay rate of 3 × 10<sup>-3</sup> s<sup>-1</sup>. This value is estimated by monitoring the decay of 5-hydroxy-2-pentanone using CIMS in the presence of 20 μm<sup>3</sup> cm<sup>-3</sup> (NH<sub>4</sub>)<sub>2</sub>SO<sub>4</sub>/H<sub>2</sub>SO<sub>4</sub> seeds at 3 % RH. This assumed decay rate is consistent with those rates measured in previous studies (Cavalli et al., 2000; Martin et al., 2002; Holt et al., 2005; Lim and Ziemann, 2009 c). The equilibrium

constant  $K$  ( $K = [4,5\text{-dihydro-2-methylfuran}]/[5\text{-hydroxy-2-pentanone}]$ ) is estimated to be ~7 at 3 % RH from the CIMS measured 5-hydroxy-2-pentanone decay curve, based on the assumption that the decrease in the 5-hydroxy-2-pentanone concentration is accompanied by stoichiometric formation of the corresponding 4,5-dihydro-2-methylfuran. Note that although the proportion of the heterogeneous conversion occurring on the chamber walls is unknown, the potential contribution of chamber walls to the particle-phase production of substituted dihydrofuran has been accounted for by employing the measured overall conversion rate in the mechanism.

The substituted dihydrofuran formed evaporates rapidly due to its high volatility and undergoes reactions with OH, O<sub>3</sub>, and NO<sub>3</sub> in the gas phase (Ziemann and Atkinson, 2012), with reaction rate constants of 2.18 × 10<sup>-10</sup>, 3.49 × 10<sup>-15</sup> cm<sup>3</sup> molecule<sup>-1</sup> s<sup>-1</sup>, and 1.68 × 10<sup>-10</sup> cm<sup>3</sup> molecule<sup>-1</sup> s<sup>-1</sup>, respectively (Martin et al., 2002; Atkinson et al., 2008). Reaction with NO<sub>3</sub> is not important under the conditions of this study. In general, the OH addition to an alkyl-substituted dihydrofuran produces either an alkyl-substituted tetrahydrofuran or a carbonyl ester; see Fig. 2a (Martin et al., 2002; Lim and Ziemann, 2005, 2009a, b, c; Jordan et al., 2008). The mechanism for the O<sub>3</sub> reaction with an alkyl-substituted dihydrofuran, as shown in Fig. 2b, was developed following the ozonolysis of 4,5-dihydro-2-methylfuran (Martin et al., 2002), alkyl vinyl ethers (Thiault et al., 2002; Klotz et al., 2004; Sadezky et al., 2006) and monoterpenes (Jenkin et al., 2000; Jenkin, 2004). The reaction of alkyl-substituted dihydrofuran with O<sub>3</sub> involves the addition of O<sub>3</sub> to the C=C double bond to produce an energy-rich primary ozonide, which rapidly decomposes into two excited Criegee intermediates. The energy-rich Criegee intermediates are either collisionally stabilized or decompose to yield OH (or OH+CO) and an additional α-carbonyl peroxy radical (or peroxy radical). The resulting α-carbonyl peroxy radical (or peroxy radical) can undergo the well-established reactions available for peroxy radicals; see Fig. 2b. The stabilized Criegee intermediates are predicted to react primarily with water (Martin et al., 2002), leading to 3-propoxy-nonanal (C<sub>12</sub>H<sub>22</sub>O<sub>3</sub>) and 3-propoxy-nonanoic acid (C<sub>12</sub>H<sub>22</sub>O<sub>3</sub>), with molar yields of 90 and 10 %, respectively. The total yield of 3-propoxy-nonanal is predicted to be 18 %, which is close to the yield of succinaldehydic acid methyl ester (23 %) from the ozonolysis of 4,5-dihydro-2-methylfuran (Martin et al., 2002).

We consider SOA formation by dodecane photooxidation, including heterogeneous formation of substituted dihydrofuran and its subsequent reaction with OH/O<sub>3</sub>. Gas-particle equilibrium partitioning of semivolatile products is assumed. The branching ratio and vapor pressure ( $P_{L,i}^0$  atm<sup>-1</sup>) at 300 K (predicted by SIMPOL.1; Pankow and Asher, 2008) of each product from the OH/O<sub>3</sub>-initiated oxidation of alkyl-substituted dihydrofuran are labeled in Fig. 2. The corresponding effective saturation concentrations

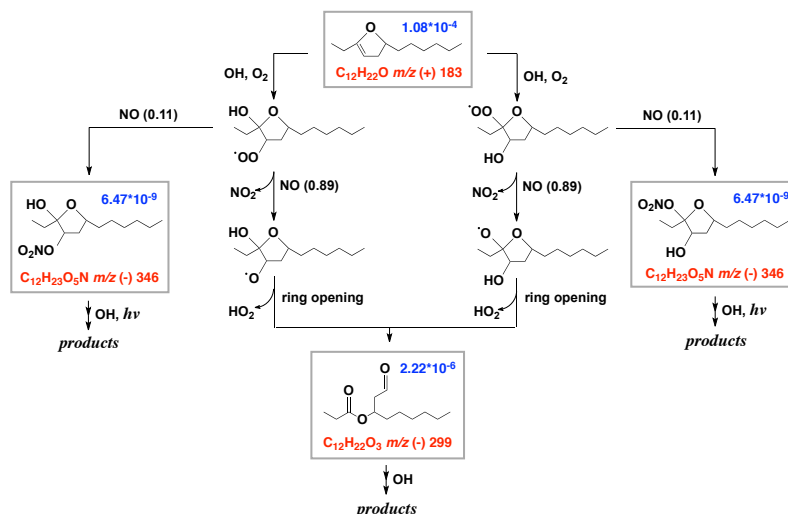


**Fig. 2a.** Proposed mechanism for the OH-initiated oxidation of alkyl-substituted dihydrofuran under high- $\text{NO}_x$  conditions. The boxes indicate compounds or reaction pathways incorporated in the model simulation. CIMS monitored species have  $m/z$  noted in red. Estimated vapor pressure (atm) of each compound is indicated in blue.

( $C^* = 10^6 P_{L,i}^0 \gamma_i \bar{M}_w / RT$ ) range from  $7.0 \times 10^1 \mu\text{g m}^{-3}$  to  $4.7 \times 10^4 \mu\text{g m}^{-3}$ , for which approximately 0.1 %  $\sim$  41.7 % of these products are in the particle phase at an organic loading of  $\sim 50 \mu\text{g m}^{-3}$ . Compounds with the lowest volatility ( $\sim 10^{-9}$  atm) are produced mostly from the  $\text{RO}_2 + \text{NO} \rightarrow \text{RONO}_2$  reaction, the branching ratio of which ranges from 0.11 to 0.28. As a result, the total amount of organic nitrates in the particle phase is relatively high; see Fig. 9c. Compounds generated from the  $\text{RO}_2 + \text{NO} \rightarrow \text{RO} + \text{NO}_2$  reaction have higher molar yields (0.72–0.89). But they are too volatile ( $\sim 10^{-6}$ – $10^{-7}$  atm) to partition significantly into the particle phase. The stabilized Criegee intermediate reaction with water is predicted to predominate over reaction with  $\text{NO}/\text{NO}_2$  at  $\text{RH} > 3\%$ . The ester containing carboxylic acid ( $\text{C}_{12}\text{H}_{22}\text{O}_4$ ) is predicted to be present in the particle phase due to its sufficiently low volatility ( $\sim 10^{-8}$  atm); see Fig. 9c.

#### 4 Results and discussion

In this section, we seek to evaluate the impact of substituted dihydrofuran chemistry on dodecane SOA formation as follows: (1) predict the yield of alkyl-substituted dihydrofuran from the photooxidation of dodecane under both high- and low- $\text{NO}_x$  conditions, and the fraction of alkyl-substituted dihydrofuran that reacts with  $\text{O}_3$  in the  $\text{O}_3$ -dominant regime (Sect. 4.1); (2) measure the time-dependent evolution of cyclic hemiacetal and alkyl-substituted dihydrofuran at 3 %,

10, 20, and 50 % RH (Sect. 4.2); (3) propose gas-phase products that are unique to dihydrofuran chemistry based on the CIMS speciation (Section 4.3); (4) compare particle-phase chemical composition under OH-dominant vs.  $\text{O}_3$ -dominant environments via identifying AMS measured ions representative of dihydrofuran oxidation products (Sect. 4.4); and (5) estimate the change in SOA yield and elemental composition by incorporating the complete substituted-dihydrofuran formation and removal pathways into the dodecane SOA prediction model (Sect. 4.5).

##### 4.1 Predicted substituted dihydrofuran formation and reaction with ozone in the dodecane system

To what extent is the formation of substituted dihydrofuran and its subsequent chemistry important in the formation of dodecane SOA? A mechanism simulation was conducted, with initial conditions similar to those employed in the chamber (Table 1), i.e., 200 ppb dodecane, 1.5 ppm  $\text{H}_2\text{O}_2$ , 100 ppb  $\text{O}_3$ , and 100 ppb + 30 ppb  $\text{h}^{-1}$   $\text{NO}$  for high- $\text{NO}_x$  conditions and 200 ppb dodecane, 4 ppm  $\text{H}_2\text{O}_2$ , 100 ppb  $\text{O}_3$ , and 0 ppb  $\text{NO}_x$  for low- $\text{NO}_x$  conditions. Figure 3 shows the predicted mass distribution of  $\delta$ -hydroxycarbonyl, alkyl-substituted dihydrofuran, together with other products of the same generation.  $\delta$ -hydroxycarbonyl is predicted to account for  $> 90\%$  total organic mass of first-generation products under high- $\text{NO}_x$  conditions (see Fig. 3a (H)), but  $< 5\%$  to the total organic mass of the third-generation products under low- $\text{NO}_x$  conditions (see Fig. 3a (L)). Inclusion of the

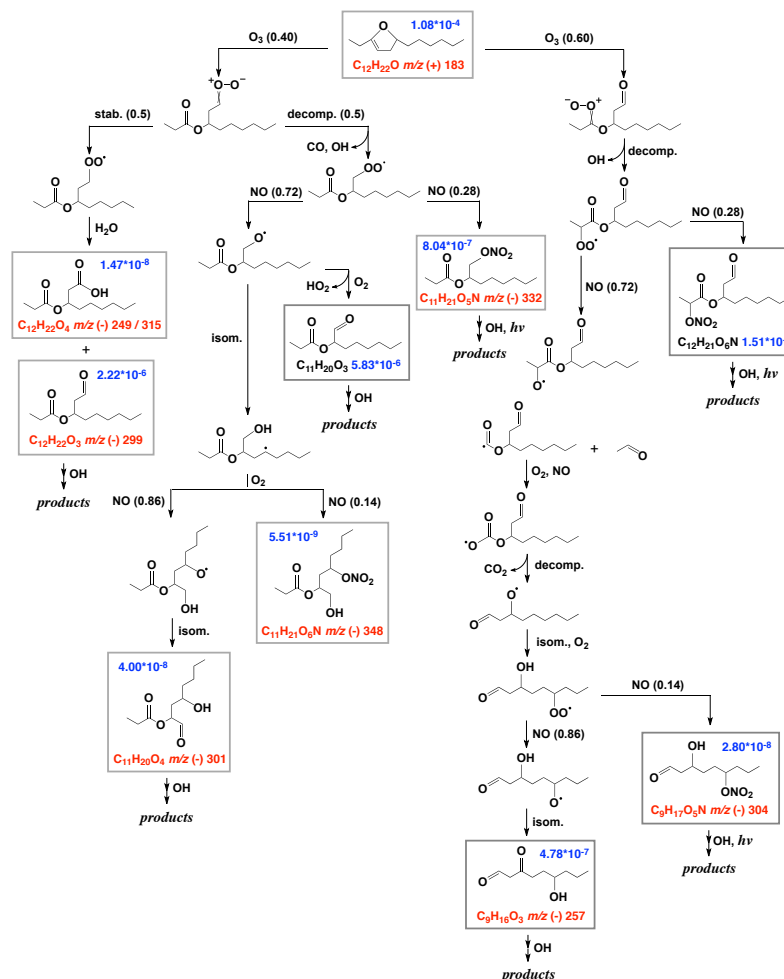


**Fig. 2b.** Proposed mechanism for the ozonolysis of alkyl-substituted dihydrofuran under high- $\text{NO}_x$  conditions. The boxes indicate compounds or reaction pathways incorporated in the model simulation. CIMS monitored species have  $m/z$  noted in red. Estimated vapor pressure (atm) of each compound is indicated in blue.

heterogeneous conversion pathway from  $\delta$ -hydroxycarbonyl to alkyl-substituted dihydrofuran is predicted to result in a rapid consumption of  $\delta$ -hydroxycarbonyl under dry conditions, as opposed to a slow decay from OH oxidation. Alkyl-substituted dihydrofuran accounts for up to 70 % of the decay of  $\delta$ -hydroxycarbonyl, as shown in Fig. 3b (H). As discussed earlier, an ozonolysis-dominant environment occurs for  $\text{O}_3 > 3$  ppb at a typical OH concentration of  $1.0 \times 10^6$  molecules  $\text{cm}^{-3}$ . In the high- $\text{NO}_x$  simulation case, ozone is predicted to lead to 82–98 % of the total alkyl-

substituted dihydrofuran loss over the course of photooxidation; see Fig. 3d (H).

The alkyl-substituted dihydrofuran is not the only product that contains a dihydrofuran structure in the dodecane photooxidation system. The first-generation product 3-dodecyl nitrate under high- $\text{NO}_x$  conditions is an example. Three pathways exist that could produce semivolatile compounds containing a dihydrofuran structure from the further photochemical reaction of 3-dodecyl nitrate: (1) photolysis of the  $-\text{ONO}_2$  group leads to an alkyl-substituted dihydrofuran, (2) abstraction of an H atom by OH potentially leads to an

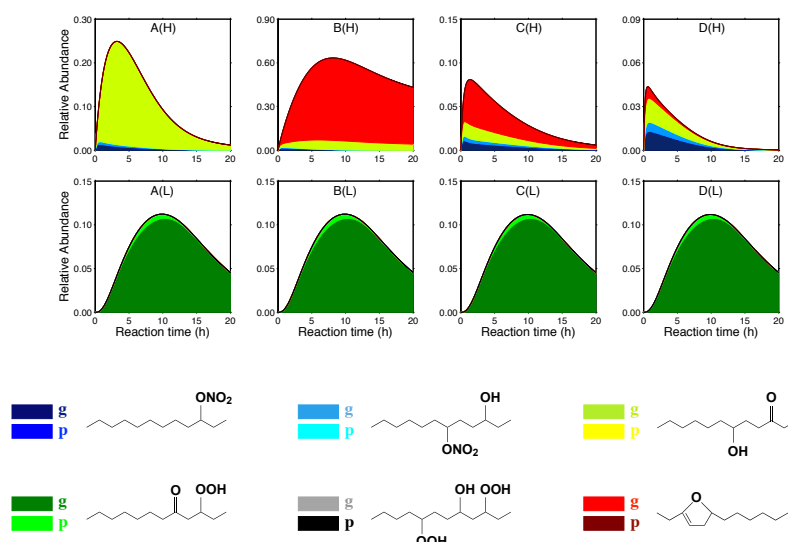


**Fig. 3.** Model-predicted relative abundance of  $\delta$ -hydroxycarbonyl and alkyl-substituted dihydrofuran, together with other first-generation products under high- $\text{NO}_x$  (H) and other third-generation products under low- $\text{NO}_x$  (L) conditions in gas (g) and particle (p) phases. All the organic masses are normalized by the initial organic mass ( $\sim 200$  ppb dodecane). (A) represents the relative abundance of products without a heterogeneous alkyl-substituted dihydrofuran formation channel, (B) represents the relative abundance of products when the heterogeneous channel is incorporated into the scheme but in the absence of any sink of alkyl-substituted dihydrofuran, (C) represents the relative abundance of products when the OH oxidation is the only sink of alkyl-substituted dihydrofuran, and (D) represents the relative abundance of products using the complete gas- and particle-phase mechanism.

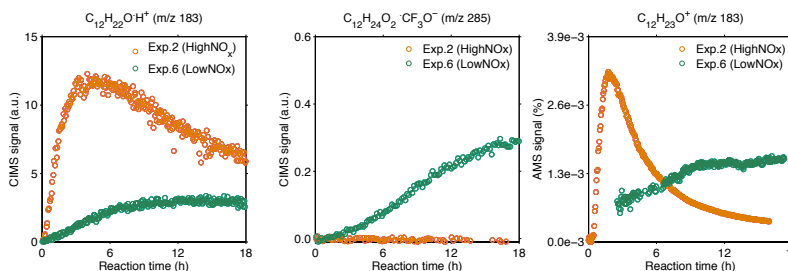


**Fig. 4.** Temporal profiles of ion  $\text{C}_{12}\text{H}_{22}\text{O}\cdot\text{H}^+$  ( $m/z = 183$ ) and  $\text{C}_{12}\text{H}_{24}\text{O}_2\cdot\text{CF}_3\text{O}^-$  ( $m/z = 285$ ) measured by CIMS and ion  $\text{C}_{12}\text{H}_{23}\text{O}^+$  ( $m/z = 183$ ) measured by AMS under high- and low- $\text{NO}_x$  conditions. Details of experimental conditions are given in Table 1.

organonitrate-substituted dihydrofuran, and (3) H-atom abstraction from a C atom with the  $-\text{ONO}_2$  functional group attached and further H-atom abstraction from a C atom potentially leads to a carbonyl-substituted dihydrofuran. It is worth noting that the gas-phase ozonolysis of alkyl-substituted dihydrofuran under high- $\text{NO}_x$  conditions contributes to most of the ozonolysis reactions because the alkyl-substituted dihydrofuran is a major first-generation product, as shown in Fig. 3b (H).

#### 4.2 Formation of cyclic hemiacetals and alkyl-substituted dihydrofuran

CIMS measurement at  $(+)\text{m/z } 183$  in positive mode represents the ion  $\text{C}_{12}\text{H}_{22}\text{O}\cdot\text{H}^+$  generated from the proton transfer reaction with alkyl-substituted dihydrofuran ( $M_w = 182$ ). An additional source of  $(+)\text{m/z } 183$  is the proton transfer reaction followed by dehydration of hydroxyl dodecanone ( $M_w = 200$ ), which is also detected as a fluoride cluster product at  $(-)\text{m/z } 285$  ( $\text{C}_{12}\text{H}_{24}\text{O}_2\cdot\text{CF}_3\text{O}^-$ ) in negative

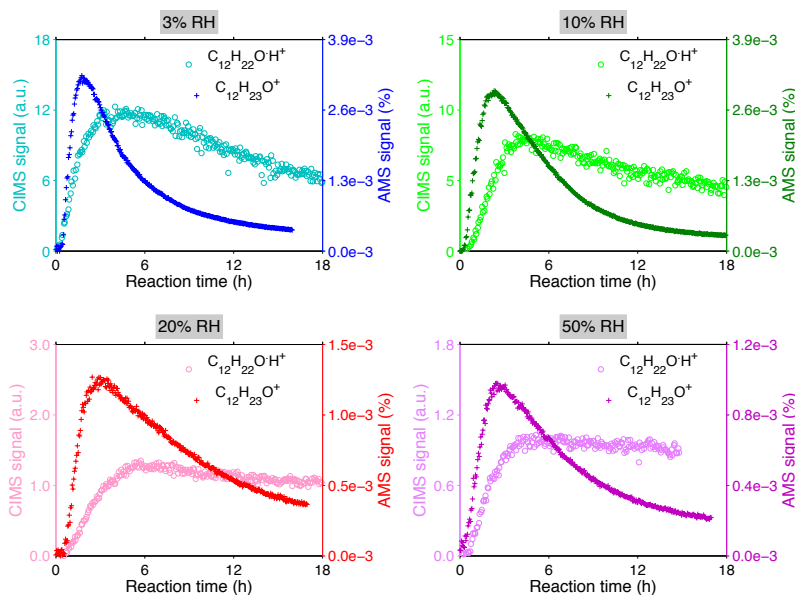


**Fig. 5.** Time-dependent evolution of ion  $\text{C}_{12}\text{H}_{22}\text{O} \cdot \text{H}^+$  ( $m/z = 183$ ) measured by CIMS and ion  $\text{C}_{12}\text{H}_{23}\text{O}^+$  ( $m/z = 183$ ) measured by AMS at 3, 10, 20, and 50% RH.

mode. Figure 4 shows temporal profiles of  $(+)\text{m}/z$  183 and  $(-)\text{m}/z$  285 monitored under both high- and low- $\text{NO}_x$  conditions (Exp. 2 vs. Exp. 6). The  $(+)\text{m}/z$  183 ion was detected in each of the two experiments, but with distinct time-dependent patterns. Under high- $\text{NO}_x$  conditions,  $(+)\text{m}/z$  183 peaks during the first 3 h of irradiation, indicating fast formation of alkyl-substituted dihydrofuran, and decays during the next 15 h of photooxidation. Under low- $\text{NO}_x$  conditions, however, the  $(+)\text{m}/z$  183 signal eventually reaches a plateau, which is more consistent with the pattern of  $(-)\text{m}/z$  285. This behavior is consistent with the mechanism prediction that the alkyl-substituted dihydrofuran is formed in significant amounts only under high- $\text{NO}_x$  conditions (Fig. 3b (H)). An alternative explanation for the temporal profiles of  $(+)\text{m}/z$  183 under low- $\text{NO}_x$  conditions is that this ion is formed by dehydration of the cyclic hemiacetal following protonation in CIMS. The occurrence of a plateau could be indicative of an absence of dehydration in the particle phase due to the lack of an acid catalyst (no  $\text{HNO}_3$  formation from  $\text{NO}_2 + \text{OH}$  reaction as in the high- $\text{NO}_x$  cases). However, based on the model prediction, cyclic hemiacetal is not likely to accumulate since the formation of its precursor,  $\delta$ -hydroxycarbonyl, is a minor pathway when the  $\text{RO}_2 + \text{HO}_2$  reaction is dominant and the photolysis of the resulting peroxide is not important.

The AMS measured  $m/z$  183 ( $\text{C}_{12}\text{H}_{23}\text{O}^+$ ) is the major characteristic ion for cyclic hemiacetal. This ion is produced by the neutral loss of OH ( $M_w = 17$ ) from the 2 po-

sition in the cyclic hemiacetal ( $M_w = 200$ ) during electron ionization (Gong et al., 2005; Lim and Ziemann, 2009c). In addition, the  $\text{C}_{12}\text{H}_{23}\text{O}^+$  ion is suggested to be the characteristic fragment of carbonyl-hydroperoxide-derived peroxyhemiacetal (Yee et al., 2012). The temporal profiles of the  $\text{C}_{12}\text{H}_{23}\text{O}^+$  ion under both high- and low- $\text{NO}_x$  conditions (Exp. 2 vs. Exp. 6) exhibit distinct growth patterns (Fig. 4). Under high- $\text{NO}_x$  conditions, the  $\text{C}_{12}\text{H}_{23}\text{O}^+$  ion signal increases rapidly to a maximum during the first 2 h and decays over the next  $\sim 14$  h. The temporal behavior of the  $\text{C}_{12}\text{H}_{23}\text{O}^+$  ion is a result of its rapid formation, i.e., uptake of  $\delta$ -hydroxycarbonyl onto particles and subsequent cyclization, and relatively slower removal, i.e., dehydration. Under low- $\text{NO}_x$  conditions, the  $\text{C}_{12}\text{H}_{23}\text{O}^+$  ion increases over the course of a 20 h experiment because of the accumulative formation of peroxyhemiacetal. During the first 3 h of irradiation under low- $\text{NO}_x$  conditions, the organic loading is below the AMS detection limit; thus the  $\text{C}_{12}\text{H}_{23}\text{O}^+$  ion signal does not appear in Fig. 4 during this period. The  $\text{C}_{12}\text{H}_{23}\text{O}^+$  ion signal under low- $\text{NO}_x$  conditions therefore potentially represents peroxyhemiacetal, since the formation of peroxides is the major reaction pathway in the  $\text{RO}_2 + \text{HO}_2$  dominant regime. This is again consistent with the mechanism prediction that the formation of alkyl-substituted dihydrofuran is unimportant under low- $\text{NO}_x$  conditions (Fig. 3b (L)).

Figure 5 shows temporal profiles of the ion  $\text{C}_{12}\text{H}_{22}\text{O} \cdot \text{H}^+$  detected by CIMS and the ion  $\text{C}_{12}\text{H}_{23}\text{O}^+$  detected by AMS

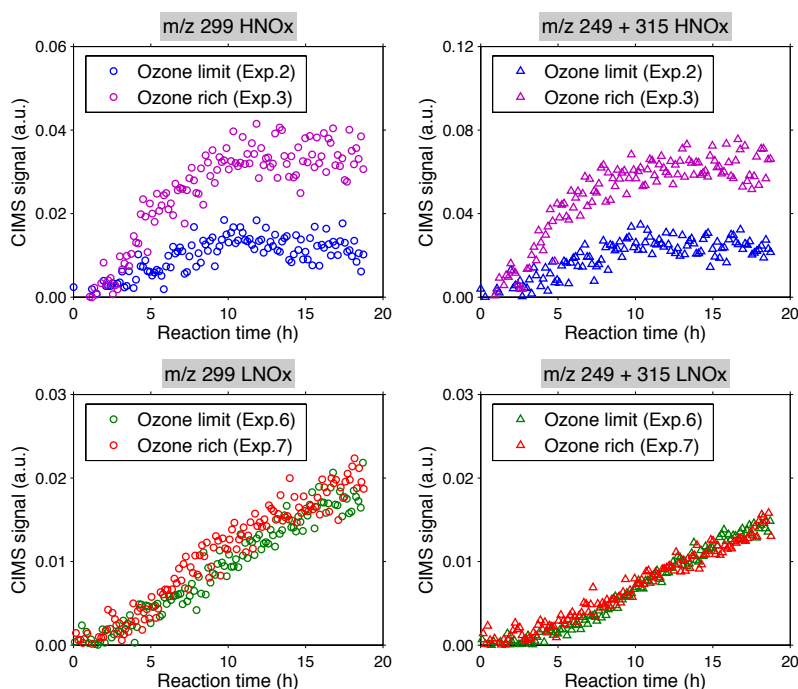


**Fig. 6.** Time-dependent evolution of CIMS measured signals at  $m/z$  299, and  $m/z$  249 and 315, as a function of  $O_3$  levels under high- and low- $NO_x$  conditions over the course of 20 h photooxidation.

in the presence of  $NO_x$  under varying RH. In general, the AMS ion  $C_{12}H_{23}O^+$  peaks  $\sim 3$  h earlier than the CIMS ion  $C_{12}H_{22}O \cdot H^+$ . The decay rates of AMS ion  $C_{12}H_{23}O^+$ , which is calculated by assuming first-order kinetics, are  $4.02 \times 10^{-3}$ ,  $3.06 \times 10^{-3}$ ,  $1.71 \times 10^{-3}$ , and  $1.37 \times 10^{-3} s^{-1}$  at RH of 3, 10, 20, and 50 %, respectively. Aerosol water content could slow down the formation and removal rate of AMS ion  $C_{12}H_{23}O^+$ , mainly because (1) water could accelerate the hydration rate, thus changing the equilibrium coefficient of the interconversion between cyclic hemiacetal and dihydrofuran, and (2) the addition of water might neutralize the particle-phase acid (e.g.,  $HNO_3$ ), which is thought to catalyze the cyclization of  $\delta$ -hydroxycarbonyl to cyclic hemiacetal (Lim and Ziemann, 2009c). The decay rates of AMS ion  $C_{12}H_{23}O^+$  are within the same order of magnitude of that measured for 5-hydroxy-2-pentanone at 3 % RH, indicating that the dehydration of cyclic hemiacetal is the rate-limiting step in the overall heterogeneous conversion process. Water vapor influences CIMS sensitivity to certain compounds in negative mode by clustering with the reagent ion  $CF_3O^-$  to form  $[H_2O \cdot CF_3O]^-$ . The decreasing intensity of the ion  $C_{12}H_{22}O \cdot H^+$  as RH increases is likely indicative of this effect.

#### 4.3 Products from alkyl-substituted dihydrofuran oxidation

Products unique to the alkyl-substituted dihydrofuran oxidation chemistry have been proposed based on CIMS measured  $m/z$  signals; see Table 2 for chemical structures. Authentic standards are not commercially available for these products. Compounds from the dodecane photooxidation route that share the same  $m/z$  signal with alkyl-substituted dihydrofuran oxidation products are also presented in Table 2. The CIMS signal ( $-$ ) $m/z$  346 is composed of 2-nitroso-2-alkyl-3-hydroxyl-5-heptyl-tetrahydrofuran and 2-carbonyl-5-hydroxyl-2-dodecyl-nitrate. The latter is a third-generation product resulting from the further oxidation of dodecyl nitrate. The branching ratio for the addition of an  $-ONO_2$  group is much lower than that for the formation of the RO radical; therefore the interference of 2-carbonyl-5-hydroxyl-2-dodecyl-nitrate in the ( $-$ ) $m/z$  346 signal can be neglected. The CIMS signal ( $-$ ) $m/z$  299 represents 3-propoxy-nonanal, which is a primary product from both OH oxidation and ozonolysis of alkyl-substituted dihydrofuran, and 8-hydroxy-3,5-dodecanedione, which is produced from the further oxidation of dodecyl nitrate. As discussed earlier,

**Table 2.** Proposed structures for CIMS ions unique to the alkyl-substituted dihydrofuran chemistry. C and T indicate the cluster and transfer product, respectively. Commercial standards are not available.

| Observed $m/z$ | Product | Chemical formula   | Proposed structure | Chemical pathway           | Interference |
|----------------|---------|--------------------|--------------------|----------------------------|--------------|
| 183(+)         | T       | $C_{12}H_{22}O$    |                    | Heterogeneous conversion   |              |
| 328(-)         | C       | $C_{12}H_{21}NO_4$ |                    | Heterogeneous conversion   | —            |
| 346(-)         | C       | $C_{12}H_{23}NO_5$ |                    | OH-oxidation               |              |
| 299(-)         | C       | $C_{12}H_{22}O_3$  |                    | OH-oxidation<br>Ozonolysis |              |
| 249(-)         | T       | $C_{12}H_{22}O_4$  |                    | Ozonolysis                 | —            |
| 315(-)         | C       | $C_{12}H_{22}O_4$  |                    | Ozonolysis                 | —            |
| 332(-)         | C       | $C_{11}H_{21}O_5N$ |                    | Ozonolysis                 | —            |
| 348(-)         | C       | $C_{11}H_{21}O_6N$ |                    | Ozonolysis                 | —            |
| 301(-)         | C       | $C_{11}H_{20}O_4$  |                    | Ozonolysis                 | —            |

the formation and transformation of dodecyl nitrate is predicted to be a minor pathway, and thus the  $(-)m/z$  299 is dominated by 3-propoxy-nonanal.

A distinct feature of proposed products from the dihydrofuran oxidation by either OH or  $O_3$  is the formation of an ester group ( $-C(O)O-$ ) or an ether group ( $-O-$ ), both of which cannot be accessed from photochemical reaction pathways initiated by the OH attack on the aliphatic hydrocar-

bon. The OH oxidation channel leads solely to the formation of tetrahydrofuran and carbonyl ester. In the ozonolysis pathway, on the other hand, the reaction of stabilized Criegee intermediates with water produces one ester group containing aldehyde (3-propoxy-nonanal) and carboxylic acid (3-propoxy-nonanoic acid); see proposed structures in Table 2. From the intact  $C_{12}$  skeleton and highly oxygenated nature, these two products are consistent with CIMS signals in

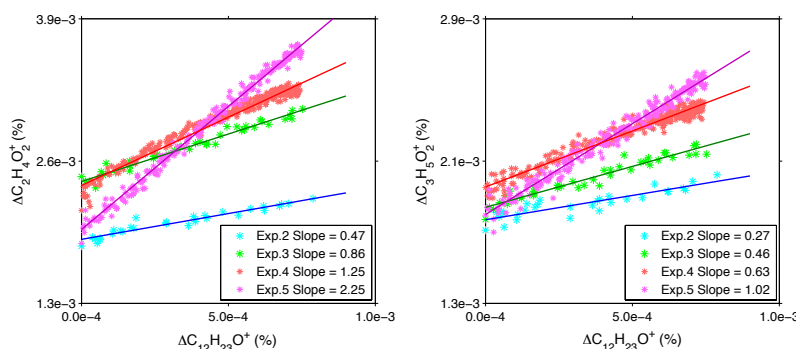


Fig. 7. Time-dependent evolution of AMS measured ion intensities of  $\text{C}_2\text{H}_4\text{O}_2^+$  and  $\text{C}_3\text{H}_5\text{O}_2^+$  as a function of decay of the  $\text{C}_{12}\text{H}_{23}\text{O}^+$  signal.

( $-$ ) $m/z$  299 and ( $-$ ) $m/z$  249 and 315 in negative mode with little interference from other products.

Figure 6 shows the temporal profiles of ( $-$ ) $m/z$  299, as well as ( $-$ ) $m/z$  249 and 315, under “ $\text{O}_3$ -limiting” (Exp. 2) and “ $\text{O}_3$ -rich” (Exp. 3) conditions. The decay rates of their precursor (+) $m/z$  183, as calculated by assuming first-order kinetics, are  $1.19 \times 10^{-5} \text{ s}^{-1}$  and  $1.44 \times 10^{-5} \text{ s}^{-1}$ , respectively. Under  $\text{O}_3$ -rich conditions, both species increase and eventually level off. When  $\text{O}_3$  reaction is less competitive, the CIMS signals start to decrease after 10 h of photooxidation. Note that these three ions were also detected under low- $\text{NO}_x$  conditions. No significant increase in their signals was observed in the  $\text{O}_3$ -rich environment (Exp. 7), compared with the  $\text{O}_3$ -limiting case (Exp. 6). If they were assigned the same chemical structures as those proposed under high- $\text{NO}_x$  conditions, their growth pattern would suggest a minor formation of their precursor alkyl-substituted dihydrofuran. This can be attributed to the slowdown or even termination of the dehydration of cyclic hemiacetal in the absence of strong acid catalysis (Atkinson et al., 2008; Lim and Ziemann, 2009c).

#### 4.4 Ozonolysis vs. OH oxidation

Carboxylic acids produce significant signals at  $m/z$  60 and 73, specifically  $\text{C}_2\text{H}_4\text{O}_2^+$  and  $\text{C}_3\text{H}_5\text{O}_2^+$ , in the AMS measurement (Aiken et al., 2008). The formation of these two ions, as a function of the time-dependent decay of the ion  $\text{C}_{12}\text{H}_{23}\text{O}^+$ , is shown under different RH conditions in Fig. 7. The largest slope of either  $\Delta\text{C}_2\text{H}_4\text{O}_2^+ / \Delta\text{C}_{12}\text{H}_{23}\text{O}^+$  or  $\Delta\text{C}_3\text{H}_5\text{O}_2^+ / \Delta\text{C}_{12}\text{H}_{23}\text{O}^+$  is associated with the highest RH, i.e., 50 %. However, the production of  $\text{C}_2\text{H}_4\text{O}_2^+$  and  $\text{C}_3\text{H}_5\text{O}_2^+$  is not significant under dry conditions. Also, the changes in slopes along with changes in RH values are consistent for both ions. This indicates that the formation of the carboxylic acid functional group detected in particles is associated with the water vapor concentration in the gas phase, consistent with the reaction of the stabilized Criegee interme-

diates with water in the substituted dihydrofuran oxidation system.

Two dominant oxygen-containing ions,  $m/z$  44 (mostly  $\text{CO}_2^+$ ) and  $m/z$  43 ( $\text{C}_3\text{H}_7^+$  and  $\text{C}_2\text{H}_3\text{O}^+$ ), have been widely used to characterize organic aerosol evolution in chamber and field observations. Previous studies have shown that  $\text{CO}_2^+$  results mostly from the thermal decarboxylation of an organic acid group (Alfarra, 2004). The  $f_{44}$  (ratio of  $m/z$  44, mostly  $\text{CO}_2^+$ , to total signal in the component mass spectrum) axis is also considered to be an indicator of photochemical aging (Alfarra et al., 2004; Aiken et al., 2008; Kleinman et al., 2008). It has been found that increasing OH exposure increases  $f_{44}$  and decreases  $f_{43}$  (ratio of  $m/z$  43, mostly  $\text{C}_2\text{H}_3\text{O}^+$ , to total signal in the component mass spectrum) for SOA generated from gas-phase alkanes (Lambe et al., 2011). The  $\text{C}_2\text{H}_3\text{O}^+$  ion at  $m/z$  43 is assumed predominantly due to nonacid oxygenates, such as saturated carbonyl groups (Ng et al., 2011). The evolution of dodecane SOA from four experiments (Table 1), characterized by different OH and  $\text{O}_3$  exposure, and different RH levels, is shown in  $f_{\text{CO}_2^+} - f_{\text{C}_2\text{H}_3\text{O}^+}$  space in Fig. 8. Overall, high- $\text{NO}_x$  dodecane SOA lies to the lower left of the triangular region derived for ambient SOA. The relatively high organic loading ( $\sim 200$  ppb dodecane) employed in this study favors partitioning of less oxidized species, which would remain in the gas phase under atmospheric conditions. For each experiment,  $f_{\text{CO}_2^+}$  decreases and  $f_{\text{C}_2\text{H}_3\text{O}^+}$  increases with increasing SOA at the beginning of irradiation. After several hours of photooxidation, the trends reverse, resulting in increasing  $f_{\text{CO}_2^+}$  and decreasing  $f_{\text{C}_2\text{H}_3\text{O}^+}$ . Curvature in  $f_{\text{CO}_2^+} - f_{\text{C}_2\text{H}_3\text{O}^+}$  space has been also observed in other chamber/flow reactor studies (Kroll et al., 2009; Ng et al., 2010; Chhabra et al., 2011; Lee et al., 2011; Lambe et al., 2011). When the organic loading is small, only the highly oxygenated and least volatile species partition to the particle phase. As particles grow, more volatile and less oxidized species are able to



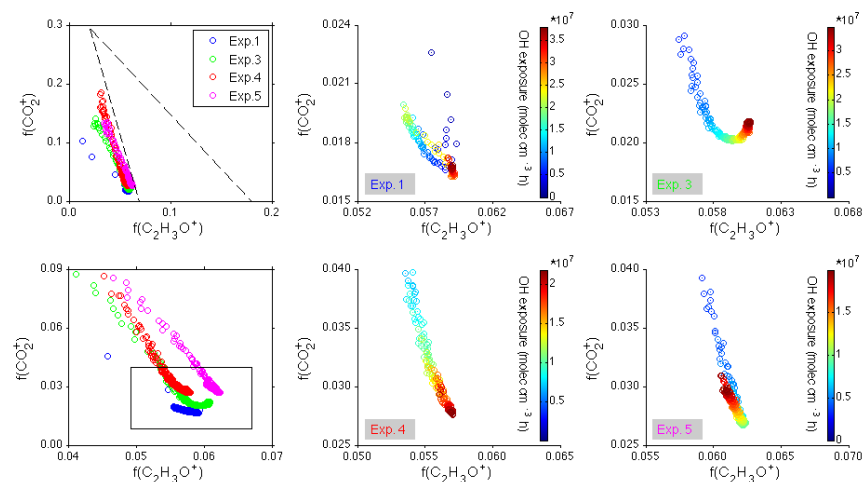


**Fig. 8.** SOA evolution as a function of OH exposure vs.  $\text{O}_3$  exposure from dodecane photochemistry under high- $\text{NO}_x$  conditions in the  $f_{44}$  vs.  $f_{43}$  space. The top-left graph shows the combination of all the data, and the bottom-left graph shows an expanded version. The other graphs show the specific behavior of each experiment: Exp. 1 corresponds to a regime in which OH oxidation of dihydrofuran is dominant. Exp. 3, 4, and 5 correspond to a regime in which ozonolysis of dihydrofuran is dominant, at 10, 20, and 50 % RH, respectively.

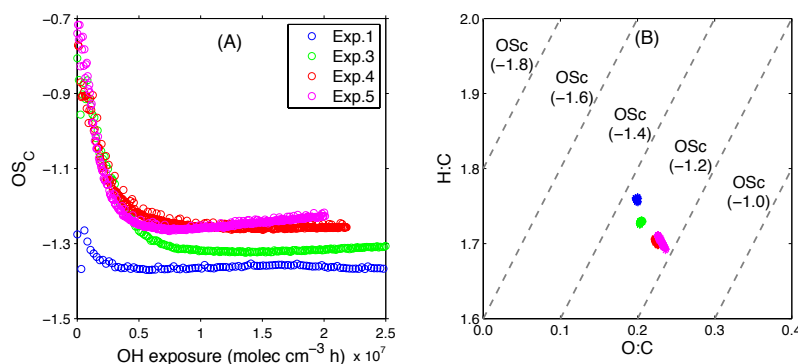


**Fig. 9.** (A) SOA average carbon oxidation state as a function of OH exposure from dodecane photochemistry under high- $\text{NO}_x$  conditions. Exp. 1 corresponds to a regime in which OH oxidation of dihydrofuran is dominant. Exp. 3, 4, and 5 correspond to a regime in which ozonolysis of dihydrofuran is dominant, at 10, 20, and 50 % RH, respectively. (B) van Krevelen diagram. AMS measured O : C vs. H : C ratios for the four experiments under the OH total exposure ranging from  $1.0 \times 10^7$  to  $2.0 \times 10^7$  molecules  $\text{cm}^{-3}$  h. Gray dashed lines denote the average carbon oxidation state.

participate in equilibrium partitioning, leading to a decrease in  $f_{\text{CO}_2^+}$ . Progressive oxidation of semivolatile products in the gas phase eventually leads to multifunctionalized species contributing to the increase of  $f_{\text{CO}_2^+}$ .

Both  $\text{O}_3$ - and OH-initiated oxidation of substituted dihydrofuran lead to the formation of  $f_{\text{CO}_2^+}$ , via the thermal decarboxylation of an organic acid group and photochemical aging, respectively. The contribution of each reaction path-

way to the intensity of  $f_{\text{CO}_2^+}$  can be evaluated based on the  $f_{\text{CO}_2^+} - f_{\text{C}_2\text{H}_3\text{O}^+}$  plot. As discussed in Sect. 2.1, Exp. 1 is designed as an OH-dominant case, in which it is estimated that >73 % of the dihydrofuran reacts with OH over the course of the experiment. Exp. 3, 4, and 5 were designed to be  $\text{O}_3$ -dominant at 10 %, 20 %, and 50 % RH, respectively. Approximately 96, 97, and 98 % of substituted dihydrofuran is predicted to react with  $\text{O}_3$  when it peaks after  $\sim 3$  h of photooxidation in Exp. 3, 4, and 5, respectively.

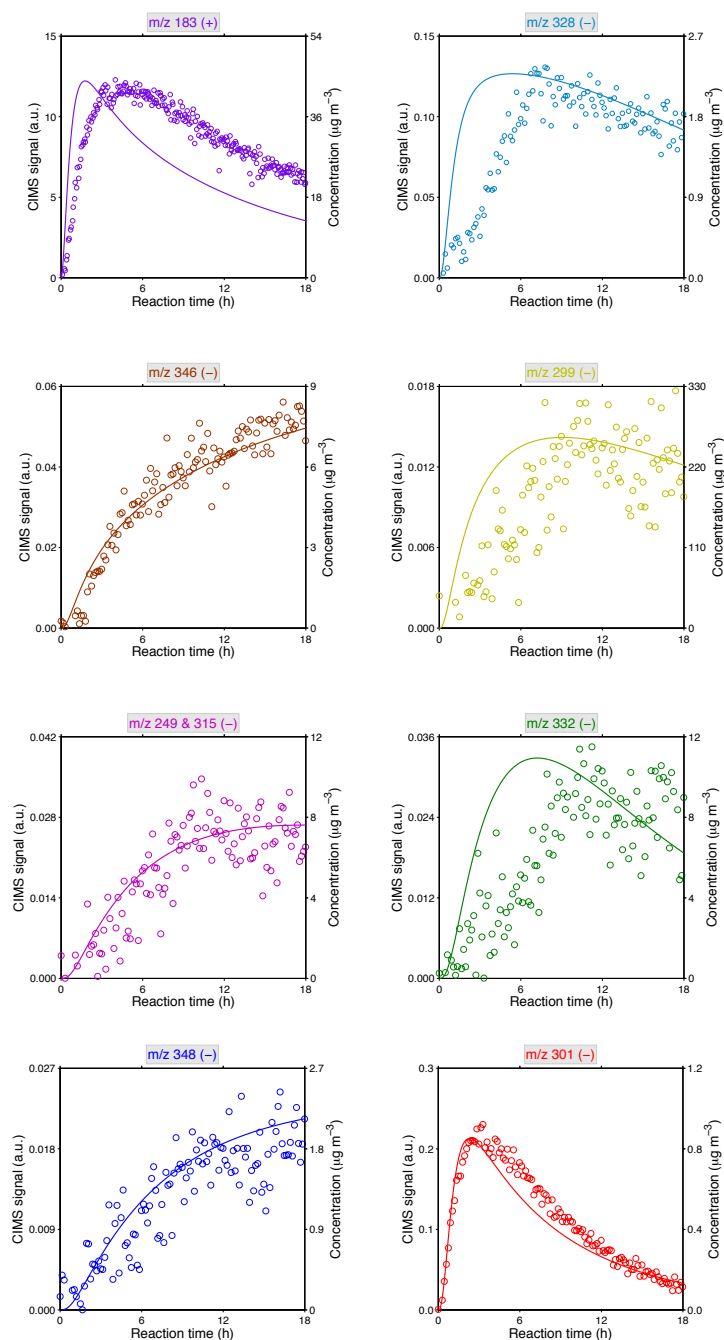


**Fig. 10.** Comparison of CIMS measured ions in positive and negative mode, with chemical structures proposed in Table 2, with model simulations using experimental conditions of Exp. 2.

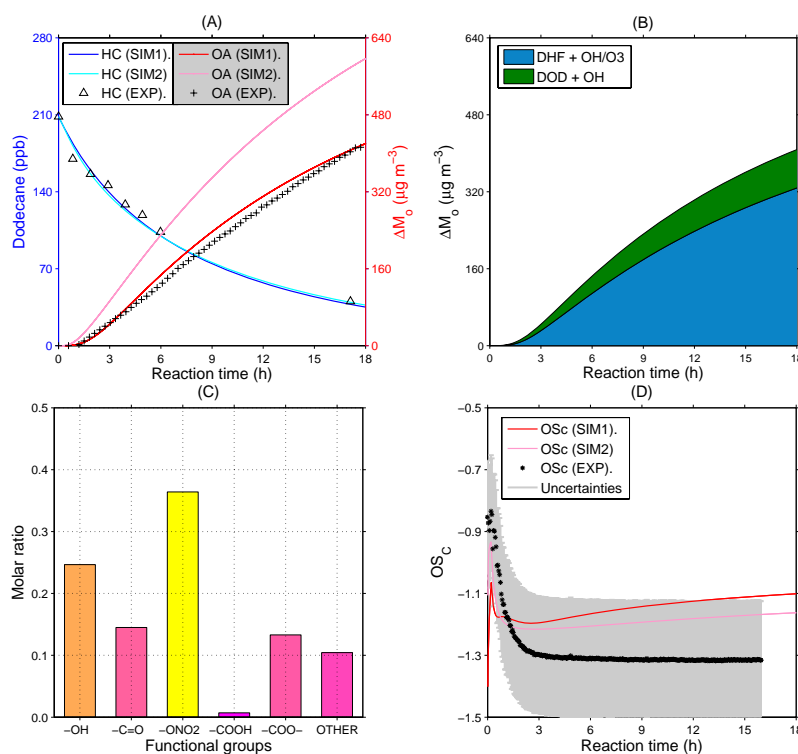


**Fig. 11.** (A) Comparison of the predicted dodecane decay and SOA growth with observations (Exp. 2). SIM1 represents the full mechanism simulations under initial conditions of Exp. 2. SIM2 is the simulations in the absence of the substituted dihydrofuran formation channel. (B) The contribution of dihydrofuran chemistry (DHF+OH/O<sub>3</sub>) vs. dodecane photochemistry (DOD+OH) to the total organic mass. (C) Molar fractions of major functional groups after 3 h of photochemical reaction (when alkyl-substituted dihydrofuran peaks and organic loading is  $\sim 50 \mu\text{g m}^{-3}$ ) as predicted by SIM1. Note that “other” includes dihydrofuran, tetrahydrofuran, and ether moieties. (D) Comparison of the predicted average carbon oxidation state with observations (Exp. 2).

As shown in Fig. 8, the intensities of  $f_{\text{CO}_2^+}$  in Exp. 1, 3, 4, and 5 are 0.019, 0.020, 0.028, and 0.030, respectively, at the same OH exposure, i.e.,  $2 \times 10^7$  molecules  $\text{cm}^{-3}$  h. The increase in  $f_{\text{CO}_2^+}$  intensities results from the increasing O<sub>3</sub> and RH levels in these four experiments. Overall, Exp. 1 exhibits the least intensity of  $f_{\text{CO}_2^+}$  at the end of the experiment, i.e., 0.017, although the total OH exposure is the highest, i.e.,  $3.8 \times 10^7$  molecules  $\text{cm}^{-3}$  h. The total OH exposures for Exp. 3, 4, and 5 are  $3.5 \times 10^7$ ,  $2.2 \times 10^7$ , and  $2.1 \times 10^7$  molecules  $\text{cm}^{-3}$  h, respectively, which are less than that in Exp. 1. However, the intensities of  $f_{\text{CO}_2^+}$  for these three experiments are 35–82 % higher than that in Exp. 1 at the end of experiments. In addition, the intensity of  $f_{\text{CO}_2^+}$  increases along with increasing RH and O<sub>3</sub> exposure for these three experiments, varying from 0.023 to 0.031. The highest  $f_{\text{CO}_2^+}$  intensity shown in Exp. 5 corresponds to the highest O<sub>3</sub> exposure and RH level, but lowest OH exposure.

The difference in elemental composition of organic particles produced from O<sub>3</sub>-dominant vs. OH-dominant environments is also examined via the AMS measured O:C and H:C ratios in the van Krevelen plot and the time-dependent evolution of the average carbon oxidation state ( $OS_C = 2 \times \text{O:C} - \text{H:C}$ ; see Fig. 9). In general, the  $OS_C$  values calculated fall into a region characterized by oxidized primary organic aerosol and semivolatile oxidized organic aerosol (Kroll et al., 2011). The measured O:C ( $\sim 0.2$ ) and H:C ( $\sim 1.7$ ) ratios at an OH exposure on the order of  $\sim 10^7$  molecules  $\text{cm}^{-3}$  h agree with those measured for organic aerosols generated from C<sub>10</sub>–C<sub>17</sub> alkanes (Lambe et al., 2011, 2012). As mentioned earlier, the four experiments (Exp. 1, 3, 4, and 5) were conducted in such a way that the total OH exposure is decreasing, whereas the total O<sub>3</sub> and RH exposure is increasing along with increasing experimental numbers (for example, Exp. 5 has the least

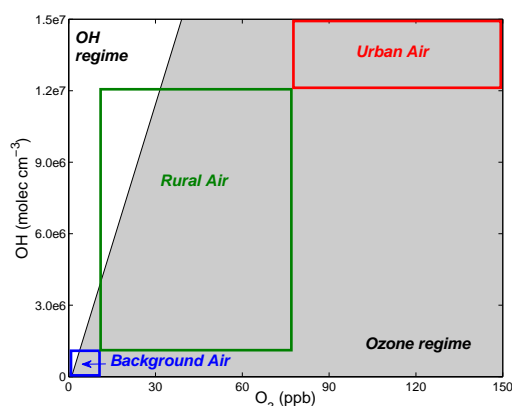


**Fig. 12.** Regimes of dominance of ozonolysis vs. OH oxidation of substituted dihydrofuran. Daily maximum OH concentrations vary by regions in the troposphere, i.e.,  $10^5$ – $10^6$  molecules  $\text{cm}^{-3}$  for background air,  $10^6$ – $10^7$  molecules  $\text{cm}^{-3}$  for rural air, and  $>10^7$  molecules  $\text{cm}^{-3}$  for urban air, with a global average concentration of  $1 \times 10^6$  molecules  $\text{cm}^{-3}$ . Daily average surface ozone mixing ratios in rural areas are between 10 and 50 ppb, but these can exceed 100 ppb in polluted urban areas.

OH exposure but the largest  $\text{O}_3$  and RH exposure). A clear trend observed from the van Krevelen plot is that O:C increases, whereas H:C decreases under elevated  $\text{O}_3$  and RH levels. The effect of ozonolysis of substituted dihydrofuran chemistry on the aerosol chemical composition can be evaluated by comparing  $\text{OS}_C$  (O:C vs. H:C) for these four experiments under the same OH exposure. Consistent with our findings in  $f_{\text{CO}_2^+} - f_{\text{C}_2\text{H}_5\text{O}^+}$  space, the highest  $\text{OS}_C$  is observed under the highest  $\text{O}_3$  exposure and RH level, but lowest OH exposure (98 % substituted dihydrofuran reacts with  $\text{O}_3$  at 55 % RH). With the same OH exposure, e.g.,  $1.5 \times 10^7$  molecules  $\text{cm}^{-3}$  h, the average carbon oxidation state increases from  $-1.36$  in  $\text{O}_3$ -limiting environments (Exp. 1) to  $-1.25$  in  $\text{O}_3$ -dominant environments (Exp. 5). In conclusion, ozonolysis of substituted dihydrofuran plays an important role in the formation of highly oxidized aerosol in alkane SOA.

#### 4.5 Experiment and model comparison

Figure 10 shows the temporal profiles of CIMS measured ions in (+/–) mode, with structures proposed in Table 2, together with the corresponding model predictions under conditions of Exp. 2. In general, four time-dependent growth patterns are observed in experiments, which are also captured by model predictions. “Pattern 1” denotes species with rapid removal pathways, e.g.,  $m/z$  301 (–), with a proposed structure of  $\delta$ -hydroxycarbonyl. In the current mechanism, the overall heterogeneous conversion rate of  $\delta$ -hydroxycarbonyl

to substituted dihydrofuran is taken as  $3 \times 10^{-3} \text{ s}^{-1}$ . The model output is consistent with the observed time-dependent trend when this rate is used. Up to  $\sim 90\%$  of  $m/z$  301 (–) is consumed due to this rapid heterogeneous reaction pathway at 3 % RH after 18 h of photooxidation. “Pattern 2” is indicative of a species that also reacts rapidly, but with a much slower consumption rate than species of pattern 1. A typical example here is  $m/z$  183 (+), which represents the alkyl-substituted dihydrofuran. The reaction rate constants of alkyl-substituted dihydrofuran with either OH or  $\text{O}_3$  are at least an order of magnitude higher than the generic reaction rate constant for the OH abstraction reaction, which is the dominant gas-phase pathway in the dodecane photooxidation mechanism. The simulated peak occurs  $\sim 2$  h earlier than observations, indicating that the formation rate of alkyl-substituted dihydrofuran might be slower than the decay rate of its precursor,  $\delta$ -hydroxycarbonyl, considering that fact that the acid-catalyzed dehydration process in the particle phase is the rate-limiting step. The extent to which the formation rate is slower than the decay rate, however, is unknown since the measurement of rate constants for individual steps is infeasible in this study. “Pattern 3” reflects the temporal profiles for a majority of ions here, e.g.,  $m/z$  328(–), 299(–), 249(–), 315(–), and 332(–). Compounds proposed for the above  $m/z$  can be categorized as semivolatile products. In the gas phase, they undergo functionalization or fragmentation, or partition into the particle phase as the precursors of SOA. Overall, the temporal profiles of species in pattern 3 are governed by the progressive photochemistry in the gas phase and gas–particle equilibrium partitioning. “Pattern 4”, including  $m/z$  346 (–) and 328 (–) here, represents “non-volatile” species. Owing to their low volatilities, they will immediately partition to the particle phase once formed and the gas-phase photooxidation becomes negligible, although it might still occur via the OH attack on C atoms.

Figure 11a shows the simulated SOA growth (SIM.1) using the initial conditions in Exp. 2, together with the observed total organic aerosol mass as a function of reaction time and OH exposure. The model reproduces the chamber measured SOA yield at 3 % RH when the conversion rate of  $3 \times 10^{-3} \text{ s}^{-1}$  is employed to represent the heterogeneous conversion of  $\delta$ -hydroxycarbonyl to dihydrofuran. A second simulation (SIM.2) was run with the complete dihydrofuran chemistry removed while other parameters were held constant. The total organic mass is  $\sim 42\%$  higher as a result after 18 h of photooxidation. The formation of alkyl-substituted dihydrofuran from  $\delta$ -hydroxycarbonyl is accompanied by an increase of vapor pressure from  $5.36 \times 10^{-7}$  to  $1.08 \times 10^{-4} \text{ atm}$  at 300 K, as predicted by SIMPOL.1, and the total organic mass formed decreases. Although the addition of OH to the C=C double bond in the substituted dihydrofuran introduces an extra OH group, the decrease of vapor pressure owing to the addition of one OH group does not compensate for the heterogeneous conversion of both  $\text{C=O}$  and  $\text{OH}$  groups in  $\delta$ -hydroxycarbonyl to an  $\text{O-}$  group in

a nonaromatic ring in dihydrofuran. The predicted average carbon oxidation state is  $\sim 7$ –15 % higher than observations. The overprediction is within the uncertainties in the O : C (31 %) and H : C (10 %) measurement by AMS (Aiken et al., 2008). Incorporation of the substituted dihydrofuran formation and removal pathways in the model leads to an increase in the simulated  $OS_C$ . Compared with compounds produced from dodecane photooxidation under high- $NO_x$  conditions, products from dihydrofuran chemistry tend to have a higher O : C but lower H : C due to the formation of ether, ester, and carboxylic acid functional groups. As a result, the calculated average carbon oxidation state is higher in the presence of chemical reactions that accelerate the aerosol aging process.

## 5 Atmospheric implications

The importance of ozone in the SOA formation from the photooxidation of long-chain alkanes under atmospherically relevant conditions depends on two factors: (1) the relative concentration of  $O_3$  vs. OH, and (2) the heterogeneous conversion rate of  $\delta$ -hydroxycarbonyls to substituted dihydrofurans. Figure 12 shows regimes of ozonolysis vs. OH oxidation of substituted dihydrofuran corresponding to ranges of OH and  $O_3$  concentrations. The OH-initiated oxidation of substituted dihydrofuran is predicted to dominate only under remote atmospheric conditions. Most alkane emissions occur in areas where ozone levels exceed 10 ppb, where the ozonolysis of dihydrofuran should be dominant.

Under conditions of the current study, the substituted dihydrofuran chemistry is predicted to account for > 95 % of the removal pathways of  $\delta$ -hydroxycarbonyl (Fig. 1d (H)) and up to  $\sim 80$  % of the total organic mass formed from dodecane photooxidation (Fig. 11b). This estimate sets the upper limit in terms of the contribution of substituted dihydrofuran chemistry to alkane SOA production in the actual atmosphere, where the RH is higher (50 % vs. 3 %), the ambient aerosols are less acidic, and the organic aerosol masses are lower ( $\sim 10 \mu\text{g m}^{-3}$ ) than in the chamber experiments ( $\sim 50 \mu\text{g m}^{-3}$  after 3 h of irradiation). Experimental evidence in this study shows that the heterogeneous conversion still occurs at 50 % RH, but with less efficiency (Fig. 3). The water vapor abundance at 50 % RH, however, compensates for the production of the less substituted dihydrofuran, leading to an eventually higher yield of carboxylic acids (Sect. 4.4). If the conversion of  $\delta$ -hydroxycarbonyl to substituted dihydrofuran occurs efficiently in the atmosphere, this could be a source of carboxylic acid in the ambient aerosols. It has been suggested that the heterogeneous formation of substituted dihydrofuran is acid-catalyzed (Atkinson et al., 2008; Lim and Ziemann, 2009a, b, c). Aerosols generated in the chamber environment in the presence of  $NO_x$  are expected to be highly acidic due to the formation of  $HNO_3$ . In the atmosphere, where ambient particles are less acidic or even neu-

tralized, the heterogeneous conversion of  $\delta$ -hydroxycarbonyl to substituted dihydrofuran might be a minor process.

In summary, two impacts of substituted dihydrofuran chemistry on alkane SOA formation are expected. First, the SOA yield from the photooxidation of long-chain alkanes can be overpredicted without accounting for substituted dihydrofuran formation and removal pathways. Second, a substantial amount of carboxylic acid, ester, and tetrahydrofuran moieties can be produced, leading to higher O : C but much lower H : C ratios, and thus a higher oxidation state of alkane SOA in general. In this manner, the dihydrofuran chemistry can be considered as a “dehydration” channel in alkane SOA formation.

**Supplementary material related to this article is available online at <http://www.atmos-chem-phys.net/14/1733/2014/acp-14-1733-2014-supplement.pdf>.**

**Acknowledgements.** This work was supported by National Science Foundation grant AGS-1057183.

Edited by: A. Laskin

## References

- Aiken, A. C., DeCarlo, P. F., and Jimenez, J. L.: Elemental analysis of organic species with electron ionization high-resolution mass spectrometry, *Anal. Chem.*, 79, 8350–8358, doi:10.1021/ac071150w, 2007.
- Aiken, A. C., Decarlo, P. F., Kroll, J. H., Worsnop, D. R., Huffman, J. A., Docherty, K. S., Ulbrich, I. M., Mohr, C., Kimmel, J. R., Sueper, D., Sun, Y., Zhang, Q., Trimborn, A., Northway, M., Ziemann, P. J., Canagaratna, M. R., Onasch, T. B., Alfarra, M. R., Prevot, A. S. H., Dommen, J., Duplissy, J., Metzger, A., Baltensperger, U., and Jimenez, J. L.: O/C and OM/OC ratios of primary, secondary, and ambient organic aerosols with high-resolution time-of-flight aerosol mass spectrometry, *Environ. Sci. Technol.*, 42, 4478–4485, 2008.
- Alfarra, M. R., Coe, H., Allan, J. D., Bower, K. N., Boudries, H., Canagaratna, M. R., Jimenez, J. L., Jayne, J. T., Garforth, A. A., Li, S. M., and Worsnop, D. R.: Characterization of urban and rural organic particulate in the lower Fraser valley using two Aerodyne aerosol mass spectrometers, *Atmos. Environ.*, 38, 5745–5758, 2004.
- Arey, J., Aschmann, S. M., Kwok, E. S. C., and Atkinson, R.: Alkyl nitrate, hydroxyalkyl nitrate, and hydroxycarbonyl formation from the  $NO_x$ -air photooxidations of  $C_5$ – $C_8$  n-alkanes, *J. Phys. Chem. A*, 105, 1020–1027, 2001.
- Atkinson, R., Arey, J., and Aschmann, S. M.: Atmospheric chemistry of alkanes: Review and recent developments, *Atmos. Environ.*, 42, 5859–5871, 2008.
- Aumont, B., Valorso, R., Mouchel-Vallon, C., Camredon, M., Lee-Taylor, J., and Madronich, S.: Modeling SOA formation from the oxidation of intermediate volatility n-alkanes, *Atmos. Chem. Phys.*, 12, 7577–7589, doi:10.5194/acp-12-7577-2012, 2012.

- Aumont, B., Camredon, M., Mouchel-Vallon, C., La, S., Ouzebidour, F., Valorso, R., Lee-Taylor, J., and Madronich, S.: Modeling the influence of alkane molecular structure on secondary organic aerosol formation, *Faraday Discuss.*, 165, 1–16, 2013.
- Bloss, C., Wagner, V., Jenkin, M. E., Volkamer, R., Bloss, W. J., Lee, J. D., Heard, D. E., Wirtz, K., Martín-Reviejo, M., Rea, G., Wenger, J. C., and Pilling, M. J.: Development of a detailed chemical mechanism (MCMv3.1) for the atmospheric oxidation of aromatic hydrocarbons, *Atmos. Chem. Phys.*, 5, 641–664, doi:10.5194/acp-5-641-2005, 2005.
- Canagaratna, M. R., Jayne, J. T., Jimenez, J. L., Allan, J. D., Alfarra, M. R., Zhang, Q., Onasch, T. B., Drewnick, F., Coe, H., Middlebrook, A., Delia, A., Williams, L. R., Trimborn, A. M., Northway, M. J., DeCarlo, P. F., Kolb, C. E., Davidovits, P., and Worsnop, D. R.: Chemical and microphysical characterization of ambient aerosols with the Aerodyne aerosol mass spectrometer, *Mass Spectrom. Rev.*, 26, 185–222, 2007.
- Cappa, C. D., Zhang, X., Loza, C. L., Craven, J. S., Yee, L. D., and Seinfeld, J. H.: Application of the Statistical Oxidation Model (SOM) to Secondary Organic Aerosol formation from photooxidation of C12 alkanes, *Atmos. Chem. Phys.*, 13, 1591–1606, doi:10.5194/acp-13-1591-2013, 2013.
- Cavalli, F., Barnes, I., and Becker, K. H.: FTIR kinetic, product, and modeling study of the OH-initiated oxidation of 1-butanol in air, *Environ. Sci. Technol.*, 36, 1263–1270, 2000.
- Chhabra, P. S., Ng, N. L., Canagaratna, M. R., Corrigan, A. L., Russell, L. M., Worsnop, D. R., Flagan, R. C., and Seinfeld, J. H.: Elemental composition and oxidation of chamber organic aerosol, *Atmos. Chem. Phys.*, 11, 8827–8845, doi:10.5194/acp-11-8827-2011, 2011.
- Craven, J. S., Yee, L. D., Ng, N. L., Canagaratna, M. R., Loza, C. L., Schilling, K. A., Yatavelli, R. L. N., Thornton, J. A., Ziemann, P. J., Flagan, R. C., and Seinfeld, J. H.: Analysis of secondary organic aerosol formation and aging using positive matrix factorization of high-resolution aerosol mass spectra: application to the dodecane low-NO<sub>x</sub> system, *Atmos. Chem. Phys.*, 12, 11795–11817, doi:10.5194/acp-12-11795-2012, 2012.
- Crounse, J. D., McKinney, K. A., Kwan, A. J., and Wennberg, P. O.: Measurement of gas-phase hydroperoxides by chemical ionization mass spectrometry, *Anal. Chem.*, 78, 6726–6732, 2006.
- DeCarlo, P. F., Kimmel, J. R., Trimborn, A., Northway, M. J., Jayne, J. T., Aiken, A. C., Gonin, M., Fuhrer, K., Horvath, T., Docherty, K. S., Worsnop, D. R., and Jimenez, J. L.: Field-deployable, high-resolution, time-of-flight aerosol mass spectrometer, *Anal. Chem.*, 78, 8281–8289, 2006.
- Fraser, M. P., Cass, G. R., Simoneit, B. R. T., Rasmussen, R. A.: Air quality model evaluation data for organics. 4. C<sub>2</sub>–C<sub>36</sub> non-aromatic hydrocarbons, *Environ. Sci. Technol.*, 31, 2356–2367, 1997.
- Gentner, D. R., Isaacman, G., Worton, D. R., Chan, A. W. H., Dallmann, T. R., Davis, L., Liu, S., Day, D. A., Russell, L. M., Wilson, K. R., Weber, R., Guha, A., Harley, R. A., and Goldstein, A. H.: Elucidating secondary organic aerosol from diesel and gasoline vehicles through detailed characterization of organic carbon emissions, *P. Natl. Acad. Sci. USA*, 109, 18318–18323, 2012.
- Gong, H. M., Matsunaga, A., and Ziemann, P. J.: Products and mechanism of secondary organic aerosol formation from reactions of linear alkenes with NO<sub>3</sub> radicals, *J. Phys. Chem. A*, 109, 4312–4324, 2005.
- Hoekman, S. K.: Speciated measurements and calculated reactivities of vehicle exhaust emissions from conventional and reformulated gasolines, *Environ. Sci. Technol.*, 26, 1206–1216, 1992.
- Holt, T., Atkinson, R., and Arey, J.: Effect of water vapor concentration on the conversion of a series of 1,4-dihydroxycarbonyls to dihydrofurans, *J. Photochem. Photobiol. A: Chem.*, 176, 231–237, 2005.
- Jathar, S. H., Miracolo, M. A., Tkacik, D. S., Donahue, N. M., Adams, P. J., and Robinson, A. L.: Secondary Organic Aerosol Formation from Photo-Oxidation of Unburned Fuel: Experimental Results and Implications for Aerosol Formation from Combustion Emissions, *Environ. Sci. Technol.*, 47, 12886–12893, 2013.
- Jenkin, M. E., Shallcross, D. E., Harvey, J. H.: Development and application of a possible mechanism for the generation of *cis*-pinic acid from the ozonolysis of  $\alpha$ - and  $\beta$ -pinene, *Atmos. Environ.*, 34, 2837–2850, 2000.
- Jenkin, M. E., Saunders, S. M., Wagner, V., and Pilling, M. J.: Protocol for the development of the Master Chemical Mechanism, MCM v3 (Part B): tropospheric degradation of aromatic volatile organic compounds, *Atmos. Chem. Phys.*, 3, 181–193, 2003, <http://www.atmos-chem-phys.net/3/181/2003/>.
- Jenkin, M. E.: Modelling the formation and composition of secondary organic aerosol from  $\alpha$ - and  $\beta$ -pinene ozonolysis using MCM v3, *Atmos. Chem. Phys.*, 4, 1741–1757, doi:10.5194/acp-4-1741-2004, 2004.
- Jordan, C. E., Ziemann, P. J., Griffin, R. J., Lim, Y. B., Atkinson, R., and Arey, J.: Modeling SOA formation from OH reactions with C<sub>8</sub>–C<sub>17</sub> n-alkanes, *Atmos. Environ.*, 42, 8015–8026, 2008.
- Isaacman, G., Chan, A. W. H., Nah, T., Worton, D. R., Ruehl, C. R., Wilson, K. R., and Goldstein, A. H.: Heterogeneous OH oxidation of motor oil particles causes selective depletion of branched and less cyclic hydrocarbons, *Environ. Sci. Technol.*, 46, 10632–10640, 2012.
- Kirchstetter, T. W., Singer, B. C., Harley, R. A., Kendall, G. R., and Traverse, M.: Impact of California reformulated gasoline on motor vehicle emissions. 1. Mass emission rates, *Environ. Sci. Technol.*, 33, 318–328, 1999.
- Kleinman, L. I., Springston, S. R., Daum, P. H., Lee, Y. N., Nunnermacker, L. J., Senum, G. I., Wang, J., Weinstein-Lloyd, J., Alexander, M. L., Hubbe, J., Ortega, J., Canagaratna, M. R., and Jayne, J.: The time evolution of aerosol composition over the Mexico City plateau, *Atmos. Chem. Phys.*, 8, 1559–1575, 2008, <http://www.atmos-chem-phys.net/8/1559/2008/Klotz>, B., Barnes, I., and Imamura, T.: Product study of the gas-phase reactions of O<sub>3</sub>, OH and NO<sub>3</sub> radicals with methyl vinyl ether, *Phys. Chem. Chem. Phys.*, 6, 1725–1734, 2004.
- Kroll, J. H., Smith, J. D., Che, D. L., Kessler, S. H., Worsnop, D. R., and Wilson, K. R.: Measurement of fragmentation and functionalization pathways in the heterogeneous oxidation of oxidized organic aerosol, *Phys. Chem. Chem. Phys.*, 11, 8005–8014, 2009.
- Kroll, J. H., Donahue, N. M., Jimenez, J. L., Kessler, S. H., Canagaratna, M. R., Wilson, K. R., Altieri, K. E., Mazzoleni, L. R., Wozniak, A. S., Bluhm, H., Mysak, E. R., Smith, J. D., Charles, E. K., and Worsnop, D. R.: Carbon oxidation state as a metric for describing the chemistry of atmospheric organic aerosol, *Nature Chem.*, 3, 133–139, 2011.

- Lambe, A. T., Onasch, T. B., Croasdale, D. R., Wright, J. P., Martin, A. T., Franklin, J. P., Massoli, P., Kroll, J. H., Canagaratna, M. R., Brune, W. H., Worsnop, D. R., and Davidovits, P.: Transitions from functionalization to fragmentation reactions of laboratory secondary organic aerosol (SOA) generated from the OH oxidation of alkanes precursors, *Environ. Sci. Technol.*, 46, 5430–5437, 2012.
- Lee, A. K. Y., Herckes, P., Leitch, W. R., Macdonald, A. M., and Abbatt, J. P. D.: Aqueous OH oxidation of ambient organic aerosol and cloud water organics: Formation of highly oxidized products, *Geophys. Res. Lett.*, 38, L11805, doi:10.1029/2011GL047439, 2011.
- Lim, Y. B. and Ziemann, P. J.: Products and mechanism of secondary organic aerosol formation from reactions of n-alkanes with OH radicals in the presence of NO<sub>x</sub>, *Environ. Sci. Technol.*, 39, 9229–9236, 2005.
- Lim, Y. B. and Ziemann, P. J.: Effects of molecular structure on aerosol yields from OH radical-initiated reactions of linear, branched, and cyclic alkanes in the presence of NO<sub>x</sub>, *Environ. Sci. Technol.*, 43, 2328–2334, 2009a.
- Lim, Y. B. and Ziemann, P. J.: Chemistry of secondary organic aerosol formation from OH radical-initiated reactions of linear, branched, and cyclic alkanes in the presence of NO<sub>x</sub>, *Aero. Sci. Technol.*, 43, 604–619, 2009b.
- Lim, Y. B. and Ziemann, P. J.: Kinetics of the heterogeneous conversion of 1,4-hydroxycarbonyls to cyclic hemiacetals and dihydrofurans on organic aerosol particles, *Phys. Chem. Chem. Phys.*, 11, 8029–8039, 2009c.
- Liu, S., Day, D. A., Shields, J. E., and Russell, L. M.: Ozone-driven daytime formation of secondary organic aerosol containing carboxylic acid groups and alkane groups, *Atmos. Chem. Phys.*, 11, 8321–8341, doi:10.5194/acp-11-8321-2011, 2011.
- Loza, C. L., Craven, J. S., Yee, L. D., Coggon, M. M., Schwantes, R. H., Shiraiwa, M., Zhang, X., Schilling, K. A., Ng, N. L., Canagaratna, M. R., Ziemann, P. J., Flagan, R. C., and Seinfeld, J. H.: Secondary organic aerosol yields of 12-carbon alkanes, *Atmos. Chem. Phys. Discuss.*, 13, 20677–20727, doi:10.5194/acpd-13-20677-2013, 2013.
- MathWorks, MATLAB, 2002.
- Martin, P., Tuazon, E. C., Aschmann, S. M., Arey, J., and Atkinson, R.: Formation and atmospheric reaction of 4,5-dihydro-2-methylfuran, *J. Phys. Chem. A*, 106, 11492–11501, 2002.
- Miracolo, M. A., Presto, A. A., Lambe, A. T., Hennigan, C. J., Donahue, N. M., Kroll, J. H., Worsnop, D. R., and Robinson, A. L.: Photooxidation of low-volatility organics found in motor vehicle emissions: production and chemical evolution of organic aerosol mass, *Environ. Sci. Technol.*, 44, 1638–1643, 2010.
- Miracolo, M. A., Hennigan, C. J., Ranjan, M., Nguyen, N. T., Gordon, T. D., Lipsky, E. M., Presto, A. A., Donahue, N. M., and Robinson, A. L.: Secondary aerosol formation from photochemical aging of aircraft exhaust in a smog chamber, *Atmos. Chem. Phys.*, 11, 4135–4147, doi:10.5194/acp-11-4135-2011, 2011.
- Ng, N. L., Canagaratna, M. R., Zhang, Q., Jimenez, J. L., Tian, J., Ulbrich, I. M., Kroll, J. H., Docherty, K. S., Chhabra, P. S., Bahreini, R., Murphy, S. M., Seinfeld, J. H., Hildebrandt, L., Donahue, N. M., DeCarlo, P. F., Lanz, V. A., Prévôt, A. S. H., Dinar, E., Rudich, Y., and Worsnop, D. R.: Organic aerosol components observed in Northern Hemispheric datasets from Aerosol Mass Spectrometry, *Atmos. Chem. Phys.*, 10, 4625–4641, doi:10.5194/acp-10-4625-2010, 2010.
- Ng, N. L., Canagaratna, M. R., Jimenez, J. L., Chhabra, P. S., Seinfeld, J. H., and Worsnop, D. R.: Changes in organic aerosol composition with aging inferred from aerosol mass spectra, *Atmos. Chem. Phys.*, 11, 6465–6474, doi:10.5194/acp-11-6465-2011, 2011.
- Pankow, J. F. and Asher, W. E.: SIMPOL.1: a simple group contribution method for predicting vapor pressures and enthalpies of vaporization of multifunctional organic compounds, *Atmos. Chem. Phys.*, 8, 2773–2796, doi:10.5194/acp-8-2773-2008, 2008.
- Paulot, F., Crounse, J. D., Kjaergaard, H. G., Kurten, A., St. Clair, J. M., Seinfeld, J. H., and Wennberg, P. O.: Unexpected epoxide formation in the gas-phase photooxidation of isoprene, *Science*, 325, 730–733, 2009.
- Presto, A. A., Miracolo, M. A., Kroll, J. H., Worsnop, D. R., Robinson, A. L., and Donahue, N. M.: Intermediate-volatility organic compounds: a potential source of ambient oxidized organic aerosol, *Environ. Sci. Technol.*, 43, 4744–4749, 2009.
- Presto, A. A., Miracolo, M. A., Donahue, N. M., and Robinson, A. L.: Secondary organic aerosol formation from high-NO<sub>x</sub> photooxidation of low volatility precursors: n-alkanes, *Environ. Sci. Technol.*, 44, 2029–2034, 2010.
- Reisen, F., Aschmann, S. M., Atkinson, R., and Arey, J.: 1, 4-Hydroxycarbonyl products of the OH radical initiated reactions of C<sub>5</sub>–C<sub>8</sub> n-alkanes in the presence of NO, *Environ. Sci. Technol.*, 39, 4447–4453, 2005.
- Robinson, A. L., Donahue, N. M., Shrivastava, M. K., Weitkamp, E. A., Sage, A. M., Grieshop, A. P., Lane, T. E., Pierce, J. R., and Pandis, S. N.: Rethinking organic aerosols: semivolatile emissions and photochemical aging, *Science*, 315, 1259–1262, 2007.
- Russell, L. M., Bahadur, R., and Ziemann, P. J.: Identifying organic aerosol sources by comparing functional group composition in chamber and atmospheric particles, *Proc. Natl. Acad. Sci.*, 108, 3516–3521, 2011.
- Sadezky, A., Chaimbault, P., Mellouki, A., Römpf, A., Winterhalter, R., Le Bras, G., and Moortgat, G. K.: Formation of secondary organic aerosol and oligomers from the ozonolysis of enol ethers, *Atmos. Chem. Phys.*, 6, 5009–5024, doi:10.5194/acp-6-5009-2006, 2006.
- Sander, S. P., Abbatt, J., Barker, J. R., Burkholder, J. B., Friedl, R. R., Golden, D. M., Huie, R. E., Kolb, C. E., J., K. M., Moortgat, G. K., Orkin, V. L., and Wine, P. H.: Chemical kinetics and photochemical data for use in atmospheric studies, Evaluation No. 17. JPL Publication 10-6, Jet Propulsion Laboratory, Pasadena, <http://jpldataeval.jpl.nasa.gov>, 2011.
- Saunders, S. M., Jenkin, M. E., Derwent, R. G., and Pilling, M. J.: Protocol for the development of the Master Chemical Mechanism, MCM v3 (Part A): tropospheric degradation of non-aromatic volatile organic compounds, *Atmos. Chem. Phys.*, 3, 161–180, doi:10.5194/acp-3-161-2003, 2003.
- Schauer, J. J., Kleeman, M. J., Gass, G. R., and Simoneit, B. R. T.: Measurement of emissions from air pollution sources. 2. C<sub>1</sub> through C<sub>30</sub> organic compounds from medium duty diesel trucks, *Environ. Sci. Technol.*, 33, 1578–1587, 1999.
- Schauer, J. J., Kleeman, M. J., Gass, G. R., and Simoneit, B. R. T.: Measurement of emissions from air pollution sources. 5. C<sub>1</sub>–

- C<sub>32</sub> organic compounds from gasoline-powered motor vehicles, *Environ. Sci. Technol.*, 33, 1578–1587, 1999.
- St. Clair, J. M., McCabe, D. C., Crounse, J. D., Steiner, U., and Wennberg, P. O.: Chemical ionization tandem mass spectrometer for the in situ measurement of methyl hydrogen peroxide, *Rev. Sci. Instrum.*, 81, 094102, doi:10.1063/1.3480552, 2010.
- Thiault, G., Thévenet, R., Mellouki, A., and Le Bras, G.: OH and O<sub>3</sub> initiated oxidation of ethyl vinyl ether, *Phys. Chem. Chem. Phys.*, 4, 613–619, 2002.
- Tkacik, D. S., Presto, A. A., Donahue, N. M., Robinson, A. M.: Secondary organic aerosol formation from intermediate-volatility organic compounds: cyclic, linear, and branched alkanes, *Environ. Sci., Technol.*, 46, 8773–8781, 2012.
- Yee, L. D., Craven, J. S., Loza, C. L., Schilling, K. A., Ng, N. L., Canagaratna, M. R., Ziemann, P. J., Flagan, R. C., and Seinfeld, J. H.: Secondary organic aerosol formation from Low-NO<sub>x</sub> photooxidation of dodecane: evolution of multi-generation gas-phase chemistry and aerosol composition, *J. Phys. Chem. A*, 116, 6211–6230, 2012.
- Zhang, X. and Seinfeld, J. H.: A functional group oxidation model (FGOM) for SOA formation and aging, *Atmos. Chem. Phys.*, 13, 5907–5926, doi:10.5194/acp-13-5907-2013, 2013.
- Zielinska, B., Sagebiel, J. C., Harshfield, G., Gertler, A. W., Pierson, W. R.: Volatile organic compounds up to C<sub>20</sub> emitted from motor vehicles, measurement methods, *Atmos. Environ.*, 30, 2269–2286, 1996.
- Ziemann, P. J. and Atkinson, R.: Kinetics, products, and mechanisms of secondary organic aerosol formation, *Chem. Soc. Rev.*, 41, 6582–6605, 2012.



**Supplementary Materials**  
**for**  
**Role of ozone in SOA formation from**  
**alkane photooxidation**

X. Zhang<sup>1</sup>, R. H. Schwantes<sup>1</sup>, M. M. Coggon<sup>2</sup>, C. C. Loza<sup>2</sup>, K. A. Schilling<sup>2</sup>,  
R. C. Flagan<sup>1,2</sup>, and J. H. Seinfeld<sup>1,2</sup>

<sup>1</sup> Division of Engineering and Applied Science, California Institute of Technology, Pasadena, CA, USA

<sup>2</sup> Division of Chemistry and Chemical Engineering, California Institute of Technology, Pasadena, CA, USA

*Correspondence to:* J. H. Seinfeld (seinfeld@caltech.edu)

## 1. Particle wall loss corrections

Two limiting assumptions can be made for the interactions between particles on the wall and suspended vapor: 1) particles deposited on the wall are assumed to interact with the suspended vapors as if they had remained suspended and 2) particles deposited on the wall are assumed to cease interaction with the suspended vapors. The first assumption gives the upper bound limit on SOA mass concentration. To invoke this assumption, one applies the time-dependent organic to sulfate ratio measured by AMS to the seed volume concentration measured by DMA. We do not usually use this assumption considering the fact that the presence of organics enhances the collection efficiency of sulfates in AMS. The second assumption is applied in the present study. In this case, particles deposited on the wall remain the same size and do not undergo continued organic growth. In order to calculate the total particle mass lost on the wall as a function of time, the size-dependent particle wall loss rate parameter ( $\beta$ ) needs to be determined. Wall loss calibration experiments were carried out by atomizing 1.0 M and 0.015 M ammonium sulfate solution ( $(\text{NH}_4)_2\text{SO}_4$ ) into the chamber and monitoring the decay of particle number distribution using a DMA. The size dependent wall loss rate parameter ( $\beta$ ) can be obtained by fitting equation S1 to the data for pure wall loss:

$$n_{i,s} = n_{i,0} \times \exp(-\beta t) \quad (\text{Equ S1})$$

where  $n_{i,s}$  is the suspended particle number distribution in size bin  $i$  at time  $t$ , and  $n_{i,0}$  is the initial particle number distribution in size bin  $i$ . The  $\beta$  values so derived were then applied to the  $\text{C}_{12}$  alkane chamber experiments. For each size bin  $i$  at each time step  $j$ , particle number distribution deposited to the wall ( $n_{w,i,j}$ ) is calculated as:

$$n_{w,i,j} = n_{s,i,j} \times [1 - \exp(-\beta \Delta t)] \quad (\text{Equ S2})$$

where  $n_{s,i,j}$  is the suspended particle number distribution in size bin  $i$  at time step  $j$ , and  $\Delta t$  is the difference between time step  $j$  and time step  $j + 1$ . The deposited particle size distribution ( $n_{w,i,j}$ ) is added to the suspended particle size distribution ( $n_{s,i,j}$ ) to give the total particle distribution ( $n_{tot,i,j}$ ):

$$n_{tot,i,j} = n_{w,i,j} + n_{s,i,j} \quad (\text{Equ S3})$$

The total number concentration in size bin  $i$  at time step  $j$  ( $N_{tot,i,j}$ ) can be calculated by converting the size distribution based on  $d(\ln D_p)$  to  $d(D_p)$ :

$$N_{tot,i,j} = n_{tot,i,j} / D_{p,i} \ln 10 \times (D_{p,i+} - D_{p,i-}) \quad (\text{Equ S4})$$

where  $D_{p,i}$  is the median particle diameter for size bin  $i$ ,  $D_{p,i+}$  is the upper limit of particle diameter for size bin  $i$ , and  $D_{p,i-}$  is the lower limit of particle diameter for size bin  $i$ . Assuming spherical particles, the total volume concentration at time step  $j$  ( $V_{tot,j}$ ) is:

$$V_{tot,j} = \sum_i^m \frac{\pi}{6} D_{p,i}^3 \times N_{tot,i,j} \quad (\text{Equ S5})$$

The total organic mass growth ( $\Delta M_{o,j}$ ) at time step  $j$  is:

$$\Delta M_{o,j} = \rho (V_{tot,j} - V_{seed}) \quad (\text{Equ S6})$$

where  $\rho$ , the density for a specific  $C_{12}$  alkane SOA under high- or low-  $NO_x$  conditions, is obtained from seed free nucleation experiments.

## 2. HR-ToF-AMS data processing protocols

All AMS data were processed with “Squirrel”, the ToF-AMS Unit Resolution Analysis Toolkit (<http://cires.colorado.edu/jimenez-group/ToFAMSResources/ToFSoftware/index.html>), in Igor Pro Version 6.22A (Wavemetrics, Lake Oswego, OR). The ToF-AMS High Resolution Analysis software tool PIKA (Peak Integration by Key Analysis) was employed for high-resolution analysis (Decarlo et al., 2006). The interference of chamber air on the particulate spectrum was corrected by adjusting parameters in the fragmentation table based on the “filter run” (AMS is collecting chamber air with a particle filter in-line) before each alkane photooxidation experiment (Chhabra et al., 2010; Craven et al., 2012). Briefly, the ion  $CO_2^+$  signal from ambient  $CO_2$ , which is estimated to be 370 ppm in the chamber, is removed to determine the organic contribution of  $CO_2^+$  to  $m/z$  44. The ion  $CO^+$  ( $m/z$  28), which is considered to be a common fragment of organic species, can be overwhelmed by ion  $N_2^+$  signal derived from ambient  $N_2$ . In this study, we used the particle-phase ratio of  $CO^+/CO_2^+$  to be unity as the default value to calculate the contribution of  $CO^+$  to the total organic signal. We also checked W-mode, which has higher resolution than V-mode, to separate the  $CO^+$  signal from  $N_2^+$  signal. The  $C_2H_4^+$  ion signal was removed because of its interference with the  $N_2^+$  signal. The signals from  $H_2O^+$ ,  $OH^+$ , and  $O^+$  can be biased by water from both gas and particle phase. We use fragmentation table parameters in Aiken et al. (2008) to estimate the organic contributions ( $H_2O^+ = 22.5\%$ ,  $OH^+ = 5.625\%$ , and  $O^+ = 0.9\%$ ).

Table S1. O<sub>x</sub>, NO<sub>x</sub>, and HO<sub>x</sub> reactions incorporated in the photochemical model

| Reaction | Reactants                                 | Products   | Rate Constants (cm <sup>3</sup> molec <sup>-1</sup> s <sup>-1</sup> ) | References |
|----------|---|--|---|------------|
| 1        | NO <sub>2</sub> + <i>hν</i>               | NO + O   | See Table S3  | a          |
| 2        | O + O <sub>2</sub> + M                    | O <sub>3</sub> + M                                 | See Table S2  | a          |
| 3        | O <sub>3</sub> + NO                       | NO <sub>2</sub> + O <sub>2</sub>                   | 3.0E-12 × EXP (-1500/TEMP)  | a          |
| 4        | O <sub>3</sub> + NO <sub>2</sub>          | NO <sub>3</sub> + O <sub>2</sub>                   | 1.2E-13 × EXP (-2450/TEMP)  | a          |
| 5        | NO <sub>3</sub> + <i>hν</i>               | NO <sub>2</sub> + O                                | See Table S3  | a          |
| 6        | NO <sub>3</sub> + <i>hν</i>               | NO + O <sub>2</sub>                                | See Table S3  | a          |
| 7        | NO + NO <sub>3</sub>                      | 2NO <sub>2</sub>                                   | 1.5E-11 × EXP (170/TEMP)  | a          |
| 8        | NO <sub>2</sub> + NO <sub>3</sub>         | NO + NO <sub>2</sub> + O <sub>2</sub>              | 4.5E-14 × EXP (-1258/TEMP)  | a          |
| 9        | NO <sub>2</sub> + NO <sub>3</sub> + M     | N <sub>2</sub> O <sub>5</sub> + M                  | See Table S2  | a          |
| 10       | N <sub>2</sub> O <sub>5</sub>             | NO <sub>2</sub> + NO <sub>3</sub>                  | See notes <sup>b</sup>  | a          |
| 11       | N <sub>2</sub> O <sub>5</sub> + <i>hν</i> | NO <sub>2</sub> + NO <sub>3</sub>                  | See Table S3  | a          |
| 12       | O <sub>3</sub> + <i>hν</i>                | O + O <sub>2</sub>                                 | See Table S3  | a          |
| 13       | O <sub>3</sub> + <i>hν</i>                | O( <sup>1</sup> D) + O <sub>2</sub>                | See Table S3  | a          |
| 14       | O( <sup>1</sup> D) + N <sub>2</sub>       | O + N <sub>2</sub>                                 | 2.2E-11 × EXP (110/TEMP)  | a          |
| 15       | O( <sup>1</sup> D) + O <sub>2</sub>       | O + O <sub>2</sub>                                 | 3.3E-11 × EXP (55/TEMP)   | a          |
| 16       | O( <sup>1</sup> D) + H <sub>2</sub> O     | 2 OH   | 1.6E-10 × EXP (60/TEMP)   | a          |
| 17       | O + O <sub>3</sub>                        | 2 O <sub>2</sub>                                   | 8.0E-12 × EXP (-2060/TEMP)  | a          |
| 18       | O + NO + M                                | NO <sub>2</sub> + M                                | See Table S2  | a          |
| 19       | O + NO <sub>2</sub>                       | NO + O <sub>2</sub>                                | 5.6E-12 × EXP (180/TEMP)  | a          |
| 20       | O + NO <sub>2</sub> + M                   | NO <sub>3</sub> + M                                | See Table S2  | a          |
| 21       | O + NO <sub>3</sub>                       | NO <sub>2</sub> + O <sub>2</sub>                   | 1.0E-11   | a          |
| 22       | HO <sub>2</sub> + HO <sub>2</sub>         | H <sub>2</sub> O <sub>2</sub> + O <sub>2</sub>     | 3.0E-13 × EXP (460/TEMP)  | a          |
| 23       | HO <sub>2</sub> + HO <sub>2</sub> + M     | H <sub>2</sub> O <sub>2</sub> + O <sub>2</sub> + M | 2.1E-33 × EXP (920/TEMP) × [M]  | a          |
| 24       | H <sub>2</sub> O <sub>2</sub> + <i>hν</i> | 2OH  | See Table S3  | a          |
| 25       | HO <sub>2</sub> + O <sub>3</sub>          | OH + 2O <sub>2</sub>                               | 1.0E-14 × EXP (-490/TEMP)   | a          |
| 26       | HO <sub>2</sub> + NO                      | OH + NO <sub>2</sub>                               | 3.3E-12 × EXP (270/TEMP)  | a          |
| 27       | OH + OH + M                               | H <sub>2</sub> O <sub>2</sub> + M                  | See Table S2  | a          |
| 28       | OH + OH                                   | O + H <sub>2</sub> O                               | 1.8E-12   | a          |
| 29       | OH + HO <sub>2</sub>                      | H <sub>2</sub> O + O <sub>2</sub>                  | 4.8E-11 × EXP (250/TEMP)  | a          |
| 30       | OH + O <sub>3</sub>                       | HO <sub>2</sub> + O <sub>2</sub>                   | 1.7E-12 × EXP (-940/TEMP)   | a          |
| 31       | OH + NO + M                               | HONO + M   | See Table S2  | a          |
| 32       | OH + NO <sub>2</sub> + M                  | HNO <sub>3</sub> + M                               | See Table S2  | a          |
| 33       | HONO + <i>hν</i>                          | OH + NO  | See Table S3  | a          |

|    |                                       |   |                            |   |
|----|---------------------------------------|---|----------------------------|---|
| 34 | OH + HONO                             | NO <sub>2</sub> + H <sub>2</sub> O                  | 1.8E-11 × EXP (-390/TEMP)  | a |
| 35 | OH + HNO <sub>3</sub>                 | NO <sub>3</sub> + H <sub>2</sub> O                  | See Notes <sup>c</sup>     | a |
| 36 | OH + H <sub>2</sub> O <sub>2</sub>    | HO <sub>2</sub> + H <sub>2</sub> O                  | 2.9E-11 × EXP (-161/TEMP)  | a |
| 37 | OH + NO <sub>3</sub>                  | HO <sub>2</sub> + NO <sub>2</sub>                   | 2.2E-11                    | a |
| 38 | HO <sub>2</sub> + NO <sub>3</sub>     | OH + NO <sub>2</sub> + O <sub>2</sub>               | 3.5E-12                    | a |
| 39 | HO <sub>2</sub> + NO <sub>2</sub> + M | HNO <sub>4</sub> + M                                | See Table S2               | a |
| 40 | HNO <sub>4</sub>                      | HO <sub>2</sub> + NO <sub>2</sub>                   | See Notes <sup>d</sup>     | a |
| 41 | HNO <sub>4</sub> + OH                 | NO <sub>2</sub> + H <sub>2</sub> O + O <sub>2</sub> | 1.3E-12 × EXP (380/TEMP)   | a |
| 42 | NO <sub>3</sub> + NO <sub>3</sub>     | 2NO <sub>2</sub> + O <sub>2</sub>                   | 8.5E-13 × EXP (-2450/TEMP) | a |

<sup>a</sup> Sander, S. P., Abbatt, J., Barker, J. R., Burkholder, J. B., Friedl, R. R., Golden, D. M., Huie, R. E., Kolb, C. E., J., K. M., Moortgat, G. K., Orkin, V. L., and Wine, P. H.: Chemical kinetics and photochemical data for use in atmospheric studies, Evaluation No. 17. JPL Publication 10-6, Jet Propulsion Laboratory, Pasadena, <http://jpldataeval.jpl.nasa.gov>, 2011.

<sup>b</sup> For Reaction No. 10, the reaction rate constant  $k_{R10} = k_{R9} / K_{eq}$ , where  $K_{eq} = 2.7E-27 \times EXP (11000/TEMP)$ .

<sup>c</sup> For Reaction No. 35, the reaction rate constant  $k_{R35} = k_1 + k_3 \times M / (1 + k_3/k_2 \times M)$ , where  $k_1 = 2.4E-14 \times EXP (460/TEMP)$ ;  $k_2 = 2.7E-17 \times EXP (2199/TEMP)$ ; and  $k_3 = 6.5E-34 \times EXP (1335/TEMP)$ .

<sup>d</sup> For Reaction No. 40, the reaction rate constant  $k_{R40} = k_{R39} / K_{eq}$ , where  $K_{eq} = 2.1E-27 \times EXP (10900/TEMP)$ .

Table S2. Termolecular reaction rate constant calculations

| Reaction                                 | $k_0^{300}$ | n   | $k_{inf}^{300}$ | m   | F   |
|--|-------------|-----|-----------------|-----|-----|
| $O + O_2 + M \rightarrow O_3 + M$        | 6.0E-34     | 2.3 | —               | —   | 0.6 |
| $NO_2 + NO_3 + M \rightarrow N_2O_5 + M$ | 2.0E-30     | 4.4 | 1.4E-12         | 0.7 | 0.6 |
| $O + NO + M \rightarrow NO_2 + M$        | 9.0E-31     | 1.5 | 3.0E-11         | 0.0 | 0.6 |
| $O + NO_2 + M \rightarrow NO_3 + M$      | 2.5E-31     | 1.8 | 2.2E-11         | 0.7 | 0.6 |
| $OH + OH + M \rightarrow H_2O_2 + M$     | 6.9E-31     | 1.0 | 2.6E-11         | 0.0 | 0.6 |
| $OH + NO + M \rightarrow HONO + M$       | 7.0E-31     | 2.6 | 3.6E-11         | 0.1 | 0.6 |
| $OH + NO_2 + M \rightarrow HNO_3 + M$    | 2.0E-30     | 3.0 | 2.5E-11         | 0.0 | 0.6 |
| $HO_2 + NO_2 + M \rightarrow HNO_4 + M$  | 2.0E-31     | 3.4 | 2.9E-12         | 1.1 | 0.6 |

Reaction rate constants are given in the form

$$k_0(T) = k_0^{300} \left( \frac{T}{300} \right)^{-n} \text{ cm}^6 \text{ molecules}^{-2} \text{ s}^{-1}$$

$$k_\infty(T) = k_\infty^{300} \left( \frac{T}{300} \right)^{-m} \text{ cm}^3 \text{ molecules}^{-1} \text{ s}^{-1}$$

To obtain the effective second-order rate constant at a given temperature and pressure (altitude z) the following formula is used:

$$k(T, z) = \left\{ \frac{k_0(T)[M]}{1 + (k_0(T)[M]/k_\infty(T))} \right\} F^{\{1 + [\log_{10}(k_0(T)[M]/k_\infty(T))]^2\}^{-1}}$$

Table S3. Photolysis rate constants in Caltech Environmental Chamber

| Photolysis Reactions                    | Value of $j$ ( $s^{-1}$ ) <sup>a</sup> |
|---|--|
| $NO_2 + h\nu \rightarrow NO + O$        | 4.629E-3                               |
| $NO_3 + h\nu \rightarrow NO_2 + O$      | 2.109E-3                               |
| $NO_3 + h\nu \rightarrow NO + O_2$      | 3.863E-5                               |
| $N_2O_5 + h\nu \rightarrow NO_2 + NO_3$ | 2.286E-5                               |
| $O_3 + h\nu \rightarrow O + O_2$        | 7.102E-6                               |
| $O_3 + h\nu \rightarrow O(^1D) + O_2$   | 5.078E-6                               |
| $H_2O_2 + h\nu \rightarrow 2OH$         | 4.660E-6                               |
| $HONO + h\nu \rightarrow OH + NO$       | 1.130E-3                               |

<sup>a</sup> Photolysis rate constants are calculated using the irradiance spectrum measured for the chamber UV lights and absorption cross section values and quantum yields from Sander et al. (2011).